frontiers | Research Topics

Applications of gravity anomalies in geophysics

Edited by
Henglei Zhang, Meixia Geng, Victor Sacek and Filippo Greco

Coordinated by
Pengfei Liu

Published in
Frontiers in Earth Science

ISSN 1664-8714
ISBN 978-2-8325-4355-9
DOI 10.3389/978-2-8325-4355-9

About Frontiers

Frontiers is more than just an open access publisher of scholarly articles: it is a pioneering approach to the world of academia, radically improving the way scholarly research is managed. The grand vision of Frontiers is a world where all people have an equal opportunity to seek, share and generate knowledge. Frontiers provides immediate and permanent online open access to all its publications, but this alone is not enough to realize our grand goals.

Frontiers journal series

The Frontiers journal series is a multi-tier and interdisciplinary set of open-access, online journals, promising a paradigm shift from the current review, selection and dissemination processes in academic publishing. All Frontiers journals are driven by researchers for researchers; therefore, they constitute a service to the scholarly community. At the same time, the *Frontiers journal series* operates on a revolutionary invention, the tiered publishing system, initially addressing specific communities of scholars, and gradually climbing up to broader public understanding, thus serving the interests of the lay society, too.

Dedication to quality

Each Frontiers article is a landmark of the highest quality, thanks to genuinely collaborative interactions between authors and review editors, who include some of the world's best academicians. Research must be certified by peers before entering a stream of knowledge that may eventually reach the public - and shape society; therefore, Frontiers only applies the most rigorous and unbiased reviews. Frontiers revolutionizes research publishing by freely delivering the most outstanding research, evaluated with no bias from both the academic and social point of view. By applying the most advanced information technologies, Frontiers is catapulting scholarly publishing into a new generation.

What are Frontiers Research Topics?

Frontiers Research Topics are very popular trademarks of the *Frontiers journals series*: they are collections of at least ten articles, all centered on a particular subject. With their unique mix of varied contributions from Original Research to Review Articles, Frontiers Research Topics unify the most influential researchers, the latest key findings and historical advances in a hot research area.

Find out more on how to host your own Frontiers Research Topic or contribute to one as an author by contacting the Frontiers editorial office: frontiersin.org/about/contact

Applications of gravity anomalies in geophysics

Topic editors

Henglei Zhang — China University of Geosciences, China
Meixia Geng — Khalifa University, United Arab Emirates
Victor Sacek — University of São Paulo, Brazil
Filippo Greco — National Institute of Geophysics and Volcanology (INGV), Italy

Topic Coordinator

Pengfei Liu — Macau University of Science and Technology, SAR China

Citation

Zhang, H., Geng, M., Sacek, V., Greco, F., Liu, P., eds. (2024). *Applications of gravity anomalies in geophysics*. Lausanne: Frontiers Media SA.
doi: 10.3389/978-2-8325-4355-9

Table of contents

frontiers | Frontiers in Earth Science

TYPE Editorial
PUBLISHED 12 January 2024
DOI 10.3389/feart.2024.1349161

OPEN ACCESS

EDITED AND REVIEWED BY
Jeroen van Hunen,
Durham University, United Kingdom

*CORRESPONDENCE
Henglei Zhang,
h.l.zhang@cug.edu.cn

RECEIVED 04 December 2023
ACCEPTED 02 January 2024
PUBLISHED 12 January 2024

CITATION
Zhang H, Greco F, Sacek V, Geng M and Liu P (2024), Editorial: Applications of gravity anomalies in geophysics.
Front. Earth Sci. 12:1349161.
doi: 10.3389/feart.2024.1349161

Editorial: Applications of gravity anomalies in geophysics

Henglei Zhang[1]*, Filippo Greco[2], Victor Sacek[3], Meixia Geng[4] and Pengfei Liu[5]

[1]School of Geophysics and Geomatics, China University of Geosciences, Wuhan, China, [2]National Institute of Geophysics and Volcanology (INGV), Roma, Italy, [3]Institute of Astronomy, Geophysics and Atmospheric Sciences, University of São Paulo, São Paulo, Brazil, [4]Technology Innovation Institute, Abu Dhabi, United Arab Emirates, [5]State Key Laboratory of Lunar and Planetary Sciences, Macau University of Science and Technology, Macao, Macao SAR, China

KEYWORDS

gravity anomalies, Moho inversion, time-varying gravity, lineaments, subsurface structure

Editorial on the Research Topic
Applications of gravity anomalies in geophysics

With the progress of cheap, lightweight, and efficient gravimeters (Carbone et al., 2020; Stray et al., 2022; Kim and Choi, 2023), gravity anomalies are expected to receive wider attention in the future, opening up new perspectives for increasing the capability of gravimetry to Earth sciences. Since the knowledge of the crustal density of a planet is important in determining its interior structure, gravity anomaly is widely used in Solid Earth and exploration geophysics, and also extended to the moon and Mars. In addition to the routine applications focusing on the crustal density structure, contributing to the characterization and definition of underground structures at various scales, time-varying gravity, microgravity survey, and gravity admittance are widely applied in order to supply unique information on the dynamics of underground processes. The goal of this Research Topic is to highlight the various extracted information from gravity anomalies in applications, toward an understanding of choosing appropriate methods dealing with gravity anomalies in varying study cases.

There are ten accepted papers on this Research Topic focusing on the following four research questions.

The first question is about the equivalent-layer technique (Oliveira Junior et al.) which present a comprehensive review of the computation aspects concerning the equivalent-layer technique. The equivalent-layer technique is used widely in processing gravity and magnetic anomalies, e.g., the downward continuation and the reduction to the pole at low latitudes. While such method is very inefficient for dealing with massive data sets, lots of computationally efficient methods have been proposed to reduce its computational cost. The authors from Observatório Nacional and Universidade do Estado do Rio de Janeiro (Brazil) present a comprehensive review of diverse strategies to solve the linear system of the equivalent layer in which the advantages and disadvantages for the existing strategies are described in detail.

The second question is about the time-varying gravity (Zhu et al.) which is used in monitoring the subsurface mass variation. Zhu et al., from China Earthquake Administration, have conducted numerous applications focusing on the time-varying gravity in earthquake research in the Chinese Mainland. The gravity changes before

and after the earthquakes were found in several earthquakes, and thus the high-precision mobile gravity observations used to survey the gravity changes possibly induced by the earthquake had attracted people's attention. Reports show that the gravity observation network in the Chinese Mainland made a relatively successful medium-term prediction for a series of earthquakes since 2008 after the serious Wenchuan *Ms*8.0 earthquake. Zhu et al. introduce some case studies and progress using the time-varying gravity in earthquake monitoring in the Chinese Mainland which put forward the gravity applications in earthquake prediction. The time-varying gravity is also applied widely in investigating the hydrological and volcano-tectonic processes controlling the present day activity of the volcano (Pivetta et al., 2023). The present studies show that the role of time-varying gravity in earthquake prediction would become increasingly significant with the progress of cheap, lightweight and efficient gravimeter. In addition to the high precision ground time-varying gravity, the time-varying gravity from satellites has played an extremely important role in hydrology, seismology, geodesy, and geophysics (Liu and Sun, 2023).

The third question is about mapping the structural lineaments (Ganguli and Pal; Sun et al.) which is used widely in geological mapping (Altinoğlu, 2023; Ashraf and Filina, 2023; Bayou et al., 2023; Ibrahim et al., 2023; Lghoul et al., 2023; Mnasri et al., 2023; Qadir et al., 2023). Such applications are based on the qualitative interpretation of gravity anomalies in which the edge detection filters are usually applied to enhance the lineament. Sun et al. propose a modified edge detection method based on the second order spectral moment to detect edges on potential field which can enhance the weak anomalies and eliminate the false edges caused by the associated anomalies. Ganguli and Pal applied second vertical derivative and tilt derivative on the potential field data to reveal very prominent NESW trending linear gravity high and low.

The fourth question is about the quantitative interpretation of gravity anomalies. Harash et al. and Liu et al. apply the gravity inversion to obtain the Moho topography. For the Moho inversion from gravity anomalies, the Parker–Oldenburg methods in Fourier domain are powerful tools (Zhang et al., 2020; Elmas and Karsl, 2021; Borghi, 2022). The other contributions in this Research Topic are focusing on the subsurface density structures modeling using gravity anomalies (Nigussie et al.; Nigussie et al.; Moura and Marangoni; Pánisová et al.). Modeling the crustal density is very useful to reveal its composition and structure, and hence it is also significantly related to the tectonic evolution and geodynamics in Earth, Moon and Mars (Affatato, 2023; Haas et al., 2023; Smith et al., 2023).

In addition to the above-mentioned research questions, the gravity anomalies have been widely used in estimation of the elastic thickness and have been extended from Earth to other planets where gravity data is available (Broquet and Wieczorek, 2019; Genova et al., 2023). Since the routine Pratt and Airy compensation modes require a lithosphere with an unrealistic and highly anisotropic mechanical behavior, the flexure model has been extensively used to interpret short-wavelength gravity anomalies due to variations in crustal thickness. The parameter that characterizes the apparent strength of the lithosphere is the effective elastic thickness (Te) of the lithosphere, and thus the estimation of Te value is important to measure of the integrated strength of the lithosphere which can be compared from region to region and interpreted in terms of the thermal and mechanical structure of the continental lithosphere. Gravity/topography admittance is first proposed to estimate Te, and the related improvements on Te estimation are becoming the focus of attention.

We hope this Research Topic would provide a helpful source of references for those working in gravity anomalies.

Author contributions

HZ: Writing–original draft, Writing–review and editing. VS: Writing–review and editing. MG: Writing–review and editing. PL: Writing–review and editing.

Funding

The authors declare financial support was received for the research, authorship, and/or publication of this article. This work was in part financially supported by National Key R&D Program of China (2022YFC3104000).

Acknowledgments

HZ thanks Prof. Dhananjay Ravat from University of Kentucky for his kindly suggestions in this Research Topic. Many thanks go to Dr. Xiaofei Ma graduated from Utah State University for his helps in polishing the English texts. The Guest Editors of this SI are grateful to all authors who contributed to this volume sharing their results with the scientific community.

Conflict of interest

The authors declare that the research was conducted in the absence of any commercial or financial relationships that could be construed as a potential conflict of interest.

Publisher's note

References

Affatato, V. (2023). *Interpretation of gravitational data from past martian missions*.

Altinoğlu, F. F. (2023). Mapping of the structural lineaments and sedimentary basement relief using gravity data to guide mineral exploration in the denizli basin gravity data to guide mineral exploration in the denizli basin. *Minerals* 13 (10), 1276. doi:10.3390/min13101276

Ashraf, A., and Filina, I. (2023). Zones of weakness within the Juan de Fuca plate mapped from the integration of multiple geophysical data and their relation to observed seismicity. *Geochem. Geophys. Geosystems* 24 (10), e2023GC010943. doi:10.1029/2023gc010943

Bayou, Y., Abtout, A., Renaut, R. A., Bouyahiaoui, B., Maouche, S., Vatankhah, S., et al. (2023). The northeastern Algeria hydrothermal system: gravimetric data and structural implication. *Geotherm. Energy* 11 (1), 14–26. doi:10.1186/s40517-023-00258-2

Borghi, A. (2022). Moho depths for Antarctica Region by the inversion of ground-based gravity data. *Geophys. J. Int.* 231 (2), 1404–1420. doi:10.1093/gji/ggac249

Broquet, A., and Wieczorek, M. A. (2019). The gravitational signature of Martian volcanoes. *J. Geophys. Res. Planets* 124 (8), 2054–2086. doi:10.1029/2019je005959

Carbone, D., Antoni-Micollier, L., Hammond, G., de Zeeuw-van Dalfsen, E., Rivalta, E., Bonadonna, C., et al. (2020). The Newton-g gravity imager: toward new paradigms for terrain gravimetry. *Front. Earth Sci.* 8. doi:10.3389/feart.2020.573396

Elmas, A., and Karsl, H. (2021). Tectonic and crustal structure of Archangelsky ridge using Bouguer gravity data. *Mar. Geophys. Res.* 42 (3), 21. doi:10.1007/s11001-021-09443-z

Genova, A., Goossens, S., Del Vecchio, E., Petricca, F., Beuthe, M., Wieczorek, M., et al. (2023). Regional variations of Mercury's crustal density and porosity from MESSENGER gravity data. *Icarus* 391, 115332. doi:10.1016/j.icarus.2022.115332

Haas, P., Ebbing, J., and Szwillus, W. (2023). Cratonic crust illuminated by global gravity gradient inversion. *Gondwana Res.* 121, 276–292. doi:10.1016/j.gr.2023.04.012

Ibrahim, A., Gemail, K. S., Bedair, S., Saada, S. A., Koch, M., and Nosair, A. (2023). An integrated approach to unravel the structural controls on groundwater potentialities in hyper-arid regions using satellite and land-based geophysics: a case study in southwestern desert of Egypt. *Surv. Geophys.* 44 (3), 783–819. doi:10.1007/s10712-022-09755-8

Kim, G., and Choi, I. M. (2023). Development of SQUID detection technology for a superconducting gravimeter. *Rev. Sci. Instrum.* 94 (9), 094505. doi:10.1063/5.0163714

Lghoul, M., Abd-Elhamid, H. F., Zelenakova, M., Abdelrahman, K., Fnais, M. S., and Sbihi, K. (2023). Application of enhanced methods of gravity data analysis for mapping the subsurface structure of the Bahira basin in Morocco. *Front. Earth Sci.* 11, 1225714. doi:10.3389/feart.2023.1225714

Liu, C., and Sun, W. (2023). GRACE time-variable gravity and its application to geoscience: quantitative analysis of relevant literature. *Earth Planet. Phys.* 7 (2), 295–309. doi:10.26464/epp2023022

Mnasri, M., Amiri, A., Nasr, I. H., Belkhiria, W., and Inoubli, M. H. (2023). Integrated geophysical approach for ore exploration: case study of sidi bou aouane–khadhkhadha Pb–Zn province–northern Tunisia. *Geophys. Prospect.* 71 (9), 1772–1791. doi:10.1111/1365-2478.13338

Pivetta, T., Riccardi, U., Ricciardi, G., and Carlino, S. (2023). Hydrological and volcano-related gravity signals at Mt. Somma–Vesuvius from ~20 yr of time-lapse gravity monitoring: implications for volcano quiescence. *Geophys. J. Int.* 235 (2), 1565–1580. doi:10.1093/gji/ggad320

Qadir, H. O., Baban, E. N., Aziz, B. Q., and Koyi, H. A. (2023). Potential field survey of subsurface structures of the NW segment of the zagros fold-thrust belt, kurdistan region. *Geophys. Prospect.* 71 (8), 1673–1690. doi:10.1111/1365-2478.13401

Smith, D. E., Goossens, S., Neumann, G. A., and Zuber, M. T. (2023). Constraining the structure under lunar impact basins with gravity lunar impact basins with gravity. *Planet. Sci. J.* 4 (11), 204. doi:10.3847/psj/acfcac

Stray, B., Lamb, A., Kaushik, A., Vovrosh, J., Rodgers, A., Winch, J., et al. (2022). Quantum sensing for gravity cartography. *Nature* 602 (7898), 590–594. doi:10.1038/s41586-021-04315-3

Zhang, H. L., Ravat, D., and Lowry, A. (2020). Crustal composition and Moho variations of the central and eastern United States: improving resolution and geologic interpretation of EarthScope USArray seismic images using gravity. *J. Geophys. Res. Solid Earth* 125, e2019JB018537. doi:10.1029/2019jb018537

frontiers | Frontiers in Earth Science

TYPE Original Research
PUBLISHED 04 January 2023
DOI 10.3389/feart.2022.1092759

OPEN ACCESS

EDITED BY
Filippo Greco,
Istituto Nazionale di Geofisica e Vulcanologia (INGV), Italy

REVIEWED BY
Valerio Acocella,
Roma Tre University, Italy
Catherine A. Meriaux,
University of Rwanda, Rwanda

*CORRESPONDENCE
Wubamlak Nigussie,
wubmulnig12@gmail.com

SPECIALTY SECTION
This article was submitted to Solid Earth Geophysics, a section of the journal Frontiers in Earth Science

RECEIVED 08 November 2022
ACCEPTED 12 December 2022
PUBLISHED 04 January 2023

CITATION
Nigussie W, Mickus K, Keir D, Alemu A, Muhabaw Y, Muluneh AA, Yehualaw E and Demissie Z (2023), Subsurface structure of magmatic segments during continental breakup: Perspectives from a gravity data analysis along the Main Ethiopian Rift.
Front. Earth Sci. 10:1092759.
doi: 10.3389/feart.2022.1092759

Subsurface structure of magmatic segments during continental breakup: Perspectives from a gravity data analysis along the Main Ethiopian Rift

Wubamlak Nigussie[1]*, Kevin Mickus[2], Derek Keir[3,4], Abera Alemu[5], Yoseph Muhabaw[1], Ameha A. Muluneh[5,6], Esubalew Yehualaw[7] and Zelalem Demissie[8]

[1]School of Earth Sciences, Bahir Dar University, Bahir Dar, Ethiopia, [2]Department of Geosciences, Missouri State University, Springfield, MO, United States, [3]School of Ocean and Earth Science, University of Southampton, Southampton, United Kingdom, [4]Dipartimento di Scienze della Terra, Università degli Studi di Firenze, Firenze, Italy, [5]School of Earth Sciences, Addis Ababa University, Addis Ababa, Ethiopia, [6]Helmholtz Centre Potsdam, GFZ German Research Centre for Geosciences, Potsdam, Germany, [7]Department of Petroleum and Geothermal Energy, Ethiopian Ministry of Mines, Addis Ababa, Ethiopia, [8]Department of Geology, Wichita State University, Wichita, KS, United States

In magma-rich continental rifts, extension is commonly localized as dike injection in discrete magmatic segments which appear from surface geology to mimic the along-axis segmentation of ocean ridges. However, the subsurface morphology of these zones of localized magma injection is unclear, and whether and at what depth range they remain with discrete subvolcanic plumbing systems is not fully understood. In addition, the relationship between zones of magma injection and tectonic faulting is also debated. The Main Ethiopian Rift (MER) provides a unique opportunity to examine the spatial scale, locus, and subsurface geometries of magmatic localization in active continental rifts. We examined spatial variations in the structure of the crust in the MER using gravity data to better understand the subsurface pattern of magma injection. Results of our study reveal discrete Bouguer gravity highs in the centers of the distinct right-stepping magmatic segments of the MER (Aluto, Gedemsa, and Boseti), and interpreted as the locus of mafic intrusions. The gravity data show that the boundary between each magmatic segment is observed down to depths of ~20 km, suggesting that magmatic segments have discrete subvolcanic plumbing systems at least down to the mid-crust. Additionally, incorporating the fault network shows that the densest faulting occurs at the tips of the zones of densest magma injection shown by Bouguer gravity highs. This is similar to the axial segmentation observed at slow and ultra-slow spreading ridges and suggests strong along-axis variations in deformation mechanism, with magma injection accommodating extension at the segment centers and faulting dominating towards the segment ends. In addition, rift margin volcanic zones (Siltie Debrezeit, Yerer Tulu, and Galema) are also inferred from bandpass gravity

anomaly maps, supported by petrologic evidence, which implies that extension by dike injection has also occurred near the rift flanks.

KEYWORDS

magmatic segment, gravity anomaly, rift-margin magmatism, Main Ethiopian Rift, continental breakup

1 Introduction

During continental rifting, extension is generally thought to initiate on rift border faults in the brittle crust, and ductile stretching and thinning in the lower crust and mantle lithosphere (McKenzie 1978; Hayward and Ebinger, 1996). As extension increases through time, extension commonly focuses into the rift due to several processes such as strain softening, and lithosphere heating and thinning (Hayward and Ebinger, 1996; Corti, 2009). In magma-rich rifts, the within-rift strain localization can also occur by magma intrusion, with diking being an efficient and effective way of accommodating extension (Ebinger and Casey, 2001; Wright et al., 2016). The magma intrusion commonly localizes to ~50–100 km long, tens of kilometer-wide magmatic segments with surface volcanic and fault morphology that mimics the segments of mid-ocean ridges (Ebinger and Casey, 2001; Acocella, 2014). As such the magmatic segments in magma-rich continental rifts are potentially thought to persist through a continental breakup and define the along-axis segmentation of the subsequent ocean ridge (Ebinger and Casey, 2001). However, the subsurface manifestation of magmatic segments in continental rifts is poorly understood and therefore it remains debated how magmatism varies along rift and to what depth in the lithosphere they have discrete plumbing systems.

The East Africa Rift System (EARS) is the Earth's longest continental divergent plate boundary and forms the Afar triple junction together with the two ocean ridges in the Red Sea and Gulf of Aden (Ebinger, 2005). The northern end of this newly formed tectonic boundary, the Main Ethiopian Rift (MER), is an ideal natural laboratory to study the ongoing process of continental breakup in an advanced stage of evolution (Ebinger and Casey, 2001; Wolfenden, et al., 2004; Kurz et al., 2007). The rift is flanked by ~60 km-long, NE-striking Miocene age border faults that separate the rift floor from the adjacent plateaus (Corti, 2009). Geological records show that strain has subsequently shifted in the rift since the Quaternary and has been localized to a series of right stepping en echelon magmatic segments (Ebinger and Casey, 2001; Casey et al., 2006). The surface morphology of the magmatic segments is dominated by Quaternary to Recent volcanic centers, NNE aligned cone fields, lava flows, and cut by a dense network of small offset but active faults (Wonji Fault Belt) (Mohr, 1968; Ebinger and Casey, 2001; Corti, 2009). Furthermore, crustal seismic tomography shows that the magmatic segments are underlain by high seismic velocity crust (interpreted as mafic intrusion) in the upper crust (Keranen et al., 2004; Daly et al., 2008). Although the axial part of the MER is accepted to be the locus of strain in existing rift models (Ebinger and Casey, 2001; Wolfenden, et al., 2004; Casey et al., 2006; Kurz et al., 2007; Corti, 2009; Beutel et al., 2010), the presence of young magmatic systems near the rift margin suggests a potentially more complex distribution of extension (Rooney et al., 2007; Chiasera et al., 2018).

The evolution of the MER has been a region of focused investigation (Ebinger and Casey, 2001; Keranen et al., 2004; Wolfenden, et al., 2004; Casey et al., 2006; Keir et al., 2006;

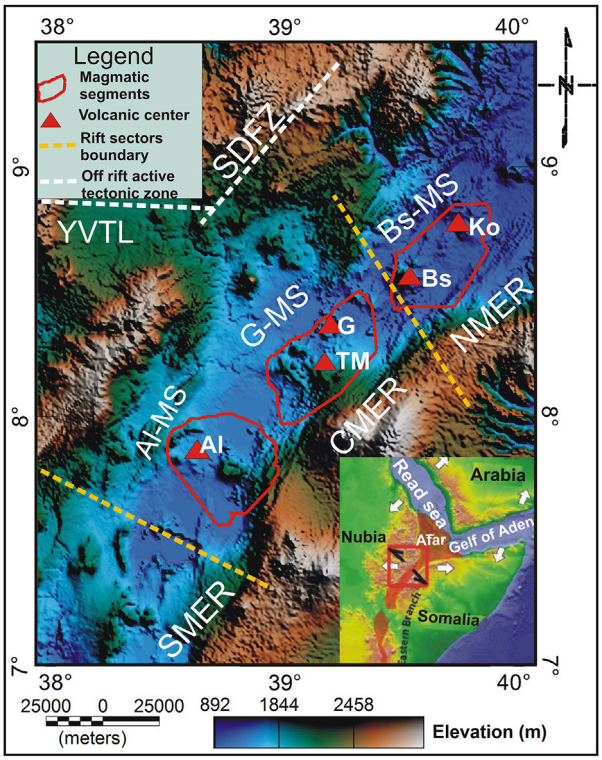

FIGURE 1
Evolution of the MER within the frame of the East African Rift System (right bottom panel): a change in Nubia-Somalia kinematics from orthogonal (white arrows) to oblique extension (black arrows) (Boccaletti et al., 1998; Wolfenden et al., 2004). The main map shows the en echelon arrangements of magmatic segments in the MER (Ebinger and Casey, 2001; Kurz et al., 2007): the rectangle in the red line is the MER (the study area) and abbreviations: SMER, Southern MER; CMER, Central MER; NMER, Northern MER; MS, magmatic segment; Al-MS, Aluto magmatic segments; G-magmatic segments, Gedemsa magmatic segments; Bs-MS, Boseti magmatic segments.

Maguire et al., 2006; Kurz et al., 2007; Corti, 2009; Beutel et al., 2010). However, the significance of the tectonic geometries and magmatic localization is still widely debated (Kurz et al., 2007). Consequently, long-standing questions including to what depth the magmatic segments maintain discrete magmatic plumbing systems, and whether magma intrusion and faulting vary along discrete segments, have remained unanswered. To address these issues, we used gravity data to image and model the subsurface characteristics of the magmatic segments in the MER. This was accomplished by creating a variety of gravity anomaly maps by using wavelength filtering and upward continuation in conjunction with two-dimensional forward modeling constrained by existing seismic models (Keranen et al., 2004; Maguire et al., 2006) and geologic information (Corti et al., 2020 and references therein). Although our study focused on the Aluto-Gedemsa-Boseti portion of the rift (Figure 1), which is the most magmatically productive middle Pleistocene to Holocene parts of the MER (Acocella et al., 2002; Abebe et al., 2007; Nicotra et al., 2021), implications are relevant to the entire EARS and other rift systems on Earth.

2 Geological and geophysical background of the MER

2.1 Geology and tectonic setting

Ethiopia's pre-rift geology comprises highly folded and foliated Proterozoic basement rocks. Overlain by Mesozoic sediments, these rocks are exposed in the southern MER, northern Afar, and western rift escarpment of the Central MER (Woldegabriel et al., 1990; Wolfenden et al., 2004; Abebe et al., 2005; Corti, 2009 and references therein). With the eruption of the Ethiopia–Yemen flood-basalt province, Ethiopian volcanism began during the Eocene-Late Oligocene (Mohr and Zanettin, 1988). Tholeiitic to alkaline lava flows (Kieffer et al., 2004) and felsic lavas with pyroclastic rocks of rhyolitic compositions inter-bedded with flood basalts characterize this volcanic phase (Mohr and Zanettin, 1988). In the Miocene period, a second stage of volcanism is marked by the development of massive basaltic shield volcanoes (Kieffer et al., 2004), whereas the third stage in the Pliocene-Quaternary is intimately tied to the opening of the MER and Afar (Wolfenden et al., 2004; Nicotra et al., 2021).

The volcanic rocks of the MER are dominated by a bimodal composition with a basalt-rhyolite association (Peccerillo et al., 2003). Basalts are associated with monogenetic vents or fissures on the side of the main central volcano (Ebinger and Casey, 2001; Acocella, 2014 and references therein), while rhyolites are associated with central volcanoes, which are usually characterized by a summit caldera (Ebinger and Casey, 2001; Acocella, 2014 and references therein). Several basaltic fields, silicic domes, and calderas are interlayered with lacustrine deposits on the rift floor (Woldegabriel et al., 1990).

From embryonic continental rifting in the south to incipient oceanic spreading in the north, the MER encompasses many phases of rift sector evolution (e.g., Hayward and Ebinger, 1996; Corti, 2009; Ebinger et al., 2017; Chiasera et al., 2021). Based on the onset of rifting and the age of volcanism (Corti, 2009; Corti et al., 2020), the MER has commonly been divided into three sectors: Southern Main Ethiopian Rift (SMER), Central Main Ethiopian Rift (CMER) and Northern Main Ethiopian Rift (NMER) (Figure 1). This division of the MER into several sectors which varies in rift architecture, melt production, and strain accommodation processes have been attributed to be affected by the Pan-African suture zone (Muluneh et al., 2017). Structurally, the MER is dominated by E-W oriented pre-existing faults, NE-SW oriented Miocene border faults and NNE-SSW oriented Quaternary-Recent rift floor faults (Korme et al., 2004; Corti, 2009 and references therein). Deformation in the central to northern MER shifted from the NE trending border faults to the rift floor over the last 2 Ma, focusing along ~20 km wide, ~60 km long, NNE striking magmatic segments aligned in a right stepping en echelon pattern (Boccaletti et al., 1998, 1999; Ebinger and Casey, 2001).

2.2 Previous geophysical studies

A variety of geophysical techniques (seismic, gravity, and magnetotellurics) have been used to investigate the lithospheric structure and the process of continental rifting in Ethiopia. The Ethiopian Afar Geoscientific Lithospheric Experiment (EAGLE) yielded a wealth of data on the lithospheric structure (Keranen et al., 2004; Bastow et al., 2005; Cornwell et al., 2006; Maguire et al., 2006; Whaler and Hautot, 2006; Mickus et al., 2007). The main geophysical results on the lithospheric structure of the MER, which are used in constraining the interpretation of our gravity data, are discussed in Sections 2.2.1, 2.2.2.

2.2.1 Upper mantle structure of the Main Ethiopian Rift

The upper mantle properties have been imaged by receiver functions, surface waves and seismic tomography (e.g., Bastow et al., 2005, 2008; Dugda et al., 2007; Rychert et al., 2012; Lavayssière et al., 2018; Chambers et al., 2022). The deeper portions of the lithosphere beneath the Ethiopian plateau has been imaged using receiver functions and surface wave tomography (Keranen et al., 2009; Rychert et al., 2012; Gallacher et al., 2016; Lavayssière et al., 2018). More specifically, Lavayssière et al., 2018 used S-p receiver functions and identified a negative phase, a decrease in velocity with depth (at 67 ± 3 km depth) beneath the Ethiopian plateau, likely associated with the lithosphere-asthenosphere boundary (LAB). This is broadly consistent with previous studies

estimating lithospheric thickness at 60–90 km beneath the Ethiopian plateau (e.g., Dugda et al., 2007). Estimates of lithospheric thickness beneath the MER generally yield lower values than for the plateau. For example, a joint inversion of teleseismic receiver functions and surfaces waves by Dugda et al. (2007) showed evidence beneath the MER for a ~50 km thick high seismic velocity lid commonly interpreted as the lithosphere. Further constraints on the nature of the mantle lithosphere come from S-p receiver functions (Rychert et al., 2012; Lavayssière et al., 2018). These studies have struggled to image a discontinuity likely associated with the LAB beneath the MER. Instead, either there is no discontinuity, or a weak discontinuity at ~50–70 km depth with the poor definition of the boundary having been interpreted to be due to melt infiltration masking the seismic contrast between lithosphere and asthenosphere (Lavayssière et al., 2018). A 3D gravity inversion by Mammo (2013) also argues for the absence of a lithospheric mantle beneath the rift.

2.2.2 Crustal structure of the Main Ethiopian Rift

The regional crustal structure beneath the MER and the adjacent plateaus has been modified during extension and magmatism as revealed by seismic and gravity modeling (Maguire et al., 2003; Keranen et al., 2004; Dugda et al., 2005; Mackenzie et al., 2005; Maguire et al., 2006; Stuart et al., 2006; Mickus et al., 2007; Figures 2B, C). The crust beneath the adjacent plateaus is considerably thicker than the MER, with values for the Ethiopian plateau ranging between 35–45 km and the Somalia plateau ranging between 30–35 km (Mackenzie et al., 2005; Stuart et al., 2006; Chambers et al., 2022). However, the Ethiopian plateau can be divided into two regions (eastern and western) with the crust of the eastern Ethiopian plateau being thicker (40–45 km) likely due to magmatic additions to the lower crust (Mackenzie et al., 2005; Stuart et al., 2006; Mammo, 2013).

In contrast, the thickness of the crust within the MER ranges between 25 and 38 km (Mackenzie et al., 2005; Mickus et al., 2007; Keranen et al., 2009; Hammond et al., 2011; Figures 2B, C). In general, the thickness decreases towards the Afar rift and the thickness is less than the adjacent plateaus except in the SMER where it is of similar thickness to beneath the Somalia plateau (Mackenzie et al., 2005; Hammond et al., 2011). The crust has been broken into several distinct layers. These are an upper and lower crust, and then also a seismically faster and denser layer at the bottom of the lower crust which has been interpreted to be a mafic magmatic addition (underplating) (Mackenzie et al., 2005; Tiberi et al., 2005; Stuart et al., 2006; Mammo, 2013). Within the upper and lower crust, both gravity and seismic models have imaged seismically faster (P-wave) and denser regions beneath the magmatic segments in the NMER and CMER (Keranen et al., 2004; Mackenzie et al., 2005; Mickus et al., 2007). Three-dimensional seismic models (Keranen et al., 2004; Daly et al., 2008) imaged 20 km wide and 50 km-long high-velocity regions at depths between 5–15 km beneath both the SDFZ and WFB and interpreted them as segmentation of the rift with distinct magmatic segments (Figures 1, 2A). Daly et al. (2008) interpreted these high P-wave velocities (6.5 km s^{-1}) and high V_p/V_s ratios (1.81–1.84) at the same depth range to be cooled mafic intrusions. S-wave velocities (V_s) from surface wave studies and Vp/Vs from receiver functions have imaged slower crustal Vs. and high V_p/V_s in portions of the MER which have been interpreted to be caused by a fluid component, such as partial melt, under the magmatic segments (Dugda et al., 2005; Keranen et al., 2009; Chambers et al., 2019). These fluid components have also been imaged as high conductivity regions by magnetotelluric modeling under the magmatic segments in the northern CMER and southern NMER (Whaler and Hautot, 2006; Hübert et al., 2018; Samrock et al., 2018).

3 Data and methods

3.1 The gravity data

The gravity data used in this study are from the Global Gravity Model Plus (GGMplus 2013) model, which is a mixture of ground, satellite, and topographic effect gravity data. These data have a resolution of 200 m × 200 m but this is due to the topographic effect of gravity data and the real resolution for subsurface density variations is approximately 10 km (Hirt et al., 2013). The data are publicly available by the International Gravimetric Bureau (IGB) *via* an available website at htt:/ddfe.curtin.edu.au/gravitymodels/GGMplus/GGMplus-readme.dat/. We used a 1-km grid interval to investigate the MER at a regional scale. A total of 61,717 gravity data points were extracted (from 38° to 40° E and 7° to 9.5° N), which are attributed to provide a reliable data coverage in both the MER floor and the adjacent plateaus, processed and analyzed to understand the subsurface spatial distribution of magma intrusion in the magma-rich continental rift in Ethiopia.

3.2 Methods

3.2.1 Gravity data reduction

The GGMplus2013 data are observed gravity values and the theoretical gravity values at each observation station were computed using the Geodetic Reference System 1967 (GRS67). Using a Free-Air gradient of 0.3086 mGal/m, a Bouguer reduction density of 2.67 g/cm^3, and mean sea level as an elevation reference, the data were corrected for Free-Air and Bouguer gravity anomalies. To obtain complete Bouguer anomalies (CBA), terrain corrections are made using a 1-km digital elevation model and a terrain density of 2.67 g/cm^3. To create a CBA map, the entire Bouguer gravity anomaly (CBA) data were gridded at a 1 km interval (Figure 3).

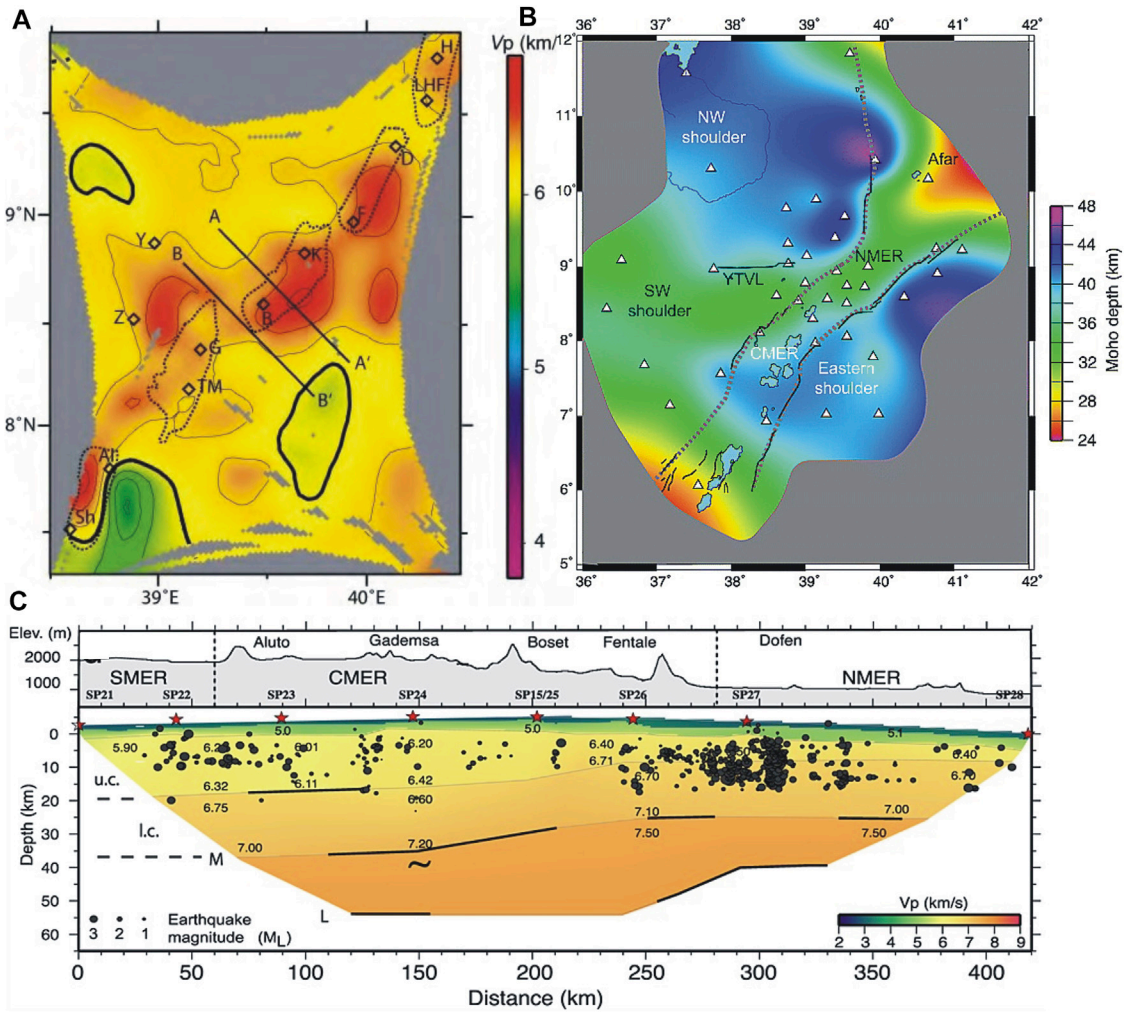

FIGURE 2
Previous seismic studies in the MER. **(A)** horizontal slice of VP at 10 km underlying TMSs (Dashed lines) and eruptive centers (Diamonds where Sh, Shala; Al, Aluto; TM, Tulu Moye; G, Gedemsa; B, Boseti; K, Kone; F, Fentale; D, Dofan; LHF, Liyado-Hayk field; H, Hertale), A-A′ and B-B′ are velocity profiles (Keranen et al., 2004). **(B)** Moho depth over the MER and adjacent plateaus with the dashed gray lines show the rift outlines, solid black lines are the rift border faults (Keranen et al., 2009) and the white triangles represent seismic stations. **(C)** Topographic profile (top) and *p* wave velocity model (bottom): Labels, u. c., upper crust; l. c., lower crust; M, Mohorovic discontinuity; and L, mid-Lithospheric reflector. Stars, shot point location and black dots, Earthquake hypocenters (Maguire et al., 2006).

3.2.2 Determination of regional-residual gravity anomalies

Gravity data can be enhanced to investigate different anomaly sizes and to isolate anomalies of certain wavelengths before one performs more quantitative modeling (Mammo, 2010). There are various methods to accomplish this enhancement including wavelength filtering, upward continuation, and isostatic residual anomalies (Abera, 2020). We used wavelength filtering on the CBA data (Figure 3) to isolate anomalies that occur within the crust. A high pass filter (HPF) with a cutoff wavelength of 130 km was applied to investigate sources of up to 35 km in depth as Abera (2020) showed that an approximate maximum depth of the density sources is one-quarter of the wavelength (Figure 4). To enhance longer wavelength anomalies which are usually due to deeper density variations, band-pass filters (BPF) with wavelengths between 20–130 km, 40–130 km, and 40–200 km were applied to the CBA data to produce three BPF gravity anomaly maps (Figures 5–7, respectively). The BPF gravity anomaly maps are used to investigate the density structure between different depths and the subsurface segmentation of magmatic features beneath the MER.

The HPF anomaly map is thought to show the gravity field response of the entire crust. To further examine the source of geologic bodies at different depth scales, we used upward continuation with continuation distances of 5, 10, 20 and 30 km (Figures 8A–D as a filtering method. Upward continuation involves mathematically projecting a gravity field from one vertical datum to

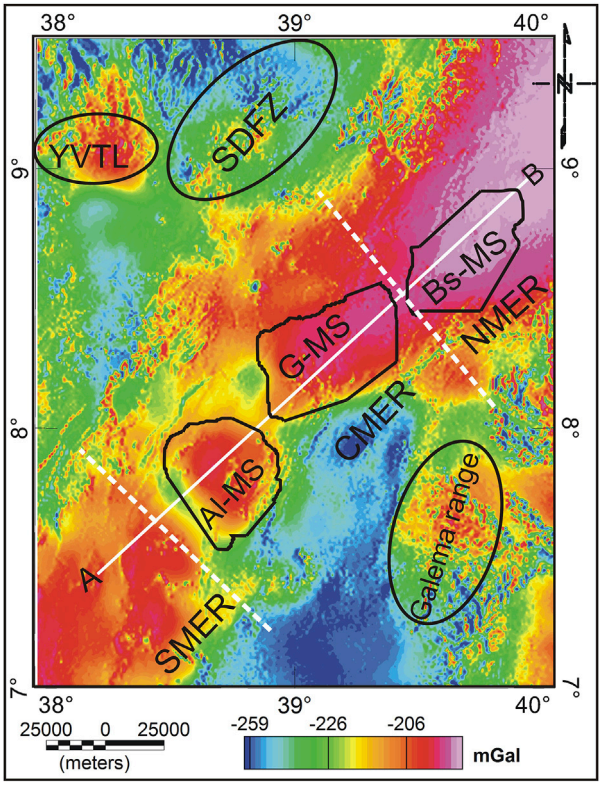

FIGURE 3
Complete Bouguer anomaly map of the MER. Labels: Al, Aluto; TM, Tulumoye; G, Gedemsa; Bs, Boseti; SDFZ, Silte Debrezeyit fault Zone; YVTZ, Yerer Tulu volcano-tectonic zone. The white broken line shows the expected boundary of the Southern, Central, and Northern MER. The curved solid lines represent the off-rift volcanic zones and the irregular polygons represent the magmatic segments along with the MER. The white line along AB is the model (Figure 9) profile line.

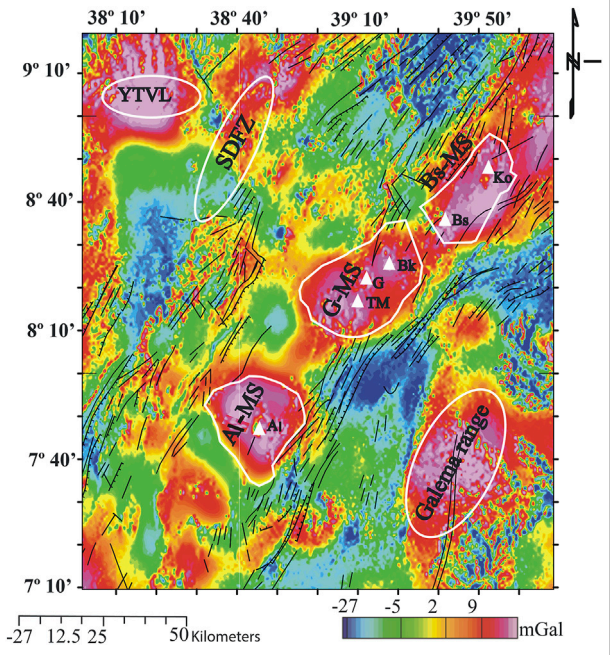

FIGURE 4
The residual gravity anomaly map of the MER was compiled using a high pass filter with a cutoff wavelength of 130 km. The elliptical-shaped solid black lines are the off-rift volcanic regions (YVTZ, SDFZ, and Galema range) and the polygons with white lines are magmatic segments. Labels: Al-MS, G-MS, and Bs-MS represent Aluto, Gedemsa, and Boseti magmatic segments respectively. The overlaid black lines represent faults (where hachured lines are border faults) within the MER.

another (Jacobsen, 1987) and smoothes the gravity field or removes high-frequency gravity signals. As a result, the resultant gravity field usually represents deeper and/or broader density variations as one continues to higher elevations. Jacobsen (1987) showed that the upward continuation height is related to the depth of the anomaly sources and that the density sources are at or deeper than one-half of the continuation height. Therefore, this method can also provide a rough estimate of the depth of the density sources.

3.2.2 Two-dimensional forward modeling

The non-uniqueness of modeling gravity data dictates independent constraints from seismic models, borehole data, geological mapping, and other geophysical data in order to obtain meaningful geological models. In our study, we used the available geophysical and geological constraints to obtain a quantitative model of the upper mantle and crustal structure of the MER through a 2D forward model (Figure 9) along profile AB (Figure 3) following the rift axis. Geometries, depths, and density constraints on the upper mantle and crustal bodies were obtained from 2D reflection/refraction models and 3D tomographic models of the EAGLE project (Keranen et al., 2004; Mackenzie et al., 2005; Maguire et al., 2006). We converted the P-wave velocities determined beneath the magmatic segments to densities using an empirical relationship between P-wave velocity and density (Christensen and Mooney, 1995). The final densities of the bodies are shown in Table 1. The CBA data were modeled using the GM-SYS forward modeling program where the modeling was performed by a trial and error process, by changing the geometries, depths, and densities, until the error (in our case 2%) between the observed and calculated gravity anomalies was acceptable.

4 Results

4.1 Gravity field of the MER

The reduced gravity data have been processed to compile the CBA map (Figure 3) and its enhanced components (Figures 4–8) aiming at examining the subsurface nature and structure of the

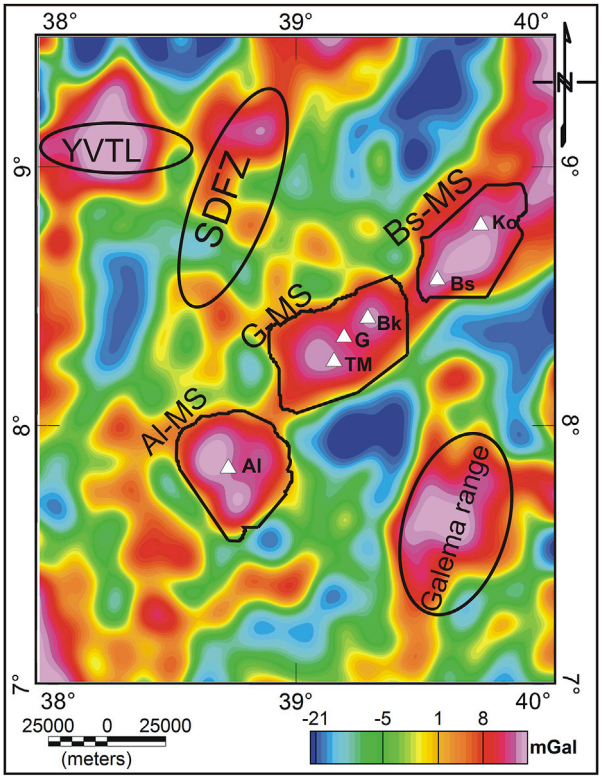

FIGURE 5
Bandpass filtered regional gravity anomaly map of the MER where wavelengths between 20 and 130 km are passed. The elliptical-shaped solid black lines are the off-rift volcanic regions (YVTZ, SDFZ, and Galema range). Labels: Al-MS, G-MS, and Bs-MS represent Aluto, Gedemsa, and Boseti magmatic segments respectively.

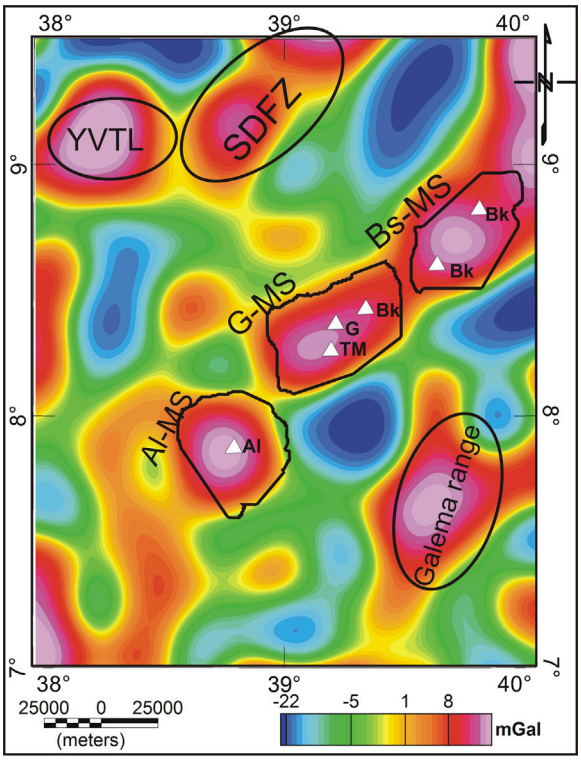

FIGURE 6
Bandpass filtered regional gravity anomaly map of the MER where wavelengths between 40 and 130 km are passed. The elliptical-shaped solid black lines are the off-rift volcanic regions (YVTZ, SDFZ, and Galema range). Labels: Al-MS, G-MS, and Bs-MS represent Aluto, Gedemsa, and Boseti magmatic segments respectively.

magmatic segments within the MER. Furthermore, a 2D gravity model (Figure 9) has been constructed along profile AB running along the rift axis (Figure 3) by sampling the entire crust and upper mantle.

4.1.1 Complete Bouguer anomalies

Figure 3 shows the CBA map of the MER where its axial portion is characterized by gravity maxima, and an increase in gravity value (>−210 mGa l) is observed after the northern termination of the Gedemsa magmatic segment. South of the Gedemsa magmatic segment, the Aluto magmatic segment is exhibited a positive gravity anomaly (>−210 mGal). The elevated platforms corresponding to the western and eastern flanks of the rift are characterized by negative gravity anomalies (<−234 mGal). The rift margin is generally not characterized by an anomalous signal, except for specific volcano-tectonic zones, Silte Debrezeyit fault zone (SDFZ), Yerer Volcano-Tectonic zone (YVTZ), and the Galema range, which are also characterized by gravity maxima. Since the CBA map (Figure 3) is the response of lithospheric scale materials existing beneath the MER and the adjacent plateaus, it does not readily provide information on the depth of the individual source bodies without some type of map transformation or modeling. Consequently, high pass filtering (Figure 4), bandpass filtering (Figures 5–7), and upward continuation (Figure 8) were applied to the CBA data (Figure 3) to obtain the anomaly components that can be used to get information regarding the depths of the individual causative bodies.

4.1.2 High pass filtered gravity anomalies

The high pass filtered gravity anomaly map (Figure 4) reveals a gravity maximum along the magmatic segments of the MER and the rift margin volcanic zones occurring at a crustal level, above 30 km in depth on the wavelength of 130 km (Abera, 2020). The magmatic segments (Figure 4) are associated with one or more Quaternary rift volcanoes. The Gedemsa magmatic segment is associated with five rift volcanoes (Bora, Bericha, Tulu Moye, Gedemsa, and Boku) (Ebinger and Casey, 2001; Nigussie et al., 2022a). The rift margin volcanic zones identified in our study are the SDFZ and YVTL on the western rift flank and

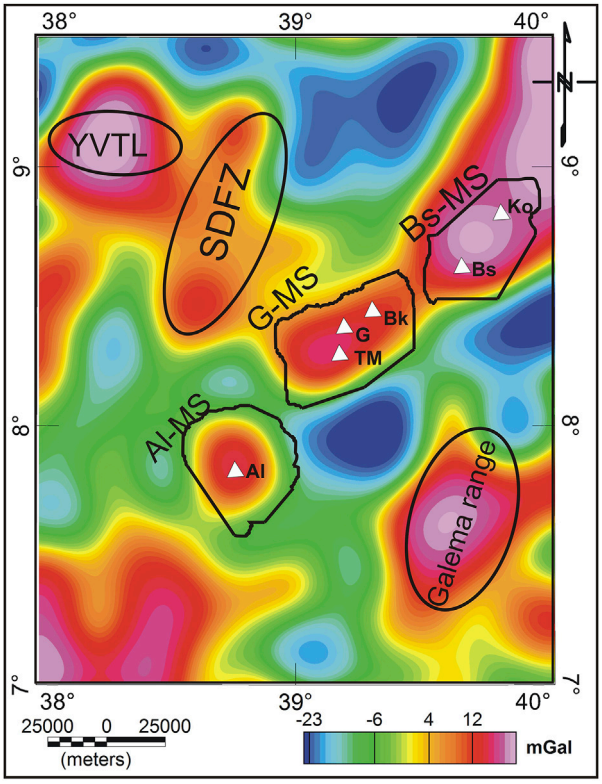

FIGURE 7
Bandpass filtered regional gravity anomaly map of the MER where wavelengths between 40 and 200 km are passed. The elliptical-shaped solid black lines are the off-rift volcanic regions (YVTZ, SDFZ, and Galema range). Labels: Al-MS, G-MS, and Bs-MS represent Aluto, Gedemsa, and Boseti magmatic segments respectively.

the Galema range on the southeastern rift flank, characterized by elongated gravity maxima.

4.1.3 Bandpass filtered gravity anomalies

The 20–130 km bandpass filtered gravity anomaly map (Figure 5) reveals information on density sources occurring between depths of 5–32.5 km. Figure 5 shows a trend of gravity maxima over the magmatic segments which consists of the rift floor volcanic complexes (Aluto, Gedemsa, Boku, and Boseti) and rift margin volcanic regions (YVTZ, SDFZ, and Galema range). Figure 6 is a 40–130 km bandpass filtered gravity anomaly which corresponds to density sources between 10 and 32.5 km. Figure 6 reveals a circular gravity maxima occurring over the above-mentioned rift volcanoes and the southwestern part of the Aluto magmatic segment is also reflected by a positive gravity response.

Figure 7 is a 40–200 km bandpass gravity anomaly map to determine if there are density sources between the mid-crust to the upper mantle. The resultant map reveals a gravity maximum that occurs along the MER axis diverted towards the northeast, toward the NMER. This anomaly has been shown by Mickus et al. (2007) to be caused by a thinning crust toward the Afar depression. Additionally, there is a positive gravity anomaly that trends toward the northwest toward YVTL and SDFZ that might be related to lower crustal bodies or undulations in the Moho surface. Gravity minima are observed northeast of SDFZ, south of the Gedemsa magmatic segment, and between the Gedemsa magmatic segment and Aluto magmatic segment and these anomalies may be related to crustal thickening. In addition, a gravity maximum is observed after the southern termination of the Aluto magmatic segment, towards the SMER, suggesting that the density source under the Aluto magmatic segment is larger than was previously known (Mickus et al., 2007).

4.1.4 Upward continuation of gravity anomalies

The high-pass filtered gravity anomaly map (Figure 4) shows the average gravity field response of density sources at a crustal scale. To further investigate the nature and approximate depth ranges of the density sources which may include magmatic intrusions at a crustal-scale, the high-pass filtered gravity anomaly data (Figure 4) were further processed through upward continuation (Figures 8A–D). A 5 km continuation (Figure 8B) indicates the removal of shallow density sources (<2.5 km) with a gravity maximum along the MER axis (Figures 4, 8A) and gravity maxima over the magmatic segments (Aluto, Gedemsa, and Boseti). In addition, rift margin volcanic zones (e.g., SDFZ, YVTL, and Galema range) (Figure 8B) are also characterized by gravity maxima.

The upward continued 10 km and 20 km gravity maps (Figures 8C, D), images density sources below 5 km and 10 km, respectively, reveal a gradual disappearance of the gravity anomalies (Figure 8B). In the 40 km upward continued residual gravity map (Figure 8E), the lenticular shaped gravity maxima responses over the SMER and CMER disappeared (e.g., Aluto and Gedemsa magmatic segments), except for a general positive gravity anomaly trend over the rift axis.

4.2 Interpretation and gravity modeling

The gravity maximum over the MER floor and the sudden increase in the gravity anomalies (>−210 mGa l) after the northern termination of the Gedemsa magmatic segment (Figure 3) are attributed to the cumulative response of the addition of magmatic underplated intrusions and northward crustal thinning (Tiberi et al., 2005; Mickus et al., 2007). The gravity maxima over rift margin volcanic zones (SDZFZ, YVTZ, and Galema range) are interpreted to be magmatic intrusions into the crust in the form of dike swarms (Chiasera et al., 2021). The gravity maxima over the magmatic segments and the rift margin volcanic zones on the rift flanks occur at a crustal level (~ < 30 km), based on the high pass

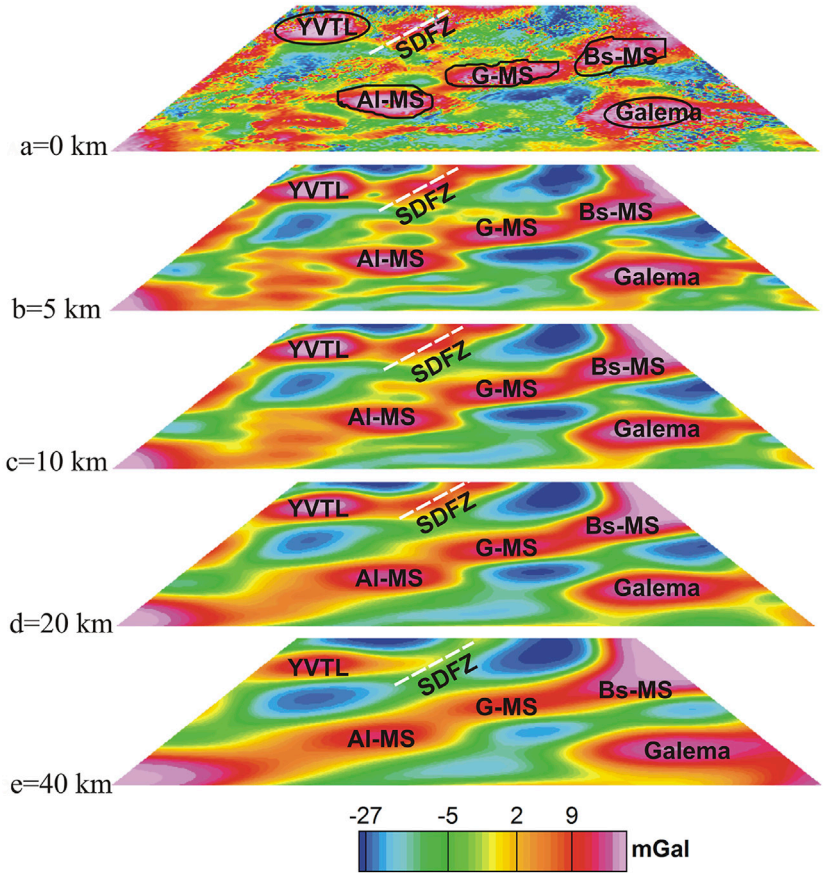

FIGURE 8
Upward continuation of the residual gravity anomaly map (Figure 8) to heights of **(A)** 0 km, **(B)** 5 km, **(C)**10 km, **(D)**20 km, and **(E)**30 km.

filtered gravity anomaly map (Figure 4), suggesting a concentrated or focused magmatic activity in these regions.

The isolated density sources along the MER axis in the bandpass filtered gravity maps (Figures 5–7) are interpreted as the subsurface continuation of the surface magmatic segments. Sampling the crust with an increasing depth in the bandpass filtered maps show a change in anomaly nature over magmatic segments as well as a diversion in gravity anomaly towards the YTVT and SDFZ (Figure 7) starting from the Gedemsa magmatic segment. This anomaly pattern is interpreted as a pre-existing NW-SE trending structure (Corti, 2009) with magmatic intrusions along it which may control the southward propagation of the MER from Afar. The upward continuation maps show similar results as the bandpass filtered gravity anomaly maps (Figures 5, 6) except it revealed more detailed depth wise information.

To characterize the nature of the magmatic segments in the crust beneath the MER quantitatively, a gravity model was constructed that estimates the subsurface density sources along the rift axis and crosses the major magmatic segments of the MER [Aluto, Gedemsa, and Boseti (Figures 3, 9)]. The gravity model along profile AB (Figure 9) has a top layer of upper volcanic and sediments (ρ=2.34 g/cm^3) covering the rift floor and its thickness is less than 4 km (Figure 9; Table 1). The second layer is the upper crust (ρ=2.7 g/cm^3) along the rift axis with its thickness varying from 17 km at the southern tip of the model (a portion of the CMER) to 6 km at the northern end of the model profile (a portion of the NMER).

The lower crust was given a density of 2.87 g/cm^3 and a thickness varying from 16 km at the NMER to 20 km at the SMER (Figure 9; Table 1). A decrease in thickness of the upper and lower crust is observed north of the Boseti magmatic segment (Figure 9). The upper mantle has a density of 3.2 g/cm^3 where the Moho depth shows a decrease in depth of 38 km–28 km from south to north. In addition, higher density bodies which are interpreted to be mafic intrusions are included in the upper and lower crust to model the short wavelength gravity maxima (Figure 9). Unlike previous studies which modeled the axial mafic intrusions under the magmatic segments of the MER with a similar density (e.g., Mickus et al., 2007; Nigussie et al., 2022b) based on crustal scale seismic model (Maguire et al., 2006), we modeled the mafic intrusions with

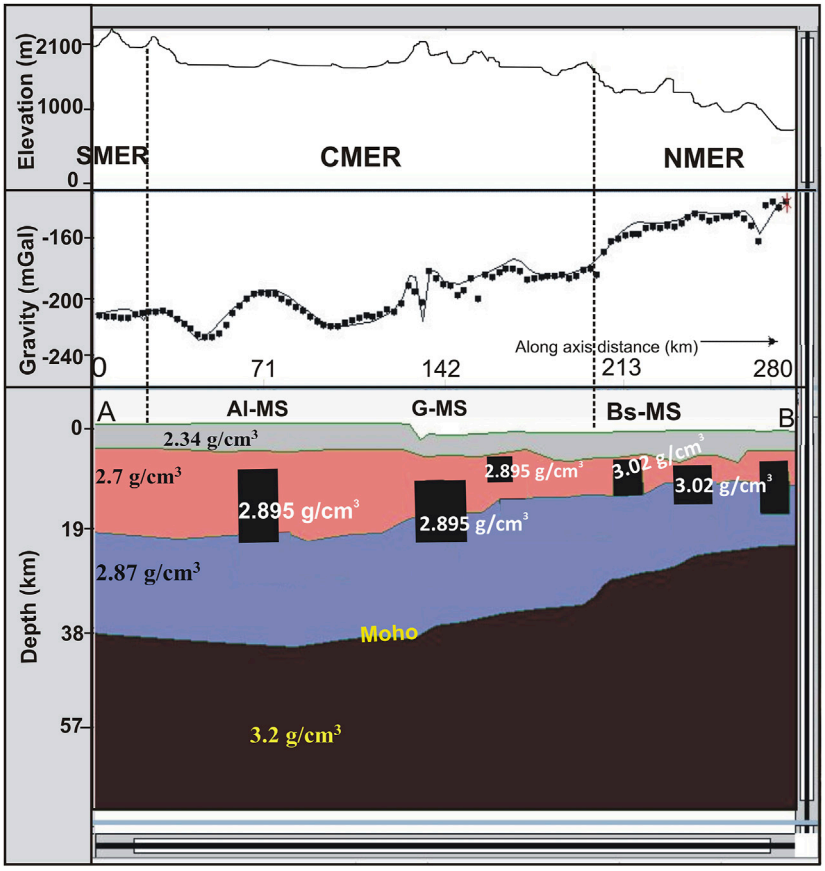

FIGURE 9
The two-dimensional gravity model of the crust and upper mantle, shows mafic intrusions, crustal thickness modification, and Moho depth undulation. The solid line of the gravity profile shows the calculated gravity and the black dots are the observed gravity values and abbreviations: SMER, Southern MER; CMER, Central MER; NMER, Northern MER; Al-MS, Aluto magmatic segments; G-magmatic segments, Gedemsa magmatic segments; Bs-MS, Boseti magmatic segments.

TABLE 1 P-wave velocities (V_p) (Maguire et al., 2006), densities (ρ), and thickness of each body in the gravity modeling.

Layer description	V_p (km/s) range	Mean V_p (km/s)	Initial model ρ (g/cm^3)	Final model ρ (g/cm^3)	Thickness (km)
Upper volcanic and sediments	4–5.2	4.5	2.34	2.34	<4
Upper crust	6.07–6.40	6.2	2.77	2.7	6–17
Lower crust	6.31–6.83	6.57	2.91	2.87	16–20
Mafic intrusions	6.65–7	6.7	2.95–3.0	2.895 3.02	-
Upper Mantle	7–8.10	7.55	3.25	3.2	?

varying densities, 2.895 g/cm^3 at the Aluto magmatic segment to 3.02 g/cm^3 at the Boseti magmatic segment, from south to north (Figure 9). This density variations of the zones of intrusions along the 280 km axial zone of the MER are based on the observed variations in the upper crust, controlled-source seismic velocity study of Keranen et al. (2004) (Figure 2A).

5 Discussion

In this section, we discuss the implications of our study for understanding the along-axis segmentation of magma intrusion and its relationship with faulting (Section 5.1). Moreover, the subsurface nature and structure of each magmatic segment with

the MER (Section 5.1) and broadly distributed strain accommodation, rift margin extension of the MER (Section 5.2) are also clearly mentioned. To support our discussion, we include interpretations of our results in comparison with other previous geophysical and geological studies that focused on the fault-dominated and magma-enhanced rifting cases of the MER.

5.1 Along-axis segmentation of the rift

Geodetic constraints and seismicity indicate that more than 80% of current extension in the upper crust is localized to the magmatic segments (Bilham et al., 1999; Kogan et al., 2012; Daniels et al., 2014; Birhanu et al., 2016). Geological records suggest that this has been the case since the Quaternary (Ebinger and Casey, 2001; Casey et al., 2006). The geological expression of the magmatic segments is localized volcanic centers, and NNE striking aligned cones and small offset fault systems oriented to the orientation of the Miocene border faults (Ebinger and Casey, 2001; Kurz et al., 2007). The spatial position of the gravity maxima we observe in the upper crust shows a clear along-rift segmented pattern (Figures 4–9). However, it does not always exactly match with the geologically mapped location of the magmatic segments and appears to be shorter and more spatially separated (e.g., Figure 9). For example, we image two discrete gravity maxima that we define as the Aluto magmatic segment and Gedemsa magmatic segment, whereas these two segments are harder to distinguish from the surface geology (Ebinger and Casey, 2001; Casey et al., 2006). The subsurface separation between these two segments is also supported by a recent gravity data analysis (Nigussie et al., 2022b) which showed that the Aluto and Gedemsa magmatic segments represent two distinct features and no linkage between the two occurs in the upper crust. An elongated NW trending gravity maxima associated with the Gedemsa magmatic segment led Nigussie et al. (2022b) to suggest that the formation of Gedemsa magmatic segment could be linked to and controlled by transversal structures within the rift. In this regard, the local gravity minimum superimposed on a larger gravity maximum over the Gedemsa magmatic segment (Figure 9) could possibly reflect the associated transversal structures, although it needs more analysis at a smaller scale, since low density bodies may cause the same response.

Closer inspection of the position of the gravity maxima shows that they are localized to major volcanic centers (e.g., Figure 4): The gravity maxima are centered on the Aluto volcanic center within the Aluto magmatic segment, on the Tulu Moye volcanic center within the Gedemsa magmatic segment, and the Boseti volcanic center within the Boseti magmatic segment. This observation suggests that the major volcanic centers are the locus of magma intrusion and that there is limited magmatism in-between the segments. Furthermore, this interpretation may also suggest that the dikes feeding the monogenic volcanoes propagate laterally in the upper crust from a magmatic center, and not vertically from deeper depths. The shorter length scale of the gravity maxima (~30 km), compared to the surface expression (~60-km) of the magmatic segments suggests that the amount of magma intrusion may vary along the rift in each segment. To explore this hypothesis further, we combined the gravity maps with the surface fault data (Figure 4). The discrete gravity maxima do not correlate to where the fault density is highest, but instead reveal that the densest fault swarms occur at the lateral tips and between the gravity maxima. This result may suggest that tectonic extension by faulting and magmatic extension by intrusion vary along the rift in a regular pattern, with faulting becoming more important away from zones of focused intrusion. A similar interpretation has been reached from surface structural geology studies of along rift variation in faulting and volcanism (Kurz et al., 2007; Siegburg et al., 2020), with magmatism being interpreted to be focused on the segment centers with faulting increasing in importance at the segment tips, and to link the segments (Illsley-Kemp et al., 2018; La Rosa et al., 2022).

The along-axis pattern and scale of gravity maxima (Figures 4–9) and their spatial relationship to volcanic centers and zones of increased faulting (Figure 4) are similar to what is observed at slow and ultra-slow spreading ridges. In the oceans, gravity maxima defining a "bulls' eye" pattern are positioned in the center of the third order segments (~50–100 km-long) of the ridge, and interpreted as zones of localized magma intrusion and magma supply (Phipps Morgan & Chen, 1993; Liu & Buck, 2020). At the surface, the axial volcanic highs of up to a few hundred meters are observed at the segment centers (Phipps Morgan & Chen, 1993; Liu & Buck, 2018). In contrast, where magma supply is lower towards the segment tips, an axial graben develops (Phipps Morgan & Chen, 1993; Liu & Buck, 2018). Therefore, we interpret the along rift variation in gravity signature (Figures 4–9) and faulting (Figure 4) in the MER to be similar to that observed at ocean spreading centers. This suggests that the mode of crustal extension seen at ocean ridges can initiate in magma-rich rifts long before continental breakup.

Previous crustal seismic imaging studies that have the resolution to image high P-wave velocities beneath discrete segments only have good resolution in the upper crust (Keranen et al., 2004; Daly et al., 2008), and that the subsurface extent and geometry of localized intrusion zones beneath segments is debated. This can be elaborated by closely examining the subsurface extent of the separation between magmatic segments by sampling the entire crust at different depths (Figures 4–9). The results indicate that discrete gravity maxima can be inferred to a mid-crust depth of 20 km. This suggests that the subvolcanic plumbing systems beneath the centers of magmatic segments remain discrete down to at least mid-crustal depths (Figure 9). Constraining their separation into the lower crust with certainity is difficult to achieve with geophysical studies, since the lower continental crust shares similar densities and seismic velocities to mafic rock (Maguire et al., 2006). However, the observation of the gravity highs at the centre of the magmatic segments and similarity to that seen at slow spreading oceanic ridges leads us to speculate that segment centres share a connection to magma supply from depth. The centres of magmatic segments may therefore represent regions where magma has risen from the upper

mantle and resides in the middle crust, where it starts to undergo fractional crystallization (Siegburg et al., 2018).

5.2 Rift margin extension by magma intrusion

The mode of strain accommodation in the central MER is much more complex than in the northern MER (Rooney et al., 2005; Rooney, 2006) where focused magmatism is observed only along the axial zone of the rift. A seismic analysis of the MER and gravity modeling indicates that there are regions of higher P-wave velocities and densities in the crust at 10 km beneath the surface expressions of the WFB, SDFZ, YVTL, and the Galema range (Keranen et al., 2004; Mickus et al., 2007; Nigussie et al., 2022b; Figure 2A). High-pass filtered (Figure 4) and bandpass filtered (Figures 5–7) gravity anomaly maps also show gravity maxima over these rift margin volcanic zones (WFB, SDFZ, YVTL, and the Galema range). Specifically, the occurrence of higher P-wave velocities in the crust at depths of approximately 10 km beneath these zones (Keranen et al., 2004; Figure 2A) is consistent with the bandpass filtered gravity anomaly map (Figure 6) which represents depths between ~10–32.5 km and is comparable to the seismic models. This correlation together with petrologic and geochemical evidence (Rooney et al., 2005; Chiasera et al., 2018) may be evidence of cooled mafic material at these depths.

The bandpass filtered gravity maps (Figures 5–7) displays an en echelon arrangement of the magmatic segments (Aluto, Gedemsa, and Boseti) and rift margin volcanic ranges (Galema range, YVTL and SDFZ) reflected by gravity maxima. This shows a process of magmatic addition to the crust not only on the rift axis but also on the margin and flanks of the rift. Although the axial part of the MER is the locus of strain in existing rift models, there is increasing evidence of ongoing rift margin and off-rift extension from petrologic studies and the gravity data analysis in this study (Rooney et al., 2007; Chiasera et al., 2018; 2021 Nigussie et al., 2022b; Figures 4–6). The occurrence of rift margin volcanic ranges (e.g., SDFZ and Galema) implies a broad distribution of strain and complex geodynamic setting of the MER.

Most of the rift magmatic segments reflect SW-NE trending gravity maxima (Mehatsente et al., 1999; Tiberi et al., 2005; Mickus et al., 2007) and high seismic velocities (Keranen et., 2004) within the WFB. However, the Gedemsa magmatic segment has an anomaly with a perturbation/shift of high velocity beneath the SDFZ (Figure 1, Keranen et., 2004) which is not seen on the gravity anomaly maps (Figures 4–6). Despite the seismic evidence (Figure 2A, Keranen et., 2004) which shows a shift in velocity highs towards the SDFZ in the vicinity of Gedemsa, subsurface evidence from gravity anomalies shows that the maxima are consistent with the surface location of the magmatic segments (Figures 4–6). There is a diversion of gravity maxima towards the SDFZ from the Gedemsa magmatic segment (not perturbation) at greater depth (Figure 7) which may reflect the existence of pre-existing weak zones. However, this dilemma needs further geochemical and geophysical investigation. The presence of this NW trending gravity maxima associated with some of the segments (e.g., Gedemsa magmatic segment) may imply that the formation of magmatic segments in the MER could be linked to and controlled by transversal structures in the rift.

6 Conclusion

Our contribution from interpreting gravity data in conjunction with previous data is to understand better the spatial distribution of magma intrusion in a magma-rich continental rift. We have used 61,717 datasets to produce higher resolution gravity anomaly maps on a large spatial scale in the MER than previously achieved. Our gravity data analysis includes creating a variety of gravity anomaly maps by using wavelength filtering and upward continuation in conjunction with two-dimensional forward modeling constrained by existing seismic models. The following conclusions have been forwarded based on the observations and interpretations made:

The along-axis gravity model combined with high pass and bandpass filtered gravity anomaly maps shows distinct 30–60 km long gravity highs in the upper crust that we interpret as focused zones of magma intrusion beneath the centers of magmatic segments. These gravity highs are shorter than the surface expression of the magmatic segments, suggesting along-rift variations in magma intrusion at the segment scale. Furthermore, our integration of our gravity maps with fault maps suggests that the fault density is highest at the tips and in between the gravity highs, supporting an interpretation that tectonic extension becomes increasingly important away from the centers of the magmatic segments. This along-segment variation in magmatism and faulting is similar to what is observed at slow and ultra-slow ocean ridges.

The presence of NW trending gravity maxima associated with some magmatic segments (e.g., Gedemsa) may imply that the formation of the magmatic segments in the MER could be linked to and controlled by transversal structures in the rift. The occurrence of rift margin volcanic zones within the CMER (e.g. SDFZ and Galema) evidenced from previous geological mapping

and petrological data reinforced by the gravity data in this study show that extension *via* magma intrusion also occurs in places at the rift margin. These results suggest that the central MER is still in a relatively immature stage of continental rifting where strain is accommodated by border faults, axial magmatic segments, and off-rift magmatic zones.

Data availability statement

The datasets presented in this study can be found in online repositories. The names of the repository/repositories and accession number(s) can be found below: https://bgi.obs-mip.fr/data-products/grids-and-models/modele-global-ggmplus2013/.

Author contributions

All authors listed have made a substantial, direct, and intellectual contribution to the work and approved it for publication.

Acknowledgments

We are thankful to the International Gravimetric Bureau for providing the gravity data which is freely available to the public (http://ddfe.curtin.edu.au/gravitymodels/GGMplus/data/).

Conflict of interest

The authors declare that the research was conducted in the absence of any commercial or financial relationships that could be construed as a potential conflict of interest.

Publisher's note

All claims expressed in this article are solely those of the authors and do not necessarily represent those of their affiliated organizations, or those of the publisher, the editors and the reviewers. Any product that may be evaluated in this article, or claim that may be made by its manufacturer, is not guaranteed or endorsed by the publisher.

References

Abebe, B., Acocella, V., Korme, T., and Ayalew, D. (2007). Quaternary faulting and volcanism in the main Ethiopian rift. *J. Afr. Earth Sci.* 48 (2-3), 115–124. doi:10.1016/j.jafrearsci.2006.10.005

Abebe, T., Manetti, P., Bonini, M., Corti, G., Innocenti, F., Mazzarini, F., et al. (2005). Geological map (scale 1: 200, 000) of the northern main Ethiopian rift and its implication for the volcano-tectonic evolution of the rift. *Geol. Soc. Am. Map Chart Ser.*, MCH094.

Acocella, V., Korme, T., and Salvini, F. (2002). Formation of normal faults along the axial zone of the Ethiopian Rift. *J. Struct. Geol.* 25 (4), 503–513. doi:10.1016/s0191-8141(02)00047-0

Acocella, V. (2014). Structural control on magmatism along divergent and convergent plate boundaries: Overview, model, problems. *Earth-Science Rev.* 136, 226–288. doi:10.1016/j.earscirev.2014.05.006

Alemu, A. (2020). *Geophysics: Principles, practices, and applications of geophysical methods to resource exploration and geohazard studies*. Addis Ababa: Aster Nega Publishing Enterprise, 500.

Bastow, I. D., Nyblade, A. A., Stuart, G. W., Rooney, T. O., and Benoit, M. H. (2008). Upper mantle seismic structure beneath the Ethiopian hot spot: Rifting at the edge of the African low-velocity anomaly. *Geochem. Geophys. Geosystems* 9 (12). doi:10.1029/2008gc002107

Bastow, I. D., Stuart, G. W., Kendall, J. M., and Ebinger, C. J. (2005). Upper-mantle seismic structure in a region of incipient continental breakup: Northern Ethiopian rift. *Geophys. J. Int.* 162 (2), 479–493. doi:10.1111/j.1365-246x.2005.02666.x

Beutel, E., van Wijk, J., Ebinger, C., Keir, D., and Agostini, A. (2010). Formation and stability of magmatic segments in the Main Ethiopian and Afar rifts. *Earth Planet. Sci. Lett.* 293, 225–235. doi:10.1016/j.epsl.2010.02.006

Bilham, R., Bendick, R., Larson, K., Mohr, P., Braun, J., Tesfaye, S., et al. (1999). Secular and tidal strain across the main Ethiopian rift. *Geophys. Res. Lett.* 26 (18), 2789–2792. doi:10.1029/1998gl005315

Birhanu, Y., Bendick, R., Fisseha, S., Lewi, E., Floyd, M., King, R., et al. (2016). GPS constraints on broad scale extension in the Ethiopian Highlands and Main Ethiopian Rift. *Geophys. Res. Lett.* 43 (13), 6844–6851. doi:10.1002/2016gl069890

Boccaletti, M., Bonini, M., Mazzuoli, R., Abebe, B., Piccardi, L., and Tortorici, L. (1998). Quaternary oblique extensional tectonics in the Ethiopian rift (horn of Africa). *Tectonophysics* 287 (1-4), 97–116. doi:10.1016/s0040-1951(98)80063-2

Boccaletti, M., Mazzuoli, R., Bonini, M., Trua, T., and Abebe, B. (1999). Plio-quaternary volcano-tectonic activity in the northern sector of the main Ethiopian rift: Relationships with oblique rifting. *J. Afr. Earth Sci.* 29 (4), 679–698. doi:10.1016/s0899-5362(99)00124-4

Casey, M. C. D. R. F. G., Ebinger, C., Keir, D., Gloaguen, R., and Mohamed, F. (2006). Strain accommodation in transitional rifts: Extension by magma intrusion and faulting in Ethiopian Rift magmatic segments. *Geol. Soc. Lond. Spec. Publ.* 259 (1), 143–163. doi:10.1144/gsl.sp.2006.259.01.13

Chambers, E., Harmon, N., Keir, D., and Rychert, C. (2019). Using ambient noise to image the northern East African rift. *Geochem. Geophys. Geosystems* 20, 2091–2109. doi:10.1029/2018gc008129

Chambers, E. L., Harmon, N., Rychert, C. A., Gallacher, R. J., and Keir, D. (2022). Imaging the seismic velocity structure of the crust and upper mantle in the northern East African Rift using Rayleigh wave tomography. *Geophys. J. Int.* 230 (3), 2036–2055. doi:10.1093/gji/ggac156

Chiasera, B., Rooney, T. O., Bastow, I. D., Yirgu, G., Grosfils, E. B., Ayalew, D., et al. (2021). Magmatic rifting in the Main Ethiopian Rift began in thick continental lithosphere; the case of the Galema Range. *Lithos* 406, 106494. doi:10.1016/j.lithos.2021.106494

Chiasera, B., Rooney, T. O., Girard, G., Yirgu, G., Grosfils, E., Ayalew, D., et al. (2018). Magmatically assisted off-rift extension—the case for broadly distributed strain accommodation. *Geosphere* 14 (4), 1544–1563. doi:10.1130/ges01615.1

Christensen, N. I., and Mooney, W. D. (1995). Seismic velocity structure and composition of the continental crust: A global view. *J. Geophys. Res. Solid Earth* 100 (B6), 9761–9788. doi:10.1029/95jb00259

Cornwell, D. G., Mackenzie, G. D., England, R. W., Maguire, P. K. H., Asfaw, L. M., and Oluma, B. (2006). Northern Main Ethiopian Rift crustal structure from new high-precision gravity data. *Geol. Soc. Lond. Spec. Publ.* 259 (1), 307–321. doi:10.1144/gsl.sp.2006.259.01.23

Corti, G. (2009). Continental rift evolution: From rift initiation to incipient break-up in the main Ethiopian rift, East Africa. *Earth-Science Rev.* 96 (1-2), 1–53. doi:10.1016/j.earscirev.2009.06.005

Corti, G., Sani, F., Florio, A. A., Greenfield, T., Keir, D., Erbello, A., et al. (2020). Tectonics of the asela-langano margin, main Ethiopian rift (East Africa). *Tectonics* 39 (8), e2020TC006075. doi:10.1029/2020tc006075

Daly, E., Keir, D., Ebinger, C. J., Stuart, G. W., Bastow, I. D., and Ayele, A. (2008). Crustal tomographic imaging of a transitional continental rift: The Ethiopian Rift. *Geophys. J. Int.* 172 (3), 1033–1048. doi:10.1111/j.1365-246x.2007.03682.x

Daniels, K. A., Bastow, I. D., Keir, D., Sparks, R. S. J., and Menand, T. (2014). Thermal models of dyke intrusion during development of continent–ocean transition. *Earth Planet. Sci. Lett.* 385, 145–153. doi:10.1016/j.epsl.2013.09.018

Dugda, M. T., Nyblade, A. A., Julia, J., Langston, C. A., Ammon, C. J., and Simiyu, S. (2005). Crustal structure in Ethiopia and Kenya from receiver function analysis: Implications for rift development in eastern Africa. *J. Geophys. Res. Solid Earth* 110 (B1), B01303. doi:10.1029/2004jb003065

Dugda, M. T., Nyblade, A. A., and Julia, J. (2007). Thin lithosphere beneath the Ethiopian Plateau revealed by a joint inversion of Rayleigh wave group velocities and receiver functions. *J. Geophys. Res. Solid Earth* 112 (B8), B08305. doi:10.1029/2006jb004918

Ebinger, C. (2005). Continental break-up: The East African perspective. *Astronomy Geophys.* 46 (2), 2.16–2.21. doi:10.1111/j.1468-4004.2005.46216.x

Ebinger, C. J., and Casey, M. (2001). Continental breakup in magmatic provinces: An Ethiopian example. *Geology* 29 (6), 527–530. doi:10.1130/0091-7613(2001)029<0527:cbimpa>2.0.co;2

Ebinger, C. J., Keir, D., Bastow, I. D., Whaler, K., Hammond, J. O., Ayele, A., et al. (2017). Crustal structure of active deformation zones in Africa: Implications for global crustal processes. *Tectonics* 36 (12), 3298–3332. doi:10.1002/2017tc004526

Gallacher, R. J., Keir, D., Harmon, N., Stuart, G. W., Leroy, S., Hammond, J. O. S., et al. (2016). The initiation of segmented buoyancy-driven melting during continental breakup. *Nat. Commun.* 7 (1), 13110–13119. doi:10.1038/ncomms13110

Hammond, J., Kendall, J., Stuart, G., Keir, D., Ebinger, C., Ayele, A., et al. (2011). The nature of the crust beneath the Afar triple junction. Geochemistry. *Geophys. Geosystems* 121, 1–24.

Hayward, N. J., and Ebinger, C. J. (1996). Variations in the along-axis segmentation of the Afar Rift system. *Tectonics* 15 (2), 244–257. doi:10.1029/95tc02292

Hirt, C., Claessens, S., Fecher, T., Kuhn, M., Pail, R., and Rexer, M. (2013). New ultrahigh-resolution picture of Earth's gravity field. *Geophys. Res. Lett.* 40 (16), 4279–4283. doi:10.1002/grl.50838

Hübert, J., Whaler, K., and Fisseha, S. (2018). The electrical structure of the central main Ethiopian rift as imaged by magnetotellurics: Implications for magma storage and pathways. *J. Geophys. Res. Solid Earth* 123 (7), 6019–6032. doi:10.1029/2017jb015160

Illsley-Kemp, F., Bull, J., Keir, D., Gerya, T., Pagli, C., Gernon, T., et al. (2018). Initiation of a proto-transform fault prior to seafloor spreading. *Geochem. Geophys. Geosystems* 19 (12), 4744–4756.

Jacobsen, B. H. (1987). A case for upward continuation as a standard separation filter for potential-field mapsfilter for potential-field maps. *Geophysics* 52, 1138–1148. doi:10.1190/1.1442378

Keir, D., Ebinger, C. J., Stuart, G. W., Daly, E., and Ayele, A. (2006). Strain accommodation by magmatism and faulting as rifting proceeds to breakup: Seismicity of the northern Ethiopian Rift. *J. Geophys. Res. Solid Earth* 111 (5). doi:10.1029/2005jb003748

Keranen, K., Klemperer, S. L., Gloaguen, R., and Group, E. W. (2004). Three-dimensional seismic imaging of a protoridge axis in the Main Ethiopian Rift. *Geology* 32 (11), 949–952. doi:10.1130/g20737.1

Keranen, K. M., Klemperer, S. L., Julia, J., Lawrence, J. F., and Nyblade, A. A. (2009). Low lower crustal velocity across Ethiopia: Is the Main Ethiopian Rift a narrow rift in a hot craton? *Geochem. Geophys. Geosystems* 10 (5). doi:10.1029/2008gc002293

Kieffer, B., Arndt, N., Lapierre, H., Bastien, F., Bosch, D., Pecher, A., et al. (2004). Flood and shield basalts from Ethiopia: Magmas from the african superswell. *J. Petrology* 45 (4), 793–834. doi:10.1093/petrology/egg112

Kogan, L., Fisseha, S., Bendick, R., Reilinger, R., McClusky, S., King, R., et al. (2012). Lithospheric strength and strain localization in continental extension from observations of the East African Rift. *J. Geophys. Res. Solid Earth* 117 (B3). doi:10.1029/2011jb008516

Kurz, T., Gloaguen, R., Ebinger, C., Casey, M., and Abebe, B. (2007). Deformation distribution and type in the main Ethiopian rift (MER): A remote sensing study. *J. Afr. Earth Sci.* 48 (2-3), 100–114. doi:10.1016/j.jafrearsci.2006.10.008

La Rosa, A., Pagli, C., Hurman, G. L., and Keir, D. (2022). Strain accommodation by intrusion and faulting in a rift linkage zone: Evidences from high-resolution topography data of the afrera plain (Afar, East Africa). *Tectonics* 41 (6). doi:10.1029/2021TC007115

Lavayssière, A., Rychert, C., Harmon, N., Keir, D., Hammond, J. O., Kendall, J. M., et al. (2018). Imaging lithospheric discontinuities beneath the Northern East African Rift using S-to-P receiver functions. *Geochem. Geophys. Geosystems* 19 (10), 4048–4062. doi:10.1029/2018gc007463

Liu, Z., and Buck, W. R. (2020). Global trends of axial relief and faulting at plate spreading centers imply discrete magmatic events. *J. Geophys. Res. Solid Earth* 125 (8), e2020JB019465. doi:10.1029/2020jb019465

Liu, Z., and Buck, W. R. (2018). Magmatic controls on axial relief and faulting at mid-ocean ridges. *Earth Planet. Sci. Lett.* 491, 226–237. doi:10.1016/j.epsl.2018.03.045

Mackenzie, G. D., Thybo, H., and Maguire, P. K. H. (2005). Crustal velocity structure across the main Ethiopian rift: Results from two-dimensional wide-angle seismic modelling. *Geophys. J. Int.* 162 (3), 994–1006. doi:10.1111/j.1365-246x.2005.02710.x

Maguire, P. K. H., Ebinger, C. J., Stuart, G. W., Mackenzie, G. D., Whaler, K. A., Kendall, J. M., et al. (2003). Geophysical project in Ethiopia studies continental breakup. *EOS, Trans. Am. Geophys. Union* 84 (35), 337–343. doi:10.1029/2003eo350002

Maguire, P. K. H., Keller, G. R., Klemperer, S. L., Mackenzie, G. D., Keranen, K., Harder, S., et al. (2006). Crustal structure of the northern Main Ethiopian Rift from the EAGLE controlled-source survey; a snapshot of incipient lithospheric break-up. *Geol. Soc. Lond. Spec. Publ.* 259 (1), 269–292. doi:10.1144/gsl.sp.2006.259.01.21

Mammo, T. (2013). Crustal structure of the flood basalt province of Ethiopia from constrained 3-D gravity inversion. *Pure Appl. Geophys.* 170 (12), 2185–2206. doi:10.1007/s00024-013-0663-0

Mammo, T. (2010). Delineation of sub-basalt sedimentary basins in hydrocarbon exploration in North Ethiopia. *Mar. petroleum Geol.* 27 (4), 895–908. doi:10.1016/j.marpetgeo.2009.12.009

McKenzie, D. (1978). Some remarks on the development of sedimentary basins. *Earth Planet. Sci. Lett.* 40, 25–32. doi:10.1016/0012-821x(78)90071-7

Mehatsente, R., Jentzsch, G., and Jahr, T. (1999). Crustal structure of the main Ethiopian rift from gravity data: 3-dimensional modeling. *Tectonophysics* 313 (4), 363–382. doi:10.1016/s0040-1951(99)00213-9

Mickus, K., Tadesse, K., Keller, G. R., and Oluma, B. (2007). Gravity analysis of the main Ethiopian rift. *J. Afr. Earth Sci.* 48 (2-3), 59–69. doi:10.1016/j.jafrearsci.2007.02.008

Mohr, P. A. (1968). Transcurrent faulting in the Ethiopian rift system. *Nature* 218 (5145), 938–941. doi:10.1038/218938a0

Mohr, P., and Zanettin, B. (1988). *The Ethiopian flood basalt province*. Kluwer Academic Publishers, 4, 63–110.

Muluneh, A. A., Cuffaro, M., and Kidane, T. (2017). Along-strike variation in deformation style inferred from kinematic reconstruction and strain rate analysis: A case study of the Ethiopian rift. *Phys. Earth Planet. Interiors* 270, 176–182. doi:10.1016/j.pepi.2017.07.009

Nicotra, E., Viccaro, M., Donato, P., Acocella, V., and De Rosa, R. (2021). Catching the Main Ethiopian Rift evolving towards plate divergence. *Sci. Rep.* 11 (1), 21821–21916. doi:10.1038/s41598-021-01259-6

Nigussie, W., Alemu, A., Mickus, K., and Muluneh, A. (2022a). Structure of the upper crust at the axis segmentation stage of rift evolution as revealed by gravity data: Case study of the Gedemsa magmatic segment, Main Ethiopian Rift. *J. Afri. Earth Sci.* 190, 104523–104611. doi:10.1016/j.jafrearsci.2022.104523

Nigussie, W., Alemu, A., Muluneh, A., Mickus, K., Muhabaw, Y., and Ballay, M. (2022b). formation of magmatic segments within the aluto-gedemsa area, main Ethiopian rift. *Italian J. Geosciences, Special volume rifts* 142, 1–14. doi:10.3301/IJG.2023.02

Peccerillo, A., Barberio, M. R., Yirgu, G., Ayalew, D., Barbieri, M. W. U. T. W., and Wu, T. W. (2003). Relationships between mafic and peralkaline silicic magmatism in continental rift settings: A petrological, geochemical and isotopic study of the Gedemsa volcano, central Ethiopian rift. *J. Petrology* 44 (11), 2003–2032. doi:10.1093/petrology/egg068

Phipps Morgan, J., and Chen, Y. J. (1993). Dependence of ridge-axis morphology on magma supply and spreading rate. *Nature* 364, 706–708. doi:10.1038/364706a0

Rooney, T., Furman, T., Bastow, I., Ayalew, D., and Yirgu, G. (2007). Lithospheric modification during crustal extension in the Main Ethiopian Rift. *J. Geophys. Res. Solid Earth* 112 (B10), B10201. doi:10.1029/2006jb004916

Rooney, T. O. (2006). "Continental rifting in central Ethiopia: Geochemical and isotopic constraints from lavas and xenoliths," (the Pennsylvania State University). PhD thesis.

Rooney, T. O., Furman, T., Yirgu, G., and Ayelew, D. (2005). Structure of the Ethiopian lithosphere: Xenolith evidence in the main Ethiopian rift. *Geochimica Cosmochimica Acta* 69 (15), 3889–3910. doi:10.1016/j.gca.2005.03.043

Rychert, C. A., Hammond, J. O., Harmon, N., Michael Kendall, J., Keir, D., Ebinger, C., et al. (2012). Volcanism in the Afar Rift sustained by decompression melting with minimal plume influence. *Nat. Geosci.* 5 (6), 406–409. doi:10.1038/ngeo1455

Samrock, F., Grayver, A. V., Eysteinsson, H., and Saar, M. O. (2018). Magnetotelluric image of transcrustal magmatic system beneath the Tulu Moye geothermal prospect in the Ethiopian Rift. *Geophys. Res. Lett.* 45 (23), 12–847. doi:10.1029/2018gl080333

Siegburg, M., Bull, J. M., Nixon, C. W., Keir, D., Gernon, T. M., Corti, G., et al. (2020). Quantitative constraints on faulting and fault slip rates in the northern

Main Ethiopian Rift. *Tectonics* 39 (8), e2019TC006046. doi:10.1029/2019tc006046

Siegburg, M., Gernon, T. M., Bull, J. M., Keir, D., Barfod, D. N., Taylor, R. N., et al. (2018). Geological evolution of the boset-bericha volcanic complex, main Ethiopian rift: 40Ar/39Ar evidence for episodic Pleistocene to Holocene volcanism. *J. Volcanol. Geotherm. Res.* 351, 115–133. doi:10.1016/j.jvolgeores.2017.12.014

Stuart, G. W., Bastow, I. D., and Ebinger, C. J. (2006). Crustal structure of the northern Main Ethiopian Rift from receiver function studies. *Geol. Soc. Lond. Spec. Publ.* 259 (1), 253–267. doi:10.1144/gsl.sp.2006.259.01.20

Tiberi, C., Ebinger, C., Ballu, V., Stuart, G., and Oluma, B. (2005). Inverse models of gravity data from the Red Sea-Aden-East African rifts triple junction zone. *Geophys. J. Int.* 163 (2), 775–787. doi:10.1111/j.1365-246x.2005.02736.x

Whaler, K. A., and Hautot, S. (2006). The electrical resistivity structure of the crust beneath the northern Main Ethiopian Rift. *Geol. Soc. Lond. Spec. Publ.* 259 (1), 293–305. doi:10.1144/gsl.sp.2006.259.01.22

Woldegabriel, G., Aronson, J. L., and Walter, R. C. (1990). Geology, geochronology, and rift basin development in the central sector of the Main Ethiopia Rift. *Geol. Soc. Am. Bull.* 102 (4), 439–458. doi:10.1130/0016-7606(1990)102<0439:ggarbd>2.3.co;2

Wolfenden, E., Ebinger, C., Yirgu, G., Deino, A., and Ayalew, D. (2004). Evolution of the northern main Ethiopian rift: Birth of a triple junction. *Earth Planet. Sci. Lett.* 224 (1-2), 213–228. doi:10.1016/j.epsl.2004.04.022

Wright, T. J., Ayele, A., Ferguson, D., Kidane, T., and Vye-Brown, C. (2016). Magmatic rifting and active volcanism: Introduction. *Geol. Soc. Lond. Spec. Publ.* 420 (1), 1–9. doi:10.1144/sp420.18

frontiers | Frontiers in Earth Science

TYPE Review
PUBLISHED 24 January 2023
DOI 10.3389/feart.2023.1124573

OPEN ACCESS

EDITED BY
Henglei Zhang,
China University of Geosciences Wuhan, China

REVIEWED BY
Lianghui Guo,
China University of Geosciences, China
Yunlong Wu,
China University of Geosciences Wuhan, China

*CORRESPONDENCE
Xiong Yang,
1076772921@qq.com

SPECIALTY SECTION
This article was submitted to Solid Earth Geophysics, a section of the journal Frontiers in Earth Science

RECEIVED 15 December 2022
ACCEPTED 09 January 2023
PUBLISHED 24 January 2023

CITATION
Zhu Y, Yang X, Liu F, Zhao Y, Wei S and Zhang G (2023), Progress and prospect of the time-varying gravity in earthquake prediction in the Chinese Mainland. *Front. Earth Sci.* 11:1124573. doi: 10.3389/feart.2023.1124573

Progress and prospect of the time-varying gravity in earthquake prediction in the Chinese Mainland

Yiqing Zhu, Xiong Yang*, Fang Liu, Yunfeng Zhao, Shouchun Wei and Guoqing Zhang

Second Crust Monitoring and Application Center, China Earthquake Administration, Xi'an, China

This paper mainly introduces the application and progress of the time-varying gravity in earthquake research in the Chinese Mainland. Since the Xingtai earthquake in 1966, China has begun mobile gravity monitoring, trying to explore the relationship between gravity changes and seismic activities. The gravity changes before and after the Haicheng M_S7.3 earthquake in 1975 and the Tangshan M_S7.8 earthquake in 1976 were observed. In 1981, a high-precision metal spring gravimeter was introduced to carry out high-precision mobile gravity observation in the key earthquake monitoring areas in western Yunnan. The gravity anomaly changes near the epicenters of the Lijiang M_S7.0 earthquakes in 1996 were observed. In 1998, a high-precision absolute gravity survey was introduced to carry out the overall scale gravity field monitoring in the Chinese Mainland, and the large-scale gravity change information before Wenchuan M_S8.0 and Yutian M_S7.3 earthquakes in 2008 was obtained, and the effective prediction opinions were given. After the Wenchuan M_S8.0 earthquake in 2008, the integration of the national network and the regional network accelerated, forming the whole gravity observation network in the Chinese Mainland, which made a relatively successful medium-term prediction for a series of earthquakes with M_S6.0 or above (such as Lushan M_S7.0, Menyuan M_S6.4, and Jiuzhaigou M_S7.0) in recent years and played an important role in the study of the earthquake mechanism and earthquake prediction level in China. Finally, the existing problems in time-varying gravity monitoring in China are pointed out, and the prospect of earthquake research using time-varying gravity monitoring data is put forward.

KEYWORDS

gravity observation, time-varying gravity, tectonic activity, earthquake precursor, earthquake prediction

1 Introduction

The time-varying gravity field is the basic physical field reflecting material migration, which directly reflects the nature and process of tectonic movement and surface mass migration in the Earth's interior. The relationship between earthquakes and gravity is closely linked to the Earth's internal tectonic movement and mass (density) change. Therefore, we can make repeated observations of the ground gravity regularly and deeply analyze and study the dynamic changes of its gravity field, which is beneficial to timely capture the precursor information on gravity before some strong earthquakes. This is the basic starting point of taking time-varying gravity as the observation means so as to deeply explore the mechanism of earthquake occurrence and carry out earthquake risk prediction.

The relationship between seismicity and gravity variation has been studied for a long time. Although there were reports of gravity field changes before strong earthquakes in the early 20th century, it was not until the application of high-precision gravimeters that the monitoring and research of seismic gravity changes began in the Soviet Union, the United States, Japan, etc., in the 1960s. At the same time, the study of time-varying gravity was regarded as an important means of earthquake prediction and analysis. Before and after the 1964 Alaska earthquake, the 1965–1967 Songdai earthquake swarm in Japan, the 1974 Izu earthquake in Japan, and the 1976 Gazley earthquake swarm in the Soviet Union (Barnes, 1966; Mao and Zhu, 2018), the time-varying information on gravity before earthquakes was observed. The landmark research achievement is that Cal Barnes, a famous geologist, made it clear in 1966 that before and after the earthquake, the local stress field in the earth's crust changed due to the fault movement, which led to the change of the density of the underground medium at the fault. At the same time, the deformation of the medium would also produce new cracks, which would increase the cracks of the existing medium. In this way, the fluid medium, such as groundwater or volcanic magma, might directly flow in (or out), causing the density of the fluid medium near the observation point to change, which might directly affect the time change of the regional gravity field (Walsh, 1975; Chen et al., 1979).

Seismology is an observational science. Earthquake research depends not only on the development of relevant basic theories but also on high-precision observation data with complete space-time before and after earthquakes. The research results in recent years show that significant gravity anomaly information may be observed in the regional gravity field before strong earthquakes (Lu et al., 1978; Chen et al., 1979; Zhu et al., 2008a; Zhu et al., 2008c; Shen et al., 2009; Shen et al., 2012; Zhu et al., 2013; Chen et al., 2015; Chen et al., 2016; Zhu et al., 2017). Using high-precision gravity measurement data to analyze the spatial distribution characteristics of gravity anomalies before earthquakes is helpful in determining the high-risk areas of future large earthquakes. Recently, researchers have made accurate medium-term predictions of some large earthquakes by using the data on gravity anomaly and the historical data on earthquakes in the study area (Zhu et al., 2005; Zhu et al., 2008a; Zhu et al., 2008c; Zhu et al., 2013; Zhu et al., 2017; Shen et al., 2020; Zhu et al., 2022). This paper briefly summarizes the application of time-varying gravity in earthquake prediction and the research results obtained.

2 Research on the dynamic change of the regional gravity field

The collision of the Indian–Eurasian plate in the west and the subduction of the Pacific plate in the east have caused frequent strong earthquakes and serious earthquake disasters in China's Mainland (Zhang et al., 2013; Zhou et al., 2017). Therefore, it is a basic national policy of China to actively carry out earthquake prevention and disaster reduction, including earthquake monitoring and prediction, and minimize earthquake risk. At present, China is the only country in the world with the main purpose of earthquake monitoring and prediction, which has built a large-scale ground gravity monitoring network and actively carried out regular gravity resurvey and earthquake prediction (Jiang et al., 2005; Shen et al., 2020).

2.1 Exploration and development stage

In order to explore the relationship between time-varying gravity and seismic activity, after the Xingtai earthquake in 1966, China began to set up mobile gravity monitoring networks, and all kinds of mobile gravity lines across faults were set up in major fault zones in North China, Sichuan, Yunnan, *etc.* On the gravity survey line from Beizhen to Zhuanghe, Liaoning Province, about 180 $\times 10^{-8}$ ms^{-2} of gravity change was observed in a year in the survey section of Gaixian–Donghuangdi before the Haicheng M_S7.3 earthquake in 1975 (Lu et al., 1978). The gravity field changes before and after the 1976 Tangshan M_S7.8 earthquake were obtained through the long baseline gravity joint survey of Beijing–Tianjin–Tangshan–Shanhaiguan; it was found that there was a 100×10^{-8} ms^{-2} gravity anomaly change (Li and Fu, 1983; Li et al., 1997), which proves the existence of gravity anomaly before the earthquake. Chen et al. (1979) pointed out in the analysis of the gravity changes before and after the Haicheng earthquake in 1975 and the Tangshan earthquake in 1976 that the gravity change is closely related to the process of earthquake preparation and occurrence. The gravity change caused by the ground elevation change estimated according to the repeated leveling data is much smaller than the observed gravity change. Therefore, it is speculated that the preparation and occurrence of some large earthquakes may be related to the mass migration in the crust and upper mantle. It is considered that most of the observed gravity changes are caused by mass transfer, and the effects of gravity changes caused by deformation and mass transfer are analyzed theoretically, but the physical process of mass transfer is not completely explained. Li et al. (1997) explained the change process of the regional gravity field before and after the Tangshan earthquake by adopting the expansion model and considered that the epicentral area before and after the Tangshan earthquake experienced the process of gravity increase (stress accumulation and compression), gravity decrease (expansion and expansion), earthquake occurrence, and post-earthquake reverse recovery, and the theoretically calculated gravity change value was in good agreement with the actual observation value (Hu et al., 2021). The gravity measurements before and after the Haicheng and Tangshan earthquakes also showed that there would be significant anomaly changes in gravity before large earthquakes, which provided a typical earthquake example for the study of earthquake prediction by using gravity measurement methods.

2.2 Observation and practice stage

Before 1981, gravimeters were mainly of quartz spring type, and their measuring accuracy was about 30×10^{-8} ms^{-2}. After 1981, due to the introduction of the LaCoste–Romberg (G) (LCR-G) metal spring gravimeter, its measurement accuracy is within 10×10^{-8} ms^{-2}, which is greatly improved compared with the quartz spring gravimeter (Zhu et al., 2008b). The China Earthquake Administration has successively carried out repeated observations of seismic gravity (mobile gravity) and laid a number of survey networks or lines throughout the country, taking provincial (municipality directly under the Central Government, autonomous region) territories as units, which are self-contained and independent of each other (Shen et al., 2020).

In 1981, the Institute of Geophysics, China Earthquake Administration, using three LCR-G gravimeters provided by the

United States, made 2–3 periods of seismic gravity observations in the Beijing–Tianjin–Tangshan–Zhangjiakou area every year to explore the gravity changes and mechanisms during the preparation of strong earthquakes (Gu et al., 1997). The data on seismic gravity measurement in the Beijing–Tianjin–Tangshan–Zhangjiakou area show that the gravity field in this area has obvious regional variation characteristics, and the most obvious is that there is a large-scale increase in gravity in the south of the survey area. The main reason for this change is that the ground subsidence caused by the extensive use of groundwater resources in the south of the survey area leads to an increase in gravity (Lu et al., 2004). The gravity change in the northern mountainous area of the survey area tends to decrease, and the decreasing amplitude is consistent with the change amount of the absolute gravity point of Xiangshan Mountain. The inherited and synchronous tectonic movement in a large mountainous area is the main reason for the trend reduction of the surface gravity change. The gravity change in the eastern part of the survey area was mainly from June 1990 to June 1994, and the gravity change showed a rapid decline and then a rapid increase, which may be the gravity change related to the preparation of the Luanxian M_S5.9 earthquake in October 1995 (Lu et al., 2004).

In 1984, the Institute of Seismology, China Earthquake Administration, in cooperation with the University of Hanover in Germany and others, set up a seismic gravity survey network at the West Yunnan Earthquake Prediction Experimental Site and carried out regular repeated surveys for 2–3 periods every year. It was observed that gravity anomalies of about 70×10^{-8} ms^{-2} occurred before the Gengma M_S7.6 earthquake in Lancang, Yunnan, in 1988 (Wu et al., 1995), gravity anomalies of about 110×10^{-8} ms^{-2} occurred before the M_S7.3 earthquake on the border between China and Myanmar in 1995 (Wu et al., 1998), and a gravity anomaly of about 120×10^{-8} ms^{-2} occurred near the epicenter before the Lijiang M_S7.0 earthquake in 1996 (Wu et al., 1997), and it was recognized that the gravity change related to earthquake preparation is not limited to the fault but presents the characteristics of the "field". Jia et al. (1995) studied the dynamic images of the gravity field of the earthquake experimental site in western Yunnan during 1985–1994 and its corresponding relationship with nine earthquakes with M_S >5.0. During the observation period, nine earthquakes with M_S >5.0 occurred in the survey area and its adjacent areas, all of which occurred near the zero line of the transition zone between positive and negative anomaly areas. Before the earthquake, there is always a positive anomaly zone, and the larger the magnitude, the larger the range and amplitude of the anomaly zone. The time scale of the gravity anomaly change before the earthquake is about 3 years, and the complete rule is that the gravity field rises first and then falls; earthquakes occur in the process of falling, and the time from turning to earthquake occurrence is within 1 year. Further comparison and analysis of the gravity field change images before the Yongsheng M_S5.1 and M_S5.4 earthquakes in December 1992, the Dayao M_S5.3 earthquakes in February 1993, and the Lijiang M_S7.0 earthquakes in February 1996 show that the positive anomaly areas before the Yongsheng M_S5.1 and M_S5.4 earthquakes in December 1992 and the Dayao M_S5.3 earthquakes in February 1993 are obvious and complete, and the gravity change gradient zones and negative anomaly areas in the southwest and northeast are clearly visible, which are two earthquake-prone areas. Combined with other relevant data, an accurate prediction opinion was put forward before the Yongsheng and Dayao earthquakes (Jia and Zhan, 2000). The magnitude of the gravity positive anomaly area before the Lijiang M_S7.0 earthquake in 1996 is seven times that before the Dayao M_S5.3 earthquake in 1993, and the anomaly area has a larger range, but the anomaly shape is incomplete, which is related to the relatively small survey network in the experimental site of western Yunnan. Therefore, it is clearly pointed out that to accurately judge the epicenter position before the earthquake of magnitude 7, it is necessary to have a range of 900 km × 900 km in the survey area, while the range of the gravity network in western Yunnan is only 300 km × 300 km. In fact, the gravity researchers of the Yunnan Earthquake Administration have long been aware of the gravity anomaly changes before the 1996 Lijiang earthquake and have made some predictions about this earthquake (Wu et al., 1997; Shen et al., 2003).

Around 1990, China built a regional gravity survey network with independent units of provinces, municipalities, and autonomous regions in North China, the North–South seismic belt, the southeast coast, and other regions. Some of the survey networks are network-like and some are strip-like, with an average range of less than 300 km × 300 km (Shen et al., 2020; Zhu et al., 2020). There are 20 companies carrying out field monitoring of mobile gravity. The gravity anomaly around the epicenter before and after the Zhangbei M_S6.2 earthquake in Hebei in 1998 (Zhang and Sun, 2001) and the gravity anomaly near the epicenter before and after the Datong M_S5.6 earthquake in Shanxi in 1999 (Li and Qin, 2001) were monitored, and the gravity anomaly at the junction area of Jiangsu, Shandong, and Anhui before the Cangshan M_S5.2 earthquake in Shandong in 1995 (Liu, 1997) was also monitored. Before the Yongdeng M_S5.8 earthquake in Gansu in 1995 and the Jingtai M_S5.9 earthquake in Gansu in 2000, an obvious gravity anomaly change was also observed in the Hexi area of North Qilian, and the medium-term predictions of these two earthquakes were made to some extent (Jiang et al., 1998; Zhu et al., 2001). During the period from 1992 to 1994, significant gravity anomalies occurred in Gulang and Wuwei areas, and the spatial range with gravity variation amplitude greater than 50 $\times10^{-8}$ ms^{-2} was more than 100 km in diameter. The Gulang–Tianzhu–Yongdeng area was a gravity variation high-gradient zone connected with the high-value area of gravity variation. The epicenter of the Yongdeng M_S5.8 earthquake on 22 July 1995 was located at the edge of this gravity variation high-gradient zone (Jiang et al., 1998). Before the Jingtai M_S5.9 earthquake in June 2000, there were two changes in the gravity field from 1998 to 1999, which were similar to those before the Yongdeng earthquake: 1) the regional gravity field showed a wide range of trend anomalies, with a high-gradient zone of gravity change along the main fault tectonic belt of Qilian Mountain, negative gravity changes in mountainous areas, and relatively positive changes in basins; 2) there are many local anomaly areas with uneven spatial changes near the epicenter of the Jingtai M_S5.9 earthquake in the east of the survey area (Zhu et al., 2001). Zhu et al. (2004) further expanded the research range and analyzed the dynamic evolution characteristics of the regional gravity field from 1992 to 2001 and its relationship with the preparation and occurrence of the Yongdeng M_S5.8 and Jingtai M_S5.9 earthquakes by using the gravity observation data on the northeast margin of the Qinghai–Tibet block obtained by the unified starting datum. It is considered that the gravity observation data on the northeast margin of the Qinghai–Tibet block obtained by overall calculation can more completely reflect the complete precursor information on the gravity field changes during the seismogenic process of the Yongdeng M_S5.8 and Jingtai M_S5.9 earthquakes, and the dynamic change

image of the gravity field can clearly reflect the relationship between the orderly evolution process of the regional gravity field and seismic activity (Zhu et al., 2004).

2.3 Application promotion stage

In 1998, the China Earthquake Administration, together with the State Bureau of Surveying and Mapping, the General Staff Bureau of Surveying and Mapping, the China Academy of Sciences, and four other ministries and commissions, built the "crustal movement observation network of China" project (referred to as the network project). With the implementation of the network project, a unified national seismic gravity network in the Chinese Mainland was built. The gravity joint survey was carried out on 25 reference stations, 56 basic stations, and more than 300 regional stations (or transition points), and the absolute gravity values of the 25 reference stations were also measured. The absolute gravity measurement is made using an FG-5 absolute gravimeter, and the absolute gravity measurement accuracy at each reference station is better than 5×10^{-8} ms^{-2}. The relative gravity joint measurement is made by LCR-G, Burris, or CG5/6 gravimeter, and the joint measurement accuracy of gravity segment difference is better than 10×10^{-8} ms^{-2}. Since 1998, the network project has carried out a joint survey of the Chinese Mainland gravity basic network every 2–3 years. In the earthquake-prone areas such as Sichuan–Yunnan and the northeastern edge of the Qinghai–Tibet Plateau, the Seismological Research Institute of the China Earthquake Administration and the Second Crust Monitoring and Application Center of the China Earthquake Administration jointly completed the joint survey of the GNSS stations in the regional gravity survey network. Connect isolated provincial gravity networks into larger regional gravity networks (Zhu et al., 2008b; Shen et al., 2020), and observe and study the dynamic change of regional gravity field and its relationship with strong earthquake preparation.

Li et al. (2009) used the network project gravity observation data to obtain the dynamic change image of the gravity field in the Chinese Mainland at the scale of 2–3 years since 1998, which better reflects the basic contour of the crustal tectonic movement and major strong earthquake activities in the Chinese Mainland. Zhu et al. (2012) obtained the dynamic change images of gravity field in the Chinese Mainland area based on absolute gravity by using the gravity observation data on a network project from 1998 to 2008 and considered that the change of gravity field in the Chinese Mainland not only has the phenomenon of uneven spatial and temporal distribution and zoning of gravity change but also is closely related to active fault structures and earthquake preparation and development. Jiang et al. (2003) analyzed that the gravity difference in the Wudaoliang–Altyn region near the epicenter of the M_S8.1 earthquake in the west of the Kunlun Pass in Qinghai in 2001 reached 100×10^{-8} ms^{-2}。. Wang et al. (2004) used repeated gravity observation data to analyze the relationship between co-seismic dislocation and gravity variation of the Lijiang M_S7.0 earthquake. Zhang and Zhang (2000) analyzed the gravity change of the Lijiang M_S7.0 earthquake based on the mechanics theory, multiplication decomposition theory, and numerical simulation in porous media and proposed that the gravity change experienced the elastic stage of the body, the elastic-plastic stage of the deformation of the body and the hole, and the stress release during the co-seismic dislocation, and then, the hole closed again (Mao and Zhu, 2018). Shen et al. (2011) analyzed the variation characteristics of the gravity field before the Yao'an M_S6.0 earthquake in Yunnan in 2009 in combination with the focal mechanism solution, pointed out that the four-quadrant distribution image of the relative gravity change in the epicenter area reflected the existence of shear stress in the seismogenic area before the earthquake (Shen et al., 2020), and proposed the precursor model of "locking shear." Zhu et al. (2009), Zhu et al. (2012), and Zhu et al. (2015b) have studied that strong earthquakes are prone to occur in the high-gradient zone where the positive and negative gravity change transition areas along the tectonic active fault, and the turning part of the gravity changes the contour line. Due to the strong differential movement and the strongest discontinuity of tectonic deformation, the tectonically active fault zone is prone to produce severe gravity changes, which is conducive to the high accumulation of stress and the preparation of earthquakes. In addition, accurate medium-term predictions have been made for the large earthquakes of M_S7.3 in Yutian, Xinjiang, and M_S8.0 in Wenchuan, Sichuan, in 2008.

2.4 Overall optimization stage

After the 2008 Wenchuan 8.0 earthquake, the China Earthquake Administration summarized and reflected on the advantages and limitations to the seismic gravity field observation in the Chinese Mainland and believed that it was necessary to connect the regional gravity measurement network into a whole and form a unified observation benchmark. According to the idea of "nationwide and regional networking," the existing conventional gravity observation tasks were coordinated (Zhu et al., 2020), and the construction of seismic gravity monitoring network and observation technology was developed rapidly. In 2009, the special task of "Strengthening, Monitoring, and Tracking of Strong Earthquakes in North China" was launched to adjust, optimize, and transform the scattered provincial seismic gravity network in North China, effectively connecting the gravity measurement network of the relevant provincial Earthquake Administration and strengthening absolute gravity control to form a new gravity monitoring network in North China as a whole (Zhu et al., 2019). In 2010, the encrypted monitoring network of the gravity field change of "Comprehensive Geophysical Field Observation of China (CGFOOC)" a key scientific research project in the earthquake industry, was launched. This project took the national basic gravity network as the overall framework and optimized and transformed the existing seismic gravity monitoring networks in the eastern margin of the Qinghai–Tibet Plateau, the surrounding areas of Ordos, and the North China by stages, connecting the scattered regional gravity networks (Hao et al., 2015; Hu et al., 2015; Zhu et al., 2019; Wei et al, 2020). In 2010, the Chinese Mainland Tectonic Environment Monitoring Network optimized and upgraded the gravity survey network on the basis of the Crustal Movement Observation Network of China and conducted joint surveys of 100 reference stations (absolute gravity survey points) and more than 600 joint survey points in the Chinese Mainland region (Xing et al., 2016; Shen et al., 2020). Through the Chinese Mainland Tectonic Environment Monitoring Network, Comprehensive Geophysical Field Observation of China, North China's strong earthquakes, and other large-scale key earthquake monitoring projects, the "scattered distribution" seismic gravity monitoring

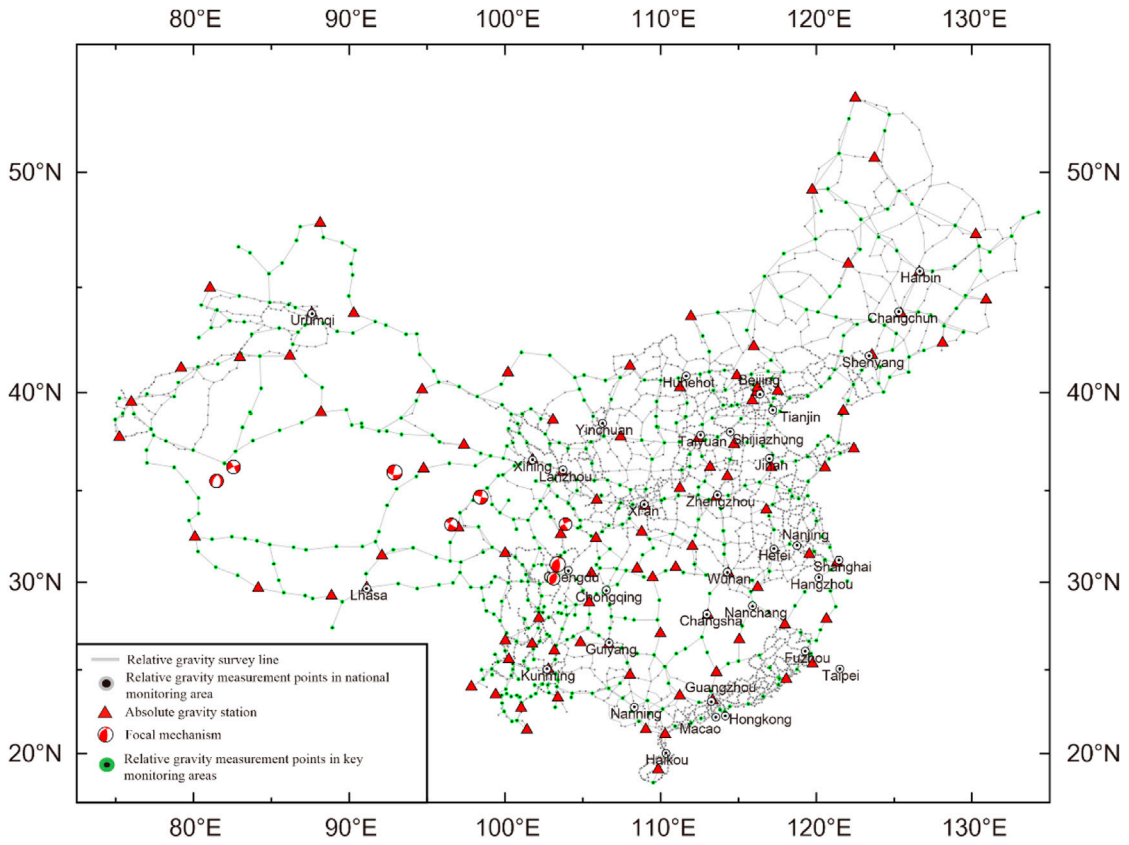

FIGURE 1
Seismic gravity monitoring network in the China continental area.

network has been optimized and transformed many times in its overall structure and gradually built into the Chinese Mainland mobile gravity seismic monitoring network consisting of the relative gravity joint measurement network and the absolute gravity control network in the Chinese Mainland (Figure 1), with regular observations every year. In addition, gravity exploration was carried out for the crustal structure of the North–South seismic belt (Zhu et al., 2019; Shen et al., 2020). According to the national gravity field change image obtained under the unified benchmark, it has played an important role in annual earthquake prediction, especially in location prediction. Many researchers have made an in-depth summary of the relationship between the gravity field change images and earthquakes (Li et al., 2009; Li et al., 2010; Zhu et al., 2010; Zhu et al., 2012; Zhu et al., 2014; Zhu et al., 2015a; Hu et al., 2019; Shen et al., 2020). Figure 1 shows the epicenters of eight earthquakes with magnitude of more than 7 in the Chinese Mainland, including the Wenchuan M_S8.0 and Yutian M_S7.3 earthquakes in 2008, the Yushu M_S7.1 earthquake in 2010, the Lushan M_S7.0 earthquake in 2013, the Yutian M_S7.3 earthquake in 2014, the Jiuzhaigou M_S7.0 earthquake in 2017, and the Maduo M_S7.4 earthquake in 2021, since the Kunlun Mountain Pass West M_S8.1 earthquake in 2001. It can be seen that there are some gravity measuring points near the epicenter of the seven other major earthquakes, except that there are no gravity measuring points near the epicenter of the Kunlun Mountain Pass west M_S8.1 earthquake in 2001. In particular, there are gravity monitoring points around the epicenter of the Wenchuan M_S8.0 earthquake in 2008, the Lushan M_S7.0 earthquake in 2013, and the Jiuzhaigou M_S7.0 earthquake in 2017, which laid a good foundation for extracting precursory information on gravity changes before strong earthquakes. In recent years, significant gravity anomalies have been observed in mobile gravity before many strong earthquakes in the Chinese Mainland. Although the manifestations of the anomalies are different, some of them occur in the high-gradient zone and zero isoline area where the positive and negative gravity anomaly areas undergo transition and some of them occur in the center of the distribution characteristics of the four-quadrants of gravity anomalies. However, according to the range and amplitude of gravity anomaly areas, the magnitude, and characteristics of the gravity anomaly gradient, we can study the location and magnitude of potential strong earthquakes (Zhu et al., 2019). Zhu et al. (2018), Zhu et al. (2019), Zhu et al. (2020), and Zhu et al. (2022), on the basis of an in-depth study on the evolution characteristics and laws of regional gravity fields with different time and space scales in the Chinese Mainland, proposed that regional gravity fields with multiple time and space scales should be used as the basis for analyzing and studying the dynamic images of gravity fields. The prediction method and judgment index of earthquake risk analysis based on the gravity field change trend, gravity anomaly shape, gravity anomaly area range, amplitude, duration, gravity anomaly gradient, and its characteristics in different time and space scales (adjacent two periods of gravity change, year-scale gravity change, cumulative gravity change, etc.) are proposed in Table 1.

TABLE 1 Relation between the gravity anomaly and earthquake preparation (Zhu et al., 2022).

Magnitude	Characteristics of the gravity field at the potential earthquake location	Trend characteristics and anomaly range/km	Duration	Anomaly magnitude/ $\times10^{-8}$ ms^{-2}
5	Gravity change high-gradient zone	Local anomaly area appears in the trend anomaly, ≥100	0.5~1a	≥50
6	The turning part of the gravity change high-gradient zone related to the tectonic activity, near the four-quadrant distribution feature center	Local anomaly area appears in the trend anomaly, ≥200	1~3a or longer	≥80
7	The turning part of the gravity change high-gradient zone related to the block boundary, near the four-quadrant distribution feature center	Positive and negative local anomaly areas appear in the trend anomaly, ≥400	3~5a or longer	≥100
8	The turning part of the gravity change high-gradient zone related to the boundary of the first-order block, near the four-quadrant distribution feature center	Positive and negative local anomaly areas appear in the trend anomaly, ≥600	5a or longer	≥120

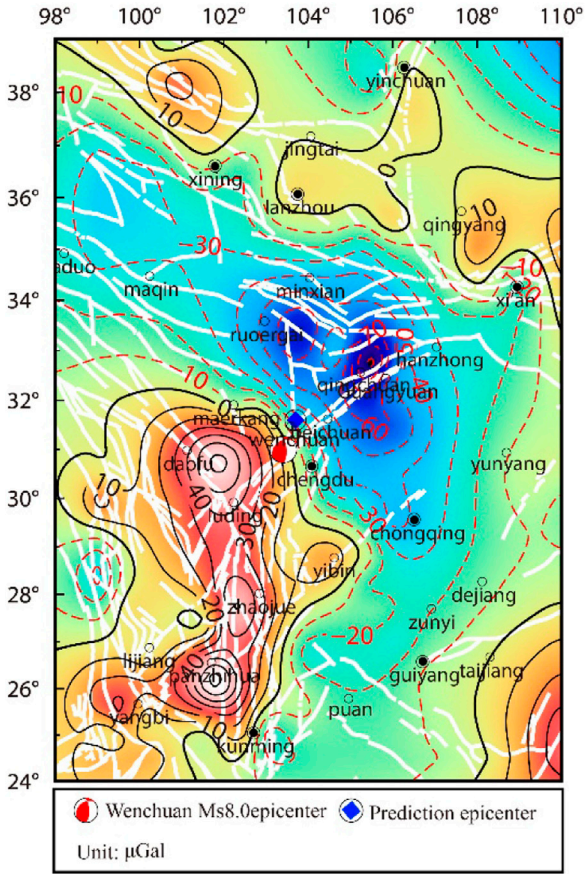

FIGURE 2
Gravity changes before the Wenchuan Ms 8.0 earthquake.

3 Time-varying gravity and strong earthquake prediction

Earthquakes are a manifestation of deformation and rupture of the medium in the crust, and the observation of gravity field changes during the earthquake preparation period can help in studying the relationship between the accumulation of the elastic strain in the crust medium and the occurrence of earthquakes (Shen et al., 2009; Chen et al., 2015). By analyzing the dynamic changes of the gravity field before and after the earthquake, we can study the source parameters, the rupture process, and the post-earthquake recovery viscoelastic deformation (Fu and Liu, 2017; Fu and Wang, 2020). At present, the gravity field change data obtained based on surface mobile gravity observation is gradually increasing, and with the continuous improvement of instrument performance indicators and the coverage of gravity survey network, much progress has been made in the study of the relationship between the dynamic changes of gravity field obtained through repeated surface gravity observation and tectonic activity (Chen et al., 2015; Shen et al., 2020; Zhu et al., 2020; Zhu et al., 2022). A large number of research results show that the gravity time-varying anomaly is one of the reliable precursor anomalies related to earthquake preparation, especially for the seismogenic process of earthquakes with $M_S \geq 6$.

1) Prediction of the Wenchuan M_S8.0 earthquake in Sichuan in 2008 (Zhu et al., 2008a; Zhu et al., 2010).

Prediction basis: The cumulative gravity change in the Sichuan–Yunnan region during 1998–2005 shows that there is a large range of positive gravity change anomaly area in the Sichuan–Yunnan rhombic block and a large range of negative gravity change anomaly area in the Sichuan region in the north of the Sichuan–Yunnan rhombic block. The difference between the two anomaly areas is more than 100 $\times10^{-8}$ ms^{-2}, and a high-gradient zone of gravity change is formed in the Maerkang–Wenchuan–Chengdu area (Figure 2).

Prediction opinion: earthquake occurrence time: 2007–2008; location of the earthquake: 103.7°E, 31.6°N as the center, with a radius of 200 km; magnitude: 6–7.

Results: The M_S8.0 Wenchuan earthquake (103.4°E, 31.0°N) occurred in the prediction area on 12 May 2008. The predicted epicenter was 72 km away from the M_S8.0 Wenchuan earthquake (Figure 2) and between the two extreme earthquake areas of Beichuan and Yingxiu (Figure 3). The time and place were correct, and magnitude 7 was mentioned.

2) Prediction of the Yutian M_S7.3 earthquake in Xinjiang in 2008 (Zhu et al., 2008c; Zhu et al., 2012).

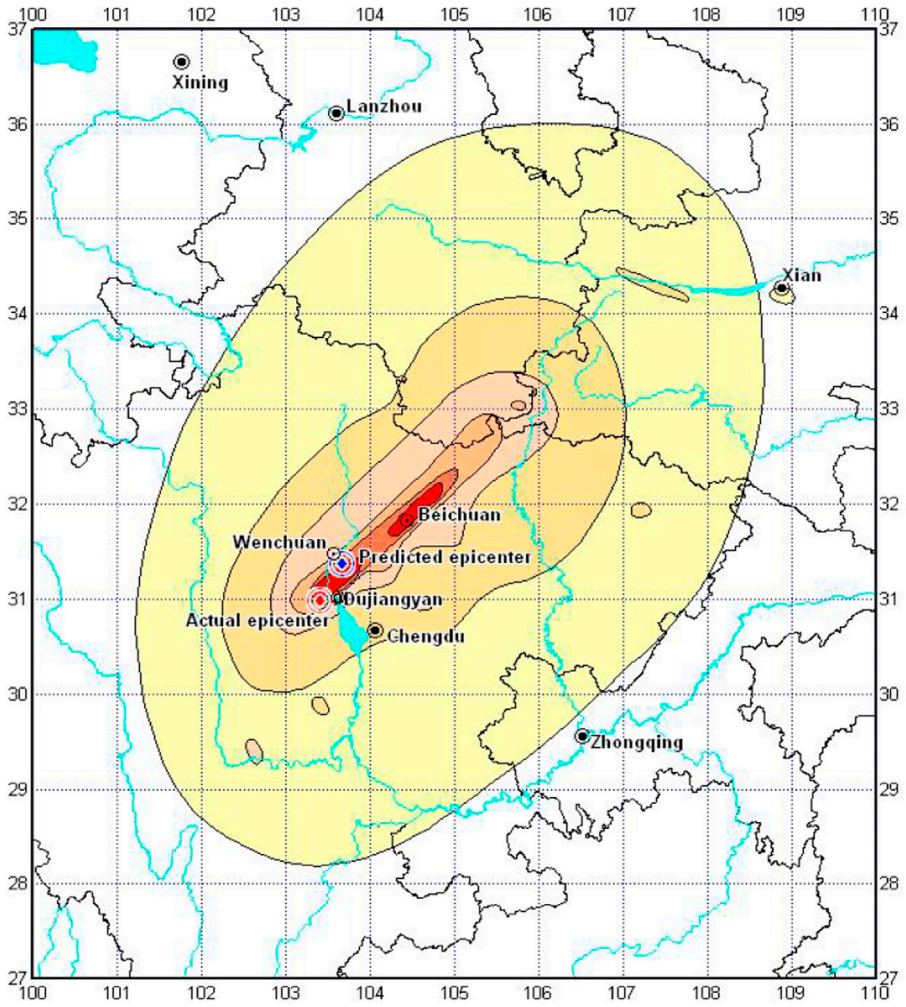

FIGURE 3
Predicted epicenter and earthquake intensity of the Wenchuan Ms 8.0 earthquake.

Prediction basis: The regional gravity change in a long period from 1998 to 2005 shows that there is a significant gravity anomaly in the border area between Xinjiang and Tibet, with the maximum difference of more than 90×10^{-8} ms^{-2}, and a significant gravity gradient zone has been formed along the boundary zone of tectonic blocks in the Yutian–Hetian area of Xinjiang.

Prediction opinion: earthquake occurrence time: 2007–2008; location of the earthquake: 80.0° E, 36.0° N as the center, with a radius of 200 km; magnitude: six to seven.

Results: The Yutian M_S7.3 earthquake (81.6° E, 35.6° N) occurred in the prediction area on 21 March 2008. The predicted epicenter is 149 km away from the Yutian M_S7.3 earthquake, which was very accurate in areas with weak earthquake monitoring ability (the distance between the measuring points in the border area between Xinjiang and Tibet is 100–200 km, and the measuring points are sparse).

After the Wenchuan earthquake in 2008, the Gravity Discipline Management Department of the China Earthquake Administration strengthened the research on gravity monitoring and prediction and actively explored the use of gravity observation data to predict the annual risk of earthquakes, made full use of increasingly abundant gravity observation data, and deeply and carefully studied the dynamic evolution characteristics and laws of regional gravity field on the basis of fine processing of regional gravity network observation data, searched for tectonic activity and earthquake precursor information from the complex and changeable gravity anomaly phenomena, carried out a retrospective study of earthquake cases, tracked and analyzed the regional gravity field anomaly changes and possible medium and short-term anomaly information, and proposed a variety of gravity field change characteristic models with different space–time scales that have prediction significance before strong earthquakes (Zhu et al., 2013; Chen et al., 2015; Zhu et al., 2016; Shen et al., 2020; Zhu et al., 2020). On the basis of strong earthquake prediction methods and judgment indicators, annual prediction and post-earthquake trend determination of seismic risk in key monitoring areas are carried out using the dynamic change data on the gravity field, which has played an important role in the determination of strong earthquake locations in key seismic risk areas in the Chinese Mainland and has achieved a certain degree of effectiveness in disaster reduction. In recent years, we have predicted many earthquakes, such as the Sichuan Lushan M_S7.0 and Gansu Minxian M_S6.6 earthquakes in 2013, the Yunnan Ludian M_S6.5 and Xinjiang Yutian

TABLE 2 Midterm prediction information on strong earthquakes with magnitude 6 or above since 2013 (Zhu et al., 2022).

Predicted epicenter	Predicted magnitude/Ms	Predicted time/ Year	Actual magnitude/Ms	Actual epicenter	Earthquake occurrence time
102.2°E, 30.2°N	About 6	2013	Lushan, Sichuan, 7.0	103.0°E, 30.3°N	2013–04–20
105.2°E, 35.5°N	6–7	2011–2013	Minxian, Gansu, 6.6	104.2°E, 34.5°N	2013–07–22
81.6°E, 35.6°N	About 7	2014	Yutian, Xinjiang, 7.3	82.5°E, 36.1°N	2014–02–12
102.1°E, 28.8°N	About 7	2014	Ludian, Yunnan, 6.5	103.3°E, 27.1°N	2014–08–03
			Kangding, Sichuan, 6.3	101.7°E, 30.3°N	2014–11–22
102.2°E, 37.5°N	About 6	2016	Menyuan, Qinghai, 6.4	101.62°E, 37.68°N	2016–01–21
75.7°E, 39.3°N	6–7	2016	Aketao, Xinjiang, 6.7	74.04°E, 39.27°N	2016–11–25
85.5°E, 43.5°N	About 6	2016	Hutubi, Xinjiang, 6.2	86.35°E, 43.83°N	2016–12–08
101.9°E,34.7°N	6–7	2016–2017	Jiuzhaigou, Sichuan, 7.0	103.82°E, 33.20°N	2017–08–08
75.8°E, 39.6°N	6–7	2020	Jiashi, Xinjang, 6.4	77.21°E, 39.83°N	2020–01–19
100.5°E, 25.8°N	About 6	2020	Yangbi, Yunnan, 6.4	99.87°E, 25.67°N	2021–05–21
101.2°E, 37.8°N	About 6	2021–2022	Menyuan, Qinghai, 6.9	101.26°E, 37.77°N	2022–01–08
102.0°E, 29.6°N	About 7	2021–2022	Luding, Sichuan, 6.8	102.08°E, 29.59°N	2022–09–05

M_S7.3 earthquakes in 2014, the Qinghai Menyuan M_S6.4 earthquake in 2016, the Sichuan Jiuzhaigou M_S7.0 earthquake in 2017, the Xinjiang Jiashi M_S6.4 earthquake in 2020, the Yunnan Yangbi M_S6.4 earthquake in 2021, and the Qinghai Menyuan M_S6.9 earthquake and Sichuan Luding M_S6.8 earthquake in 2022, especially the determination of the location of strong earthquakes. The following table lists the prediction of more than 10 strong earthquakes in the Chinese Mainland since 2013 by gravity observation data in recent years, as shown in Table 2.

As can be seen from Table 2, in recent years, the medium-term prediction of strong earthquakes/large earthquakes with magnitude 6 or above occurred in areas with monitoring ability in the western Chinese Mainland has been made accurately by using mobile gravity data. However, there are also cases of strong earthquakes which were missed, such as the earthquakes with M_S6.9 in Milin, Tibet, on 18 November 2017, and the earthquake with M_S6.6 in Nima, Tibet, on 23 July 2020; all occurred in areas with weak gravity monitoring capability on the Qinghai–Tibet Plateau, so they cannot be effectively monitored.

In general, the mobile gravity observation data can better reflect the gravity anomaly changes in the process of earthquake preparation and occurrence, especially for strong earthquakes with a magnitude of 6 or above. Through timely and careful analysis and research of mobile gravity observation data, it is possible to make more accurate medium-term predictions of future strong earthquakes/large earthquakes, especially the determination of strong earthquake locations. For example, in the prediction of the locations of the Menyuan M_S6.9 and Luding M_S6.8 earthquakes in Qinghai in 2022 (see Table 2), the predicted epicenters of the two earthquakes are less than 10 km away from the epicenter of the earthquake, which is basically the same (Zhu et al., 2022).

4 Problems and prospects

Obtaining reliable earthquake precursor information is the precursor of realizing earthquake prediction. Gravity change measurement is the most precise and difficult work in geodesy at present, and seismic monitoring acquires 10^{-8} ms^{-2} level changes. The observation technology is very important, and data processing is also very critical. At present, the relative gravity measurement under the control of absolute gravity is the main method, so data processing is particularly important. The data processing and analysis should be strengthened to ensure the reliability of the first-hand data. In addition, gravity changes caused by different environmental and physical factors should also be considered, such as environmental changes, groundwater, air pressure, and post-glacial rebound.

4.1 Problems

In China, gravimetry, as a means of studying and predicting earthquakes, has gone through a history of more than 50 years. Through constant exploration and practice, it has gradually recognized and captured the typical gravity variation characteristics related to the preparation and occurrence of strong earthquakes, providing an important basis for the mid-year and annual earthquake trend discussion of the China Earthquake Administration, and it has obtained many successful cases of mid-term prediction (Mao and Zhu, 2018; Shen et al., 2020; Zhu et al., 2022). Before the strong earthquake comes, there are four-quadrant of ascending and descending changes or the gravity gradient zone along the main tectonic belts, and the epicenter is often located in the low-value area of gravity isoline, which is also the successful experience of earthquake research and prediction by gravity monitoring in recent 20 years. Shen et al. (2011) and Shen et al. (2020) put forward the basic criterion for judging large earthquakes and the locking shear model from the point of view of energy accumulation and rupture and considered that tectonic earthquakes originated from the deep crust, and when the stress and strain energy of the medium accumulated to a certain extent, it

would cause shear rupture, resulting in the four-quadrant distribution characteristics of the surface gravity field along the fault tectonic belt. The four-quadrant distribution image of the relative change in the epicenter area reflected the pre-existing shear stress of the seismogenic body, which provided a theoretical basis for earthquake prediction and mechanism explanation. Many researchers have carried out a lot of mathematical statistics and analysis based on the relationship between the anomaly range, magnitude and duration of gravity changes, and strong earthquakes in previous earthquake cases (Jia and Zhan, 2000; Hu et al., 2019; Zhu et al., 2019; Shen et al., 2020; Zhu et al., 2022), which provides methodological experience for earthquake prediction. Although gravity time-varying monitoring has gained successful experience in earthquake monitoring and research in the Chinese Mainland, it is still insufficient to meet the needs of disaster reduction, such as earthquake prediction and prevention, and there are mainly the following problems:

1) The actual monitoring ability of gravity directly determines the ability to study the evolution of the gravity field and its relationship with seismic activity in key areas of the Chinese Mainland. The current monitoring network in the Chinese Mainland is unevenly distributed, and the gravity monitoring points are mainly distributed in the North China and the North-South seismic belt, while being less distributed in the Qinghai–Tibet Plateau and its surrounding areas, with an insufficient spatial and temporal resolution, and the information obtained is incomplete. Therefore, it is still incapable of monitoring strong earthquakes with magnitude 6, and it is impossible to effectively capture the complete precursor information during the preparation and occurrence of strong earthquakes.
2) The calibration and control degree of absolute gravity are relatively low, and the absolute gravity and relative gravity are not measured in a quasi-synchronous manner, which cannot eliminate the system error caused by the calibration of the scale value of the relative gravimeter. The fusion degree of continuous gravity and flowing gravity is relatively low, and the number of micro-drift and high stability instruments represented by superconducting gravimeters is scarce.
3) Time-varying gravity measurement is the most precise and difficult work in current seismic monitoring, and what seismic gravity monitoring obtains is the 10^{-8} ms^{-2} level change. The observation technology is very important, and the timeliness of data processing is also critical. The Chinese Mainland Basic Gravity Network is jointly completed by several ministries and commissions. As a result of the unsynchronized observation, the fieldwork lasts for 5–6 months, or even longer, so it is impossible to timely and effectively integrate all monitoring data. Therefore, the timeliness of data processing is particularly important to ensure the timeliness and reliability of the calculation results.
4) In the study of time-varying gravity, the influence of structure and water is the biggest factor that causes the change of ground gravity. How to deduct the influence of surface ice and snow, lakes, and groundwater on the change of gravity and effectively extract the signal reflecting the change of structure and dynamics is an urgent task.
5) In terms of in-depth understanding of the characteristics of gravity field changes before earthquakes, some models such as mass migration, density change, fault dislocation and creep, joint expansion, and locking shear force have been put forward successively, and some progress has been made in revealing the physical mechanism of gravity field changes. However, earthquake prediction is an international scientific problem, so we should actively carry out international cooperation and vigorously develop strong earthquake numerical prediction and application research based on various gravity observation data through a large number of anatomical studies of earthquake cases.

4.2 Outlook

Among all kinds of natural disasters, earthquake is the one that has the most serious impact on human life. It is conceivable that it is very important for the benefit of mankind to accurately predict when and where a big earthquake will occur through earthquake monitoring and prediction. However, it is very difficult to predict earthquakes. Earthquake prediction has always been recognized as a scientific problem in the world, and its mechanism is extremely complex, but it is not completely unknown. The occurrence of earthquakes is the deformation process of underground tectonic movement from slow to fast. The question is whether it can be observed and recorded, and even if it is observed, whether it can be identified (Ma, 2016).

In recent years, thanks to the continuous optimization and improvement of the Chinese mainland Seismic Gravity Observation Network, mobile gravity plays an increasingly important role, and many successful cases of medium-term predictions have been obtained. However, at present, there are few absolute gravimeters, and there is a certain zero drift in relative gravimeters, which greatly reduces the efficiency of ground flow observation data. Therefore, in the long run, we should develop high-precision absolute gravity observation technology to replace relative gravity observation technology. Low-altitude satellite gravity observation technology should be developed to make up for the deficiency of ground gravity observation technology (Zhu et al., 2020). In the future, with the progress of observation technology and the enhancement of spatial–temporal monitoring resolution of the gravity field, based on the fusion of multi-source gravity observation data and the further study of the relationship between gravity anomaly and seismic activity, the role of time-varying gravity in earthquake prediction and research will become increasingly significant.

Author contributions

YZ and XY both contributed to topic selection, writing, and editing of the manuscript. FL contributed to the discussion section, and review and editing of the manuscript. YZ and SW contributed to data processing, and review and editing of the manuscript. GZ contributed to drawing, review, and editing of the manuscript.

Funding

This research was funded by the National Natural Science Foundation of China (No.41874092, No.U1939205). The authors express their appreciation to the National Natural Science Foundation of China (No.41874092, No.U1939205) for the financial support of this work.

Conflict of interest

The authors declare that the research was conducted in the absence of any commercial or financial relationships that could be construed as a potential conflict of interest.

Publisher's note

References

Barnes, D. F. (1966). Gravity changes during the Alaska earthquake. *J. Geophys. Res.* 71 (2), 451–456. doi:10.1029/jz071i002p00451

Chen, S., Liu, M., Xing, L. L., Xu, W., Wang, W., Zhu, Y., et al. (2016). Gravity increase before the 2015 M_W7.8 Nepal earthquake[J]. *Geophys. Res. Lett.* 43, 111–117. doi:10.1002/2015gl066595

Chen, S., Xu, W. M., and Jiang, C. S. (2015). Relationship between gravity variation and seismic hazards in the Western China[J]. *Acta Seismol. Sin.* 37 (4), 575–587. (in Chinese). doi:10.11939/jass.2015.04.005

Chen, Y. T., Gu, H. D., and Lu, Z. X. (1979). Variations of gravity before and after the Haicheng earthquake, 1975, and the Tangshan earthquake, 1976. *Phys. Earth Planet. Interiors* 18, 330–338. doi:10.1016/0031-9201(79)90070-0

Fu, G. Y., and Liu, T. (2017). A user-friendly code for Calculating post-seismic displacements and gravity changes on a symmetric viscoelastic spherical Earth[J]. *J. Geodesy Geodyn.* 37 (7), 661–667. (in Chinese). doi:10.14075/j.jgg.2017.07.001

Fu, G. Y., and Wang, Z. Y. (2020). Crustal structure, isostatic anomaly and flexure mechanism around the Jinghe Ms6.6 earthquake in Xinjiang[J]. *J. Geophys.* 63 (6), 2221–2229. (in Chinese).

Gu, G. X., Kuo, J. T., and Liu, K. R. (1997). Seismogenesis and occurrence of earthquakes as observed by temporally continuous gravity variations in China[J]. *Chin. Sci. Bull.* 42 (18), 1919–1930.

Hao, H. T., Li, H., Hu, M. Z., and Zhu, Y. Q. (2015). Gravity variation observed by scientific expedition of Lushan earthquake[J]. *J. Geodesy Geodyn.* 35 (2), 331–335. (in Chinese). doi:10.14075/j.jgg.2015.02.035

Hu, M. Z., Hao, H. T., and Han, Y. F. (2021). Gravity flexural isostasy background of the 2021 Maduo(Qinghai)Ms7.4 earthquake and gravity change before the earthquake[J]. *J. Geophys.* 64 (9), 3135–3149. (in Chinese). doi:10.6038/cjg2021O0527

Hu, M. Z., Hao, H. T., and Li, H. (2019). Quantitative analysis of gravity changes for earthquake prediction[J]. *Earthq. Res. China* 35 (3), 417–430. (in Chinese).

Hu, M. Z., Li, H., and Liu, Z. X. (2015). The gravity change over Sichuan-Yunnan region in 2010-2013 and the earthquake monitoring ability of the gravimetric network[J]. *J. Geodesy Geodyn.* 35 (4), 616–620. (in Chinese). doi:10.14075/j.jgg.2015.04.016

Jia, M. Y., Xing, C. F., and Sun, S. A. (1995). Two dimensional image of gravity variation in Western Yunnan and its relationship with earthquakes above magnitude 5 (M_S)[J]. *Crustal Deformation Earthquakes* 15 (3), 9–19. (in Chinese).

Jia, M. Y., and Zhan, J. H. (2000). The structure and ability of the China seismological gravity monitoring system[J]. *Acta Seismol. Sin.* 22 (4), 360–367. (in Chinese). doi:10.3321/j.issn:0253-3782.2000.04.004

Jiang, Z. S., Ren, J. W., and Li, Z. X. (2005). Strategic countermeasures for promoting earthquake prediction research[J]. *Recent Dev. World Seismol.* 35 (5), 168–173. (in Chinese).

Jiang, Z. S., Zhang, X., and Zhu, Y. Q. (2003). Regional tectonic deformation background before the MS8.1 earthquake in the west of the Kunlun Mountains Pass[J]. *Sci. China (Series D)* 33 (S1), 163–172. (in Chinese). doi:10.3969/j.issn.1674-7240.2003.z1.018

Jiang, Z. S., Zhu, Y. Q., and Wang, Q. L. (1998). On fault deformation and geodynamic characteristics during seismogenic progress of Yongdeng M_W5.8 earthquake[J]. *Acta Seismol. Sin.* 20, 264–271. doi:10.1088/0256-307X/16/9/027

Li, H., Shen, C. Y., and Sun, S. A. (2009). Dynamic gravity change in recent years in China continent[J]. *J. Geodesy Geodyn.* 29 (3), 1–10. (in Chinese). doi:10.3969/j.issn.1671-5942.2009.03.001

Li, H., Xu, R. G., and Shen, C. Y. (2010). Fractal characteristics of seismological dynamic gravity network in northern China. *JJ J. Geodesy Geodyn.* 30 (5), 15–18. (in Chinese). doi:10.3969/j.issn.1671-5942.2010.05.003

Li, Q. L., and Qin, J. Z. (2001). Variation of gravity field and deep dynamic process before and after Datong M_S5.6 earthquake [J]. *Crustal Deformation Earthq.* 21 (4), 43–51. (in Chinese). doi:10.3969/j.issn.1671-5942.2001.04.006

Li, R. H., and Fu, Z. (1983). The gravity changes before and after the Tangshan earthquake (M=7.8) and dilatation process[J]. *Tectonophysics* 97, 159–169. doi:10.1016/0040-1951(83)90143-9

Li, R. H., Huang, J. L., and Li, H. (1997). The mechanism of gravity changes before and after the Tangshan earthquake[J]. *Acta Seismol. Sin.* 19, 399–407. (in Chinese).

Liu, C. H. (1997). Temporal variation of gravity field in northeast Anhui and the junction of Anhui and Jiangsu before cangshan M_S5.2 earthquake[J]. *Crustal Deformation Earthq.* 17 (1), 109–111. (in Chinese).

Lu, H. Y., Zheng, J. H., and Liu, D. F. (2004). Gravity variation in beijing Tianjin tangzhang area from 1985 to 2003[J]. *Prog. Geophys.* 19 (4), 887–892. (in Chinese).

Lu, Z. X., Fang, C. L., and Shi, Z. T. (1978). Variation of the gravity field and the Haicheng earthquake[J]. *Chin. J. Geophys.* 21 (1), 1–8. (in Chinese).

Ma, J. (2016). On “whether earthquake precursors help for prediction do exist”. *Chin. Sci. Bull.* 61 (Z1), 409–414. (in Chinese). doi:10.1360/n972015-01239

Mao, J. L., and Zhu, Y. Q. (2018). Progress in the application of ground gravity observation data in earthquake prediction[J]. *Adv. Earth Sci.* 33 (3), 236–247. (in Chinese).

Shen, C. Y., Li, H., and Fu, G. Y. (2003). Study on a gravity precursor sormode of Lijiang earthquake with M_S=7.0[J]. *Acta Seismol. Ainica* 25 (2), 163–171. (in Chinese).

Shen, C. Y., Li, H., and Sun, S. A. (2009). Dynamic variations of gravity and the preparation process of the Wenchuan M_S8.0 earthquake[J]. *Chin. J. Geophys.* 52 (10), 2547–2557. (in Chinese). doi:10.3969/j.issn.0001-5733.2009.10.013

Shen, C. Y., Tan, H. B., and Hao, H. T. (2011). Mechanism of precursory gravity change before Yaoan M_S6.0 earthquake in 2009[J]. *J. Geodesy Geodyn.* 31 (2), 17–47. (in Chinese). doi:10.3969/j.issn.1671-5942.2011.02.005

Shen, C. Y., Xing, L. L., and Tan, H. B. (2012). The absolute gravity change in the eastern margin of the Qinghai-Tibetan Plateau before and after Yushu M_S7.1 earthquake in 2010 [J]. *Prog. Geophys.* 27 (6), 2348–2357. (in Chinese). doi:10.6038/j.issn.1004-2903.2012.06.010

Shen, C. Y., Zhu, Y. Q., and Hu, M. Z. (2020). Monitoring of gravity field time variation and prediction of strong earthquakes in Chinese mainland[J]. *Earthq. Res. China* 36 (4), 729–743. (in Chinese).

Walsh, J. B. (1975). An analysis of local changes in gravity due to deformation. *Pure Appl. Geophys.* 113, 97–106. doi:10.1007/bf01592902

Wang, Y., Zhang, W. M., and Zhan, J. G. (2004). Gravity change detected by repeated absolute gravity measurements in the Western Yunnan and Lhasa China and its implication[J]. *Chin. J. Geophys.* 47 (1), 95–100. (in Chinese). doi:10.3321/j.issn:0001-5733.2004.01.014

Wei, S. C., Zhu, Y. Q., and Zhao, Y. F. (2020). Study on characteristics of gravity variation before and after Hutubi M_S6.2 earthquake[J]. *Seismol. Geol.* 42 (4), 923–935. (in Chinese). doi:10.3969/j.issn.0253-4967.2020.04.010

Wu, G. H., Luo, Z. X., and Lai, Q. (1998). Gravity variation of West Yunnan test site before the M_S7.3 earthquake on the China Myanmar border in Menglian, Yunnan[J]. *Earthquake* 18 (2), 146–154. (in Chinese).

Wu, G. H., Luo, Z. X., and Lai, Q. (1995). Lancang Gengma earthquake in 1988 and gravity variation at the test site in Western Yunnan[J]. *Crustal Deformation Earthquakes* 15 (2), 66–73. (in Chinese).

Wu, G. H., Luo, Z. X., and Lai, Q. (1997). Variation characteristics of gravity anomaly in West Yunnan test site before and after Lijiang M_S7.0 earthquake[J]. *Earthq. Res.* 20 (1), 101–107. (in Chinese).

Xing, L. L., Li, H., and Li, J. G. (2016). Establishment of absolute gravity datum in CMONOC and its application[J]. *Acta Geod. Cartogr. Sinica* 45 (5), 538–543.

Zhang, J., and Sun, B. C. (2001). Discussion on gravity anomaly and anomaly mechanism before Zhangbei M_S6.2 earthquake[J]. *Earthquake* 21 (2), 75–78. (in Chinese). doi:10.3969/j.issn.1000-3274.2001.02.012

Zhang, P. Z., Deng, Q. D., and Zhang, Z. Q. (2013). Active fault, earthquake hazards and associated geodynamic processes in continental China [J]. *Scientia Sinica Terrae* 43 (10), 1607–1620. (in Chinese).

Zhang, Y. Z., and Zhang, K. S. (2000). The gravity variation during the breaking process in Earth crust[J]. *Crustal Deformation Earthq.* 20 (1), 8–16. (in Chinese). doi:10.3969/j.issn.1671-5942.2000.01.002

Zhou, S. Y., Wu, Y., and Jiang, Z. S. (2017). Earthquake geodesy and earthquake prediction: Progress, Innovations and problems over fifty years[J]. *J. Geodesy Geodyn.* 37 (6), 551–562. (in Chinese). doi:10.14075/j.jgg.2017.06.001

Zhu, Y. Q., Chen, B., and Zhang, X. (2001). Study of the gravity changes before and after the Jingtai M_S5.9 earthquake[J]. *Earthq. Res. China* 17 (4), 356–363. (in Chinese). doi:10.3969/j.issn.1001-4683.2001.04.004

Zhu, Y. Q., Fu, G. Y., and Liang, W. F. (2015b). Spatial-temporal gravity changes before the ludian M_S6.5, lushan M_S7.0 and wenchuan M_S8.0 earthquakes[J]. *Seismol. Geol.* 37 (1), 319–330. (in Chinese). doi:10.3969/j.issn.0253-4967.2015.25

Zhu, Y. Q., Hu, B., and Zhu, G. Z. (2005). Research on the variation of gravity field before Minle M_S6.1 and Minxian M_S5.2 earthquakes[J]. *J. Geodesy Geodyn.* 25 (1), 24–29. (in Chinese). doi:10.3969/j.issn.1671-5942.2005.01.005

Zhu, Y. Q., Li, H., and Zhu, G. Z. (2004). Gravity evolution and earthquake actives of the northeastern edge of Qinghai-Xizang block[J]. *Acta Seismol. Sin.* 26 (S1), 71–78. (in Chinese).

Zhu, Y. Q., Li, T., and Hao, M. (2016). Gravity changes before the menyuan, Qinghai M_S6.4 earthquake of 2016[J]. *Chin. J. Geophys.* 59 (10), 3744–3752. (in Chinese).

Zhu, Y. Q., Liang, W. F., and Xu, Y. M. (2008a). Medium-term prediction of M_S8.0 earthquake in Wenchuan, Sichuan by mobile gravity[J]. *Recent Dev. World Seismol.* 38 (7), 36–39. (in Chinese).

Zhu, Y. Q., Liang, W. F., and Zhan, F. B. (2012). Study on dynamic change of gravity field in China continent[J]. *Chin. J. Geophys.* 55 (3), 804–813. (in Chinese).

Zhu, Y. Q., Liang, W. F., and Zhang, S. (2018). Earthquake precursors: Spatial-temporal gravity changes before the great earthquakes in the sichuan-yunnan area. *J. Seismol.* 22 (1), 217–227. doi:10.1007/s10950-017-9700-2

Zhu, Y. Q., Liang, W. F., and Zhao, Y. F. (2017). Gravity changes before the Jiuzhaigou, sichuan, M_S7.0 earthquake of 2017[J]. *Chin. J. Geophys.* 60, 4124–4131. (in Chinese). doi:10.ssss/j.issn.0001-5733.2017.10.036

Zhu, Y. Q., Liu, F., and Li, T. M. (2015a). Dynamic variation of the gravity field in the Sichuan-Yunnan region and its implication for seismic risk[J]. *Chin. J. Geophys.* 58 (11), 4187–4196. (in Chinese). doi:10.6038/cjg20151125

Zhu, Y. Q., Liu, F., and Zhang, G. Q. (2022). Mobile gravity monitoring and earthquake prediction in China[J]. *Geomatics Inf. Sci. Wuhan Univ.* 47 (6), 820–829. (in Chinese). doi:10.13203/j.whugis20220127

Zhu, Y. Q., Liu, F., Zhang, G. Q., and Xu, Y. M. (2019). Development and prospect of mobile gravity monitoring and earthquake forecasting in recent ten years in China. *Geodesy Geodyn.* 10 (6), 485–491. doi:10.1016/j.geog.2019.05.006

Zhu, Y. Q., Wang, Q. L., and Xu, Y. M. (2008b). Thoughts on the development of earthquake monitoring and prediction in mobile gravity[J]. *Recent Dev. World Seismol.* 38 (9), 19–25. (in Chinese). doi:10.3969/j.issn.0253-4975.2008.09.004

Zhu, Y. Q., Wen, X. Z., and Sun, H. P. (2013). Gravity changes before the lushan, sichuan, M_S=7.0 earthquake of 2013[J]. *Chin. J. Geophys.* 56 (6), 1887–1894. (in Chinese). doi:10.6038/cjg20130611

Zhu, Y. Q., Xu, Y. M., and Liang, W. F. (2008c). Medium-term prediction of yutian, Xinjiang M_S7.3 earthquake in 2008[J]. *J. Geodesy Geodyn.* 28 (5), 13–15. (in Chinese). doi:10.3969/j.issn.1671-5942.2008.05.003

Zhu, Y. Q., Xu, Y. M., and Lü, Y. P. (2009). Relations between gravity variation of Longmenshan fault zone and Wenchuan M_S8.0 earthquake[J]. *Chin. J. Geophys.* 2 (10), 2538–2546. (in Chinese). doi:10.3969/j.issn.0001-5733.2009.10.012

Zhu, Y. Q., Zhan, F. B., Zhou, J. C., Liang, W., and Xu, Y. (2010). Gravity measurements and their variations before the 2008 wenchuan earthquake. *Bull. Seismol. Soc. Am.* 100, 2815–2824. doi:10.1785/0120100081

Zhu, Y. Q., Zhang, Y., Zhang, G. Q., Liu, F., and Zhao, Y. (2020). Gravity variations preceding the large earthquakes in the Qinghai-Tibet Plateau from 21st century. *Chin. Sci. Bull.* 65 (7), 622–632. (in Chinese). doi:10.1360/tb-2019-0153

Zhu, Y. Q., Zhao, Y. F., and Li, T. M. (2014). Dynamic variation of gravity field before and after the Minxian-Zhangxian M_S6.6 earthquake on July 22, 2013, Gansu, China[J]. *Seismol. Geol.* 36 (3), 667–376. (in Chinese). doi:10.3969/j.issn.0253-4967.2014.03.010

frontiers | Frontiers in Earth Science

TYPE Original Research
PUBLISHED 05 May 2023
DOI 10.3389/feart.2023.1162187

OPEN ACCESS

EDITED BY
Henglei Zhang,
China University of Geosciences Wuhan, China

REVIEWED BY
Luan Thanh Pham,
VNU University of Science, Vietnam
Ahmed M. Eldosouky,
Suez University, Egypt

*CORRESPONDENCE
Xiangzhi Zeng,
zengxiangzhi01@126.com

RECEIVED 09 February 2023
ACCEPTED 11 April 2023
PUBLISHED 05 May 2023

CITATION
Sun Y, Zeng X, Yang W, Li X, Zhang W and Zhang X (2023), Mapping structural lineaments using the edge filters of the potential field: a case study of the Rizhao–Lianyungang area, East China. *Front. Earth Sci.* 11:1162187. doi: 10.3389/feart.2023.1162187

Mapping structural lineaments using the edge filters of the potential field: a case study of the Rizhao–Lianyungang area, East China

Yanyun Sun[1], Xiangzhi Zeng[2]*, Wencai Yang[3], Xiao Li[1], Wan Zhang[1] and Xuanjie Zhang[1]

[1]China Aero Geophysical Survey & Remote Sensing Center for Natural Resources, Beijing, China, [2]Donghai Crustal Activity in Continental Deep Hole National Observation and Research Station, Jiangsu, China, [3]School of Earth Sciences, Zhejiang University, Zhejiang, China

Background: Edge enhancement plays an important role in potential field data processing and interpretation, which facilitate regional tectonic studies, mineral and energy exploration. This is because edges on potential field often indicate linear geological structures such as fractures, edges of geological bodies and so on. With the development of meticulous edge enhancement on potential field, the phenomenon of false edges caused by the associated anomalies when detect ing edges from magnetic field cannot be ignored.

Methods: Aiming at this problem, we proposes a modified magnetic edge detection method (SP Mag) based on the second order spectral moment. This method has been tested on both synthetic and field data. The synthetic test show that SP Mag cannot only balanced edges no matter from strong or weak anomalies, but also eliminates those false edges caused by the associated anomalies in magnetic field, which provide more effective information for subsequent interpretation.

Results: We apply this new method to the RTP aero magnetic field and gravity field of Rizhao Lianyungang area. The lineaments recognized by the SP Mag method correspond well with geologic structures through comparing with geological maps.

Discussion: The results illustrate the usefulness of the method for potential field interpretation. Furthermore, more geological and geophysical data should be still combined for comprehensive interpretation in the actual interpretation, though the SP Mag method can recognize lineaments effectively.

KEYWORDS

magnetic field, edge enhancement, the second-order spectral moment, false edges, faults

1 Introduction

Edges detected from the potential field often correspond to geological linear structures such as faults, geological contracts, and sources' boundaries, which can play an important role in geotectonic research, energy and mineral exploration, etc. Therefore, developing many edge-enhancing methods is highly desired. Edge enhancement in the early stage is mainly based on horizontal and vertical derivatives. For example, these high-pass filters include vertical derivatives (Evjen, 1936), horizontal gradient (HGA) (Cordell, 1979; Fedi and Florio, 2001), fitting paraboloid on the horizontal gradient (Blakely and Simpson, 1986), and analytic signal methods (Nabighian, 1972; Roest, 1992; Hu et al., 1995; Guan and Yao, 1997). As is known, methods based on horizontal and vertical derivatives often detect boundaries of sources with lager amplitude well but not very effective for edges of small-amplitude sources (Sun et al., 2016a). Therefore, the tilt angle method (Miller and Singh, 1994) was proposed to balance different amplitude anomalies, which was the first balanced filter. However, it is not an edge-detection method. Then, the balanced edge-enhancing methods emerge endlessly, such as the total horizontal derivative of the tilt angle (Verduzco et al., 2004), theta map (Wijins et al., 2005), calculating the tilt angle on the total horizontal derivative (Francisco et al., 2013), and the curvature of the total horizontal gradient amplitude (Hansen and de Ridder, 2006; Phillips et al., 2007). In order to detect more details but with less noise interference, numerous excellent edge-enhancing filters are proposed (Cooper and Cowan, 2008; Cooper, 2009; Cooper and Cowan, 2011; Wang et al., 2013), for example, the normalized standard deviation (NSTD), the orthogonal Hilbert transforms of analytic signal amplitudes, and the generalized derivative operator. On the basis of NSTD, the normalized anisotropy variance method was developed by Zhang et al. (2014) to recognize linear structures and meanwhile suppress noise. Ma et al. (2012) proposed balancing filters and enhanced local-phase filters to detect edges, which showed higher resolution and less sensitivity to noise than the theta map method. Hu et al. (2019) presented the normalized facet edge-detection method to enhance weak and noisy signals produced by shallow and deep mass anomalies. Pham et al. (2020a), Pham et al. (2020b), and Pham et al. (2021) proposed some excellent filters, of which the application for interpreting geological structures showed that it can balance edges from both strong and weak anomalies avoiding producing the spurious edges (Pham et al., 2021; Eldosouky et al., 2022). For example, the method based on an arcsine function uses the ratio of the vertical gradient to the total gradient of the amplitude of the horizontal gradient field (EHGA) (Pham et al., 2020b), the improved logistic (IL) filter (Pham et al., 2020a), and the enhanced total gradient (ETG) method (Prasad et al., 2022).

Our previous work has proposed an edge-enhancing method based on the second-order spectral moment (SP-Gra for short) on the potential field (Sun et al., 2016a). Both synthetic data and real data experiments show that it has strong ability on weak boundary enhancing and spatial discrimination. With the deepening of research, we find that many "false edges" are also outlined, producing false information for the following interpretation. This is because the relationship between magnetic anomaly and susceptibility is much more complicated than the positive correlation between gravity anomaly and density. The center of a perpendicularly magnetized magnetic anomaly is generally positive to the magnetic susceptibility, but there often exist associated anomalies opposite to magnetic susceptibility anomalies (Figures 2B, C). If we apply the SP-Gra method, both the main boundaries of anomalies and associated anomalies can be detected simultaneously. In addition, the boundaries of the associated anomaly are the "false edges." In fact, in addition to the SP-Gra method, many edge-enhancing methods (e.g., NSTD method) also outline the "false edges," and the stronger the edge-enhancing ability is, the more obvious the "false edges" detected are. If these "false edges" caused by associated anomalies are not eliminated, false information will be provided for later geological interpretation.

In this paper, we propose a modified magnetic edge-detection method on the basis of Poisson's formula aiming at edge detection from the magnetic field, which is named the SP-Mag method. It can balance the boundaries of sources with both high and low amplitudes well and then the recognized boundaries when detecting edges from the magnetic field. Furthermore, it can also eliminate false edges produced by the associated anomalies, meanwhile providing more accurate information for the later geological interpretation.

2 Magnetic edge enhancements using the second-order spectral moment

2.1 The gradient norm of the pseudo-gravity field

Geophysical potential fields include gravity and magnetic fields, but they show different features (Zeng et al., 2018). As is well known, there is a more complicated relationship between magnetic field and magnetic susceptibility than that between gravity field and density. In addition, the magnetic field can be mathematically related to the pseudo-gravity through Poisson's formula (Zeng et al., 2018), which is

$$U = k \cdot \nabla V. \tag{1}$$

Here, $k = -\frac{M}{4\pi G\rho}$, where k is a constant, M is the geomagnetic field intensity, and ρ is the equivalent density difference; U is the magnetic potential; and V is the pseudo-gravity potential field.

From Eq. 1, the magnetic scalar potential field that is vertically magnetized equals to the pseudo-gravity field

$$U_{\perp} = k \cdot \frac{\partial V}{\partial z} = k \cdot g, \tag{2}$$

where g is the pseudo-gravity field.

$$\begin{cases} k\dfrac{\partial g}{\partial x} = \dfrac{\partial U_{\perp}}{\partial x} = Hax_{\perp}, \\ k\dfrac{\partial g}{\partial y} = \dfrac{\partial U_{\perp}}{\partial y} = Hay_{\perp}. \end{cases} \tag{3}$$

The total horizontal derivative of g is defined as

$$B = |k|\sqrt{\left(\partial_x g\right)^2 + \left(\partial_y g\right)^2} = \sqrt{Hax_{\perp}{}^2 + Hay_{\perp}{}^2}. \tag{4}$$

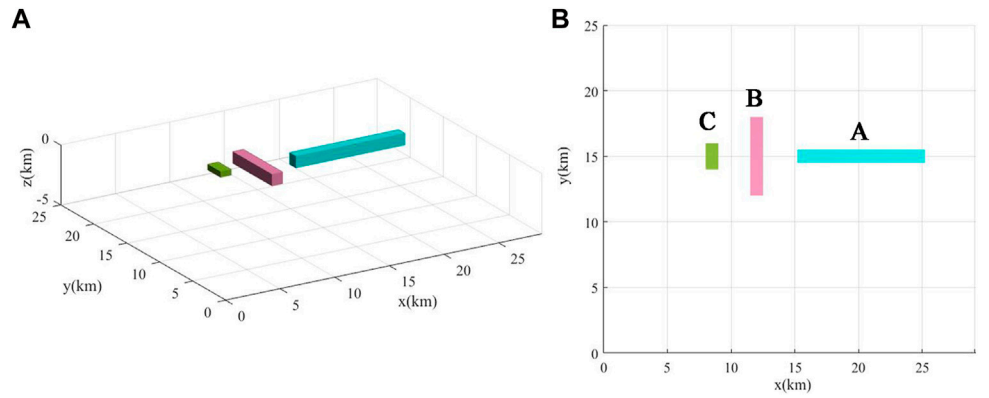

FIGURE 1
3D view **(A)** and top view **(B)** of the first simple magnetic model.

From this formula 1, one can see that the ridges of $B(x, y, z = z_0)$ correspond to the edges of $g(x, y, z = z_0)$. In addition, we use the idea of the pseudo-gravity field, but there is no need to calculate it at all. Instead, we calculate two horizontal components, *Hax* and *Hay*, of the magnetic anomaly.

2.2 The edge coefficient

According to random process theory (Thomas, 1982), the (p + q)th order discrete spectral moment of a surface is (Sun et al., 2016a; Sun et al., 2016b)

$$m_{pq} = \sum_{v=1}^{n}\sum_{u=1}^{m} G(f_u, f_v) f_u{}^p f_v{}^q \Delta f_u \Delta f_v, \tag{5}$$

where $G(f_u,f_v)$ represents the two-dimensional power spectral density; f_u and f_v represent the discrete x- and y-directional spatial frequencies, respectively; and m and n are the sizes of the surface.

When sliding a moving window (w_1) point by point on the surface B, the three elements' spatial expressions of the second spectral moment of the small windowed surface can be calculated by the derived formula (Yang et al., 2015; Sun et al., 2016b; Yang and Sun, 2016; Yang et al., 2017; Sun et al., 2022), which are

$$\begin{cases} m_{20} = \sum_{i=1}^{N_\alpha}\sum_{j=1}^{M_\alpha}\left(\partial_x B(x_j, y_i)\right)^2, \\ m_{02} = \sum_{i=1}^{N_\alpha}\sum_{j=1}^{M_\alpha}\left(\partial_y B(x_j, y_i)\right)^2, \\ m_{11} = \sum_{i=1}^{N_\alpha}\sum_{j=1}^{M_\alpha}\partial_x B(x_j, y_i)\partial_y B(x_j, y_i), \end{cases} \tag{6}$$

where $B(x_j, y_i)$ is the total horizontal derivative of pseudo-gravity within the sliding window w_1; $i = 1,2, \ldots N_\alpha$; $j = 1,2, \ldots M_\alpha$.

From Eq. 6, one can see that if the coordinates rotate, the spectral moments will change. Therefore, one can define the statistically invariable quantities (M_2 and $\triangle_2$) independent of the system rotation, which are (Sun et al., 2016a, Yang et al., 1992; Huang, 1985; Thomas, 1982)

$$M_2 = m_{20} + m_{02}, \tag{7}$$

$$\Delta_2 = m_{20}m_{02} - m_{11}^2. \tag{8}$$

Here, M_2 represents the variance of the two-dimensional slope of B in the window w_1, showing the edges' magnitudes. $\triangle_2$ indicates the anisotropy of surface B in the window w_1.

In order to bring more details of small anomalies, the edge coefficient is defined as (Sun et al., 2016a; Li et al., 2000)

$$\Lambda = -sign(\nabla^2 B) \cdot \frac{2\sqrt{\Delta_2}}{M_2}. \tag{9}$$

Here, ∇^2 is the Laplacian operator. $\frac{\sqrt{\Delta_2}}{M_2}$ increases sharply near the maximum or minimum values of the scalar field B. When $\nabla^2 B > 0$, they correspond to the minimum values (valleys); when $\nabla^2 B < 0$, they correspond to the maximum values (ridges). From the aforementioned analysis, the ridges of B (x, y, z=z_0) correspond to the edges of g (x, y, $z = z_0$). Therefore, values of Λ>0 reflect the anisotropy of surface B (x, y, $z = z_0$) or edges of the surface of the pseudo-gravity field g (x, y, $z = z_0$).

The key of the SP-Mag method to eliminate false edges caused by the associated anomalies is that we define the variable B (formula 4) and modify the integral kernel by the variable B of m_{02}, m_{11}, and m_{20} which are the most basic elements of the second-order spectral moment. This also shows the difference between the SP-Mag and SP-Gra (Sun et al., 2016a) methods. Furthermore, though we use the Poisson formula to derive and construct B, there is no need to calculate the pseudo-gravity field at all, which can avoid losing details caused by truncation errors.

3 Tests on synthetic data

We test the proposed SP-Mag method on two synthetic magnetic datasets without and with noise. Figures 1A, B display the 3D and ground view of the first simple model that consists of three prisms. The plan view of the model consisting of three cuboids A, B, and C is shown in Figure 2A. Cuboid A is with the size of 10 km × 1 km × 2 km and with a buried depth of 1.5 km; cuboid B is

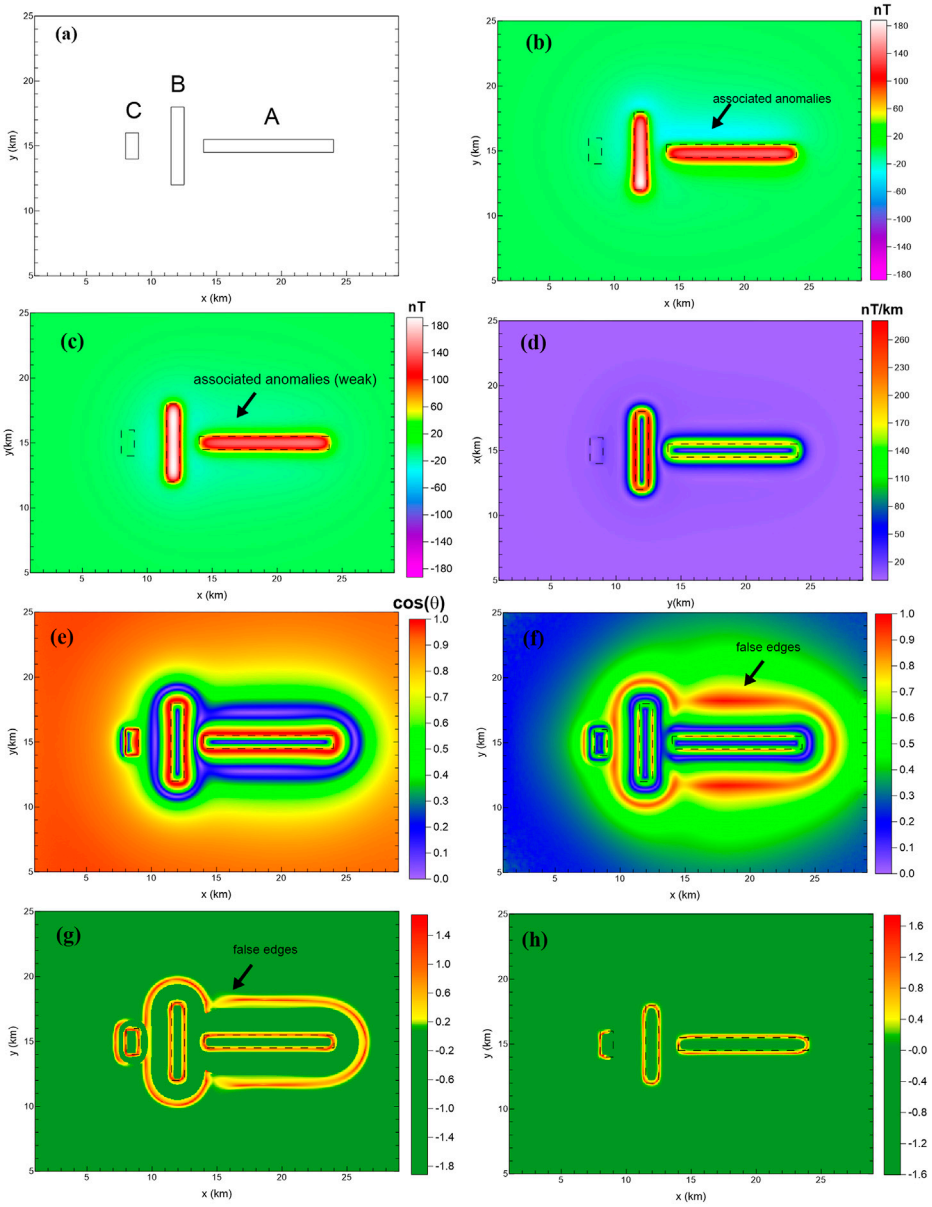

FIGURE 2
Comparison of the edge-enhancing methods. **(A)** Plane graph of the model; **(B)** synthetic magnetic anomaly of the model in Figure 1; **(C)** RTP magnetic anomaly; edge-detection results outlined from the RTP magnetic anomaly using **(D)** HGA; **(E)** theta map; **(G)** SP-Gra; and **(H)** SP-Mag.

with the size of 1 km × 6 km × 1 km and with a buried depth of 1 km; and cuboid C is with the size of 1 km × 2 km × 0.5 km and with a buried depth of 0.5 km. The magnetic intensities of cuboids A, B, and C are 0.6, 1, and 0.02 A/m, respectively. We compute the synthetic data on a grid of 20 km × 25 km with 0.05-km spacing.

The magnetic anomalies are calculated by the 3D forward modeling algorithm (Guan, 2005), and Figure 2Bshows the magnetic anomaly under oblique magnetization with the declination of 0° and inclination of 60°. There are two kinds of anomalies: the strong positive anomalies and the weaker negative anomalies. In addition, the weaker negative anomaly is the associated anomaly (indicated by the black arrow). The RTP (reduced to the pole) magnetic anomaly is shown in Figure 2C. Compared to Figure 2B, the RTP magnetic anomaly can not only reduce the positional deviation between the magnetic source and magnetic anomaly caused by the oblique magnetization but also suppress the associated anomalies. However, from Figure 2C, one can also see that the RTP magnetic anomaly can suppress associated anomalies but cannot eliminate them (indicated by the arrow in Figure 2C).

For comparison, we present edge-detection results outlined from the RTP magnetic anomaly (Figure 2C) using HGA, theta map, NSTD, and SP-Gra (Figures 2D–G, respectively). The HGA method (Figure 2D) can effectively identify the edges of prisms A and B with strong anomalies, while the boundary of prism C with the weaker anomaly has not been effectively identified. The theta map,

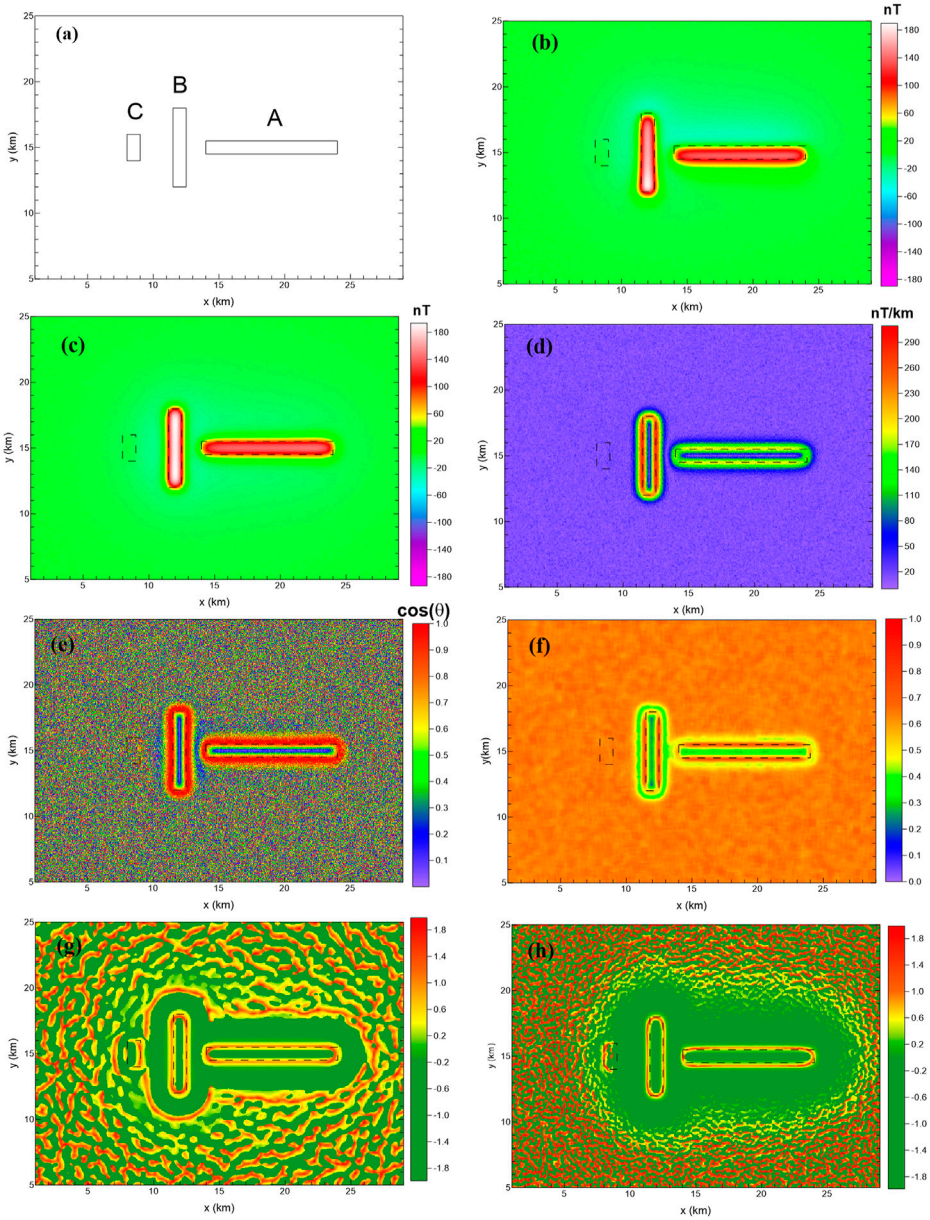

FIGURE 3
Edges detected by the methods. **(A)** Plane graph of the model; **(B)** synthetic magnetic anomaly, with an added noise of amplitude 0.5% of the maximum data magnitude; **(C)** RTP magnetic anomaly with noise; edge-detection results outlined from the RTP magnetic anomaly with noise using **(D)** HGA; **(E)** theta map; **(F)** NSTD; **(G)** SP-Gra; and **(H)** SP-Mag.

NSTD, and SP-Gra methods have strong ability to enhance the weak boundary, so the boundaries of prisms A, B, and C are all well recognized. However, as the methods' ability to enhance the weak boundary becomes stronger, the false boundaries (pointed by the arrow) caused by the associated anomaly gradually become prominent, which could interfere with the final interpretation.

Figure 2H shows the edges detected by the SP-Mag method that is proposed in this paper. Compared with HGA (Figure 2D), the SP-Mag method has a strong ability to enhance the weak boundary, so that edges detected from prism C with the weak magnetic anomaly are at the same magnitude as the edges detected from prisms A and B. Compared with the results of the theta map (Figure 2E), NSTD (Figure 2F), and SP-Gra (Figure 2G), the SP-Mag method has a good ability to eliminate the false edges caused by the associated anomalies. One can also observe that the boundary of prism C on the right side has not been recognized. This is because the definition of B (the total horizontal derivative of g in formula 4) is one order lower than the magnetic field, and the detected details are not as clear as the magnetic field.

In fact, the SP-Mag method is modified from the SP-Gra method. Thus, the SP-Mag method maintains the weak-edge-enhancing ability while eliminating the false edge caused by the magnetic field-associated anomalies, which can provide a more effective reference map for the subsequent interpretation. It is worth noting that when we apply the SP-Mag method, we do not

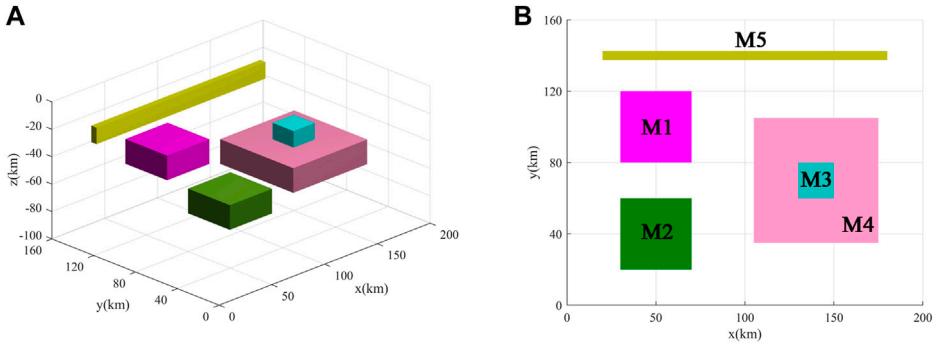

FIGURE 4
3D view **(A)** and top view **(B)** of the second magnetic model.

TABLE 1 Parameters of the second synthetic magnetic model.

Parameter	M1	M2	M3	M4	M5
x-coordinates of the center (km)	50	50	140	140	100
y-coordinates of the center (km)	100	40	70	70	140
z-coordinates of the center (km)	5.5	8.5	6	8.5	4
Length (km)	40	40	20	70	160
Width (km)	40	40	20	70	5
Height (km)	3	3	2	3	2
Inclination (°)	90	90	90	90	90
Declination (°)	0	0	0	0	0
Magnetization (A/m)	−1	1	1.1	1.5	1

need to compute the pseudo-gravity field at all but calculate two horizontal components of the magnetic anomaly—*Hax* and *Hay* (see Eqs 3, 4 for details) so that the problem of detail loss caused by the truncation error can be avoided.

In order to test the sensitivity of methods to noise, we add random noise to the synthetic magnetic anomaly, as shown in Figure 2B. The random noise has the amplitude of 0.5% of the maximum data magnitude. The magnetic anomaly with noise and the RTP is shown in Figures 3B, C, respectively. The results detected from the RTP magnetic anomaly with noise, as shown in Figure 3C, using HGA, theta map, NSTD, and SP-Gra methods are shown in Figures 3D–G. The HGA, theta map, and NSTD methods can identify the edges of prisms A and B, but the boundary of prism C cannot be effectively identified because of the influence of noise.

The SP-Gra methods can suppress noise, and the boundaries of prisms A and B, as well as the boundaries of prism C, can be recognized basically. The "false edges" affected by the noise become faintly visible. Because the SP-Gra method has a similar theoretical definition and calculation process to the SP-Mag method and both methods are based on the second-order spectral moment, the SP-Mag method has the similar ability to suppress noise. In addition, the SP-Mag method (Figure 3H) recognized the edges of prisms A and B and basically identified the edges of prism C except for the edges on the right side.

Figures 4A, B display the 3D and ground view of the second magnetic model that consists of two bodies (M1 and M2) with the same size but different depths, two overlapped sources (M3 and M4), and one thin source (M1). The geometric and magnetic parameters are shown in Table 1. The magnetic anomalies (Figure 5A) of the model are computed on a grid of 200 km × 160 km with 0.25-km spacing. Figure 5B shows the edges estimated by the HGA method. One can see that the results are dominated by the edges from the stronger source anomalies. Figures 5C, D show the edges estimated by the theta map and NSTD method, respectively. We can see that the two filters produce many false edges around and above the sources, and the theta map filter does not exhibit sharp peaks over the sources edges. Figures 5C, D show the results of the SP-Gra and SP-Mag filters. Both SP-Gra and SP-Mag filters provide the results with high resolution, but SP-Mag has the ability to avoid false edges in the map.

We also added random noise to the synthetic magnetic anomaly (Figure 5A) to estimate the effectiveness of the method in a noisy environment (Figure 6A). The random noise was introduced with an amplitude of 0.5% of the maximum data magnitude. The HGA (Figure 6B) and theta map (Figure 6C) filters can outline the edges of all sources, but the edges were blurred because of the effect of noise. Figure 6D shows the results of the NSTD method. We can see that the NSTD filter is less effective in outlining the edges of bodies M2, M3, and M4. Figure 6E shows the edges estimated by the SP-Gra method. In addition, the false edges affected by the noise become faintly visible. The edges estimated by SP-Mag are shown in Figure 6F. We can see that the SP-Mag provides a better outcome than the other filters, which can not only detect edges of all model bodies with high resolution but also show less sensitivity to noise and avoid bringing false edges in the map.

4 Application to field data

To test the performance of the SP-Mag method, it is applied together with the other four edge-enhancing methods to the RTP aeromagnetic anomaly of the Rizhao–Lianyungang area (indicated by the red rectangle in Figure 7). The magnetic field (Figure 8A) provides the high-accuracy aeromagnetic measurement with a grid cell size of 1 km × 1 km. The flight height of the data is 200 m, and

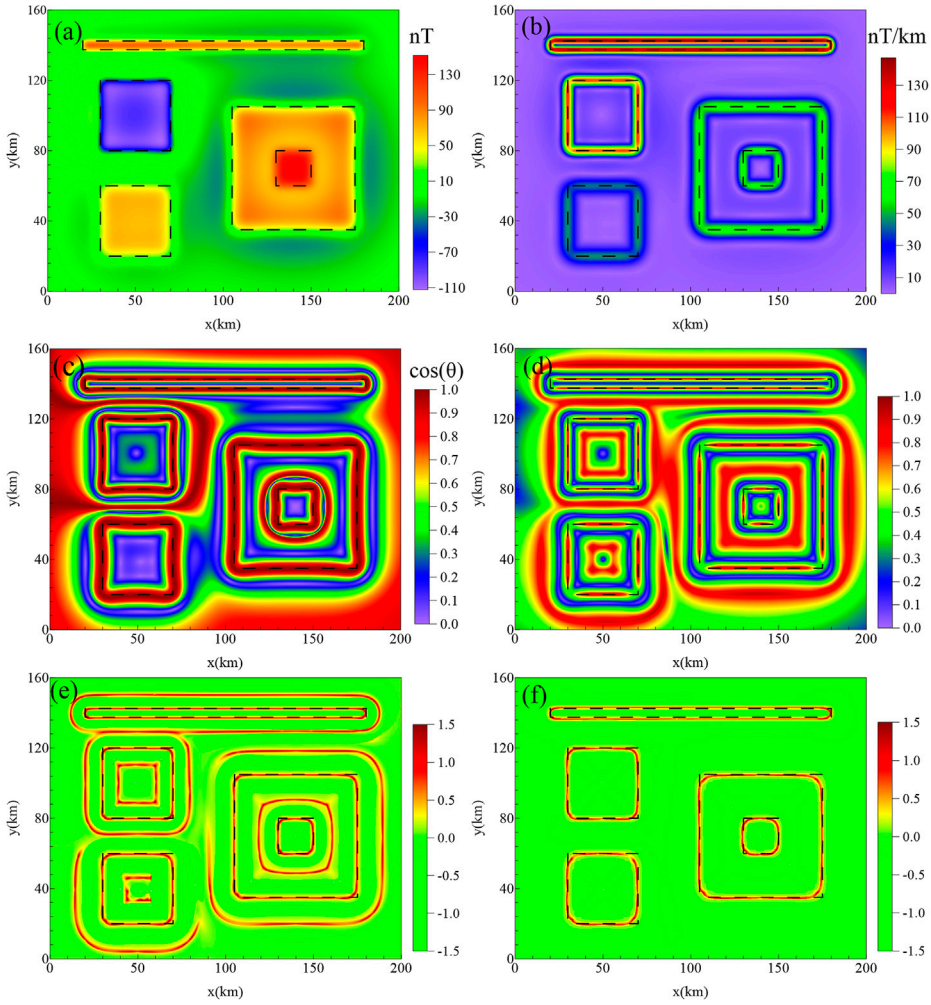

FIGURE 5
Example of the second synthetic model. **(A)** Synthetic magnetic anomaly caused by the five prisms; **(B)** HGA; **(C)** theta map; **(D)** NSTD; **(E)** SP-Gra; and **(F)** SP-Mag.

the total measurement accuracy after leveling is ±1.35 nT. The aeromagnetic field is positive to the north and negative to the south on a whole and can be divided into two magnetic regions with Wenquan–Xufu–Rizhao as the boundary between them. The northern magnetic field is located in the large Jiaodong Peninsula with NE magnetic anomaly belts, which are characterized by strong magnetic anomaly intensity and local anomaly development. The eastern part of the southern magnetic region mainly corresponds to the Haizhouwan area, and the western part of this region is mainly covered by the Quaternary. In addition, the stratigraphy or magnetic rocks are only exposed in Donghai, Lianyungang, Guanyun, etc.

Edges outlined by the SP-Mag, HGA, theta map, NSTD, and SP-Gra methods from the RTP aeromagnetic anomaly of the Rizhao–Lianyungang area are shown in Figure 9. From Figure 9, one can obviously observe that regardless of the result detected by the SP-Gra method (Figure 9A) from the aeromagnetic anomaly or the results highlighted by the SP-Gra (Figure 9B), theta map (Figure 9D), and NSTD (Figure 9E) methods from the RTP aeromagnetic anomaly, all exhibit obvious false boundaries (e.g., areas declined by ellipse A). Compared with Figure 9A, the false edges detected by the SP-Gra (Figure 9B) from the RTP aeromagnetic anomaly were suppressed slightly (e.g., indicated by the arrow a), but they were still obvious. This is because the reduction to the pole can suppress the associated anomalies, but it cannot eliminate them. Figure 9C shows the result of the SP-Mag method. Compared with the other results, the SP-Mag significantly eliminates the false edges caused by the associated anomalies (e.g., area delineated by ellipse A in Figure 9C). The result of the SP-Mag method (Figure 9F) is more efficient for the later geological interpretation. For example, the boundary indicated by the rectangular box B in Figure 9C is the Lianyungang fault, which is difficult to be clearly identified in the other detected results because of the influence of false boundaries.

In addition, SP-Mag can maintain the strong ability to enhance weak edges while eliminating the false boundary caused by the associated anomalies. For example, compared with the edges outlined by the HGA, the SP-Mag detects much edge information, especially in the southeast of the

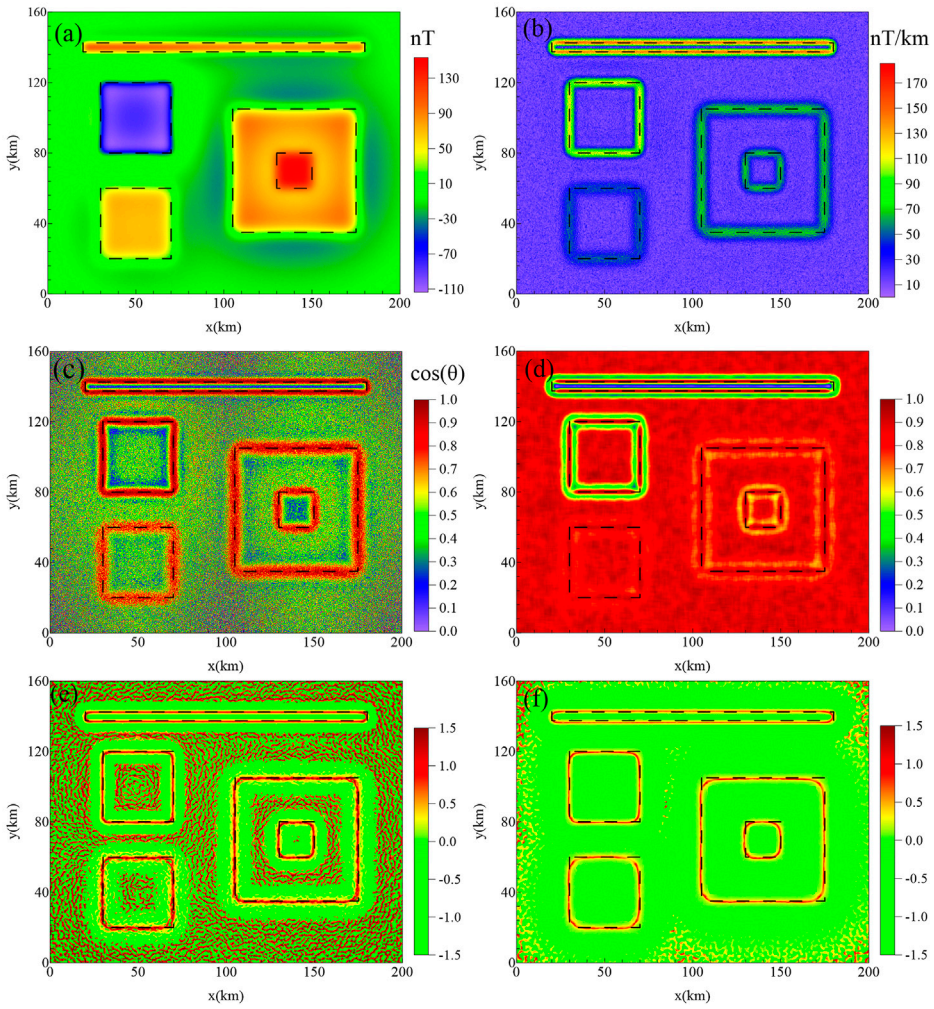

FIGURE 6
Synthetic magnetic anomaly of the second model corrupted by random noise with an amplitude equal to 0.5% of the maximum data magnitude, **(A)** synthetic magnetic anomaly caused by the five prisms; **(B)** HGA; **(C)** theta map; **(D)** NSTD; **(E)** SP-Gra; and **(F)** SP-Mag.

study area. In addition, edges detected by the SP-Mag are sharper than those detected from being covered by the strong boundaries. So the result of the SP-Mag can be more conducive to identify and track faults.

It is because the SP-Mag method eliminates the false boundary caused by the associated anomalies and the detected results can reflect the tectonic divisions more clearly. The result of the SP-Mag method (Figure 10A) is consistent with the tectonic division (Zhang et al., 2018) of the study area (Figure 11A). Figure 10A shows four obvious long and continuous belts A, B, C, and D that correspond to Yuli–Dadian, Wulian–Taoyuan, Donghai–Ganyu, and Sangxu–Lianyungang faults.

In order to learn the features of these faults, we also applied this method to the gravity field of the Rizhao–Lianyungang area. Figure 8B shows the airborne Bouguer gravity. The gravity field is measured with a grid cell size of 500 m × 500 m. The flight height of the data is 1,200 m, and the total measurement accuracy after leveling is ± 2.0×10^{-5} m/s^2. The gravity and magnetic anomalies in the study area have good homology. The Bouguer gravity field is high in the south and low in the north on a whole. The high-gravity anomalies spread to the NE direction and are mainly distributed in the Haizhouwan area and its southern land. The gravity anomalies in Qibaoshan and Xiazhuang–Nangu areas in the northwest of the study area are also relatively high, showing NNE-trending distribution, which are caused by the Precambrian basement uplift. The most obvious low-gravity anomaly is distributed in the Jiaonan area, which is mainly caused by the large area of Archaeo-Paleoproterozoic intermediate to acid rock mass.

The edge-enhanced results of the gravity field are shown in Figure 10B. It can be seen that the strikes of the detected edges are consistent with those of the magnetic field, reflecting the main structural strikes of NE and NNE in the study area. In addition, there are also obvious long and continuous belts A′, B′, and D′ corresponding to Yuli–Dadian, Wulian–Taoyuan, and Sangxu–Lianyungang faults. It is noteworthy that the Yuli–Dadian fault belongs to the Tanlu fault zone and is the eastern boundary of the Tanlu fault zone in the study area. Therefore, we can also find there are parallel lines on the left side of belt A′ in gravity edge-enhanced results. However, the belt C' corresponding to the Donghai–Ganyu fault is no longer continuous anymore because

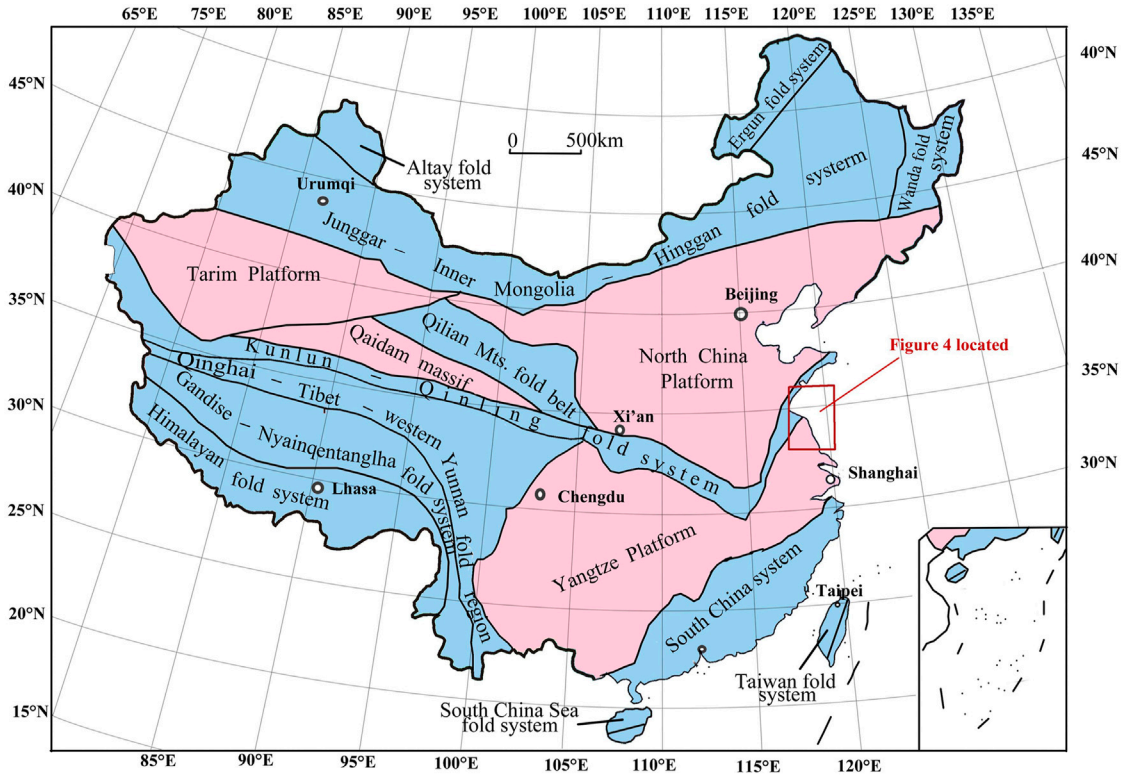

FIGURE 7
Geological sketch map of China (Sun et al., 2016a). The Rizhao–Lianyungang area in Figure 4 is indicated by the red rectangle. The pink color represents platform or massifs. The blue color represents tectonic or orogenic belts.

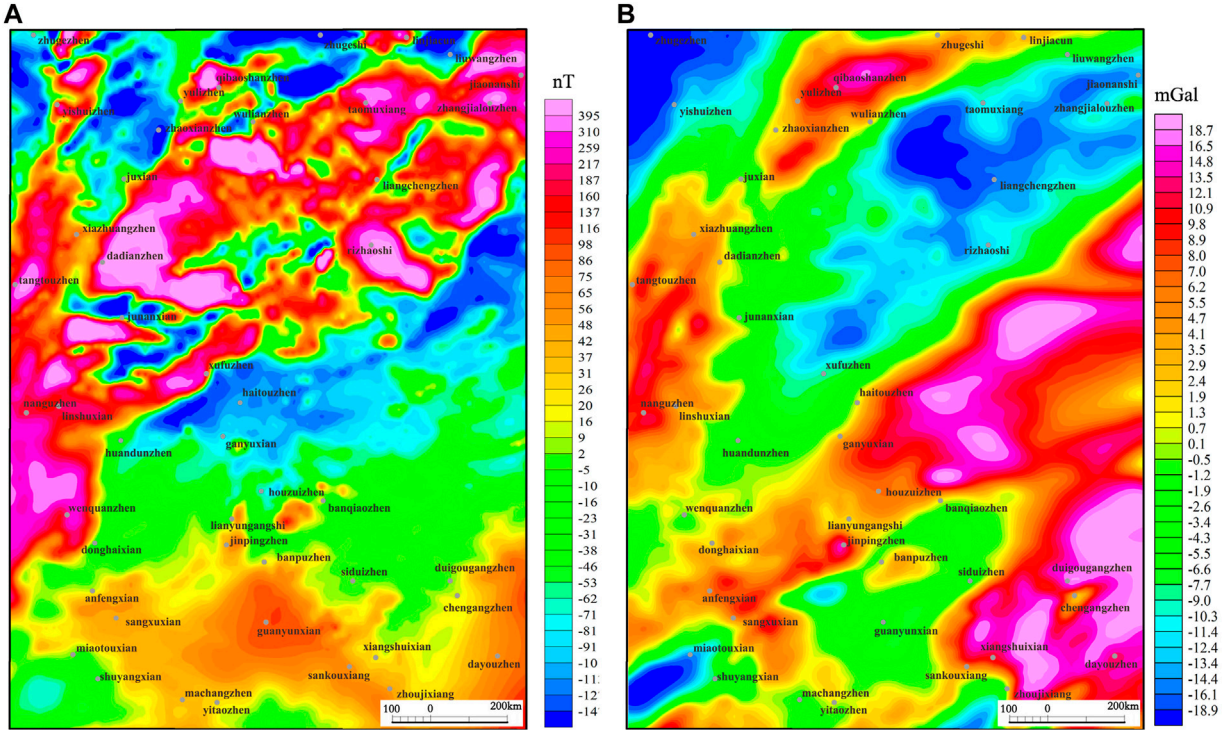

FIGURE 8
RTP aeromagnetic anomaly **(A)** and airborne gravity anomaly **(B)** of the Rizhao–Lianyungang area.

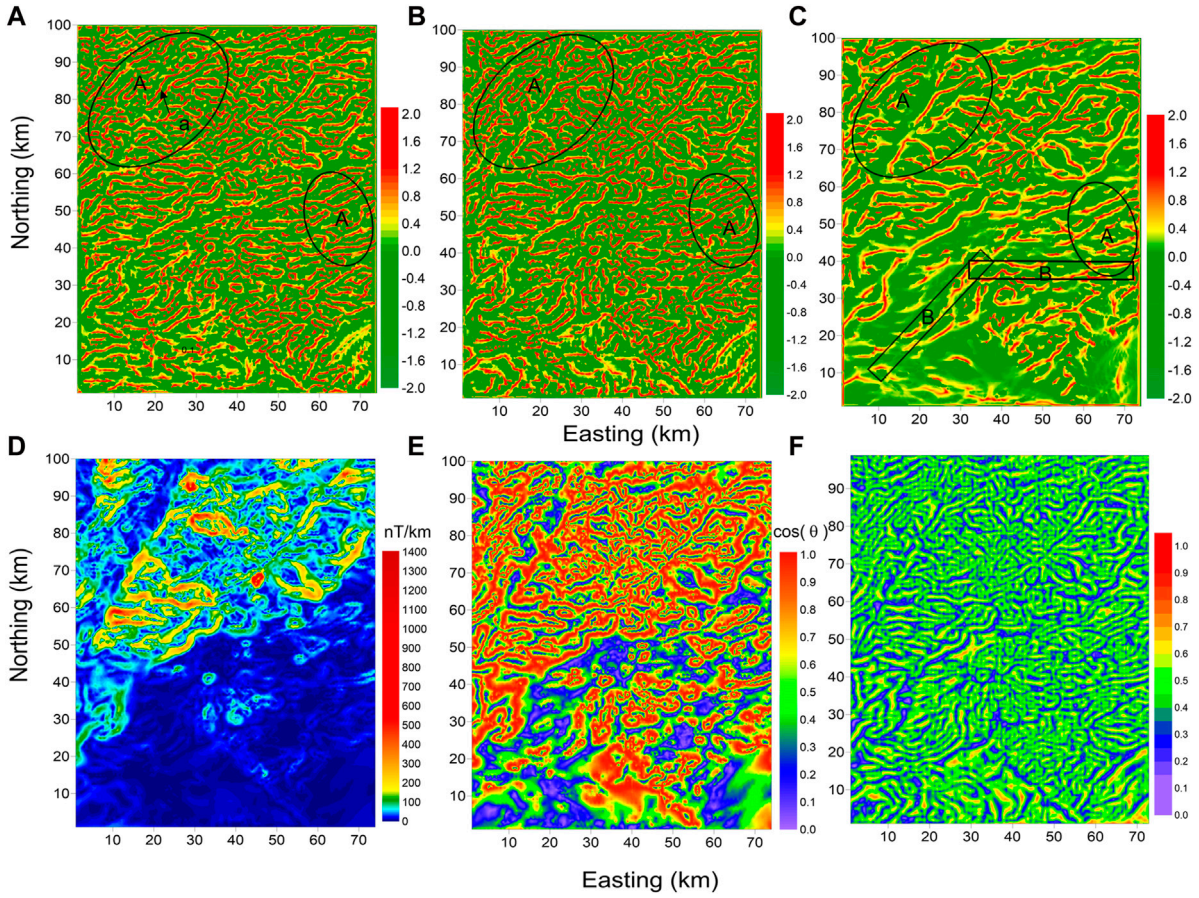

FIGURE 9
Test cases of edge-enhancing methods on the aeromagnetic anomaly of the Rizhao–Lianyungang area. The location has been outlined in the red rectangle in Figure 3. **(A)** SP-Gra from the aeromagnetic anomaly; **(B)** SP-Gra from the RTP aeromagnetic anomaly; **(C)** SP-Mag; **(D)** HGA from the RTP aeromagnetic anomaly; **(E)** theta map from the RTP aeromagnetic anomaly; and **(F)** NSTD from the RTP aeromagnetic anomaly.

the fault was staggered by late NW tectonic activities. It is well known that the magnetic field reflects magnetization information from the upper crust, while the gravity field can reflect density information from the whole crust. Yuli–Dadian, Wulian–Taoyuan, Donghai–Ganyu, and Sangxu–Lianyungang faults exist in the detected results from both magnetic and gravity fields, indicating they are all deep and large faults.

Furthermore, these four faults divided the study area into five structural regions and sub-regions (Figure 11A): west Shandong uplift zone (I_1), north Jiaodong uplift (I_2), south Jiaodong uplift (II_1), Lianyungang uplift (II_2), and north Jiangsu depression (III). The geometrical characteristics of the boundaries are obviously different in different structural partitions. Because of the control of the NNE Tanlu fault zone, boundaries in the west Shandong uplift zone are in the NE trends, while most boundaries in the south Jiaodong uplift zone are in the trends of EW direction. There develop several groups of NE parallel boundaries in north Jiangsu depression, and the boundaries in the Lianyungang uplift zone are disorderly, indicating crustal deformation is stronger here.

The edges detected by the SP-Mag method have also been compared with the fault structures. Figure 11B illustrates the edges recognized by the SP-Mag method, which is superimposed over a simplified geologic map (Zhang et al., 2018). The Rizhao–Lianyungang area has developed fault structures. In addition, the tectonic framework is composed of NE and NNE trending faults. The deep and large faults in the study area, which play an important role in controlling the regional structure, are the Tanlu fault zone (F1), Wulian–Taoyuan fault (F14), Sangxu–Lianyungang fault (F6), Rizhao–Liuwang fault (F2), Donghai–Ganyu fault (F5), and Yishui–Juxian fault (F13) (Zhang et al., 2018). Figure 11B displays that the edge coefficients show a good correlation with the geologic structures.

5 Discussion

It is well known that the short wavelength lineaments are mostly associated with shallower depth, whereas the longer wavelength lineaments are mostly related to the deep interior inside the Earth (Pham et al., 2020a). The HGA is dominated by the short wavelength lineaments (Figure 9D), and the SP-Gra, theta map, NSTD, and SP-Mag can delineate both the longer and smaller wavelengths' structural and tectonic boundaries (Figures 9B, C, E, F). The SP-Gra, theta map, and NSTD maps indicate that the NE–SW and NW–SW trends are dominant in the data (Figures 9B, E, F). Although the SP-Gra, theta

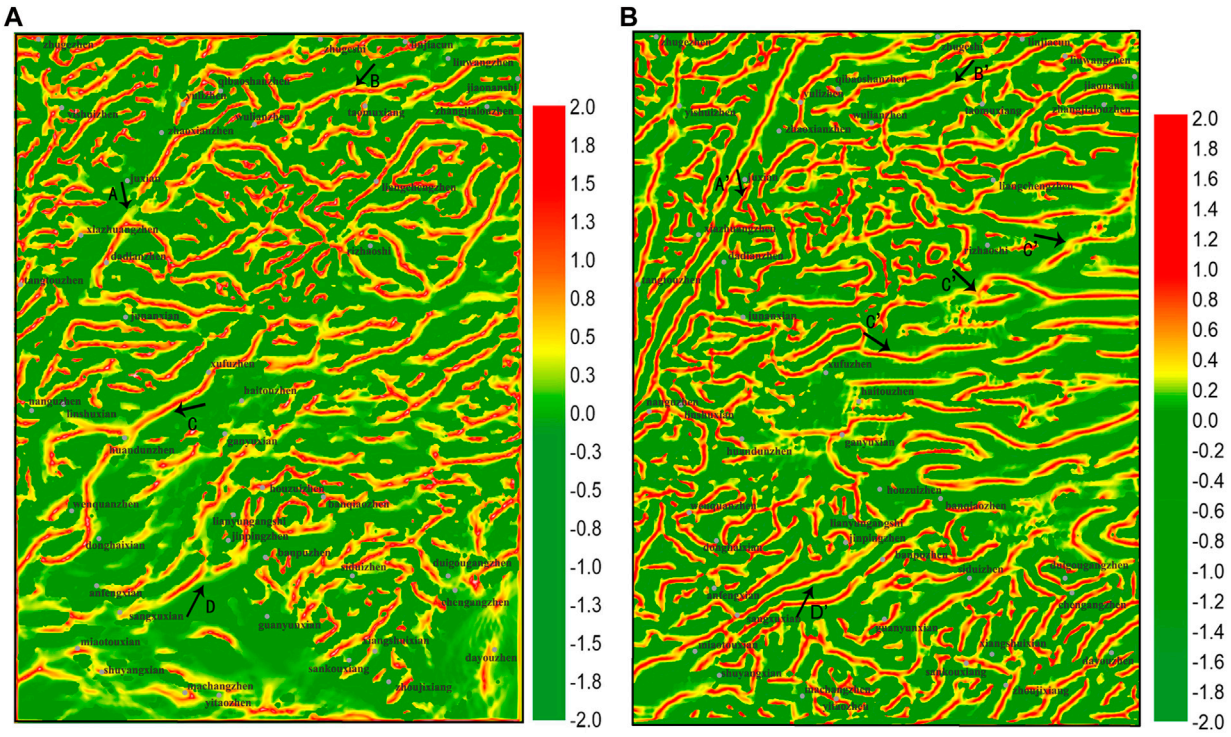

FIGURE 10
Edges detected from the aeromagnetic field **(A)** and airborne gravity field **(B)** by using the SP-Mag method.

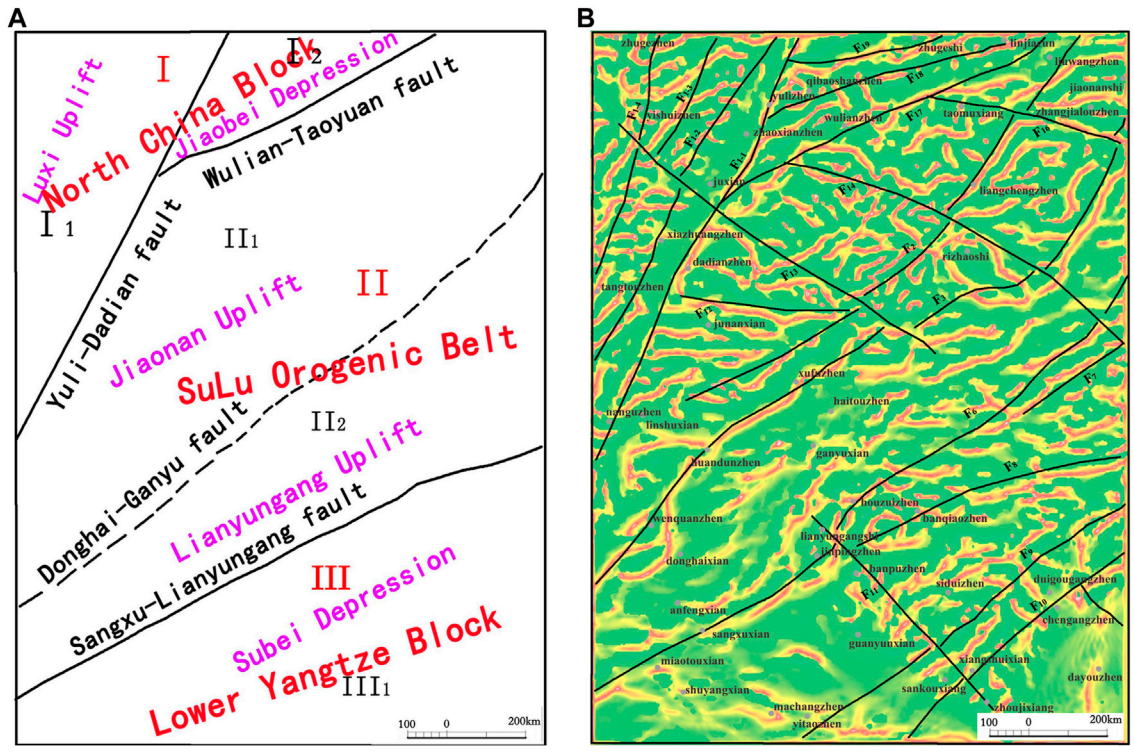

FIGURE 11
(A) Tectonic division sketch map; **(B)** map of the edges detected by using the SP-Mag method superimposed with the simplified geological map of the study region.

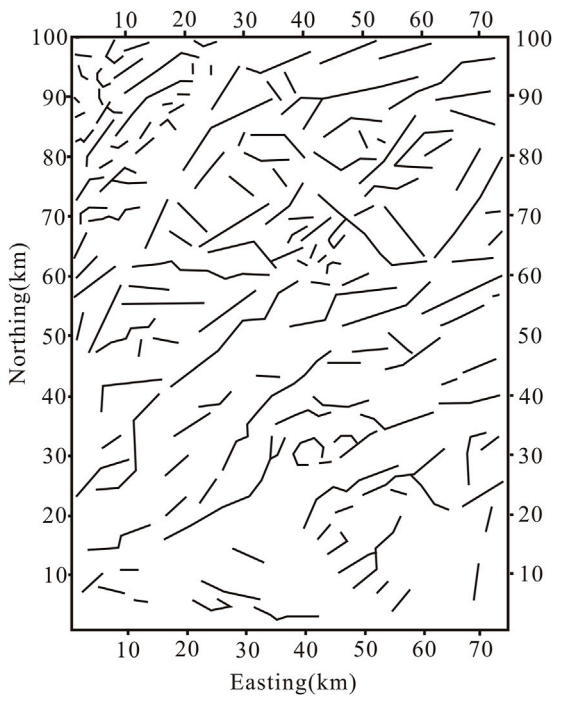

FIGURE 12
Lineaments detected from the SP-Mag map of the magnetic data.

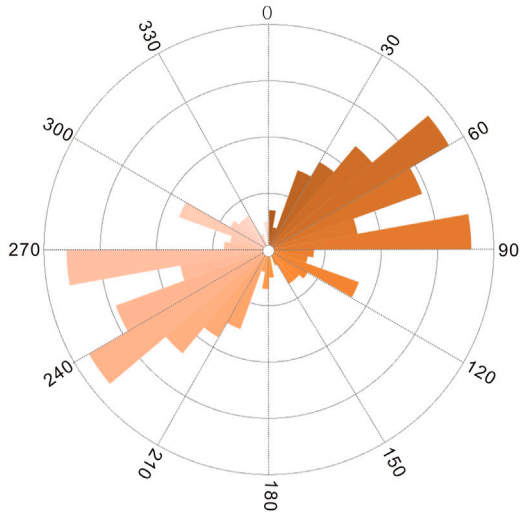

FIGURE 13
Rose diagram of the lineaments in Figure 12.

map, NSTD, and SP-Mag are effective in balancing lineaments associated with both shallow and deep depth, meanwhile the SP-Mag can eliminate false edges caused by the associated anomalies. In the practical application, a large amount of false edges and some small-scale partial boundaries are eliminated; thus, the detected edges are more suitable to highlight the whole structure pattern and trace the faults. Figure 12 shows the lineaments detected by the SP-Mag map. In addition, the trend analysis of the mapped lineaments has been statistically computed in the form of the rose diagram (Figure 13). The diagram shows the dominant lineament trends in NE–SW and NW–SW orientations, which is in accordance with the fault trends shown in Figure 6. The obtained results illustrate the usefulness of the SP-Mag for potential field interpretation.

The proposed method uses the idea of the pseudo-gravity field, but there is no need for the calculation of the pseudo-gravity field. Instead, we calculate two horizontal components of magnetic anomaly—*Hax* and *Hay*—and hence avoid losing details caused by the local truncation errors. In addition, when the associated anomalies are not very serious in the magnetic field in the study area, we can use the SP-Gra method directly to outline the edges; when the regional magnetic field is with serious associated anomalies, one can select the SP-Mag method to detect these edges. Although the SP-Mag can recognize lineaments effectively, more geological and geophysical data should be still combined for comprehensive interpretation in the actual interpretation.

Furthermore, we have conducted some three-component aeromagnetic surveys, obtaining data *Hax*, *Hay*, and *Za*. Therefore, the SP-Mag method can directly use the two horizontal components *Hax* and *Hay* to enhance the edges. Furthermore, this work will be carried out in the following study.

6 Conclusion

We have proposed a modified magnetic edge-detection method (SP-Mag) based on the second-order spectral moment. This method has been demonstrated using both synthetic and field data. The synthetic test shows that SP-Mag can not only balance edges regardless of strong or weak anomalies but also eliminate those false edges caused by the associated anomalies in the magnetic field, which provides more effective information for subsequent interpretation. Using the RTP aeromagnetic field of the Rizhao–Lianyungang area as an example, the detected results can provide clearer details, and the lineaments detected by the SP-Mag method are consistent with geological structures.

Data availability statement

The data analyzed in this study are subjected to the following licenses/restrictions: the original aeromagnetic data are unavailable. The analyzed data are available from the authors upon reasonable request and by permission of China Aero Geophysical Survey and Remote Sensing Center for Natural Resources. Requests to access these datasets should be directed to Sun Yanyun, yysun2009@126.com.

Author contributions

YS conceived the idea and made overarching research goals and aims and wrote the manuscript. XZe contributed to the conception of the study and helped to deduce the formula. WY contributed to analysis and manuscript preparation, critical

review, and commentary or revision—including pre- or post-publication stages. XL contributed to data processing through software and codes. WZ contributed to the geological interpretations of the edge results extracted from the aeromagnetic data. XZh contributed to the analysis with constructive discussions. All authors approved the final draft of the manuscript.

Funding

The authors gratefully acknowledge the financial support from the National Science Foundation of China (Grant No. 42104138) and the Geological Survey Project (No. DD20221715, No. DD20230069).

Conflict of interest

The authors declare that the research was conducted in the absence of any commercial or financial relationships that could be construed as a potential conflict of interest.

Publisher's note

References

Blakely, R. J., and Simpson, R. W. (1986). Approximating edges of source bodies from magnetic or gravity anomalies. *Geophysics* 51, 1494–1498. doi:10.1190/1.1442197

Cooper, G. R. J. (2009). Balancing images of potential field data. *Geophysics* 74 (3), 17–20. doi:10.1190/1.3096615

Cooper, G. R. J., and Cowan, D. R. (2011). A generalized derivative operator for potential field data. *Geophys. Prospect.* 59, 188–194. doi:10.1111/j.1365-2478.2010.00901.x

Cooper, G. R. J., and Cowan, D. R. (2008). Edge enhancement of potential-field data using normalized statistics. *Geophysics* 73 (3), 1–4. doi:10.1190/1.2837309

Cordell, L. (1979). "Gravimetric expression of graben faulting in santa Fe country and the espanola basin," in *30th field conference* (New Mexico: Geological Society Guidebook), 59–64.

Eldosouky, A. M., Pham, L. T., and Henaish, A. (2022). High precision structural mapping using edge filters of potential field and remote sensing data: A case study from wadi umm ghalqa area, south eastern desert, Egypt. *Egypt J. Remote Sens. Space Sci.* 25 (2), 501–513. doi:10.1016/j.ejrs.2022.03.001

Evjen, H. M. (1936). The place of the vertical gradient in gravity interpretation. *Geophysics* 1, 127–136. doi:10.1190/1.1437067

Fedi, M., and Florio, G. (2001). Detection of potential fields source boundaries by enhanced horizontal derivative method: Potential field sources boundaries by EHD method. *Geophys. Prospect.* 49, 40–58. doi:10.1046/j.1365-2478.2001.00235.x

Francisco, F. J., de Souza, A., Bongiolo, A. B. S., and Castro, L. G. (2013). Enhancement of the total horizontal gradient of magnetic anomalies using the tilt angle. *Geophysics* 78 (3), J33–J41. doi:10.1190/GEO2011-0441.1

Guan, Z. L. (2005). *Geomagnetic field and magnetic exploration*. Beijing: Geological Publishing House Press.

Guan, Z. L., and Yao, C. L. (1997). Inversion of the total gra dient modulus of magnetic anomaly due to dipping dike (in Chinese). *Earth Sci. J. China Uni. Geosci.* 22 (1), 81–85.

Hansen, R. O., and de Ridder, E. (2006). Linear feature analysis for aeromagnetic data. *Geophysics* 71 (6), L61–L67. doi:10.1190/1.2357831

Hu, S. G., Tang, J. T., and Ren, Z. Y. (2019). Normalized facet edge detection and enhancement in potential field sources with the scale-space technique. *Chin. J. Geophys.* 62 (1), 331–342. doi:10.6038/cjg2019L0317

Huang, Y. Y. (1985). Geometrical interpretation and graphical solution of second order spectrum moments and statistical invariants for random surface characterization. *J. Zhejiang Univ.* 6 (19), 143–153.

Hu, Z. G., Yu, Q. F., and Lou, H. (1995). 3-D analytic signal method (in Chinese). *Computing techniques for geophysical and geochemical exploration* 17 (3), 36–42.

Li, C. G., Dong, S., and Zhang, G. X. (2000). Evaluation of the anisotropy of machined 3D surface topography. *Wear* 237, 211–216. doi:10.1016/S0043-1648(99)00327-0

Ma, G. Q., Huang, D. N., Yu, P., and Li, L. L. (2012). Application of improved balancing filters to edge identification of potential field data (in Chinese). *Chin. J. Geophys.* 55 (12), 4288–4295. doi:10.6038/j.issn.0001-5733.2012.12.040

Miller, H. G., and Singh, V. (1994). Potential field tilt - a new concept for location of potential field sources. *J. Appl. Geophys.* 32, 213–217. doi:10.1016/0926-9851(94)90022-1

Nabighian, M. N. (1972). The analytic signal of two-dimensional magnetic bodies with polygonal cross-section: Its properties and use for automated anomaly interpretation. *Geophysics* 37, 507–517. doi:10.1190/1.1440276

Pham, L. T., Eldosouky, A. M., Melouah, O., Abdelrahman, K., Alzahrani, H., Oliveira, S. P., et al. (2021). Mapping subsurface structural lineaments using the edge filters of gravity data. *J. King Saud. Univ. Sci.* 33 (8), 101594. doi:10.1016/j.jksus.2021.101594

Pham, L. T., Eldosouky, A. M., Oksum, E., and Saada, S. A. (2020a). A new high resolution filter for source edge detection of potential field data. *Geocarto Int.* 37, 3051–3068. doi:10.1080/10106049.2020.1849414

Pham, L. T., Van Vu, T., Le Thi, S., and Trinh, P. T. (2020b). Enhancement of potential fieldsource boundaries using an improved logistic filter. *Pure Appl. Geophys* 177 (11), 5237–5249. doi:10.1007/s00024-020-02542-9

Phillips, J. D., Hansen, R. O., and Blakely, R. J. (2007). The use of curvature in potential-field interpretation. *Explor. Geophys.* 38, 111–119. doi:10.1071/EG07014

Prasad, K. N. D., Pham, L. T., Singh, A. P ., Eldosouky, A. M., Abdelrahman, K., Fnais, M. S., et al. (2022). A novel EnhancedTotal gradient (ETG) forInterpretation of magnetic data. *Minerals* 12, 1468. doi:10.3390/min12111468

Roest, W. R., Verhoef, J., and Pilkington, M. (1992). Magnetic interpretation using the 3-D analytic signal. *Geophys.* 57, 116–125. doi:10.1190/1.1443174

Sun, Y. Y., Yang, W. C., Zeng, X. Z., and Zhang, Z. Y. (2016a). Edge enhancement of potential field data using spectral moments. *Geophysics* 81, G1–G11. doi:10.1190/geo2014-0430.1

Sun, Y. Y., Yang, W. C., and Yu, C. Q. (2016b). Multi-scale scratch analysis in Qinghai-Tibet plateau and its geological implications. *Pure Appl. Geophys.* 173, 1197–1210. doi:10.1007/s00024-015-1153-3

Sun, Y. Y., Yang, W. C., Zeng, X. Z., Zhao, T. Y., Zhang, W., Zhang, X. J., et al. (2022). Scratch recognition and analysis of gravity field in Chinese continent. *Acta Geophys.* 70, 2001–2012. doi:10.1007/s11600-022-00899-0

Thomas, T. R. (1982). *Rough surfaces*. London: Longman Group UK Limited.

Verduzco, B., Fairhead, J. D., Green, C. M., and MacKenzie, C. (2004). New insights into magnetic derivatives for structural mapping. *Lead. Edge* 23, 116–119. doi:10.1190/1.1651454

Wang, Y. G., Zhang, F. X., Wang, Z. W., Meng, L. S., and Zhang, J. (2013). Edge detection of potential field using normalized differential (in Chinese). *J. Jilin Univ. (Earth Sci. Ed.* 43 (2), 591–602.

Wijins, C., Perez, C., and Kowalczyk, P. (2005). Thetamap: Edge detection in magnetic data. *Geophysics* 70 (4), L39–L43. doi:10.1190/1.1988184

Yang, S. Z., Wu, Y., and Xuan, J. P. (1992). *Time series analysis in engineering and application*. Wuhan: Huazhong University of Science and Technology Press.

Yang, W. C., and Sun, Y. Y. (2016). Discovering crustal deformation bands by processing regional gravity field. *Acta Geol. Sin. Engl. Ed.* 90 (2), 66–74. doi:10.1111/1755-6724.12642

Yang, W. C., Sun, Y. Y., Hou, Z. Z., and Yu, C. Q. (2015). A multi scale scratch analysis method for quantitative interpretation of regional gravity fields. *Chin. J. Geophys.* 58, 41–53. doi:10.1002/cjg2.20154

Yang, W. C., Sun, Y. Y., Hou, Z. Z., and Yu, C. Q. (2017). A study on spectral moments of gravity field with application to crustal structure imaging of Tarim basin (in Chinese). *Chin. J. Geophys.* 60(8), 3140–3150. doi:10.6038/cjg20170821

Zeng, X. Z., Sun, Y. Y., Yu, C. Q., and Liu, S. B. (2018). *Edge enhancement of magnetic field based on spectral moments and pseudo-gravity field*. California, CA: Soc Exploration Geophysicists, 1494–1498.

Zhang, H. L., Dhananjay, R., Marangoni, Y. R., and Hu, X. Y. (2014). NAV- Edge: Edge detection of potential-field sources using normalized anisotropy variance. *Geophysics* 79 (3), J43–J53. doi:10.1190/geo2013-0218.1

Zhang, W., Zhang, X. J., Tong, J., and Fan, Z. (2018). Gravity and magnetic anomaly characteristics and its geological interpretation in rizhao-lianyungang areas. *Earth-Science* 43 (12), 4490–4497. doi:10.3799/dqkx.2018.518

frontiers | Frontiers in Earth Science

TYPE Original Research
PUBLISHED 12 May 2023
DOI 10.3389/feart.2023.1143637

OPEN ACCESS

EDITED BY
Henglei Zhang,
China University of Geosciences (Wuhan), China

REVIEWED BY
Ning Qiu,
South China Sea Institute of Oceanology (CAS), China
Alessandra Borghi,
National Institute of Geophysics and Volcanology (INGV), Italy

*CORRESPONDENCE
Guangliang Yang,
vfory@aliyun.com

RECEIVED 13 January 2023
ACCEPTED 05 May 2023
PUBLISHED 12 May 2023

CITATION
Liu Y, Yang G, Zhang J and Zhao B (2023), Papua New Guinea Moho inversion based on XGM 2019e gravity field model. *Front. Earth Sci.* 11:1143637. doi: 10.3389/feart.2023.1143637

Papua New Guinea Moho inversion based on XGM 2019e gravity field model

Yijun Liu[1], Guangliang Yang[1,2]*, Jie Zhang[3] and Bingjie Zhao[4]

[1]Key Laboratory of Earthquake Geodesy, Institute of Seismology, China Earthquake Administration, Wuhan, China, [2]Hubei Earthquake Agency, Wuhan, China, [3]Southern University of Science and Technology, Shenzhen, China, [4]Zachry Department of Civil and Environmental Engineering, Texas A&M University, Texarkana, TX, United States

The construction of the high-resolution Moho depth model is significant for studying the characteristics of the complex tectonic movement (seafloor spreading, plate subduction phenomena) in Papua New Guinea. We calculate the region's Moho relief and lithosphere thinning factor using the XGM 2019e gravity field model and nonlinear fast gravity inversion method under the GEMMA Moho depth model's constraint considering the influence of lithosphere thermal gravity anomaly. The calculation result shows that the Moho depth is between 6—34 km, forming two large depressions in Woodlark Basin (WB) and Solomon Sea Plate (SSP) with deep scattered islands. In addition, the findings suggest that Significant differences exist in the shape and tectonic movement intensity of the North and South oceanic crust at the WB. Nevertheless, the lithosphere extends evenly in Manus Basin (MB). WB collided with the Solomon Islands at a higher angle than the SSP subducted under Bismarck Sea Plate (BSP); strong earthquakes may frequently occur on both sides and in deeper positions at West New Britain Trench in the future.

KEYWORDS

Papua New Guinea, gravity inversion, Moho depth, plate subduction, seafloor spreading

1 Introduction

Papua New Guinea is in the northeast of Australia and southwest of the Pacific Ocean, situated at the junction of the Pacific Plate and the Indo-Australian plate, composed of several microplates (Wallace et al., 2004; Davies, 2012) (Figure 1). The region has undergone a series of tectonic movements such as plate subduction, arc-continent collision, and seafloor spreading (Curtis, 1973), which indirectly or directly led to strong earthquakes and tsunamis (Borrero et al., 2003; Xu et al., 2020). Since the Cretaceous, the convergence and subduction of the Indo-Australian and Pacific plate caused the rise of seafloor sediments, which in turn rose to form arcs and collided with the Australian continent (Pigram and Davies, 1987; Haddad and Watts, 1999). There are still intricate motions between multiple microplates or accretion blocks. For instance, WB subducted into the Solomon Islands; SSP subducted beneath BSP; BSP moved southwest due to the Finisterre collision (Wallace et al., 2004); Finisterre, Adelbert block ran into Guinea Plateau. The interaction between microplates leads to strong plate coupling (Mann et al., 1998), which results in regional uplift and folds (Curtis, 1973). The phenomenon of seafloor spreading primarily occurs in three areas, namely, WB, MB, and SSP, with varying intensities, periods, and forms. The spreading center of WB moves from east to west at a quick speed of 14 cm/yr from 3.6 Ma and continuously goes through the spreading center nucleation, expansion, and standstill (Taylor et al., 1999).

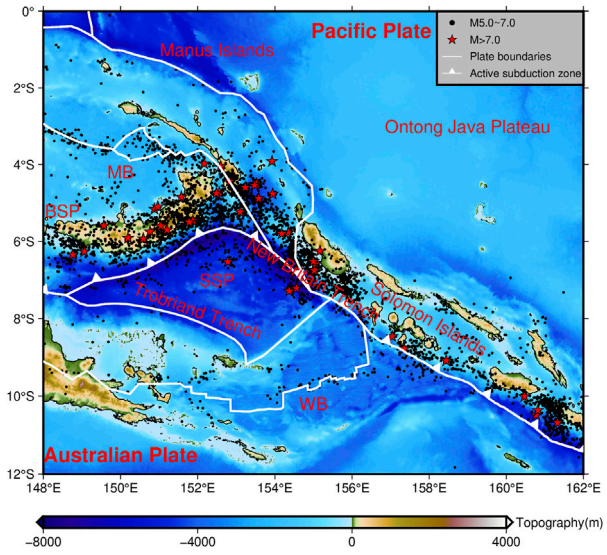

FIGURE 1
Topography and earthquake occurrence in Papua New Guinea. The earthquake data comes from United States Geological Survey (USGS) (e.g., earthquakes with a magnitude greater than 5.0 since 1980 are considered); topography data are obtained from General Bathymetric Chart of the Oceans 2021 (GEBCO 2021); plate boundary data is taken from Bird. (2003).

In the young (<1 Ma) back-arc MB (Dyriw et al., 2021), Martinez and Taylor (1996) found that the spreading center diffuses outward at a rate of 9.2 cm/yr to form a wedge-shaped oceanic crust. The SSP spread at a relatively slow rate of 5.8 cm/yr for a long time (Joshima et al., 1987), which is partially subducted below the BSP and Trobriand Trench (Honza et al., 1987).

Previous research has investigated variable tectonic movements from various perspectives. Nonetheless, our understanding of the overall deep structure characteristics remains limited due to a few previous research on this aspect, and the existing Moho depth models have low resolution (up to 0.5°×0.5°). The Moho relief and lithosphere thinning factor are critical parameters that present deep structure features: the former describes the overall crustal structure (Zhu, 2000) and is closely linked to tectonic evolution, such as plate subduction; the latter indicates the degree of thinning of the lithosphere, which can measure the extent and intensity of seafloor spreading. Solving both data with higher resolution can help us better understand the details and characteristics of the deep structure of the region.

In recent studies, the Moho relief has been determined through five different methods: seismic refraction, receiver functions, seismic reflection profiles, seismic tomography, and gravity inversion (Aitken et al., 2013). While several seismic techniques provide relatively accurate Moho depth results, they are limited to individual points, sections, or strip areas. They are not suitable for large-scale research due to high costs. As a result, using gravity data has become a more popular alternative approach in geophysics due to its high resolution, extensive coverage, and richer sources. Nonetheless, some hyperparameters must be selected during the gravity inversion, such as Moho reference depth (the depth of the normal Earth) and crust-mantle density contrast. To enhance the accuracy of Moho depth inversion results, many researchers use seismic data as constraint information to determine hyperparameters by minimizing the misfit between the gravimetric solution and the seismic data. For example, Gaulier et al. (1997) determined the Moho reference depth and crust-mantle density contrast of the Liguro-Provençal Basin's Moho depth based on seismic refraction and reflection data. The Moho depth obtained by the seismic method was broadly consistent with the gravity inversion result, with a difference of less than 2 km; Aitken. (2010) also inverted the Australian Moho depth using various interface models and seismic data constraints, revealing that seismically-constrained gravity inversion can generate a well-constrained and detailed Moho depth model (Abrehdary et al., 2015).

Gravity corrections are crucial for improving the accuracy of Moho depth inversion results. In addition to topography and other common corrections, lithosphere thermal gravity anomaly correction is essential in Papua New Guinea. Seafloor spreading results in the extension and thinning of the oceanic lithosphere and adjacent rifted continental margin lithosphere, resulting in the geothermal rise and lithosphere lateral density change (Chappell and Kusznir, 2008), which generates significant lithosphere thermal gravity anomaly, reaching the maximum at the ocean ridge (Alvey et al., 2008). Chappell and Kusznir. (2008) obtained lithosphere thermal gravity anomaly through iterative calculation combined with the lithosphere thinning temperature field model proposed by McKenzie. (1978). He considered the existence of the crustal melting thickness (White and McKenzie, 1989) and evaluated the sensitivity of the thermal model. Alvey et al. (2008) established multiple plate reconstruction models to estimate the age of the oceanic lithosphere, providing more methods for calculating lithosphere thermal gravity anomaly. After correcting the lithosphere thermal gravity anomaly, the inversion result will be more accurate and closer to the actual geological structure (Cowie and Kusznir, 2012; Constantino and Sacek, 2020).

Based on the reasons mentioned above, we propose to use the Moho depth of the GEMMA model as constraint information, along with Bouguer gravity anomaly data (After lithosphere thermal gravity anomaly correction) to obtain the Moho depth and distribution of lithosphere thinning factors in Papua New Guinea through gravity inversion, focusing on the Moho relief, seafloor spreading and microplate subduction. The paper is structured as follows: 1) Data source: presentation of the Bouguer gravity anomaly data required for gravity inversion, the GEMMA Moho depth data, and the relevant data for calculating the lithosphere thermal gravity anomaly. 2) Methodology: presentation of the gravity inversion and lithosphere thermal gravity anomaly calculation methods. 3) Results and discussion: description and analysis of the Moho inversion results, lithosphere thermal gravity anomaly, lithosphere thinning factor results, the seafloor spreading features at WB and MB, and microplate subduction at SSP and WB. 4) Conclusion: summary of the work carried out.

2 Data source

We use the combined global gravity field model XGM 2019e (Zingerle et al., 2020) as the raw gravity data. This model integrates

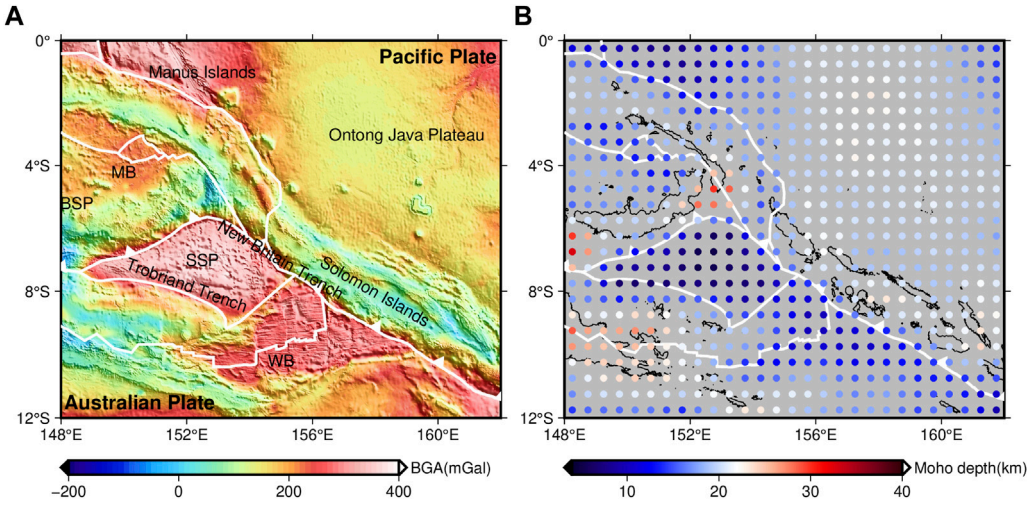

FIGURE 2
(A) The calculated Bouguer gravity anomaly, **(B)** Moho depth of GEMMA model.

terrestrial and satellite altimetry data based on the spherical harmonic domain. Its spherical harmonic is 2' (the spatial resolution is about 4 km). According to the GNSS/levelling validation test and Ocean Mean Dynamic Topography (MDT) calculation results, XGM 2019e′s performance is more consistent globally than preceding models, especially in the ocean.

For the terrain correction, we use the spherical approximation classical gravity anomaly obtained from the model minus the attraction of the Bouguer plate, in which the topography spherical harmonic model of ETOPO1 data (Amante and Eakins, 2009) up to the same maximum degree is used (Standard density of 2,670 kg/m^3 for the continents, −1,025 kg/m^3 for the oceans), then resample the calculations into Bouguer gravity anomaly data with a spatial resolution of 3′for gravity inversion. The overall variation range is about −200–400 mGal, showing apparent high anomaly in several oceanic basins and low anomaly in densely distributed islands (Figure 2A). There are two major gravity anomaly gradient zones with drastic variation, located at the junction of plate subduction, which are the areas where earthquakes occur frequently. They are the SE-NW trend of SSP-MB and the SW-NE trend of WB - Solomon Islands-Ontong Java Plateau.

In the study area, only a few Moho depth point data values obtained by the seismic method exists at WB and Manus Islands, so we can't understand the characteristics of Moho relief as a whole. We only use this data to verify our Moho depth inversion result. Therefore, this paper intends to use the Moho depth (with respect to sea level) provided by the GEMMA Earth crust model (Reguzzoni and Sampietro, 2015) as the depth constraint information. The spatial resolution of the model is 0.5° × 0.5°, and the Moho depth error standard deviation is 3.4 km globally. It is calculated using a uniformly distributed GOCE gravity satellite dataset and CRUST2.0 seismic information through least squares inversion, considering many factors, such as differences between major geological provinces and lateral density variations of the upper mantle. The model's gravitational effects are more consistent with the actual gravity field, so it can be used as a reference for studying Moho relief in some places lacking seismic data. We select 1760 Moho depth points from the model, as shown in Figure 2B. Model's Moho depth is between 5~40 km. Along the SW-NE direction, the depth decreases slowly, then increases sharply, and finally decreases gradually. The minimum depth is found at the SSP and WB, while the maximum depth is at the Solomon Islands and locations close to the Ontong Java Plateau.

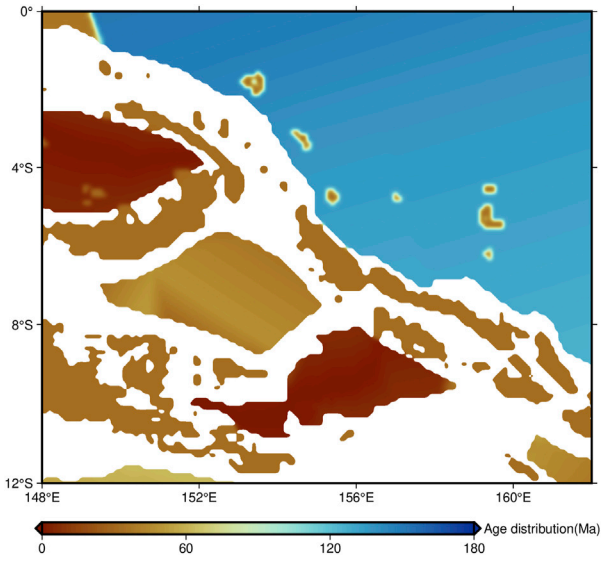

FIGURE 3
Distribution of lithosphere thermal equilibration time in Papua New Guinea.

Lithosphere thermal equilibration time (Figure 3) are needed to calculate the lithosphere thermal gravity anomaly. In oceanic lithosphere, the lithosphere thermal equilibration time is the age of oceanic crust, which is taken from Müller et al. (2019). In

continental margin lithosphere, the lithosphere thermal equilibration time is the age since continental breakup, we set it as 32 Ma (Wu et al., 2017).

3 Methodology

3.1 Gravity inversion

The fast nonlinear gravity inversion based on spatial spherical coordinate proposed by Uieda and Barbosa. (2017) is adopted to study the Moho depth's solution. This approach considers the influence of Earth curvature on the calculation result (Uieda et al., 2015). Moreover, it enhances the inversion calculation efficiency by using Silva et al. (2014) of replacing Jacobian matrix with a Bouguer plate.

To reduce the ill-posed solution of the inversion problem, regularization constraint is introduced to make the inversion result smoother and closer to the real situation (Silva et al., 2001). The inversion objective function $\Gamma(\boldsymbol{P})$ constructed according to the gravity data fitting term and regularization term is as follows:

$$\Gamma(\boldsymbol{P}) = \left[\boldsymbol{d}^0 - \boldsymbol{d}(\boldsymbol{p})\right]^T \left[\boldsymbol{d}^0 - \boldsymbol{d}(\boldsymbol{p})\right] + \mu \boldsymbol{p}^T \mathbf{R}^{\mathrm{T}} \mathbf{R} \boldsymbol{p} \tag{1}$$

Where $\boldsymbol{p}$ represents the Moho depth parameter vector, $\boldsymbol{d}(\boldsymbol{p})$ is the gravity anomaly prediction data vector calculated by $\boldsymbol{p}$, $\boldsymbol{d}^0$ is the gravity anomaly observation data vector, $\mathbf{R}$ is the first-order difference matrix representing the depth of adjacent spherical prisms, and μ is the regularization parameter.

The Gauss-Newton iteration method minimizes the objective function. The perturbation vector $\Delta\boldsymbol{p}$ updates the parameter vector $\boldsymbol{p}$ through the iteration process until the objective function reaches the optimal solution. At the $k+1$st iteration, the parameter vector $\boldsymbol{p}^{k+1}$ is updated as follows:

$$\boldsymbol{p}^{k+1} = \boldsymbol{p}^k + \Delta\boldsymbol{p}^k \tag{2}$$

The perturbation vector of the kth iteration is obtained by solving linear Eq. (3):

$$\left[\mathbf{A}^{\mathrm{k}^{\mathrm{T}}} \mathbf{A}^{\mathrm{k}} + \mu \mathbf{R}^{\mathrm{T}} \mathbf{R}\right] \Delta\boldsymbol{p}^k = \mathbf{A}^{\mathrm{k}^{\mathrm{T}}} \left[\boldsymbol{d}^0 - \boldsymbol{d}\left(\boldsymbol{p}^k\right)\right] - \mu \mathbf{R}^{\mathrm{T}} \mathbf{R} \boldsymbol{p}^k \tag{3}$$

$$\mathbf{A} = 2\pi \mathrm{G} \Delta\rho \mathbf{I} \tag{4}$$

In which G is the gravitational constant, $\Delta\rho$ is the crust-mantle density contrast, and $\mathbf{I}$ is the identity matrix.

We determine the three hyperparameters needed for the inversion by two cross-validations: The Moho reference depth (z^{ref}), crust-mantle density contrast ($\Delta\rho$), and regularization parameters (μ). The specific process is as follows:

(1) Divide the Bouguer gravity anomaly data into two data sets: test set and training set. The grid spacing of the training set is twice that of the test set. We apply the training set to invert the Moho depth given three different parameters, while the test set data is used to determine the values of hyperparameters;
(2) Perform the first cross-validation to determine μ. We set the value range and interval of three hyperparameters, choose one z^{ref} and $\Delta\rho$ randomly and calculate the mean square error (MSE) between the gravity anomaly obtained by forward calculation of Moho depth obtained by inversion and the test set when different μ is selected. The μ corresponding to the minimum MSE is taken as the final μ;
(3) Perform the second cross-validation to determine z^{ref} and $\Delta\rho$. Calculating the MSE between the Moho depth obtained by inversion and the constraint information while selecting different combinations of z^{ref} and $\Delta\rho$. The z^{ref}, $\Delta\rho$ correspond to the minimum MSE that is taken as the optimal solution.

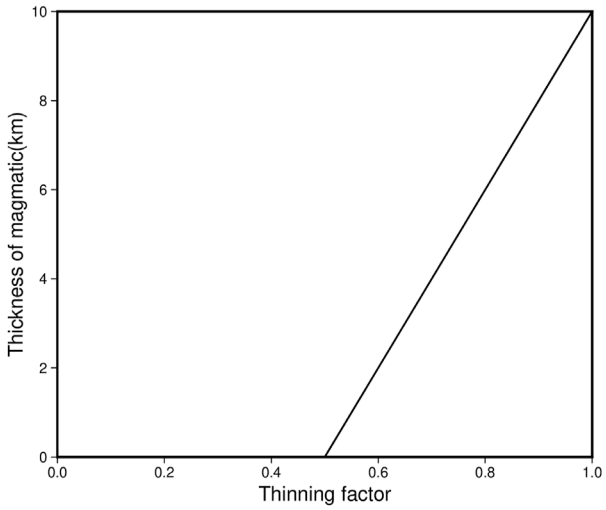

FIGURE 4
Predicted thickness of magmatic as a function of thinning factor.

3.2 Lithosphere thermal gravity anomaly correction

To calculate lithosphere thermal gravity anomaly, we first need to estimate temperature anomaly at different depths in the lithosphere. We divide the study region into 141×121 grids with a vertical spacing of 5 km and utilize the lithosphere thinning temperature field model (McKenzie, 1978) to calculate the temperature anomaly caused by lithosphere stretching based on the assumption that the stretching degree of the lithosphere is equal to the crust. The temperature anomaly in °C, T_z, at depth z is:

$$T_z = \frac{2\mathrm{T_m}}{\pi} \sum_{n=0}^{\infty} \frac{(-1)^{n+1}}{n} \left[\frac{\beta}{n\pi} \sin\left(\frac{n\pi}{\beta}\right) \times \exp\left(-\frac{n^2 t}{\tau}\right) \sin\left(\frac{n\pi z}{\mathrm{a}}\right)\right] \tag{5}$$

where the base-lithosphere temperature $\mathrm{T_m}$ = 1,300°C, lithosphere cooling thermal decay constant τ = 65 Ma, and the equilibrium lithosphere thickness a = 125 km (Greenhalgh and Kusznir, 2007). The description of lithosphere thermal equilibration time t is provided in the Data Source section.

The selection of lithosphere stretching factor β can be divided into two cases. For oceanic lithosphere, $\beta = \infty$. For continental margin lithosphere, the original crustal thickness $\mathrm{Ct_{init}}$ is set as

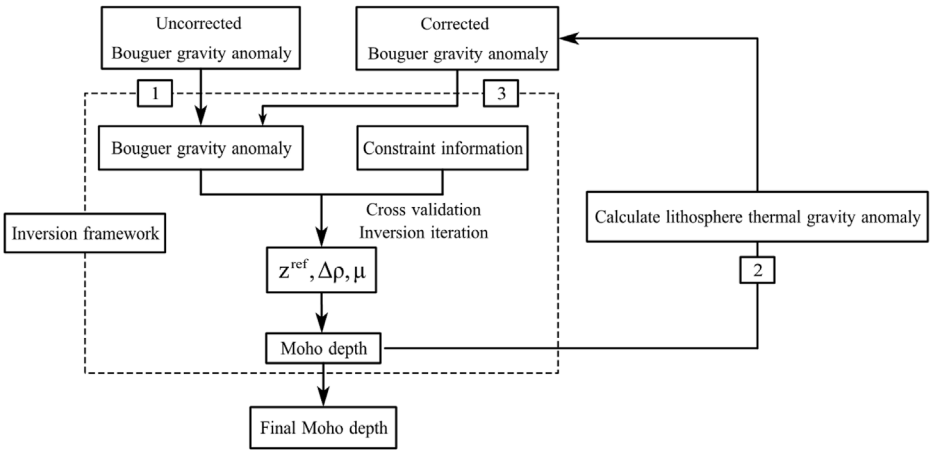

FIGURE 5
Iterative calculation flow chart.

32 km (Wu et al., 2017), and β is equal to the ratio of the original crustal thickness Ct_{init} to the current crustal thickness Ct_{now} derived from gravity inversion. At the rifted continental margin, decompression melting makes the crust thick until the seafloor spreads to form a new oceanic crust. Therefore, thickness of magmatic should be considered and β is calculated as follows:

$$\beta = \frac{Ct_{init}}{Ct_{now} - Ct_{mag}} \tag{6}$$

where Ct_{mag} is the thickness of magmatic. We use the relationship between the thinning factor and thickness of magmatic (White and McKenzie, 1989) to calculate β, set the critical thinning factor $(1 - 1/\beta_{crit}) = 0.5$ and the maximum oceanic crust thickness $Ct_{max} = 10$ km (Greenhalgh and Kusznir, 2007) (Figure 4). When the lithosphere thinning factor $(1 - 1/\beta)$ is less than 0.5, $Ct_{mag} = 0$. On the contrary, the influence of magma on crustal stretching needs to be considered.

When the temperature anomaly is calculated, the second step is to calculate the density anomaly. The transition relationship between temperature anomaly and density anomaly is given by:

$$\Delta\rho = -\alpha\rho\Delta T \tag{7}$$

in which thermal expansion coefficient $\alpha = 3.28 \times 10^{-5}\ K^{-1}$, and $\rho = 3300\ kg/m^3$ (Greenhalgh and Kusznir, 2007).

We set each horizontal layer of the grid represents a 5 km thick layer and calculate the lithosphere thermal gravity anomaly of each layer in spherical coordinate. Therefore, the total lithosphere thermal gravity anomaly is the sum of the anomaly calculated for each layer.

3.3 Calculation process

The final Moho relief is obtained by the following steps (Figure 5):

TABLE 1 Hyperparameters' selection before lithosphere thermal gravity anomaly correction, where z^{ref} is Moho reference depth, $\Delta\rho$ is crust-mantle density contrast, and μ is regularization parameters.

Hyperparameters	Value range	Interval/ Number	Result
μ	$10^{-15} \sim 10^{-5}$	20 points	3.6×10^{-15}
z^{ref}	20–40 km	2.5 km	25 km
$\Delta\rho$	400–700 kg/m^3	25 kg/m^3	625 kg/m^3

TABLE 2 Hyperparameters' selection after lithosphere thermal gravity anomaly correction, where z^{ref} is Moho reference depth, $\Delta\rho$ is crust-mantle density contrast, and μ is regularization parameters.

Hyperparameters	Value range	Interval/ Number	Result
μ	$10^{-15} \sim 10^{-5}$	20 points	1.1×10^{-14}
z^{ref}	20–40 km	2.5 km	25 km
$\Delta\rho$	500–800 kg/m^3	25 kg/m^3	775 kg/m^3

(1) Obtain the initial Moho relief. The Bouguer gravity anomaly data without lithosphere thermal gravity anomaly correction is used for inversion;
(2) Calculate lithosphere thermal gravity anomaly. The crustal thickness is further calculated from the Moho depth obtained in the previous step, and lithosphere thermal anomaly is computed according to the method described above;
(3) Obtain the final Moho relief. The final Moho depth is got through inversion using the Bouguer gravity anomaly data with lithosphere thermal gravity anomaly correction.

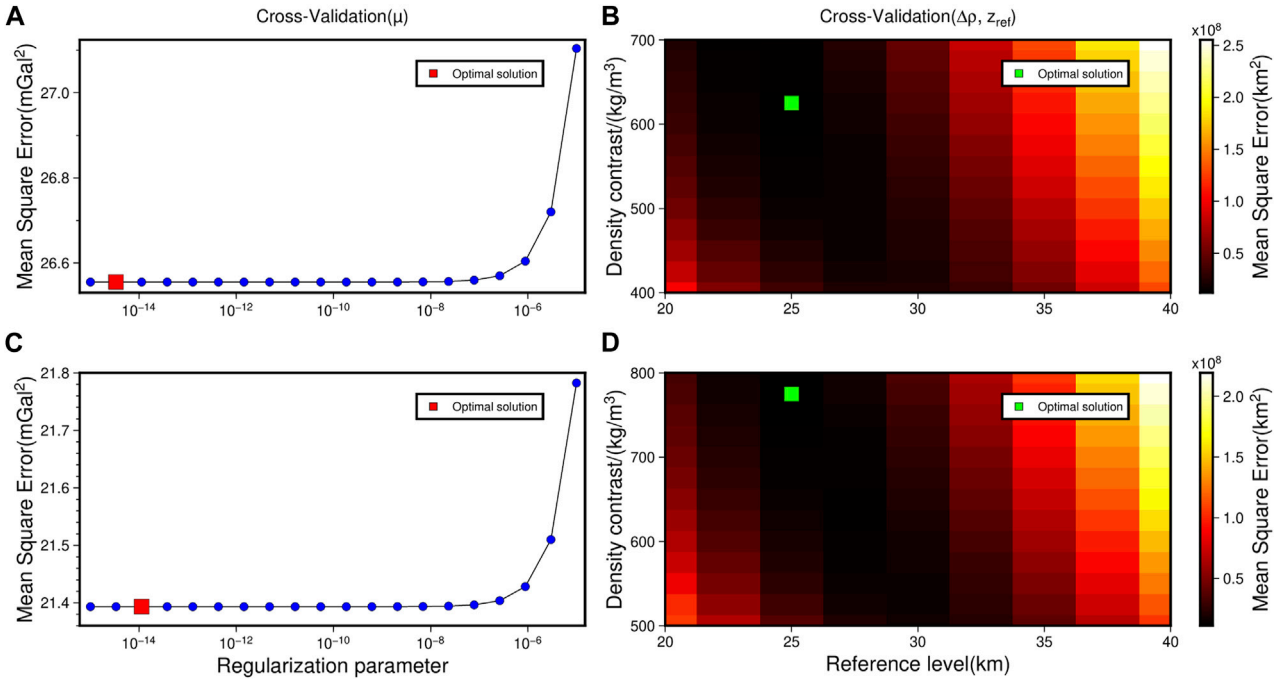

FIGURE 6
Visualization of hyperparameters' selection. **(A, B)** are the hyperparameters selection for gravity inversion without lithosphere thermal gravity anomaly correction; **(C, D)** are the hyperparameters selection for gravity inversion with lithosphere thermal gravity anomaly correction.

4 Results and discussion

4.1 Moho depth inversion results

The spatial resolution of Moho depth inversion results is 0.1 °× 0.1 ° and the relevant information on the hyperparameters' selection is shown in Tables 1, 2; Figure 6.

The final inversion result after lithosphere thermal gravity anomaly correction (Figure 7B) shows that the Moho relief is consistent with the geological structure and Bouguer gravity anomaly distribution. The Moho depth ranges from 6 to 34 km. The Moho depth at SSP is the lowest (6–8 km), WB is about 10–15 km, and they form two large depressions. Fragmented islands' Moho is deep, up to 28–34 km. The Moho relief fluctuates gently at Ontong Java Plateau (17–19 km) and MB (12–14 km). There are two depth gradient zones with drastic changes along the strike of SSP-MB and WB-Solomon Islands-Ontong Java Plateau.

Compared to the inversion results without lithosphere thermal gravity anomaly correction (Figures 7A,C), the final inversion result is overall 2–6 km shallower than before. The Moho depth is significantly reduced at locations with young oceanic crust, such as WB (4–6 km), MB (3–5 km), and SSP (1–2 km), which are currently active parts of seafloor spreading, with significant geothermal upwelling and large lateral density variations. This produces large lithosphere thermal gravity anomaly, resulting in great changes in depth after correction. In contrast, Ontong Java Plateau's Moho depth decreases only by 1–2 km in a wide range, where the oceanic crust is old, and there is no active seafloor spreading, therefore no significant changes in depth after correction.

The misfit analysis all presents normal distribution (Figures 8C, 9C). The residuals between the gravity anomaly obtained by the inversion result's forward calculation and the gravity anomaly observation have a mean of 0.047 mGal and a Standard deviation (Std) of 6.59 mGal (Figure 8C). The mean depth difference between the inversion result and the GEMMA equals −0.3 km, and Std equals 3.45 km (Figure 8D). After correction, gravity residuals' mean value of 0.04 mGal and standard deviation of 6.29 mGal (Figure 9C); the depth differences' mean is 0.18 km, and the standard deviation is 3.31 km (Figure 9D), both of which are reduced from the previous values, indicating that the lithosphere thermal gravity anomaly correction has a positive impact on improving the accuracy of the inversion results.

The depth difference between the final inversion result and the GEMMA model is smaller in SSP and Ontong Java Plateau than without lithosphere thermal gravity anomaly correction (Figures 8B, 9B), which is because these areas no longer experience active seafloor spreading movements, and the lithosphere thermal gravity anomaly can be more accurately calculated, so these areas' Moho depth can better be fitted with the GEMMA model after minor correction. In contrast, the Moho depth in the final inversion result is smaller than in the GEMMA model at the southwest corner of MB and WB (Figure 9B). This difference may arise due to the omission of the lithosphere thermal gravity anomaly in the GEMMA model calculation, or it could be attributed to the present-day active seafloor spreading motion, which leads to errors in the gravity anomaly and oceanic crust age data, resulting in inaccuracy in

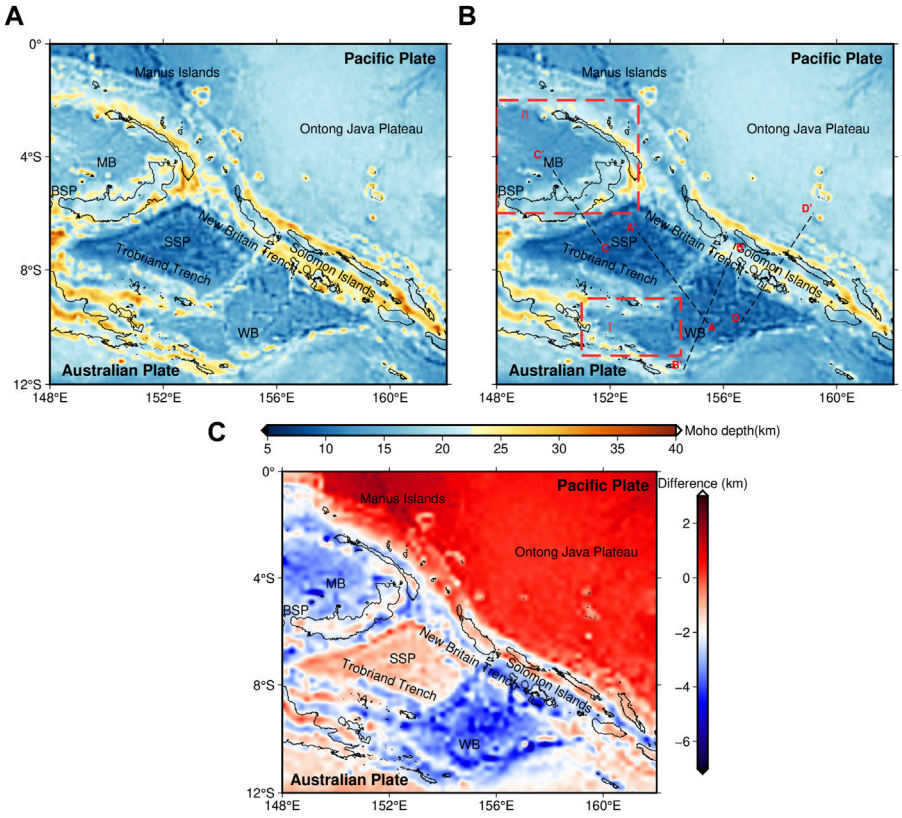

FIGURE 7
Moho depth inversion results. **(A)** Result without lithosphere thermal gravity anomaly correction, **(B)** result with lithosphere thermal gravity anomaly correction. The black dotted line is the section profiles. The red dashed rectangular selection range is the area to be studied below. **(C)** Depth difference between the inversion results after lithosphere thermal gravity anomaly correction and uncorrected inversion results.

the calculation of the lithosphere thermal gravity anomaly and overcorrection.

Gravity residuals are mainly distributed in the trenches (Figures 8A, 9A), and the maximum Moho depth difference is also primarily located there (Figures 8B, 9B), reaching 8–16 km. This result could be attributed to the fact that trenches are formed by the collision between oceanic and continental plates and are situated at the transition zone between oceanic and continental crust, with a complex geological structure. As a result, gravity anomaly data may be inaccurate and lead to significant discrepancies in Moho depth calculations.

4.2 Lithosphere thinning factor and thermal gravity anomaly calculation results

Figure 10A presents the calculated lithosphere thinning factor (LTF), which shows the highest values at SSP and Manus Islands, at around 1.0, followed by WB, with values ranging from 0.7 to 0.9. The values at MB are slightly larger than that at Ontong Java Plateau (0.3–0.4) by 0.1–0.2. The values at fragmented islands range from 0 to 0.3. Additionally, Figure 10B shows that the lithosphere thermal gravity anomaly (LTGA) is inversely proportional to the age of the oceanic crust, with the largest at WB (−200~−160 mGal), followed by MB (−160~ −110 mGal). The values at the SSP range from −137 mGal to −110 mGal. Other areas, such as the Manus Islands and Solomon Islands, are usually between −100 and −70 mGal. In contrast, the values at Ontong Java Plateau are only −20~−60 mGal.

The lithosphere thinning factor and lithosphere thermal gravity anomaly exhibit significant differences between WB and SSP. The SSP continued to spread over the following 10 Ma due to the development of the Solomon rift in the early Oligocene, reaching its peak in the late Oligocene (Honza et al., 1987). Consequently, it underwent prolonged lithosphere stretching and experienced a high degree of thinning. In contrast, WB has a much faster seafloor spreading rate, higher temperature anomaly, and thicker crustal thickness (Figure 13A) than the SSP. The generation of the thin oceanic crust may be due to colder asthenosphere temperature and very slow seafloor spreading rate (Greenhalgh and Kusznir, 2007). Therefore, we speculate that WB has a higher asthenosphere temperature and more intense seafloor spreading activity than the SSP. These factors may explain why the thinning factor at the SSP is higher than that in WB, but the lithosphere thermal gravity anomaly is lower at the SSP.

The problem with the current study of the lithosphere thermal gravity anomaly in Papua New Guinea is that we assumed that the extension of the crust is equivalent to the extension of the lithosphere. However, there is a significant

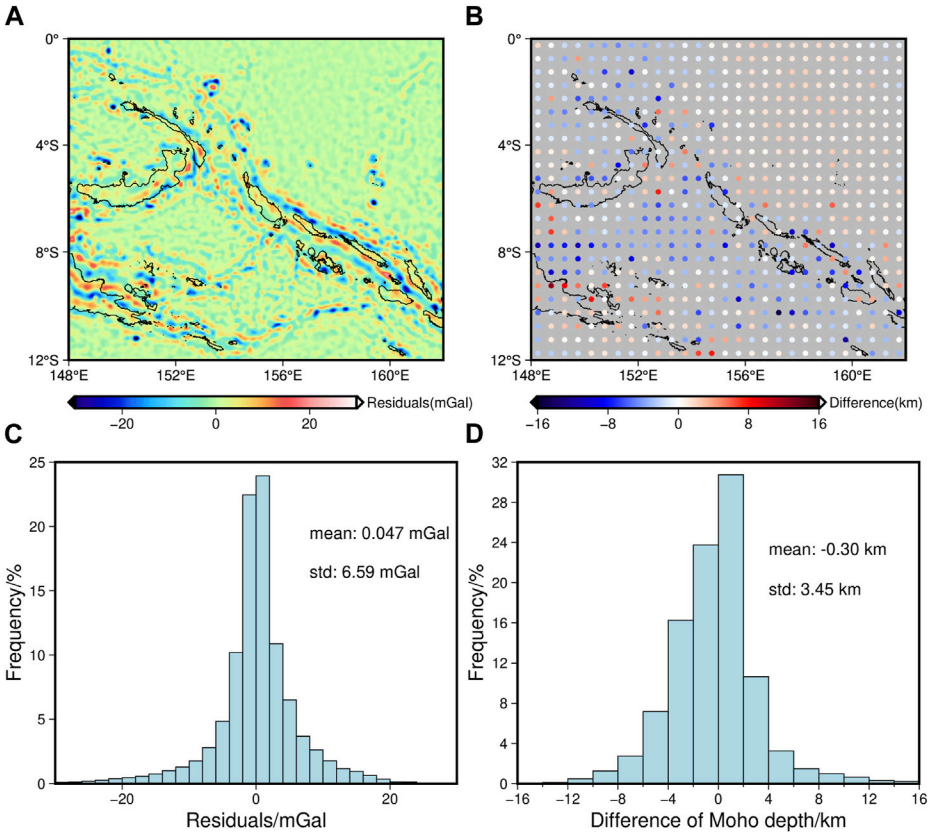

FIGURE 8
The misfit analysis of Moho depth inversion result without lithosphere thermal gravity anomaly correction. **(A)** The residuals between the gravity anomaly obtained by the inversion result's forward calculation and the gravity anomaly observation, **(B)** the Moho depth differences between the inversion result and the GEMMA, **(C)** histogram of the gravity residuals, and **(D)** histogram of the Moho depth differences.

stretching difference between these units in the actual evolution process, which we have not yet discussed in our current calculations. We will focus on this issue in more depth in a follow-up study.

4.3 Seafloor spreading

Lithosphere thinning factor and crust thickness variation are critical parameters that describe the extent and intensity of seafloor spreading. Sudden thinning of the crustal thickness may be attributed to seafloor spreading (Bown and White, 1994). Meanwhile, the lithosphere thinning factor measures the degree of thinning of the lithosphere. Hence, we decide to use these data to analyse the characteristics of seafloor spreading in two typical areas (Part of WB and MB).

Study area I is in the southwest corner of the WB, between Trobriand Trench and Owen Stanley Fault Zone. WB has expanded from northeast to southwest since 3.4 Ma, and the spreading centre keeps moving southward. The crustal thickness is significantly thinner by 10–15 km compared with the surrounding area (The Solomon Islands and the Australian plate) (Figure 13B). Seafloor spreading from 1 Ma to the present has occurred in 151°40′E~152°30′E, 9°30'S~10°30'S (Benes et al., 1994), SE-NW trend. The oceanic crust gradually decreases from southeast to northwest (Solid orange lines in Figure 11A), the corresponding Moho depth is shallower than the surrounding area, and the variation range is almost consistent with the oceanic crust (Figure 11A). The spreading centre is practically located in the central area of the oceanic crust. It spreads laterally to form a younger oceanic crust (<0.78 Ma, the dark blue solid line in Figure 11A) with a more significant thinning.

The oceanic crust displays apparent asymmetry on its northern and southern sides, with the southern side exhibiting a wider range and steeper inclination angle than the other one (Figure 11A). Abers et al. (2002) provided a north-south profile of Moho depth at the southwest corner of the WB using receiver function data at 150.8°E. We compared a portion of these results (9°S-11°S, the solid red line in Figure 11A) with our inversion results and the GEMMA model. We found that the inversion results fit the trend of the receiver function results more closely than the GEMMA model. The gravity inversion results match well with the receiver function results to the south direction from the point of coordinate (150.8°E, 10°S), with differences basically between 0 and 8 km. However, the Moho depth inversion results are generally lower than the receiver function results towards the south direction (>8 km) (Figure 12). This discrepancy may be

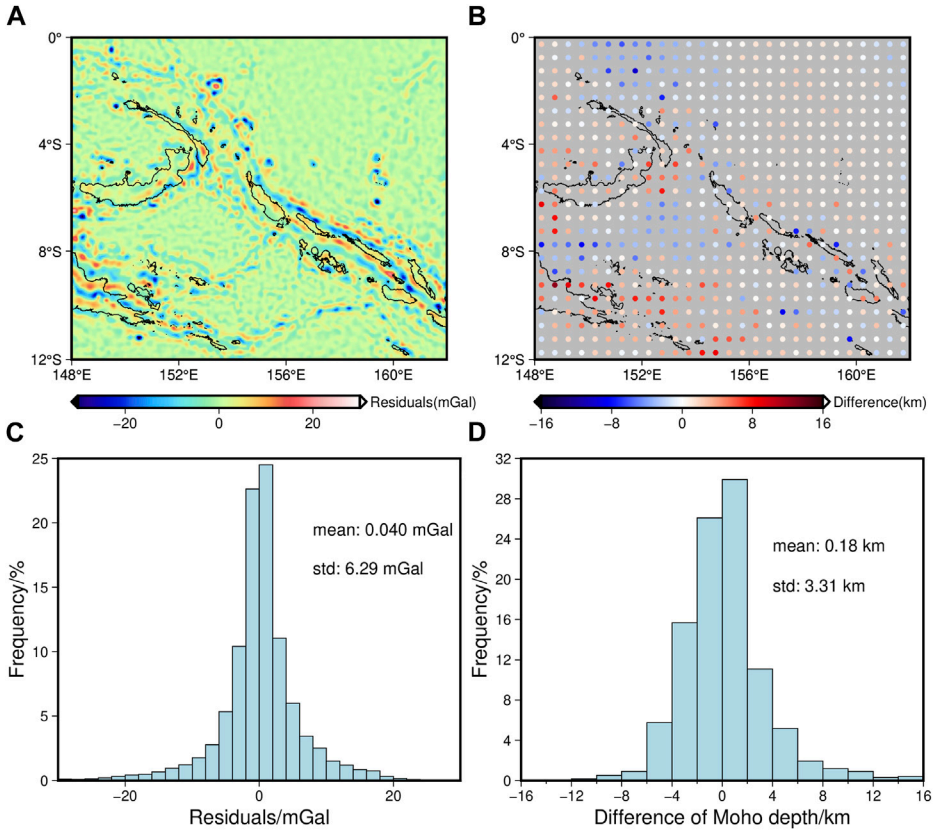

FIGURE 9
The misfit analysis of Moho depth inversion result with lithosphere thermal gravity anomaly correction. The introduction of **(A–C)**, and **(D)** is the same as that of the corresponding pictures in Figure 8.

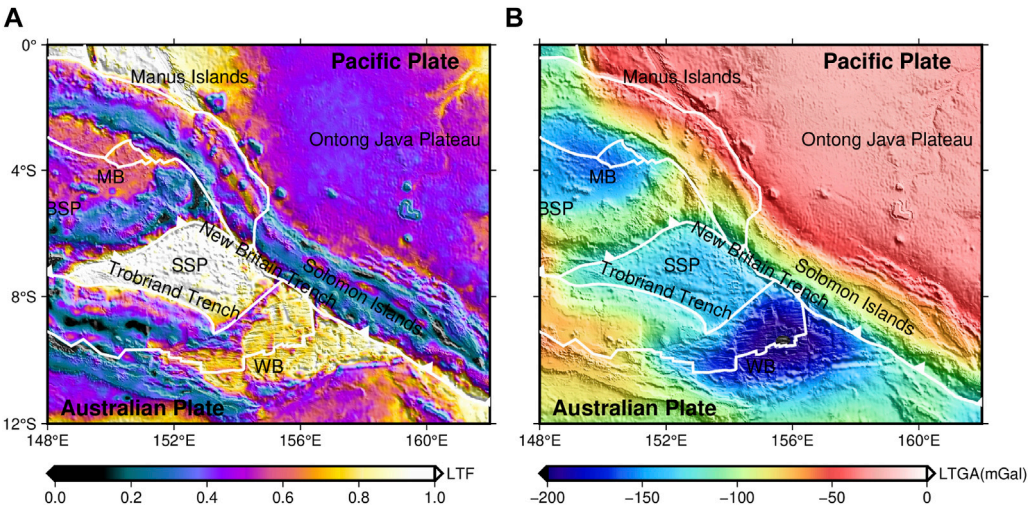

FIGURE 10
Distribution of lithosphere thinning factor and lithosphere thermal gravity anomaly in Papua New Guinea. **(A)** Lithosphere thinning factor (LTF), **(B)** lithosphere thermal gravity anomaly (LTGA).

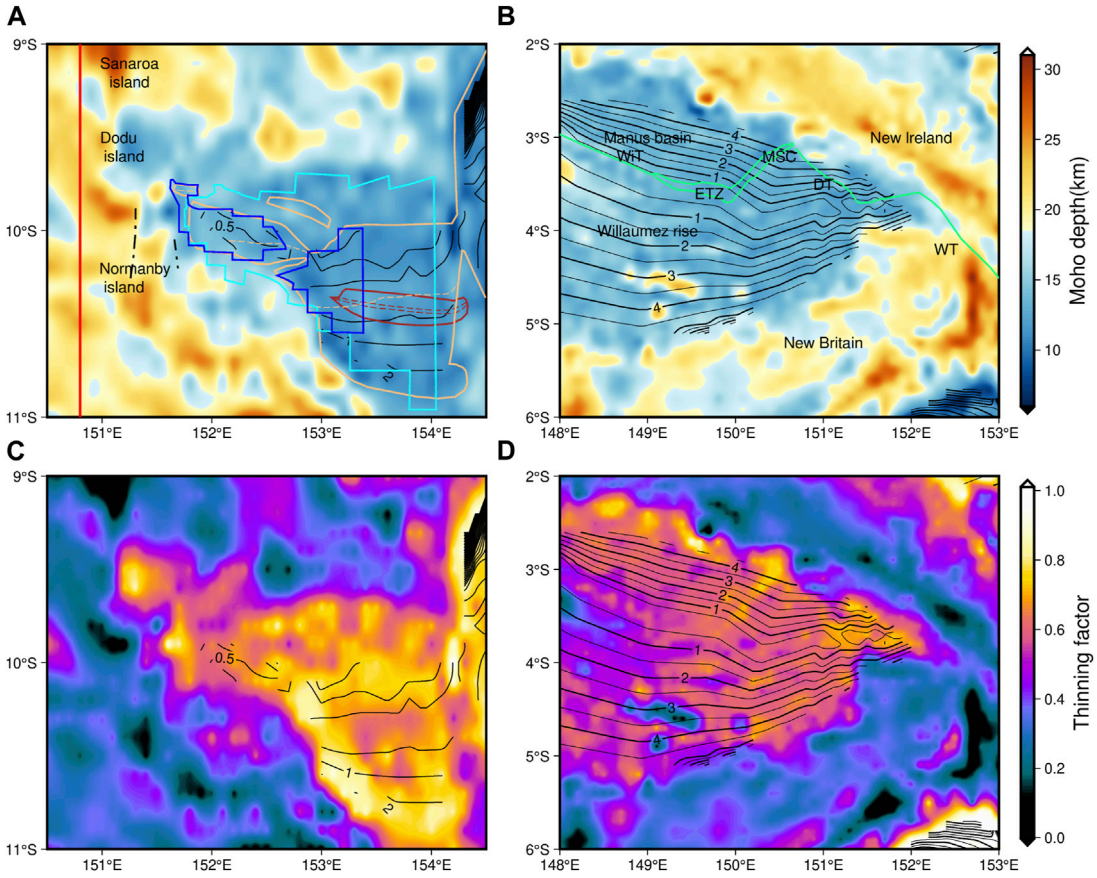

FIGURE 11
Distribution of Moho depth, thinning factor in the study area I and II. The first column **(A, C)** is the two data distribution details of study area I; the second column is the data distribution details of study area II. CBGA is the abbreviation of corrected Bouguer gravity anomaly. Previous research results are drawn in Figure 11A. The solid brown line represents the COB, where the dotted brown line is the spreading centre (Taylor et al., 1999). The solid orange line represents the oceanic crust since 1.2 Ma, where the dotted orange line is the spreading centre (Goodliffe and Taylor, 2022). The light blue solid line is the scope of the oceanic crust older than 0.73 Ma (Benes et al., 1994). The area surrounded by the dark blue line is the younger new-born oceanic crust, less than 0.73 Ma (Benes et al., 1997). The solid red line is the location of the receiver function line result of Abers et al. (2002). Martinez and Taylor. (1996) refer to the area enclosed by the solid green line in Figure 11B. ETZ represents the extensional transform zone. WiT, DT, and WT are transformed faults. The contours in the figures show the age of oceanic crust.

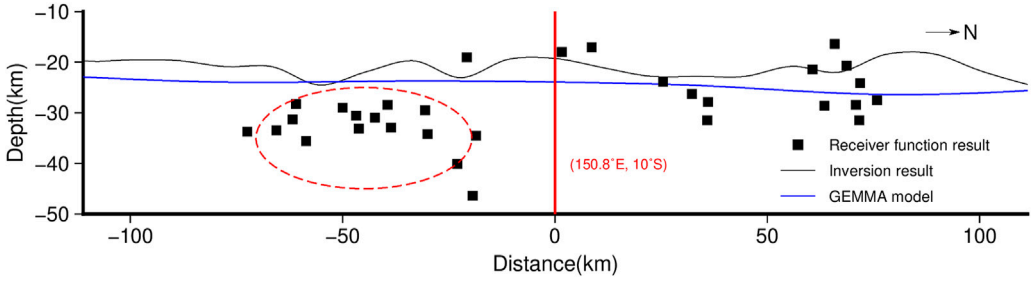

FIGURE 12
Comparison between the previous research results and this paper's results at WB.

caused by simple shear acting on the rift margin of the southern side of the lithosphere, resulting in a more complex geological structure on this side (Benes et al., 1994). Additionally, Taylor et al. (1999) provided the location of the Continent-Ocean Boundary (COB) (solid brown line in Figure 11A), which is situated in the narrow region between longitude 153°–154°5' E on the south side of the oceanic crust, representing the boundary between the thinning continental crust and the normal oceanic

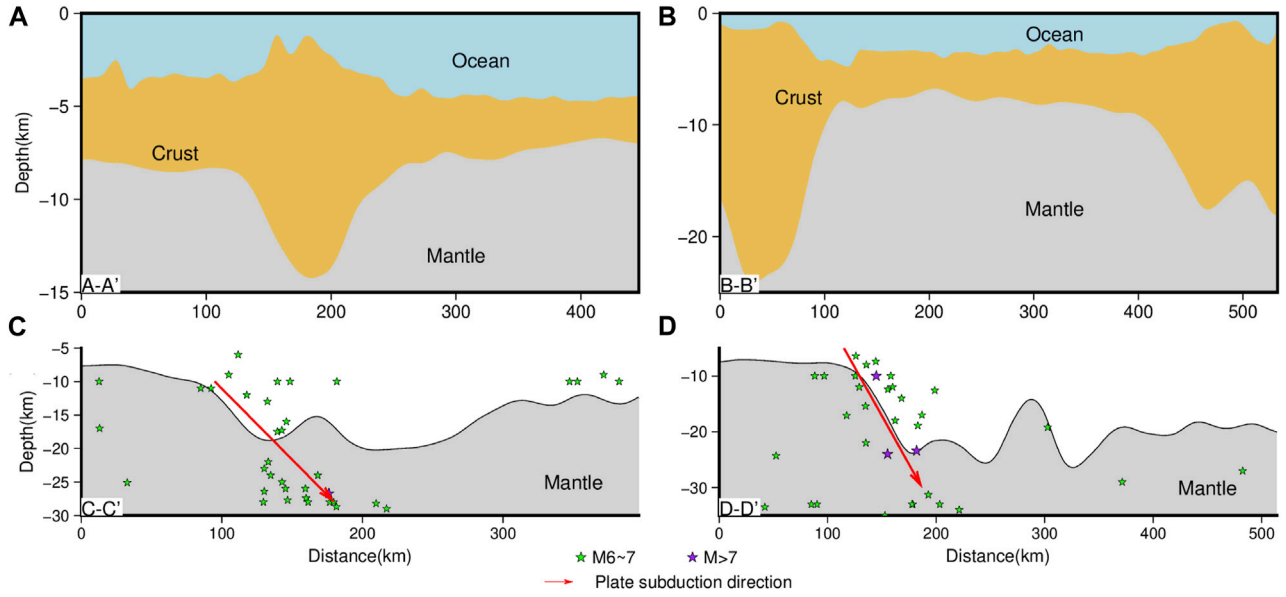

FIGURE 13
Four selected profiles, of which the locations of the profiles are shown in Figure 7B.

crust. Meanwhile, the thinning factor is greater on the southern than on the northern side (>0.8, Figure 11C). These two pieces of evidence suggest the stronger tectonic movement on the southern side of the oceanic crust.

At 151°40′E, 9°–11°S, there are significant variations in crustal thickness and thinning factor, characterized by rapid crustal thickening (12–16 km) and drastic changes in thinning factor (0.8–0.3). Towards the west direction from 151°40′E, the terrain is transformed into a series of mounds and graben structures associated with continental rift (Benes et al., 1994) lies a narrow transition zone between seafloor spreading and continental rifting (Ferris et al., 2006), which is balanced by transition fault systems (Black dotted line in Figure 11A) (Benes et al., 1997).

Study area II is primarily situated in the Manus Basin (MB), which is bordered by New Ireland and New Britain. Receiver function analysis has determined a Moho depth point of 19.2 km at the Manus Islands (Xu et al., 2022), which is very close to our inversion results with a difference of only 0.4 km. The Manus spreading centre is located in the southeast corner of the MB, accompanied by an extensional transform zone to its left, together constituting the seafloor spreading segment. The relationship between continental rifting and seafloor spreading is balanced by three transform fault systems: WiT, DT, and WT (Martinez and Taylor, 1996). The crustal thickness in the MB and its vicinity remains relatively stable, primarily at 15 km. Moreover, the thinning factor is symmetrically distributed along the north and south sides of the spreading segment, indicating that the lithosphere may be uniformly stretched along the spreading part. Dyriw et al. (2021) also indicate that the back-arc crust was partially extended before seafloor spreading, suggesting that the spreading centre uniformly diffused along the spreading axis (Martinez and Taylor, 1996).

4.4 Microplates subduction and seismic activity

We select two profiles with distinct subduction features under the tectonic background and project the relative earthquakes within 150 km along with the profiles onto them to analyse the relationship between the Moho relief, earthquakes, and microplate subduction (Figures 7B, 13C, D).

Profile C-C′ traverses the Western New Britain Trench, SSP, and BSP. The Australian Crustal front is embedded within a portion of the accretion block, influenced by arc-continent collision and block accretion. It provides upward heat flow (Holm and Richards, 2013), forming an active West Bismarck volcanic arc. In the first half of the profile, the Moho depth increases gradually from 10 km to 17 km; strong earthquakes are primarily distributed along the direction indicated by the red arrow (Figure 13C), which should be the angle of the SSP subducted beneath the BSP, severe subduction leads to the generation of fault systems in the deep crust (Abers, 1994).

Profile D-D' across WB, East New Britain Trench, Solomon Islands, and Ontong Java Plateau shows that the Moho depth rapidly deepens from 8 to 23 km, and earthquakes are primarily distributed in the deep crust. The red arrow in Figure 13D may indicate the angle of WB subducted into the Solomon Islands. Therefore, we can assume that WB subducted into the Solomon Islands at a higher angle than SSP subducted beneath BSP according to Moho relief and earthquake distribution, which further suggests that the Solomon Islands are in a high-stress state, earthquakes on the west side of WB might be affected by it (Yoneshima et al., 2005).

Earthquakes are primarily concentrated in the Moho depth gradient zone of Papua New Guinea, particularly on both sides of the New Britain Trench. The lithosphere thinning factor varies significantly there, indicating intense stretching and strong deep crustal tectonic movement. Moreover, the anti-isostatic effect is most significant in the West New Britain Trench, demonstrating that underground materials' distribution is exceptionally uneven and has a strong trend of isostatic adjustment (Yang et al., 2018), which may further trigger strong earthquakes.

In addition, the seismic distribution of SSP is mainly concentrated in the shallow crust. In contrast, the seismic distribution of BSP decreases gradually from shallow to medium-deep sources, which means BSP has lower integrity and is less stable than the former. Therefore, strong earthquakes near the West New Britain Trench tend to extend further under BSP with the development of microplate movement.

5 Conclusion

We discuss the characteristics of regional seafloor spreading and microplate subduction combined with other geophysical data from the perspective of the lithosphere thinning factor, Moho depth inversion result based on the gravity field model XGM 2019e by removing the lithosphere thermal gravity anomaly. The main conclusions are as follows:

(1) The Moho depth of Papua New Guinea is between 6 and 34 km. The lithosphere thinning factor is the largest at Solomon Sea Plate and Manus Islands, values at fragmented islands are close to 0. The maximum value of lithosphere thermal gravity anomaly is −200 mGal at Woodlark Basin.
(2) More intense tectonic movement occurred in the southern oceanic crust at the southwest of Woodlark Basin. Within Manus Basin, new oceanic crust expends uniformly on both sides along the spreading axis.
(3) The earthquakes and the Moho relief are closely related to microplate movement. Woodlark Basin subducted into the Solomon Islands at a higher Angle than Solomon Sea Plate beneath the Bismarck Sea Plate.

Data availability statement

The original contributions presented in the study are included in the article/supplementary material, further inquiries can be directed to the corresponding author.

Author contributions

YL contributed to the application of methods, original draft writing and review. GY, JZ, and BZ contributed to the draft review and its scientific development. All authors revised the manuscript and approved the final version for publication validation for the program. All authors contributed to the article and approved the submitted version.

Funding

This study was supported by the National Natural Science Foundation of China under Grant No. 42174104, U1939204 and Hubei Provincial Natural Science Foundation of China (2022CFB350).

Conflict of interest

The authors declare that the research was conducted in the absence of any commercial or financial relationships that could be construed as a potential conflict of interest.

Publisher's note

References

Abers, G. A., Ferris, A., Craig, M., Davies, H., Lerner-Lam, A. L., Mutter, J. C., et al. (2002). Mantle compensation of active metamorphic core complexes at Woodlark rift in Papua New Guinea. *Nature* 418 (22), 862–865. doi:10.1038/nature00990

Abers, G. A., and McCaffrey, R. (1994). Active arc-continent collision: Earthquakes, gravity anomalies, and fault kinematics in the Huon-Finisterre collision zone, Papua New Guinea. *Tectonics* 13 (2), 227–245. doi:10.1029/93TC02940

Abrehdary, M., Sjöberg, L. E., and Bagherbandi, M. (2015). Combined Moho parameters determination using CRUST1.0 and vening meinesz-moritz model. *J. Earth Sci.* 26 (4), 607–616. doi:10.1007/s12583-015-0571-6

Aitken, A. R. A. (2010). Moho geometry gravity inversion experiment (MoGGIE): A refined model of the Australian Moho, and its tectonic and isostatic implications. *Earthpl. Sci. Lett.* 297, 71–83. doi:10.1016/j.epsl.2010.06.004

Aitken, A. R. A., Salmon, M. L., and Kennett, B. L. N. (2013). Australia's Moho: A test of the usefulness of gravity modelling for the determination of Moho depth. *Tectonophysics* 609, 468–479. doi:10.1016/j.tecto.2012.06.049

Alvey, A., Gaina, C., Kusznir, N. J., and Torsvik, T. H. (2008). Integrated crustal thickness mapping and plate reconstructions for the high Arctic. *Earthpl. Sci. Lett.* 274 (3-4), 310–321. doi:10.1016/j.epsl.2008.07.036

Amante, C., and Eakins, B. W. (2009). "ETOPO1 1 arc-minute global relief model: Procedures, data sources and analysis," in *NOAA technical memorandum NESDIS NGDC-24* (National Geophysical Data Center, NOAA). doi:10.7289/V5C8276M

Benes, V., Bocharova, N., Popov, E., Scott, S. D., and Zonenshain, L. (1997). Geophysical and morpho-tectonic study of the transition between seafloor spreading and continental rifting, Western Woodlark Basin, Papua New Guinea. *Mar. Geol.* 142, 85–98. doi:10.1016/S0025-3227(97)00042-X

Benes, V., Scott, S. D., and Binns, R. A. (1994). Tectonics of rift propagation into a continental margin: Western Woodlark Basin, Papua New Guinea. *J. Geophys. Res. Solid Earth* 99 (B3), 4439–4455. doi:10.1029/93JB02878

Bird, P. (2003). An updated digital model of plate boundaries. *Geochem. Geophys. Geosystems* 4 (3), 1027. doi:10.1029/2001GC000252

Borrero, J. C., Bu, J., Saiang, C., UsJu, B., Freckman, J., Gomer, B., et al. (2003). Field Survey and preliminary modeling of the wewak, Papua New Guinea earthquake and tsunami of 9 september 2002. *Seismol. Res. Lett.* 74 (4), 393–405. doi:10.1785/gssrl.74.4.393

Bown, J. W., and White, R. S. (1994). Variation with spreading rate of oceanic crustal thickness and geochemistry. *Earthpl. Sci. Lett.* 121, 435–449. doi:10.1016/0012-821X(94)90082-5

Chappell, A. R., and Kusznir, N. J. (2008). Three-dimensional gravity inversion for Moho depth at rifted continental margins incorporating a lithosphere thermal gravity anomaly correction. *Geophys. J. Int.* 174, 1–13. doi:10.1111/j.1365-246X.2008.03803.x

Constantino, R. R., and Sacek, V. (2020). Thermal correction for Moho depth estimations on west philippine basin: A Python code to calculate the gravitational effects of lithospheric cooling under oceanic crust. *Pure Appl. Geophys* 177, 5225–5236. doi:10.1007/s00024-020-02581-2

Cowie, L., and Kusznir, N. (2012). Gravity inversion mapping of crustal thickness and lithosphere thinning for the eastern Mediterranean. *Lead. Edge* 31 (7), 810–814. doi:10.1190/tle31070810.1

Curtis, J. W. (1973). Plate tectonics and the papua—new Guinea—Solomon islands region. *J. Geol. Soc. Aust.* 20 (1), 21–35. doi:10.1080/14400957308527892

Davies, H. L. (2012). The geology of New Guinea - the cordilleran margin of the Australian continent. *Episodes* 35 (1), 87–102. doi:10.18814/epiiugs/2012/v35i1/008

Dyriw, N. J., Bryan, S. E., Richards, S. W., Parianos, J. M., Arculus, R. J., and Gust, D. A. (2021). Morphotectonic analysis of the east Manus Basin, Papua New Guinea. *Front. Earth Sci.* 8, 596727. doi:10.3389/feart.2020.596727

Ferris, A., Abers, G. A., Zelt, B., Taylor, B., and Roecker, S. (2006). Crustal structure across the transition from rifting to spreading: The Woodlark rift system of Papua New Guinea. *Geophys. J. Int.* 166, 622–634. doi:10.1111/j.1365-246X.2006.02970.x

Gaulier, J. M., Chamot-Rooke, N., and Jestin, F. (1997). Constraints on Moho depth and crustal thickness in the Liguro-Provençal Basin from a 3d gravity inversion: Geodynamic implications. *Rev. l'Institut Français Pétrole, EDP Sci.* 52 (1), 557–583. doi:10.2516/ogst:1997060

Goodliffe, A. M., and Taylor, B. (2022). The boundary between continental rifting and sea-floor spreading in the Woodlark Basin, Papua New Guinea. *Geol. Soc. Spec. Publ.* 282, 217–238. doi:10.1144/sp282.11

Greenhalgh, E. E., and Kusznir, N. J. (2007). Evidence for thin oceanic crust on the extinct Aegir Ridge, Norwegian Basin, NE Atlantic derived from satellite gravity inversion. *Geophys. Res. Lett.* 34, L06305. doi:10.1029/2007GL029440

Haddad, D., and Watts, A. B. (1999). Subsidence history, gravity anomalies, and flexure of the northeast Australian margin in Papua New Guinea. *Tectonics* 18 (5), 827–842. doi:10.1029/1999TC900009

Holm, R. J., and Richards, S. W. (2013). A re-evaluation of arc–continent collision and along-arc variation in the Bismarck Sea region, Papua New Guinea. *Aust. J. Earth Sci.* 60 (5), 605–619. doi:10.1080/08120099.2013.824505

Honza, E., Davies, H. L., Keene, J. B., and Tiffin, D. L. (1987). Plate boundaries and evolution of the Solomon sea region. *Geo-Mar Lett.* 7, 161–168. doi:10.1007/BF02238046

Joshima, M., Okuda, Y., Murakami, F., Kishimoto, K., and Honza, E. (1987). Age of the Solomon sea basin from magnetic lineations. *Geo-Mar Lett.* 6, 229–234. doi:10.1007/BF02239584

Mann, P., Taylor, F. W., Lagoe, M. B., Quarles, A., and Burr, G. (1998). Accelerating late Quaternary uplift of the New Georgia Island Group (Solomon island arc) in response to subduction of the recently active Woodlark spreading center and Coleman seamount. *Tectonophysics* 295, 259–306. doi:10.1016/S0040-1951(98)00129-2

Martinez, F., and Taylor, B. (1996). Backarc spreading, rifting, and microplate rotation, between transform faults in the Manus Basin. *Mar. Geophys. Res.* 18, 203–224. doi:10.1007/BF00286078

Mckenzie, D. (1978). Some remarks on the development of sedimentary basins. *Earth Planet. Sci. Lett.* 40, 25–32. doi:10.1016/0012-821X(78)90071-7

Müller, D. R., Zahirovic, S., Williams, E. S., Cannon, J., Seton, M., Bower, D. J., et al. (2019). A global plate model including lithospheric deformation along major rifts and orogens since the Triassic. *Tectonics* 38, 1884–1907. doi:10.1029/2018TC005462

Pigram, C. J., and Davies, H. L. (1987). Terrranes and the accretion history of the new Guinea orogen: Bmr. *J. Aust. Geol. Geophys.* 10, 193–211.

Reguzzoni, M., and Sampietro, D. (2015). Gemma: An Earth crustal model based on GOCE satellite data. *Int. J. Appl. Earth Obs. Geoinf* 35 (A), 31–43. doi:10.1016/j.jag.2014.04.002

Silva, J., Medeiros, W., and Barbosa, V. (2001). Potential-field inversion: Choosing the appropriate technique to solve a geologic problem. *Geophysics* 66 (2), 511–520. doi:10.1190/1.1444941

Silva, J., Santos, D., and Gomes, K. (2014). Fast gravity inversion of basement relief. *Geophysics* 79 (5), G79–G91. doi:10.1190/geo2014-0024.1

Taylor, B., Goodliffe, A. M., and Martinez, F. (1999). How continents break up: Insights from Papua New Guinea. *J. Geophys. Res. Solid Earth* 104 (B4), 7497–7512. doi:10.1029/1998JB900115

Uieda, L., Barbosa, V. C. F., and Braitenberg, C. (2015). Tesseroids: Forward-modeling gravitational fields in spherical coordinates. *Geophysics* 81 (5), 41–48. doi:10.1190/geo2015-0204.1

Uieda, L., and Barbosa, V. C. F. (2017). Fast nonlinear gravity inversion in spherical coordinates with application to the South American Moho. *Geophys. J. Int.* 208, 162–176. doi:10.1093/gji/ggw390

Wallace, L. M., Stevens, C., Silver, E., McCaffrey, R., Loratung, W., Hasiata, S., et al. (2004). GPS and seismological constraints on active tectonics and arc-continent collision in Papua New Guinea: Implications for mechanics of microplate rotations in a plate boundary zone. *J. Geophys. Res. Solid Earth* 109 (B05404), 1–16. doi:10.1029/2003JB002481

White, R., and Mckenzie, D. (1989). Magmatism at rift zones: The generation of volcanic continental margins and flood basalts. *J. Geophys. Res. Solid Earth* 94 (86), 7685–7729. doi:10.1029/JB094iB06p07685

Wu, Z. C., Gao, J. Y., Ding, W. W., Shen, Z. Y., Zhang, T., and Yang, C. G. (2017). Moho depth of the South China Sea basin from three-dimensional gravity inversion with constraint points. *Chin. J. Geophys.* 60 (4), 368–383. doi:10.6038/cjg20170709

Xu, C., Xing, J. H., Gong, W. W., Zhang, H., Xu, H. W., and Xu, X. (2022). Density structure of the Papua New Guinea-Solomon arc subduction system. *J. Ocean. Univ. China* 22 (3), 1–8. doi:10.1007/s11802-023-5425-8

Xu, Z., Feng, W. P., Du, H. L., Li, L., Wang, S., Yi, L., et al. (2020). The 2018 $M_{<i>w</i>}$ 7.5 Papua New Guinea earthquake: A possible complex multiple faults failure event with deep-seated reverse faulting. *Geophys. Res. Lett.* 47, e2020GL089271. doi:10.1029/2019EA000966

Yang, G. L., Shen, C. Y., Wang, J. P., Xuan, S. B., Wu, G. J., and Tan, H. B. (2018). Isostatic anomaly characteristics and tectonism of the New Britain Trench and neighboring Papua New Guinea. *Geod. Geodyn.* 9 (5), 404–410. doi:10.1016/j.geog.2018.04.006

Yoneshima, S., Mochizuki, K., Araki, E., Hino, R., Shinohara, M., and Suyehiro, K. (2005). Subduction of the Woodlark Basin at new Britain trench, Solomon islands region. *Tectonophysics* 397, 225–239. doi:10.1016/j.tecto.2004.12.008

Zhu, L. P., and Kanamori, H. (2000). Moho depth variation in southern California from teleseismic receiver functions. *J. Geophys. Res. Solid Earth* 105 (B2), 2969–2980. doi:10.1029/1999JB900322

Zingerle, P., Pail, R., Gruber, T., and Oikonomidou, X. (2020). The combined global gravity field model XGM2019e. *J. Geod.* 94 (7), 66. doi:10.1007/s00190-020-01398-0

frontiers | Frontiers in Earth Science

TYPE Original Research
PUBLISHED 24 May 2023
DOI 10.3389/feart.2023.1171884

OPEN ACCESS

EDITED BY
Paolo Capuano,
University of Salerno, Italy

REVIEWED BY
Umberto Riccardi,
University of Naples Federico II, Italy
Yosuke Aoki,
The University of Tokyo, Japan

*CORRESPONDENCE
Filippo Greco,
filippo.greco@ingv.it

RECEIVED 22 February 2023
ACCEPTED 15 May 2023
PUBLISHED 24 May 2023

CITATION
Pánisová J, Greco F, Carbone D, Branca SF and Vajda P (2023), New insights into geological setting of the summit area of mount Etna volcano (Italy) inferred from 2D gravity data modelling. *Front. Earth Sci.* 11:1171884. doi: 10.3389/feart.2023.1171884

New insights into geological setting of the summit area of mount Etna volcano (Italy) inferred from 2D gravity data modelling

Jaroslava Pánisová[1], Filippo Greco[2]*, Daniele Carbone[2], Stefano Felice Branca[2] and Peter Vajda[1]

[1]Earth Science Institute of the Slovak Academy of Sciences, Bratislava, Slovakia, [2]Istituto Nazionale di Geofisica e Vulcanologia—Sezione di Catania—Osservatorio Etneo, Catania, Italy

Gravimetric observations were carried out in 2015, to image the uppermost portion of the volcanic plumbing system of Mt. Etna (Italy). Gravity measurements were performed using two relative gravimeters, along a profile that crosses the summit craters area (elevations between 2,820 and 3,280 m a.s.l.). Accurate positioning of the gravity observation points was determined through GPS measurements. After applying elevation and terrain corrections, the reduced gravity data were used to build a 2D density model of the uppermost part of the volcano edifice. This model was constrained using to-date knowledge of the structural setting of the area and the available volcanological data. We highlighted the presence of low-density material below the summit craters, down to the depth of about 2.1 km, interpreted as highly altered, fumarolized and structurally weakened material. It is also likely that the close presence of the conduits feeding the summit craters of the volcano contributes to the gravity low in the SW half of the measurement profile. Conversely, the gravity low observed at the northern edge of the profile could reflect the high concentration of faults and eruptive fissures in the Pizzi Deneri area, in correspondence of the Ellittico caldera rim.

KEYWORDS

gravity, density model, plumbing system, Etna volcano, volcano eruption

Introduction

One of the most important elements characterizing volcanism is the structural setting of the uppermost section of the volcano's plumbing system. It consists of interconnected magma conduits and reservoirs (Cashman et al., 2017), which directly govern the mobilisation and storage, as well as the transport/ascent, evolution and eruption of magma.

Over the last few decades, significant advances in using geophysical techniques to image the structure of magma plumbing systems have enabled the identification of zones of melt accumulation, crystal mush development, and magma migration (Magee et al., 2018).

Mount Etna (Italy) is an active open-conduit volcano characterized by almost persistent mild explosive activity from the summit craters. This "steady state" is sometimes interrupted by phases of stronger activity from the summit craters or from flank fissures (Calvari et al., 2020). Since detailed information is rarely available about the characteristics of buried

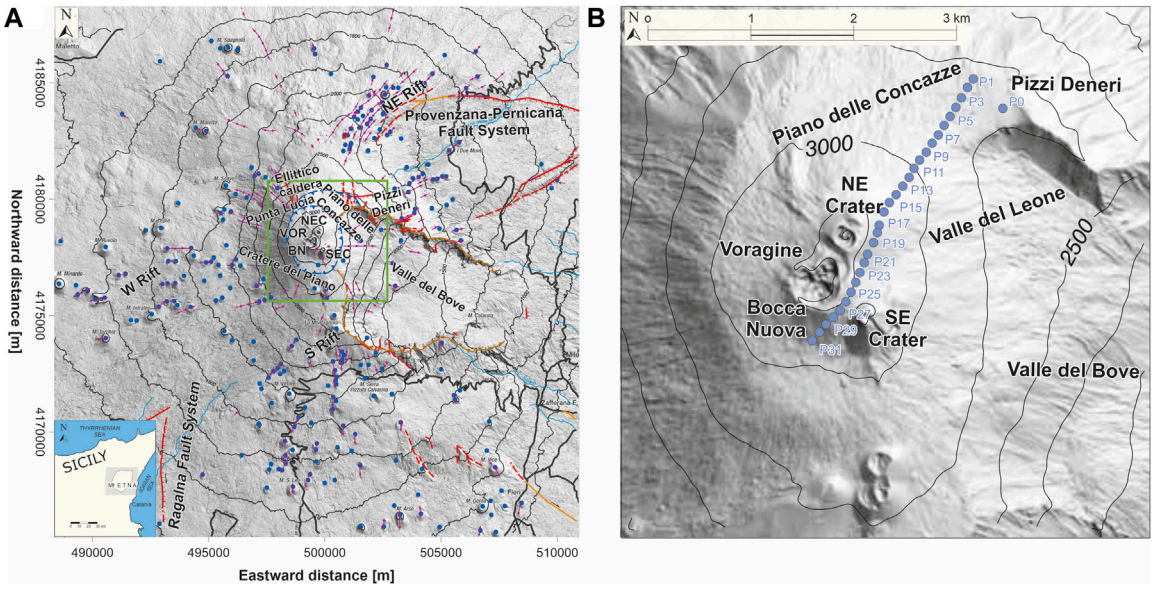

FIGURE 1
(A) Sketch map of Etna showing location of the volcano-tectonic landforms (modified after Azzaro et al. (2012): faults (solid or dashed red lines with barbs); caldera rims (solid or dashed blue lines with barbs); flank collapse rims (solid or dashed brown lines with rounded barbs); eruptive fissures (purple lines with circles); pyroclastic cones (blue points). The inset at the bottom left shows the location of Etna volcano with respect to Sicily. The green square represents the area indicated in **(B)**, which includes the gravimetric profile with 31 measuring points. Geographical coordinates are expressed in UTM projection, zone 33 N.

structures and faults, it is not clear which role they could play during a magmatic intrusion, and, in particular, if they could be activated and become preferential pathways for magma ascent.

In these conditions, gravity investigations have proven valuable in delivering information about magma chambers, dykes, and sill complex locations and geometries (Locke et al., 1993; Kauahikaua et al., 2000; Schiavone and Loddo, 2007; Fedi et al., 2018; Magee et al., 2018).

With the aim of investigating the geological structure of the uppermost part of the plumbing system of Mt. Etna, a gravity survey was undertaken in the summit craters area. The survey set-up and field work were conditioned by the accessibility of the area, due to the ongoing activity of Mt. Etna.

By means of 2D density modelling, constrained by surface and subsurface geological information, we studied the uppermost portion of the volcanic plumbing system and here we present results on the structural features of this part of the volcano edifice.

This work demonstrates how gravimetry can provide knowledge useful for studying and understanding the processes occurring in the uppermost portion of the volcano edifice.

Geological evolution of the summit part of Mt. Etna

Volcanic activity in the Etna area started more than half a million years ago (De Beni et al., 2011), both with submarine and subaerial fissural eruptions. They covered large portions of the territory with volcanic products that, however, did not build up important reliefs (Branca et al., 2008; Branca et al., 2011a; Branca et al., 2011b). About 110,000 years ago, fissural volcanic activity evolved into central-type activity, and stratovolcanoes began to grow, whose eruptive axes shifted over time along the SE—NW direction (Branca et al., 2008; Branca et al., 2011a; Branca et al., 2011b). Starting from around 60,000 years ago, the main stratovolcano, named Ellittico, began to grow, reaching a maximum elevation of about 3,600 m. The Ellittico activity ended ~15,000 years ago, with caldera-forming plinian eruptions (Coltelli et al., 2000; Del Carlo et al., 2017). They formed a wide summit caldera, whose preserved rim currently crops out in the Pizzi Deneri (2,846 m a.s.l.) and Punta Lucia (2,930 m a.s.l.) areas (Figure 1A). Inside this caldera, volcanic activity resumed roughly along the same eruptive axis, forming the present volcanic centre, named Mongibello.

In 122 BC the largest explosive eruption of Mongibello volcano in Holocene time occurred. This was a Plinian eruption of a basaltic magma (Coltelli et al., 1998) that produced the formation of a new summit caldera (Cratere del Piano; Figure 1A) and caused the disruption of the Ellittico caldera southern rim. The reconstructed original shape of this historical caldera appears slightly elliptical, with diameters of 2.7 and 2.3 km along the N-S and E-W axes (Azzaro et al., 2012; Figure 1A). The eruptive activity of the past 2 ka produced the filling of the Cratere del Piano caldera and the formation of the present-day Etna summit cone. The latter comprises the Central Crater, divided into Voragine (VOR) and Bocca Nuova (BN), surrounded by two craters named Northeast Crater (NEC) and Southeast Crater (SEC), formed in 1911 and 1971, respectively (Figure 1B).

The upper portion of the volcano is characterized by three main rift zones that radiate from the summit (Neri et al., 2011; Azzaro

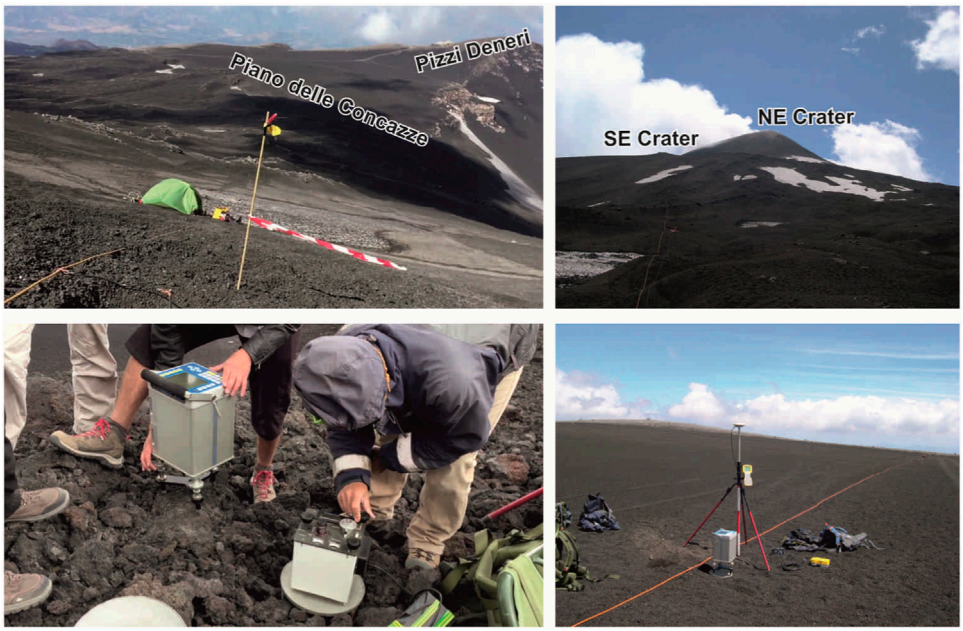

FIGURE 2
Photos taken during the gravimetric survey carried out in 2015. The top pictures provide a view of the investigated area, while, in the bottom pictures, the instruments used for data acquisition (gravimeters and GPS receiver) are shown.

et al., 2012; Cappello et al., 2012): the NE Rift, the S Rift and the W Rift (Figure 1A). These rifts are not directly connected to deep magma reservoirs, but are frequently fed by dikes radiating from the central volcanic conduit (Bousquet and Lanzafame, 2001; Acocella and Neri, 2003; Neri et al., 2011).

Besides occurring from the summit craters or from the rift zones, less frequent eruptions (sub-terminal) can take place from fissures that open in close spatial and structural relation to the summit cones, i.e., on their slopes or at their foot.

Etna's summit area is also affected by extensional processes in part related to the seaward displacement of its eastern and southern flanks (Borgia et al., 1992; Solaro et al., 2010; Bonforte et al., 2011; Ruch et al., 2012). This unstable area is confined to the north by the Pernicana Fault System (Neri et al., 2004) and to the SW by the Ragalna Fault System (Neri et al., 2007; Branca et al., 2011b). Wide fracture fields formed both around and inside the summit craters, and, after 1995, these fractures developed into a main N–S structural system (Neri and Acocella, 2006). During 1998–2001, this system consisted of a N–S fracture zone with orthogonal extension. In 2004, the fractures propagated towards the SE, cutting the SEC and triggering the 2004–2005 eruption (Neri and Acocella, 2006). The Piano delle Concazze area is also affected by different N–S trending faults that represent extension-accommodation features linked to the extensional tectonic regime of the North-East Rift (Azzaro et al., 2012). These N–S trending faults, whose field evidence is sometimes obscured by accumulation of pyroclastic deposits, were recently investigated (geometry, depth, etc.) through magnetic measurements (Napoli et al., 2021).

Data acquisition and analysis

In 2015 gravity measurements were collected along a profile passing through the summit craters area of Mt. Etna volcano, along a NE-SW direction (Figure 1B). The profile is 3.3 km long and comprises 31 measurement points, with average inter-point distance of 100 m (elevations between 2,820 and 3,280 m a.s.l.; Figure 1B). The profile ranges from the Pizzi Deneri area to the pass between Bocca Nuova and SE Crater, crossing Piano delle Concazze, and arrives at the SW rim of the Cratere del Piano (Figure 1B).

Gravity data were acquired in 3 days between 30 June and 6 July 2015. Measurements were taken using in parallel a Scintrex CG5 and a LaCoste and Romberg mod. G relative gravimeters (Figure 2). The absolute gravity station (P0; Figure 1B), at the Pizzi Deneri volcanological observatory (PDN; 2,820 m a.s.l.), was used as reference (Pistorio et al., 2011; Greco et al., 2012; 2022). At least three readings were taken with both gravimeters at each measurement point of the profile. Furthermore, in order to achieve a reliable model of the daily instrumental drift, we performed measurements at the absolute reference station at the beginning and at the end of each working day, using both gravimeters. Tidal effects were corrected for using the Eterna 3.4 software (Wenzel, 1996). We evaluated an average measurement error on the order of 10 μGal. Spatial coordinates of each point were determined by GPS observations, performed at the same time as the gravity measurements, using a Trimble 5700 GPS receiver (Figure 2). The precision achieved for both horizontal and vertical coordinates is on the order of a few centimetres. Consequently, the maximum error in gravity

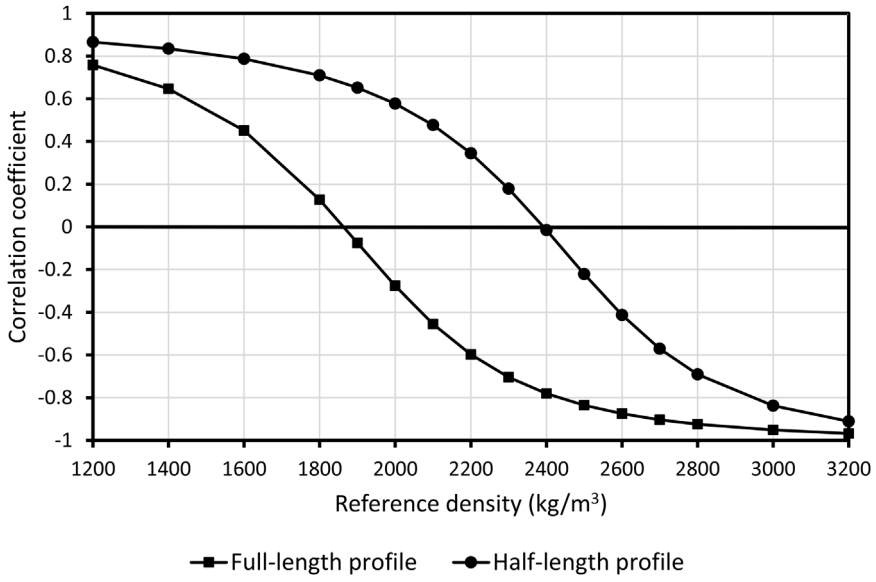

FIGURE 3
Correlation of Bouguer anomalies and topography for different reference densities.

determinations due to the uncertainty in the elevation data is lower than 0.05 mGal.

In order to be used for imaging the subsurface density distribution, gravity measurements need to be reduced for (i) the difference in altitude between the reference (P0; Figure 1B) and each observation point (free-air correction) and (ii) the effect of the different distribution of above-ground masses around each measurement point (complete Bouguer correction). Once these corrections are accomplished, gravity measurements are reduced to Bouguer anomalies (Deroussi et al., 2009), which reflect anomalies in the subsurface density structure. Differences in elevation retrieved from the GPS measurements were used to perform the free-air correction. Conversely, the complete Bouguer effect was evaluated at each observation point as the cumulative gravity effect of two arrays of vertically elongated cells (square-based vertical parallelepipeds), having common bottom elevation (bottom of the "Bouguer plate") and top elevation defined by two DEMs. In particular, the DEM developed by De Beni et al. (2015), featuring a spatial resolution of 4.5 m, was used to define the height of the cells in the near field (an almost square area with sides ~2 km away from the edge points of the profile), while the DEM by Favalli et al. (2009), featuring a spatial resolution of 10 m, was used to define the height of the cells in the far field (an area of about 26 km x 26 km around the measurement profile). To define their gravity effect, a constant density of 2,400 kg/m^3 was assumed for all the prism cells in both the near and far fields.

Direct information (i.e., from boreholes) on the density of the rocks in the summit area of Etna are not available. To choose the most appropriate reference density for the 2D model, we started from the classical Nettleton's method (Nettleton, 1939). However, this method can lead to misleading estimates of the reference density if applied to data from areas where the properties of rock change significantly (Long and Kaufmann, 2013). In order to obtain a reliable estimate of the reference density, we calculated a set of correlation coefficients between Bouguer anomalies and topography for several lengths of the profile and densities (1,200–3,200 kg/m^3; Figure 3). The minimal correlation between the calculated gravity anomaly and the topography is achieved for a density of 2,400 kg/m^3 and for a reduced profile length (profile truncated from SW to about half-length). This value is thus chosen as the reference density for the 2D model. It is worth noting that using the whole length of the profile in the calculation leads to underestimation of the reference density, due to the presence of lighter material beneath the summit area of Mt. Etna (curve with square symbols in Figure 3).

The resulting Bouguer anomalies across the measurement profile are shown in the top panel of Figure 4 (grey solid line; referred as "observed gravity"). The main anomaly has a peak-to-peak amplitude of about 6 mGal and a wavelength of about 2.5 km. Lowest values occur in correspondence of the summit craters area, while moving towards NE and SW, progressively higher values are encountered (upper panel in Figure 4).

2D density modelling with IGMAS+

It is well-known that the inherent ambiguity in the interpretation of potential fields (gravity and magnetic) implies that a non-unique mathematical model can explain the same observable (Götze, 2014). To constrain the 2D model of the Bouguer gravity anomaly across the uppermost part of the Mt. Etna's volcano edifice (top panel in Figure 4), we used the to-date knowledge of the structural setting of the area and the available volcanological data (Branca et al., 2011a; b; Branca and Ferrara, 2013; Barreca et al., 2018).

Data modelling was carried out using the IGMAS+ (Interactive Geophysical Modelling Assistant) software, under the assumption of

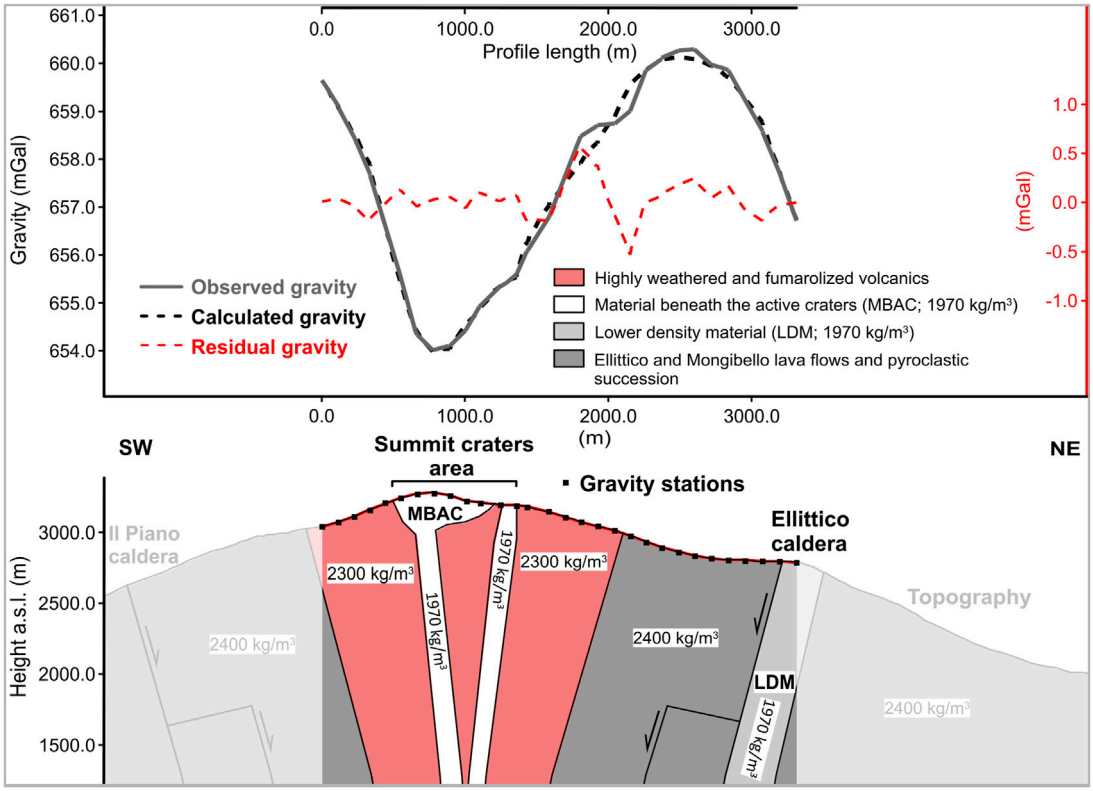

FIGURE. 4
Top panel: observed (solid grey curve) and calculated (black dashed curve) Bouguer profiles. Residuals (observed minus calculated gravity) are depicted by the red dashed curve. Bottom panel: 2D density model of Mt. Etna's summit area down to a depth of about 2.1 km below the point of the profile at highest elevation. On both sides, the density model is extended beyond the gravity profile (shaded parts), in order to avoid edge effects.

homogeneous density within each modelled geological formations. IGMAS+ allows 3D potential field modelling at different scales (Schmidt et al., 2011; 2015). Based on the analytical solution of Götze and Lahmeyer (1988), it utilizes polyhedrons with triangulated surfaces to approximate deep structures. Triangulated surfaces can be combined with voxel cubes to produce complex ("hybrid") models, thus allowing to describe the geological structures in a more realistic way (Schmidt et al., 2011; Alvers et al., 2014). The IGMAS+ software can also be used for 2D forward density modelling, as in the present case.

The bottom panel of Figure 4 shows the cross section of Mt. Etna's summit zone along the SW-NE gravity profile. The 2D density model is defined from the surface down to an elevation of about 1,200 m (about 2.1 km below the highest point of the profile). In order to avoid edge effects, the modelled vertical section is i) extended beyond the edges of the gravity profile (bottom panel of Figure 4) and ii) its edge mirrors (Schmidt et al., 2015) are set far enough (model geometry extended by 50 km). As the geological formations crossed by the profile are lithologically very similar, when developing the model, we aimed at the best compromise between fitting the observed gravity data, while using anomalous bodies with as smaller as possible density contrasts. To constrain the geometry of individual structures, the available scheme published in Barreca et al. (2018), based on geological interpretation, is adopted. Results show a reasonable fit between the calculated (dashed black line) and observed (solid grey line) Bouguer anomalies, with a misfit (dashed red line in Figure 4) ranging between −0.52 and +0.56) mGal and RMS of 0.20 mGal across the whole profile. The proposed model includes the following structural elements (see also the legend in Figure 4).

- ✓ Material beneath the active summit craters (MBAC, white coloured) having a negative density contrast of −430 kg/m³;
- ✓ Lower density material in the Pizzi Deneri zone corresponding with the Ellittico caldera rim (LDM, light grey coloured) having a negative density contrast of −430 kg/m³;
- ✓ Ellittico and Mongibello lava flows and pyroclastic succession (grey coloured) with a zero density contrast;
- ✓ Highly weathered and fumarolized volcanics (light red coloured) having a negative density contrast of −100 kg/m³.

The marked low in the left part of the Bouguer anomaly curve (top panel of Figure 4) indicates the presence of low-density material below the summit craters. To fit this anomaly, we considered two almost vertical bodies, centered beneath the active summit craters (part of the MBAC structural element), whose lateral and vertical extensions are within 100 m and about 2 km (the maximum model depth is controlled by the length of the observation profile), respectively. Considering the position of the gravity profile with respect to the summit craters (Figure 1B), it is likely that the observed Bouguer anomaly is not affected by each volcanic conduit individually, but, rather it images the cumulative near-

field gravity effect of the conduits feeding the different craters. Accordingly, it is probable that the conduits feeding the Central (Voragine and Bocca Nuova) and SE craters induce a single gravity effect on the Bouguer curve, while the conduit feeding the NE crater is "seen" as a separate effect. Following this view, the MBAC structural element includes two vertical sub-structures (bottom panel of Figure 4).

Discussion

Our density model (bottom panel of Figure 4) involves three sources of anomaly, with different negative density contrasts, namely, MBAC, LDM and the altered volcanics beneath the active craters zone. The geometries of and boundaries between the modelled structures were defined on the grounds of the available geological constraints.

The dominating gravity low in the left half of the Bouguer curve (top panel of Figure 4) indicates a mass deficiency beneath the summit craters area, due to low-density material. In particular, this gravity low can be attributed to the presence of (i) the conduits feeding the summit craters and (ii) altered and fumarolized rock, weakened by the sustained passage of volcanic gases. A mass deficiency was also detected through gravimetric measurements beneath the summit of Mt. Vesuvius and along its vertical axis (Celli et al., 2007) and interpreted as due to the presence of low-density shattered lava rocks from internal break-ups and collapses during explosive eruptions (Rolandi et al., 2004).

The NE edge of the profile crosses the Pizzi Deneri area, that is cut by several faults and eruptive fissures (Figure 1A). The presence of these structures lowers the overall local density, thus explaining the gravity low observed at the northern edge of the profile (LDM structure in Figure 4). It is important to mention that, with the data at our disposal, we cannot spot possible density differences between the Mongibello and Ellittico volcanics, since the SW edge of the measurement profile does not cross the boundary between these volcanics in the Cratere del Piano area (Figure 1).

The strongest discrepancies between observed and calculated Bouguer curves, namely, the +0.56 mGal and −52 mGal, occurring at distances of between 1,800 and 2,200 from the SW edge of the profile (red dashed curve; top panel of Figure 4) could be due to either unknown shallow geological structures, not accounted for in the 2D model, or errors in the DEM data used to perform the terrain correction, or to a combination of both. It is worth stressing that the morphology of the summit active area of Mt. Etna may undergo rapid and drastic changes, in consequence of intense eruptive activity, and relief changes that are not captured in the DEM data can have significant impact on the accuracy of the terrain correction.

Further errors could come from projecting the complex morpho-tectonic setting onto a 2D profile.

Conclusion

Using gravity and GPS data collected in the summit craters area of Mt. Etna, we produced the first density model of its upper plumbing system. To reduce ambiguities, we used all the available information, mainly geological knowledge and volcanological considerations. Despite their limits, our results represent a valuable starting point for further studies.

One weakness of our results dwells in the fact that a complex setting in an area of steep topography is studied in 2D. In the follow-up work we therefore plan to complement the existing gravity data by new observations, allowing to perform 3D modelling. However, it is noteworthy that harsh environmental conditions and security reasons limit accessibility to the summit area of Mt. Etna.

Another weakness comes from the lack of DEM data acquired at the same time as the gravity data. This may introduce some systematic bias in the computed Bouguer anomalies, which, in turn, translates into bias in the subsurface density model. The acquisition of new gravity data should be thus complemented by the production of an updated DEM of the studied area.

The production of a more detailed 3D density model, covering a deeper portion than the current model, would improve our knowledge of Mt. Etna's uppermost plumbing system, with important implications for hazard assessments, considering the key role this part of the volcano edifice plays in controlling eruptive activity.

Data availability statement

The raw data supporting the conclusions of this article will be made available by the authors, without undue reservation.

Author contributions

JP performed data modelling. FG designed the work, collected and analysed gravity and GPS data. DC collected and analysed gravity and GPS data. SB provided the volcanological constraints. PV conceptualized the work. All authors contributed to the article and approved the submitted version.

Acknowledgments

This work was partially supported by the Slovak VEGA grant agency under project No. 2/0002/23.

Conflict of interest

The authors declare that the research was conducted in the absence of any commercial or financial relationships that could be construed as a potential conflict of interest.

Publisher's note

References

Acocella, V., and Neri, M. (2003). What makes flank eruptions? The 2001 Etna eruption and its possible triggering mechanisms. *Bull. Volcanol.* 65 (7), 517–529. doi:10.1007/s00445-003-0280-3

Alvers, M. R., Götze, H.-J., Barrio-Alvers, L., Plonka, C., Schmidt, S., and Lahmeyer, B. (2014). A novel warped-space concept for interactive 3D-geometry-inversion to improve seismic imaging. *First Break* 32, 61–67. doi:10.3997/1365-2397.32.4.74375

Azzaro, R., Branca, S., Gwinner, K., and Coltelli, M. (2012). The volcano-tectonic map of Etna volcano, 1:100.000 scale: An integrated approach based on a morphotectonic analysis from high-resolution DEM constrained by geologic, active faulting and seismotectonic data. *Italian J. Geosciences* 131 (1), 153–170. doi:10.3301/ijg.2011.29

Barreca, G., Branca, S., and Monaco, C. (2018). Three-Dimensional modeling of mount Etna volcano: Volume assessment, trend of eruption rates, and geodynamic significance. *Tectonics* 37, 842–857. doi:10.1002/2017tc004851

Bonforte, A., Guglielmino, F., Coltelli, M., Feretti, A., and Puglisi, G. (2011). Structural assessment of mount Etna volcano from permanent scatterers analysis. *Geochem. Geophys. Geosystems* 12 (2), 1–19. doi:10.1029/2010gc003213

Borgia, A., Ferrari, L., and Pasquarè, G. (1992). Importance of gravitational spreading in the tectonic and volcanic evolution of Mount Etna. *Nature* 357, 231–235. doi:10.1038/357231a0

Bousquet, J. C., and Lanzafame, G. (2001). New interpretation of the flank eruption fractures on Mt. Etna: Consequences for the tectonic framework of the volcano. *Bull. Soc. Geol. Fr.* 172 (4), 455–467. doi:10.2113/172.4.455

Branca, S., Coltelli, M., De Beni, E., and Wijbrans, J. (2008). Geological evolution of Mount Etna volcano (Italy) from earliest products until the first central volcanism (between 500 and 100 ka ago) inferred from geochronological and stratigraphic data. *Int. J. Earth Sci.* 97, 135–152. doi:10.1007/s00531-006-0152-0

Branca, S., Coltelli, M., and Groppelli, G. (2011b). Geological evolution of a complex basaltic stratovolcano: Mout Enta, Italy. *Italian J. Geosciences (Bolletino della Soc. Geol. Italiana)* 130 (3), 306–317.doi:10.3301/IJG.2011.13

Branca, S., Coltelli, M., Groppelli, G., and Lentini, F. (2011a). Geological map of Etna volcano 1:50,000 scale. *Italian J. Geosciences (Bolletino della Soc. Geol. Italiana)* 130 (3), 265–291. doi:10.3301/ijg.2011.15

Branca, S., and Ferrara, V. (2013). The morphostructural setting of Mount Etna sedimentary basement (Italy): Implications for the geometry and volume of the volcano and its flank instability. *Tectonophysics* 586, 46–64. doi:10.1016/j.tecto.2012.11.011

Calvari, S., Di Traglia, F., Ganci, G., Giudicepietro, F., Macedonio, G., Cappello, A., et al. (2020). Overflows and pyroclastic density currents in march-april 2020 at Stromboli volcano detected by remote sensing and seismic monitoring data. *Remote Sens. (Basel).* 12 (18), 3010. doi:10.3390/rs12183010

Cappello, A., Neri, M., Acocella, V., Gallo, G., Vicari, A., and Del Negro, C. (2012). Spatial vent opening probability map of Etna volcano (Sicily, Italy). *Bull. Volcanol.* 74 (9), 2083–2094. doi:10.1007/s00445-012-0647-4

Cashman, K. V., Sparks, R. S. J., and Blundy, J. D. (2017). Vertically extensive and unstable magmatic systems: A unified view of igneous processes. *Science* 355 (6331), eaag3055. doi:10.1126/science.aag3055

Cella, F., Fedi, M., Florio, G., Grimaldi, M., and Rapolla, A. (2007). Shallow structure of the Somma–Vesuvius volcano from 3D inversion of gravity data. *J. Volcanol. Geotherm. Res.* 161, 303–317. doi:10.1016/j.jvolgeores.2006.12.013

Coltelli, M., De Carlo, P., and Vezzoli, L. (1998). Discovery of a Plinian basaltic eruption of Roman age at Etna volcano, Italy. *Geology* 26 (12), 1095–1098. doi:10.1130/0091-7613(1998)026<1095:doapbe>2.3.co;2

Coltelli, M., Del Carlo, P., and Vezzoli, L. (2000). Stratigraphic constraints for explosive activity in the past 100 ka at Etna Volcano, Italy. *Int. J. Earth Sci.* 89, 665–677. doi:10.1007/s005310000117

De Beni, E., Behncke, B., Branca, S., Nicolosi, I., Carluccio, R., D'Ajello Caracciolo, F., et al. (2015). The continuing story of etna's new Southeast Crater (2012–2014): Evolution and volume calculations based on field surveys and aerophotogrammetry. *J. Volcanol. Geotherm. Res.* 303, 175–186. doi:10.1016/j.jvolgeores.2015.07.021

De Beni, E., Branca, S., Coltelli, M., Groppelli, G., and Wijbrans, J. R. (2011). $^{40}Ar/^{39}Ar$ isotopic dating of Etna volcanic succession. *Italian J. Geosciences* 130 (3), 292–305. doi:10.3301/ijg.2011.14

Del Carlo, P., Branca, S., and D'Oriano, C. (2017). New findings of Late Glacial Etna pumice fall deposits in NE Sicily and implications for distal tephra correlations in the Mediterranean area. *Bull. Volcanol.* 79, 50–17. doi:10.1007/s00445-017-1135-7

Deroussi, S., Diament, M., Feret, J. B., Nebut, T., and Staudacher, Th. (2009). Localization of cavities in a thick lava flow by microgravimetry. *J. Volcanol. Geotherm. Res.* 184 (1-2), 193–198. doi:10.1016/j.jvolgeores.2008.10.002

Favalli, M., Fornaciai, A., and Pareschi, M. T. (2009). LIDAR strip adjustment: Application to volcanic areas. *Geomorphology* 111 (3), 123–135. doi:10.1016/j.geomorph.2009.04.010

Fedi, M., Cella, F., D'Antonio, M., Florio, G., Paoletti, V., and Morra, V. (2018). Gravity modeling finds a large magma body in the deep crust below the Gulf of Naples, Italy. *Italy. Sci. Rep.* 8, 8229. doi:10.1038/s41598-018-26346-z

Götze, H.-J., and Lahmeyer, B. (1988). Application of three-dimensional interactive modeling in gravity and magnetics. *Geophysics* 53, 1096–1108. doi:10.1190/1.1442546

Götze, H.-J. (2014). "Potential method and geoinformation systems," in *Handbook of geomathematics*. Editors W. Freeden, M. Z. Nashed, and T. Sonar (Berlin Heidelberg: Springer-Verlag), 1–21.

Greco, F., Bonforte, A., and Carbone, D. (2022). A long-term charge/discharge cycle at Mt. Etna volcano revealed through absolute gravity and GPS measurements. *J. Geodesy* 96, 101. doi:10.1007/s00190-022-01692-z

Greco, F., Currenti, G., D'Agostino, G., Germak, A., Napoli, R., Pistorio, A., et al. (2012). Combining relative and absolute gravity measurements to enhance volcano monitoring. *Bull. Volcanol.* 74, 1745–1756. doi:10.1007/s00445-012-0630-0

Kauahikaua, J., Hildenbrand, T., and Webring, M. (2000). Deep magmatic structures of Hawaiian volcanoes, imaged by three-dimensional gravity models. *Geology* 28 (10), 883–886. doi:10.1130/0091-7613(2000)028<0883:dmsohv>2.3.co;2

Locke, C. A., Cassidy, J., and MacDonalds, A. (1993). Three-dimensional structure of relict stratovolcanoes in taranaki, New Zealand: Evidence from gravity data. *J. Volcanol. Geotherm. Res.* 59 (1-2), 121–130. doi:10.1016/0377-0273(93)90081-2

Long, L. T., and Kaufmann, R. D. (2013). *Acquisition and analysis of terrestrial gravity data*. Cambridge: Cambridge University Press, 171.

Magee, C., Stevenson, C. T. E., Ebmeier, S. K., Keir, D., Hammond, J. O. S., Gottsmann, J. H., et al. (2018). Magma plumbing systems: A geophysical perspective. *J. Petrology* 59 (6), 1217–1251. doi:10.1093/petrology/egy064

Napoli, R., Currenti, G., and Sicali, A. (2021). Magnetic signatures of subsurface faults on the northern upper flank of Mt. Etna. *Ann. Geophys.* 64 (1), PE108.doi:10.4401/ag-8582

Neri, M., Acocella, V., Behncke, B., Giammanco, S., Mazzarini, F., and Rust, D. (2011). Structural analysis of the eruptive fissures at Mount Etna (Italy). *Ann. Geophys.* 54 (5), 464–479.doi:10.4401/ag-5332

Neri, M., Acocella, V., and Behncke, B. (2004). The role of the Pernicana Fault System in the spreading of Mt. Etna (Italy) during the 2002–2003 eruption. *Bull. Volcanol.* 66 (5), 417–430. doi:10.1007/s00445-003-0322-x

Neri, M., and Acocella, V. (2006). The 2004–2005 Etna eruption: Implications for flank deformation and structural behaviour of the volcano. *J. Volcanol. Geotherm. Res.* 158 (1-2), 195–206. doi:10.1016/j.jvolgeores.2006.04.022

Neri, M., Guglielmino, F., and Rust, D. (2007). Flank instability on Mount Etna: Radon, radar interferometry and geodetic data from the southwestern boundary of the unstable sector. *J. Geophys. Res.* 112 (B4), B04410. doi:10.1029/2006jb004756

Nettleton, L. L. (1939). Determination of density for reduction of gravimeter observations. *Geophysics* 4 (3), 176–183. doi:10.1190/1.0403176

Pistorio, A., Greco, F., Currenti, G., Napoli, R., Sicali, A., Del Negro, C., et al. (2011). High-precision gravity measurements using absolute and relative gravimeters at Mount Etna (Sicily, Italy). *Ann. Geophys.* 54 (5), 500–509.doi:10.4401/ag-5348

Rolandi, G., Bellocci, F., and Cortini, M. (2004). A new model for the formation of the Somma Caldera. *Mineral. Petrol.* 80, 27–44. doi:10.1007/s00710-003-0018-0

Ruch, J., Pepe, S., Casu, F., Acocella, V., Neri, M., Solaro, G., et al. (2012). How do volcanic rift zones relate to flank instability? Evidence from collapsing rifts at Etna. *Geophys. Res. Lett.* 39 (20), L20311. doi:10.1029/2012gl053683

Schiavone, D., and Loddo, M. (2007). 3-D density model of Mt. Etna Volcano (Southern Italy). *J. Volcanol. Geotherm. Res.* 164 (3), 161–175. doi:10.1016/j.jvolgeores.2007.04.016

Schmidt, S., Barrio-Alvers, L., and Götze, H. J. (2015). IGMAS+: Interactive geophysical modelling ASistant. Available at: http://www.potentialgs.com.59

Schmidt, S., Plonka, C., Götze, H.-J., and Lahmeyer, B. (2011). Hybrid modelling of gravity, gravity gradients and magnetic fields. *Geophys. Prospect.* 59 (6), 1046–1051. doi:10.1111/j.1365-2478.2011.00999.x

Solaro, G., Acocella, V., Pepe, S., Ruch, J., Neri, M., and Sansosti, E. (2010). Anatomy of an unstable volcano from InSAR: Multiple processes affecting flank instability at Mt. Etna, 1994–2008. *J. Geophys. Res.* 115 (B10), B10405. doi:10.1029/2009jb000820

Wenzel, H. G. (1996). "Thenanogal software: Earth tide data processing package ETERNA 3.30," in *Marees terrestres bulletin informations*. Editor P. Melchior (Bruxelles: Association Internationale de G′eod′esie), 124, 9425–9439.

frontiers | Frontiers in Earth Science

TYPE Original Research
PUBLISHED 05 June 2023
DOI 10.3389/feart.2023.1195485

OPEN ACCESS

EDITED BY
Filippo Greco,
National Institute of Geophysics and Volcanology (INGV), Italy

REVIEWED BY
Alessandra Borghi,
National Institute of Geophysics and Volcanology (INGV), Italy
Ameha Atnafu Muluneh,
Addis Ababa University, Ethiopia

*CORRESPONDENCE
Fayez Harash,
f.harash@hotmail.com
Nadhir Al-Ansari,
nadhir.alansari@ltu.se

RECEIVED 28 March 2023
ACCEPTED 18 May 2023
PUBLISHED 05 June 2023

CITATION
Harash F, Khalaf A, Al-Ansari N, Chen C, Alrawi I, Al-Khafaji H and Tageldin M (2023), Local Moho distribution in the eastern Mediterranean region from gravity inversion: eastern Mediterranean Sea.
Front. Earth Sci. 11:1195485.
doi: 10.3389/feart.2023.1195485

Local Moho distribution in the eastern Mediterranean region from gravity inversion: eastern Mediterranean Sea

Fayez Harash[1,2]*, Amin Khalaf[3], Nadhir Al-Ansari[4]*, Chao Chen[5], Imad Alrawi[6], Harith Al-Khafaji[7] and Mohammed Tageldin[7]

[1]State Key Laboratory of Geological Processes and Mineral Resources, School of Geophysics & Geomatics, China University of Geosciences, Wuhan. China, [2]Geology Department, Faculty of Science s, Damascus University, Damascus. Syria, [3]Sorbonne Universite, EPHE, Milieux Environnementaux, Transferts et Interactions dans les hydrosyst' emes et les Sols, METIS, France, [4]Water Resources Engineering, Department of Civil, Environmental and Natural Resources Engineering, Lulea University of Technology, Lulea, Sweden, [5]Hubei Subsurface Multi-Scale Imaging Key Laboratory, School of Geophysics & Geomatics, China University of Geosciences, Wuhan. China, [6]School of Earth Sciences and Resources, China University of Geosciences (Beijing), Beijing, China, [7]Department of Petroleum Engineering, School of Earth Resources, China University of Geosciences, Wuhan, China

This study investigates the variations of surface Moho inverted from Bouguer gravity data beneath the northwestern Arabian plate. The results were obtained by applying the 3DINVER program developed in a MATLAB environment using the Parker–Oldenburg method. The calculation results show that the maximum Moho depth observed in the western Arabian shield approaches more than 40 km, while the minimum values of 16–20 km are mainly concentrated beneath the Mediterranean Sea. A key innovation of this study is its implementation of exponential density contrast decrease in the sediment–basement interface in the Syrian part of the Arabian plate. The gravity anomaly of the sediment is computed using a density contrast which varies exponentially with depth, leading to a more accurate representation of the subsurface structure and offering valuable insights into the geodynamic processes and seismogenic potential of the area. To validate the inverted results from the 3DINVER program, the study compares these findings with seismic results that show good agreement with our results from the same region. This leads to a better understanding of the crustal structure and provides insights into its implications for the geodynamic and seismogenic nature of the northwestern Arabian plate—critical for assessing the potential for earthquakes and other geological hazards. The density contrast between the Earth's crust and mantle can be related to variations in the composition, temperature, and pressure of the rocks. These factors influence the mechanical properties of the crust, ultimately affecting the tectonic processes and seismic activity in the region.

KEYWORDS

basement boundary, eastern Mediterranean Sea, gravity inversion, Moho depth, Bouguer gravity

1 Introduction

The northwestern Arabian plate is a very interesting region because of the tectonic separation from the African plate in the south and the collision with the Anatolian microplate in the north, as well as the Red Sea spreading and movement in the Suez Gulf (Figure 1) and the Dead Sea rift (Ben-Avraham, 1985).

The Dead Sea Fault System (DSFS) starts in the south from the northern part of the Gulf of Aqaba to the Kara Su Valley in the north, with a total length of about 1,100 km that crosses four countries: through the Arab Wadi, Jordan Valley in Jordan, the Beqa'a Valley in Lebanon, and the Al-Ghab Graben in Syria (Figure 1).

The Cornell Syria project has already surveyed Syria with its prominent tectonic features represented by the Zagros fold in the far northeastern boundary with Iraq that extends northwest into western Iraq and western Iran, the Palmyride fold belt in central Syria, the Euphrates fault system crossing Syria from north to east, and the Abd el Aziz and Sinjar folds in eastern Syria near the border with Iraq (Brew et al., 2000). This project described paleogeography and tectonic deformation using geological data but did not use gravity data to investigate the deep Moho depth in this area.

Many functions were used to observe the density contrast variation. For example, Murthy and Rao (1979) developed a linear function, Rao et al. (1990) assumed the change in density contrast as a quadratic function, Silva et al. (2006) simulated a hyperbolic function, and Chakravarthi et al. (2016) discovered that the density contrast differed as an exponential function with depth.

Our study discusses the Moho depth inverted from Bouguer gravity measurements and seeks to understand the difference in Moho depth in the study area. We focus on the Syrian part of the plate and the surrounding areas because Syria has not been studied as specifically comprising oceanic and continental crust, and no sedimentary corrections have been attempted as the density contrast changes following an exponential function with depth. Some authors have considered the sedimentary density in the surrounding area as being uniform (Ben-Avraham et al., 2002; Michal Rosenthal, 2015).

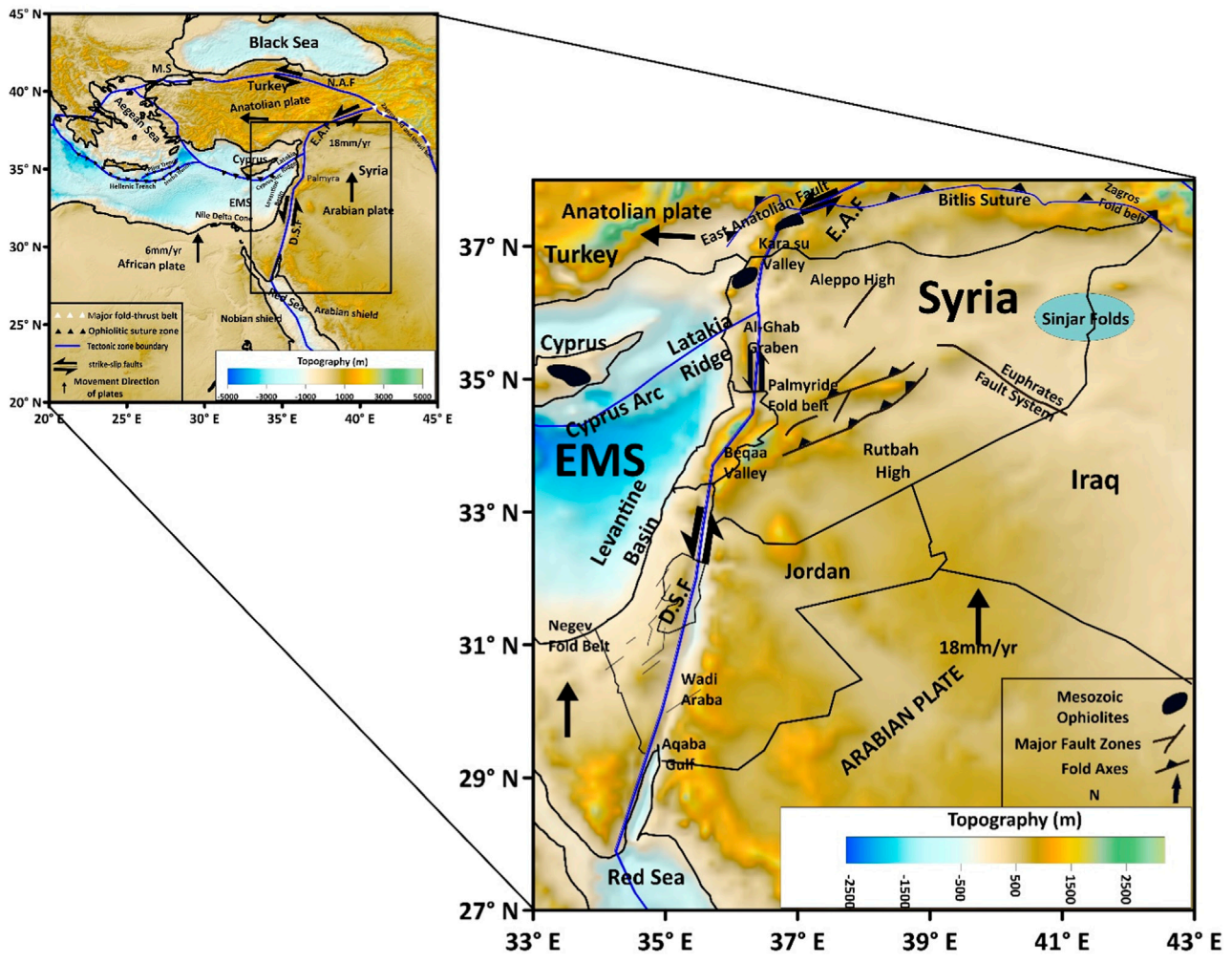

FIGURE 1
Location of the study area (WMS Demo Server). Simplified tectonic and topographic map of the eastern Mediterranean. Thick lines show the main plate boundaries. Approximate plate velocity vectors are shown in black (Stern & Johnson, 2010). E. A. F, East Anatolian Fault; D. S. F, Dead Sea Fault; EMS, eastern Mediterranean Sea, modified from Barazangi et al. (1993).

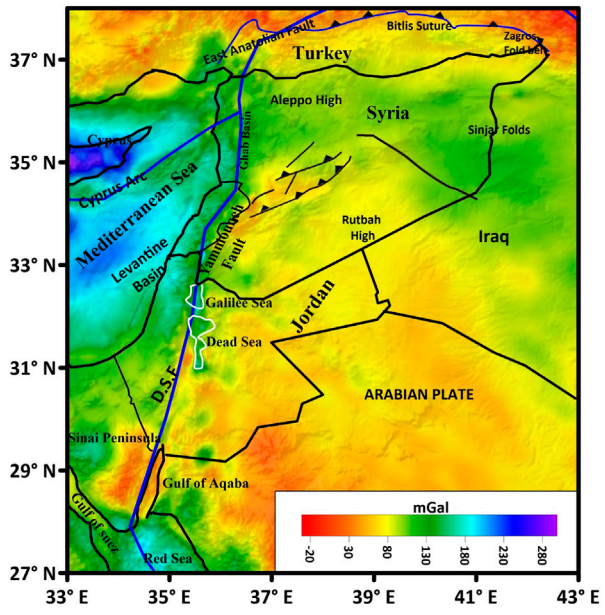

FIGURE 2
Bouguer gravity map (in mGal) of the study region.

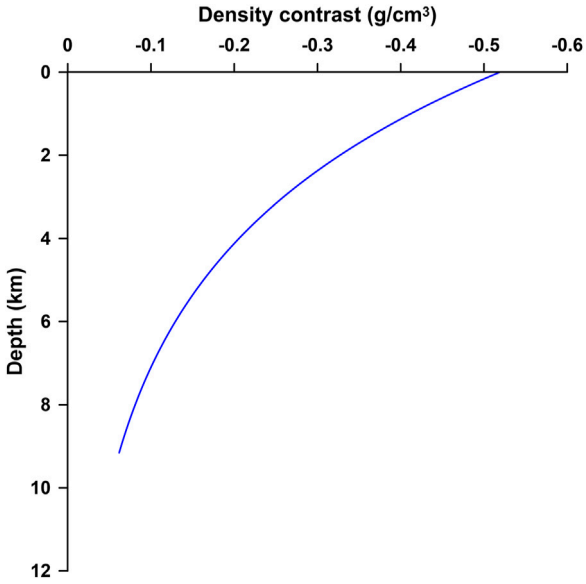

FIGURE 3
Exponential density contrast variation in the study region.

2 Geological setting

The tectonics of the northwestern Arabian plate are still active, as represented in its tectonic boundaries. Those in the east comprise the thrust belt and Zagros fold that form the collision zone between the Arabian and Iranian plates, the eastern Anatolian fault in the north, and, in the south, the Red Sea and Dead Sea faults that separate the Arabian plate and the Levantine microplate (Brew et al., 2003). There are many clear features in the region that derive from this complicated history, such as the Dead Sea, which separates the Arabian and African plates. The tectonic movement of the plate boundaries controls the tectonic deformation in the region, especially in Syria, as observed in the Palmyride fold and the Euphrates system (Barazangi et al., 1993). The Levant basin was opened in the eastern Mediterranean Sea as a result of the separation of the Arabian from the African plate. The eastern Mediterranean region has a complicated geological history that extends from the late Triassic to the early Jurassic (Garfunkel, 1998). The varied stratigraphic evolution of the eastern Mediterranean region represents the complicated Cenozoic and pre-Cenozoic boundary (McBride et al., 1990).

Syria has been geologically influenced because of the movement of the Arabian plate, with Syria being in its northwest (Brew et al., 2000). Syria has many consequent tectonic features like the Aleppo Plateau in the north, the Rutbah uplift in the south, the intercontinental Palmyride fold belt in the center, and the Abd el Aziz fold in its northeast.

The Al-Ghab depression is formed at the northern end of the Levant rift that extends from south of the Dead Sea rift to the north in Turkey. It is considered to have been a left-lateral strike-slip fault since the mid-Cenozoic (Chaimov et al., 1993) and has been studied by many researchers (Trifonov et al., 1991; Domas, 1994). The central portion of the graben is a plain covered by a thin bed of Pleistocene and Holocene sediment covered with lacustrine Pliocene deposits which may reach 1 km in thickness, and a base that may go 700 m below sea level. The flanks of this rift are controlled by faults with blocks and scraps. Basaltic magma was very active during the late Miocene–Pliocene in the southern Al-Ghab depression and moved to the north of this basin during the late Pliocene–early Pleistocene (Sharkov, 1997).

This study aims to determine the Moho depth based on Bouguer gravity data inversion, assuming that the density contrast decreases exponentially with depth (Chakravarthi, 2003; Chakravarthi et al., 2016; Pham et al., 2018). Although many authors consider the sedimentary density uniform, two maps will be presented here: one from our inversion results and the other from the seismological map. Our inversion results will be compared to the seismological Moho map (Mechie et al., 2013).

3 Materials and methods

3.1 Bouguer gravity data

Bouguer gravity data are a useful tool for inverting the Moho boundary. The gravity data for the region we investigated were acquired from the Earth Geopotential Model EGM2008 estimated from altimetry missions, ground data, and the GRACE satellite mission (Pavlis et al., 2013), with a resolution (1′ × 1′) as demonstrated in Figure 2.

Figure 2 represents the Bouguer anomaly map related to the crust–mantle boundary observed over the eastern Mediterranean region. Gravity anomaly is high in the Mediterranean Sea and through the DSFS, with a total amplitude of over 150 mGal crossing the DSFS. The area has an extent of 10° and 11° in longitude and latitude, respectively.

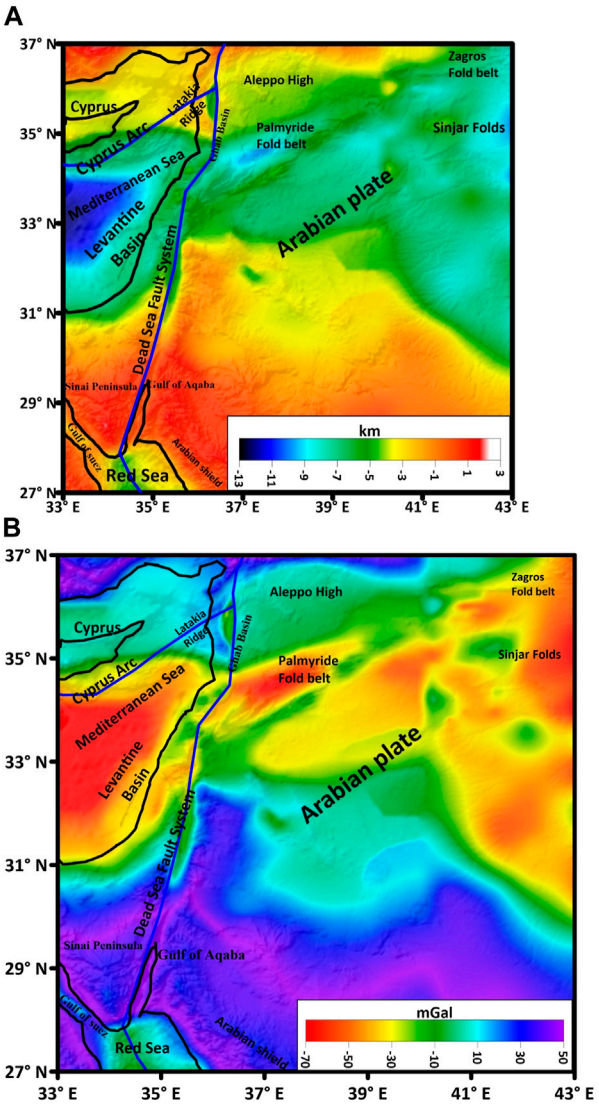

FIGURE 4
(A) Top boundary (in km) of basement rocks (modified after Michel Rybakov, 2004; Jassim and Goff, 2006); **(B)** gravitational attraction of this boundary in mGal.

We corrected the Bouguer gravity anomalies to eliminate the gravitational effects of the sediment–basement because of their lower density. We concluded that density contrast decreases following an exponential function with depth, based on seismic velocity measurements provided by the Syrian Petroleum Company (Figure 3). This exponential function was used in Granser's method (Chakravarthi et al., 2003; Pham et al., 2018) to compute the Bouguer gravity effect of sediment–basement from the basement data digitized by Rybakov (2004) and Jassim and Goff (2006). Bouguer gravity was corrected for the sediment–basement effect before inverting the data. We obtained the residual Bouguer gravity data that were ready to implement in the inversion process. Before performing the inversion, we applied some processes to achieve the gravity anomaly from the Moho boundary (g_m).

Many anomalies and trends are clearly observed on the simplified Bouguer map. The Bouguer gravity anomaly has a clear variation in southern and northern Syria, and with maximum anomalies values of 270 mGal in western Syria and minimum values of −70 mGal (Figure 2).

3.2 Methodology

Density is considered an important parameter that plays a significant role in the impact of gravity anomalies. It is useful to distinguish the lithology by investigating its conduct as it changes with depth.

The density contrast values change exponentially with depth (Chakravarthi et al., 2016; Pham et al., 2018) according to this equation:

$$\Delta\rho = \Delta\rho_0 e^{-\lambda z}, \tag{1}$$

where z represents depth in km, $\Delta\rho_0$ represents the surface density contrast, and λ represents the decreasing constant. Density is calculated by using Gardner's equation (Gardner et al., 1974) that depends on the relationship between seismic velocity (V) and density (ρ) as follows:

$$\rho = 0.31V^{0.25}. \tag{2}$$

To forward compute the gravity effect of the sediment–basement, the exponential density contrast function that varies with depth following Granser's (1987a) equation should be taken into account:

$$\Delta g = \frac{2\pi\gamma\Delta\rho_0}{\lambda}\left(1 - e^{-\lambda z_0}\right) + 2\pi\gamma\Delta\rho_0 e^{-\lambda z_0} \times F^{-1}\left[\frac{e^{-|k|z_0}}{|k| + \lambda}\left(F\left[1 - e^{(-\lambda\Delta h)}\right] - \sum_{n=1}^{\infty}\frac{(-|k|)^n}{n!}F\left[e^{-\lambda\Delta h}\Delta h^n\right]\right)\right], \tag{3}$$

where $e^{-|k|z_0}$ denotes the upward continuation, k denotes the wave number, γ is the gravitational constant, and F^{-1} represents the inverse Fourier function.

The basement depths used in the aforementioned algorithm were digitized from Rybakov (2004) and Jassim & Goff (2006) over an area of (33–43°N and 27–37°E) described in Figure 4A. The resulting gravity data will be subtracted from the Bouguer gravity data to obtain the residual gravity effect of the Moho discontinuity that will be used in the inversion procedures as

$$g_m = \Delta g - (g_{sed} + g_{sb}). \tag{4}$$

The result obtained for gravitational Bouguer anomaly g_m is used for inversion to calculate the Moho depth over our study area. Gómez-Ortiz and Agarwal (2005) modified the Parker–Oldenburg iterative method to construct a Moho map under the eastern Mediterranean study area by inverting the gravity anomaly along the horizontal density interface geometry. This code was modified again because it misused Parker's formula by giving incorrect forward and inversion results (Gao & Sun, 2019).

This technique depends on the Fourier transform for the topography interface, the gravity anomaly, and the relationship between them. Many authors have established methods to determine Moho depth (e.g., Cordell & Henderson, 1968; Rao et al., 1990).

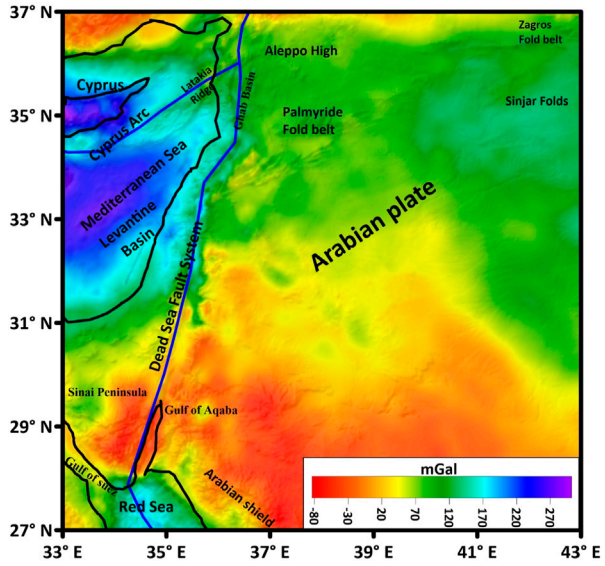

FIGURE 5
Observed gravity anomaly (in mGal) resulting from Moho topography after removing the gravitational effect of Cenozoic sedimentary and shallow blocks.

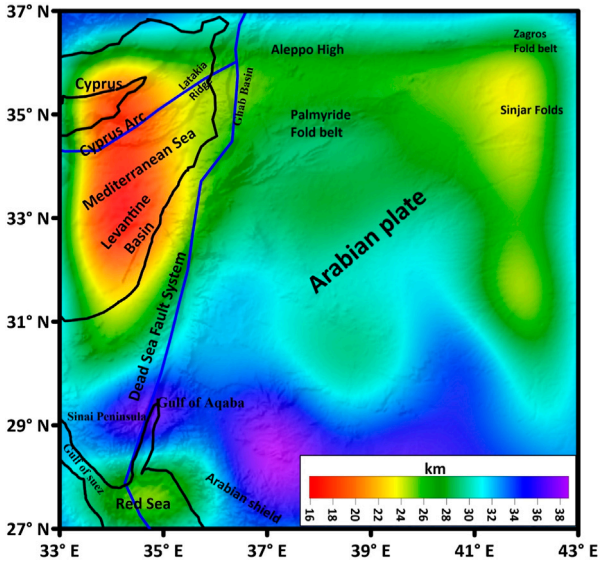

FIGURE 6
Map of Moho depth (in km) computed by applying 3D inversion MATLAB code.

Eq. 5 represents the Fourier transform of gravity data (Parker, 1973) in a one-dimensional direction as

$$F[\Delta g(x)] = -2\pi\gamma\rho e^{(-|k|z_0)}\sum_{n=1}^{\infty}\frac{(-|k|)^{n-1}}{n!}F[h^n(x)]. \quad (5)$$

The depth to the uneven interface is computed using MATLAB code with several iterative procedures based on Oldenburg's (1974) equation.:

$$h(x) = F^{(-1)}\left[-\frac{F[\Delta g(x)]e^{|k|z_0}}{2\pi\gamma\rho} - \sum_{n=2}^{\infty}\frac{(|k|)^{n-1}}{n!}F[h^n(x)]\right], \quad (6)$$

where $F(\Delta g)$ denotes the Fourier transform of the gravity anomaly ρ and the term $h(x)$ represents the interface topography at the horizontal interface average depth z_0.

The inversion needs to set parameters that are z_0 in km, which is the mean Moho depth, with ρ in g/cm^{-3} referring to the density contrast. Inversion implementation has a shortcoming at high frequencies, so these high frequencies should be removed by applying a high-cut wave filter during the inversion process.

The root mean square error (RMS) can be calculated using the following formula:

$$RMS = \sqrt{\frac{\sum_{i=1}^{M}\sum_{j=1}^{N}\left(h_{i,j}^{t+1} - h_{i,j}^{t}\right)^2}{M \times N}}, \quad (7)$$

where M and N stand for the grid size and t means the iteration step.

A low-pass filter is used during the process to assure the convergence of the inversion steps in the equation (Oldenburg, 1974):

$$B(k) = \left\{\frac{1}{2}\left[1 + \cos\left(\frac{k - 2\pi WH}{2(SH - WH)}\right)\right]\right\}, \quad (8)$$

for $WH < h < SH$, $B(k) = 0$ for $k > SH$, and $B(k) = 1$ for $k < WH$, where WH and SH are the roll-off frequencies in the applied filter.

4 Results

Figure 4B shows the forwarding results of the compiled crystalline basement depth data generated by applying Granser's method (1987a) to compute the gravitational effect between the Cenozoic sediment and the basement (Pham et al., 2018). The exponential decrease in density contrast with depth $\Delta\rho = -0.52e^{-0.1728z}$ gcm^{-3} is shown in Figure 3, where the density contrast and the decay constant are −0.52 g/cm^{-3} and -0.1728 g/cm^{-3}, respectively. The density which differs from the depth taken from seismic measurements in Syria was provided by the Syrian Petroleum Company.

We removed the gravity effect of the Cenozoic sediments g_{sed} (Trung et al., 2018), computing the forward gravity effect of the layer of the digitized crystalline basement.

The obtained data still have high-frequency anomalies resulting from shallow blocks, so they were removed by a low-pass filter to eliminate the gravitational effect of shallow blocks g_{sb} (Trung et al., 2018), with cut-wave number (0.1 rad) equivalent to 63 km as the wavelength obtained by the power density spectrum. We subtracted these data from the Bouguer gravity data by Eq. 4, resulting in (Figure 5)—the residual gravity data of Moho discontinuity.

The inversion needs parameters of z_0 = 32 km, where the mean Moho depth used the inversion procedure reported by Koulakov & Sobolev (2006) for the eastern Mediterranean study region, ρ = 0.45 g/cm^{-3} refers to the density contrast (Michal Rosenthal et al., 2015), and the cut wavelength filter was chosen as 85 km based on

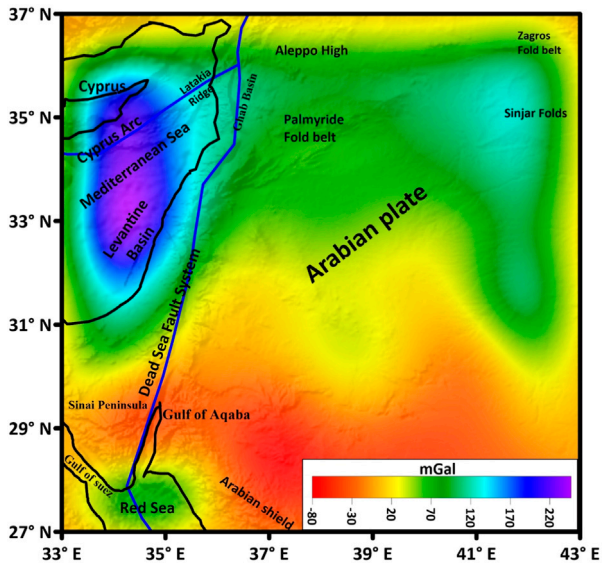

FIGURE 7
Map of gravity anomaly (in mGal) computed from the 3D Moho relief map derived from the present inversion process.

the power spectrum method (Spector & Grant, 1970; Blakely, 1995). The convergence was set at 0.01 mGal.

The sum of the columns and rows is 301 × 301. The truncation window data length was chosen as 10% of the extended data length.

The inversion procedures needed 10 iterations to compute the anomalies and calculate the desired Moho depth. In the last step of the inversion, the RMS error was 0.009 according to Eq. 7.

Figure 6 shows the Moho discontinuity depth resulting from the inversion of Bouguer gravity anomalies corrected for the gravity effect of the sediment–basement (Figure 5). The Moho depth ranges from 12–48 km over the study area (Figure 6). The maximum values tending toward the south under the western Arabian shield determine the deep roots beneath those chains; the minimum depth is observed in western Syria beneath the Mediterranean Sea.

The minimum Bouguer anomalies coincide with the high mountains over the western Arabian shield, Palmyride in central Syria, and the Zagros chains. Crustal thickness plays an important role in the increase and decrease of Bouguer anomaly values. The Moho depths reached more than 44 km beneath the western Arabian shield and more than 35 km in central Syria, where the Palmyride is located. The low Moho depth tends toward western Syria, reaching less than 15 km—except under Cyprus and the Eratosthenes seamount because of the overlying continental crust.

5 Discussion

The prominent tectonic features in Syria are a result of the separation of the Arabian plate from the African plate, which created the increase and decrease of Moho depth and may be associated with the Neo-Tethys Ocean.

Figure 4A illustrates the top boundary between the Cenozoic sediment and basement blocks, while its gravity effect is constructed by applying Granser's (1987a) forward method with contrast density decreasing exponentially with the depth (Figure 4B).

The Bouguer gravity anomaly in Figure 4B increases to the south in the Red Sea with a value of approximately 35 mGal. It is relatively reduced to −50 mGal in central Syria (Palmyria) and in eastern Syria close to the Syria–Iraq border. It reaches a maximum of approximately 35 mGal at the northern Mediterranean Sea.

The Moho gravity effect after correction by removing the gravity anomaly of the sedimentary–basement boundary and shallow blocks is presented in Figure 5. The anomaly ranges between −60 mGal and 300 mGal. We note the negative anomalies centered beneath the western Arabian shield chains while the maximum values are located in the Mediterranean Sea. The gravity anomaly values range from 100–150 mGal in Syria. These data will be used in the inversion process to obtain the Moho depth under the eastern Mediterranean Sea.

A comparison of the two maps in Figures 5, 7 shows good agreement where the gravity anomaly values are almost the same, especially in the northeast. The inverted Bouguer anomaly coincides with the theoretical gravity data at many parts of the study region. The RMS error was just 0.009 mGa l with few differences.

There are two unique regions in the Mediterranean Sea that have a great Moho depth: 22 km under Cyprus at 33.5 E, 35 N and 27 km at 33 E, 33.5 N beneath the Eratosthenes seamount, and toward the south in the Mediterranean Sea; the great Moho depth here is because of continental crust (Netzeband et al., 2006).

The maximum values of Moho depth are located in the east toward the destructive margin of the Arabian plate, while the minimum depths are at the constructive margin near the Red Sea.

The Moho depth values range from approximately 16 km to 40 km; the lowest value is observed in the eastern Mediterranean Sea and near the Red Sea with constructive edges, and the highest value appears in the northeastern corner of the investigation area with destructive edges.

Moho depth in Syria has an extended trend between 27 and 32 km. A large part of the Arabian region has a value between 30 and 35 km, which represents the mantle–crust boundary in the Arabian area, especially in the southeastern corner. The maximum value reaches 40 km in south Turkey near northeastern Syria. The Bouguer gravity anomaly in the southern part of the DSFS is very small, representing deep Moho depth variations caused by left-lateral movement along the fault (Group. et al., 2004). From north to south alongside the DSFS, where the Ghab depression is considered an extended graben of the Dead Sea rift, the Moho depth has a small value ranging from 27–29 km, decreasing toward offshore and increasing to the east, in agreement with Segev et al. (2006).

It is clear that the crustal thinning is to the north of the Red Sea under the Mediterranean Sea; north of 36 N, the crustal thickness increases to more than 40 km in the western corner of the map. The lowest Moho depth value in the study area is observed to be approximately 16 km at 33 N on the eastern Mediterranean coast.

The Moho depth from Lebanon in the south along the Mediterranean coast varies from 27 km to 32 km in the north

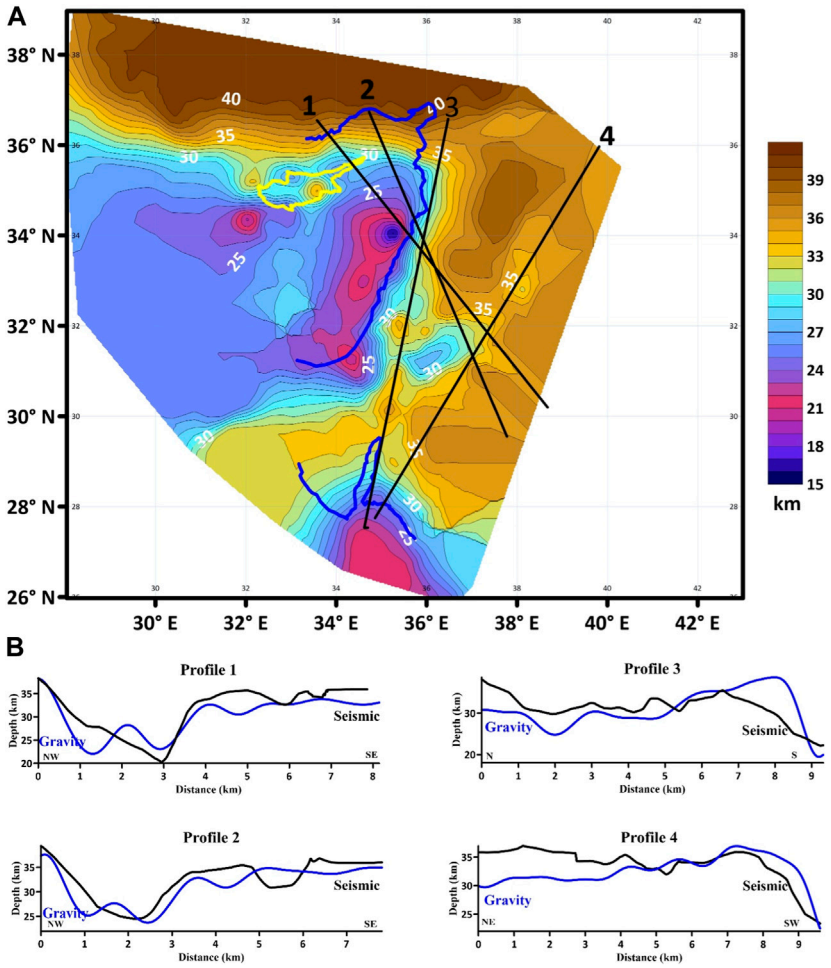

FIGURE 8
Comparison between Moho gravity depth and seismic Moho depth. **(A)** Seismic Moho depth map (in km) modified after Koulakov & Sobolev (2006); **(B)** profiles of both Moho gravity depth (blue color) and seismic Moho depth (black color).

(Bekaa) and increases toward eastern Syria, which agrees with Tiberghien (1974). The higher gravity anomaly along the Lebanon coast and the Levant basin means a higher Moho depth due to tectonic forces and active dynamism (Segev et al., 2006). The Moho depth beneath the Palmyride is approximately 37 km and may be caused by a high density penetrated body (Barazangi et al., 1993).

A comparison between the north-east of Syria and the southern Syrian boundaries shows an increase in the south approaching 33 km and a decrease in the north of approximately 27 km, while the increment toward the east of Syria near the Iraqi border reaches more than 30 km and continues beneath the Zagros Mountains in the northern Arabian boundaries with Iran.

The sediments in the Arabian shield are not evident (Seber et al., 2000). Triassic rifting plays a major role in the depth of the Moho in Palmyride in central Syria (Brew et al., 2003). Under the Arabian shield, the Moho depth was too deep at approximately 48 km, in agreement with Mooney et al. (1985) who provide a seismic velocity of 8 km.s^{-1}.

It is clear that there is a sharp and major difference of the Moho depth between offshore and onshore areas on the inversion and seismological maps. Both maps coincide with the shallowing of the Moho depth toward the west of the DSFS beneath the Mediterranean Sea. Both maps show the same tendency of increment and shallowing in Moho depths in the study region. Moho depth increases under eastern Syria to approximately 37 km toward the destructive margin of the eastern boundaries of the Arabian with the Eurasian Plate. On the other hand, the decrease in the southern DSFS under the Red Sea is approximately 27 km, at the constructive margin of the Arabian Plate. The Moho depth decreases west of the DSFS under the Mediterranean Sea, except under the two unique continental regions of Cyprus and the Eratosthenes seamount (roughly 28 km).

In comparing the Moho depth results obtained by seismic data (Koulakov and Sobolev, 2006) in Figure 8A and gravity data we inverted (Figure 6), the Moho depth, seismically calculated, ranges between 15 and 42 km, where the maximum values of 42 km are located near the Red Sea and in the northern Mediterranean Sea to the south of Turkey, with the minimum of approximately 15 km in western Syria.

Four profiles are plotted to compare the Moho discontinuity inverted from seismological and gravity data. In the first profile, we see the compatibility of two profiles, where seismic and gravity data give the same Moho depth value of 39 km under the northern Mediterranean Sea. Both profiles continue fluctuating, matching well (Figure 8). In the second profile, the Moho depth given by seismic and gravity data is almost the same as in the first profile.

We can observe the difference in the third and fourth profiles. Even though both have different starting points, they share with the end point the inversion of the same Moho depth. The unique feature in the third profile is that it is located along the DSFS from north to south; when the DSFS approaches Turkey, gravity and seismological data give different Moho depths while giving the same results along this fault.

In central Syria (Palmyride fold belt), we can find the coincidence between gravity and seismic results where the Moho depth value is 37 and 38 km, respectively, while, in western Syria, the Moho depth minimum is 15 km.

Despite the similarity of the Moho depth in the two maps, there is a still difference where the seismic Moho depth is deeper than the Bouguer Moho depth. This difference is not standard, varying from 2 km in central Syria to 5 km under the Mediterranean Sea due to density contrast over the study area, so the results obtained from gravity data could be changed by a change in this contrast. This comparison is thus very important.

The average crustal thickness is over 42 km in the southern and eastern continental parts of Syria, whereas, in the south where the western Arabian shield is located, a minimum thinning of the crust is observed in the western part of Syria beneath the Mediterranean Sea ranging 15–18 km. This may be a result of the increased density contrast in the Mediterranean Sea. The results obtained by seismic and gravity data corroborate the high Moho depths located in the continental areas beneath the Palmyride, Zagros Mountains, and the western Arabian shield, while the low Moho depth values in the Mediterranean Sea are because of the ocean crust and high density.

6 Conclusion

We have applied the 3DINVER program developed in a MATLAB environment using the Parker–Oldenburg method to determine the Moho depth inverted from the Bouguer gravity anomaly with many iterations. Prior to executing the inversion process, we conducted some corrections to remove the gravity effect of the sedimentary–basement boundary by forward modeling Granser's (1987a) method that takes into account the variation of density contrast exponentially with the depth.

It is clear that there is a sharp and major difference in Moho depth between offshore and onshore areas, confirmed by the inversion of the seismological and gravity data. Both maps coincide with the shallowing of Moho depth toward the west of the DSFS toward the Mediterranean Sea because of the ocean crust and high density. Both maps give the same tendency of increment and shallowing in Moho depths in the study region. The computed Moho depth ranging from 16 km to 40 km coincides with results obtained from seismic data. The deepest Moho depth was beneath the Arabian shield, with an approximate value of 40 km. The Moho depth increases over the eastern Mediterranean Sea toward eastern Syria near the Iraqi border with a maximum value of 42 km and may continue toward the destructive margin of the eastern edges of the Arabian and Eurasian plates. Conversely, the Moho depth decreases in the western Dead Sea rift under the Mediterranean Sea due to the thinning of the oceanic crust. However, an exception is observed beneath Cyprus and the Eratosthenes seamount because of the continental crust, with a maximum depth of approximately 30 km. This research sheds light on the variations in Moho depth across the region, providing valuable insights into the geophysical characteristics of the region.

In this research, we have not only analyzed the Moho depth variations but have also used the density contrasts, which play a crucial role in understanding the geodynamics and seismogenic nature of the northwestern Arabian plate. This study provides valuable insights into the composition and structure of the lithosphere, which directly influences the geodynamic behavior of the region. In the study area, density contrasts are influenced by several factors, including the presence of both continental and oceanic crust, variations in crustal thickness, and the distribution of different rock types. The variations in Moho depth across the northwestern Arabian plate provide critical insights into the geodynamics and seismogenic nature of the region. The study highlights the importance of considering both depth and density contrasts when investigating the complex tectonic processes and seismic activity in the area. Further study in this field will help expand our understanding of the geophysical characteristics of the region and contribute to better hazard assessment and mitigation strategies (Dyrelius and Vogel, 1972; Sawaf et al., 1990).

Data availability statement

The original contributions presented in the study are included in the article/Supplementary Material; further inquiries can be directed to the corresponding authors.

Author contributions

Conceptualization, FH and CC; methodology, FH, AK, HA, and IA; software, FH, MT, and IA; validation, CC and NA; formal analysis, FH, MT, HA, and AK; investigation, CC; resources, CC; data curation, FH, MT, and AK; writing—original draft preparation, FH, CC, and AK; writing—review and editing, FH, CC, HA, and MT; visualization, CC and NA; supervision, CC; project administration, CC; funding acquisition, CC and NA. All authors contributed to the article and approved the submitted version.

Funding

The publication fees were paid gratefully by Lulea University of Technology (Sweden). This work was supported by Natural Science Foundation of China (Nos. 42174090 and 41604060), the MOST Special

Fund from the State Key Laboratory of Geological Processes and Mineral Resources (MSFGPMR2022-4), China University of Geosciences.

Acknowledgments

The authors express many thanks to Qing Liang, Jinsong Du, and Dr. Shida Sun for their sincere criticisms and helpful advice during this research. Thanks are due to Prof. Jamal Abou-deeb of Damascus University for revising the manuscript. This work was supported by the National Natural Science Foundation of China (No. 41604060). The gravity data of the investigated region were acquired from the Earth Geopotential Model EGM2008 estimated from altimetry missions, ground data, and GRACE satellite mission (Pavlis et al., 2013) with resolution ($1' \times 1'$) shown in Figure 2.

Conflict of interest

The authors declare that the research was conducted in the absence of any commercial or financial relationships that could be construed as a potential conflict of interest.

Publisher's note

References

Barazangi, M., Seber, D., Chaimov, T., Best, J., Litak, R., Al-Saad, D., et al. (1993). Tectonic evolution of the northern Arabian Plate in western Syria. *Recent Evol. Seismicity Mediterr. Region*, 117–140. doi:10.1007/978-94-011-2016-6_5

Ben-Avraham, Z. (1985). Structural framework of the Gulf of elat (Aqaba), northern Red Sea. *J. Geophys. Res.* 90 (B1), 703–726. doi:10.1029/JB090iB01p00703

Ben-Avraham, Z., Ginzburg, A., Makris, J., and Eppelbaum, L. (2002). Crustal structure of the Levant basin, eastern mediterranean. *Tectonophysics* 346 (1–2), 23–43. doi:10.1016/S0040-1951(01)00226-8

Blakely, R. (1995). *Potential theory in gravity and magnetic applications*. Cambridge, UK: Cambridge University Press.

Brew, G., Barazangi, M., Sawaf, T., and Al-Maleh, K. (2000). "A new tectonic map of Syria and surrounding regions," in 4th Middle East Geosciences Conference GEO, Manama, Bahrain, February 2000.

Brew, G., Best, J., Barazangi, M., and Sawaf, T. (2003). Tectonic evolution of the NE Palmyride mountain belt, Syria: The bishri crustal block. *J. Geol. Soc.* 160 (5), 677–685. doi:10.1144/0016-764902-161

Chakravarthi (2003). *Digitally implemented method for automatic optimization of gravity fields*. US6615139B1, 2.12

Chakravarthi, V., Pramod Kumar, M., Ramamma, B., and Rajeswara Sastry, S. (2016). Automatic gravity modeling of sedimentary basins by means of polygonal source geometry and exponential density contrast variation: Two space domain based algorithms. *J. Appl. Geophys.* 124, 54–61. doi:10.1016/j.jappgeo.2015.11.007

Cordell, L., and Henderson, N. D. G. (1968). Iterative three dimensional solution of gravity anomaly data using a digital computer. *Geophysics* 33, 596–601. doi:10.1190/1.1439955

Domas (1994). *The late Cenozoic of the al ghab rift.pdf*. Al ghab, Cyria: Al ghab rift.

Dyrelius, D., and Vogel, A. (1972). Improvement of convergency in iterative gravity interpretation. *Geophys. J. R. Astronomical Soc.* 27 (2), 195–205. doi:10.1111/j.1365-246X.1972.tb05771.x

Gao, X., and Sun, S. (2019). Comment on "3DINVER.M: A matlab program to invert the gravity anomaly over a 3D horizontal density interface by parker-oldenburg's algorithm". *Comput. Geosciences* 127, 133–137. doi:10.1016/j.cageo.2019.01.013

Gardner, G. H. F., Gardner, L. W., and Gregory, A. R. (1974). Formation velocity and density—The diagnostic basics for stratigraphic traps. *Geophysics* 39 (6), 770–780. doi:10.1190/1.1440465

Garfunkel, Z. (1998). Constrains on the origin and history of the Eastern Mediterranean basin. *Tectonophysics* 298 (1–3), 5–35. doi:10.1016/S0040-1951(98)00176-0

Gómez-Ortiz, D., and Agarwal, B. N. P. (2005). 3-3DINVER.M: A matlab program to invert the gravity anomaly over a 3D horizontal density interface by parker-oldenburg's algorithm. *Comput. Geosciences* 31 (4), 513–520. doi:10.1016/j.cageo.2004.11.004

Granser, H. (1987). *U S I N G a N exponential density-depth*. Tulsa, Oklahoma: Seg Library, 1030–1041.

Group, D., Weber, M., Abueladas, A., Agnon, A., Babeyko, A., Bartov, Y., et al. (2004). The crustal structure of the Dead Sea transform. *Geophys. J. Int.* 156, 655–681. doi:10.1111/j.1365-246X.2004.02143.x

Jassimand Goff (2006). *Geology of Iraq*. Iraq: Google Books.

Koulakov, I., and Sobolev, S. V. (2006). Moho depth and three-dimensional P and S structure of the crust and uppermost mantle in the Eastern Mediterranean and Middle East derived from tomographic inversion of local ISC data. *Geophys. J. Int.* 164, 218–235. doi:10.1111/j.1365-246X.2005.02791.x

McBRIDE (1990). *Seismic inMcBride_Palmyrides_AAPG_90*. Columbia, Canada: McBRIDE.

Mechie, J., Ben-avraham, Z., Weber, M. H., Götze, H., Koulakov, I., Mohsen, A., et al. (2013). The distribution of Moho depths beneath the Arabian plate and margins. *Tectonophysics* 609, 234–249. doi:10.1016/j.tecto.2012.11.015

Michal Rosenthal, A. S. (2015). 1-The deep structure and density distribution of northern Israel and its surroundings. Report No.: GSI/12/2015.

Mooney, W. D., Gettings, M. E., Blank, H. R., and Healy, J. H. (1985). Saudi arabian seismic-refraction profile: A traveltime interpretation of crustal and upper mantle structure. *Tectonophysics* 111 (3–4). doi:10.1016/0040-1951(85)90287-2

Murthy, I. V. R. (1979). Gravity anomalies of two-dimensional bodies of irregular cross-section with density contrast varying with depth. *Geophysics* 44. doi:10.1190/1.1441023

Netzeband, G. L., Gohl, K., Hübscher, C. P., Ben-avraham, Z., Dehghani, G. A., Gajewski, D., et al. (2006). *Levantine Basin — crustal Struct. Orig.* 418, 167–188. doi:10.1016/j.tecto.2006.01.001

Oldenburg (1974). The inversion and interpretation of gravity anomalies. *Geophysics* 39 (4), 526–536. doi:10.1190/1.1440444

Parker, R. L. (1973). The rapid calculation of potential anomalies. *Geophys. J. R. Astronomical Soc.* 31, 447–455. doi:10.1111/j.1365-246X.1973.tb06513.x

Pavlis, N. K., Holmes, S. A., Kenyon, S. C., and Factor, J. K. (2013). Erratum: Correction to the development and evaluation of the Earth gravitational model 2008 (EGM2008). *J. Geophys. Res. Solid Earth* 118 (5), 2633. doi:10.1002/jgrb.50167,2013

Pham, T. P., Oksum, E., and Do, T. D. (2018). GCH_gravinv: A MATLAB-based program for inverting gravity anomalies over sedimentary basins. *Comput. Geosciences* 120, 40–47. doi:10.1016/j.cageo.2018.07.009

Rao, D. B., Prakash, M. J., and Babu, N. R. (1990). 3D and 2½ D modelling of gravity anomalies with variable density contrast. *Geophys. Prospect.* 38 (4), 411–422. doi:10.1111/j.1365-2478.1990.tb01854.x

Rybakov, M. (2004). 4-Top of the crystalline basement in the Levant. *J. Metrics*, 1–8. doi:10.1029/2004GC000690

Sawaf, T., Gebran, A., and Resources, M. (1990). Crustal shortening in the Palmyride fold belt, Syria, and implications for movement along the Dead Sea fault system. *Tectonics* 9 (6), 1369–1386. doi:10.1029/TC009i006p01369

Seber, D., Steer, D., Sandvol, E., Sandvol, C., Brindisi, C., and Barazangi, M. (2000). Design and development of information systems for the geosciences: An application to the Middle East. *Geoarabia* 5 (2). doi:10.2113/geoarabia0502269

Segev, A., Rybakov, M., Lyakhovsky, V., and Hofstetter, A. (2006). The structure, isostasy and gravity field of the Levant continental margin and the southeast Mediterranean area the structure. *isostasy gravity field Levant Cont. margin southeast Mediterr. area* 425. doi:10.1016/j.tecto.2006.07.010

Sharkov, E. V. (1997). The el-ghab rift depression in Syria: Its structure, stratigraphy, and history of development. *Stratigr. Geol. Correl.*5 (4), 362–374.

Silva, J. B., Costa, D. C., and Barbosa, V. C. (2006). Gravity inversion of basement relief and estimation of density contrast variation with depth. *Geophysics* 71 (5), J51–J58. doi:10.1190/1.2236383

Spector and Grant (1970). Statistical models for interpreting aeromagnetic data. *GEOPHYSICS* 35 (2), 293–302. doi:10.1190/1.1440092

Trung, N. N. (2018). Moho depth of the northern Vietnam and Gulf of Tonkin from 3D inverse interpretation of gravity anomaly data to. *J. Geophys. Eng.* 15. doi:10.1088/1742-2140/aabf48

frontiers | Frontiers in Earth Science

TYPE Original Research
PUBLISHED 19 July 2023
DOI 10.3389/feart.2023.1190106

OPEN ACCESS

EDITED BY
Henglei Zhang,
China University of Geosciences Wuhan, China

REVIEWED BY
Ahmed M. Eldosouky,
Suez University, Egypt
Khalid Essa,
Cairo University, Egypt

*CORRESPONDENCE
Shuva Shankha Ganguli,
shuvaganguli@gmail.com,
shuva.ganguli@gsi.gov.in

RECEIVED 20 March 2023
ACCEPTED 29 June 2023
PUBLISHED 19 July 2023

CITATION
Ganguli SS and Pal SK (2023), Gravity-magnetic appraisal of the southern part of the Cauvery Basin, Eastern Continental Margin of India (ECMI): evidence of a volcanic rifted margin.
Front. Earth Sci. 11:1190106.
doi: 10.3389/feart.2023.1190106

Gravity-magnetic appraisal of the southern part of the Cauvery Basin, Eastern Continental Margin of India (ECMI): evidence of a volcanic rifted margin

Shuva Shankha Ganguli[1]* and Sanjit K. Pal[2]

[1]PSS-P&M-I, Geological Survey of India, Kolkata, India, [2]Department of Applied Geophysics, Indian Institute of Technology (Indian School of Mines), Dhanbad, India

The Cauvery sedimentary basin of India, a part of the Eastern Continental Margin of India (ECMI), has evolved as a consequence of its breakup from East Antarctica in the early Cretaceous. This study covers approximately 10,000 km^2 in the southern part of the Cauvery basin. A total of 5,161 gravity-magnetic observations were made in an area bounded by 78°–79°E longitude and 9°–10°N latitude. The gravity anomaly map shows a dominant NE-SW trend with a total relief of 83 mGal from −77 mGal to 6 mGal. The map reveals very prominent NE-SW trending linear gravity high bands and two circular/elliptical gravity lows around Madurai and Ramanathapuram, respectively. The residual gravity map reveals NE-SW trending alternative bands of gravity highs and lows, revealing a ridge-depression structure. The gravity modeling shows the presence of underplated material, which may be related to magmatic activity during the Cretaceous. The magnetic map reveals two prominent E-W trending linear structures, which probably represent the disposition of a shear zone under the Cauvery Basin. Based on the filtered magnetic and gravity map, we have prepared an interpreted basement geology map. The magnetic map and residual gravity map suggest that the basement rock of the basin is crystalline (granite/gneiss) and may not comprise a high-grade metamorphic rock Eastern Ghat Orogeny.

KEYWORDS

gravity-magnetic, cauvery basin, eastern continental margin of India (ECMI), regional-residual analysis, gravity modeling

Introduction

Massive igneous activity is usually associated with continental rifting as the continents are stretched prior to their break up (White and M^{c}kenzie, 1989). The Western Continental Margin of India (WCMI, Figure 1B) evolved due to the disintegration of India from Madagascar and Seychelles, which was associated with the extrusion of huge areas of flood basal approximately 65 Ma. A thick (~18 km) high-velocity layer (HVL) was reported in the lower crust of the west coast of India, which is considered a part of magmatism that characterizes a volcanic rifted margin (Saikia et al., 2017). The Cauvery Sedimentary Basin (CSB), southernmost among the string of Mesozoic rift basins along the east coast, is a part of the Eastern Continental Margin of India (ECMI) and has evolved as a consequence of fragmentations of India and East Antarctica in the early Cretaceous (Powel et al., 1988); however, evidence of volcanic activity at the surface is absent and may be buried under thick sedimentary cover. Additionally, the seismological and

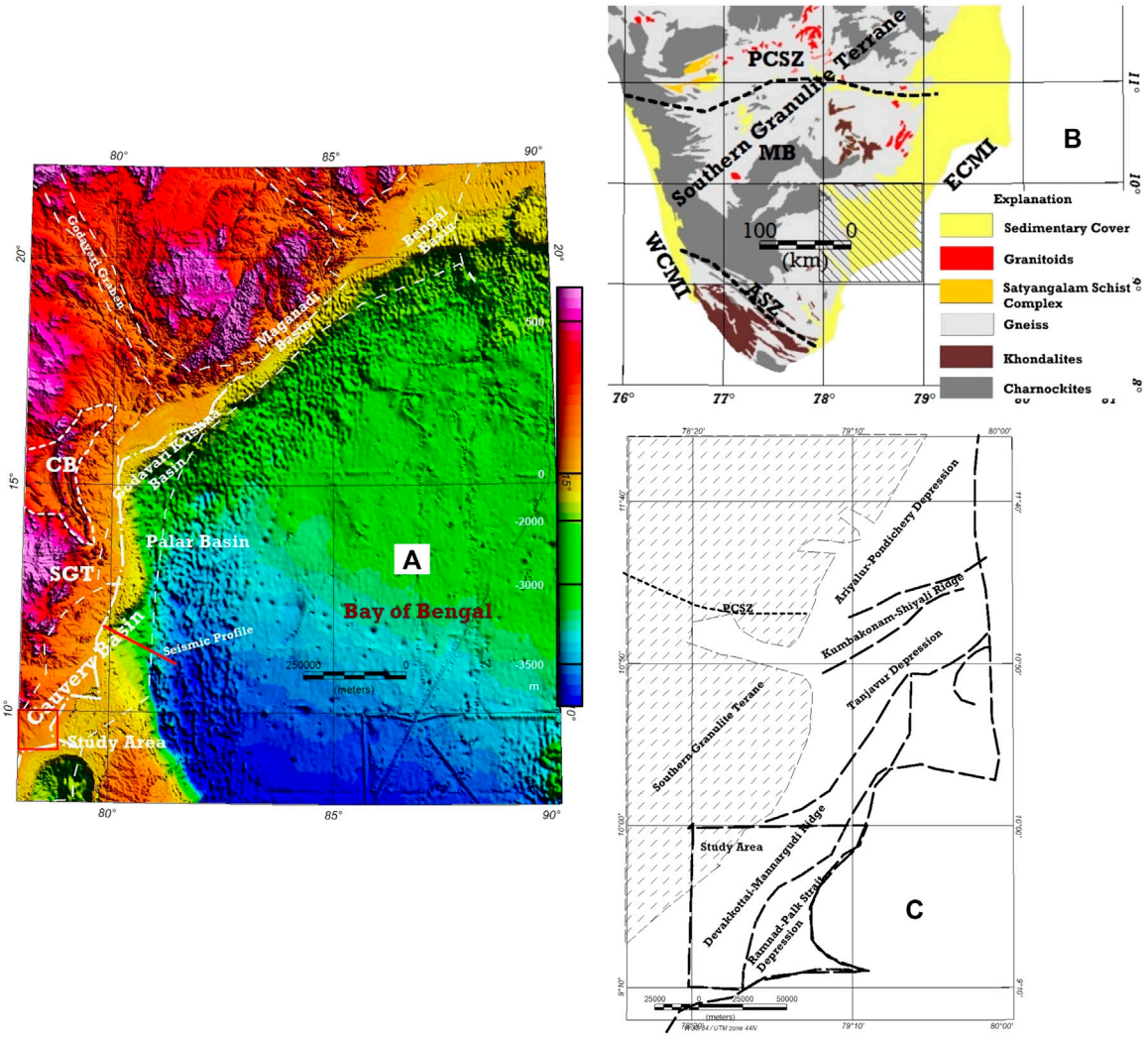

FIGURE 1
(A) The prominent basins of the Eastern Continental Margin of India (ECMI), including the location of the Cauvery Sedimentary Basin. SGT, Southern Granulite Terrane; CB, Cuddapah Basin. **(B)** Generalized geological map of parts of the SGT. MB, Madurai Block; PCSZ, Palghat Cauvery Shear Zone; ASZ, Achankovil Shear Zone. The hatched box indicates the study area; WCMI, Western Continental Margin of India. **(C)** Prominent structures of the Cauvery Sedimentary Basin.

magnetotelluric (MT) studies are also inadequate with regard to the east coast of India; therefore, the deeper crustal architecture is elusive. The east coast of India comprises five sedimentary basins, from north to south. These are Bengal, Mahanadi, Godavari-Krishna, Palar, and Cauvery (Figure 1A; Sastri et al., 1981), and the Cauvery Basin forms a Category-I sedimentary basin or an oil province with an established commercial production (Mazumder et al., 2019). For the past few decades, a large amount of data has been accrued during the exploration for hydrocarbons. The geophysical studies in the East Indian coast have revealed an alternating set of NE-SW trending ridge-depression structural features in all of the basins (Sastri et al., 1973, 1981; Behara et al., 2004; Bastia et al., 2010; Radhakrishna et al., 2012). The studies based on the satellite-derived potential field and seismic data encompassing onshore and offshore areas provided broad crustal configurations, lithospheric strength, and subsidence history of the Godavari-Krishna and Palar-Cauvery basins (Singh and Rao, 2021, Twinkle et al., 2016a; Radhakrishna et al., 2012; Rao and Radhakrishna, 2021). The present study area is mostly covered by sediments, except in western parts; therefore, the structural features and basement geology remain elusive. The potential field data have been effectively used for structural studies attempting to better understand basement geometry (Castro et al., 2014; Curto et al., 2014; Essa et al., 2018; Eldosouky and Mohamed, 2021; Hamimi et al., 2023) and mineral investigations (Blundell et al., 2019; Eassa et al., 2022) in different parts of the world, especially over sediment-covered terrain. However, insights into the shallow crustal structure and deep crustal architecture based on high data density and systematic coverage of the ground gravity-magnetic data are limited, especially for the southern part of the Cauvery Basin. The present study is based on an analysis of high-resolution ground gravity magnetic and aims to reveal basement

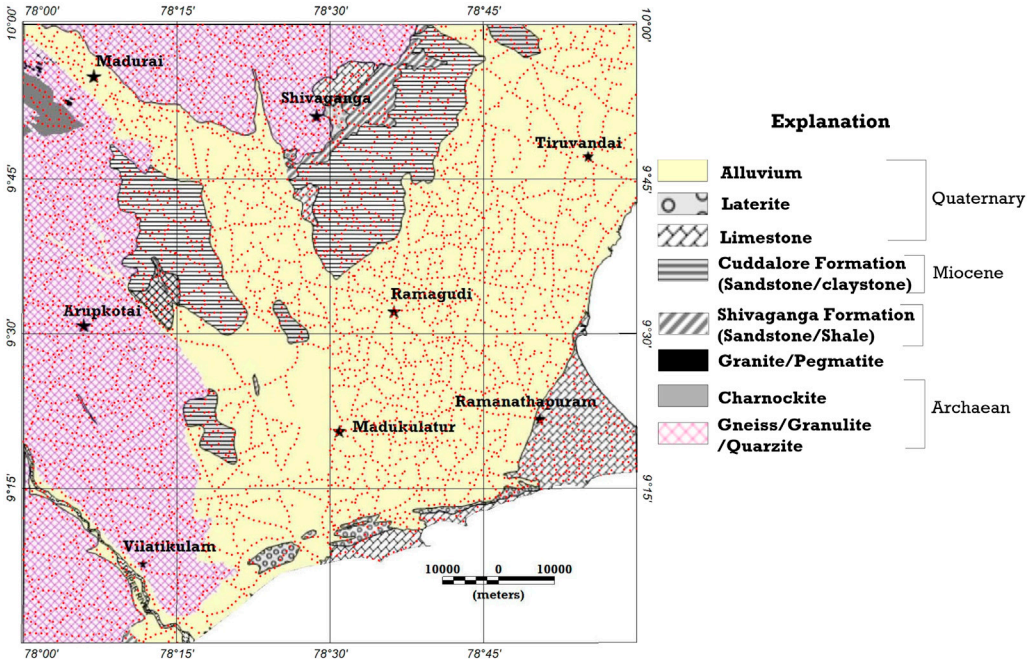

FIGURE 2
Geological map of the study area. The red dots represent gravity-magnetic data locations.

geometry and structure. Additionally, the study aims to understand the tectonic regime that caused the evolution of the Cauvery Basin. We have applied several geophysical filters and generated a residual-regional gravity anomaly map of the study area based on the spectral analysis, analytical signal map, and tilt derivative map of the magnetic data and two-dimensional gravity modeling. The study reveals the alternate ridge-depression structure, some oblique structures to the east coast, and the occurrence of a high-density unit on the deeper crust, which might be the impact of plume lithospheric interaction.

Regional geology and tectonics

The Eastern Continental Margin of India (ECMI) bears the imprints of drifting because of the disintegration of Gondwanaland with a time window stretching from the Permian to the Early Cretaceous (Sastri et al., 1981). The margin consists of five river basins. From north to south these are the Bengal, Mahanadi, Godavari-Krishna, Palar, and Cauvery (Fig. 1 a) basins, and the sediment thickness in these basins varies from 3 to 5 km in the onshore depressions to more than 10 km in the thick deltaic sedimentation regions of the onshore (Sastri et al., 1973). The seismic studies reveal that the underlying basement is characterized by NE-SW ridge-depression structures that are parallel to the east coast of India. The geophysical studies suggest the margin is a composite of two segments: the northern part (north of 16° N), with a rifted margin character, and the transformed segment southern part that has developed due to shearing during the early stages of continental separation (Subrahmanyam et al., 1999; Chand et al., 2001; Krishna et al., 2009; Yatheesh, 2020). The effective elastic thickness (Te), which indicates the mechanical character of the underlying lithosphere, varies from 10 to 25 km for the northern part of the ECMI and less than 5 km for the southern part of the ECMI (Chand et al., 2001).

The Cauvery Basin is an intracratonic rift basin (Chari et al., 1995) that came into existence due to the break-up of Eastern Gondwanaland during the Late Jurassic to Early Cretaceous. The westerly bordering Southern Granulite Terrane (SGT) forms the basement of the basin (Figure 1). The SGT is made of exhumed lower crustal rocks, such as the gneisses, charnockite, khondolite, intrusive granites, and other high-grade metamorohic rocks (Chetty 2021). The Palghat Cauvery Shear Zone (PCSZ) is a crustal scale E-W trending shear zone that separates the SGT in the northern block in the north and the Madurai block (MB; Chetty, 2021) in the south (Figure 1B). The disposition of the PCSZ beneath the Cauvery Basin played a major role in shaping the basement structure and morphology of the basin (Majumder et al., 2019). Additionally, apart from the shear zone, the basement was subjected to three episodes of tectonism, which also shaped the basin geometry. The oldest episode was associated with N-S trending faults that developed during the late Permian followed by the principle event associated with NE trending rifts during the late Jurassic to Early Cretaceous. The rifting was caused by the separation of the India-Sri Lanka system from Antarctica and Australia. The NW-SE trending oblique structures developed due to rifting and strike-slip moment (Majumder et al., 2019).

The Cauvery Basin encompasses an area of approximately 25,000 km^2 on land (Chari et al., 1995), and the basement is characterized by ridge and graben morphology. The depth to the basement for depression varies from 5,400 to 3,000 m, as estimated

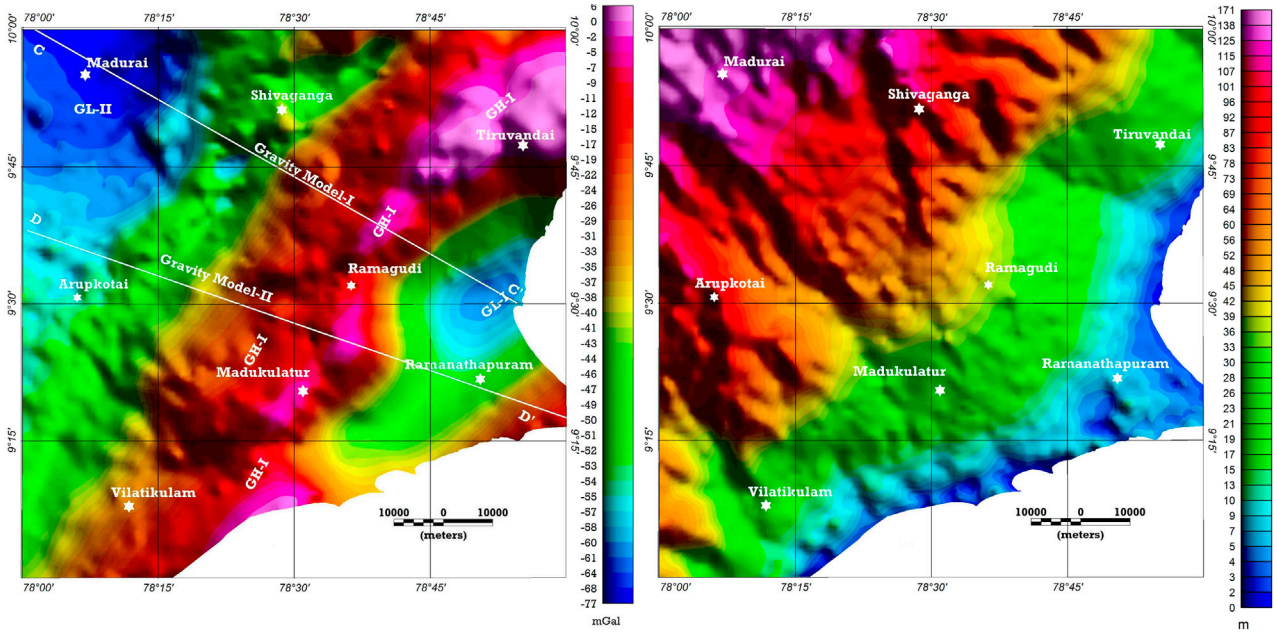

FIGURE 3
(A) Bouguer Gravity Anomaly Map of the study area. The warm color indicates gravity high zones and the lighter color indicates gravity low zones. Note the NE-SW trending moderate-to-high gravity anomaly (GH-I) zone and two gravity low zones (GL-I and GL-II). Gravity modeling is carried along C–C′ and D–D′. **(B)** Topographic image of the study area.

from the seismic refraction survey (Sastri et al., 1973). The sedimentary thickness over the ridges varies from 250 to 2,440 m (Sastri et al., 1973). The present study covers an approximately 10,000-km^2 area of the southern part of the Cauvery Basin. The Khondolite and Charnockite group of rocks of the SGT forms the basement (Figure 2). The basement is unconformably overlain by Triassic-Cretaceous Shivganga formations comprising alternating shale, sandstone, and grit. Coal seams occasionally occur in the formation. The Cuddalore formation overlies the Miocene Shivganga formation. The formation mainly comprises sandstone. The major part of the area is covered by Quaternary alluvium of arenaceous and calcareous origin, with patches of laterite cover over the Tertiary formations. The area has a gentle seaward slope with an elevation that varies from 171 m to 1 m (amsl).

Methodology and analysis

The Bouguer gravity anomalies (BGA) are essentially caused by subsurface density inhomogeneity, and therefore, reflect the lateral variations in the density of subsurface rocks. The magnetic anomalies (MA), which are caused by the variations in the magnetic susceptibility in crustal rocks, formed at temperatures above the Curie point. The magnetic susceptibility of rocks is inversely correlated with rock silica content (Teknik et al., 2023) and directly proportional with magnetite content. Magnetic anomaly maps are efficient tools for mapping concealed subsurface magmatic structures and basement configurations where overlying sedimentary units are not embedded by magnetic bodies (e.g., basaltic intrusions). Thus, both gravity and magnetic anomalies provide important insights into the tectonic nature of crustal domains and help in building a regional scale representation of the basement configuration. The gravity-magnetic data were acquired as part of the National Geophysical Mapping Programme (NGPM) of the GSI between 2010 and 2012, along with all the available roads with 1–2-km station intervals. The present data set includes more than 5,000 gravity-magnetic observations covering an area of approximately 10,000 sq. Km (Figure 2). The gravity data were acquired using a CG-5 gravimeter and magnetic data were acquired using a proton precession magnetometer (GSM-19T), and the orthometric height of each gravity station was measured by deploying the 'Total Station' leveling instrument. The entire acquired data, which was tied with the IGSN-1971 gravity bases, was corrected for drift, tidal, elevation, and latitude effects to arrive at the Bouguer gravity anomaly (BGA). The magnetic data were subjected to diurnal correction and IGRF correction (Epoch-2010). The gravity, magnetic, and elevation data were gridded using the minimum curvature method with a cell size of 1,000 m.

Bouguer gravity anomaly (BGA)

The Bouguer gravity map shows some distinct anomaly patterns with a total variation of 83 mGa l from −77 mGa l to six mGa l (Figure 3). The high gravity anomaly values may indicate the reduction of crustal thickness and the presence of underplated high-

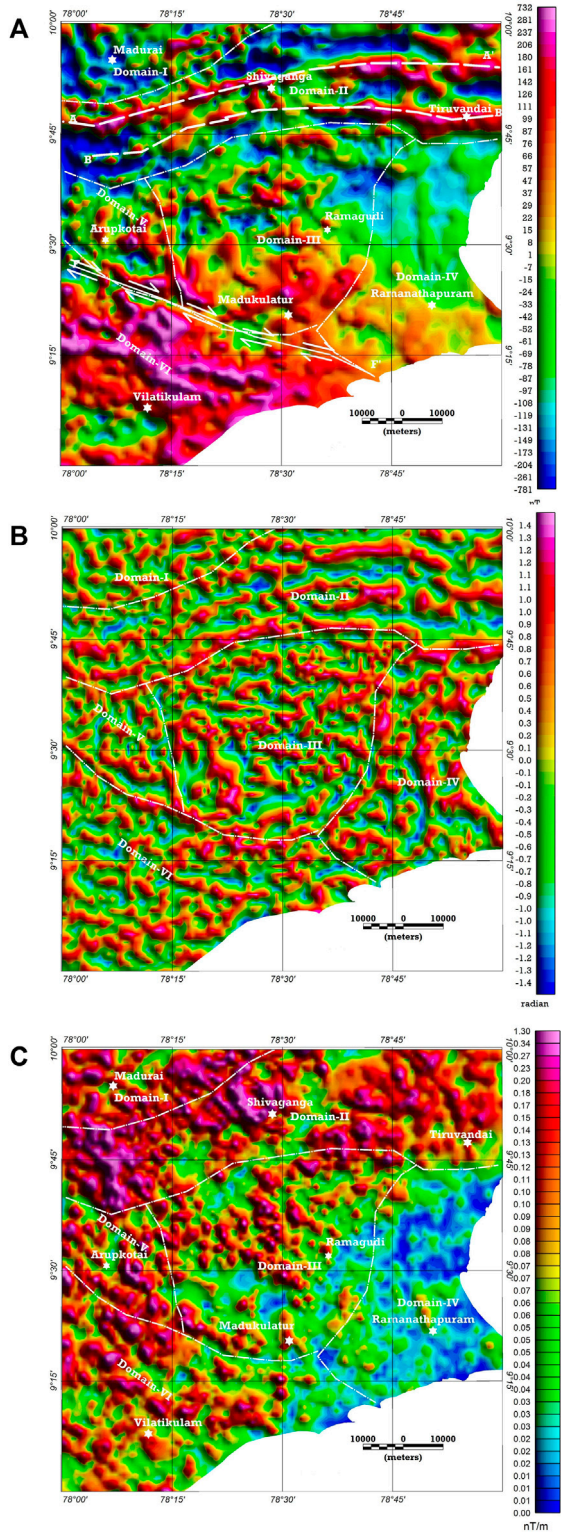

FIGURE 4
(A) Magnetic (RTP) anomaly map of the study area. The warm color indicates magnetic high zones and the lighter color indicates magnetic low zones. Note the curvilinear approximate E-W trending magnetic features (A–A′ and B–B′) in domain II. F–F′ is the inferred structural feature (see text for details). **(B)** Tilt derivative of the magnetic anomaly map (TDR). The study area is divided in five zones based on the tilt derivative signatures. **(C)** Analytical Signal (AS) map of the study area.

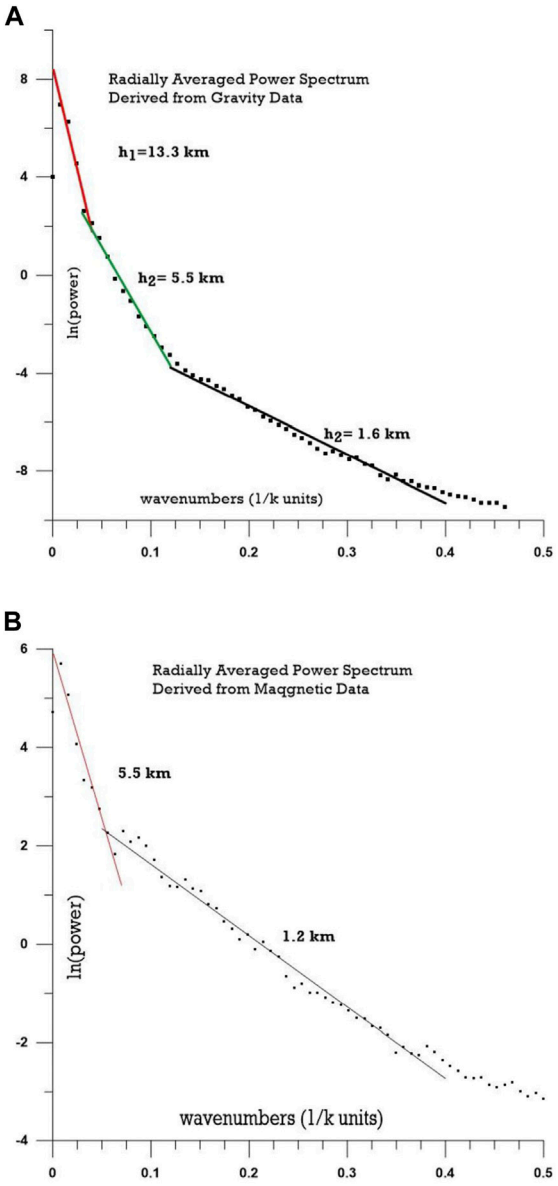

FIGURE 5
Radially average power spectrum for gravity **(A)** and magnetic data **(B)**.

density material. The very prominent NE-SW trending linear gravity high zone (−35 to six mGa l) anomaly values separate the entire study area into two-halves. The high anomaly zone may indicate the emplacement of a high-density plug into the mid-crustal level. The map shows circular and elliptical gravity lows around Madurai and Ramanathapuram, respectively (Figure 3), which may indicate the occurrence of low-density granites within the basement.

Magnetic anomaly (MA)

The magnetic anomaly map shows some distinct anomaly patterns; however, we have applied a reduced to pole filter (RTP) to center the magnetic anomalies over their causative features,

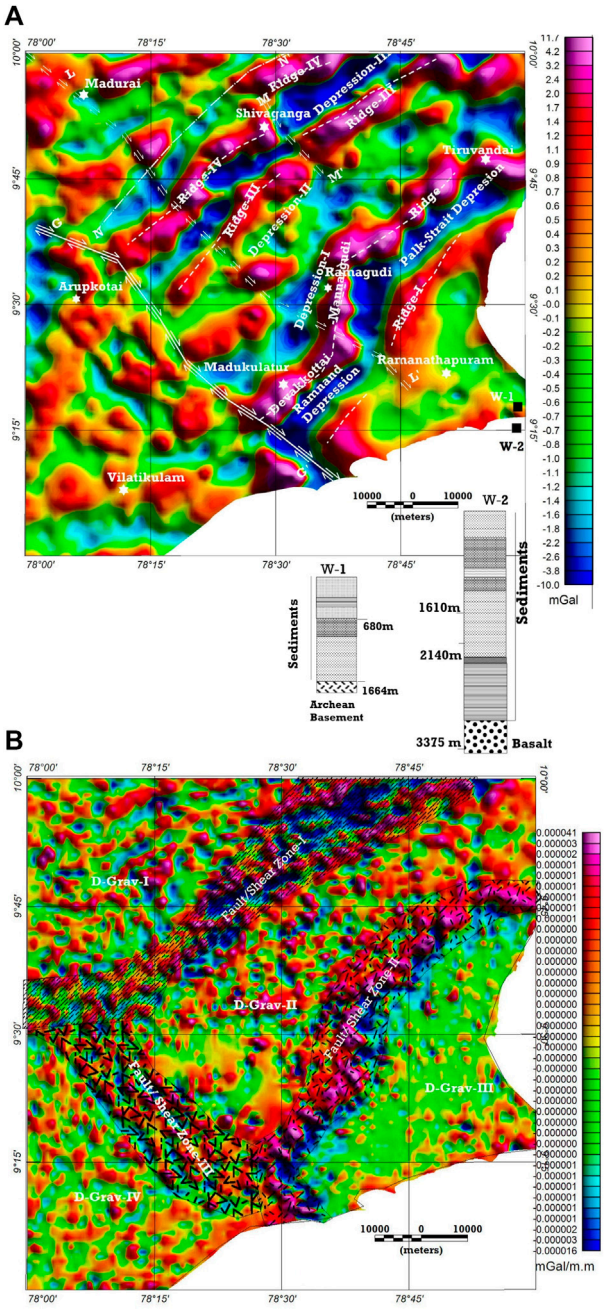

FIGURE 6
(A) Residual gravity anomaly map of the study area. W-1 and W-2 bore well locations are indicated. M–M′, L–L′, and G–G′ are the inferred faults. N–N′ is the inferred western boundary of the basin. Note the alternative high and low anomalies revealing the ridge depression structure of the study area. See text for details. **(B)** Second vertical derivative of the gravity anomaly map. Based on the gravity trend, the entire study area can be divided into several domains.

which makes the interpretation easier and more reliable (Castro et al., 2014; Essa et al., 2022). The present study lies in a low magnetic latitude, hence a pseudo-inclination factor of 60°–85° was used to suppress the amplitude and power in and near the declination direction at low magnetic latitudes (Blakely R. J., 1996). Generally high amplitude high-frequency anomalies are caused by highly magnetized rocks at a shallow depth, and low-amplitude low-frequency anomalies are likely to be sourced from deep magnetic bodies (Teknik et al., 2023). The magnetic anomaly values (Figure 4A) show a relief of approximately 1,500 nT, which suggests susceptibility does not vary widely among the litho-units and non-magnetic litho-units are dominant within the study area. The western part of the study area is characterized by higher frequency anomalies than the eastern part. It suggests that in the western part, the causative sources of the anomalies are occurring at a shallow depth and magnetic minerals are present in the causative litho-units. We have generated an RTP, analytical signal (AS), and tilt derivative magnetic anomaly map of the study area to enhance the shape and pattern of the magnetic anomalies. The application of an RTP filter on the magnetic data centers the magnetic anomaly over a causative source but the filter does not take account of the remanent magnetization (Leseane et al., 2020; Essa et al., 2021). The tilt derivative (TDR) is an arc-tan geometrical function that normalizes the vertical derivative by the total horizontal derivative (Miller and Singh, 1994; Blakely RJ. 1996; Essa et al., 2022). The TDR acts as an automatic gain control filter (AGF) and responds equally to both shallow and deeper sources. The peaks of the transformed data are positioned directly over the body's center (Ferreira et al., 2013). The function is very useful in enhancing the structural trend and linear features in magnetic data (Stewart and Miller, 2018). Based on the RTP anomaly and tilt derivative (TDR) (Castro et al., 2014; Ganguli et al., 2022), the entire study area is classified into five magnetic domains: domains I, II, III, IV, V, and VI (Figure 4A, B). 'Domain I' is characterized by high-frequency negative anomalies, with a few patches of positive anomalies (Figure 4A). The magnetic fabric did not show any predominant trend (Figure 4B). A strong approximate E-W trending positive linear magnetic anomaly (A-A'; Figure 4A) runs across domain II. Another near parallel linear magnetic anomaly (B-B'; Figure 4A) runs just south of it. The same pattern is also evident in the TDR map (Figure 4B). The pattern cuts across the dominant NE-SW structural and gravity anomaly trend of the study area, and the causative magnetic source may not be outcropping but corroborates well with the trend of PCSZ (Figure 1B). Domain III is characterized by moderate-to-high frequency positive and negative anomalies. Domain IV is characterized by negative-to-near positive long-wavelength anomalies, which indicate the presence of thick sedimentary rock over the dominantly non-magnetic or silicic basement. The WNW-ESE trending linear feature separates domains IV and VI, which otherwise shows a similar anomaly pattern. This linear feature is interpreted as a fault. The southern part of domain IV covers the Ramanathapuram Sub-basin. The anomaly pattern suggests a comparatively shallow mafic basement. Based on the analysis of the magnetic data, an inferred geological map was prepared and is presented in Figure 4C.

Regional-residual analysis of the gravity data

The gravity and magnetic anomaly map represent the superposition of the anomalies of various frequencies associated

with sources with different depth levels. The spectral analysis and subsequent wavelength filtering of the gravity and magnetic anomaly are useful for separating anomalies resulting from shallow causative sources and deeper causative sources (Telford et al., 1990; Ganguli et al., 2020, 2022).

The radially averaged power spectrums (Spector and Grant, 1970; Blakely R. J., 1996; Ganguli et al., 2021, Teknik et al., 2023) were generated for both the gravity and magnetic data (Figure 5). The radially averaged power spectrum of the gravity data shows three density interfaces at 13.3 km, 5.5 km, and 1.6 km. The radially averaged power spectrum for the magnetic data shows two magnetic interfaces: a deeper interface at 5.5 km and a shallower one at 1.2 km. The results of the spectral analysis suggest there is a density and magnetic interface at 5.5 km, which may indicate the average basement for the sedimentary depressions, while the density interface at 1.7 km may indicate average sedimentary thickness over the ridges and the magnetic interface at 1.2 km may indicate the top of a buried magnetic source. Here, we have observed that the deepest density interface is at 13.3 km but the magnetic deepest magnetic interface is at 5.5 km. This suggests that geological sources at a greater depth contribute more to the gravity anomaly map than they do to the magnetic anomaly map. Additionally, it is possible that the crust below 5.5 km is magnetically homogeneous.

Residual gravity map

The cutoff wavenumber (0.04 units) separating the regional and residual gravity maps were derived from the results of the spectral analysis of gravity data. The residual anomaly map, which manifests a near-surface density distribution (Figure 6), was generated by applying a band-pass anomaly map with a passband from 0.04–0.4 units. The residual gravity map shows the variation of 18 mGa l and NE-SE trending linear bands of gravity residual highs and lows, which are the distinct features of the map. We have corroborated the geologically mapped ridge-depression structure (Sastri et al., 1981) with the residual gravity map (Figure 1B) and observed that the NE-SW trending most prominent positive gravity anomaly in the eastern part of the study area corroborates well with the Devakkottai-Mannargudi Ridge and the adjacent linear gravity low Ramnand-Palk-Strait Depression (Sastri et al., 1981). Additionally, similar anomaly patterns were observed over the Mahanadi Basin, where gravity 'highs' lie over the shallow basement ridges and the 'low' corroborates with the basement depressions over which thick sediments have been deposited (Behara et al., 2004). Hence, we have inferred that linear gravity lows are associated with depression and linear highs are associated with ridges and marked them in the residual gravity map. The present study, for the first time, brought out the subsurface ridge depression structure, which had otherwise been concealed. It is interesting to note that the ridge-depression structures abut along the line G–G' (Figure 6A) in the south, which we have inferred as a fault oblique to the primary NE-SW trend. Additionally, we have identified some faults (L–L', M–M'; Figure 6) parallel to this fault. We further notice that the residual high signature associated with the Devvakotai-Mannargudi Ridge exhibits three deformation sets (NE-SW, N-S, and NW-SE). NE-SW is the oldest and NW-SE is the youngest. Moderate-to-high residual gravity signatures were observed in Madurai and Ramanathapuram sub-basin, respectively. Over the Ramanathapuram sub-basin or Ramnand-Palk Strait depression, the basement thickness reaches almost 3.5 km (Sastri et al., 1981). Therefore, the moderate-to-high residual gravity anomaly may indicate the presence of mafic rock underneath the sediments. The drilling data does indicate the presence of basalts at a depth of ~1,650 m.

Second vertical derivative (SVD)

The second vertical derivative of the gravity data enhances the subtle effects caused by near-surface density discontinuities, which are otherwise blurred by the density variation in the deeper subsurface. The spectral analysis shows that the deepest density interface is approximately 13 km, while the deepest magnetic interface is at a depth of approximately 5 km (Figure 5). Therefore, magnetic data are more influenced by near surface geological units than the gravity data. Again, the cutoff wavelength used to derive the residual gravity anomaly was approximately 25 km. Hence, the residual anomaly is dominated by a signal from a crustal column at least 5 km thick. To carry out a comparative study between the magnetic and gravity anomaly maps, we generated an SVD gravity map that is dominated by signals from a much shallower depth. Based on the SVD of the gravity data (Figure 6B), we have again classified the study area in different domains (Figure 6B). The SVD brings out two prominent NE-SW trending litho-contacts (Litho-Contact-I and Litho-Contact-II, Figure 6B) and another NW-SE trending litho-contact (Fault/Shear Zone-III, Figure 6B). These prominent structures divide the entire study area into four domains (Figure 6B). Litho contact-I is probably indicating the contact between basement granulites and sedimentaries. Litho contact-II is probably the western boundary of the Ramnathapuram sub-basin. The basement is exposed over domains 'D-Grav-I' and 'D-Grav- IV' (Figure 6B) and consists of high-grade metamorphic rocks of the Southern Granulite Terrane (SGT). However, there is difference in structural trends over these two domains. Domain 'D-Grav-II' is covered by sediments, but it appears that the basement occurs at a shallow depth and granulites may form the basement. The sediments are thicker over domain 'D-Grav-III', which represents the Ramanathpuram sub-basin.

Regional gravity map

The regional gravity map almost mimics the Bouguer gravity maps and have a high frequency due to the elimination of shallow sources (Figure 7). The strong linear NE-SW trending gravity high band is a distinct feature of the map, and it further emphasizes the emplacement of a high-density plug into mid-crustal levels. The two distinct gravity lows near Madurai and Ramanathapuram persist in the regional gravity map, which indicates emplaced low-density rocks within the basement. Moderate-to-high residual anomalies were observed (Figure 6) at these two places.

The signature of the regional and residual Bouguer gravity anomalies, magnetic anomaly, and surface geology along two profiles was examined (Figure 8). The residual gravity profile shows a sinusoidal gravity anomaly pattern in the southeastern part under the sedimentary cover (Figure 8A, B). The anomaly pattern depicts a concealed ridge basin structure in the SE part of the study area. The regional gravity anomaly for Profile-1 (Figure 8A) shows a strong gravity high with a peak amplitude of −18 mGa l. The anomaly has a wavelength of approximately 70 km (Profile-1), which suggests the emplacement of a high-density plug at the mid-crustal level. This regional gravity high is followed by a regional gravity low (−60 mGal) of approximately 25 km wavelength in the SE, which

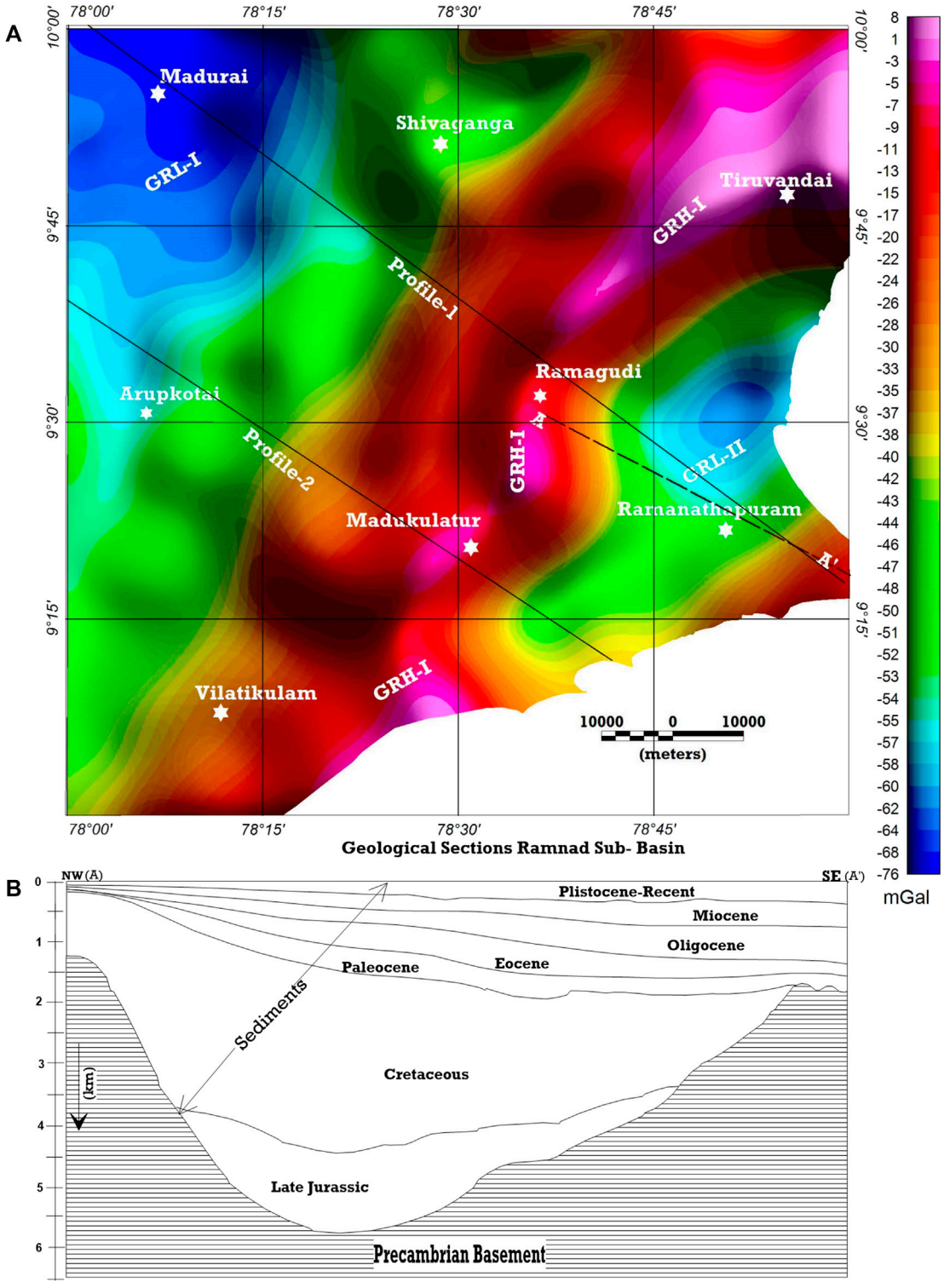

FIGURE 7
(A) Regional gravity anomaly map of the study area. See the NE-SW trending moderate-to-high gravity anomaly (GRH-I) zone and two gravity low zones (GRL-I and GRL-II). The gravity magnetic anomaly response over the outcrop geology was studied along the two profiles (Profile-I and Profile-II) indicated by black lines. **(B)** The available geological section (Chaudhuri et al., 2010) along A–A′ based on a bore well study is presented below.

indicates the presence of low-density granitoid within the basement. Additionally, a similar feature was also observed in Profile-2 (Figure 8B). The profile shows a Bouguer anomaly low over a regional gravity high extends in the southeast. The NW part of the profiles are dominated by high-frequency magnetic anomalies (Figure 8A, B), indicating the shallow presence of

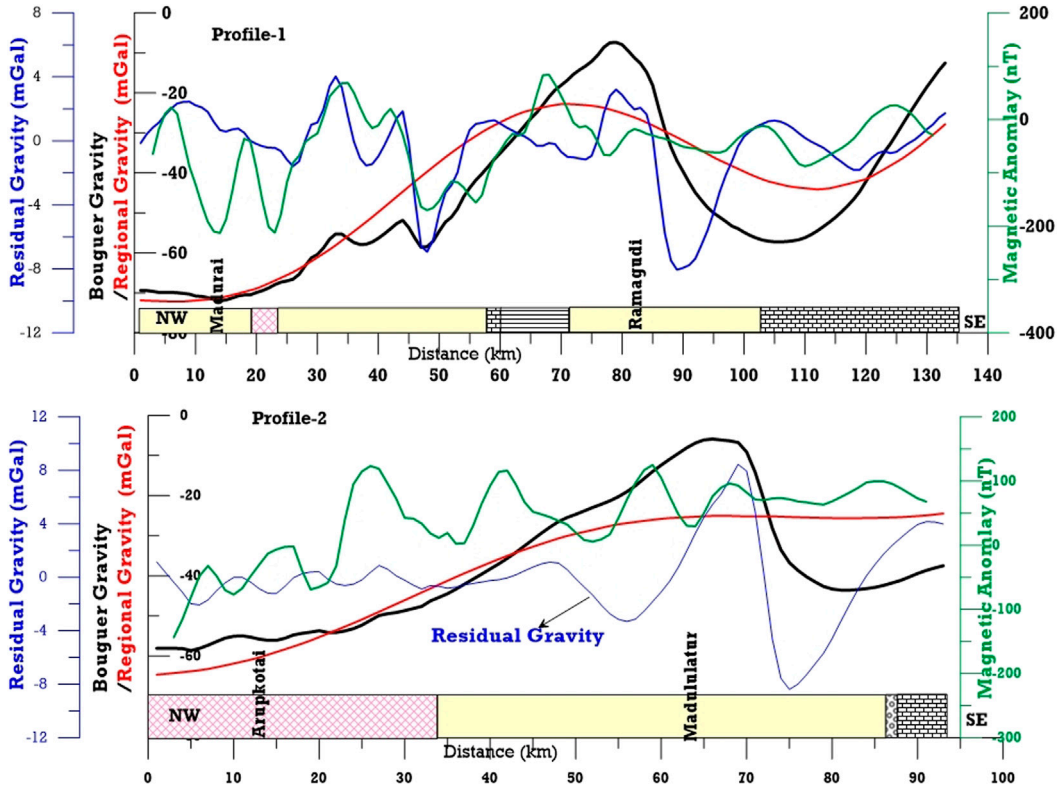

FIGURE 8
Gravity, regional gravity, residual gravity, and magnetic (RTP) response over the lithology along profiles one and 2 (Figure 7).

magnetic sources. In the south-eastern (SE) part, the low-frequency magnetic anomalies suggest the deeper occurrence of magnetic sources and the non-magnetic nature of the basement sediments underneath.

Bouguer gravity elevation relationship

The Bouguer gravity anomaly (BGA) bears a definite direct relationship with surface elevation, which depends on the subsurface density distributions and crust-mantle density difference (Verma and Mukhopadhyay, 1976). The BGA varies linearly with a negative regression coefficient (−112 mGa l/km) in a region with isostatic equilibrium; however, in some areas, non-linear relationships and a positive regression coefficient are also observed (Qureshy, 1971). In the present case, we have observed that gravity and elevation overall maintain an inverse relationship with a regression coefficient of −305.6 mGa l/km (Figure 9A). However, the data are segregated into two clusters. For surface elevations up to 25 m, the gravity data bears no distinct linear relationship with surface elevation; rather, the least-square fitted line shows a positive regression coefficient (932.2 mGa l/km). The gravity data for surface elevations of 25 m or more maintain an inverse relationship, with a negative regression coefficient of −483.6 mGa l/km. To analyze this observation, we undertook an isostatic study (Blakely RJ., 1996; Lowrie and Fichtner, 2020). The gravity field that originates due to the compensation of long wavelength topographic features is called an isostatic regional gravity field, which is manifested by Moho relief and also indicates the mechanical strength of the lithosphere. The gravity field that remains after subtracting the isostatic regional field from the Bouguer gravity field is known as an isostatic residual anomaly (Ussami et al., 1993; Kumar et al., 2011). The isostatic residual anomalies are caused by the intracrustal masses and sources that are not involved in isostatic compensation. Assuming the Airy–Heiskanen model for local isostasy, the crust-mantle interface was derived by using the formula.

$$w(x,y) = H(x,y) + \left[\frac{h(x,y)\cdot\rho_c}{\rho_m - \rho_c}\right]$$

where $w(x,y)$ is the crust-mantle interface and $H(x,y)$ is the reference depth, and for the present study, we have taken $H(x,y)$ as 34.0 km as per the CRUST.1 model (Laske et al., 2012). ρ_m is the mantle density, and the assigned value is 3.3 g/cm^3. ρ_c is the crustal density, and for the present study, we have considered the value as 2.67 g/cm^3. $h(x,y)$ is the elevation at the location (x,y). The regional gravity field was derived (Figure 10A) based on the Parker algorithm (Ussami et al., 1993; Kumar et al., 2011). Additionally, from the regional gravity field, we have calculated crustal thickness (Figure 10C). The parameter used to derive crustal thickness is given in Table 1. Crustal thickness varied from approximately 34 km–35 km, i.e., a relief of approximately 1 km, and the prominent gravity anomalies (Figure 10B) are caused by intracrustal mass distribution rather than Moho undulation.

Therefore, we may infer that the area bordered by a 25 m elevation contour is subject to emplacement of high-density masses, which are not part of the isostatic compensation.

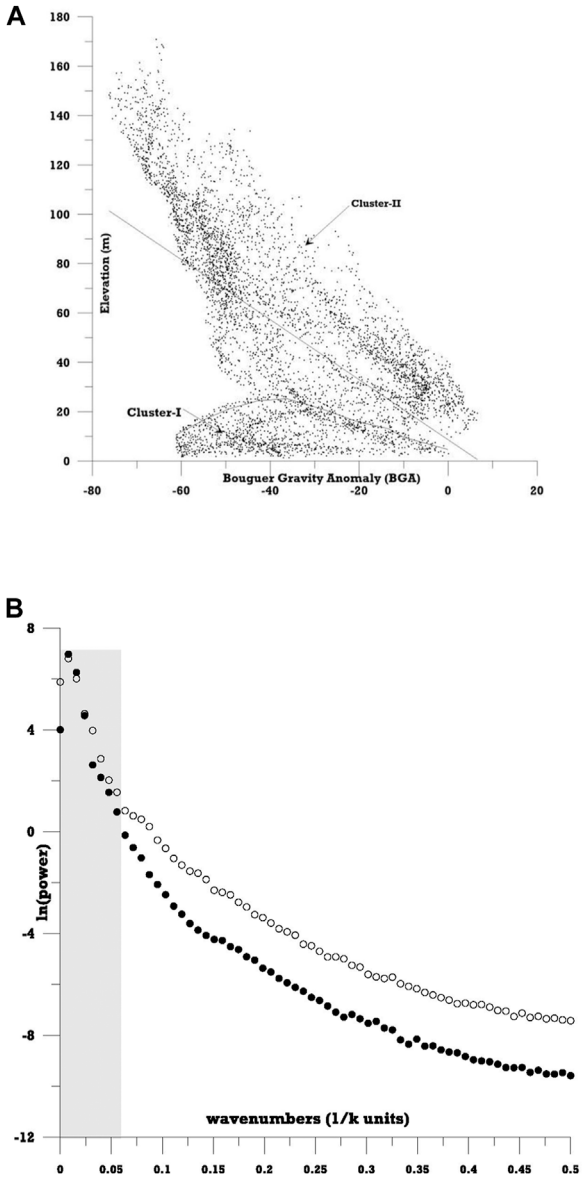

FIGURE 9
(A) Scatter diagram of station elevation against the Bouguer gravity anomaly (BGA) over the study area. The plot can be classified in two clusters (Cluster-I and Cluster-II). **(B)** Radially averaged power spectrum of the Bouguer gravity and topography over the study area. Note the increase in offset between the spectrums for wavenumbers more than 0.06 units.

Furthermore, we studied the spectral relationship between surface elevation and gravity data (Figure 9B). The gravity data has a good coherence with surface elevation up to a wavenumber of 0.06 units. The shallow crustal units represented by a wavelength less than approximately 16.5 km may not have been involved in isostatic compensation.

2.5D gravity modeling

The 2.5D gravity modeling (Vasanthi and Santosh, 2021; Kumar et al., 2009) was performed along the profiles in C–C' and D–D' (Figure 3, Figure 11) to arrive at a realistic geological model. The geological section derived from gravity modeling suffers from non-uniqueness (Singh et al., 2014). However, if the model is constrained from any other independent data sets, the ambiguity reduces, which leads to a realistic geological model (Motaghi et al., 2014; Kumar et al., 2009). For gravity modeling, two parameters, i.e., the density and geometry of geological bodies, need to be calibrated. The densities of the representative rock samples were collected from the available reports (Table 2) of the Geological Survey of India (GSI).

A northwest-southeast trending geological section (Figure 7) across the Ramnand basin shows that the basement depth varies from approximately 5.5 km–1.5 km (Chaudhuri et al., 2010). The basement of rock comprised Archean gneiss, granite, and other metamorphic rocks (Sastri et al., 1973); therefore, we have assumed a velocity of 6.2 km/s for the upper crust as it belongs to the Southern Granulite Terrane (SGT), and accordingly the basement density is considered as 2,720 kg m^{-3} (Sinha et al., 2015). The value was obtained from converting the reported seismic velocity (6.2 km/s) to density (Barton, 1986). The seismic velocity for the Cretaceous, Tertiary formations, and Quaternaries were not available. We have initially assumed a density of 2,450 kg m^{-3} (Lasitha et al., 2019) for the sedimentary formations, and this was increased or decreased systematically to match the observed and calculated gravity response.

The results from receiver function analysis enumerating the velocity structure of the crust are not available over the southern part of the ECMI or Cauvery Basin. The receiver function analysis over the Eastern Ghat Mobile Belt (EGMB) shows that crustal thickness varies from 38 to 36 km (Chaudhuri et al., 2016). An east-west trending seismic profile on the onshore region of the Cauvery basin shows a three-layer crustal segment (Sinha et al., 2016), with the upper and lower crust interface at 21 km. The upper crust dips towards the east with an average depth of 6 km underneath sediments. The mantle dips toward the west and the depth varies from 28 to 35 km from east to west. We have used the aforementioned information to set the initial crustal configurations. The velocity-depth relationship provided by Barton (1986) was used for the conversion of velocity to density. The seismic velocity in the upper mantle at the ECMI (Radhakrishna et al., 2012) for continental crust ranges from 8.1 to 8.2 km/s, and the density for the mantle is uniformly assigned as 3.3 g/cc. The reported lower crustal velocity over the southern part of the SGT is 7.1 km/s (Reddy et al., 2003); accordingly, the density value was assigned for the lower crust.

The central regional gravity high (Figure 6) bears a wavelength of approximately 70 km; at the same time from the spectral analysis, we have observed a density interface at 13.6 km, which argued for a deeper source, and accordingly, we have incorporated a high-density rock unit with an initial density value of 3,000 kg m^{-3}, as we believe that the high-density body is sourced from the mantle. At the same time, isostatic studies suggest that the high gravity is not caused by an upward raised Moho in any way. Additionally, two low-density rock units were incorporated to account for regional gravity lows with an initial density value of 2,650 kg m^{-3}.

We have calculated the gravity response of the model and compared it with the observed gravity profile; subsequently, the model was iteratively inverted until a satisfactory fit between the calculated response and the observed gravity was obtained (Figure 11A, B).

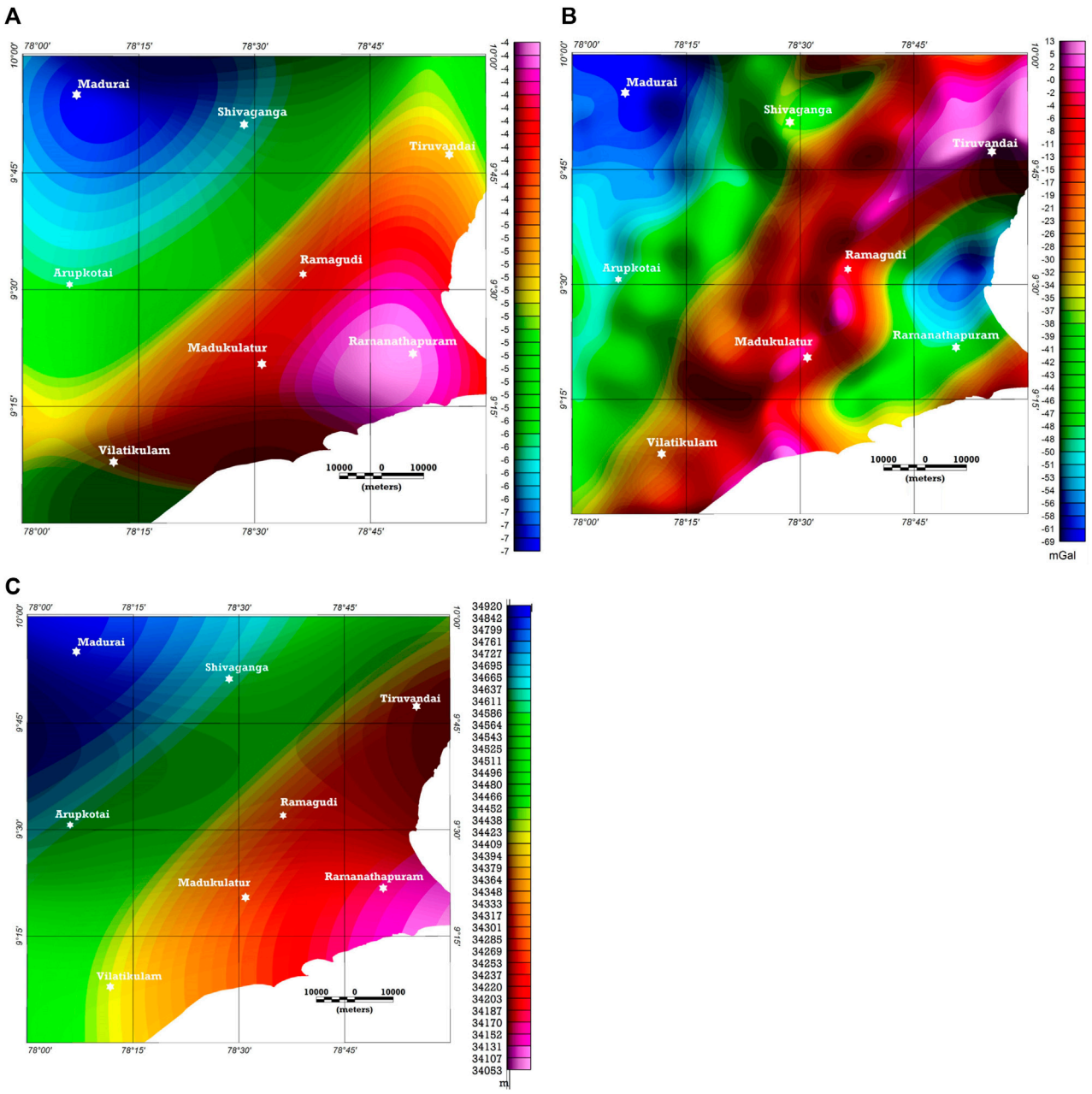

FIGURE 10
(A) Isostatic regional anomaly map. **(B)** Isostatic residual anomaly map. **(C)** Crustal thickness map.

TABLE 1 Model Parameters considered for the Moho relief calculation.

The density of contrast between the crust and mantle	0.33 g/cm^3	References
Poisson's ratio	0.25	Chand et al. (2001)
Young's modulus (G Pa)	100	
Effective elastic thickness (Te) in km	5.0	

Discussion

The ECMI has a rifted passive margin that has evolved as a consequence of the separation of eastern Gondwanaland from Antarctica in the Early Cretaceous (Biswas et al., 1993; Figure 12). The present study shows the presence of the NE-SW elongated high-density rock at a depth of approximately 12 km, which extends to a depth of 23–24 km. The emplacement of high-

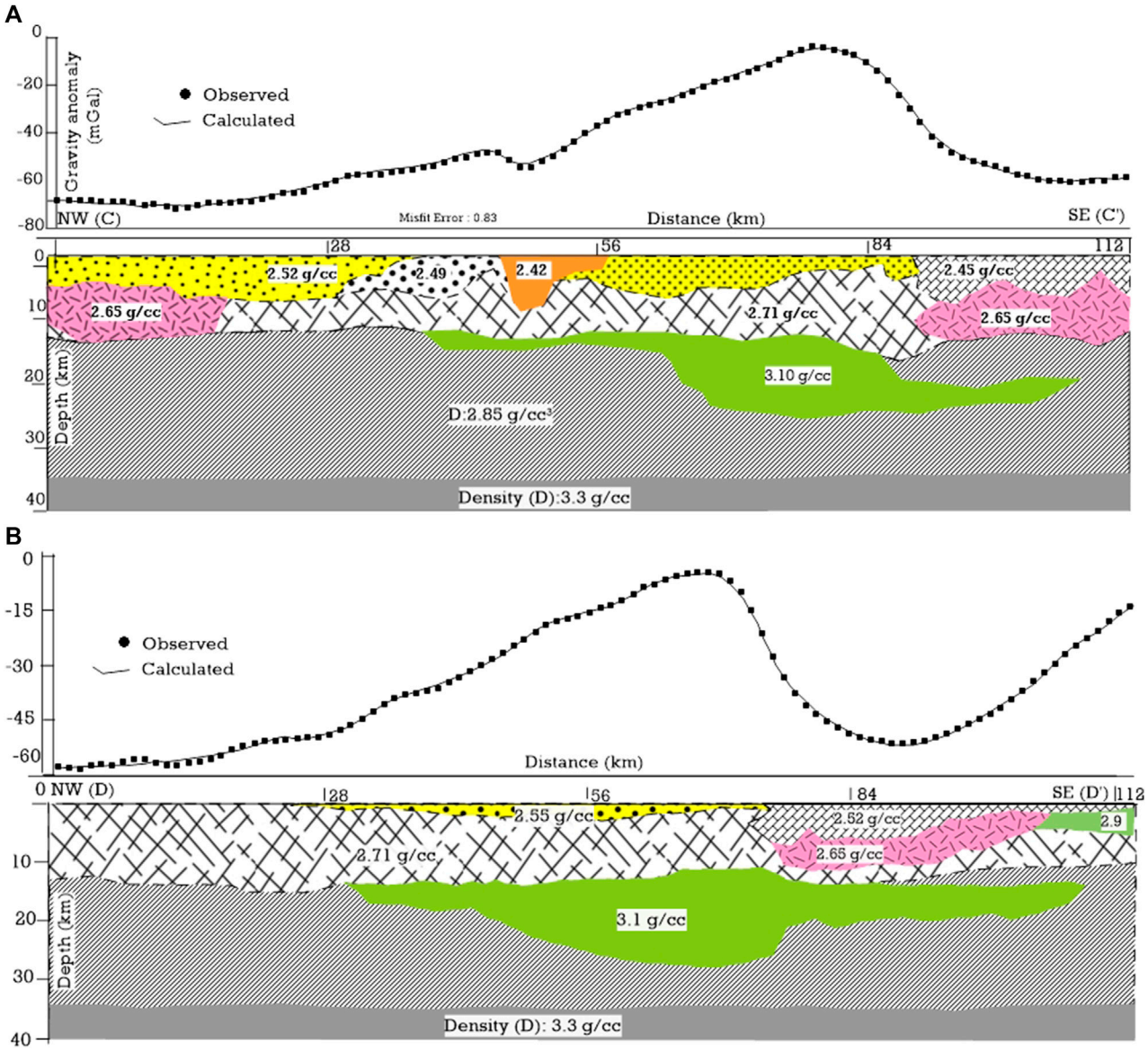

FIGURE 11
Gravity model along profiles C–C′ **(A)** and D–D′ **(B)**.

TABLE 2 Density values of the representative rock samples from the study area.

Rock type	No. of samples	Density range in g/cc	Mean g/cc
Granite	10	2.62–2.70	2.65
Biotite gneiss	25	2.67–2.74	2.72
Charnockitie	12	2.65–3.00	2.80
Quartzite	4	2.55–2.70	2.64

density rock may be due to mafic underplating via mantle diapirism in a pull-apart rift system. The presence of a large volcanic province underlying the Bengal Basin, related to the exposed Rajmahal Trap volcanism at 118–110 Ma, is reported (Baksi, 1995, Figure 12.e) in ECMI India and corresponds to the breakup of greater India and Antarctica. The magmatic activities have been related to the Kerguelen hot spot, which was located under the India-Antarctica Sector for a long time (Behara et al., 2004, Figure 12). The emplacement high-density body may be related to magmatic activity at 118–110 Ma. Additionally, a similar kind of high-density

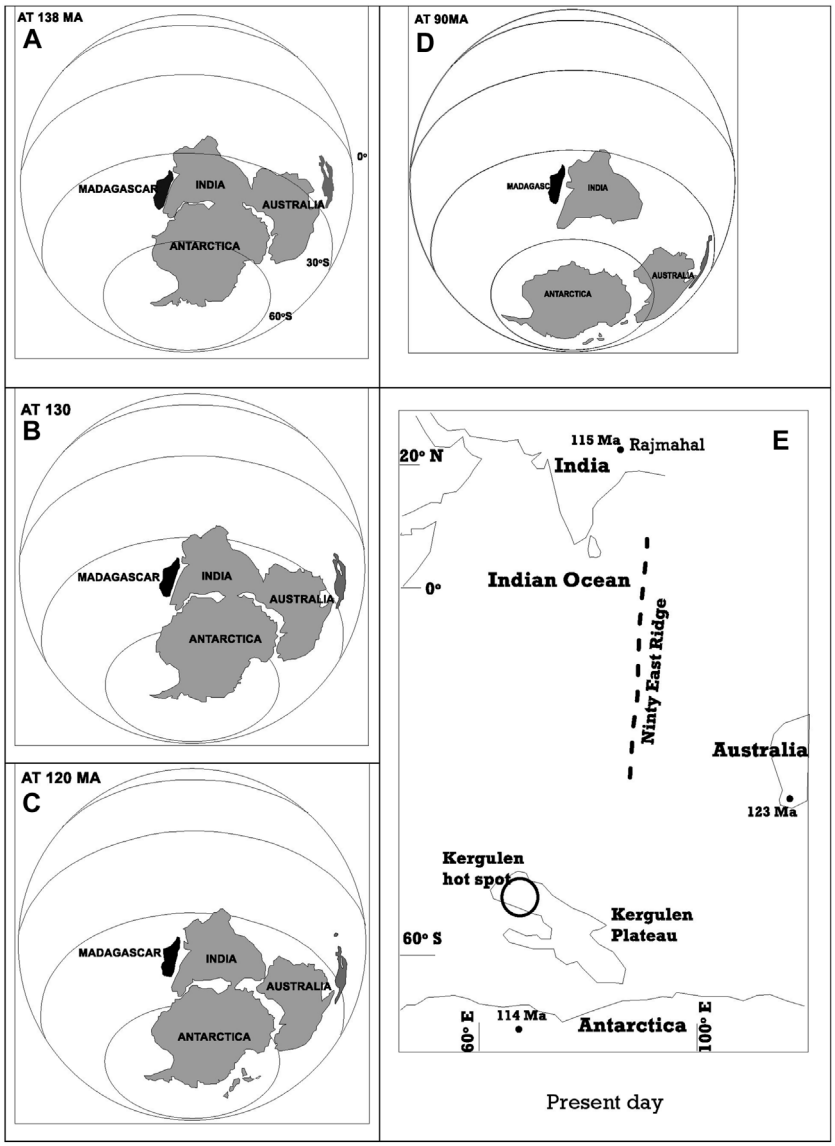

FIGURE 12
Present position of India, Antarctica, and Australia. Ages of dated basalts (in Ma). At ca. 120 Ma, the three continents were adjacent to the Kerguelen hot spot. From 115 to 40 Ma, India moved rapidly northward and the Ninety East Ridge marks the track of the hot spot on the Indian Plate. Inset: reconstruction of Greater India in Gondwana at 170 Ma based on the paleomagnetic studies (Figure modified from Frisch et al., 2011; van Hinsbergen et al., 2019).

high-velocity layer in the upper crust was reported in the Mahanadi Delta (Behara et al., 2004). The upwelling plume head of the Kerguelen hot spot had caused thermal perturbations and generated the extensional force. The high-density mafic material might have been transported to the shallow depth through weak zones/conduits and formed intrusively. The high-density rock may be alkaline in nature as the magnetic signature is not evident. The depth to the Curie-point isotherm is approximately 23 km in the Cauvery basin (Twinkle et al., 2016b).

A similar type of gravity anomaly has been observed over the Red Sea, which has evolved due to rift-related magmatic systems above a hotspot in the mantle (Almalki et al., 2015). A linear positive gravity anomaly extends along the crest of the Red Sea. The forward modeling of the gravity data shows the occurrence of a high-density body at the upper crust extending up to the lower crust (Izzeldin, 1987). The Aravalli-Delhi Mobile Belt (ADMB) in the northwestern part of India has evolved through rifting during the Proterozoic period. The gravity modeling shows the presence of a high-density domal-shaped body (3.04 g/cm^3) extending from a depth of approximately 20–30 km (Mishra et al., 2000), which has been suggested to represent underplated mantle material at the lower crust emplaced due to upwelling in an extensional regime during the Proterozoic. The Cambay Basin is a marginal rift basin in the Western Continental Margin of India (WCMI) that has been affected by the Reunion plume–lithosphere interactions (Danda et al., 2020). A high-density (3.15 g/cm^3) lower crustal rock unit,

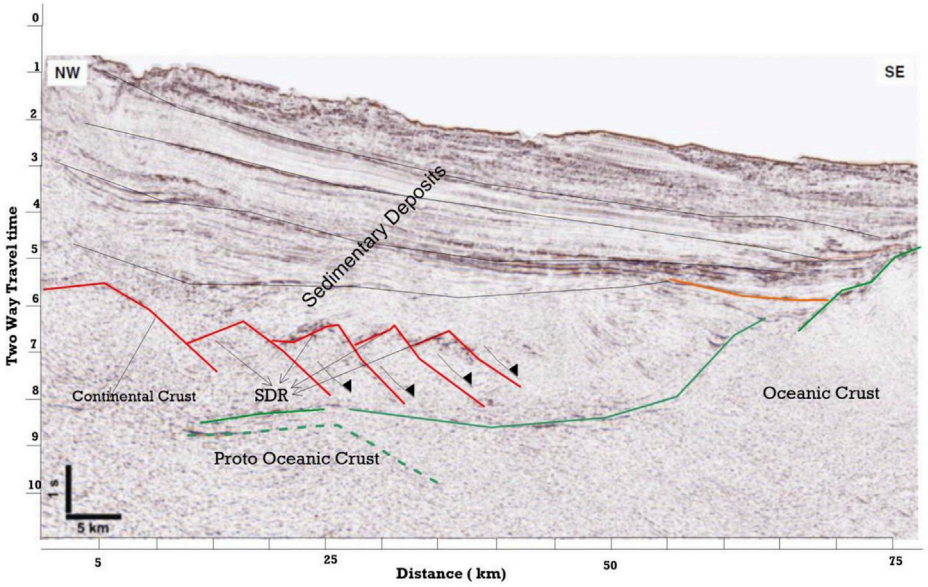

FIGURE 13
Seismic section along the seismic profile marked in Figure 1A.

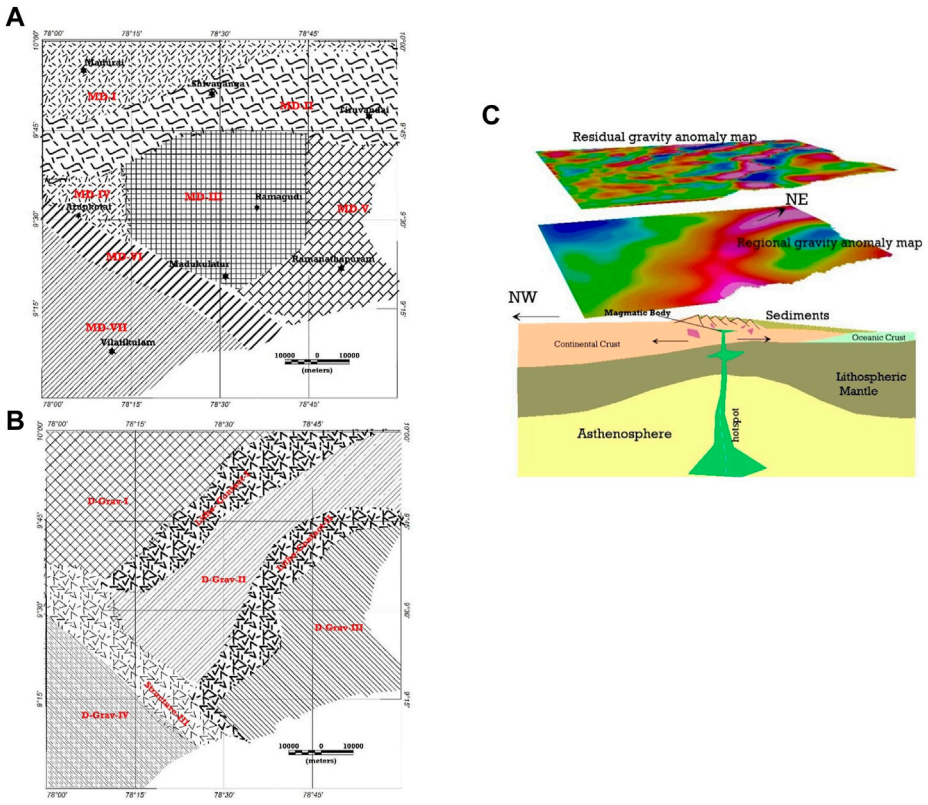

FIGURE 14
Interpreted shallow subsurface tectonic sketch of the southern part of the Cauvery Basin from magnetic **(A)** and gravity data **(B, C)** A cartoon illustration of the proposed evolution of the Cauvery Basin, indicating thick underplated material and the conjectural source marked by a plume head. The ridge-depression structure developed due to extensional forces.

resulting from mantle upwarp and crustal thinning within the basin, was attributed for the observed gravity high over the basin (Tewari et al., 1991). The high-density bodies in the lower crust are generally found the world over in all periods (Baldridge et al., 1995). The "magmatic underplating" as suggested by the present study below Cauvery Basin is in agreement with similar observations along passive volcanic margins all over the world, many of them interpreted as "plume-induced" (Coffin and Eldholm, 1994).

The gravity studies also suggest the presence of low-density granitoid in the upper crust, which indicates bimodal volcanism (Figures 7–11). After the intrusion into the continental crust, the volcanic mantle melts generate acidic crustal melts, which can explain the bimodal distribution of magmatism. The low-density acidic magmas occur in graben regions of greater crustal extension and higher continuous magmatic activity (Frisch et al., 2011).

The SDR (Sea Dipping Reflector) is a common feature of volcanic passive margins worldwide (Mutter, 1985; Geoffroy, 2005; McDermott, 2019). The details of the signatures for identifying the SDR have been well described by Mutter (1985). We have analyzed a published reflection profile (Figure 13; Misra and Dasgupta, 2018) over the onshore area near to the study area. To the best of our knowledge, a published seismic profile over the offshore area of the Cauvery Basin is not available. In the seismic profile, we have identified the SDR and other features, such as the top of the continental crust and the top of the oceanic crust. Models of the origin of the SDR are widely debated but are associated with voluminous volcanic loading and predates, accompanies, or post dates continental break up (Mutter, 1985; Geoffroy, 2005). The presence of the SDR in the onshore area and the presence of high-density rock over the offshore area at the mid crust, as derived from the present level, strongly suggest a volcanic rifted margin.

The Grabens or rifts are narrow fault-bounded elongated structures developed in the continental lithosphere, where crust and lithospheric mantle is thinned. The present study shows an NE-SW trending ridge-depression structure (Figures 6–14) that might have formed due to stretching of the crust as a result of the emplacement of high-density rocks (Figure 11; Figure 14C). The gravity modeling (Figure 11) shows that the maximum depth to the Palk Strait depression is 3.8 km, which is bounded by another ridge-like structure to the east. Depression two in the western part of the Devakkottai-Mannargudi Ridge (DMR; Figure 6) may be the southern extension of the Thanjavur Depression (Figure 1B). The residual anomaly reveals the presence of at least another two ridges and depression structures in the west of the DMR and one of the depressions is very sharp, extending up to 5.8 km in depth, and might be a coal deposit. The concealed basement structural highs can act as an effective reservoir for hydrocarbons (Mazumder et al., 2019). The gravity map suggests the ridge depression structure extends approximately 80 km west from the shore. The NE-SW trending ridge depression structure divides the basin into a number of fault-bound ridges and sub-basin areas. The NE-SW trending structure that has shaped the morphology of the Cauvery Basin was associated with the separation of the India-Sri Lanka system from Antarctica and Australia during the Late Jurassic and Early Cretaceous (Mazumder et al., 2019).

The magnetic anomalies in the northern part exhibit two prominent E-W trending linear structures that are sympathetic to the trend of the Palghat Cauvery Shear Zone (PCSZ, Figures 1–4). The prominent linear structures may indicate the disposition of a shear zone underneath the Cauvery Basin, as the magnetic signature of the Palghat Cauvery Shear Zone is also similar. Additionally, the magnetic features may represent a dyke and the high-density lower crustal body may be the feeder unit. The E-W trending linear magnetic features indicate intense volcanism that has affected the entire crustal column. The ridge-depression structure is not reflected in the magnetic map. This suggests that the geological units that caused the ridge-depression structures do not exhibit appreciable lateral contrast in magnetic properties. The magnetic fabric in domains I, III, and V (Figure 4B) do not exhibit any predominant trend, suggesting that the basement is formed of granulitic rock. However, in magnetic domain IV, the N-S trending fabric is clear. This may indicate that the basement was affected by the episode's N-S trending tectonism during the Late Carboniferous (Mazumder et al., 2019) and may also suggest the presence of N-S trending mafic supracrustal rock over the basement. A prominent NE-SW trending linear magnetic feature (F–F′, Figure 4A), which also corroborates the inferred structures from the residual gravity map (G–G′, Figure 6A), is a cross trending feature. The trend might have developed due to N-S strike-slip faulting and NE-SW rifting (Mazumder et al., 2019). The gravity and magnetic maps suggest NE-SW, N-S, and NW-SE are the major structural trends of the study area. Figure 4B; Figure 6B suggest that the Ramnathapuram Sub-Basin (domain IV, Figure 4B, and D-Grav-III, Figure 6B) can be easily identified in both maps. The NW-SE structural element (Figure 14A, B) is also well reflected in both maps, but the NE-SW trending gravity features are not well reflected in the magnetic map. The NE-SW trending features may indicate litho-contact, and magnetic properties may not vary laterally across the litho-contact.

A systematic magnetotelluric (MT) study and a seismological study integrated with the gravity-magnetic survey will bring out the comprehensive crustal architecture, fluid, thermal imprints, and magmatic processes at various depths.

Conclusion

This study reveals coast parallel ridge depression structures covered under Quaternary alluvium. The NE-SW trending structures are attributed to extensional tectonics or wrench faulting induced due to rifting of India and Antarctica during the Cretaceous. The depression structures have economic importance in terms of coal, and ridges can act as a reservoir of hydrocarbons. Based on the gravity magnetic anomalies, the study area is classified into several domains, which suggests the basement rock underneath the alluvium cover has different structural fabrics and each domain is bounded by faults/shear zones. The high-density plug that was emplaced at a mid-crustal level and the presence of SDRs in the onshore areas probably indicate a large-scale volcanic eruption that initiated the rift between India and Antarctica. The magnetic map reveals two prominent E-W trending linear structures that may indicate the disposition of a shear zone underneath sediments.

Data availability statement

The datasets presented in this article are not readily available because authors do not have the permission to share raw data. Requests to access the datasets should be directed to shuvaganguli@gmail.com.

Author contributions

SG: Data acquisition, processing, interpretation, Software, Methodology, Writing–original draft. SP: Supervision, Writing–review and editing. All authors contributed to the article and approved the submitted version.

Acknowledgments

The authors wish to declare their appreciation of all the geophysicists of the GSI, SR who painstakingly collected the baseline geophysical data under the National Geophysical Mapping Programme (NGPM). We also gratefully acknowledge the kind permission from the Director General of the GSI to publish this work. Additionally, the authors express sincere thanks to Henglei Zhang, Editor, Frontiers in Earth Science, for the comprehensive review and suggested modifications that improved the initial draft.

Conflict of interest

The authors declare that the research was conducted in the absence of any commercial or financial relationships that could be construed as a potential conflict of interest.

Publisher's note

References

Almalki, K. A., Betts, P. G., and Ailleres, L. (2015). The Red Sea–50 years of geological and geophysical research. *Earth-Sci. Rev.* 147, 109–140. doi:10.1016/j.earscirev.2015.05.002

Baksi, A. K. (1995). Petrogenesis and timing of volcanism in the Rajmahal flood basalt province, north-eastern India. *Chem. Geol.* 21, 73–90. doi:10.1016/0009-2541(94)00124-q

Baldridge, M. S., Keller, G. R., and Braila, L. W. (1995). "Continental rifting a final perspective, continental rifts: Evolution, structure the tectonics," in *Development in geotectonics*. Editor K. H. Olsen (Amsterdam, Netherlands: Elsevier), 453–459.

Barton, P. J. (1986). The relationship between seismic velocity and density in the continental crust—A useful constraint? *Geophys. J. Int.* 87 (1), 195–208. doi:10.1111/j.1365-246x.1986.tb04553.x

Bastia, R., Radhakrishna, M., Srinivas, T., Satyabrata, N., Nathaniel, D. M., and Biswal, T. K. (2010). Structural and tectonic interpretation of geophysical data along the Eastern Continental Margin of India with special reference to the deep water petroliferous basins. *J. Asian Earth Sci.* 39, 608–619. doi:10.1016/j.jseaes.2010.04.031

Behera, L., Sain, K., and Reddy, P. R. (2004). Evidence of underplating from seismic and gravity studies in the Mahanadi delta of eastern India and its tectonic significance. *J. Geophys. Res. Solid Earth* 109 (12), B12311. doi:10.1029/2003jb002764

Biswas, S. K., Bhasin, A. L., and Ram, Jokhan (1993). Classification of Indian sedimentary basins in the framework of plate tectonics. *Proc. second seminar petroliferous basins India* 1, 1–46.

Blakely, R. J. (1996b). *Potential theory in gravity and magnetic applications*. Cambridge, England: Cambridge University Press.

Blakely, R. J. (1996a). *Potential theory in gravity and magnetic applications*. Cambridge, England: Cambridge University Press.

Blundell, C. C., Armit, R., Ailleres, L., Micklethwaite, S., Martin, A., and Betts, P. (2019). Interpreting geology from geophysics in poly-deformed and mineralised terranes; the otago schist and the hyde-macraes shear zone. *N. Z. J. Geol. Geophys.* 62 (4), 550–572. doi:10.1080/00288306.2019.1579741

Chand, S., Radhakrishna, M., and Subrahmanyam, C. (2001). India–East Antarctica conjugate margins: Rift-shear tectonic setting inferred from gravity and bathymetry data. *EPSL* 185, 225–236. doi:10.1016/s0012-821x(00)00349-6

Chari, M. V. N., Sahu, J. N., Banerjee, B., Zutshi, P. L., and Chandra, K. (1995). Evolution of the Cauvery basin, India from subsidence modelling. *Mar. Petrol. Geol.* 12, 667–675. doi:10.1016/0264-8172(95)98091-i

Chaudhuri, A., Rao, M. V., Dobriyal, J. P., Saha, G. C., Chidambaram, L., Mehta, A. K., et al. "Prospectivity of Cauvery Basin in deep synrift sequences, SE India," in Proceedings of the AAPG Search and Discovery Article, Denver, Colorado, USA, June2010.

Chaudhuri, K., Borah, K., and Gupta, S. (2016). Seismic evidence of crustal low velocity beneath eastern Ghat mobile Belt, India. *Phys. Earth Planet. Inter* 261, 207–216. doi:10.1016/j.pepi.2016.10.004

Coffin, M. F., and Eldholm, O. (1994). Large igneous provinces: Crustal structure, dimensions, and external consequences. *Rev. Geophys.* 32 (1), 1–36. doi:10.1029/93rg02508

Curto, J. B., Vidotti, R. M., Fuck, R. A., Blakely, R. J., Alvarenga, C. J., and Dantas, E. L. (2014). The tectonic evolution of the Transbrasiliano Lineament in northern Paraná Basin, Brazil, as inferred from aeromagnetic data. *J. Geophys. Res. Solid Earth* 119 (3), 1544–1562. doi:10.1002/2013jb010593

Danda, N., Rao, C. K., Kumar, A., Rao, P. R., and Rao, P. S. (2020). Implications for the lithospheric structure of Cambay rift zone, Western India: Inferences from a magnetotelluric study. *Geosci. Front.* 11 (5), 1743–1754. doi:10.1016/j.gsf.2020.01.014

de Castro, D. L., Fuck, R. A., Phillips, J. D., Vidotti, R. M., Bezerra, F. H., and Dantas, E. L. (2014). Crustal structure beneath the Paleozoic Parnaíba Basin revealed by airborne gravity and magnetic data, Brazil. *Braz. Tectonophys.* 614, 128–145. doi:10.1016/j.tecto.2013.12.009

Eldosouky, A. M., and Mohamed, H. (2021). Edge detection of aeromagnetic data as effective tools for structural imaging at Shilman area, South Eastern Desert, Egypt. *Arabian J. Geosciences* 14, 13–10. doi:10.1007/s12517-020-06251-4

Essa, K. S., Abo-Ezz, E. R., and Géraud, Y. (2021). Utilizing the analytical signal method in prospecting gravity anomaly profiles. *Environ. Earth Sci.* 80, 1–21.

Essa, K. S., Munschy, M., Youssef, M. A., and Khalaf, E. E. D. A. H. (2022). Aeromagnetic and radiometric data interpretation to delineate the structural elements and probable precambrian mineralization zones: A case study, Egypt. *Min. Metallurgy Explor.* 39 (6), 2461–2475. doi:10.1007/s42461-022-00675-0

Essa, K. S., Nady, A. G., Mostafa, M. S., and Elhussein, M. (2018). Implementation of potential field data to depict the structural lineaments of the Sinai Peninsula, Egypt. *J. Afr. Earth Sci.* 147, 43–53. doi:10.1016/j.jafrearsci.2018.06.013

Frisch, W., Meschede, M., and Blakey, R. (2011). "Continental graben structures," in *Plate tectonics* (Berlin, Germany: Springer), 27–41.

Ganguli, S. S., Pal, S. K., Rao, J. V. R., and Raj, B. S. (2020). Gravity–magnetic appraisal at the interface of Cuddapah Basin and Nellore Schist Belt (NSB) for shallow crustal architecture and tectonic settings. *J. Earth Syst. Sci.* 129 (1), 1–17. doi:10.1007/s12040-020-1354-8

Ganguli, S. S., Pal, S. K., Singh, S. L., Rama Rao, J. V., and Balakrishna, B. (2021). Insights into crustal architecture and tectonics across Palghat Cauvery Shear Zone, India from combined analysis of gravity and magnetic data. *Geol. J.* 56 (4), 2041–2059. doi:10.1002/gj.4041

Ganguli, S. S., Mondal, S., Pal, S. K., Lakshamana, M., and Mahender, S. (2022). Combined analysis of remote sensing, gravity and magnetic data across moyar

bhavani shear zone, southern granulite Terrane (SGT), India: Appraisals for crustal architecture and tectonics. *Geocarto Int.* 37, 13973–14004. doi:10.1080/10106049.2022.2086627

Geoffroy, L. (2005). Volcanic passive margins. *Comptes Rendus Geosci.* 337 (16), 1395–1408. doi:10.1016/j.crte.2005.10.006

Hamimi, Z., Eldosouky, A. M., Hagag, W., and Kamh, S. Z. (2023). Large-scale geological structures of the Egyptian nubian shield. *Sci. Rep.* 13 (1), 1923. doi:10.1038/s41598-023-29008-x

Izzeldin, A. Y. (1987). Seismic, gravity and magnetic surveys in the central part of the Red Sea: Their interpretation and implications for the structure and evolution of the Red Sea. *Tectonophysics* 143, 269–306. doi:10.1016/0040-1951(87)90214-9

Krishna, K. S., Laju, M., Bhattacharyya, R., and Majumdar, T. J. (2009). Geoid and gravity anomaly data of conjugate regions of Bay of Bengal and Ender by Basin, new constraints on breakup and early spreading history between India and Antarctica. *J. Geophys. Res.* 114 (B03102), 21. doi:10.1029/2008JB005808

Kumar, N., Singh, A. P., Rao, M. P., Chandrasekhar, D. V., and Singh, B. (2009). Gravity signatures, derived crustal structure and tectonics of Achankovil Shear Zone, southern India. *Gondwana Res.* 16 (1), 45–55. doi:10.1016/j.gr.2008.11.003

Kumar, N., Singh, A. P., and Singh, B. (2011). Insights into the crustal structure and geodynamic evolution of the southern granulite terrain, India, from isostatic considerations. *Pure Appl. Geophys.* 168, 1781–1798. doi:10.1007/s00024-010-0210-1

Laske, G., Masters, G., Ma, Z., and Pasyanos, M. E. (2012). CRUST1. 0: An updated global model of Earth's crust. *Geophys Res. Abs* 14 (3), 743.

Lowrie, W., and Fichtner, A. (2020). *Fundamentals of geophysics*. Cambridge, England: Cambridge University Press.

Mazumder, S., Tep, B., Pangtey, K. K. S., and Mitra, D. S. (2019). Basement tectonics and shear zones in Cauvery Basin (India): Implications in hydrocarbon exploration. *Tect. Struct. Geol. Indian context*, 279–311. doi:10.1007/978-3-319-99341-6_9

McDermott, C., Collier, J. S., Lonergan, L., Fruehn, J., and Bellingham, P. (2019). Seismic velocity structure of seaward-dipping reflectors on the South American continental margin. *Earth Planet. Sci. Lett.* 521, 14–24. doi:10.1016/j.epsl.2019.05.049

Mishra, D. C., Singh, B., Tiwari, V. M., Gupta, S. B., and Rao, M. B. S. V. (2000). Two cases of continental collisions and related tectonics during the proterozoic period in India—Insights from gravity modelling constrained by seismic and magnetotelluric studies. *Precambrian Res.* 99 (3-4), 149–169. doi:10.1016/s0301-9268(99)00037-6

Misra, A. A., and Dasgupta, S. (2018). "Transform margin in the Cauvery Basin, Indian east coast passive margin," in *Atlas of structural geological interpretation from seismic images* (Hoboken, New Jersey, United States: Wiley), 235–239.

Motaghi, K., Tatar, M., Priestley, K., Romanelli, F., Doglioni, C., and Panza, G. F. (2015). The deep structure of the Iranian Plateau. *Gondwana Res.* 28 (1), 407–418. doi:10.1016/j.gr.2014.04.009

Mutter, J. C. (1985). Seaward dipping reflectors and the continent-ocean boundary at passive continental margins. *Tectonophysics* 114 (1-4), 117–131. doi:10.1016/0040-1951(85)90009-5

Powell, C. M., Roots, S. R., and Veevers, J. J. (1988). Pre-breakup continental extension in East Gondwanaland and the early opening of the eastern Indian Ocean. *Tectonophysics* 155 (1-4), 261–283. doi:10.1016/0040-1951(88)90269-7

Qureshy, M. N. (1971). Relation of gravity to elevation and rejuvenation of blocks in India. *J. Geophys. Res.* 76 (2), 545–557. doi:10.1029/jb076i002p00545

Radhakrishna, M., Twinkle, D., Nayak, S., Bastia, R., and Rao, G. S. (2012). Crustal structure and rift architecture across the Krishna–Godavari basin in the central Eastern Continental Margin of India based on analysis of gravity and seismic data. *Mar. Petroleum Geol.* 37 (1), 129–146. doi:10.1016/j.marpetgeo.2012.05.005

Reddy, P. R., Rajendra Prasad, B., Vijay Rao, V., Sain, K., Prasad Rao, P., Prakash, K., et al. (2003). "Deep seismic reflection and refraction/wide angle reflection studies along Kuppam–Palani transect in the southern Granulite terrain of India," in *Tectonics of southern granulite terrain: Kuppam–palani geotransect*. Editor M. Ramakrishnan (Kolkata, India: Geological Society of India Memoir), 79–106.

Saikia, U., Das, R., and Rai, S. S. (2017). Possible magmatic underplating beneath the west coast of India and adjoining Dharwar craton: Imprint from Archean crustal evolution to breakup of India and Madagascar. *Earth Planet. Sci. Lett.* 462, 1–14. doi:10.1016/j.epsl.2017.01.004

Sastri, V. V., Sinha, R. N., Singh, G., and Murti, K. V. S. (1973). Stratigraphy and tectonics of sedimentary basins on East Coast of peninsular India. *AAPG Bull.* 57 (4), 655–678.

Sastri, V. V., Venkatachala, B. S., and Narayanan, V. (1981). The evolution of the East Coast of India. *Palaeogeogr. Palaeoclimatol. Palaeoecol.* 36 (1-2), 23–54. doi:10.1016/0031-0182(81)90047-x

Singh, A., and Rao, G. S. (2021). Crustal structure and subsidence history of the Mannar basin through potential field modelling and backstripping analysis: Implications on basin evolution and hydrocarbon exploration. *J. Petroleum Sci. Eng.* 206, 109000. doi:10.1016/j.petrol.2021.109000

Singh, B., Rao, M. P., Prajapati, S. K., and Swarnapriya, C. (2014). Combined gravity and magnetic modeling over Pavagadh and Phenaimata igneous complexes, Gujarat, India: Inference on emplacement history of Deccan volcanism. *J. Asian Earth Sci.* 80, 119–133. doi:10.1016/j.jseaes.2013.11.005

Sinha, S. T., Nemčok, M., Choudhuri, M., Sinha, N., and Rao, D. P. (2016). The role of break-up localization in microcontinent separation along a strike-slip margin: the East India–elan bank case study. *Geol. Soc. Lond. Spec. Publ.* 431 (1), 95–123. doi:10.1144/sp431.5

Subrahmanyam, C., Thakur, N. K., Gangadhara Rao, T., Ramana, M. V., and Subrahmanyam, V. (1999). Tectonics of the bay of bengal: New insights from satellite-gravity and ship-borne geophysical data. *Earth Planet. Sci. Lett.* 171, 237–251. doi:10.1016/s0012-821x(99)00148-x

Telford, W. M., Telford, W. M., Geldart, L. P., and Sheriff, R. E. (1990). *Applied geophysics*. Cambridge, England: Cambridge University Press.

Teknik, V., Artemieva, I. M., and Thybo, H. (2023). Geodynamics of the central tethyan Belt revisited: Inferences from crustal magnetization in the anatolia-caucasus-black Sea region. *Tectonics* 42 (2), e2022TC007282. doi:10.1029/2022tc007282

Tewari, H. C., Dixit, M. M., Sarkar, D., and Kaila, K. L. (1991). A crustal density model across the Cambay basin, India, and its relationship with the Aravallis. *Tectonophysics* 194, 123–130. doi:10.1016/0040-1951(91)90276-x

Twinkle, D., Rao, G. S., Radhakrishna, M., and Murthy, K. S. R. (2016b). Crustal structure and rift tectonics across the Cauvery-Palar basin, Eastern Continental Margin of India based on seismic and potential field modelling. *J. Earth Syst. Sci.* 125 (2), 329–342. doi:10.1007/s12040-016-0669-y

Twinkle, D., Rao, G. S., Radhakrishna, M., and Murthy, K. S. R. (2016a). Crustal structure and rift tectonics across the Cauvery–Palar basin, Eastern Continental Margin of India based on seismic and potential field modelling. *J. Earth Syst. Sci.* 125 (2), 329–342. doi:10.1007/s12040-016-0669-y

Ussami, N., de Sá, N. C., and Molina, E. C. (1993). Gravity map of Brazil: 2. Regional and residual isostatic anomalies and their correlation with major tectonic provinces. *J. Geophys. Res. Solid Earth* 98 (B2), 2199–2208. doi:10.1029/92jb01398

van Hinsbergen, D. J., Lippert, P. C., Li, S., Huang, W., Advokaat, E. L., and Spakman, W. (2019). Reconstructing Greater India: Paleogeographic, kinematic, and geodynamic perspectives. *Tectonophysics* 760, 69–94. doi:10.1016/j.tecto.2018.04.006

Verma, R. K., and Mukhopadhyay, M. (1976). Tectonic significance of anomaly-elevation relationships in north-eastern India. *Tectonophysics* 34 (1-2), 117–133. doi:10.1016/0040-1951(76)90180-3

Yatheesh, V. (2020). Structure and tectonics of the continental margins of India and the adjacent deep ocean basins: Current status of knowledge and some unresolved problems. *Episodes* 43 (1), 586–608. doi:10.18814/epiiugs/2020/020039

frontiers | Frontiers in Earth Science

TYPE Original Research
PUBLISHED 26 July 2023
DOI 10.3389/feart.2023.1181533

OPEN ACCESS

EDITED BY
Victor Sacek,
University of São Paulo, Brazil

REVIEWED BY
Catherine A. Meriaux,
University of Rwanda, Rwanda
Tim Greenfield,
University of Cambridge, United Kingdom
Mohammad Youssof,
University of Copenhagen, Denmark

*CORRESPONDENCE
Wubamlak Nigussie,
wubmulnig12@gmail.com

RECEIVED 07 March 2023
ACCEPTED 13 July 2023
PUBLISHED 26 July 2023

CITATION
Nigussie W, Alemu A, Mickus K, Keir D, Demissie Z, Muhabaw Y, Muluneh AA, Corti G and Yehualaw E (2023), Subsurface structural control of geothermal resources in a magmatic rift: gravity and magnetic study of the Tulu Moye geothermal prospect, Main Ethiopian Rift.
Front. Earth Sci. 11:1181533.
doi: 10.3389/feart.2023.1181533

Subsurface structural control of geothermal resources in a magmatic rift: gravity and magnetic study of the Tulu Moye geothermal prospect, Main Ethiopian Rift

Wubamlak Nigussie[1]*, Abera Alemu[2], Kevin Mickus[3], Derek Keir[4,5], Zelalem Demissie[6], Yoseph Muhabaw[1,7], Ameha A. Muluneh[2,8], Giacomo Corti[9] and Esubalew Yehualaw[10]

[1]School of Earth Sciences, Bahir Dar University, Bahir Dar, Ethiopia, [2]School of Earth Sciences, Addis Ababa University, Addis Ababa, Ethiopia, [3]Department of Geosciences, Missouri State University, Springfield, MA, United States, [4]School of Ocean and Earth Science, University of Southampton, Southampton, United Kingdom, [5]Dipartimento di Scienze Della Terra, Università Degli Studi di Firenze, Florence, Italy, [6]Department of Geology, Wichita State University, Wichita, KS, United States, [7]Department of Earth and Environmental Sciences, University of Rochester, Rochester, NY, United States, [8]Helmholtz Centre Potsdam, GFZ German Research Centre for Geosciences, Potsdam, Germany, [9]Consiglio Nazionale Delle Ricerche, Istituto di Geoscienze e Georisorse, Firenze, Italy, [10]Department of Geothermal Energy, Ministry of Mine and Energy, Addis Ababa, Ethiopia

Since the Quaternary, extension and magmatism in the Main Ethiopian Rift (MER) have been mainly focused into narrow magmatic segments that have numerous volcanic centers and caldera collapses that offer favorable conditions for the occurrence of geothermal resources. However, the subsurface structure of the volcanic systems (0–10 km) and their link to the distribution of shallow geothermal resources remain unclear. To investigate the role of subsurface structures on the occurrence of these resources, we conducted gravity and magnetic studies combined with geological constraints within the Tulu Moye Geothermal Prospect (TMGP), one of the current geothermal prospects in the central MER associated with caldera collapses. Gravity data from the Global Gravity Model plus (GGMplus 2013) and ground magnetic data transformed into residual and derivative maps reveal that shallow magmatic intrusions occur under the volcanic centers (Tulu Moye, Bora, and Bericha). Our interpretation along with recent magnetotelluric model suggests that only the intrusion beneath Tulu Moye is currently magmatically active and includes partial melt, consistent with it being a primary heat source for the geothermal system. A new caldera formation model is proposed where the TMGP hosts an older large caldera (about 25 km diameter) within which there are several smaller nested caldera systems associated with the Bora, Bericha, and Tulu Moye volcanoes. Along with existing geologic, seismic, and magnetotelluric studies, our gravity and magnetic analysis indicate the interaction between NNE-SSW (rift-parallel) and NW-SE (cross-rift) trending faults, along with shallow magmatic intrusions and caldera systems, suggesting that such a large geothermal system is possible under these conditions.

KEYWORDS

East African Rift, gravity/magnetic anomalies, geothermal resources, subsurface structure, Tulu Moye geothermal prospect

1 Introduction

Geothermal energy is a carbon-neutral source of energy and continental rifts are among the best candidates for hosting these resources (King and Metcalf, 2013; Samrock et al., 2015). The occurrences of geothermal resources within volcanically and tectonically active rift zones are commonly controlled by subsurface geological structures (Omenda, 1998; Teklemariam, 2011; Hutchison et al., 2015). However, the nature of these features is often not clearly understood using surface geology alone, and commonly requires modeling and interpretation from geophysical data (Hutchison et al., 2015; Reinsch et al., 2017; Wilks et al., 2017; Mulugeta et al., 2021).

The East Africa Rift System (EARS) is the largest continental rift on Earth and is a region of major geothermal potential (Varet et al., 2020), with the rift segments of Ethiopia being especially rich (Teklemariam, 2011; Samrock et al., 2015; Varet et al., 2020; Burnside et al., 2021). Varet et al. (2020) showed that the largest geothermal sites in the EARS are Olkaria in Kenya, Tulu Moye (TM) Geothermal Prospect (TMGP) in the Main Ethiopian Rift (MER), and Era Boru in Afar, with all of these geothermal sites being located within the most volcanically and tectonically active regions. Ethiopia has an estimated geothermal energy potential of over 1,000 MW which is more than double of its current power generating capacity from all other sources including hydropower (Burnside et al., 2021).

More than 31 volcanoes hosting hydrothermal systems with the potential to generate geothermal power have been reported along the MER (Greenfield et al., 2019). Geological and geophysical studies in the MER suggest that the greatest melt supply (Kendall et al., 2006; Abebe et al., 2007; Bastow et al., 2010) and geothermal potential (Varet et al., 2020) lies in the central and northern MER between the Aluto and Dofan volcanoes. This sector of the rift includes the TMGP, the largest geothermal site within the MER (Varet et al., 2020). The TMGP consists of several Quaternary-Recent caldera-forming volcanic centers (Gedemsa, Geregendi, Tulu Moye, Boku, and Bora) (Figure 1) with various surface manifestations (fumaroles, steaming, and thermally-altered ground) (Varet and Birba, 2018). Ground deformation detected by an InSAR analysis at Tulu Moye (Biggs et al., 2011; Albino and Biggs, 2021; Kebede et al., 2023)

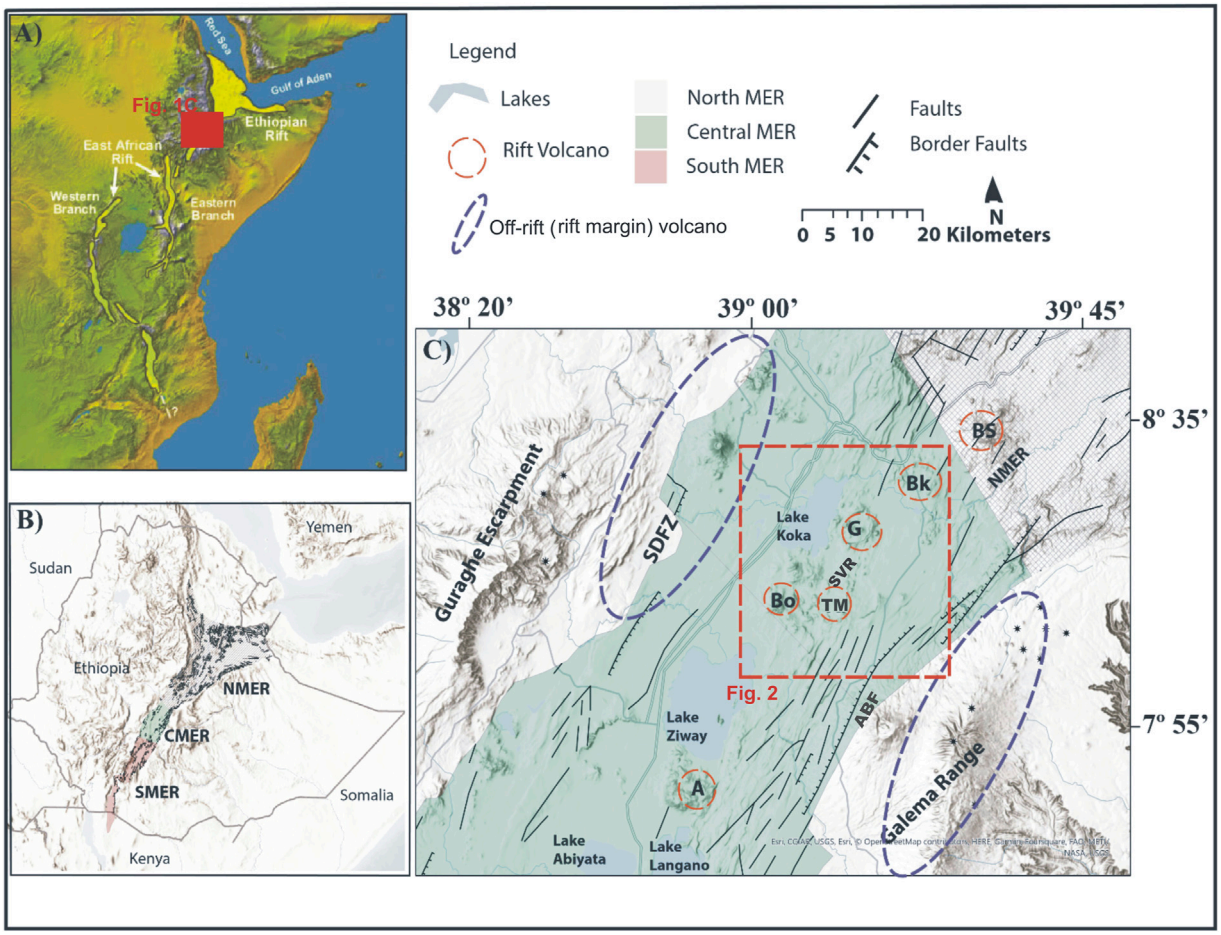

FIGURE 1
(A) Location of the study area (red square) in the frame of the East African Rift (EARS), marked in light yellow. **(B)** Map of the Main Ethiopian Rift (MER) showing its three different segments: southern MER-SMER, central MER-CMER and northern MER-NMER represented by red, blue and grey colors, respectively. **(C)** Structural map of the northern CMER-southern NMER which indicated the study area (red broken rectangle). A, Aluto volcano; Bo, Bora volcano; Bk, Boku Volcano; TM, Tulu Moye volcano; G, Gedemsa caldera; Bs, Boseti volcano; SVR, Salen Volcanic Ridge; CMER, central Main Ethiopian rift; NMER, northern Main Ethiopian rift; ABF, Asela border fault.

indicated that magmatic processes (e.g., continuous pressurization of large magmatic reservoirs) are ongoing.

From a geothermal resource exploration point of view, geophysical methods can provide constraints on subsurface magma plumbing and fault systems, with both being important for the understanding of a geothermal system (Hersir and Björnsson, 1991). Previous geophysical studies in the TMGP have used magnetotellurics (MT) and micro-seismicity (e.g., Samrock et al., 2018; Greenfield et al., 2019) which provide good constraints on locating fluid phases (partial melt and hydrothermal fluids) within the crust. However, these studies do not provide a full picture of the subsurface distribution of caldera and rift-related fault and fracture systems, and their relationship to loci of magmatism, fluid flow and related geothermal resources. Therefore, this study is intended to outline the overall upper crustal scale subsurface structure, with an emphasis on better understanding the interaction between caldera and rift fault systems in controlling the occurrence of geothermal resources, beneath the TMGP.

In this study, magnetic and gravity data are used via map analysis and forward modeling to constrain the subsurface structural control on the occurrence of geothermal resources within the TMGP. The map analysis includes the construction of residual anomaly maps to understand the gravity and magnetic source within the upper crust and derivative methods (horizontal derivatives and analytic signals) to determine linear features that might be related to subsurface structures (e.g., faults, lineaments and fractures). The forward models were constrained by the existing MT and seismic studies to determine the location of potential geothermal resources. Although we used the TMGP as an example, our study helps to fully understand the occurrence of geothermal resources in the MER as a whole.

2 Geology, tectonic and geothermal setting of the Tulu Moye-Gedemsa magmatic segment

Since the Quaternary period, extension in the MER has been localized into ~20 km wide, ~70 km long belts called magmatic segments that contain recent faults (Wonji Fault Belt, WFB) and aligned Quaternary-Recent volcanic centers and lava flows (Boccaletti et al., 1992; Ebinger and Casey, 2001; Acocella and Korme, 2002; Kurtz et al., 2007; Corti, 2009; Corti et al., 2020; Muhabaw et al., 2022; Nigussie et al., 2023). These magmatic segments strike in NNE direction and are arranged in a right stepping en echelon fashion and are seismically active (Keranen et al., 2004; Casey et al., 2006; Keir et al., 2006). Extension in these magmatic segments is thought to be largely dominated by episodic magmatic intrusions (Ebinger and Casey, 2001; Casey et al., 2006; Kurtz et al., 2007; Nigussie et al., 2023).

The TMGP lies within the TM-Gedemsa magmatic segment which includes the Gedemsa caldera at the northern end and the TM volcanic complex in the south (Figures 1C, 2). The TM volcanic complex includes the TM caldera, Bora, and Boku volcanic centers; in the TMGP, which are cut by WFB faults (Figures 1C, 2). In addition, NW-SE trending cross-rift structures control the magma transfer and emplacement and distribution of the volcanic activity in the area (Benvenuti et al., 2023).

The geology of the TMGP consists mainly of volcanic rocks, related to the MER volcanic activity, and thin sequences of Quaternary-Recent alluvial and lacustrine sediments (Abebe et al., 2005; Abebe et al., 2010; Figure 2). The volcanic rocks are characterized by bimodal volcanism of mafic and felsic types (Woldegabriel et al., 1990; Boccaletti et al., 1999; Mazzarini et al., 1999) related to three major volcanic episodes. The oldest episode (11–8 Ma) is related to the eruption of basaltic to trachytic lavas, and pyroclastic flows (Peccerillo et al., 2003; Abebe et al., 2005; Corti, 2009). These units occur southeast of the TM volcano, along the rift margins, and can be up to 700 m thick along the eastern margin (Abebe et al., 2010). The second episode (5–3 Ma) is associated with several rhyolitic domes and erupted rhyolitic and trachytic lava, and several layers of pyroclastic flows (Peccerillo et al., 2003; Corti, 2009; Figure 2). The last episode (<3 Ma) is characterized by the formation of central and caldera-forming volcanoes (Gedemsa, Bora, TM, Bericha, Boku, and Boseti; Figures 1, 2), scoria cones and fissure eruptions (Peccerillo et al., 2003; Abebe et al., 2010). A thermometry and barometry modeling study at TMGP suggests that the basaltic magmas are stored at high temperatures (1,070°C–1,190°C) at mid-to-deep-crustal levels (~7–29 km), whereas the peralkaline rhyolite melts are stored at a lower temperature (700°C–900°C) at shallow crustal levels (~4 km) (Tadesse et al., 2023).

The TM volcanic complex is one of the most important volcanic systems in the region and consists of an undated caldera that is thought to have been active between 320–265 ka forming an elliptically-shaped caldera system (Acocella et al., 2002). After the major explosive caldera/crater-forming activity occurred, volcanism continues to the present day mainly on the eastern side of the volcanic complex. The volcanic features include scoria cones and basaltic flows of various-sized, and rhyolitic (obsidian) domes mainly along the WFB, with the youngest eruptions being historical (~1,900) (Wadge et al., 2016).

The TMGP and its geothermal features are mostly related to the faults within the WFB (Admasu and Worku, 2015; Guðbrandsson et al., 2020), where the faults cut the central to eastern portions of the volcanic complex and where hydrothermal alteration and surface manifestations (hot ground, steam vents, and fumaroles) are common (Varet and Birba, 2018) (Figure 2). A Curie point depth, geothermal gradient and heat flow analysis by Kassa et al. (2022) in the central MER revealed that the TMGP is characterized by a shallow Curie point depth (7.68–13.1 km), high heat flow (141 mW/m^2) and high geothermal gradient (65°C/km) values, with all these values are greater than the Aluto geothermal prospect, south of TMGP. These values along with surface thermal manifestations make TMGP the most promising geothermal system in the region. The reservoir temperature has been estimated to be 360°C based on gas geothermometry measurements (Varet and Birba, 2018). However, Kahsay and Yehualaw (2023) have shown that from six boreholes drilled between 2,600–3,000 m in depth, the maximum temperature is only <220°C, which implies the need for future subsurface studies to precisely locate the geothermal resources.

A MT study by Samrock et al. (2018) and Samrock et al. (2021) revealed a shallow (<3 km) high conductivity structure consistent with a clay cap above a resistive hydrothermal recharge zone, and a localized high conductivity anomaly at 5–7 km depth beneath the TM volcano which is interpreted to be a magma reservoir. Microseismic observations within the TMGP during 2016 and

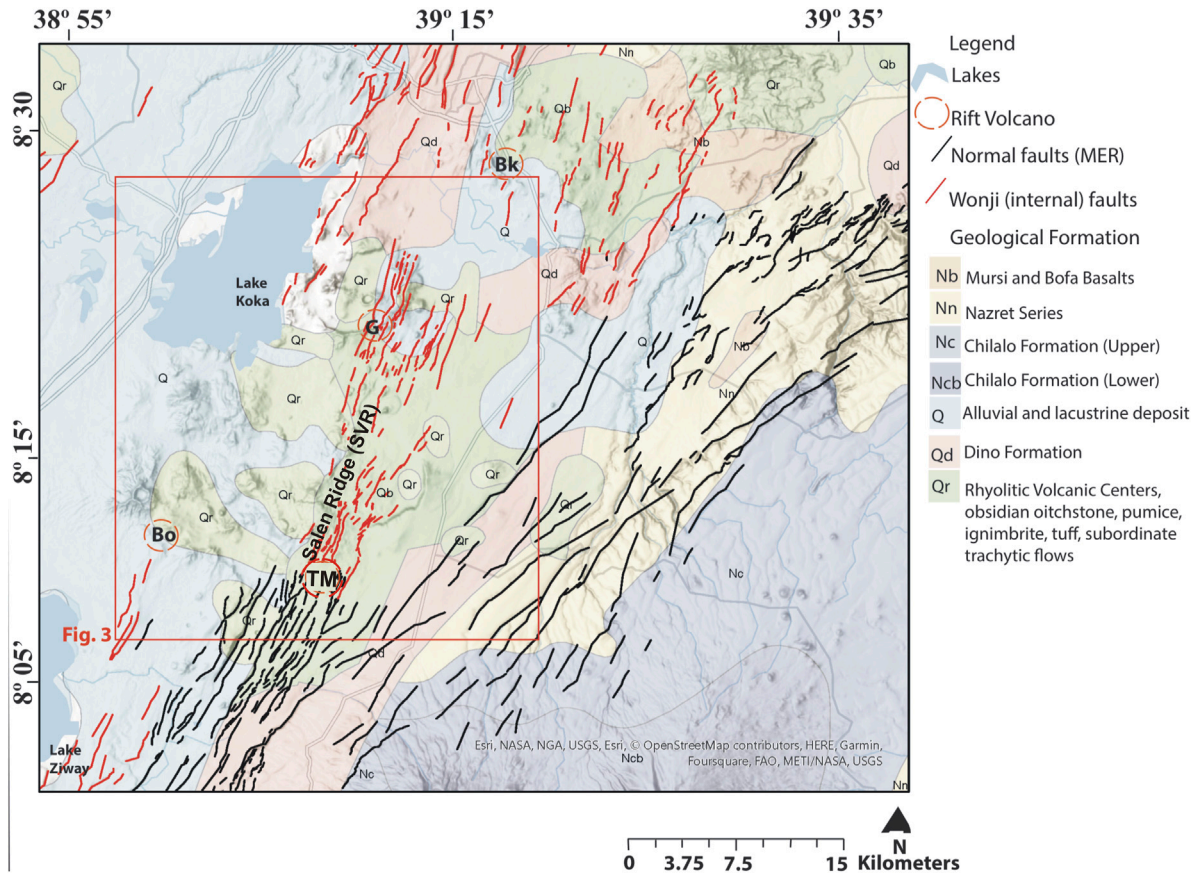

FIGURE 2
Geological map of the Tulu Moye-Gedemsa geothermal prospect. Abbreviations: Bo, Bora volcano; Bk, Boku Volcano; TM, Tulu Moye volcano; G, Gedemsa caldera (after Abebe et al., 2005).

2017 revealed swarms of seismicity mainly in the upper ~5 km and were interpreted to have been caused by hydrothermal circulation along both rift parallel and rift perpendicular fault systems (Greenfield et al., 2019). Low-frequency earthquakes occur at a depth and location coincident with the low resistivity anomaly beneath TM volcano and are therefore interpreted to be caused by melt motion (Greenfield et al., 2019). Despite several surface (Fontijn et al., 2018; Guðbrandsson et al., 2020; Kebede et al., 2023; Tadesse et al., 2023) and subsurface (e.g., Keranen et al., 2004; Maguire et al., 2006; Mickus et al., 2007; Cornwell et al., 2010; Samrock et al., 2018; Darge et al., 2019; Greenfield et al., 2019; Nigussie et al., 2022a; Nigussie et al., 2022b; Nigussie et al., 2023) studies on the structural setting and hydrothermal fluids of the area, the role of shallow subsurface structures on the occurrence of geothermal resources is not fully understood within the study area.

3 Data and methods

3.1 Data

3.1.1 Gravity data

The gravity data used in this study is part of the Global Gravity model plus (GGMplus 2013), downloaded freely from the International Gravimetric Bureau website (https://ddfe.curtin.edu.au/gravitymodels/GGMplus/GGMplus-readme.dat/). GGMplus2013 is an augmentation of satellite gravity (GOCE/GRACE), EGM2008 gravity model, and the topographic gravity effect determined from a high-pass filtered terrain model (Hirt et al., 2013). The EGM2008 gravity model includes GRACE satellite gravity and all publicly available land and airborne gravity data (Hirt et al., 2013). The resolution of GGMplus2013 is approximately 200 m and it is applicable, especially in regions where ground gravity is available (Hirt et al., 2013) including the MER. A total of 2,602 gravity data points were extracted from 38.95^0 to 39.25^{0}E and 8^0 to 8.30^{0}N by re-sampling the data with a 1 km resolution which is attributed to be sufficient to investigate the role of subsurface structures on the occurrence of geothermal resources in the study area.

The theoretical gravity value at each station was calculated using the Geodetic Reference System 1967 (GRS67). Free air and Bouguer gravity corrections were applied using mean sea level as a datum and a Bouguer density of 2.67 g/cm^3. Terrain corrections were calculated using a 1 km horizontal-resolution digital elevation model (DEM), with an accuracy of ~0.3 m, and 2.67 g/cm^3 for the terrain density to obtain complete Bouguer gravity anomalies (CBA). These data were gridded at a 1 km interval using the minimum curvature technique to produce a CBA map (Figure 4).

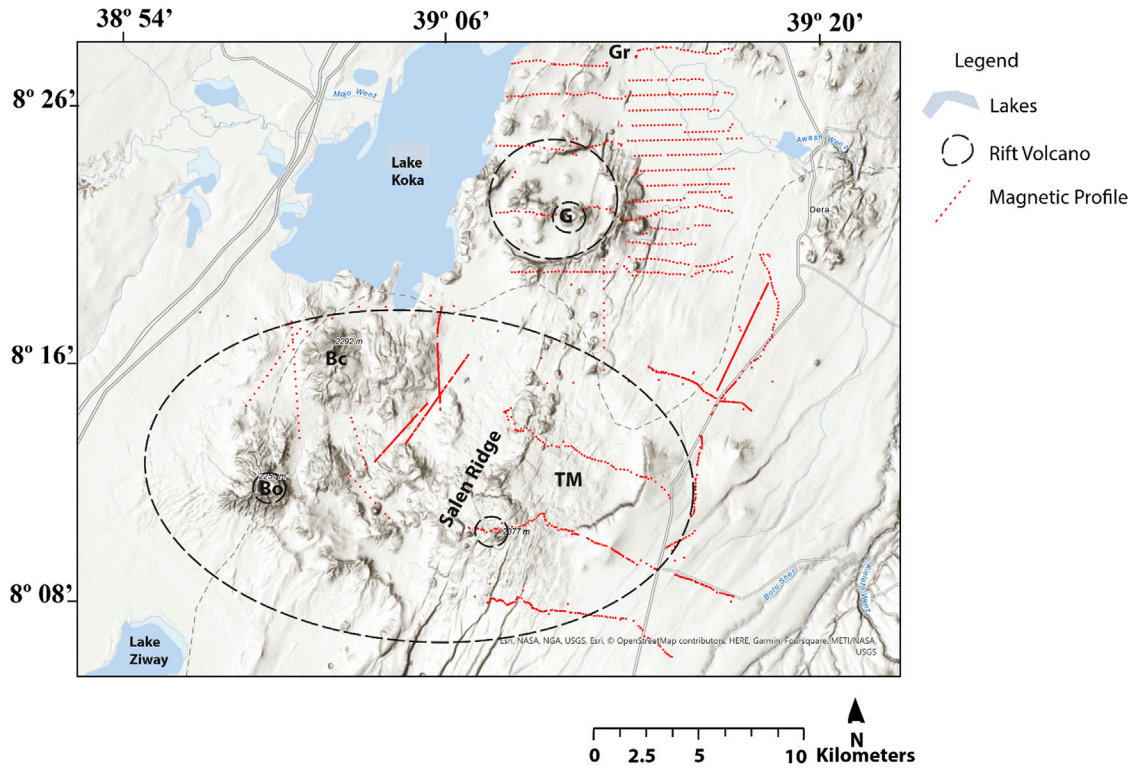

FIGURE 3
Shaded relief map of the study area showing the location of the magnetic stations (red dots) within the Tulu Moye-Gedemsa geothermal prospect. The circular broken line outlines the Gedemsa caldera and the dashed elliptical broken line outlines a proposed collapsed caldera system (Fontijn et al., 2018). Bo, Bora volcano; Bc, Bericha volcano; TM, Tulu Moye volcano; G, Gedemsa caldera; Gr, Geregendi hot spring.

3.1.2 Magnetic data

Ground magnetic data were collected using a GSM-T19 proton precession magnetometer, with a resolution and accuracy of 0.01 and 0.02 nT respectively over its full range temperature. A total of 1,440 stations were collected by the Geological Survey of Ethiopia (940 stations) and the researchers of this study (500 stations) in March 2020 (Figure 3). The data were collected with an average station spacing of 0.3–0.6 km with base stations being established to determine the diurnal variation of the Earth's magnetic field, in addition to avoiding data collection in stormy conditions and nearby power lines. Our magnetic data contains about 30 magnetic survey profile lines with varying lengths, separation distances and station distribution. Since most of the faults and magmatic alignments in the region are NNE and NE, most of the survey lines were chosen to be aligned E-W across the rift floor (Figure 3).

The magnetic data were processed by averaging the readings at each station, removing the diurnal magnetic field determined by the base stations. To remove the regional magnetic field, the 2020 International Geomagnetic Reference Field was removed from the field data to produce a total magnetic anomaly dataset. The total magnetic anomaly dataset was then reduced to the north magnetic pole (RTP) using an inclination of 1.94°, declination of 0.3°, and amplitude correction of 1.9° to remove the dipolar effect of the magnetic field at inclinations that are not at the north magnetic pole (Beard, 2000). The RTP dataset was then gridded at a 1.5 km interval using the minimum curvature technique to produce a RTP magnetic anomaly map (Figure 9A).

3.2 Data enhancement

Despite having physical property differences, the methods used in interpreting gravity and magnetic methods are similar (Alemu, 2020). Gravity and magnetic data can be transformed so that information (anomaly shape and size, physical property edges and depth of causative sources) can be extracted using various filtering techniques (Mammo, 2010; Alemu, 2020) including wavelength filtering, polynomial trend surfaces, derivative methods (Blakley and Simpson, 1986; Ansari and Alamdar, 2009) and upward continuation (Jacobsen, 1987). In this regard, we used a variety of data enhancement or filtering techniques (Table 1) to get an insight into subsurface structures beneath the TMGP.

3.2.1 Residual gravity and magnetic anomalies

The gravity or magnetic effect of all subsurface density or magnetic susceptibility variations is represented by the CBA or RTP data, respectively (Hinze et al., 2013). As a result, the physical property response of shallow seated bodies or distributions of interest (residual gravity or magnetic anomalies) can be estimated by removing the gravity or magnetic effect of deeper-seated bodies in which one is not interested (regional gravity or magnetic anomalies)

TABLE 1 Data enhancement techniques for this study.

Filtering technique		The mathematical basis of the filter		Application of the filter
		Gravity	Magnetics	
1	GF			Isolate residual from regional anomalies
2	HDR	$H(x,y) = \sqrt{(a)^2 + (b)^2}$	$H(x,y) = \sqrt{(a)^2 + (b)^2}$	Geologic contacts (Blakely and Simpson, 1986)
3	AS	$A(x,y) = \sqrt{(a)^2 + (b)^2 + (c)^2}$	$\lvert A(x,y)\rvert = \sqrt{(a)^2 + (b)^2 + (b)^2}$	Edge/vertical discontinuities (Ansari and Alamdar, 2009, Table 1)
4	RTP		$L(\theta) = \frac{1}{[\sin(I) + i\cos(I)\cos(D-\theta)^2]}$	-Avoid the polar effect (Beard, 2000)
5	UC	$\Delta g_p = Gdm\frac{z+h}{[(x-x_0)^2 + (y-y_0)^2 + (z+h)^2]^{3/2}}$	$\Delta M_p = kdQ\frac{z+h}{[(x-x_0)^2 + (y-y_0)^2 + (z+h)^2]^{3/2}}$	-Separate deeper geology from shallower (Jacobsen, 1987)

Abbreviations: GF, Gaussian filter; HDR, horizontal derivative; AS, analtyic signal; RTP, reduction to pole; and UC, Upward Continuation. Symbols: a = $\frac{\partial\Delta g}{\partial x} = \frac{\partial\Delta M}{\partial x}$, b = $\frac{\partial\Delta g}{\partial y} = \frac{\partial\Delta M}{\partial y}$, c = $\frac{\partial\Delta g}{\partial z} = \frac{\partial\Delta M}{\partial z}$ where Δg = gravity anomaly and ΔM = magnetic field anomaly, θ = wave number direction D = Declination and I = inclination, k is constant, Q is the pole strength.

from either the CBA or RTP data. The separation of the residual anomaly field from the regional field usually involves mathematical methods that are not commonly related to the actual geological conditions (Mickus et al., 1992). The most commonly used methods include upward continuation (Jacobsen, 1987), wavelength filtering (Blakely, 1995), polynomial trend surfaces (Lewi et al., 2016), and phase-match filtering (Phillips, 2001).

All of the above methods were attempted in creating residual gravity and magnetic anomaly maps. All the methods created similar anomaly amplitudes and shapes, so, we used a Gaussian-based wavelength filter where anomalies greater than 30 km were removed from the CBA data and anomalies greater than 28 km were removed from the RTP data. These wavelengths were chosen as they present density and magnetic susceptibility sources from the surface to between 7.5 and 10 km (Alemu, 2020) which are the depths of interest for subsurface structures related to the occurrence of geothermal resources within the TMGP. The subsequent residual gravity and magnetic anomaly maps are shown in Figures 5, 9B, respectively.

4 Results

4.1 Gravity anomaly maps

4.1.1 The complete Bouguer and residual gravity anomaly maps

The CBA map (Figure 4) indicates three different regions of gravity anomalies: high (>−188 mGal) over volcanic centers (TM-Bora-Bericha, Gedemsa, and Boku), intermediate (−188 to −202 mGal) over the rift floor in general, and low (<−202 mGal) towards the rift margins, regions outside the Gedemsa-magmatic segment. On the CBA map (Figure 4), the shorter wavelength anomalies are masked by a longer wavelength anomaly caused by density variations resulting from changes in crustal thickness (Mackenzie et al., 2005; Mickus et al., 2007) which masks the anomalies due to upper crustal density sources. To emphasize the shorter wavelength anomalies, a residual gravity anomaly map was created for the TMGP (Figure 5).

The residual gravity anomaly map (Figure 5) emphasizes density variations at depths less than 7.5–10 km. In general, the rift floor is characterized by gravity maxima (anomalies 1–5, Figure 5), while the region away from the margin of the magmatic segment is characterized by gravity minima (anomalies 6–7, Figure 5). Circular gravity maxima occur over some of the volcanic centers (Gedemsa and Boku) with adjacent gravity minima (Figure 5) while the TM volcanic center is associated with gravity maxima. The adjacent sides of the rift floor close to its margins are generally characterized by gravity minima (anomalies 8–11, Figure 5). The Salen Volcanic Range (SVR) is also characterized by elongated NNE-SSW gravity minimum (anomaly 12, Figure 5).

4.1.2 Horizontal derivative and analytic signal gravity anomalies

The horizontal derivative (HDR) method (Blakley and Simpson, 1986) is a technique to determine the edges of either density or magnetic susceptibility sources, where the maximum horizontal gradient occurs over the edge of planar bodies. The method was applied to the residual gravity anomaly data to aid in determining linear features that might be related to subsurface structures (e.g., faults, lineaments, and fractures) (Figure 6A). Figure 6A has several linear anomalies which are marked by black lines and could represent subsurface density discontinuities. For comparison of the subsurface mapping with the surface mapping, the surface volcano-structural mapping of the region (Figure 6B) is shown together with the HDR map. The linear features in the HDR map mainly trend either NW-SE or NE-SW with some NE-SW trending linear features being within the WFB (anomalies 1–3, Figure 6A) which agrees well with the surface data (Figure 6B). The later linear features are probably associated with the rift parallel dike intrusions. The volcanic centers (Boku, Gedemsa, TM) are bounded by linear anomalies implying some sort of structural control of the location of these volcanoes.

The analytic signal (AS) method is a total derivative method that may generate maximum anomalies over the peak of the density or magnetic susceptibility body (Dentith and Mudges, 2014). The method works well on shallow source bodies (Li, 2006) and should be combined with the HDR map to indicate which maxima are related to vertical contacts. The HDR method produces linear anomalies that are commonly continuous (Figure 6A), while the AS method produces more circular anomalies (Figure 7) that are less continuous (Phillips, 2000). However, the AS solution is more accurate and if the HDR and AS solutions overlie each other, then the contact is vertical

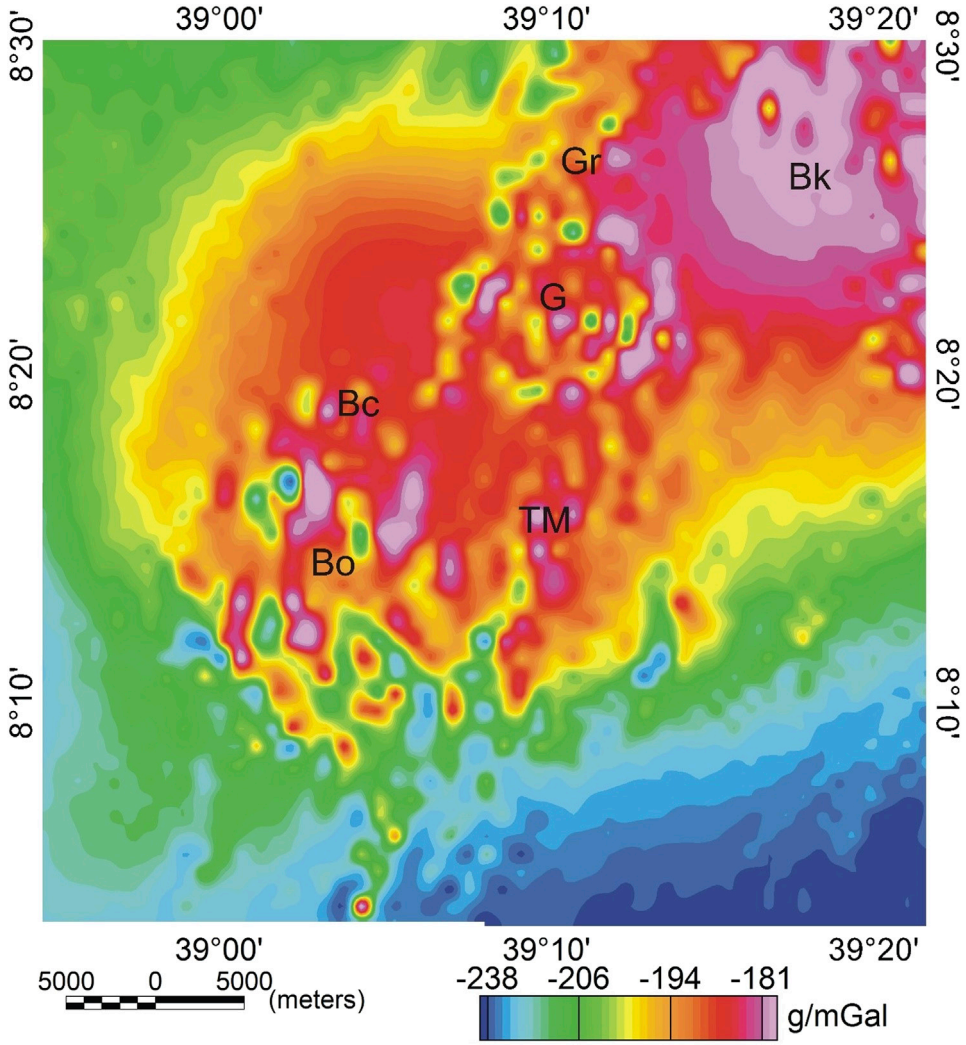

FIGURE 4
Complete Bouguer gravity anomaly map of the Tulu Moye-Gedemsa geothermal prospect. Abbreviations as in Figure 3.

(Phillips, 2000). If the HDR contacts are offset from the AS contacts, then the contacts are dipping (Phillips, 2000). The AS method was applied to the residual gravity anomaly map (Figure 5) to generate the AS map (Figure 7) which is characterized by a series of roughly circular anomalies that are in general in the same region as the HDR maxima (Figure 6A). The majority of anomalies are at the same location (Figure 7) as the HDR maxima (Figure 6A). This implies that the density source edges are vertical. However, anomalies 1-3, are not coincident with their corresponding HDR maxima, implying dipping density source edges. The location of the edges for our study should be estimated from the AS map (Figure 7).

4.1.3 Upward continuation of the residual gravity anomalies

The residual gravity anomaly map (Figure 5) highlights anomalies due to lateral variations in density but does not provide information on the depths of the source bodies. To determine a general depth to both shallow and deeper density bodies, upward continuation (Jacobsen, 1987; Kebede et al., 2020) was applied to the residual gravity anomaly data (Figure 5). Upward continuation is a low pass filter (Alemu, 2020; Kebede et al., 2020) that attenuates noise and emphasizes the anomalies from the deeper sources (Hinze et al., 2013) without changing the physical significance of the data. Jacobsen. (1987) showed that upward continuing a gravity field to a specific height implies that anomaly sources are at and below a depth of one-half of the continuation height. Figures 8A–D show the upward continuation of the residual gravity anomaly map (Figure 5) for different heights (1, 2, 4, and 8 km) to indicate the depth of the sources are at or below 0.5 km, 1 km, 2 km, and 4 km, respectively.

The upward continued gravity anomaly maps (Figures 8A–D) show that the gravity field becomes smoother as the continuation height increases. The 1 km upward continuation gravity anomaly map (Figure 8A) basically looks like the residual gravity anomaly map (Figure 5) but enhances the gravity maxima (outlined) especially those associated with the volcanic centers. As the continuation height increases, the number of maxima decreases as there are four sets of circular-shaped gravity maxima over the volcanic centers within the WFB: Bora, Bericha, TM, and Boku (Figures 8B, C).

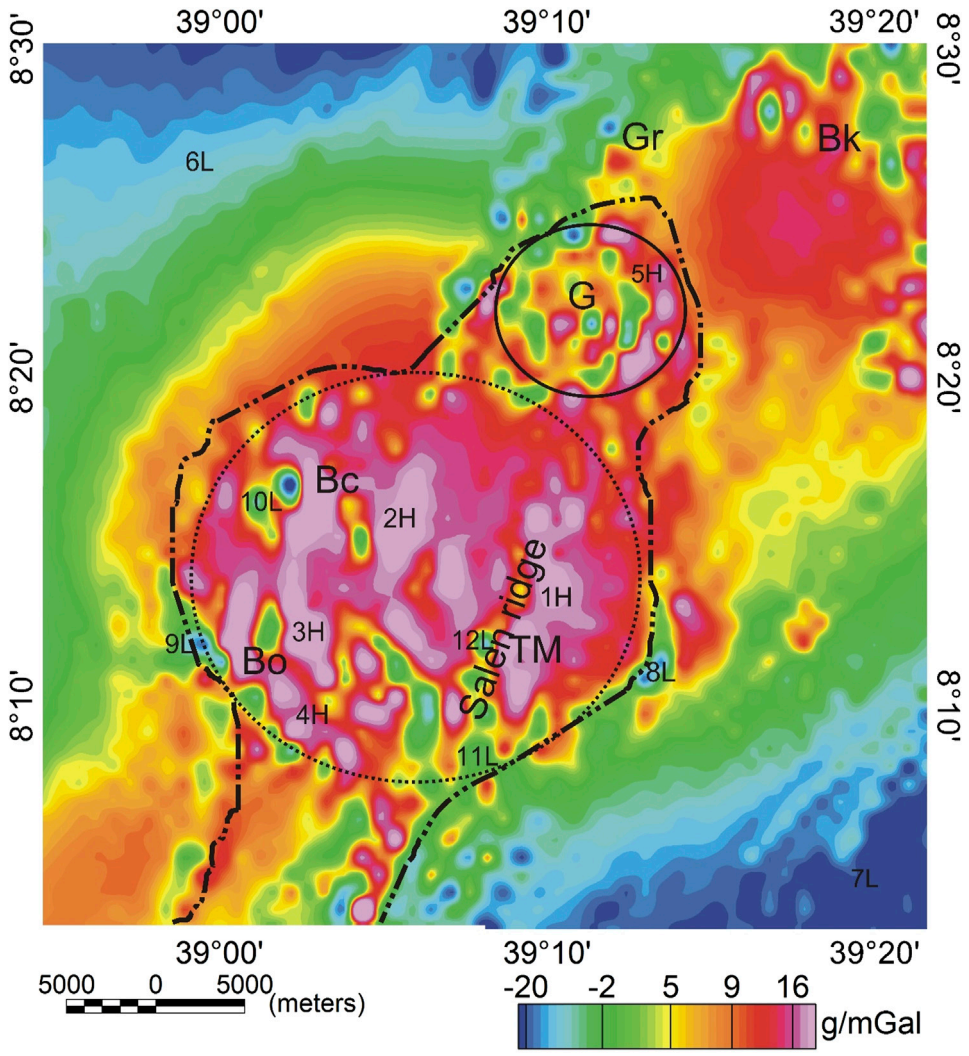

FIGURE 5
Residual gravity anomaly map. Abbreviations as in Figure 3 and solid circular black line outline the Gedemsa caldera. The dashed circular black line outlines a proposed collapsed caldera system (Fontijn et al., 2018). The dashed thick line polygon outline represents the Tulu Moye-Gedemsa magmatic segment. Numbers and associated letters are references for high (H) and Low (L) anomalies discussed in the text.

4.2 Magnetic anomaly maps

4.2.1 Total and residual magnetic anomaly maps

The magnetic survey was conducted to identify magnetically anomalous regions within the upper crust to assist and support the interpretation of the gravity data. Figure 9A reveals the presence of magnetic minima (anomalies 1, 2, and 3, Figure 9A) (as low as −450 nT) in the western and central part of the study area and magnetic maxima (anomalies 4–6, Figure 9A) (up to 300 nT) in the eastern portion of the study area. The residual magnetic anomaly map removes anomalies greater than 28 km in wavelength (Figure 9B). The resultant map basically mimics the RTP map (Figure 9A) but enhances the anomalies seen on the RTP map. This indicates that, unlike the regional gravity field which varies smoothly due to crustal thickness variations, the regional magnetic field is basically linear within the study area except under the major volcanic centers. Linear magnetic maxima (anomalies 1 and 2, Figure 9B) are seen surrounding the TM volcano (Figure 9B) although the floor of the volcano is reflected by magnetic minima (anomaly 3). The Gedemsa caldera and the surrounding area are characterized by magnetic minima (Figure 9B) and magnetic maxima. While the SVR is characterized by a SW-NE trending minima (Figure 9B).

4.2.2 Analytic signal magnetic anomaly map

The AS filter can be applied to magnetic data and it has the advantage of being independent of magnetization direction but the strength of magnetization (Ansari and Alamdar, 2009). The AS filter was applied to the residual magnetic anomaly data (Figure 9B) to aid in identifying lineaments within the magnetic data. The AS magnetic map (Figure 10) shows maxima at the peak of the magnetic susceptibility bodies. The AS method enhances short-wavelength anomalies and the AS magnetic map (Figure 10) shows maxima over the volcanics within the TM and Gedemsa caldera. Anomalies 1 and

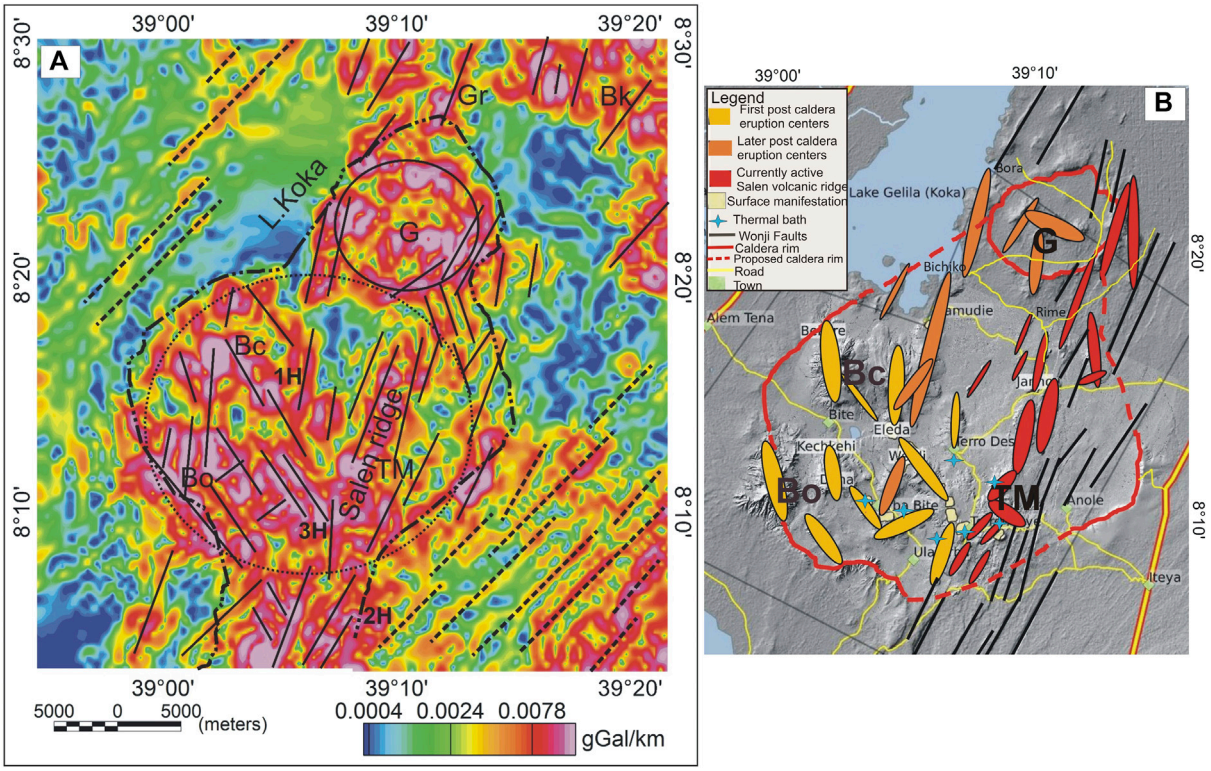

FIGURE 6
(A) Horizontal derivatives of the residual gravity anomaly map. Abbreviations as in Figure 3 and solid circular black line outline the Gedemsa caldera. The dashed circular black line outlines a proposed collapsed caldera system (Fontijn et al., 2018). The dashed thick line polygon outline represents the Tulu Moye-Gedemsa magmatic segment. Straight black lines are lineaments determined from the derivative analysis. Numbers and associated letters are references for high (H) and Low (L) anomalies discussed in the text. **(B)** Schematic volcano-structural interpretation of the TMGP (After Varet and Birba, 2018).

2 roughly outline the edges of the magnetic minimum (Figure 9B) associated with TM. Anomalies 4 and 5 trends NE-SW, are associated with the WFB (Kebede et al., 2022). The AS magnetic maxima in the Gedemsa caldera outline the magnetic susceptibility sources imaged on the residual magnetic anomaly map (Figure 9B). Most of the anomaly features in Figure 10 trend NW-SE and are in the same location as similar lineaments imaged in the gravity data (Figure 6A) and surface volcano-structural features (Figure 6B). These NW-SE trending lineaments may connect to faults that were imaged to the south in the Aluto volcano region (Kebede et al., 2022).

4.3 Interpretation of gravity and magnetic anomalies

4.3.1 Qualitative interpretation

The large-scale gravity maxima over the TMGP (Figure 5) are attributed to the response of the varying thickness of the volcanic rocks and mafic intrusions added into the upper crust as imaged in previous geophysical studies (Keranen et al., 2004; Mickus et al., 2007). In addition, the separate circular gravity maxima associated with the Gedemsa caldera and the Boku volcano are attributed to either intruded material (Kebede et al., 2022) or the result of higher density volcanic material which has built each volcanic center (Scandone, 1990). On the other hand, the surrounding gravity minima associated with the Gedemsa caldera and the Boku volcano, and possibly TM (Figure 5) may be caused by the thick, low-density volcanic ash within the caldera after collapsing or may reflect the reworked material of caldera collapse infill (Scandone, 1990). The SVR, west of TM, is also characterized by elongated NNE-SSW gravity minima (Figure 5) that may be related to the presence of partial melt at shallow depth.

Closely examining the upward continuation map (Figures 8A–D) reveals that as the continuation height increases, the individual gravity maxima under Bora, TM, and Bericha are merged into one gravity maximum, best explained as a zone of dense mafic intrusions. This could imply that there is a deep source for the three volcanic centers with smaller high-density bodies at a shallower depth under each individual volcanic center. This phenomenon has been observed at other magmatic centers in the northern MER using three-dimensional gravity and magnetic modeling (Mickus et al., 2009; Kebede et al., 2022). The larger body may represent a deeper zone of magma accumulation, from where the magma migrated upward and accumulated at shallower depths under each individual volcanic center. Combining the maxima anomalies from the residual gravity anomaly, upward continuation maps and the analytic signal maps (Figures 5, 7, 8A–D) over the TM-Gedemsa magmatic segment indicates that there was a large

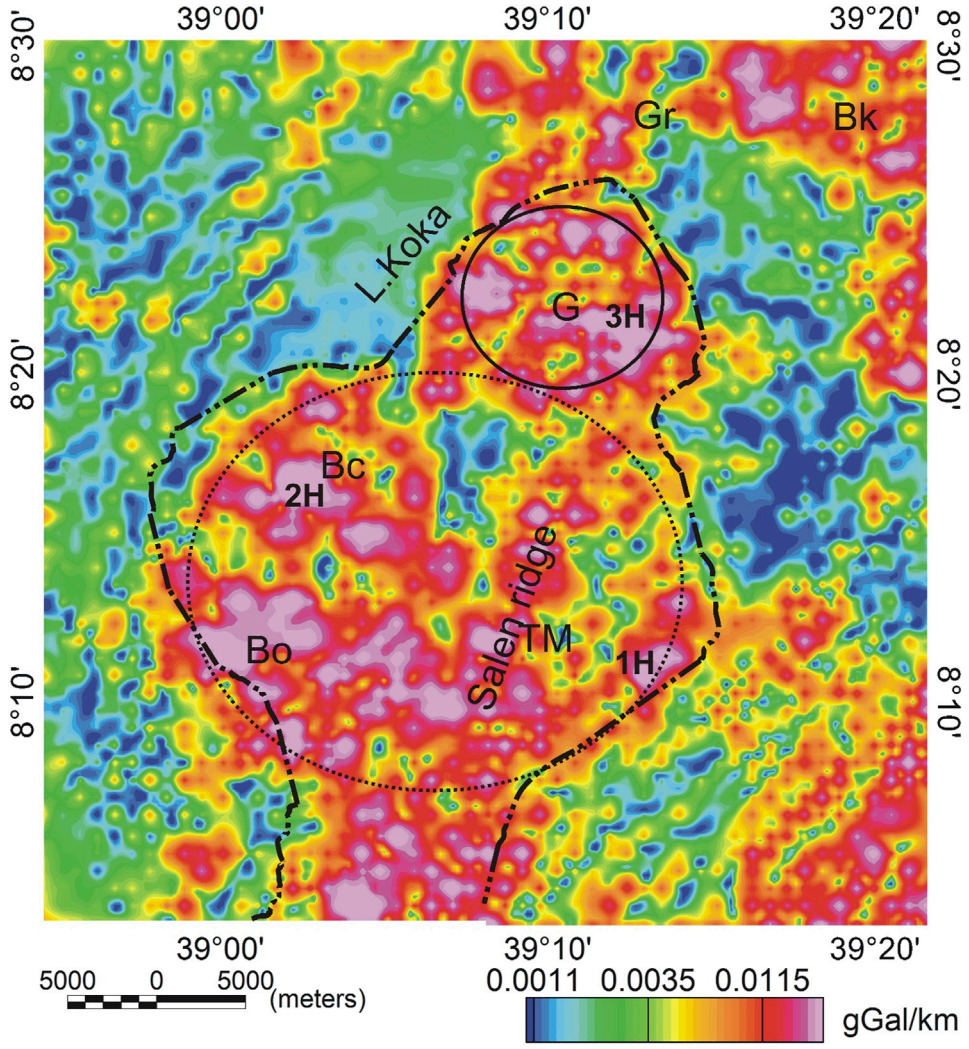

FIGURE 7
Analytic signal anomalies of the residual gravity anomalies of the Tulu Moye-Gedemsa geothermal prospect. Abbreviations as in Figure 3. Solid black circular line outlines the Gedemsa caldera. Dashed circular black line outlines a proposed collapsed caldera system (Fontijn et al., 2018). Dashed thick line polygon outline represent the Tulu Moye-Gedemsa magmatic segment. Numbers and associated letters are reference for high (H) and Low (L) anomalies discussed in the text.

amount of mafic material added to the crust under this magmatic segment.

Additionally, the HDR map (Figure 6A) in conjunction with the surface mapping (Figure 6B) indicates several NNE-SSW and NW-SE linear features which may be related to the WFB (NNE trending) and previously unknown faults (NW trending). These linear features, if they are fractures or faults and especially where they intersect, could be favorable sites for the migration of partial melt and geothermal fluids. The alteration zones and thermal baths surrounding and to the west of the TM volcanic center (Figure 6B) could be controlled by such conditions. Such a scenario was shown to be important to the south of the study area in the Aluto-Langano geothermal field, where MT studies indicated that the geothermal fluids originated to the northwest of the Aluto volcano (Samrock et al., 2015) and a magnetic analysis suggested linear magnetic anomalies interpreted as faults were the conduits of the geothermal fluids to the Aluto area (Kebede et al., 2022).

The residual magnetic anomaly map (Figure 9B) shows a series of relatively short wavelength maxima and minima that can only roughly be correlated with the surface geology (Figure 2). There are no magnetic susceptibility measurements in the study area but measurements to the south of the study area in the Aluto volcano region indicate that the near-surface pyroclastic material has low values, while the Bofa basalts and ignimbrites have high values (Kebede et al., 2022). The other lithologies in the study area, including the scoria deposits, rhyolite flows, and rhyolite domes, commonly have low magnetic susceptibilities (Mackie and Cunningham, 1982) and thus probably are not the sources of the magnetic maxima. Thicker occurrences of any of these lithologies may be the source of the magnetic minima. Accordingly, anomaly 13 (Figure 9B) possibility reflects rhyolite domes and flows (Figure 2). Based on magnetic forward modeling in the Aluto volcano region (Kebede et al., 2022), the majority of the larger amplitude magnetic maxima are caused by magmatic intrusions in the upper crust

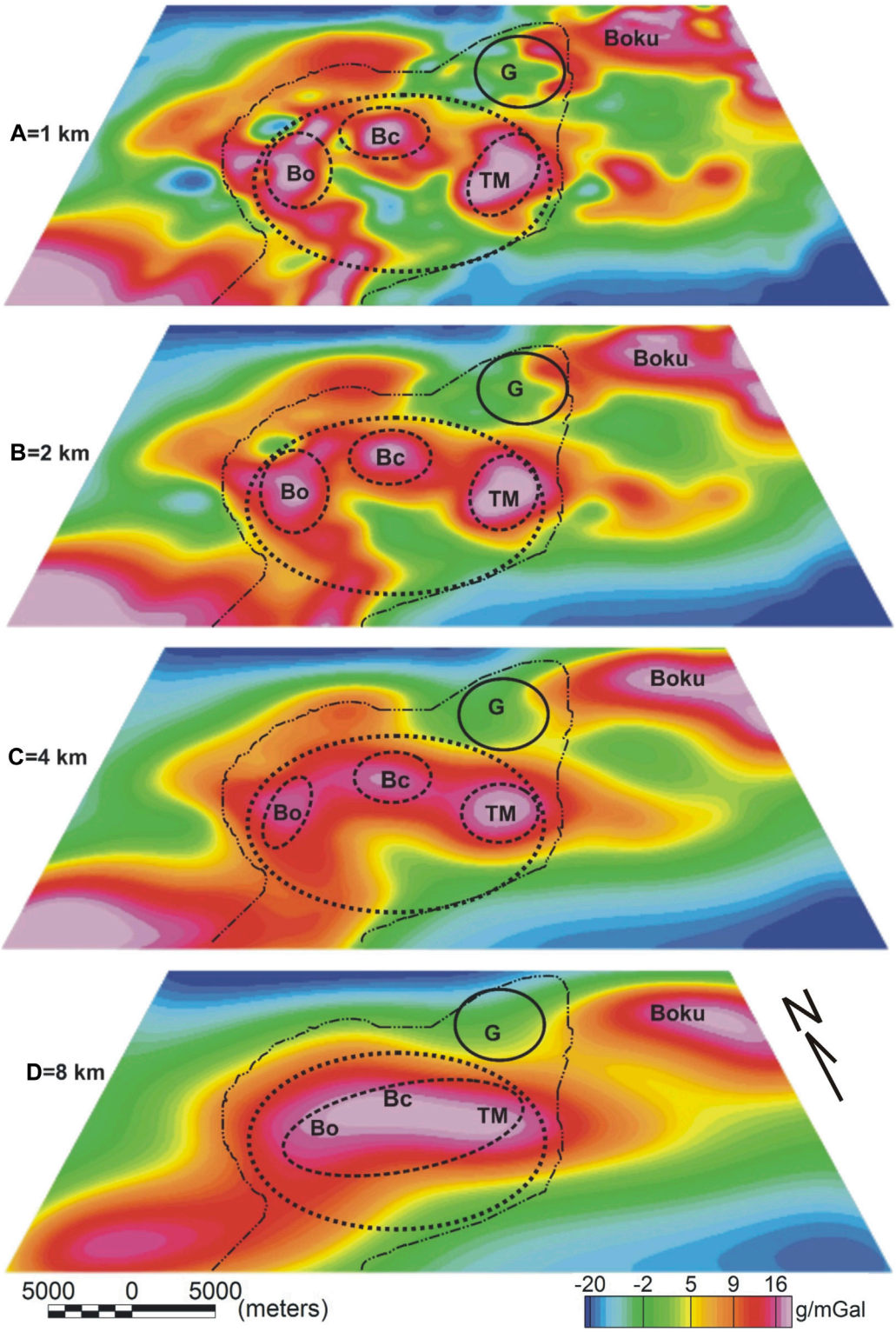

FIGURE 8
Upward continuation of the residual gravity data (Figure 5) to a height of **(A)** 1 km, **(B)** 2 km, **(C)** 4 km, and **(D)** 8 km. Abbreviations as in Figure 3. Solid black lines outline the Gedemsa caldera and the dashed black line outlines a proposed collapsed caldera system (Fontijn et al., 2018). The white line outlines the Tulu Moye-Gedemsa magmatic segment.

(<6 km in depth). A number of the magnetic maxima in the TMGP are linear in nature and occur along the WFB or along suspected fault systems that trend NW-SE determined from the gravity and magnetic derivative analysis (Figures 5, 6A, 7, 10). These anomalies may be mafic intrusions at a depth that were intruded sub-parallel to the faults. The Bora and Bericha volcanoes are associated with

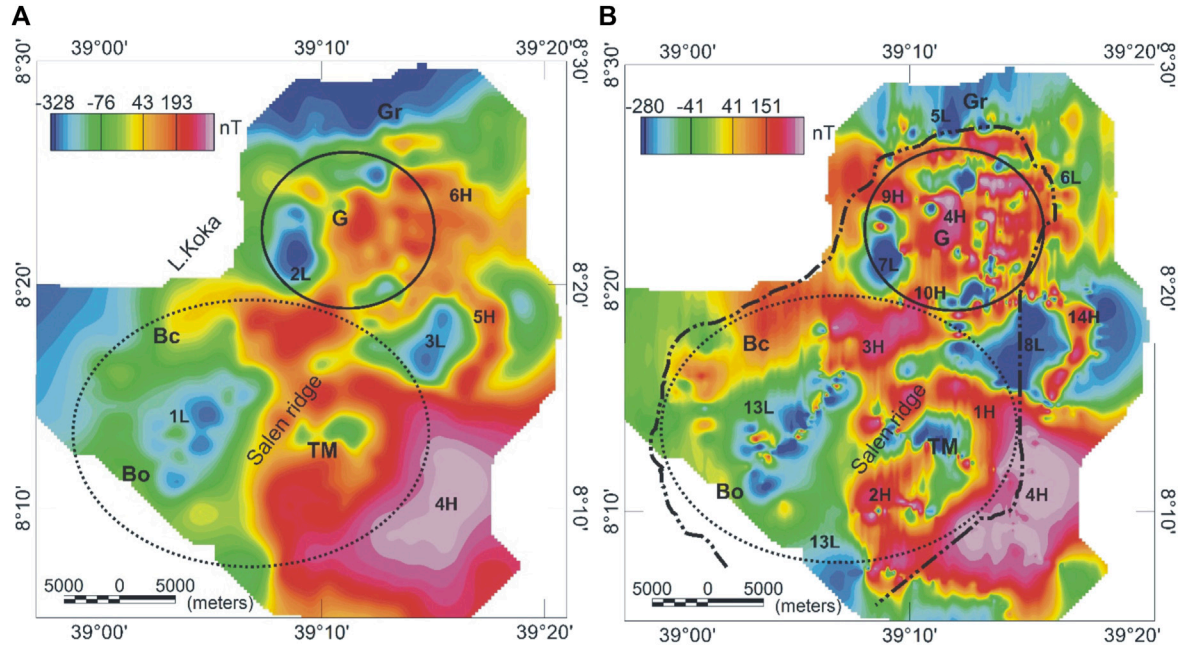

FIGURE 9
(A) RTP magnetic anomaly map and **(B)** residual magnetic anomaly map of the Tulu Moye geothermal prospect and surrounding area. Abbreviations as in Figure 3. Solid black lines outline the Gedemsa caldera and the dashed white line outlines a proposed collapsed caldera system (Fontijn et al., 2018). The white line outlines the Tulu Moye-Gedemsa magmatic segment. Numbers and associated letters are references for high (H) and Low (L) anomalies discussed in the text.

magnetic maxima and have pyroclastic flows at the surface (Figure 9B). However, the pyroclastic materials may not have sufficient magnetic susceptibility (Kebede et al., 2022) and the amplitude of these maxima suggests that they may be related to deeper mafic intrusions. (Figure 9B). The SW-NE trending aligned magnetic minima (Figure 9B) that occur over the SVR possibly reflect either thick non-magnetic lithologies or demagnetized lithologies due to hydrothermal fluid alteration as shown near the TM volcanic center in surface mapping (Figure 6B). The magnetic minima could be the response of partial melt at shallow depth associated to the active volcano-tectonic feature in support of surface-based geologic studies (Varet and Birba, 2018; Fontijn et al., 2018; Guðbran dsson et al., 2020; Figure 2) and our interpretation for the gravity data (Figure 5).

4.3.2 Quantitative interpretation

To obtain better quantitative subsurface information, we re-interpreted the 2D gravity (Figure 11) and 3D geologic (Figure 12) models from Nigussie et al. (2022a) in terms of subsurface volcanic networks and their link to the geothermal resource occurrences. The 2D model was constructed by forward modeling of the gravity data (Figure 11). This process suffers from non-uniqueness, but when combined with constraints from seismic models, borehole data, and geological mapping, it can be a powerful tool in providing additional constraints on the crustal structure. In our models (Figure 11), the available geophysical and geological constraints were used to obtain quantitative models of the upper crustal structure (Figure 11) along a profile that crossed the TMGP (Nigussie et al., 2022a). The constraints on the geometry, depths and densities of the crustal bodies were derived from seismic models (Keranen et al., 2004; Mackenzie et al., 2005; Maguire et al., 2006). Since there are few constraints on the detailed stratigraphy of the area, the majority of the rock types and thicknesses of the upper-most layers were estimated based on geological mapping in the MER (Woldegabriel et al., 1990; Abebe et al., 2005; 2010), and their densities were estimated from the measurement of common rock types (Telford et al., 1990). A residual gravity anomaly data was modeled with the density, geometry, and depth values being varied by 10% from the available constraints during the modeling process, until the difference between the observed and calculated gravity anomalies was <2%.

The final density model (Figure 11) included a top layer of Quaternary rift sediments (ρ = 2.38 g/cm^3) and a second layer consisting of both pre-rift and syn-rift volcanics (ρ = 2.6 g/cm^3) (Corti, 2009). The volcanic rocks are underlain by Mesozoic sediments of shale and claystone (ρ =2.49 g/cm^3) followed by the Antalo formation (ρ = 2.42 g/cm^3) and Adigrat formation (ρ = 2.17 g/cm^3) which lies unconformably over the crystalline basement (ρ = 2.69 g/cm^3). In addition, the models (Figures 11, 12) included a high-density body (ρ = 3 g/cm3) which is interpreted to be a mafic intrusion in the mid-upper crust (Ebinger and Casey, 2001; Keranen et al., 2004; Casey et al., 2006; Kurtz et al., 2007; Nigussie et al., 2023). This magmatic intrusion zone is beneath the WFB and is attributed to be a locus of Quaternary extension by magma intrusion (Figures 11, 12).

5 Discussion

Our discussion sections focused on explaining our results in conjunction with the existing data on constraining caldera

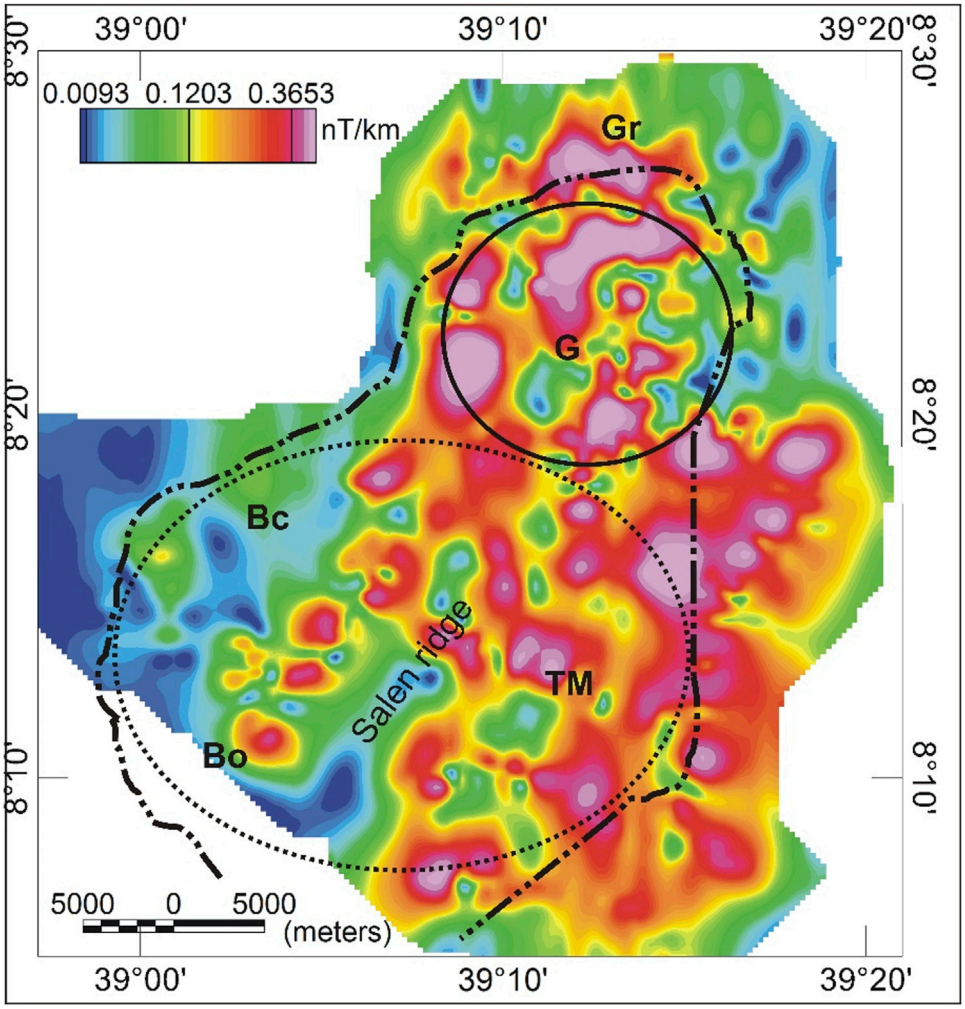

FIGURE 10
Analytic signal anomalies of the residual magnetic data. Abbreviations as in Figure 3. Solid black circular line outline the Gedemsa caldera and the dashed black circular line outlines a proposed collapsed caldera system (Fontijn et al., 2018). The black polygon outlines the Tulu Moye-Gedemsa magmatic segment.

formation mechanisms (Section 5.1), as well as the geothermal heat sources and the role of subsurface structures (Section 5.2) within the TMGP. In this regard, we re-interpreted the 2D gravity model (Figure 11) and 3D subsurface geologic model (Figure 12) of Nigussie et al. (2022a), which are constructed to understand the structure of the upper crust, in terms of geothermal resources occurrence point of view within the TMGP in conjunction with our gravity and magnetic anomaly maps (Figures 4–10).

5.1 Caldera formation scenarios in the Tulu Moye geothermal prospect

Caldera collapse is a common geological process in active volcanic regimes, especially in continental rifts (Holohan et al., 2005; Maestrelli et al., 2021b), and many mechanisms have been proposed to explain this process (Acocella et al., 2001; Troll et al., 2002; Ruch et al., 2012; Coumans and Stix, 2016). Determining which mechanism is correct for a given caldera is hindered by the rapid formation of the caldera and post-caldera volcano-tectonic processes and sediments that cover the caldera features (Holohan et al., 2005; Maestrelli et al., 2021a). Thus, geophysical methods are important in delineating caldera structures, which are common potential sites of geothermal activity (Cole et al., 2005), and determining a correct mechanism to explain their development.

Despite there being several known calderas within the MER (e.g., Gedemsa, Gariboldi; Fentale, and Dofan) (Hunt et al., 2020; Acocella et al., 2002; Maestrelli et al., 2021a; b; Casey et al., 2006), there are several volcanic complexes with calderas that have been not well studied (e.g., TM volcanic complex). The TM volcanic complex consists of several volcanic centers (TM, Bora, and Bericha, Figure 2) with visible caldera rims, although there is not a common consensus on the number and nature of the calderas in the area. Geothermal exploration studies (Fontijn et al., 2018; Varet and Birba, 2018; Guðbrandsson et al., 2020) have proposed the presence of one large caldera system for the TMGP (e.g., Figures 3, 5). If this hypothesis is correct, the TMGP is a single

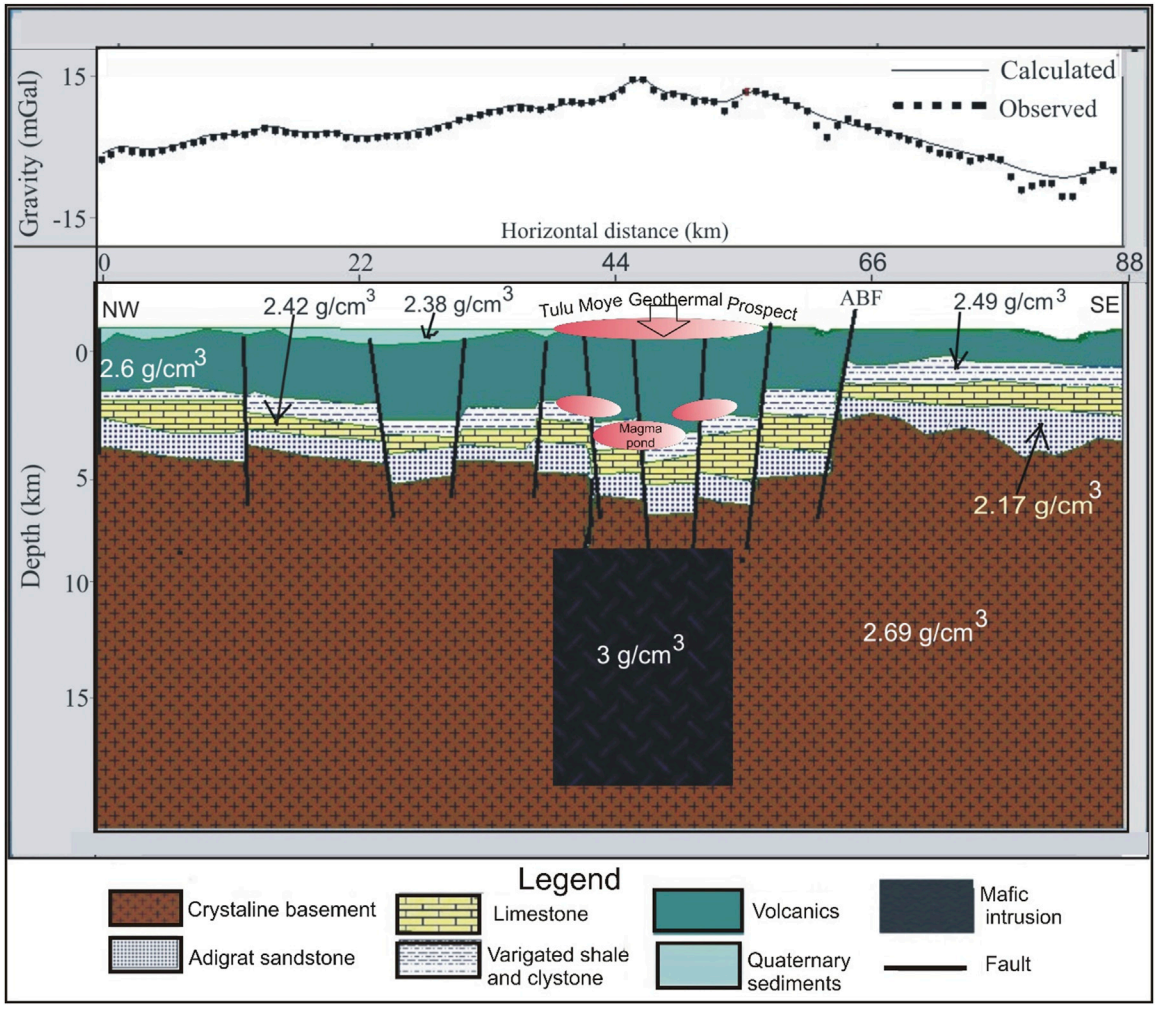

FIGURE 11
Two-dimensional gravity model across the Gedemsa TMS including the Tullu Moye volcano center along profile P1 (Figure 6 of Nigussie et al., 2022a). ABF-Asela border fault.

large caldera (~25 km in diameter and covering ~500 km^2) bounded by the younger (340 ky) Gedemsa caldera on its northern edge (Figures 5–7). However, Kebede (2021) used aerial images and field mapping data to suggest that the TMGP consists of nested or overlapping of three individual calderas, each with a different age.

The residual gravity anomaly map (Figure 6) and derivative maps (Figures 5, 6) revealed a spatially large circular maximum with overlapping smaller elliptical to circular-shaped maxima. The large circular region (Figures 3, 5, 6) could be evidence for the single large caldera model (Fontijn et al., 2018; Varet and Birba, 2018; Guðbrandsson et al., 2020) whereas, overlapping smaller elliptical-circular positive gravity anomalies could reveal a nested caldera system (Kebede, 2021). This observation can be interpreted as that the TMGP consists of an older large caldera, about 25 km in diameter followed by several smaller, younger calderas (Bora, Bericha, and TM) (Figure 12). Caldera rims are not visible in many locations due to modification by erosion and post-caldera volcano-tectonic activities associated with the Quaternary-Recent NNE-SSW trending structures related to the WFB and the cross-rift (NW-SE) structures (Figures 5–7) (Kebede, 2021).

Our interpretations are similar to the formation of other nested calderas (Aluto, Dofan, Fantale, Kone, Shala, and Corbetti) within the MER (Maestrelli et al., 2021b). However, unlike the elongated characteristics of these calderas, our subsurface interpretations revealed an almost circular shaped caldera for the TMGP (Figures 5, 6, 12), and specifically the Gedemsa caldera has a circular shape based on the gravity analysis (Figures 5–7). The larger TMGP caldera rim can also be considered fault-controlled as its southwestern margin is affected by NW-SE trending structures (Figure 6) and its eastern margin is affected by the NNE-SSW trending structures of the WFB (Figure 6).

5.2 Geothermal heat sources and roles of subsurface structures in the Tulu Moye geothermal prospect

The TM-Gedemsa volcanic complex consists of prospective geothermal sites including TM, Geregendi, and Boku (Samrock et al., 2018; Greenfield et al., 2019; Varet et al., 2020). The

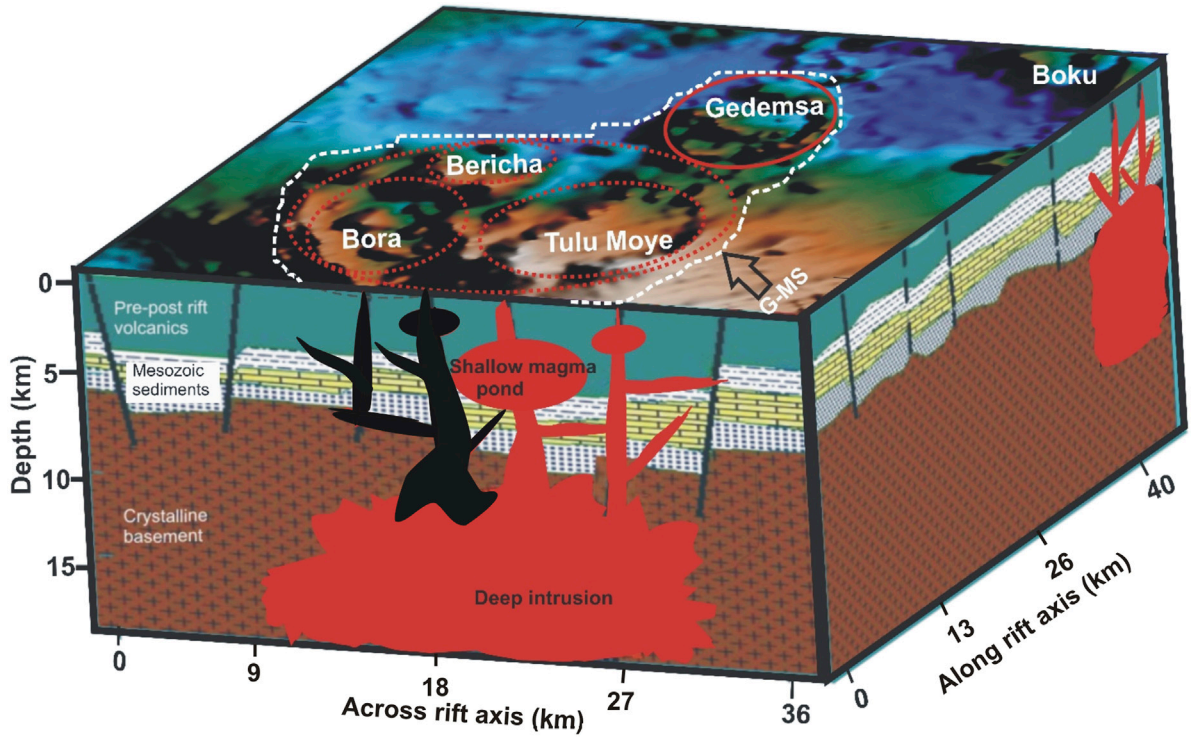

FIGURE 12
3D geology of the Tulu Moye-Gedemsa volcanic complex, showing the interaction of shallow magma chambers with deep mafic intrusions through quaternary faults (modified from Nigussie et al., 2022a), the magma plumbing system in black color beneath Bericha and Bora volcano represents extinct (volcanically inactive) zones.

interpretation of gravity data alone is not indicative of geothermal resource occurrences, but when interpreted in conjunction with magnetic data, one can obtain a better model of the structural controls on the geothermal resource occurrences. Our combined interpretations of gravity and magnetic data provided insight into the role of subsurface geological structures on the occurrence of geothermal resources in the area. The gravity maxima on the CBA map (Figure 4) and upward continued (Figures 8A–D) maps can be explained by dense mafic intrusion beneath the TMGP to at least mid-crustal depths, as the anomaly signal response increases with upward continuation height. The depth of the top of this mafic intrusion zone is as shallow as 7.5 km, as imaged by 2D gravity (Figure 11) and 3D geologic (Figure 12) models (Nigussie et al., 2022a). The geological record suggests that these mafic intrusions represent the magmatic addition to the mid-crustal level beneath the MER since the Quaternary (Ebinger and Casey, 2001; Wolfenden et al., 2004; Abebe et al., 2007). Our evidence from gravity data along with the surface thermal manifestation (Figure 6B), recent geological units (Varet and Birba, 2018; Guðbrandsson et al., 2020), low magnetic anomaly (Figures 9A, B) and high heat flow as well as a shallow Curie point depth (Kassa et al., 2022) of the TM volcanic center and SVR supports the presence of an active melt supply.

The short wavelength circular-shaped anomalies (Figures 5, 8A–C) occurring over the Bora, Bericha, and TM volcanoes are probably caused by shallow mafic intrusions as suggested by previous gravity modeling (Mickus et al., 2009). The 2D gravity model (Figure 10) and 3D geologic interpretation (Figure 12) suggest the presence of mafic intrusion at a depth of ~5 km beneath the TM, Bora, and Bericha volcanoes. Of these, only the anomaly beneath TM is imaged with high conductivity in MT surveys (Samrock et al., 2018), and we therefore interpret this specific body to be currently magmatically active and include partial melt, consistent with it being a primary heat source for the geothermal system (Figures 11, 12). In addition, the residual magnetic anomaly map (Figure 9B) reflects a SW-NE aligned minimum following the SVR, which is also reflected by thermal bath and surface alteration zones especially close to the TM volcanic center (Figure 6B). These magnetic minima parallel to this active volcano-tectonic range may indicate the existence of a zone that has been hydrothermally altered as observed on the surface structural mapping (Figure 6B) or could reflect the presence of partial melt between 2–3 km depth, as interpreted from the gravity minima (Section 4.3; Figure 5). If the anomaly is from the current partial melt, then it could be an additional heat source. This interpretation is consistent with microseismic observations where low-frequency earthquakes occur at similar depths caused by melt motion (Greenfield et al., 2019). Our interpretation of discrete and shallow loci of intrusion beneath the volcanic centers is also consistent with petrological modeling which suggests the rhyolite lavas were derived from ~4 km deep reservoirs (Tadesse et al., 2023). The magmas evolved from a basaltic primary melt (Tadesse et al., 2023) of high temperature

(1,070°C–1,190°C), which likely dominates the intruded and solidified reservoir.

The interlinking of structural zones (caldera features as well as NNE and NNW faults) (Figures 6A, B) and geothermal prospect regions implies that the geothermal resources within the area are linked to and controlled by rift structures (Admasu and Worku, 2015; Hutchison et al., 2015; 2016). The distribution of linear features along and across rift anomalies in the horizontal derivative map (Figure 6A), is similar to the surface fault pattern and alignment of volcanic systems (Figure 6B) (Boccaletti et al., 1998; Boccaletti et al., 1999; Corti, 2009; Admasu and Worku, 2015). This suggests that the Quaternary-Recent NE to NNE- and NW-trending faults and fractures are persistent and intersect below a depth of 0.5 km within the rift floor (Figures 11, 12). The region between the Salen ridge, and the TM and Bora volcanoes in particular shows dense intersections between faults striking across and along the rift, and with the caldera rims, and is also a region of most surface thermal baths (Figure 6B) and hydrothermal alteration (Kebede et al., 2023). Our horizontal derivative map suggests the surface fault system persists to significant depth and likely to contribute significantly to the movement of geothermal fluids in these areas. Therefore, we interpret that the interactions between rift and caldera related faults creates the high permeability that controls lateral and vertical hydrothermal fluid flow and results in a large geothermal system in the region (Figure 12).

At greater depths, our upward continuation analysis and 2D gravity model suggest a deeper zone of mafic intrusion beneath ~7.5 km depth. The depth of this intrusion zone is consistent with the thermometry and barometry modeling of the basaltic lavas from the TMGP, which suggest a zone of basaltic storage with higher temperature (1,070°C–1,190°C) at 7–29 km deep (Tadesse et al., 2023). These results are also consistent with a Curie point depth (7.68–13.1 km) (Kassa et al., 2022). Our gravity data and model together with the position of surface manifestation zones suggest a deep geothermal reservoir directly beneath the TMGP (Figures 6B, 11, 12), and slightly offset to the east of the west-dipping high conductivity anomaly at similar depths observed in MT data (Samrock et al., 2018). Since the high conductivities in MT show zones of partial melt currently in the crust, while the gravity data are sensitive to time-averaged locus of intrusion, we suggest that the locus of magma migration from depth beneath the TMGP has changed through time.

Haile and Tamiru. (2012) showed that the Gedemsa caldera hosts a geothermal system and is the heat source for the Geregendi thermal spring. However, geochemical evidence (Thrall, 1973) and the absence of thermal manifestations in the area suggested that Gedemsa caldera may be an extinct/or dormant volcano. This is supported by the results of a magnetic maxima (Figure 9B) which implies the presence of shallow crystalline intrusions. The absence of large-scale magnetic minima, reflecting hydrothermal alteration of magnetic minerals, implies the absence of hydrothermal fluids. The gravity data also support this argument as the gravity minima over the Gedemsa caldera (Figures 5, 8A, B) suggest that the deep intrusion beneath Gedemsa volcanic system (Figures 11, 12) does not supply enough or any heat to support shallow magma chambers near Gedemsa. This hypothesis supports the idea that this region is an extinct/or dormant volcano (Thrall, 1973).

6 Conclusion

Interpretation of gravity and magnetic data in conjunction with previous geological, seismicity, and magnetotelluric analysis have provided insights into the subsurface volcanic network and the role of subsurface structures on the occurrence of geothermal resources in the Tulu Moye geothermal prospect (TMGP), central MER. The main findings are:

1. Interpretation of gravity and magnetic anomaly maps combined with geological, seismicity, and magnetotelluric studies indicate the occurrence of potential geothermal heat sources beneath the Tulu Moye volcano.
2. Gravity and magnetic anomaly maps in conjunction with 2D gravity model and 3D geologic interpretation suggest that there are upper crustal dense mafic intrusions under each caldera (Tulu Moye, Bora and Bericha). However, our interpretation along with recent magnetotelluric surveys suggests that only the intrusion beneath Tulu Moye is currently magmatically active and includes partial melt, consistent with it being a primary heat source for the geothermal system.
3. Magnetic minima following the SVR are probably related to hydrothermal alteration of magnetic minerals and circular gravity maxima over the SVR combined with surface thermal manifestations are indicators of the presence of deeper geothermal resources.
4. Intersection of caldera features with NNE-SSW and NW-SE trending lineaments determined by the magnetic and gravity derivative maps correlated well with the pattern of surface faulting and hydrothermal manifestations. This suggests that the surface fault pattern continues to depth with the intersection between caldera and rift-related faults providing high permeability that controls vertical and lateral hydrothermal fluid flow and results in a large geothermal system in the region.

Data availability statement

Publicly available datasets were analyzed in this study. This data can be found here: https://bgi.obs-mip.fr/data-products/grids-and-models/modele-global-ggmplus2013/.

Author contributions

WN and AA framed the conceptualization and methodology, and participated in data processing and curation followed by writing-original draft preparation. KM, DK, and ZD have participated in visualization, investigation and supervision as well as software processing and validation. With all coauthors, YM, AM, GC, and EY edit, re-write and review the final manuscript. All authors contributed to the article and approved the submitted version.

Funding

Natural Environment Research Council under NERC Grant NE/L013932/1 Ministero dell'Università e della Ricerca (MiUR) through PRIN grant 2017P9AT72.

Acknowledgments

We thank the International Gravimetric Bureau and the Geological Survey of Ethiopia for providing gravity and magnetic data respectively to use in this study. Moreover, we are thankful to Reykjavik Geothermal for supplying the magnetometer, transport, and camp services for our fieldwork.

Conflict of interest

The authors declare that the research was conducted in the absence of any commercial or financial relationships that could be construed as a potential conflict of interest.

Publisher's note

All claims expressed in this article are solely those of the authors and do not necessarily represent those of their affiliated organizations, or those of the publisher, the editors and the reviewers. Any product that may be evaluated in this article, or claim that may be made by its manufacturer, is not guaranteed or endorsed by the publisher.

References

Abebe, B., Acocella, V., Korme, T., and Ayalew, D. (2007). Quaternary faulting and volcanism in the main Ethiopian rift. *J. Afr. Earth Sci.* 48, 115–124. doi:10.1016/j.jafrearsci.2006.10.005

Abebe, T., Balestrieri, M. L., and Bigazzi, G. (2010). The central main Ethiopian rift is younger than 8 Ma: Confirmation through apatite fission-track thermochronology. *Terra nova.* 22, 470–476. doi:10.1111/j.1365-3121.2010.00968.x

Abebe, T., Manetti, P., Bonini, M., Corti, G., Innocenti, F., Mazzarini, F., et al. (2005). *Geological map of the northern Main Ethiopian Rift and its implication for the volcano-tectonic evolution of the rift*. Colorado: Geological Society of America. doi:10.1130/2005042

Acocella, V., Cifelli, F., and Funiciello, R. (2001). The control of overburden thickness on resurgent domes: Insights from analogue models. *J. Volc. Geoth. Res.* 111, 137–153. doi:10.1016/s0377-0273(01)00224-4

Acocella, V., and Korme, T. (2002). Holocene extension direction along the main Ethiopian rift, east Africa. *Terra nova.* 14, 191–197. doi:10.1046/j.1365-3121.2002.00403.x

Acocella, V., Korme, T., Salvini, F., and Funiciello, R. (2002). Elliptic calderas in the Ethiopian rift: Control of pre-existing structures. *J. Volc. Geoth, Res.* 119, 189–203. doi:10.1016/s0377-0273(02)00342-6

Admasu, E., and Worku, S. (2015). Characterization of Quaternary extensional structures: Tulu Moye geothermal prospect, Ethiopia. *GRC Trans.* 39, 25–32.

Albino, F., and Biggs, J. (2021). Magmatic processes in the East African Rift System: Insights from a 2015– 2020 sentinel-1 InSAR survey. *Geochem. Geophys. Geosystems* 22 (3), e2020GC009488. doi:10.1029/2020gc009488

Alemu, A. (2020). *Geophysics: Principles, practices, and applications of geophysical methods to resource exploration and geohazard studies*. Addis Ababa: Aster Nega Publishing Enterprise, 500.

Ansari, A., and Alamdar, K. (2009). Reduction to the pole of magnetic anomalies using analytic signal. *World Appl. Sci. J.* 7, 405–409.

Bastow, I. D., Pilidou, S., Kendall, J. M., and Stuart, G. W. (2010). Melt induced seismic anisotropy and magma assisted rifting in Ethiopia: Evidence from surface waves. *Geochem. Geophys., Geosys.* 11, 05–11. doi:10.1029/2010gc003036

Beard, L. (2000). Detection and identification of north-south trending magnetic structures near the magnetic equator: Low latitude magnetic anomalies. *Geophys. Pros.* 48, 745–761. doi:10.1046/j.1365-2478.2000.00214.x

Benvenuti, M., Corti, G., Keir, D., and Sani, F. (2023). Transverse tectonics control on the late quaternary development of the central main Ethiopian rift. *Ital. J. Geosci.* 142, 42–56. doi:10.3301/IJG.2023.05

Biggs, J., Bastow, I. D., Keir, D., and Lewi, E. (2011). Pulses of deformation reveal frequently recurring shallow magmatic activity beneath the Main Ethiopian Rift. *Geochem. Geophys. Geosystems* 12 (9). doi:10.1029/2011gc003662

Blakely, R. J. (1995). *Potential theory in gravity and magnetic applications*. Cambridge: Cambridge University Press, 321.

Blakely, R. J., and Simpson, R. W. (1986). Approximating edges of source bodies from magnetic or gravity anomalies. *Geophysics* 51, 1494–1498. doi:10.1190/1.1442197

Boccaletti, M., Assefa, G., and Tortorici, L. (1992). The main Ethiopian rift: An example of oblique rifting. *Ann. Tect.* 6, 20–25.

Boccaletti, M., Bonini, M., Mazzuoli, R., Abebe, B., Piccardi, L., and Tortorici, L. (1998). Quaternary oblique extensional tectonics in the Ethiopian rift (horn of Africa). *Tectonophysics* 287, 97–116. doi:10.1016/s0040-1951(98)80063-2

Boccaletti, M., Mazzuoli, R., Bonini, M., Trua, T., and Abebe, B. (1999). Plio-quaternary volcanotectonic activity in the northern sector of the main Ethiopian rift: Relationships with oblique rifting. *J. Afr. Earth Sci.* 29, 679–698. doi:10.1016/s0899-5362(99)00124-4

Burnside, N., Montcoudiol, N., Becker, K., and Lewi, E. (2021). Geothermal energy resources in Ethiopia: Status review and insights from hydrochemistry of surface and groundwaters. *Wiley Interdiscip. Rev. Water* 8 (6), e1554. doi:10.1002/wat2.1554

Casey, M., Ebinger, C. J., Keir, D., Gloaguen, R., and Mohamad, F. (2006). Strain accommodation in transitional rifts: Extension by magma intrusion and faulting in Ethiopian rift magmatic segments. *Geol. Soc. Lond. Spec. Publ.* 259, 143–163. doi:10.1144/gsl.sp.2006.259.01.13

Cole, J. W., Milner, D. M., and Spinks, K. D. (2005). Calderas and caldera structures: A review. *Earth Sci. Rev.* 69, 1–26. doi:10.1016/j.earscirev.2004.06.004

Cornwell, D. G., Maguire, P. K. H., England, R. W., and Stuart, G. W. (2010). Imaging detailed crustal structure and magmatic intrusion across the Ethiopian Rift using a dense linear broadband array. *Geochem. Geophys. Geosystems* 11 (1), 2637. doi:10.1029/2009gc002637

Corti, G. (2009). Continental rift evolution: From rift initiation to incipient break-up in the Main Ethiopian Rift, East Africa. *Earth Sci. Rev.* 96, 1–53. doi:10.1016/j.earscirev.2009.06.005

Corti, G., Sani, F., Florio, A., Greenfield, T., Keir, D., Erbello, A., et al. (2020). Tectonics of the asela-langano margin, main Ethiopian rift (east Africa). *Tectonics* 39, e2020TC006075. doi:10.1029/2020tc006075

Coumans, J., and Stix, J. (2016). Caldera collapse at near-ridge seamounts: An experimental investigation. *Bull. Volcanol.* 78, 70. doi:10.1007/s00445-016-1065-9

Darge, Y. M., Hailu, B. T., Muluneh, A. A., and Kidane, T. (2019). Detection of geothermal anomalies using Landsat 8 TIRS data in Tulu Moye geothermal prospect, Main Ethiopian Rift. *Int. J. Appl. Earth Observation Geoinformation* 74, 16–26. doi:10.1016/j.jag.2018.08.027

Dentith, M., and Mudge, S. (2014). *Geophysics for the mineral exploration geoscientist*. New York: Cambridge University Press, 426.

Ebinger, C. J., and Casey, M. (2001). Continental breakup in magmatic provinces: An Ethiopian example. *Geol* 29, 527–530. doi:10.1130/0091-7613(2001)029<0527:cbimpa>2.0.co;2

Fontijn, K., McNamara, K., Zafu, A., Pyle, D., Dessalegn, F., Hutchison, W., et al. (2018). Contrasting styles of post-caldera volcanism along the Main Ethiopian Rift: Implications for contemporary volcanic hazards. *J. Volcanol. Geotherm. Res.* 356, 90–113. doi:10.1016/j.jvolgeores.2018.02.001

Greenfield, T., Keir, D., Kendall, J. M., and Ayele, A. (2019). Seismicity of the bora-tullu Moye volcanic field, 2016–2017. *Geochem. Geophys. Geosyst.* 20, 548–570. doi:10.1029/2018gc007648

Guàbrandsson, S., Eysteinsson, H., Mamo, T., Cervantes, C., and Gíslason, G. (2020). "Geology and conceptual model of the Tulu Moye geothermal project, Oromia, Ethiopia," in *Proceedings world geothermal congress 2020* (Iceland: Reykjavik), 8.

Haile, T., and Tamiru, A. (2012). The interference of a deep thermal system with a shallow aquifer: The case of sodere and gergedi thermal springs, main Ethiopian rift, Ethiopia. *Hydrogel* 20, 561–574. doi:10.1007/s10040-012-0832-8

Hersir, G. P., and Björnsson, A. (1991). *Geophysical exploration for geothermal resources: Principles and application*. Reykjavik: The united nations university.

Hinze, W. J., von Frese, R. R., and Saad, A. H. (2013). *Gravity and magnetic exploration: Principles, practices, and applications*. New York: Cambridge University Press, 550.

Hirt, C., Claessens, S. J., Fecher, T., Kuhun, M., Pail, R., and Rxer, M. (2013). New ultra high resolution picture of Earth's gravity field. *Geophys. Res. Let.* 140, 4279–4283. doi:10.1002/grl.50838

Holohan, E. P., Troll, V. R., Walter, T. R., Münn, S., McDonnell, S., and Shipton, Z. K. (2005). Elliptical calderas in active tectonic settings: An experimental approach. *J. Volcanol. Geotherm. Res.* 144 (1-4), 119–136. doi:10.1016/j.jvolgeores.2004.11.020

Hunt, J., Mather, T., and Pyle, D. (2020). Morphological comparison of distributed volcanic fields in the Main Ethiopian Rift using high-resolution digital elevation models. *J. Volc. Geoth. Res.* 393, 106732. doi:10.1016/j.jvolgeores.2019.106732

Hutchison, Pyle, W.,D., Mather, T. A., Yirgu, G., Biggs, J., Cohen, B. E., Barfod, N. B., et al. (2016). The eruptive history and magmatic evolution of Aluto volcano: New insights into silicic peralkaline volcanism in the Ethiopian rift. *J. Volcanol. Geotherm. Res.* 328, 9–33. doi:10.1016/j.jvolgeores.2016.09.010

Hutchison, W., Mather, T., Pyle, D., Biggs, J., and Yirgu, G. (2015). Structural controls on fluid pathways in an active rift System: A case study of the Aluto volcanic complex. *Geol. Soc. Am. Bull.* 8, 542–562. doi:10.1130/ges01119.1

Jacobsen, B. H. (1987). A case for upward continuation as a standard separation filter for potential-field maps. *Geophysics* 52, 1138–1148. doi:10.1190/1.1442378

Kahsay, L., and Yehualaw, Es. (2023). Tulu Moye geothermal operation project phase 1 GD1 and GD2 report. *Ethiop. Ministry Mines* 2023 Technical Report, 19.

Kassa, M., Alemu, A., and Muluneh, A. (2022). Determination of Conrad and Curie point depth relationship with the variations in lithospheric structure, geothermal gradient and heat flow beneath the central main Ethiopian rift. *Heliyon* 8 (11), e11735. doi:10.1016/j.heliyon.2022.e11735

Kebede, B., Pagli, C., Sigmundsson, F., Keir, D., LaRosa, A., and Gudbrandsson, S. (2023). Constraints on ground deformation processes at the Tulu Moye volcanic complex, Main Ethiopian Rift. *J. Volcanol. Geotherm. Res.* 438, 107810. doi:10.1016/j.jvolgeores.2023.107810

Kebede, B. (2021). The relationship between the Tulu Moye geothermal system, the ziway–asela area and the tectonic structure of the Ethiopian rift. MS Thesis. Iceland: Univ. of Iceland.

Kebede, H., Alemu, A., and Fisseha, S. (2020). Upward continuation and polynomial trend analysis as a gravity data decomposition, case study at Ziway-Shala basin, central Main Ethiopian rift. *Heliyon* 6 (1), e03292. doi:10.1016/j.heliyon.2020.e03292

Kebede, H., Alemu, A., and Mickus, K. (2022). Magnetic anomaly patterns and volcano-tectonic features associated with geothermal prospect areas in the Ziway-Shala Lakes Basin, Central Main Ethiopian Rift. *Geothermics* 105, 102484. doi:10.1016/j.geothermics.2022.102484

Keir, D., Ebinger, C. J., Stuart, G. W., Daly, E., and Ayele, A. (2006). Strain accommodation by magmatism and faulting as rifting proceeds to breakup: Seismicity of the northern Ethiopian rift. *J. Geophys. Res. Solid Earth* 111 (B5), 3748. doi:10.1029/2005jb003748

Kendall, J. M., Pilidou, S., Keir, D., Bastow, I. D., Stuart, G. W., and Ayele, A. (2006). Mantle upwellings, melt migration and the rifting of Africa: Insights from seismic anisotropy. *Geol. Soc. Lond. Spec. Publ.* 259, 55–72. doi:10.1144/gsl.sp.2006.259.01.06

Keranen, K., Klemperer, S. L., and Gloaguen, R.the EAGLE working group (2004). Three dimensional seismic imaging of a protoridge axis in the Main Ethiopian rift. *Geol* 32, 949–952. doi:10.1130/g20737.1

King, D., and Metcalfe, E. (2013). "Rift zones as a case study for advancing geothermal occurrence models," in *Proceedings thirty-eighth workshop on geothermal reservoir engineering* (Stanford, California: SGP-TR), 11–13.

Kurtz, T., Gloaguen, R., Ebinger, C., Casey, M., and Abebe, B. (2007). Deformation distribution and type in the main Ethiopian rift (MER): A remote sensing study. *J. Afr. Earth Sci.* 48, 100–114. doi:10.1016/j.jafrearsci.2006.10.008

Lewi, E., Keir, D., Birhanu, Y., Blundy, J., Stuart, G., Wright, T., et al. (2016). Use of a high-precision gravity survey to understand the formation of oceanic crust and the role of melt at the southern Red Sea rift in Afar, Ethiopia. *Geol. Soc. Lond. Spec. Publ.* 420, 165–180. doi:10.1144/sp420.13

Li, X. (2006). Understanding 3D analytic signal amplitude. *Geophysics* 71, L13–L16. doi:10.1190/1.2184367

Mackenzie, G. D., Thybo, H., and Maguire, P. K. H. (2005). Crustal velocity structure across the main Ethiopian rift: Results from two-dimensional wide-angle seismic modelling. *Geophys. J. Int.* 162 (3), 994–1006. doi:10.1111/j.1365-246x.2005.02710.x

Mackie, R., and Cunningham, C. (1982). Density and magnetic susceptibility measurements of igneous rocks from the Marysville volcanic field, west-central Utah. USGS open-file report 82-892.

Maestrelli, D., Bonini, M., Corti, G., Del Ventisette, C., Moratti, G., and Montanari, D. (2021b). A database of laboratory analogue models of caldera collapse testing the role of inherited structures. *Front. Earth Sci.* 9. doi:10.3389/feart.2021.618258

Maestrelli, D., Corti, G., Bonini, M., Montanari, D., and Sani, F. (2021a). Caldera collapse and tectonics along the main Ethiopian rift: Reviewing possible relationships. *Sci. Planète* 353, 91–109. doi:10.5802/crgeos.63

Maguire, P. K. H., Keller, G. R., Klemperer, S. L., Mackenzie, G. D., Keranen, K., Harder, S., et al. (2006). Crustal structure of the northern Main Ethiopian Rift from the EAGLE controlled-source survey; a snapshot of incipient lithospheric break-up. *Geol. Soc. Lond. Spec. Publ.* 259 (1), 269–292. doi:10.1144/gsl.sp.2006.259.01.21

Mammo, T. (2010). Delineation of sub-basalt sedimentary basins in hydrocarbon exploration in north Ethiopia. *Mar. Pet. Geol.* 27, 895–908. doi:10.1016/j.marpetgeo.2009.12.009

Mazzarini, F., Abebe, T., Innocent, F., Manetti, P., and Pareschi, M. T. (1999). Geology of the Debre Zeyit area (Ethiopia) (with a geological map at scale 1:100.000). *Acta Vulcanol.* 11, 131–141.

Mickus, K., Kennedy, W., and Aiken, C. (1992). Regional-residual gravity anomaly separation using the minimum-curvature technique. *Geophysics* 56, 279–283. doi:10.1190/1.1443041

Mickus, K., Ketsela, K., Keller, G., and Oluma, B. (2009). Three-dimensional gravity modeling of the magmatic segments within the Main Ethiopian Rift. *Tanzanian J. Earth Sci.* 1, 96–106. doi:10.13140/RG.2.1.3879.9524

Mickus, K., Tadesse, K., Keller, G. R., and Oluma, B. (2007). Gravity analysis of the main Ethiopian rift. *J. Afr. Earth Sci.* 48, 59–69. doi:10.1016/j.jafrearsci.2007.02.008

Muhabaw, Y., Muluneh, A. A., Nugsse, K., Gebru, E. F., and Kidane, T. (2022). Paleomagnetism of Gedemsa magmatic segment, main Ethiopian rift: Implication for clockwise rotation of the segment in the early pleistocene. *Tectonophysics* 838, 229475. doi:10.1016/j.tecto.2022.229475

Mulugeta, B., Fujimitsu, Y., Nishijima, J., and Saibi, H. (2021). Interpretation of gravity data to delineate the subsurface structures and reservoir geometry of the Aluto–Langano geothermal field, Ethiopia. *Geothermics* 94, 102093. doi:10.1016/j.geothermics.2021.102093

Nigussie, W., Alemu, A., Mickus, K., and Muluneh, A. (2022a). Structure of the upper crust at the axis segmentation of rift evolution, Case study of the Gedemsa magmatic segment, Main Ethiopian Rift. *J. Afri. Earth Sci.* 190, 1–11. doi:10.1016/j.jafrearsci.2022.104523

Nigussie, W., Alemu, A., Muluneh, A. A., Mickus, K., Muhabaw, Y., and Ballay, M. (2022b). Formation of magmatic segments within the aluto-gedemsa area, main Ethiopian rift. *Ital. J. Geosci.* 142 (1), 28–41. doi:10.3301/IJG.2023.02

Nigussie, W., Mickus, K., Keir, D., Alemu, A., Muhabaw, Y., Muluneh, A. A., et al. (2023). Subsurface structure of magmatic segments during continental breakup: Perspectives from a gravity data analysis along the Main Ethiopian Rift. *Front. earth Sci.* 10, 92759. doi:10.3389/feart.2022.1092759

Omenda, P. (1998). "The geothermal activity of the East African Rift," in *Short course IV on exploration for geothermal resources* (Lake Naivasha, Kenya: UNU-GTP), 1–12.

Peccerillo, A., Barberio, M. R., Yirgu, G., Ayalew, D., Barbieri, M. W. U. T. W., and Wu, T. W. (2003). Relationships between mafic and peralkaline silicic magmatism in continental rift settings: A petrological, geochemical and isotopic study of the Gedemsa volcano, central Ethiopian rift. *J. Petrology* 44 (11), 2003–2032. doi:10.1093/petrology/egg068

Phillips, J. (2001). Designing matched bandpass and azimuthal filters for the separation of potential-field anomalies by source region and source type. *Aust. Soc. Explor. Geophys.* 4, 1–4. doi:10.1071/aseg2001ab110

Phillips, J. (2000). "Locating magnetic contacts: A comparison of horizontal gradient, analytic signal and local wavenumber methods," in *Soc. of Explor. Geophys. extended abstracts with programs* (Oklahoma: SEG). doi:10.1190/1.1816078

Reinsch, T., Dobson, P., Asanuma, H., Huenges, E., Poletto, F., and Sanjuan, B. (2017). Utilizing geothermal systems: A review of past ventures and ongoing research activities. *Geotherm. Energy* 5, 1–5. doi:10.1186/s40517-017-0075-y

Ruch, J., Acocella, V., Geshi, N., Nobile, A., and Corbi, F. (2012). Kinematic analysis of vertical collapse on volcanoes using experimental models time series. *J. Geophys. Res.* 117, B07301. doi:10.1029/2012jb009229

Samrock, F., Grayver, A. V., Bachmann, O., Karakas, O., and Saar, M. O. (2021). Integrated magnetotelluric and petrological analysis of felsic magma reservoirs: Insights from Ethiopian rift volcanoes. *Earth Planet Sci. Lett.* 559, 116765. doi:10.1016/j.epsl.2021.116765

Samrock, F., Grayver, A. V., Eysteinsson, H., and Saar, M. O. (2018). Magnetotelluric image of transcrustal magmatic system beneath the Tullu Moye geothermal prospect in the Ethiopian Rift. *Geophys. Res. Lett.* 45, 12–847. doi:10.1029/2018GL080333

Samrock, F., Kuvshinov, A., Bakker, J., Jackson, A., and Fisseha, S. (2015). 3-D analysis and interpretation of magnetotelluric data from the Aluto-Langano geothermal field, Ethiopia. *Geophys. J. Int.* 202, 1923–1948. doi:10.1093/gji/ggv270

Scandone, R. (1990). Chaotic collapse of calderas. *J. Volc. Geoth. Res.* 42, 285–302. doi:10.1016/0377-0273(90)90005-z

Tadesse, A. Z., Fontijn, K., Caricchi, L., Bégué, F., Gudbrandsson, S., Smith, V. C., et al. (2023). Pre-eruptive storage conditions and magmatic evolution of the Bora-Baricha-Tullu Moye volcanic system, Main Ethiopian Rift. *Lithos* 442-443, 107088. doi:10.1016/j.lithos.2023.107088

Teklemariam, M. (2011). "Overview of geothermal resource exploration and development in the East African rift system," in *Short course VI on exploration for geothermal resources* (Kenya: UNU-GTP, GDC).

Telford, W. S., Geldart, L. P., and Sheriff, R. E. (1990). *Applied Geophysics*. second ed. Cambridge: Cambridge University Press.

Thrall, R. (1973). Gedemsa caldera, Ethiopia. *Cent. Astrophysics* 280, 412–426.

Troll, V., Walter, T., and Schmincke, H. (2002). Cyclic caldera collapse: Piston or piecemeal subsidence? Field and experimental evidence. *Geology* 30, 135–138. doi:10.1130/0091-7613(2002)030<0135:cccpop>2.0.co;2

Varet, J., and Birba, E. (2018). "Tulu Moye geothermal project (oromia, Ethiopia)," in *Proceedings of the 7th African rift geothermal conf* (Kigali, Rwanda: African Rift Geothermal), 231–235.

Varet, J., Omenda, P., and Birba, E. (2020). "Giant geothermal sites along the East Africa Rift System (EARS): The determinant volcano-structural setting," in *Proceedings, 8th African Rift geothermal conference* (Nairobi, Kenya: African Rift Geothermal), pp16.

Wadge, G., Biggs, J., Lloyd, R., and Kendall, J. (2016). Historical volcanism and the state of stress in the East African Rift System. *Front. Earth Sci.* 4, 1–24. doi:10.3389/feart.2016.00086

Wilks, M., Kendall, J. M., Nowacki, A., Biggs, J., Wookey, J., Birhanu, Y., et al. (2017). Seismicity associated with magmatism, faulting, and hydrothermal circulation at Aluto Volcano, Main Ethiopian Rift. *J. Volcanol. Geotherm. Res.* 340, 52–67. doi:10.1016/j.jvolgeores.2017.04.003

Woldegebrel, G., Aronson, J. L., and Walter, R. C. (1990). Geology, geochronology, and rift basin development in the central sector of the Main Ethiopia Rift. *Geol. Soc. Am. Bull.* 102, 439–458. doi:10.1130/0016-7606(1990)102<0439:ggarbd>2.3.co;2

Wolfenden, E., Ebinger, C., Yirgu, G., Deino, A., and Ayalew, D. (2004). Evolution of the northern main Ethiopian rift: Birth of a triple junction. *Earth Planet. Sci. Let.* 224, 213–228. doi:10.1016/j.epsl.2004.04.022

frontiers | Frontiers in Earth Science

TYPE Original Research
PUBLISHED 31 August 2023
DOI 10.3389/feart.2023.1214828

OPEN ACCESS

EDITED BY
Henglei Zhang,
China University of Geosciences Wuhan, China

REVIEWED BY
Chong Zhang,
Chinese Academy of Geological Sciences, China
Natasha Stanton,
Rio de Janeiro State University, Brazil

*CORRESPONDENCE
Denise Silva de Moura,
denisemoura@outlook.com

†These authors share first authorship

RECEIVED 30 April 2023
ACCEPTED 11 August 2023
PUBLISHED 31 August 2023

CITATION
Moura DS and Marangoni YR (2023), Lithosphere density structure of southeastern South America sedimentary basins from the analysis of residual gravity anomalies.
Front. Earth Sci. 11:1214828.
doi: 10.3389/feart.2023.1214828

Lithosphere density structure of southeastern South America sedimentary basins from the analysis of residual gravity anomalies

Denise Silva de Moura*† and Yára Regina Marangoni†

Department of Geophysics, Institute of Astronomy, Geophysics and Atmospheric Sciences, University of São Paulo, São Paulo, Brazil

We conduct a gravity study of the lithosphere beneath three large sedimentary basins in southeastern South America: Paraná, Chaco-Paraná, and Pantanal. We compile a massive gravity database and estimate the free-air and Bouguer gravity anomalies, resulting in a novel complete Bouguer anomaly map for the study area. To discern the influence of crustal loads with known lithologies, including sediments, basalts, and topography variations of the Moho discontinuity, we calculate their gravity effects and subsequently remove them from the complete Bouguer anomaly, leading to the development of our residual Bouguer anomaly map. This map highlights unknown anomalous masses within the lithosphere. To aid in the interpretation of these residual anomalies, we perform a 2D forward modeling. Based on our results, we propose new boundaries for the Paranapanema block and the Luiz Alves craton. Additionally, we propose that the Ponta Grossa swarm dike has a more substantial impact on the crust and lithosphere than previously considered, and delimit the region of influence of this magmatism in the lithosphere. Moreover, tectonic features such as the São Francisco paleocontinent and the Rio de La Plata craton appear to be associated with negative residual Bouguer anomaly regions. Furthermore, we identify and emphasize the significance of the Western Paraná Suture, which acts as a demarcation between the Paraná Basin region and the Pantanal and Chaco-Paraná basins. Remarkably, this suture appears to play a more important role in shaping the density structure of the southwest of South America than the age and tectonic history of the sedimentary basins.

KEYWORDS

Paraná basin, Chaco-Paraná basin, Pantanal basin, gravity corrections, Bouguer anomaly, forward modeling, lithosphere density structure

1 Introduction

The South American platform is the relatively stable Precambrian portion of South America bounded by the Andean orogeny and the Patagonian block (Heilbron et al., 2017), which consists of a mosaic of interconnected Archean and Proterozoic cratonic nuclei interspersed with mobile belts (Brito Neves and Fuck, 2014). Many of these mobile belts were formed during the Brasiliano collage, a series of Neoproterozoic tectonic events that contributed to the amalgamation of Gondwana (Brito Neves et al., 2014).

Despite its geological significance, studying the South American platform poses challenges due to the depths of the sedimentary layers, which can reach up to 6 km and

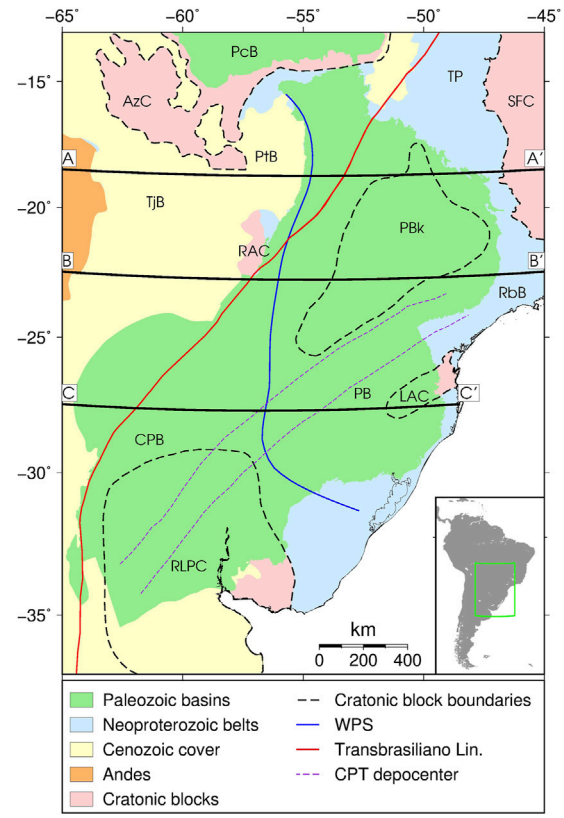

FIGURE 1
Tectonic map of the study area. AzC: Amazonian craton, PcB: Parecis basin, PtB: Pantanal basin, TjB: Tarija basin, RAC: Rio Apa craton, TP: Tocantins province, SFC: São Francisco craton, PBk: Paranapanema block, RbB: Ribeira belt, PB: Paraná basin, CPB: Chaco-Paraná basin, LAC: Luiz Alves craton, RLPC: Rio de La Plata craton (contours by Cordani et al., 2016); WPS: Western Paraná Suture (Dragone et al., 2021); CPT: Central Paranaense trough (Veroslavsky et al., 2021). The three profiles are the same as in Figure 7.

7 km in the Chaco-Paraná and Paraná basins, respectively, overlaying the crystalline basement. However, geophysical methods have been employed to overcome these challenges, leading to new insights into the density structure beneath the southern portion of the South American platform. Among these methods, gravity and geoid anomalies have proven successful in characterizing tectonic structures within the region (Ussami and Molina, 1999; Mariani et al., 2013; Chaves et al., 2016; Dragone et al., 2017). Additionally, seismic tomography has played a crucial role in providing velocity distributions that are representative of the lithosphere (Feng et al., 2007; Rocha et al., 2019a; Affonso et al., 2021; Ciardelli et al., 2022; Nascimento et al., 2022), refining our understanding of the tectonic framework in the area.

This study provides new insights into the major density structure of the Southeast region of the South American lithosphere, encompassing the Paraná, Chaco-Paraná, and Pantanal basins. Utilizing new free-air and complete Bouguer anomaly maps, along with a Bouguer residual model accounting for gravity effects of known masses and interfaces, we aim to reevaluate known lithosphere structures from literature and identify potential unknown density anomalies linked to unknown tectonic features or those proposed by other geophysical methods.

2 Study area

The study area focuses on the southern part of the South American platform, an extensive area covering approximately five million km^2. This region is predominantly covered by sedimentary basins, with particular emphasis on the Paleozoic Paraná and Chaco-Paraná basins (PB and CPB in Figure 1). These two basins share similarities in terms of sedimentary composition and history but exhibit differences related to the physical properties of their lithospheres (Dragone et al., 2017). Additionally, our investigation includes the Pantanal basin (PtB in Figure 1), a Quaternary deposit located to the west of the Paraná basin, which presents a shallower sedimentary layer of about 500 m (Ussami et al., 1999; Assine et al., 2016). The objective is to explore whether significant density disparities exist when comparing this basin with the lithosphere beneath the Paleozoic basins.

The Paraná and Chaco-Paraná intracratonic basins share a similar tectonic evolution (Milani et al., 1998). Due to the thick sedimentary package of approximately 7 km (Milani et al., 2007), the age and composition of their basement are difficult to constrain and are still subjects of study. In the Paraná basin, the oldest sedimentary sequence is Ordovician (Milani, 2004; Milani et al., 2007), while in the Chaco-Paraná basin, it is Devonian (Veroslavsky et al., 2021 and references therein). The Pantanal basin, on the other hand, developed during the Quaternary period after the Andean reactivation approximately 2.5 million years ago (Ussami et al., 1999; Assine and Soares, 2004). The basement of the Pantanal basin is believed to be associated with the Neoproterozoic terranes of the Paraguay fold thrust belt (Ussami et al., 1999).

Among the three basins, the Paraná basin has been the subject of the most extensive study. Gravity and seismological data have revealed a heterogeneous lithosphere resulting from different geological scenarios for the basement. Some researchers have proposed the presence of a single cratonic nucleus, with different suggested positions and boundaries (e.g., Cordani, 1984; Mantovani and Brito Neves, 2005; Affonso et al., 2021). Milani and Ramos (1998) proposed that the basement consists of a few blocks or a nucleus altered by a few events (Milani et al., 1998). Zalán et al. (1990), Assine et al. (1998), and Milani et al. (2007) proposed that events following the Brasiliano-Pan-African orogenic cycle have influenced the lithosphere in the region. The Paraná-Etendeka Magmatic Province adds complexity to the tectonic history of the region, a Cretaceous magmatism in which the extrusive part in Brazil is named Serra Geral Formation (Frank et al., 2009).

Verozlavsky et al. (2021) presented a revised tectono-sedimentary evolution model for the Chaco-Paraná basin. They divided the basin's basement into three units based on age: the Archean-Proterozoic Rio de La Plata craton, the Nico-Pérez terrane to the west, and the Paleozoic Dom Feliciano belt to the east. According to their classification, the southern part of the study area predominantly consists of Archean-Proterozoic terranes, along with a younger coastal orogenic belt. They proposed an NNE-SSW depocenter zone, known as the Central Paranaense Trough (CPT in Figure 1), spanning 600 km and bounded by crustal faults, which divides the Paraná and the Chaco-Paraná basins into the southern and northern regions.

Ussami et al. (1999), relying on gravity data, seismic sections, and boreholes, suggest that the Pantanal basin formed as an uplift and flexural extension of the Paraguay fold belt, which constitutes its basement. The seismic sections reveal Cenozoic fragments of limestones and sandstones over the faulted basement. The origin of the Pantanal basin, associated with the reactivation of the Andes

approximately 2.5 million years ago, differs from the long tectono-sedimentary history spanning from the Ordovician to the Neogene observed in the Paraná and Chaco-Paraná basins.

(Dragone et al. 2017; Dragone et al. 2021) proposed an evolutionary model for the three basins. Using gravity and magnetotelluric data, they suggested the existence of a suture or shear zone named the Western Paraná Suture (WPS in Figure 1) between the lithospheres of the Paraná basin and the surrounding Chaco-Paraná and Pantanal basins. According to their model, the lithosphere of the Paraná basin may result from the accommodation of several cratonic nuclei along an older suture zone. They propose that the lithosphere beneath the Pantanal basin is composed of the Rio Apa craton, while the lithosphere beneath the Chaco-Paraná basin by the Rio de La Plata and Rio Tebicuary cratons.

3 Materials and methods

3.1 Ground data

We collected a total of 81,078 ground gravity stations from different databases. These stations included 66,707 points from the Potential Methods Lab at the Institute of Astronomy, Geophysics, and Atmospheric Sciences of the University of São Paulo, 6,860 points from the Topography and Geodesy Lab at the School of Engineering of the University of São Paulo, most of which were unpublished, and 7,511 points from the Instituto Geográfico Nacional in Argentina (Figure 2). These data were collected from 1950 until the present.

The measurement of orthometric heights for the gravity stations relied on several methodologies over time, which implies different data precision. Before the 1990s, common approaches included the use of benchmarks with centimeter precision, barometric leveling with precision ranging from 1 to 3 m, and geometric leveling with centimeter precision. Geometric leveling is still employed in detailed surveys for mineral prospecting in Brazil. The introduction of GPS in the late 1990s popularized the use of double-frequency GPS for altitude surveys. It is important to note that GPS height measurements are based on the WGS-84 system, providing geometric heights, while other measurements are referenced to mean sea level or the geoid. In Brazil, a common practice in gravity research is to transform geometric heights into orthometric heights using the Brazilian Continuous Monitoring GNSS System (RBMC—https://www.ibge.gov.br/en/geosciences/geodetic-positioning/geodetic-networks), maintained by the Brazilian Geography and Statistics Institute (IBGE).

The least accurate techniques for determining the heights and locations of some of our stations are the barometer and topographic maps, which have uncertainties of up to 3 and 200 m, respectively. Considering these values, along with a maximum gravimeter uncertainty of 0.01 mGal and negligible errors in the terrain correction model, the maximum uncertainty is 1.1 mGal for the free-air anomaly map and 1.5 mGal for the complete Bouguer anomaly map.

3.2 Database analysis and processing

The gravity acceleration measured on the Earth's surface is influenced by different factors, including equipment drift, Earth's tide, topography, and mass variation within the crust and mantle.

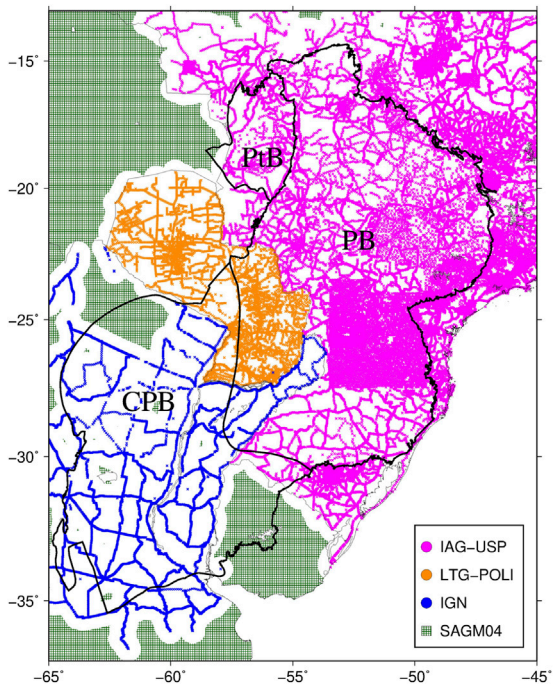

FIGURE 2
Gravity ground data distribution and model complement where no ground data is available. The black lines delimit the basin contours: Paraná basin (PB), Chaco-Paraná basin (CPB), and Pantanal basin (PtB). Notice the uneven distribution and the absence of data in some areas of the Paraná and the Chaco-Paraná basins.

To highlight mass variations, particularly in the crust and upper mantle, it is necessary to apply corrections, such as the free-air and Bouguer corrections. Then, to isolate anomalies stemming from the crust and upper mantle conventional mathematical methods are often employed, e.g., upward continuation and spectral analyses.

In our study, we adopt a different approach to isolate density anomalies in the crust and upper mantle. We first calculate the gravitational attraction of known masses, such as sedimentary deposits, large volcanic rock volumes, and density differences between crust and mantle rocks due to variations in the Moho discontinuity topography. These known contributions are then subtracted from the observed complete Bouguer anomaly map, yielding a residual map. We resume the entire procedure in a flowchart (Figure 3). We utilize GMT (Wessel et al., 2013) tools and Oasis Montaj software for many steps of the analysis.

In the first step, we calculate the normal gravity. As Brazilian institutions usually use the 1967 Normal Gravity Formula (IAG, 1971), we decided to recalculate all the anomalies whenever possible using it. In cases where gravity or height data are unavailable, we retain the Bouguer and free-air anomalies from the existing database. For the Bouguer correction, we adopt a density of 2,670 kg/m^3.

Next, in step 2, we evaluate the data and remove points that exhibit discrepancies in the topography compared to the ETOPO1 (Olson et al., 2014) model, as well as discrepancies in the free-air or Bouguer anomalies compared to the EGM08 (Pavlis et al., 2012) global model. The ETOPO1 model provides a precision of 1 arc-minute (30.9 m) for

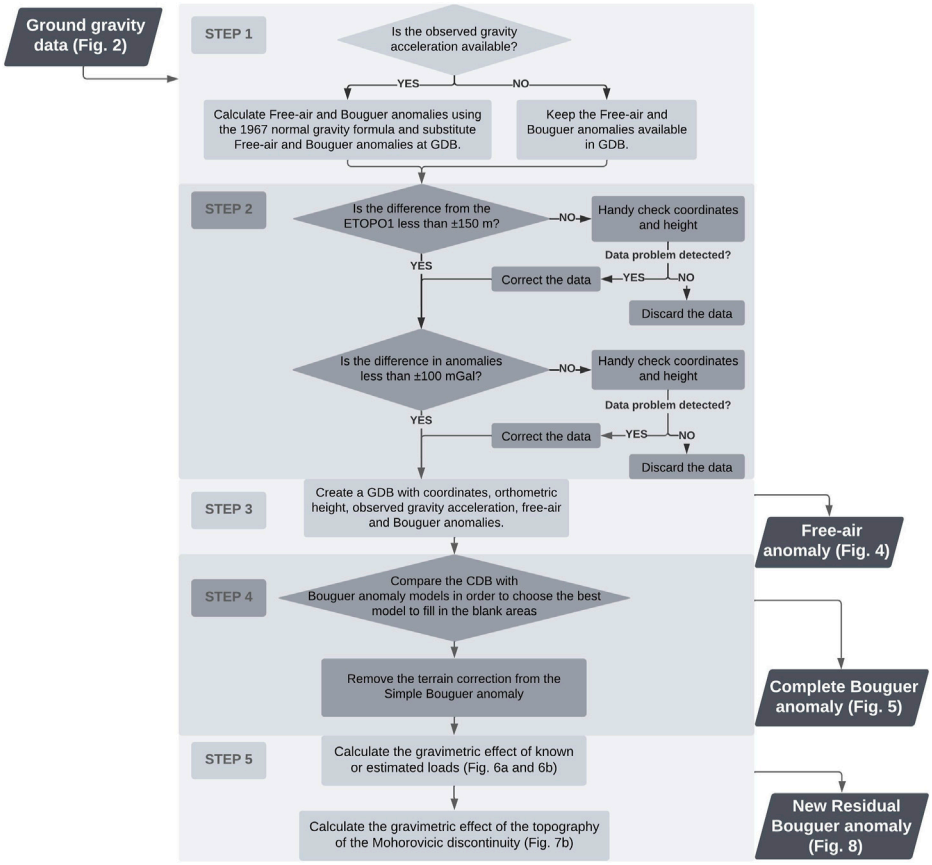

FIGURE 3
Flowchart description of database analysis and calculation of the gravimetric anomalies and components.

planar coordinates, and the altimetry precision varies depending on the adopted database (Olson et al., 2014). For continental topography, ETOPO1 employs the GLOBE model. Matos (2005) estimates that for Brazil the altimetry precision is 50 m comparing the GLOBE model with topographic charts. EGM08 has 5 arc-minute (154.5 m) precision for planar coordinates, 2 mGal precision for oceanic basins, and varied precision for continental areas. Using Figure 6A of Pavlis et al. (2012), a variation between −4 and +14 mGal is acceptable for the precision in the study area. Considering the ETOPO1 and EGM08 errors, we removed from our database the points with a discrepancy greater than 150 m or 100 mGals. This results in the removal of 70 data points, which corresponds to 0.09% of the data. These outliers are scattered across the study region and generate gravity anomalies that are not supported by global models. Additionally, these points exhibit differences that surpass our predetermined thresholds and significantly differ from neighboring measurements.

In step 3, after analyzing the data and calculating the anomalies, we generate a ground gravity database. From this database, we produce a new free-air anomaly map (Figure 4) with a 5′x5′ grid, only for the portion of the study area with ground data (Figure 2).

To fill areas without data, in step 4, we evaluate a Bouguer anomaly global model by comparing our ground data (Figure 2) with widely used gravity models for the region, namely, the Global Model EGM08 (Pavlis et al., 2012) and the South America Continental Model SAGM04 (Sá, 2004), both calculated by combining ground and satellite data. The difference between the ground data and the global gravity models varies from −30 to +30 mGal, also the zero mGal average difference is more common for the SAGM04 than for the EGM08 in the Brazilian and Argentinian data sets (Supplementary Figure S1), leading us to adopt the SAGM04 model to fill areas with no available data (Figure 2). Subsequently, we apply the terrain correction to the simple Bouguer anomaly using a 5′ x 5′ resolution grid, provided by personal correspondence with Dr. Ana Cristina de Oliveira Cancoro de Matos (Center of Geodesy Studies), which is an update of the terrain corrections presented in Matos (2005). Consequently, we generate a complete Bouguer anomaly grid for the southeast of the South American continent (Figure 5).

In step 5, we calculate the gravity effect of load masses in the crust using the Parker (1973) method with the routine from Chaves et al. (2016). To account for the effect of Moho discontinuity topography, we use the Nagy et al. (2000) formulation through the package Fatiando a Terra (Uieda et al., 2013). We adopt the CRUST1.0 (Laske et al., 2013) model for the geometries of the sediments, and Molina et al. (1988) for the geometries of the basalts. The density contrast adopted is −200 kg/m^3 for the sediments and +200 kg/m^3 for the basalts, around the average value of 2,670 kg/m^3 for the crust (Hinze, 2003), thus, we used density values of 2,470 kg/m^3 (Laske and Masters, 1997) and 2,870 kg/m^3 for sediments and basalts, respectively. Regarding the Moho topography, we adopt the RCM10 model (Chaves et al., 2016) and assume 37 km as the average depth of the crust, which is the average depth of the study area

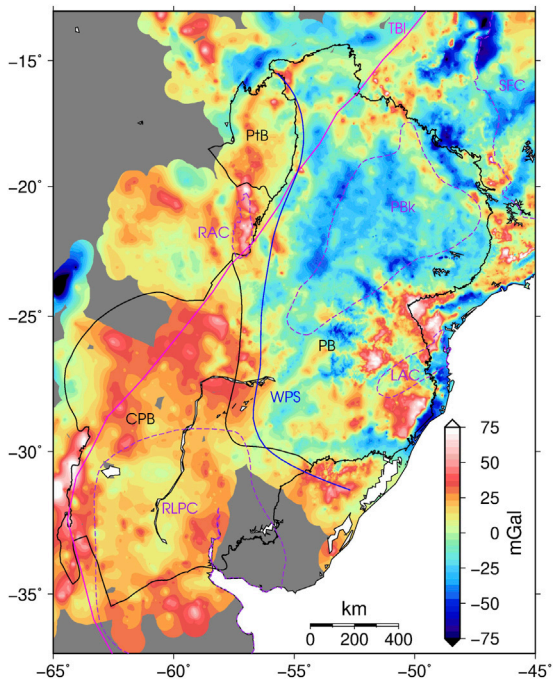

FIGURE 4
Free-air anomaly map of the database. The abbreviations are the same as in Figure 1.

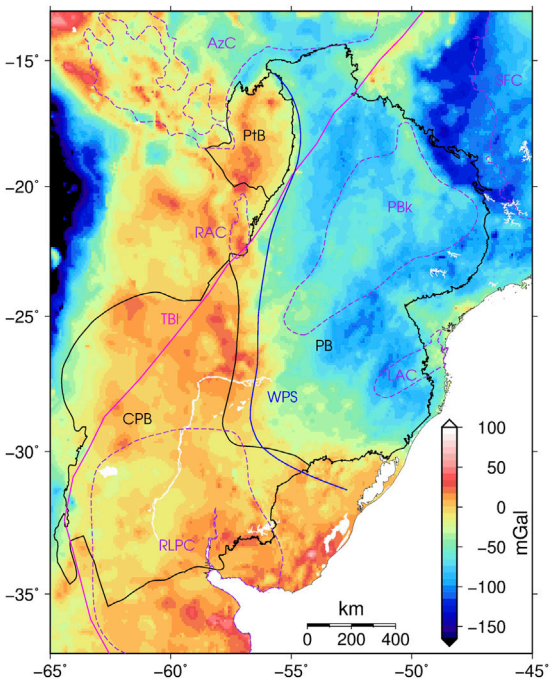

FIGURE 5
Complete Bouguer anomaly map of the database combined with the SAGM04 (Sá, 2004). The abbreviations are the same as in Figure 1.

calculated with the RCM10. The density contrast is determined based on the variable CRUST1.0 model values for the lower crust and mantle (Supplementary Figure S2). By subtracting the gravity effect of the known masses from the complete Bouguer anomaly, we obtain the residual Bouguer anomaly (Figure 8) grid with a resolution of 5′ x 5′, which highlights mass anomalies in the crust and upper mantle.

Finally, for aiding in the interpretation of the residual Bouguer anomaly map, we perform a forward 2D modeling along three profiles using GRAVMAG software (Pedley et al., 1993 updated by Jones, 2012), to estimate density variations. The lithosphere-asthenosphere boundary is determined using the global model EMC-CAM2016 (Priestley et al., 2018). We consider only lateral density variations in our model, without any vertical changes within each block, so we expect to have higher density contrasts in the real scenario. The contrast density values of the forward models do not directly stem from real geology structures, they are a simplification intended to aid the interpretation process.

4 Results

4.1 Free-air and complete Bouguer anomaly maps

The free-air anomaly map (Figure 4) exhibits positive anomalies in the Pantanal and Chaco-Paraná areas, while the Paraná basin shows a more heterogeneous pattern with negative anomalies. The magnitude of the anomalies ranges from 25 to 40 mGal at the borders of the Chaco-Paraná basin and is around 0 mGal at the center. In the center of the Paraná basin, the anomalies range from −25 to −50 mGal, whereas its eastern border displays strong positive anomalies ranging from 50 to 75 mGal. Additionally, a linear positive anomaly extends through the Pantanal basin in a north-south direction and enters the Rio Apa cratonic block to the south of the basin.

The complete Bouguer anomaly map (Figure 5) exhibits similar behavior to the free-air anomaly map. The Pantanal and Chaco-Paraná areas display a positive average anomaly, while the Paraná area shows a negative average anomaly varying by more than 100 mGals. The Bouguer anomalies in the Paraná basin are approximately 60 mGal more negative compared with the Chaco-Paraná and Pantanal basins, which exhibit Bouguer anomaly values close to 0 mGal.

Most of the tectonic features depicted in Figures 4, 5, as well as Figure 1, do not demonstrate a strong correspondence with the free-air and Bouguer anomalies. The Rio Apa craton exhibits a relatively better correspondence with the free-air anomaly, which may be attributed to the higher elevation of the area. The lowest free-air anomalies within the Paraná basin rest along the border of the Paranapanema block (Figure 4). In the complete Bouguer anomaly map (Figure 5), the Paranapanema block is characterized by anomalies of approximately −30 mGal anomaly, surrounded by a −110 mGal anomaly. The Western Paraná Suture, which delineates the boundary between the Pantanal and Chaco-Paraná basins and the Paraná basin, is also highlighted in the complete Bouguer anomaly, as a lineament that separates a positive anomaly in the west from a negative anomaly in the east.

4.2 Residual Bouguer anomaly map

With the aim of highlighting both known and potentially unmapped tectonic features, we derived a residual Bouguer anomaly map by

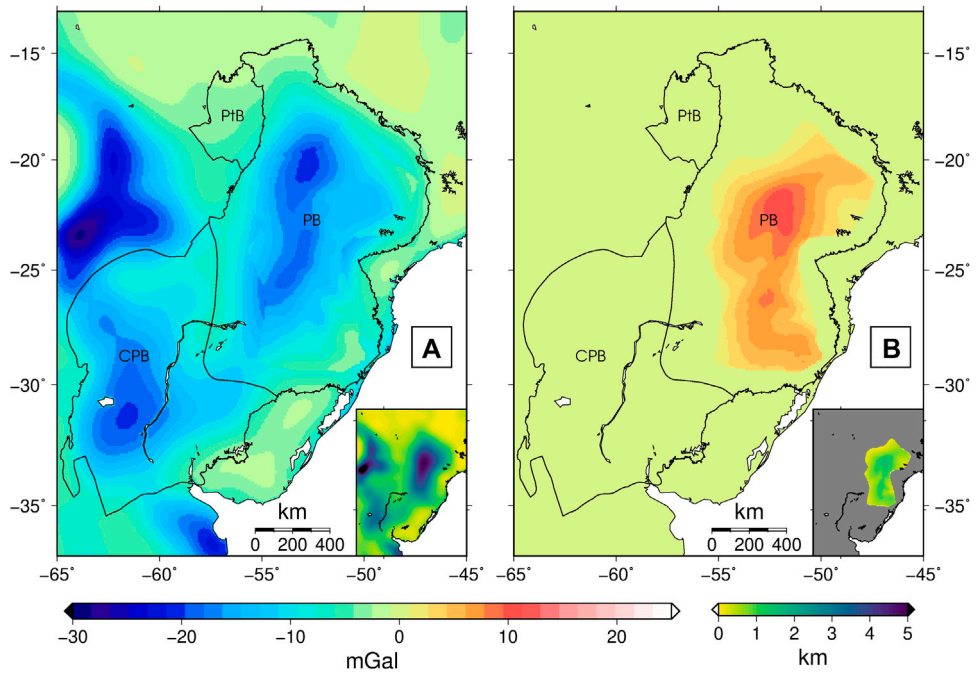

FIGURE 6
Gravity effect of **(A)** sedimentary basins infill, calculated with −200 kg/m^3 density contrast, and of **(B)** Serra Geral Fm. tholeiitic basalts, calculated with +200 kg/m^3 density contrast. PtB, Pantanal basin; PB, Paraná basin; CPB, Chaco-Paraná basin. On the inset of each map is exhibited the thickness of the layers, and the color scale is in km.

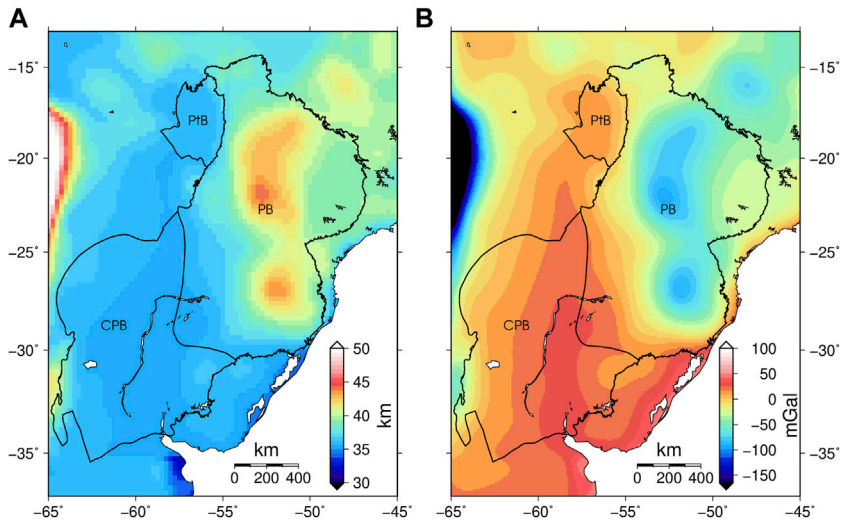

FIGURE 7
(A) Moho discontinuity depth from RCM10 model (Chaves et al., 2016), and **(B)** gravimetric component due to Moho discontinuity relief obtained using densities from CRUST 1.0 model (Laske et al., 2013). PtB, Pantanal basin; PB, Paraná basin; CPB, Chaco-Paraná basin.

subtracting the gravity effect of known masses from the complete Bouguer anomaly map. The gravity effects and thickness of sediments and basalts are presented in Figure 6, while Figure 7 displays the Moho depth and the gravity effect of the Moho topography.

Figure 6A shows that the most negative gravity anomaly, approximately −20 mGal, is associated with the depocenter of the Paraná and Chaco-Paraná basins. The Pantanal basin does not exhibit any significant effect on the sedimentary load. The basalts of Serra Geral Fm. are located in the Paraná basin, with a maximum thickness of 1,500 m, according to Molina et al. (1988). The estimated gravity anomaly resulting from the basalt load can reach values of up to +12 mGal at the center of the Paraná basin (Figure 6B), where the basalt thickness is maximum. Notice that the basalt load does not affect the Chaco-Paraná and Pantanal basins.

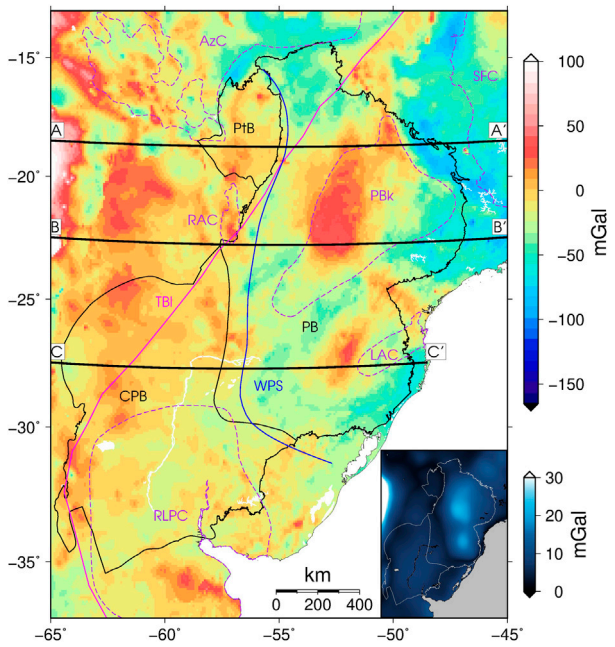

FIGURE 8
Residual Bouguer anomaly map after the correction for the gravimetric effect of density contrasts belonging to sediment infill, basalt thickness, and Moho discontinuity relief. The abbreviations are the same as in Figure 1. On the inset map is exhibited the maximum uncertainty of the residual Bouguer anomaly map, including the uncertainties of the complete Bouguer anomaly and of all the gravity effects, as described in the text.

The Moho discontinuity depth in the study area varies between 34 and 45 km, with an average value of 37 km (Figure 7A). Figure 7A emphasizes the greater crust thicknesses observed in the Paraná basin, where the maximum crustal thickness coincides with the maximum gravity anomaly and sediment/basalt loads. In contrast, the Chaco-Paraná basin exhibits a minimum crustal thickness of 36 km, unrelated to the maximum thickness of the sediments or basalts. The contrast densities between the lower crust and upper mantle, based on CRUST1.0, range from 250 to 550 kg/m³ (Supplementary Figure S2).

As expected, the calculated gravity effect (Figure 7B) reveals negative values in regions where the Moho depth exceeds the average value of 37 km. This negative effect is more pronounced in the Paraná basin, where the Moho is deeper compared with the Pantanal and Chaco-Paraná basins (Figure 7A). The Chaco-Paraná basin exhibits positive anomaly values, corresponding to a shallower Moho depth that is consistent with the Andes back-arc basin's location. The Pantanal basin is situated between two regions with low gravity effects, resulting in a gravimetric gradient of approximately 0.15 mGa l/km.

The residual Bouguer anomaly map (Figure 8) highlights mass distribution in the crust and upper mantle by excluding sediment and basalt distribution. To aid in the analyses of the residual Bouguer anomaly map, we estimate the uncertainties associated with each of the three components, considering a 10% uncertainty for the depths and density contrast values. A similar approach was employed by Chaves et al. (2016). The average uncertainties for the basins' areas are 2.2, 0.2, and 4.4 mGal for sediments, basalts, and Moho discontinuity, respectively. The maximum uncertainties, observed in the depocenter of the Paraná basin are 4.3, 2.1, and 14.5 mGal for sediments, basalts, and Moho discontinuity, respectively. The map depicting the maximum uncertainty for the study area is presented in Figure 8.

The maximum uncertainties of the residual Bouguer anomalies are higher in the central region of the Paraná basin, reaching approximately 17 mGal (Figure 8), while in other basins, they remain below 10 mGal. It is worth noting that these values represent the maximum uncertainties and that the average uncertainties are lower than 10 mGal for the entire study area, with the exception of the Andes region to the west, where uncertainties may impede the interpretation of the residual anomalies.

Paraná basin displays two positive anomalies of approximately +40 mGal surrounded by negative values ranging from −10 to −40 mGal. One of these anomalies coincides with the location of the Paranapanema block, which is also evident in the complete Bouguer anomaly map (Figure 5). The Pantanal and Chaco-Paraná basins exhibit similar residual Bouguer values, close to 0 mGal, with some regions displaying positive anomalies of less than 15 mGal (Figure 8). The Western Paraná Suture continues to mark an anomaly gradient between the west and east, albeit with a reduced variation compared with the complete Bouguer anomaly map.

4.3 Forward gravity modeling and possible anomalous mass distribution in the lithosphere

We conducted the modeling of the lithosphere density structure along three profiles (AA', BB', and CC' in Figure 8) to help with the interpretation of the Residual Bouguer anomaly map. The density modeling of the profiles helps us analyze the influence of the lithosphere, including the LAB depth. Removing the LAB topography from the residual Bouguer is complex due to the density variation in the asthenosphere being predominantly influenced by temperature rather than composition, which would introduce higher uncertainties in our model. That is why we prefer to realize the forward modeling to assist the analyses.

Considering the study area as a collage of distinctive lithospheres with varying ages, thicknesses, and densities, we assigned density values in the model based on lithospheric age, following the proposal by Poudjom-Djomani et al. (2001). Specifically, we adopt density values of −20 kg/m³ for the Archean lithosphere, between 0 and −10 kg/m³ for the Proterozoic lithospheres, and positive values for Phanerozoic lithospheres.

The forward model yielded a satisfactory fit between the model and data for the large-scale wavelength of the residual Bouguer anomaly. However, the small-scale anomalies were not fully fitted since our modeling approach employed large block dimensions without considering lateral and vertical variations within them. Across all profiles, density contrasts vary within the range of −20 and 25 kg/m³ constrained by the LAB. Notably, the highest density contrast value of 25 kg/m³ is observed in the profile AA', corresponding to the Andes region where the uncertainties in our model are higher (Figure 8). Thus, the major density contrast we can interpret is the 10 kg/m³ at the Paraná basin

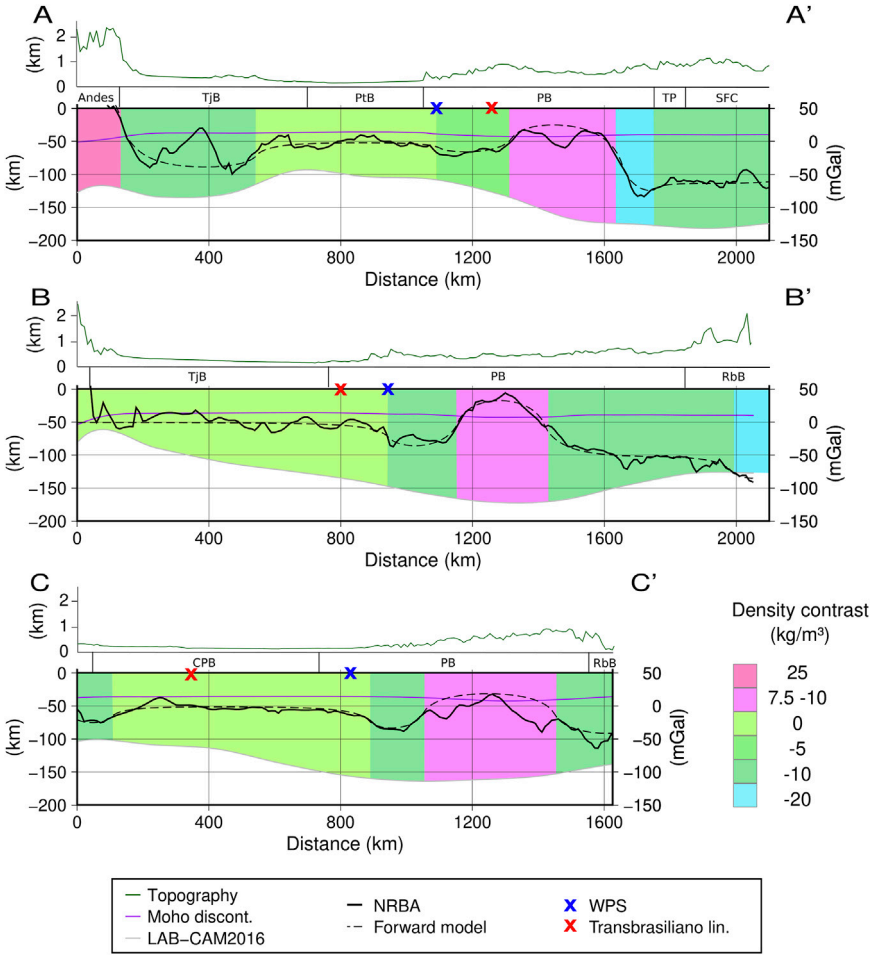

FIGURE 9
Density model for the three W-E profiles **(AA'–CC')**, whose locations are in Figure 8. Colors relate to age: blue for Archean/Proterozoic, green for Proterozoic, and pink for Phanerozoic. The topography is shown at the top of the profiles with a 30x vertical exaggeration to assist in the interpretation. TjB—Tarija basin, PtB–Pantanal basin, PB–Paraná basin, TP–Tocantins province, SFC–São Francisco craton, RbB–Ribeira belt, CPB–Chaco-Paraná basin.

(PB in Figure 9) at profiles AA' and CC', corresponding to the approximately 40 mGal residual Bouguer anomaly observed in Figure 8.

The lithosphere thickness and topography exhibit a correlation with the density contrasts, as depicted in Figure 9. The region of the Paraná basin (PB in Figure 9) displays the thickest lithosphere and most significant positive density contrasts. However, our simplified model did not incorporate the relative lows within these pink blocks (Profiles AA' and CC') as we aimed to maintain the blocks as simple and homogeneous as possible. The areas of the thinnest lithosphere generally exhibit minimal density contrasts and correspond to the lowest topography (indicated by the green line in Figure 9), but the thick lithosphere does not always correspond to high topography in the South American Platform.

The Western Paraná Suture (indicated by blue x in Figure 9) is located between regions with zero density contrast in the west and a more heterogeneous lithosphere region in the east, associated with the Paraná basin. The other lineament identified in the profiles (indicated by red x in Figure 9), the Transbrasiliano lineament, does not appear to be related to the boundaries of density blocks.

5 Discussion

5.1 The updated map of the complete Bouguer anomaly

The uncertainties associated with global gravity anomaly models in our study area have been recognized as a significant challenge (Mariani et al., 2013). To address this issue and improve the accuracy of our analysis, we have calculated a new complete Bouguer anomaly map for the study area. This map aims to reduce uncertainties and provide a more precise representation of the gravity anomalies in the region.

Our new map exhibits notable differences compared to the EGM08 model, particularly in the western part of the Paraná basin, where we have incorporated additional data from the Topography and Geodesy Lab at the School of Engineering of the University of São Paulo (depicted in orange in Figure 2). The discrepancies between our map and the EGM08 model can reach up to 60 mGal in certain regions. For a detailed comparison between our map, the EGM08 model, and the SAGM04 model, please refer to Supplementary Figure S3 in the supplementary file.

5.2 Tectonic features on the gravity anomaly maps

The free-air and complete Bouguer anomaly maps serve as valuable tools in revealing the tectonic structures within our study area. The gravity anomalies prominently highlight the Paranapanema block and the Western Paraná Suture, which aligns with our expectations, considering that both of these features were previously proposed and delineated using gravity anomaly maps (Mantovani and Brito Neves, 2005; Dragone et al., 2017).

Another noteworthy tectonic feature in the study area is the Rio Apa craton, whose free-air and Bouguer anomalies agree with the boundaries proposed by Cordani et al. (2016). However, it is important to exercise caution in attributing the positive free-air and Bouguer anomalies solely to the Rio Apa craton, as the literature lacks a consensus on its exact boundaries, which varies depending on geological (e.g., Cordani et al., 2016), gravity (e.g., Dragone et al., 2017), or seismological-based approaches (e.g., Affonso et al., 2021). Further investigations are needed to conclusively establish the correlation between these anomalies and the specific geological features in that particular location.

By removing the contributions of known masses from the gravity anomaly, we can isolate density variations associated with unknown masses in our residual Bouguer anomaly map. As a result, this map exhibits density variations that are either unrelated or only weakly related to factors such as sediments, exhumed magmatism of the Serra Geral formation, and Moho topography.

Notably, the sediments exhibit relatively higher amplitude anomalies in the Paraná basin compared to the basalts. This observation indicates that the positive anomalies identified in the complete Bouguer anomaly map cannot be solely attributed to the presence of massive volumes of basalts within the sedimentary column, coherent with previous findings by Mariani et al. (2013).

Furthermore, the anomalies of the Moho topography gravity effect show a range of approximately 100 mGal (Figure 7), which nearly corresponds to the full range of the complete Bouguer anomalies (Figure 5). Consequently, the removal of the Moho topography effect leads to significant changes in the gravity map, enabling the identification and better delineation of previously recognized as well as unrecognized anomalies.

Even after removing the known mass effects, noticeable differences persist between the west and east sides of the Western Paraná Suture, corroborating Dragone et al.'s (2017; 2021) hypothesis of a suture zone between two distinct lithospheres: a thinner lithosphere in the west compared to the eastern portion. This feature allows us to partition the study area into two distinct regions.

On the western side of the Western Paraná Suture, where the anomalies range between −20 and 60 mGal, except for the high positive anomaly at the east border of the AA' profile, a region with more than 30 mGal uncertainty (inset map in Figure 8), we observe a smoother variation of the anomalies, particularly in the Pantanal and Chaco-Paraná basins. In this same region, between the profiles AA' and BB', where the Tarija sedimentary basin is located (TjB in Figure 1), we identify a positive anomaly near its depocenter. Although this basin is beyond the scope of our specific study, the presence of this feature, not apparent in the complete Bouguer anomaly, offers a valuable opportunity for future investigations to better understand these anomalies and provide insights into the history and current architecture of the Tarija basin.

On the eastern side of the Western Paraná Suture, the density modeled profiles (Figure 9) generally exhibit a negative contrast density, except for four positive regions. Among these positive regions, three will be further presented and delimited in the next section, while the other is situated north of the Paraná basin, in the western part of the Tocantins province (TP in Figure 1). This positive anomaly encompasses the Goias Magmatic arc and the Araguaia/Paraguay belts of the Tocantins province. The negative anomaly in the same province is related to the Brasilia belt, which has been included in a paleocontinent named São Francisco paleocontinent (e.g., Rocha et al., 2019) or São Francisco-Congo when considering its African counterpart (e.g., Kuchenbecker and Barbuena, 2023).

Additionally, the negative anomaly south of the Paranapanema block seems to delineate an NNW-SSE lineament that goes until the Chaco-Paraná basin and could be related to the Central Paranaense Trough (CPT in Figure 1) since the region is the same. However, it is noteworthy that this fault-bounded depocenter proposed by Verozlavsky et al. (2021), primarily associated with the Chaco-Paraná basin, extends longer than the negative residual anomaly. Therefore, we hold back from proposing a definitive association based solely on our results.

5.3 Delimitations of lithospheric density features from the residual Bouguer anomaly

We delimited three positive anomalies, all situated within or on the border of the Paraná basin, as they exhibit larger amplitudes and may share a similar tectonic history. These anomalies are related to the Paranapanema block, the Luiz Alves craton, and the Ponta Grossa arch (indicated by red dashed contours in Figure 10). Previous studies have already delimited the first two features in similar positions. Mantovani and Brito Neves (2005) used gravity anomalies to propose and delineate the Paranapanema block, and Affonso et al. (2021) delimited the Luiz Alves craton based on a high-velocity anomaly in their P-wave seismic tomography. The third positive anomaly, located within the Ponta Grossa arch, has also been associated with a positive Bouguer anomaly by Santos et al. (2022).

The *Paranapanema block* is a well-studied tectonic feature within the Paraná basin, although its formation and nature remain a topic of debate. In the literature, there are hypotheses suggesting that it is a craton, with some proposing a single nucleus (Cordani, 1984; Mantovani and Brito Neves, 2005; Rocha et al., 2019a; Affonso et al., 2021) while others suggest that the craton is currently divided into several blocks (Milani, 1997; Milani and Ramos, 1998; Julià et al., 2008). Chaves et al. (2016) proposed that the densification of the lithosphere may be related to mantle refertilization. Mariani et al. (2016) suggested that the positive anomaly is caused by a surplus mass in the crust, a theory previously supported by Molina et al. (1988), Vidotti et al. (1998), and Piccirillo et al. (1989). The position of the surplus mass in the base of the crust was motivated by the deep Moho discontinuity estimated from seismologic data (Assumpção et al.,

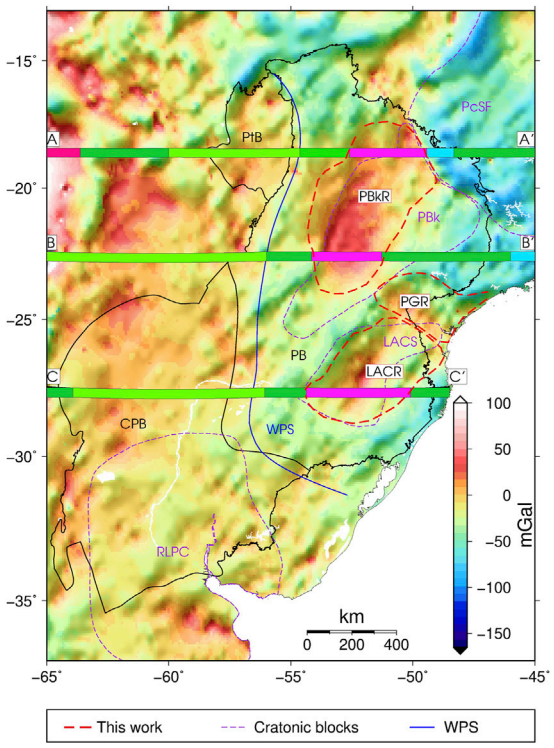

FIGURE 10
Residual Bouguer anomaly map, the colors of the **(AA'–CC')** profiles are the same as in Figure 9. WPS by Dragone et al. (2021). PtB: Pantanal basin, PB: Paraná basin, CPB: Chaco-Paraná basin, and PBk: Paranapanema block by Cordani et al. (2016); PcSF: Paleocontinent São Francisco by Rocha et al. (2019b); LACS: Luiz Alves craton from seismic tomography by Affonso et al. (2021); PBkR: Paranapanema block from residual Bouguer anomaly, PGR: Ponta Grossa arch from residual Bouguer anomaly and LACR: Luiz Alves craton from residual Bouguer anomaly by this work.

2013), which contrasts with the isostatic Moho expected by Airy's hypothesis. While our data and methodology cannot distinguish between these hypotheses or determine the depth of the excess mass causing the positive residual Bouguer anomaly, we were able to laterally delineate the region of the positive anomaly, which may assist future studies on the Paranapanema block. Our proposed boundaries (PBkR in Figure 10) extend approximately 100 km to the west from the region proposed by Cordani et al. (2016), encompassing an area of approximately 2,000 km^2.

Regarding the *Luiz Alves craton*, the boundary proposed by Cordani et al. (2016) (LAC in Figures 1, 4, 5, 8) covers a much smaller area than our proposal (LACR in Figure 10); however, the exact limits of this cratonic area remain unclear in the literature (Cordani and Sato, 1999; Cordani et al., 2016; Santos et al., 2019). Affonso et al. (2021) delimited a boundary for the Luiz Alves craton based on their seismic tomography (LACS in Figure 10), which is similar to our proposal. We extended their boundaries to the east, incorporating the area from Cordani et al. (2016), encompassing an area of approximately 1,500 km^2. We also identify a high S-velocity anomaly at the same location in the first adjoint waveform tomography for South America (SAAM23 by Ciardelli et al., 2022) that may be correspondent to the Luiz Alves craton as well.

The *Ponta Grossa arch* (PGR in Figure 10) is a tectonic and magmatic feature associated with a dike swarm of the Mesozoic rifting (Santos et al., 2022). Santos et al. (2022) have associated this structure with positive gravity anomalies, the latter even calculated the regional residual Bouguer anomaly using the polynomial method to analyze the arch's area. Their residual anomaly highlighted the same region with the highest amplitude as ours; however, they were not able to delimit the entire arch, which mainly consists of four lineaments, all within the area delimited by our study, covering approximately 1,150 km^2.

5.4 Comparison between the lithosphere density structure of the sedimentary basins

Our residual Bouguer anomaly map (Figure 10) provides compelling evidence that the lithosphere beneath the Paraná and Chaco-Paraná Paleozoic basins and the Pantanal Quaternary basin exhibits a heterogeneous density structure, which is consistent with its complex tectonic evolution. As previously discussed in Section 5.2, the residual anomalies are distinct to the west and east of the Western Paraná Suture (WPS in blue), which is also reflected in the density models of the three profiles (Figure 9 and color profiles Figure 10). This information highlights significant density differences in the lithosphere below the basins. Remarkably, despite the marked differences in the tectonic history and duration of deposition of the Pantanal and Chaco-Paraná basins, they present a more similar lithospheric density structure, compared with the Paraná basin.

The density modeling of the profiles helps us analyze the influence of the lithosphere, considering the LAB depth. Through the forward model, we were able to confirm that the density contrast is different along the Paraná basin compared to the Pantanal and Chaco-Paraná basins even with the LAB difference between them. Moreover, the density contrast of the lithosphere below the Pantanal and Chaco-Paraná basins is the same, equals to zero.

The *Paraná basin* presents the most complex density structure in the study area, with its residual Bouguer anomaly (PB Figure 10) characterized by a negative baseline with three positive anomalies, which we have delimited in this work and presented the details in the last section. The complete Bouguer anomaly (Figure 5) exhibits this negative anomaly with a higher amplitude, which was partially reduced by the removal of the Moho topography gravity effect (Figure 7B), though it still persists in the residual anomaly. This indicates that the lithosphere of this basin indeed differs from the lithosphere below the Chaco-Paraná basin, which supports the Western Paraná Suture hypothesis (Dragone et al., 2017; Dragone et al., 2021).

Furthermore, in the residual Bouguer anomaly map (Figure 10), we observe distinct gravity anomalies in the northern and southern of the *Chaco-Paraná basin*, the southern part coinciding with the area of the Rio de La Plata craton (RLPC in Figure 10), a feature that was not evident in the complete Bouguer anomaly map (Figure 5). This association could be linked to the craton, similar to the negative anomaly related to the São Francisco paleocontinent discussed in Section 5.2 of this manuscript. Notably, the primary deposition of this basin is the Las Breñas Fm., located in the northern portion of the Chaco-Paraná basin (Meeßen et al., 2018), where the basin's

depocenter is also situated. While the maximum of the residual Bouguer anomaly is not exactly at this location, the higher amplitude in the north could be related to the basin's formation or post-tectonic evolution, similar to the positive residual Bouguer anomaly observed in the north of the Paraná basin, coinciding with the Rio Ivai supersequence, the oldest units of the Paraná basin (Milani and Ramos, 1998).

Finally, the *Pantanal basin*, the youngest and smallest sedimentary basin under investigation, was included in the study to compare its geophysical characteristics with those of the Paleozoic basins. The complete Bouguer anomaly map (Figure 5) reveals a prominent positive anomaly covering the entire Pantanal basin, and the residual Bouguer anomaly also exhibits a positive anomaly, near to zero value. A noteworthy observation is the presence of an NS-oriented positive high anomaly lineament that almost bisects the basin, likely linked to the terranes comprising the lithosphere of the basin. Surprisingly, we observed no significant difference in the residual Bouguer anomaly between this younger basin and the Paleozoic Chaco-Paraná basin. However, it is worth noting that the lithosphere of the latter may have undergone alterations during its evolution (Meeßen et al., 2018), potentially influencing its overall density contrast. The alteration of the lithosphere below the Chaco-Paraná basin would explain the zero density contrast, that following our scale is related to a Proterozoic lithosphere.

6 Conclusion

Our study presents a residual Bouguer anomaly map for the Paraná, Chaco-Paraná, and Pantanal basins calculated by a new approach. Unlike conventional methods that rely on regional filters, like upward continuation or isostatic model compensation, we calculated the gravity effect of known masses in the sedimentary infill, basalt flood, and Moho topography, allowing us to remove their influence from the complete Bouguer anomaly. This approach has provided us with a more accurate and detailed representation of the lithosphere's density structures in the study area.

Through our residual Bouguer anomaly map and forward gravity modeling of the three profiles, we have not only reaffirmed density structures already reported in the literature but also revealed new insights. Notably, we propose a revised location for the Paranapanema block, situated more to the west than previously suggested, and with a limited southwestern extension. Additionally, we have identified a larger Luis Alves craton for the first time using gravity data, which is consistent with recent seismological proposals (Affonso et al., 2021). Our analysis of the Ponta Grossa swarm dike has shed light on its significant impact on the lithosphere's density structure, leading to the identification of a new anomaly. Furthermore, the western and eastern sides of the Western Paraná Suture exhibit contrasting residual Bouguer anomalies, with positive anomalies dominating the west and a mix of positive and negative anomalies with strong gradients in the eastern portion, supporting the hypothesis proposed by Dragone et al. (2017; 2021) of a suture between two different lithospheric compositions.

In summary, our findings contribute to a deeper understanding of the tectonic evolution and lithospheric density structures of the Paraná, Chaco-Paraná, and Pantanal basins, and their surrounding areas. By employing gravity data and modeling techniques, we have provided valuable geophysical insights that will aid future studies and enhance the knowledge of this complex geological region.

Data availability statement

The data analyzed in this study is subject to the following licenses/restrictions: The authors are not proprietary of the datasets analyzed for this study. Gridded files generated in this work may be available by request to the corresponding author and will be at the USP data repository after August 2024. Data from Brazil can be retrieved at BNDG (https://www.gov.br/anp/pt-br/assuntos/exploracao-e-producao-de-oleo-e-gas/dados-tecnicos/legislacao-aplicavel/bndg-banco-nacional-de-dados-gravimetricos). Requests to access these datasets should be directed to DM, denisemoura@outlook.com; YM, yaramaran@usp.br.

Author contributions

DM: main contribution to the research. YM: senior contribution to the research. All authors contributed to the article and approved the submitted version.

Acknowledgments

DM acknowledges FAPESP for scholarship grant 2018/19562-2. The authors thank LTG-Poli-USP for providing access to data from Paraguay; Carlos Alberto Moreno Chaves for sharing programs for data analysis and helping in the interpretation of the results; Gabriel Negrucci Dragone for contributing to the discussion of the results; and André Vinícius de Sousa Nascimento for reviewing the manuscript. We are thankful for the comments of two reviewers, which improved the manuscript.

Conflict of interest

The authors declare that the research was conducted in the absence of any commercial or financial relationships that could be construed as a potential conflict of interest.

Publisher's note

Supplementary material

The Supplementary Material for this article can be found online at: https://www.frontiersin.org/articles/10.3389/feart.2023.1214828/full#supplementary-material

References

Affonso, G. M. P. C., Rocha, M. P., Costa, I. S. L., Assumpcao, M., Fuck, R. A., Albuquerque, D. F., et al. (2021). Lithospheric architecture of the Paranapanema block and adjacent nuclei using multiple-frequency P -wave seismic tomography. *J. Geophys. Res. Solid Earth* 126 (4). doi:10.1029/2020jb021183

Assine, M. L., Merino, E. R., Pupim, F. N., Warren, L. V., Guerreiro, R. L., and McGlue, M. M. (2016). "Geology and geomorphology of the Pantanal basin," in *Dynamics of the pantanal wetland in south America*. Editors I. Bergier and M. L. Assine (Berlin, Germany: Springer), 23–50.

Assine, M. L., Perinotto, J. A. J., Alvarenga, C. J. S. D., and Petri, S. (1998). Arquitetura estratigráfica, tratos deposicionais e paleogeografia da Bacia do Paraná (Brasil) no Neo-Ordoviciano/Eo-Siluriano. *Rev. Bras. Geociências* 28 (1), 61–76.

Assine, M. L., and Soares, P. C. (2004). Quaternary of the pantanal, west-central Brazil. *Quat. Int.* 114 (1), 23–34. doi:10.1016/S1040-6182(03)00039-9

Assumpção, M., Bianchi, M., Julià, J., Dias, F. L., França, G. S., Nascimento, R., et al. (2013). Crustal thickness map of Brazil: data compilation and main features. *J. S. Am. Earth Sci.* 43, 74–85. doi:10.1016/j.jsames.2012.12.009

Brito Neves, B. B., Fuck, R. A., and Pimentel, M. M. (2014). The Brasiliano collage in south America: A review. *Braz. J. Geol.* 44, 493–518. doi:10.5327/Z2317-4889201400030010

Brito Neves, B. B., and Fuck, R. A. (2014). The basement of the South American platform: half Laurentian (N-NW)+half Gondwanan (E-SE) domains. *Precambrian Res.* 244, 75–86. doi:10.1016/j.precamres.2013.09.020

Chaves, C., Ussami, N., and Ritsema, J. (2016). Density and P-wave velocity structure beneath the Paraná Magmatic Province: refertilization of an ancient lithospheric mantle. *Geochem. Geophys. Geosystems* 17 (8), 3054–3074. doi:10.1002/2016GC006369

Ciardelli, C., Assumpção, M., Bozdağ, E., and van der Lee, S. (2022). Adjoint waveform tomography of South America. *J. Geophys. Res. Solid Earth* 127 (2), e2021JB022575. doi:10.1029/2021JB022575

Cordani, U. G. (1984). Estudo preliminar de integração do Pré-Cambriano com os eventos tectônicos das bacias sedimentares brasileiras. Bol. Ciênc. Técn. Petról. 15, 1–70.

Cordani, U. G., Ramos, V. A., Fraga, L. M., Cegarra, M., Delgado, I., Souza, K. G. D., et al. (2016). Tectonic map of South America. *CGMW-CPRM-SEGEMAR*. doi:10.14682/2016TEMSA

Cordani, U. G., and Sato, K. (1999). Crustal evolution of the South American Platform, based on Nd isotopic systematics on granitoid rocks. *Episodes J. Int. Geoscience* 22 (3), 167–173. doi:10.18814/epiiugs/1999/v22i3/003

Dragone, G. N., Bologna, M. S., Ussami, N., Gimenez, M. E., Alvarez, O., Klinger, F. G. L., et al. (2021). Lithosphere of South American intracratonic basins: electromagnetic and potential field data reveal cratons, terranes, and sutures. *Tectonophysics* 811, 228884. doi:10.1016/j.tecto.2021.228884

Dragone, G. N., Ussami, N., Gimenez, M. E., Klinger, F. G. L., and Chaves, C. A. M. (2017). Western Paraná suture/shear zone and the limits of Rio Apa, Rio Tebicuary and Rio de la Plata cratons from gravity data. *Precambrian Res.* 291, 162–177. doi:10.1016/j.precamres.2017.01.029

Feng, H. Q., Wu, D. J., and Chao, J. K. (2007). Size and energy distributions of interplanetary magnetic flux ropes. *J. Geophys. Res. Space Phys.* 112 (A2). doi:10.1029/2006JA011962

Frank, H. T., Gomes, M. E. B., and Formoso, M. L. L. (2009). Review of the areal extension and volume of the serra GERAL FORMATION, paraná basin, south America. *Pesqui. em Geociências* 36 (1), 49–57. doi:10.22456/1807-9806.17874

Heilbron, M., Cordani, U. G., and Alkmim, F. F. (2017). "The São Francisco craton and its margins," in *São Francisco craton, eastern Brazil: Tectonic genealogy of a miniature continent* (Berlin, Germany: Springer), 3–13.

Hinze, W. J. (2003). Bouguer reduction density, why 2.67? *Geophysics*, 68(5), 1559–1560. doi:10.1190/1.1620629

IAG - International Association of Geodesy (1971). "Geodetic reference system 1967," in *Publi. Spéc. n° 3 du Bulletin Géodésique* (Paris: Springer).

Jones, C. H. Updaters for GravMag, 2012. Available at: http://cires.colorado.edu/people/jones.craig/GSSH/updaters/GravMag.html (Accessed October, 3, 2020).

Julià, J., Assumpção, M., and Rocha, M. P. (2008). Deep crustal structure of the Paraná Basin from receiver functions and Rayleigh-wave dispersion: evidence for a fragmented cratonic root. *J. Geophys. Res. Solid Earth* 113 (B8). doi:10.1029/2007JB005374

Kuchenbecker, M., and Barbuena, D. (2023). Basement inliers of the araçuaí-west Congo orogen: key pieces for understanding the evolution of the São Francisco-Congo paleocontinent. *J. S. Am. Earth Sci.* 125, 104299. doi:10.1016/j.jsames.2023.104299

Laske, G., and Masters, G. (1997). A global digital map of sediment thickness. *EOS Trans. Am. Geophys. Union* 78, F483.

Laske, G., Masters, G., Ma, Z., and Pasyanos, M. (2013). "Update on CRUST1. 0—a 1-degree global model of earth's crust," in *Geophysical research abstracts* (Vienna, Austria: EGU General Assembly), 2658.

Mantovani, M. S. M., and de Brito Neves, B. B. (2005). The Paranapanema lithospheric block: its importance for Proterozoic (Rodinia, Gondwana) supercontinent theories. *Gondwana Res.* 8 (3), 303–315. doi:10.1016/S1342-937X(05)71137-0

Mariani, P., Braitenberg, C., and Ussami, N. (2013). Explaining the thick crust in Paraná basin, Brazil, with satellite GOCE gravity observations. *J. S. Am. Earth Sci.* 45, 209–223. doi:10.1016/j.jsames.2013.03.008

Matos, A. C. D. O. C. (2005). "Implementação de modelos digitais de terreno para aplicações na área de geodésia e geofísica na América do Sul,". Doctoral Thesis (Brazil: Universidade de São Paulo).

Meeßen, C., Sippel, J., Scheck-Wenderoth, M., Heine, C., and Strecker, M. R. (2018). Crustal Structure of the Andean foreland in Northern Argentina: results from data-integrative three-dimensional density modeling. *J. Geophys. Res. Solid Earth* 123 (2), 1875–1903. doi:10.1002/2017JB014296

Milani, E. J., Araujo, L. M., Cupertino, J. A., Faccini, U. F., and Scherer, C. M. (1998). Sequences and stratigraphic hierarchy of the parana basin (ordovician cretaceous), southern Brazil. *Bol. IG-USP. Série Científica* 29.

Milani, E. J. (2004). "Comentários sobre a origem e evolução tectônica da Bacia do Paraná," in *Geologia do Continente Sul-Americano: Evolução da obra de Fernando Flávio Marques de Almeida,*. Editors V. Mantesso-Neto and A. BartorelII, 265–291.

Milani, E. J. (1997) Evolução tectono-estratigráfica da Bacia do Paraná e seu relacionamento com a geodinâmica fanerozóica do Gondwana Sul-ocidental, Doctoral thesis (São Paulo, Brazil: Universidade de São Paulo).

Milani, E. J., Melo, J. H. G., Souza, P. A., Fernandes, L. A., and França, A. B. (2007). Bacia do Paraná. *Bol. Geociências Petrobras* 15 (2), 265–287.

Milani, E. J., and Ramos, V. A. (1998). Orogenias paleozóicas no domínio sul-ocidental do Gondwana e os ciclos de subsidência da Bacia do Paraná. *Rev. Bras. Geociências* 28 (4), 473–484. doi:10.25249/0375-7536.1998473484

Molina, E. C., Ussami, N., De Sá, N. C., Blitzkow, D., and Miranda Filho, O. F. (1988). "Deep crustal structure under the Paraná Basin (Brazil) from gravity study," in *The mesozoic flood volcanism of the Paraná Basin: Petrogenetic and geophysical aspects*. Editors E. M. Piccirillo, A. J. Melfi, and org (São Paulo, Brazil: São Paulo, Instituto Astronômico e Geofísico - Universidade de São Paulo), 271–283.

Nagy, D., Papp, G., and Benedek, J. (2000). The gravitational potential and its derivatives for the prism. *J. Geodesy* 74, 552–560. doi:10.1007/s001900000116

Nascimento, A. V. S., França, G. S., Chaves, C. A. M., and Marotta, G. S. A. (2022). Rayleigh wave group velocity maps at periods of 10–150 s beneath South America. *Geophys. J. Int.* 228 (2), 958–981. doi:10.1093/gji/ggab363

Olson, C. J., Becker, J. J., and Sandwell, D. T. (2014). A new global bathymetry map at 15 arcsecond resolution for resolving seafloor fabric: SRTM15_PLUS. *AGU Fall Meet. Abstr.* 2014, OS34A–03.

Parker, R. L. (1973). The rapid calculation of potential anomalies. *Geophys. J. Int.* 31 (4), 447–455. doi:10.1111/j.1365-246X.1973.tb06513.x

Pavlis, N. K., Holmes, S. A., Kenyon, S. C., and Factor, J. K. (2012). The development and evaluation of the earth gravitational model 2008 (EGM2008). *J. Geophys. Res. Solid Earth* 117 (B4). doi:10.1029/2011JB008916

Pedley, R. C., Busby, J. P., and Dabek, Z. K. (1993). *GRAVMAG user manual–interactive 2.5 D gravity and magnetic modeling*. Nottingham, UK: British Geological Survey, 73. Technical Report WK/93/26/R.

Piccirillo, E. M., Civetta, L., Petrini, R., Longinelli, A., Bellieni, G., Comin-Chiaramonti, P., et al. (1989). Regional variations within the Paraná flood basalts (southern Brazil): evidence for subcontinental mantle heterogeneity and crustal contamination. *Chem. Geol.* 75 (1-2), 103–122. doi:10.1016/0009-2541(89)90023-5

Poudjom-Djomani, Y. H. P., O'Reilly, S. Y., Griffin, W. L., and Morgan, P. (2001). The density structure of subcontinental lithosphere through time. *Earth Planet. Sci. Lett.* 184 (3-4), 605–621. doi:10.1016/S0012-821X(00)00362-9

Priestley, K., McKenzie, D., and Ho, T. (2018). A lithosphere–asthenosphere boundary—a global model derived from multimode surface-wave tomography and petrology. *Lithospheric discontinuities*, 111–123. doi:10.1002/9781119249740.ch6

Rocha, M. P., Assumpção, M., Affonso, G. M. P. C., Azevedo, P. A., and Bianchi, M. (2019a). Teleseismic P wave tomography beneath the pantanal, Paraná, and chaco-paraná basins, SE South America: delimiting lithospheric blocks of the SW Gondwana assemblage. *J. Geophys. Res. Solid Earth* 124 (7), 7120–7137. doi:10.1029/2018JB016807

Rocha, M. P., Azevedo, P. A., Assumpção, M., Pedrosa-Soares, A. C., Fuck, R., and Von Huelsen, M. G. (2019b). Delimiting the neoproterozoic São Francisco paleocontinental block with P-wave traveltime tomography. *Geophys. J. Int.* 219 (1), 633–644. doi:10.1093/gji/ggz323

Sá, N. C. de (2004). *O campo de gravidade, o geoide e a estrutura crustal na américa do sul: Novas estratégias de representação*. São Paulo: Thesis (Livre

Docência) – Instituto de Astronomia, Geofísica e Ciências Atmosféricas, Universidade de São Paulo.

Santos, J. O., Chernicoff, C. J., Zappettini, E. O., McNaughton, N. J., and Hartmann, L. A. (2019). Large geographic and temporal extensions of the Río de la Plata Craton, South America, and its metacratonic eastern margin. *Int. Geol. Rev.* 61 (1), 56–85. doi:10.1080/00206814.2017.1405747

Santos, M. D., Ladeira, F. S. B., Batezelli, A., Nunes, J. O. R., Salamuni, E., Silva, C. L. D., et al. (2022). Interactions between tectonics, bedrock inheritance and geomorphic responses of rivers in a post-rifting upland (Ponta Grossa Arch region, Brazil). *Braz. J. Geol.* 52, e20210002. doi:10.1590/2317-4889202220210002

Uieda, L., Oliveira, V. C., and Barbosa, V. C. (2013). "Modeling the earth with fatiando a terra," in Proceedings of the 12th Python in Science Conference, Austin, Texas, June 2013, 96–103.

Ussami, N., and Molina, E. C. (1999). Flexural modeling of the neoproterozoic Araguaia belt, central Brazil. *J. S. Am. Earth Sci.* 12 (1), 87–98. doi:10.1016/S0895-9811(99)00007-3

Ussami, N., Shiraiwa, S., and Dominguez, J. M. L. (1999). Basement reactivation in a sub-Andean foreland flexural bulge: the Pantanal wetland, SW Brazil. *Tectonics* 18 (1), pp25–39. doi:10.1029/1998TC900004

Veroslavsky, G., Rossello, E. A., López-Gamundí, O., de Santa Ana, H., Assine, M. L., Marmisolle, J., et al. (2021). Late paleozoic tectono-sedimentary evolution of eastern Chaco-Paraná basin (Uruguay, Brazil, Argentina and Paraguay). *J. S. Am. Earth Sci.* 106, 102991. doi:10.1016/j.jsames.2020.102991

Vidotti, R. M., Ebinger, C. J., and Fairhead, J. D. (1998). Gravity signature of the western Paraná basin, Brazil. *Earth Planet. Sci. Lett.* 159 (3-4), 117–132. doi:10.1016/S0012-821X(98)00070-3

Wessel, P., Smith, W. H., Scharroo, R., Luis, J., and Wobbe, F. (2013). Generic mapping tools: improved version released. *Eos, Trans. Am. Geophys. Union* 94 (45), 409–410. doi:10.1002/2013eo450001

Zalán, P. V., Wolff, S. J. C. J., Conceição, J. D. J., Marques, A., Astolfi, M. A. M., Vieira, I. S., et al. (1990). *Bacia do Paraná. Origem e evolução das bacias sedimentares*. Rio de Janeiro, Brazil: Boletim de Geociências da Petrobras, 135–168.

frontiers | Frontiers in Earth Science

TYPE Review
PUBLISHED 13 November 2023
DOI 10.3389/feart.2023.1253148

OPEN ACCESS

EDITED BY
Henglei Zhang,
China University of Geosciences Wuhan, China

REVIEWED BY
Dan Zhu,
China University of Geosciences Wuhan, China
Luan Thanh Pham,
VNU University of Science, Vietnam

*CORRESPONDENCE
Valéria C. F. Barbosa,
valcris@on.br

RECEIVED 04 July 2023
ACCEPTED 14 September 2023
PUBLISHED 13 November 2023

CITATION
Oliveira Junior VC, Takahashi D, Reis ALA and Barbosa VCF (2023), Computational aspects of the equivalent-layer technique: review.
Front. Earth Sci. 11:1253148.
doi: 10.3389/feart.2023.1253148

Computational aspects of the equivalent-layer technique: review

Vanderlei C. Oliveira Junior[1], Diego Takahashi[1], André L. A. Reis[2] and Valéria C. F. Barbosa[1]*

[1]Observatório Nacional, Department of Geophysics, Rio de Janeiro, Brazil, [2]Department of Applied Geology, Universidade do Estado do Rio de Janeiro, Rio de Janeiro, Brazil

Equivalent-layer technique is a powerful tool for processing potential-field data in the space domain. However, the greatest hindrance for using the equivalent-layer technique is its high computational cost for processing massive data sets. The large amount of computer memory usage to store the full sensitivity matrix combined with the computational time required for matrix-vector multiplications and to solve the resulting linear system, are the main drawbacks that made unfeasible the use of the equivalent-layer technique for a long time. More recently, the advances in computational power propelled the development of methods to overcome the heavy computational cost associated with the equivalent-layer technique. We present a comprehensive review of the computation aspects concerning the equivalent-layer technique addressing how previous works have been dealt with the computational cost of this technique. Historically, the high computational cost of the equivalent-layer technique has been overcome by using a variety of strategies such as: moving data-window scheme, column- and row-action updates of the sensitivity matrix, reparametrization, sparsity induction of the sensitivity matrix, iterative methods using the full sensitivity matrix, iterative deconvolution by using the concept of block-Toeplitz Toeplitz-block (BTTB) matrices and direct deconvolution. We compute the number of floating-point operations of some of these strategies adopted in the equivalent-layer technique to show their effectiveness in reducing the computational demand. Numerically, we also address the stability of some of these strategies used in the equivalent-layer technique by comparing with the stability via the classic equivalent-layer technique with the zeroth-order Tikhonov regularization. We show that even for the most computationally efficient methods, which can save up to 10^9 flops, the stability of the linear system is maintained. The two most efficient strategies, iterative and direct deconvolutions, can process large datasets quickly and yield good results. However, direct deconvolution has some drawbacks. Real data from Carajás Mineral Province, Brazil, is also used to validate the results showing a potential field transformation.

KEYWORDS

equivalent layer, gravity methods, fast algorithms, computational cost, stability analysis

1 Introduction

The equivalent-layer technique has been used by exploration geophysicists for processing potential-field data since the late 1960s (Dampney, 1969). This technique is based on a widely accepted principle, which states that a discrete set of observed potential-field data due to 3D sources can be approximated by that due to a discrete discrete set of virtual sources (such as point masses, dipoles, prisms, doublets). From a theoretical point of view, the equivalent-layer technique is grounded on potential theory (Kellogg, 1967) and consists in considering that the potential field data can be approximated by a linear combination of harmonic functions describing the potential field due to the virtual sources. These sources, commonly called equivalent sources, are arranged on a layer with finite horizontal dimensions and located below the observations. In the classical approach, a linear inverse problem is solved to estimate the physical property of each equivalent source subject to fit the observations. Then, the estimated physical-property distribution on the equivalent layer is used to accomplish the desired potential-field transformation (e.g., interpolation, upward/downward continuation, reduction to the pole). The later step is done by multiplying the estimated physical-property distribution by the matrix of Green's functions associated with the desired potential-field transformation.

Because the linear inverse problem to be solved in the equivalent-layer technique is set up with a full sensitivity matrix, its computational cost strongly depends on the number of potential-field observations and can be very inefficient for dealing with massive data sets. To overcome this problem, computationally efficient methods based on equivalent-layer technique have arose in the late 1980s. This comprehensive review discusses specific strategies aimed at reducing the computational cost of the equivalent-layer technique. These strategies are addressed in the following articles: Leão and Silva (1989); Cordell (1992); Xia et al. (1993); Mendonça and Silva (1994); Guspí and Novara (2009); Li and Oldenburg (2010); Oliveira Jr. et al. (2013); Siqueira et al. (2017); Jirigalatu and Ebbing (2019); Takahashi et al. (2020, 2022) Mendonça (2020); and Soler and Uieda (2021);

To our knowledge, the first method towards improving the efficiency was proposed by Leão and Silva (1989), who used an overlapping moving-window scheme spanning the data set. The strategy adopted in Leão and Silva (1989) involves solving several smaller, regularized linear inverse problems instead of one large problem. This strategy uses a small data window and distributes equivalent sources on a small regular grid at a constant depth below the data surface, with the sources' window extending beyond the boundaries of the data window. Because of the spatial layouts of observed data and equivalent sources in Leão and Silva (1989), the small sensitivity submatrix containing the coordinates of the data and equivalent sources within a window remains constant for all data windows. This holds true regardless of the specific locations of the data and equivalent sources within each window. For each position of the data window, this scheme consists in computing the processed field at the center of the data window only, and the next estimates of the processed field are obtained by shifting the data window across the entire dataset. More recently, Soler and Uieda (2021) extended the method introduced by Leão and Silva (1989) to accommodate irregularly spaced data collected on a non-flat surface. Unlike Leão and Silva (1989), in the generalization proposed by Soler and Uieda (2021), the sensitivity submatrix that includes the coordinates of the data and equivalent sources needs to be computed for each window. Soler and Uieda (2021) developed a computational approach to further enhance the efficiency of the equivalent-layer technique by combining two strategies. The first one—the block-averaging source locations—reduces the number of model parameters and the second strategy—the gradient-boosted algorithm—reduces the size of the linear system to be solved by iteratively fitting the equivalent source model along overlapping windows. It is worth noting that the equivalent-layer strategy of using a moving-window scheme either in Leão and Silva (1989) or in Soler and Uieda (2021) is similar to discrete convolution.

As another strategy to reduce the computational workload of the equivalent-layer technique, some authors have employed column- and row-action updates, which are commonly applied to image reconstruction methods (e.g., Elfving et al., 2017). These methods involve iterative calculations of a single column and a single row of the sensitivity matrix, respectively. Following the strategy column-action update, Cordell (1992) proposed a computational method in which a single equivalent source positioned below a measurement station is iteratively used to compute both the predicted data and residual data for all stations. In Cordell's method, a single column of the sensitivity matrix is calculated per iteration, meaning that a single equivalent source contributes to data fitting in each iteration. Guspí and Novara (2009) further extended Cordell's method by applying it to scattered magnetic observations. Following the strategy of column-action update, Mendonça and Silva (1994) developed an iterative procedure where one data point is incorporated at a time, and a single row of the sensitivity matrix is calculated per iteration. This strategy adopted by Mendonça and Silva (1994) is known as *equivalent data concept*. This concept is based on the principle that certain data points within a dataset are redundant and, as a result, do not contribute to the final solution On the other hand, there is a subset of observations known as equivalent data, which effectively contributes to the final solution and fits the remaining redundant data. In their work, Mendonça and Silva (1994) adopted an iterative approach to select a substantially smaller subset of equivalent data from the original dataset.

The next strategy involves reparametrizing the equivalent layer with the objective of solving a smaller linear inverse problem by reducing the dimension of the model space. Oliveira Jr. et al. (2013) reduced the model parameters by approximating the equivalent-source layer by a piecewise-polynomial function defined on a set of user-defined small equivalent-source windows. The estimated parameters are the polynomial coefficients for each window and they are much smaller than the original number of equivalent sources. By using the subspace method, Mendonça (2020) reparametrizes the equivalent layer, which involves reducing the dimension of the linear system from the original parameter-model space to a lower-dimensional subspace. The subspace bases span the parameter-model space and they are constructed by applying the singular value decomposition to the matrix containing the gridded data.

Following the strategy of sparsity induction, Li and Oldenburg (2010) transformed the full sensitivity matrix into a sparse one using orthonormal compactly supported wavelets. Barnes and Lumley (2011) proposed an alternative approach to introduce sparsity based on the use of quadtree discretization to group equivalent sources far

from the computation points. Those authors explore the induced sparsity by using specific iterative methods to solve the linear system.

The strategy named iterative methods estimates iteratively the parameter vector that represents a distribution over an equivalent layer. Xia and Sprowl (1991) and Xia et al. (1993) have developed efficient iterative algorithms for updating the distribution of physical properties within the equivalent layer in the wavenumber and space domains, respectively. Specifically, in Xia and Sprowl's (1991) method the physical-property distribution is updated by using the ratio between the squared depth to the equivalent source and the gravitational constant multiplied by the residual between the observed and predicted observation at the measurement station. Siqueira et al. (2017) developed an iterative solution where the sensitivity matrix is transformed into a diagonal matrix with constant terms through the use of the *excess mass criterion* and of the positive correlation between the observed gravity data and the masses on the equivalent layer. The fundamentals of the Siqueira et al.'s method is based on the Gauss' theorem (e.g., Kellogg, 1967, p. 43) and the total excess of mass (e.g., Blakely, 1996, p. 60). All these iterative methods use the full and dense sensitivity matrix to calculate the predicted data and residual data in the whole survey data per iteration. Hence, the iterative methods proposed by Xia and Sprowl (1991), Xia et al. (1993) and Siqueira et al. (2017) neither compress nor reparametrize the sensitivity matrix. Jirigalatu and Ebbing (2019) also proposed an iterative equivalent layer that uses the full and dense sensitivity matrix. However, in their approach, Jirigalatu and Ebbing (2019) efficiently compute the predicted data and residual data for the entire survey per iteration in the wavenumber domain.

Following the strategy of the iterative deconvolution, Takahashi et al. (2020, 2022) developed fast and effective equivalent-layer techniques for processing, respectively, gravity and magnetic data by modifying the forward modeling to estimate the physical-property distribution over the equivalent layer through a 2D discrete fast convolution. These methods took advantage of the Block-Toeplitz Toeplitz-block (BTTB) structure of the sensitivity matrices, allowing them to be calculated by using only their first column. In practice, the forward modeling uses a single equivalent source, which significantly reduces the required RAM memory.

The method introduced by Takahashi et al. (2020, 2022) can be reformulated to eliminate the need for conjugate gradient iterations. This reformulation involves employing a *direct deconvolution* approach (e.g., Aster et al., 2019, p. 220) with *Wiener filter* (e.g., Gonzalez and Woods, 2002, p. 263).

Here, we present a comprehensive review of diverse strategies to solve the linear system of the equivalent layer alongside an analysis of the computational cost and stability of these strategies. To do this analysis, we are using the floating-point operations count to evaluate the performance of a selected set of methods (e.g., Leão and Silva (1989); Cordell (1992); Oliveira Jr. et al. (2013); Siqueira et al. (2017); Mendonça (2020); Takahashi et al. (2020); Soler and Uieda (2021); and direct deconvolution). To test the stability, we are using the linear system sensitivity to noise as a comparison parameter for the fastest of these methods alongside the classical normal equations. A potential-field transformation will also be used to evaluate the quality of the equivalent sources estimation results using both synthetic and real data from Carajás Mineral Province, Brazil.

In the following sections, we will address the theoretical bases of the equivalent-layer technique, including aspects such as the sensitivity matrix, layer depth and spatial distribution and the total number of equivalent sources. Then, we will explore the general formulation and solution of the linear inverse problem for the equivalent-layer technique, including discussions on linear system solvers. Additionally, we will quantify the required arithmetic operations for a given equivalent-layer method, assessing the number of floating-point operations involved. Next, we will evaluate the stability of the estimated solutions obtained from applying specific equivalent-layer methods. Finally, we will delve into the computational strategies adopted in the equivalent-layer technique for reducing computational costs. These strategies encompass various approaches, such as the moving data-window scheme, column-and row-action updates of the sensitivity matrix, reparametrization, sparsity induction of the sensitivity matrix, iterative methods using the full sensitivity matrix, iterative deconvolution using the concept of block-Toeplitz Toeplitz-block (BTTB) matrices, and direct deconvolution.

2 Fundamentals

Let $\mathbf{d}$ be a $D \times 1$ vector, whose ith element d_i is the observed potential field at the position (x_i, y_i, z_i), $i \in \{1{:}D\}$, of a topocentric Cartesian system with x, y and z-axes pointing to north, east and down, respectively. Consider that d_i can be satisfactorily approximated by a harmonic function

$$f_i = \sum_{j=1}^{P} g_{ij} p_j , \quad i \in \{1{:}D\}, \tag{1}$$

where, p_j represents the scalar physical property of a virtual source (i.e., monopole, dipole, prism) located at (x_j, y_j, z_j), $j \in \{1{:}P\}$ and

$$g_{ij} \equiv g\left(x_i - x_j, y_i - y_j, z_i - z_j\right) , \quad z_i < \min\left\{z_j\right\} , \quad \forall i \in \{1{:}D\}, \tag{2}$$

is a harmonic function, where $\min\{z_j\}$ denotes the minimum z_j, or the vertical coordinate of the shallowest virtual source. These virtual sources are called *equivalent sources* and they form an *equivalent layer*. In matrix notation, the potential field produced by all equivalent sources at all points (x_i, y_i, z_i), $i \in \{1{:}D\}$, is given by:

$$\mathbf{f} = \mathbf{G}\mathbf{p}, \tag{3}$$

where $\mathbf{p}$ is a $P \times 1$ vector with jth element p_j representing the scalar physical property of the jth equivalent source and $\mathbf{G}$ is a $D \times P$ matrix with element g_{ij} given by Eq. 2.

The equivalent-layer technique consists in solving a linear inverse problem to determine a parameter vector $\mathbf{p}$ leading to a predicted data vector $\mathbf{f}$ (Eq. 3) *sufficiently close to* the observed data vector $\mathbf{d}$, whose ith element d_i is the observed potential field at (x_i, y_i, z_i). The notion of *closeness* is intrinsically related to the concept of *vector* norm (e.g., Golub and Van Loan, 2013, p. 68) or *measure of length* (e.g., Menke, 2018, p. 41). Because of that, almost all methods for determining $\mathbf{p}$ actually estimate a parameter vector $\tilde{\mathbf{p}}$ minimizing a length measure of the difference between $\mathbf{f}$ and $\mathbf{d}$ (see Subsection 3.1). Given an estimate $\tilde{\mathbf{p}}$, it is then possible to compute a potential field transformation

$$\mathbf{t} = \mathbf{A}\tilde{\mathbf{p}}, \tag{4}$$

where $\mathbf{t}$ is a $T\times 1$ vector with kth element t_k representing the transformed potential field at the position (x_k, y_y, z_k), $k \in \{1{:}T\}$, and

$$a_{kj} \equiv a\left(x_k - x_j, y_k - y_j, z_k - z_j\right), \quad z_k < \min\left\{z_j\right\}, \quad \forall k \in \{1{:}T\}, \quad (5)$$

is a harmonic function representing the kj-th element of the $T\times P$ matrix $\mathbf{A}$.

2.1 Spatial distribution and total number of equivalent sources

There is no well-established criteria to define the optimum number P or the spatial distribution of the equivalent sources. We know that setting an equivalent layer with more (less) sources than potential-field data usually leads to an underdetermined (overdetermined) inverse problem (e.g., Menke, 2018, p. 52–53). Concerning the spatial distribution of the equivalent sources, the only condition is that they must rely on a surface that is located below and does not cross that containing the potential field data Soler and Uieda (2021) present a practical discussion about this topic.

From a theoretical point of view, the equivalent layer reproducing a given potential field data set cannot cross the true gravity or magnetic sources. This condition is a consequence of recognizing that the equivalent layer is essentially an indirect solution of a boundary value problem of potential theory (e.g., Roy, 1962; Zidarov, 1965; Dampney, 1969; Li et al., 2014; Reis et al., 2020). In practical applications, however, there is no guarantee that this condition is satisfied. Actually, its is widely known from practical experience (e.g., Gonzalez et al., 2022) that the equivalent-layer technique works even for the case in which the layer cross the true sources.

Regarding the depth of the equivalent layer, Dampney (1969) proposed a criterion based on horizontal data sampling, suggesting that the equivalent-layer depth should be between two and six times the horizontal grid spacing, considering evenly spaced data. However, when dealing with a survey pattern that has unevenly spaced data, Reis et al. (2020) adopted an alternative empirical criterion. According to their proposal, the depth of the equivalent layer should range from two to three times the spacing between adjacent flight lines. The criteria of Dampney (1969) and Reis et al. (2020) are valid for planar equivalent layers. Cordell (1992) have proposed and an alternative criterion for scattered data that leads to an undulating equivalent layer. This criterion have been slightly modified by Guspí et al. (2004), Guspí and Novara (2009) and Soler and Uieda (2021), for example, and consists in setting one equivalent source below each datum at a depth proportional to the horizontal distance to the nearest neighboring data points. Soler and Uieda (2021) have compared different strategies for defining the equivalent sources depth for the specific problem of interpolating gravity data, but they have not found significant differences between them. Regarding the horizontal layout, Soler and Uieda (2021) proposed the block-averaged sources locations in which the survey area is divided into horizontal blocks and one single equivalent source is assigned to each block. The horizontal coordinates of the single source in a given block is defined by the average horizontal coordinates of the observation points at the block. According to Soler and Uieda (2021), this block-averaged layout may prevent aliasing of the interpolated values, specially when the observations are unevenly sampled. This strategy also reduces the number of equivalent sources without affecting the accuracy of the potential-field interpolation. Besides, it reduces the computational load for estimating the physical property on the equivalent layer.

2.2 Matrix G

Generally, the harmonic function g_{ij} (Eq. 2) is defined in terms of the inverse distance between the observation point (x_i, y_i, z_i) and the jth equivalent source at (x_j, y_j, z_j),

$$\frac{1}{r_{ij}} \equiv \frac{1}{\sqrt{\left(x_i - x_j\right)^2 + \left(y_i - y_j\right)^2 + \left(z_i - z_j\right)^2}}, \quad (6)$$

or by its partial derivatives of first and second orders, respectively given by

$$\partial_\alpha \frac{1}{r_{ij}} \equiv \frac{-\left(\alpha_i - \alpha_j\right)}{r_{ij}^3}, \quad \alpha \in \{x, y, z\}, \quad (7)$$

and

$$\partial_{\alpha\beta} \frac{1}{r_{ij}} \equiv \begin{cases} \dfrac{3\left(\alpha_i - \alpha_j\right)^2}{r_{ij}^5}, & \alpha = \beta, \\ \dfrac{3\left(\alpha_i - \alpha_j\right)\left(\beta_i - \beta_j\right)}{r_{ij}^5} - \dfrac{1}{r_{ij}^3}, & \alpha \neq \beta, \end{cases} \quad \alpha, \beta \in \{x, y, z\}. \quad (8)$$

In this case, the equivalent layer is formed by punctual sources representing monopoles or dipoles (e.g., Dampney, 1969; Emilia, 1973; Leão and Silva, 1989; Cordell, 1992; Oliveira Jr. et al., 2013; Siqueira et al., 2017; Reis et al., 2020; Takahashi et al., 2020; Soler and Uieda, 2021; Takahashi et al., 2022). Another common approach consists in not defining g_{ij} by using Eqs. 6–8, but other harmonic functions obtained by integrating them over the volume of regular prisms (e.g., Li and Oldenburg, 2010; Barnes and Lumley, 2011; Li et al., 2014; Jirigalatu and Ebbing, 2019). There are also some less common approaches defining the harmonic function g_{ij} (Eq. 2) as the potential field due to plane faces with constant physical property (Hansen and Miyazaki, 1984), doublets (Silva, 1986) or by computing the double integration of the inverse distance function with respect to z (Guspí and Novara, 2009).

A common assumption for most of the equivalent-layer methods is that the harmonic function g_{ij} (Eq. 2) is independent on the actual physical relationship between the observed potential field and their true sources (e.g., Cordell, 1992; Guspí and Novara, 2009; Li et al., 2014). Hence, g_{ij} can be defined according to the problem. The only condition imposed to this function is that it decays to zero as the observation point (x_i, y_i, z_i) goes away from the position (x_j, y_j, z_j) of the jth equivalent source. However, several methods use a function g_{ij} that preserves the physical relationship between the observed potential field and their true sources. For the case in which the observed potential field is gravity data, g_{ij} is commonly defined as a component of the gravitational field produced at (x_i, y_i, z_i) by a point mass or prism located at (x_j, y_j, z_j), with unit density. On the other hand, g_{ij} is commonly defined as a component of the magnetic

induction field produced at (x_i, y_i, z_i) by a dipole or prism located at (x_j, y_j, z_j), with unit magnetization intensity, when the observed potential field is magnetic data.

The main challenge in the equivalent-layer technique is the computational complexity associated with handling large datasets. This complexity arises because the sensitivity matrix $\mathbf{G}$ (Eq. 3) is dense regardless of the harmonic function g_{ij} (Eq. 2) employed. In the case of scattered potential-field data, the structure of $\mathbf{G}$ is not well-defined, regardless of the spatial distribution of the equivalent sources. However, in a specific scenario where 1) each potential-field datum is directly associated with a single equivalent source located directly below it, and 2) both the data and sources are based on planar and regularly spaced grids, Takahashi et al. (2020, 2022) demonstrate that $\mathbf{G}$ exhibits a block-Toeplitz Toeplitz-block (BTTB) structure. In such cases, the product of $\mathbf{G}$ and an arbitrary vector can be efficiently computed using a 2D fast Fourier transform as a discrete convolution.

3 Linear inverse problem of equivalent-layer technique

3.1 General formulation

A general formulation for almost all equivalent-layer methods can be achieved by first considering that the $P \times 1$ parameter vector $\mathbf{p}$ (Eq. 3) can be reparameterized into a $Q \times 1$ vector $\mathbf{q}$ according to:

$$\mathbf{p} = \mathbf{H}\,\mathbf{q}, \tag{9}$$

where $\mathbf{H}$ is a $P \times Q$ matrix. The predicted data vector $\mathbf{f}$ (Eq. 3) can then be rewritten as follows:

$$\mathbf{f} = \mathbf{G}\,\mathbf{H}\,\mathbf{q}. \tag{10}$$

Note that the original parameter vector $\mathbf{p}$ is defined in a P-dimensional space whereas the reparameterized parameter vector $\mathbf{q}$ (Eq. 9) lies in a Q-dimensional space. For convenience, we use the terms P-space and Q-space to designate them.

In this case, the problem of estimating a parameter vector $\tilde{\mathbf{p}}$ minimizing a length measure of the difference between $\mathbf{f}$ (Eq. 3) and $\mathbf{d}$ is replaced by that of estimating an auxiliary vector $\tilde{\mathbf{q}}$ minimizing the goal function

$$\Gamma(\mathbf{q}) = \Phi(\mathbf{q}) + \mu\,\Theta(\mathbf{q}), \tag{11}$$

which is a combination of particular measures of length given by

$$\Phi(\mathbf{q}) = (\mathbf{d} - \mathbf{f})^{\top}\mathbf{W}_d\,(\mathbf{d} - \mathbf{f}), \tag{12}$$

and

$$\Theta(\mathbf{q}) = (\mathbf{q} - \bar{\mathbf{q}})^{\top}\mathbf{W}_q\,(\mathbf{q} - \bar{\mathbf{q}}), \tag{13}$$

where the regularization parameter μ is a positive scalar controlling the trade-off between the data-misfit function $\Phi(\mathbf{q})$ and the regularization function $\Theta(\mathbf{q})$; $\mathbf{W}_d$ is a $D \times D$ symmetric matrix defining the relative importance of each observed datum d_i; $\mathbf{W}_q$ is a $Q \times Q$ symmetric matrix imposing prior information on $\mathbf{q}$; and $\bar{\mathbf{q}}$ is a $Q \times 1$ vector of reference values for $\mathbf{q}$ that satisfies

$$\bar{\mathbf{p}} = \mathbf{H}\,\bar{\mathbf{q}}, \tag{14}$$

where $\bar{\mathbf{p}}$ is a $P \times 1$ vector containing reference values for the original parameter vector $\mathbf{p}$.

After obtaining an estimate $\tilde{\mathbf{q}}$ for the reparameterized parameter vector $\mathbf{q}$ (Eq. 9), the estimate $\tilde{\mathbf{p}}$ for the original parameter vector (Eq. 3) is computed by

$$\tilde{\mathbf{p}} = \mathbf{H}\,\tilde{\mathbf{q}}. \tag{15}$$

The reparameterized vector $\tilde{\mathbf{q}}$ is obtained by first computing the gradient of $\Gamma(\mathbf{q})$,

$$\nabla\Gamma(\mathbf{q}) = -2\,\mathbf{H}^{\top}\mathbf{G}^{\top}\mathbf{W}_d\,(\mathbf{d} - \mathbf{f}) + 2\,\mu\,\mathbf{W}_q\,(\mathbf{q} - \bar{\mathbf{q}}). \tag{16}$$

Then, by considering that $\nabla\Gamma(\tilde{\mathbf{q}}) = \mathbf{0}$ (Eq. 16), where $\mathbf{0}$ is a vector of zeros, as well as adding and subtracting the term $(\mathbf{H}^{\top}\mathbf{G}^{\top}\mathbf{W}_d\mathbf{G}\,\mathbf{H})\,\bar{\mathbf{q}}$, we obtain

$$\tilde{\boldsymbol{\delta}}_q = \mathbf{B}\,\boldsymbol{\delta}_d, \tag{17}$$

where

$$\tilde{\mathbf{q}} = \tilde{\boldsymbol{\delta}}_q + \bar{\mathbf{q}}, \tag{18}$$

$$\boldsymbol{\delta}_d = \mathbf{d} - \mathbf{G}\,\mathbf{H}\,\bar{\mathbf{q}}, \tag{19}$$

$$\mathbf{B} = \left(\mathbf{H}^{\top}\mathbf{G}^{\top}\mathbf{W}_d\,\mathbf{G}\,\mathbf{H} + \mu\,\mathbf{W}_q\right)^{-1}\mathbf{H}^{\top}\mathbf{G}^{\top}\mathbf{W}_d, \tag{20}$$

or, equivalently (Menke, 2018, p. 62),

$$\mathbf{B} = \mathbf{W}_q^{-1}\,\mathbf{H}^{\top}\mathbf{G}^{\top}\left(\mathbf{G}\,\mathbf{H}\,\mathbf{W}_q^{-1}\,\mathbf{H}^{\top}\mathbf{G}^{\top} + \mu\mathbf{W}_d^{-1}\right)^{-1}. \tag{21}$$

Evidently, we have considered that all inverses exist in Eqs. 20, 21.

The $Q \times D$ matrix $\mathbf{B}$ defined by Eq. 20 is commonly used for the case in which $D > Q$, i.e., when there are more data than parameters (overdetermined problems). In this case, we consider that the estimate $\tilde{\mathbf{q}}$ is obtained by solving the following linear system for $\tilde{\boldsymbol{\delta}}_q$ (Eq. 18):

$$\left(\mathbf{H}^{\top}\mathbf{G}^{\top}\mathbf{W}_d\,\mathbf{G}\,\mathbf{H} + \mu\,\mathbf{W}_q\right)\tilde{\boldsymbol{\delta}}_q = \mathbf{H}^{\top}\mathbf{G}^{\top}\mathbf{W}_d\,\boldsymbol{\delta}_d. \tag{22}$$

On the other hand, for the cases in which $D < Q$ (underdetermined problems), matrix $\mathbf{B}$ is usually defined according to Eq. 21. In this case, the general approach involves estimating $\tilde{\mathbf{q}}$ in two steps. The first consists in solving a linear system for a dummy vector, which is subsequently used to compute $\tilde{\mathbf{q}}$ by a matrix-vector product as follows:

$$\begin{aligned} \left(\mathbf{G}\,\mathbf{H}\,\mathbf{W}_q^{-1}\,\mathbf{H}^{\top}\mathbf{G}^{\top} + \mu\mathbf{W}_d^{-1}\right)\mathbf{u} &= \boldsymbol{\delta}_d \\ \tilde{\boldsymbol{\delta}}_q &= \mathbf{W}_q^{-1}\,\mathbf{H}^{\top}\mathbf{G}^{\top}\mathbf{u} \end{aligned}, \tag{23}$$

where $\mathbf{u}$ is a dummy vector. After obtaining $\tilde{\boldsymbol{\delta}}_q$ (Eqs. 22, 23), the estimate $\tilde{\mathbf{q}}$ is computed with Eq. 18.

3.2 Formulation without reparameterization

Note that, for the particular case in which $\mathbf{H} = \mathbf{I}_P$ (Eq. 9), where $\mathbf{I}_P$ is the identity of order P, $P = Q$, $\mathbf{p} = \mathbf{q}$, $\bar{\mathbf{p}} = \bar{\mathbf{q}}$ (Eq. 14) and $\tilde{\mathbf{p}} = \tilde{\mathbf{q}}$ (Eq. 15). In this case, the linear system (Eqs. 22, 23) is directly solved for

$$\tilde{\boldsymbol{\delta}}_p = \tilde{\mathbf{p}} - \bar{\mathbf{p}}, \tag{24}$$

instead of $\tilde{\boldsymbol{\delta}}_q$ (Eq. 18).

3.3 Linear system solvers

According to their properties, the linear systems associated with over and underdetermined problems (Eqs. 22, 23) can be solved by using *direct methods* such as LU, Cholesky or QR factorization, for example, (Golub and Van Loan, 2013; Sections 3.2, Section 4.2 and Section 5.2). These methods involve factorizing the linear system matrix in a product of "simple" matrices (i.e., triangular, diagonal or orthogonal). Here, we consider the *Cholesky factorization*, (Golub and Van Loan, 2013, p. 163).

Let us consider a real linear system $\mathbf{M}\,\mathbf{x} = \mathbf{y}$, where $\mathbf{M}$ is a symmetric and positive definite matrix (Golub and Van Loan, 2013, p. 159). In this case, the Cholesky factorization consists in computing

$$\mathbf{M} = \mathcal{G}\mathcal{G}^{\top}, \tag{25}$$

where $\mathcal{G}$ is a lower triangular matrix called *Cholesky factor* and having positive diagonal entries. Given $\mathcal{G}$, the original linear system is replaced by two triangular systems, as follows:

$$\begin{aligned} \mathcal{G}\,\mathbf{s} &= \mathbf{y} \\ \mathcal{G}^{\top}\mathbf{x} &= \mathbf{s} \end{aligned} \tag{26}$$

where $\mathbf{s}$ is a dummy vector. For the overdetermined problem Eq. 22, $\mathbf{M} = \left(\mathbf{H}^{\top}\mathbf{G}^{\top}\mathbf{W}_d\,\mathbf{G}\,\mathbf{H} + \mu\,\mathbf{W}_q\right)$, $\mathbf{x} = \tilde{\boldsymbol{\delta}}_q$ and $\mathbf{y} = \left(\mathbf{H}^{\top}\mathbf{G}^{\top}\mathbf{W}_d\,\boldsymbol{\delta}_d\right)$. For the underdetermined problem (Eq. 23), $\mathbf{M} = \left(\mathbf{G}\,\mathbf{H}\,\mathbf{W}_q^{-1}\,\mathbf{H}^{\top}\mathbf{G}^{\top} + \mu\mathbf{W}_d^{-1}\right)$, $\mathbf{x} = \mathbf{u}$ and $\mathbf{y} = \boldsymbol{\delta}_d$.

The use of direct methods for solving large linear systems may be problematic due to computer 1) storage of large matrices and 2) time to perform matrix operations. This problem may be specially complicated in equivalent-layer technique for the cases in which the sensitivity matrix $\mathbf{G}$ does not have a well-defined structure (Section 2.2).

These problems can be overcame by solving the linear system using an iterative method. These methods produce a sequence of vectors that typically converge to the solution at a reasonable rate. The main computational cost associated with these methods is usually some matrix-vector products per iteration. The *conjugate gradient* (CG) is a very popular iterative method for solving linear systems in equivalent-layer methods. This method was originally developed to solve systems having a square and positive definite matrix. There are two adapted versions of the CG method. The first is called *conjugate gradient normal equation residual* (CGNR) Golub and Van Loan (2013, Section 11.3) or *conjugate gradient least squares* (CGLS) (Aster et al., 2019, p. 165) and is used to solve overdetermined problems (Eq. 22). The second is called *conjugate gradient normal equation error* (CGNE) method Golub and Van Loan (2013), sec. 11.3) and is used to solve the underdetermined problems (Eq. 23). Algorithm 1 outlines the CGLS method applied to the overdetermined problem (Eq. 22).

Initialization :
1 Compute $\mathbf{G}$;
2 Set $\mathbf{r} = \mathbf{d}$ and compute $\delta = \|\mathbf{r}\|/_D$;
3 Compute $\boldsymbol{\vartheta} = \mathbf{G}^{\top}\mathbf{r}$ and $\rho_0 = \boldsymbol{\vartheta}^{\top}\boldsymbol{\vartheta}$;
4 Set $\tilde{\mathbf{p}} = \mathbf{0}$, $\tau = 0$ and $\boldsymbol{\eta} = \mathbf{0}$;
5 $m = 1$;
6 **while** $(\delta > \epsilon)$ **and** $(m <$ ITMAX$)$ **do**
7 Update $\boldsymbol{\eta} \leftarrow \boldsymbol{\vartheta} + \tau\,\boldsymbol{\eta}$;
8 Compute $\boldsymbol{\nu} = \mathbf{G}\,\boldsymbol{\eta}$;
9 Compute $\upsilon = \rho_0/(\boldsymbol{\nu}^{\top}\boldsymbol{\nu})$;
10 Update $\tilde{\mathbf{p}} \leftarrow \tilde{\mathbf{p}} + \upsilon\,\boldsymbol{\eta}$;
11 Update $\mathbf{r} \leftarrow \mathbf{r} - \upsilon\,\boldsymbol{\nu}$ and $\delta \leftarrow \|\upsilon\,\boldsymbol{\nu}\|/_D$;
12 Compute $\boldsymbol{\vartheta} = \mathbf{G}^{\top}\mathbf{r}$ and $\rho = \boldsymbol{\vartheta}^{\top}\boldsymbol{\vartheta}$;
13 Compute $\tau = \rho/\rho_0$;
14 Update $\rho_0 \leftarrow \rho$;
15 $m \leftarrow m + 1$;
16 **end**

Algorithm 1. Generic pseudo-code for the CGLS applied to the overdetermined problem (Eq. 22) for the particular case in which $\mathrm{H} = \mathrm{I}_P$ (Eq. 9; subsection 3.2), $\mu = 0$ (Eq. 11), $\mathrm{W}_d = \mathrm{I}_D$ (Eq. 12) and $\bar{\mathrm{p}} = 0$ (Eq. 14), where I_P and I_D are the identities of order *P* and *D*, respectively.

4 Floating-point operations

Two important factors affecting the efficiency of a given matrix algorithm are the storage and amount of required arithmetic. Here, we quantify this last factor associated with different computational strategies to solve the linear system of the equivalent-layer technique (Section 7). To do it, we opted by counting *flops*, which are floating point additions, subtractions, multiplications or divisions (Golub and Van Loan, 2013, p. 12–14). This is a non-hardware dependent approach that allows us to do direct comparison between different equivalent-layer methods. Most of the flops count used here can be found in Golub and Van Loan (2013, p. 12, 106, 107 and 164).

Let us consider the case in which the overdetermined problem (Eq. 22) is solved by Cholesky factorization (Eqs. 25, 26) directly for the parameter vector $\tilde{\mathbf{p}}$ by considering the particular case in which $\mathbf{H} = \mathbf{I}_P$ (Eq. 9; Subsection 3.2), $\mu = 0$ (Eq. 11), $\mathbf{W}_d = \mathbf{I}_D$ (Eq. 12) and $\bar{\mathbf{p}} = \mathbf{0}$ (Eq. 14), where $\mathbf{I}_P$ and $\mathbf{I}_D$ are the identities of order *P* and *D*, respectively. Based on the information provided in Table 1, the total number of flops can be determined by aggregating the flops required for various computations. These computations include the matrix-matrix and matrix-vector products $\mathbf{G}^{\top}\mathbf{G}$ and $\mathbf{G}^{\top}\mathbf{d}$, the Cholesky factor $\mathcal{G}$, and the solution of triangular systems. Thus, we can express the total number of flops as follows:

$$f_{\texttt{Cholesky}} = 1/3D^3 + 2D^2 + 2\left(P^2 + P\right)D. \tag{27}$$

The same particular overdetermined problem can be solved by using the CGLS method (Algorithm 1). In this case, we use Table 1 again to combine the total number of flops associated with the matrix-vector and inner products defined in line 3, before starting the iteration, and the 3 saxpys, 2 inner products and 2 matrix-vector products per iteration (lines 7–12). By considering a maximum number of iterations ITMAX, we obtain

$$f_{\texttt{CGLS}} = 2PD + \texttt{ITMAX}\left(4PD + 4D\right). \tag{28}$$

The same approach used to deduce (Eqs. 27, 28) is applied to compute the total number of flops for the selected equivalent-layer methods discussed in Section 7.

To simplify our analysis, we do not consider the number of flops required to compute the sensitivity matrix $\mathbf{G}$ (Eq. 3) or the matrix $\mathbf{A}$ associated with a given potential-field transformation (Eq. 4) because they depend on the specific harmonic functions g_{ij} and a_{ij} (Equations 2 and 5). We also neglect the required flops to compute $\mathbf{H}$, $\mathbf{W}_d$, $\mathbf{W}_q$ (Eqs. 9, 12 and 13), $\bar{\mathbf{p}}$ (Eq. 14), retrieve $\tilde{\mathbf{q}}$ from $\tilde{\boldsymbol{\delta}}_q$ (Eq. 18) and computing $\boldsymbol{\delta}_d$ (Eq. 19).

TABLE 1 Total number of flops associated with some useful terms according to Golub and Van Loan (2013, p. 12). The number of flops associated with Eqs. 25, 26 depends if the problem is over or underdetermined. Note that $P = Q$ for the case in which $\mathrm{H} = \mathrm{I}_P$ (Subsection 3.2). The term $\boldsymbol{\eta} \leftarrow \boldsymbol{\vartheta} + \tau\,\boldsymbol{\eta}$ is a vector update called *saxpy* (Golub and Van Loan, 2013, p. 4). The terms defined here are references to compute the total number of flops throughout the manuscript.

References	Term	Flops
Equation 10	$\mathbf{G}\mathbf{H}$	$2DQP$
Equation 15	$\mathbf{H}\,\tilde{\mathbf{q}}$	$2PQ$
Equation 22	$(\mathbf{G}\,\mathbf{H})^\top(\mathbf{G}\,\mathbf{H})$	$2Q^2D$
Equation 22	$(\mathbf{G}\,\mathbf{H})^\top\boldsymbol{\delta}_d$	$2QD$
Equation 23	$(\mathbf{G}\,\mathbf{H})\,(\mathbf{G}\,\mathbf{H})^\top$	$2D^2Q$
Equation 23	$(\mathbf{G}\,\mathbf{H})^\top\mathbf{u}$	$2QD$
Equation 25	lower triangle of $\boldsymbol{\mathcal{G}}$	$D^3/3$ or $Q^3/3$
Equation 26	solve triangular systems	$2D^2$ or $2Q^2$
Algorithm 1	$\boldsymbol{\eta} \leftarrow \boldsymbol{\vartheta} + \tau\,\boldsymbol{\eta}$	2Q
Algorithm 1	$\boldsymbol{\vartheta}^\top\boldsymbol{\vartheta}$	2Q
Algorithm 4	scale factor σ	$2DP + 4D$

5 Numerical stability

All equivalent-layer methods aim at obtaining an estimate $\tilde{\mathbf{p}}$ for the parameter vector $\mathbf{p}$ (Eq. 3), which contains the physical property of the equivalent sources. Some methods do it by first obtaining an estimate $\tilde{\mathbf{q}}$ for the reparameterized parameter vector $\mathbf{q}$ (Eq. 9) and then using it to obtain $\tilde{\mathbf{p}}$ (Eq. 15). The stability of a solution $\tilde{\mathbf{p}}$ against noise in the observed data is rarely addressed. Here, we follow the numerical stability analysis presented in Siqueira et al. (2017).

For a given equivalent-layer method (Section 7), we obtain an estimate $\tilde{\mathbf{p}}$ assuming noise-free potential-field data $\mathbf{d}$. Then, we create L different noise-corrupted data $\mathbf{d}^\ell$, $\ell \in \{1{:}L\}$, by adding L different sequences of pseudorandom Gaussian noise to $\mathbf{d}$, all of them having zero mean. From each $\mathbf{d}^\ell$, we obtain an estimate $\tilde{\mathbf{p}}^\ell$. Regardless of the particular equivalent-layer method used, the following inequality (Aster et al., 2019, p. 66) holds true:

$$\Delta p^\ell \leq \kappa\,\Delta d^\ell\,, \quad \ell \in \{1{:}L\}\,, \tag{29}$$

where κ is the constant of proportionality between the model perturbation

$$\Delta p^\ell = \frac{\|\tilde{\mathbf{p}}^\ell - \tilde{\mathbf{p}}\|}{\|\tilde{\mathbf{p}}\|}\,, \quad \ell \in \{1{:}L\}\,, \tag{30}$$

and the data perturbation

$$\Delta d^\ell = \frac{\|\mathbf{d}^\ell - \mathbf{d}\|}{\|\mathbf{d}\|}\,, \quad \ell \in \{1{:}L\}\,, \tag{31}$$

with $\|\cdot\|$ representing the Euclidean norm. The constant κ acts as the condition number associated with the pseudo-inverse in a given linear inversion. The larger (smaller) the value of κ, the more unstable (stable) is the estimated solution. Because of that, we designate κ as *stability parameter*. Equation 29 shows a linear relationship between the model perturbation Δp^ℓ and the data perturbation Δd^ℓ (Eqs. 30 and 31). We estimate the κ (Eq. 29) associated with a given equivalent-layer method as the slope of the straight line fitted to the *numerical stability curve* formed by the L points $\left(\Delta p^\ell\,,\,\Delta d^\ell\right)$.

6 Notation for subvectors and submatrices

Here, we use a notation inspired on that presented by Van Loan (1992, p. 4) to represent subvectors and submatrices. Subvectors of $\mathbf{d}$, for example, are specified by $\mathbf{d}[\mathbf{i}]$, where $\mathbf{i}$ is a list of integer numbers that "pick out" the elements of $\mathbf{d}$ forming the subvector $\mathbf{d}[\mathbf{i}]$. For example, $\mathbf{i} = (1,6,4,6)$ gives the subvector $\mathbf{d}[\mathbf{i}] = [d_1\ d_6\ d_4\ d_6]^\top$. Note that the list $\mathbf{i}$ of indices may be sorted or not and it may also have repeated indices. For the particular case in which the list has a single element $\mathbf{i} = (i)$, then it can be used to extract the ith element $d_i \equiv \mathbf{d}[i]$ of $\mathbf{d}$. Sequential lists can be represented by using the colon notation. We consider two types of sequential lists. The first has starting index is smaller than the final index and increment of 1. The second has starting index is greater than the final index and increment of −1. For example,

$$\begin{aligned}
\mathbf{i} = (3{:}8) &\Leftrightarrow \mathbf{d}[\mathbf{i}] = [d_3\ d_4\ \ldots\ d_8]^\top \\
\mathbf{i} = (8{:}3) &\Leftrightarrow \mathbf{d}[\mathbf{i}] = [d_8\ d_7\ \ldots\ d_3]^\top \\
\mathbf{i} = (:8) &\Leftrightarrow \mathbf{d}[\mathbf{i}] = [d_1\ d_2\ \ldots\ d_8]^\top\,, \\
\mathbf{i} = (3:) &\Leftrightarrow \mathbf{d}[\mathbf{i}] = [d_3\ d_4\ \ldots\ d_D]^\top
\end{aligned}$$

where D is the number of elements forming $\mathbf{d}$.

The notation above can also be used to define submatrices of a $D \times P$ matrix $\mathbf{G}$. For example, $\mathbf{i} = (2,7,4,6)$ and $\mathbf{j} = (1,3,8)$ lead to the submatrix

$$\mathbf{G}[\mathbf{i},\mathbf{j}] = \begin{bmatrix} g_{21} & g_{23} & g_{28} \\ g_{71} & g_{73} & g_{78} \\ g_{41} & g_{43} & g_{48} \\ g_{61} & g_{63} & g_{68} \end{bmatrix}.$$

Note that, in this case, the lists $\mathbf{i}$ and $\mathbf{j}$ "pick out", respectively, the rows and columns of $\mathbf{G}$ that form the submatrix $\mathbf{G}[\mathbf{i},\mathbf{j}]$. The ith row of $\mathbf{G}$ is given by the $1 \times P$ vector $\mathbf{G}[i,:]$. Similarly, the $D \times 1$ vector $\mathbf{G}[:,j]$ represents the jth column. Finally, we may use the colon notation to define the following submatrix:

$$\mathbf{i} = (2{:}5)\,,\mathbf{j} = (3{:}7) \Leftrightarrow \mathbf{G}[\mathbf{i},\mathbf{j}] = \begin{bmatrix} g_{23} & g_{24} & g_{25} & g_{26} & g_{27} \\ g_{33} & g_{34} & g_{35} & g_{36} & g_{37} \\ g_{43} & g_{44} & g_{45} & g_{46} & g_{47} \\ g_{53} & g_{54} & g_{55} & g_{56} & g_{57} \end{bmatrix},$$

which contains the contiguous elements of $\mathbf{G}$ from rows 2 to 5 and from columns 3 to 7.

7 Computational strategies

The linear inverse problem of the equivalent-layer technique (Section 3) for the case in which there are large volumes of potential-field data requires dealing with.

(i) the large computer memory to store large and full matrices;
(ii) the long computation time to multiply a matrix by a vector; and
(iii) the long computation time to solve a large linear system of equations.

Here, we review some strategies aiming at reducing the computational cost of the equivalent-layer technique. We quantify the computational cost by using flops (Section 4) and compare the results with those obtained for Cholesky factorization and CGLS (Eqs. 27, 28). We focus on the overall strategies used by the selected methods.

7.1 Moving window

The initial approach to enhance the computational efficiency of the equivalent-layer technique is commonly denoted *moving window* and involves first splitting the observed data d_i, $i \in \{1{:}D\}$, into M overlapping subsets (or data windows) formed by D^m data each, $m \in \{1{:}M\}$. The data inside the mth window are usually adjacent to each other and have indices defined by an integer list $\mathbf{i}^m$ having D^m elements. The number of data D^m forming the data windows are not necessarily equal to each other. Each data window has a $D^m \times 1$ observed data vector $\mathbf{d}^m \equiv \mathbf{d}[\mathbf{i}^m]$. The second step consists in defining a set of P equivalent sources with scalar physical property p_j, $j \in \{1{:}P\}$, and also split them into M overlapping subsets (or source windows) formed by P^m data each, $m \in \{1{:}M\}$. The sources inside the mth window have indices defined by an integer list $\mathbf{j}^m$ having P^m elements. Each source window has a $P^m \times 1$ parameter vector $\mathbf{p}^m$ and is located right below the corresponding mth data window. Then, each $\mathbf{d}^m \equiv \mathbf{d}[\mathbf{i}^m]$ is approximated by

$$\mathbf{f}^m = \mathbf{G}^m \mathbf{p}^m, \tag{32}$$

where $\mathbf{G}^m \equiv \mathbf{G}[\mathbf{i}^m, \mathbf{j}^m]$ is a submatrix of $\mathbf{G}$ (Eq. 3) formed by the elements computed with Eq. 2 using only the data and equivalent sources located inside the window mth. The main idea of the moving-window approach is using the $\tilde{\mathbf{p}}^m$ estimated for each window to obtain 1) an estimate $\tilde{\mathbf{p}}$ of the parameter vector for the entire equivalent layer or 2) a given potential-field transformation $\mathbf{t}$ (Eq. 4). The main advantages of this approach is that 1) the estimated parameter vector $\tilde{\mathbf{p}}$ or transformed potential field are not obtained by solving the full, but smaller linear systems and 2) the full matrix $\mathbf{G}$ (Eq. 3) is never stored.

Leão and Silva (1989) presented a pioneer work using the moving-window approach. Their method requires a regularly-spaced grid of observed data on a horizontal plane z_0. The data windows are defined by square local grids of $\sqrt{D'} \times \sqrt{D'}$ adjacent points, all of them having the same number of points D'. The equivalent sources in the mth data window are located below the observation plane, at a constant vertical distance Δz_0. They are arranged on a regular grid of $\sqrt{P'} \times \sqrt{P'}$ adjacent points following the same grid pattern of the observed data. The local grid of sources for all data windows have the same number of elements P'. Besides, they are vertically aligned, but expands the limits of their corresponding data windows, so that $D' < P'$. Because of this spatial configuration of observed data and equivalent sources, we have that $\mathbf{G}^m = \mathbf{G}'$ Eq. 32 for all data windows (i.e., $\forall\, m \in \{1{:}M\}$), where $\mathbf{G}'$ is a $D' \times P'$ constant matrix.

Initialization :
1 Set the indices $\mathbf{i}^m$ for each data window, $m \in \{1 : M\}$;
2 Set the indices $\mathbf{j}^m$ for each source window, $m \in \{1 : M\}$;
3 Set the constant depth $z_0 + \Delta z_0$ for all equivalent sources ;
4 Compute the vector $\mathbf{a}'$ associated with the desired potential-field transformation ;
5 Compute the matrix $\mathbf{G}'$;
6 Compute the matrix $\mathbf{B}'$ (equation 34) ;
7 Compute the vector $(\mathbf{a}')^\top \mathbf{B}'$;
8 $m = 1$;
9 **while** $m < M$ **do**
10 | Compute t_c^m (equation 33) ;
11 | $m \leftarrow m + 1$;
12 **end**

Algorithm 2. Generic pseudo-code for the method proposed by Leão and Silva (1989).

By omitting the normalization strategy used by Leão and Silva (1989), their method consists in directly computing the transformed potential field t_c^m at the central point $(x_c^m, y_c^m, z_0 + \Delta z_0)$ of each data window as follows:

$$t_c^m = (\mathbf{a}')^\top \mathbf{B}'\, \mathbf{d}^m\,, \quad m \in \{1{:}M\}, \tag{33}$$

where $\mathbf{a}'$ is a $P' \times 1$ vector with elements computed by Eq. 5 by using all equivalent sources in the mth window and only the coordinate of the central point in the mth data window and

$$\mathbf{B}' = (\mathbf{G}')^\top \left[\mathbf{G}'\,(\mathbf{G}')^\top + \mu\, \mathbf{I}_{D'}\right]^{-1} \tag{34}$$

is a particular case of matrix $\mathbf{B}$ associated with underdetermined problems Eq. 21 for the particular case in which $\mathbf{H} = \mathbf{W}_q = \mathbf{I}_{P'}$ (Eqs. 9, 13), $\mathbf{W}_d = \mathbf{I}_{D'}$ (Eq. 12), $\tilde{\mathbf{p}} = \mathbf{0}$ (Eq. 14), where $\mathbf{I}_{P'}$ and $\mathbf{I}_{D'}$ are identity matrices of order P' and D', respectively, and $\mathbf{0}$ is a vector of zeros. Due to the presumed spatial configuration of the observed data and equivalent sources, $\mathbf{a}'$ and $\mathbf{G}'$ are the same for all data windows. Hence, only the data vector $\mathbf{d}^m$ is modified according to the position of the data window. Note that Eq. 33 combines the potential-field transformation (Eq. 4) with the solution of the undetermined problem (Eq. 23).

The method proposed by Leão and Silva (1989) can be outlined by the Algorithm 2. Note that Leão and Silva (1989) directly compute the transformed potential t_c^m at the central point of each data window without explicitly computing and storing an estimated for $\mathbf{p}^m$ (Eq. 32). It means that their method allows computing a single potential-field transformation. A different transformation or the same one evaluated at different points require running their moving-data window method again.

The total number of flops in Algorithm 2 depends on computing the $P' \times D'$ matrix $\mathbf{B}'$ (Eq. 34) in line 6 and use it to define the $1 \times P'$ vector $(\mathbf{a}')^\top \mathbf{B}'$ (line 7) before starting the iterations and computing an inner product (Eq. 33) per iteration. We consider that the total number of flops associated with $\mathbf{B}'$ is obtained by the matrix-matrix product $\mathbf{G}'(\mathbf{G}')^\top$, its inverse and then the premultiplication by $(\mathbf{G}')^\top$. By using Table 1 and considering that inverse is computed via Cholesky factorization, we obtain that the total number of flops for lines 6 and 7 is $2(D')^2P' + 7(D')^3/6 + 2(D')^2P'$. Then, the total number of flops for Algorithm 2 is

$$f_{\mathrm{LS89}} = 7/6(D')^3 + 4P'(D')^2 + M\,2P'. \tag{35}$$

Soler and Uieda (2021) generalized the method proposed by Leão and Silva (1989) for irregularly spaced data on an undulating surface. A direct consequence of this generalization is that a different

Initialization :
1 Set the indices $\mathbf{i}^m$ for each data window, $m \in \{1:M\}$;
2 Set the indices $\mathbf{j}^m$ for each source window, $m \in \{1:M\}$;
3 Set the depth of all equivalent sources ;
4 Set a $D \times 1$ residuals vector $\mathbf{r} = \mathbf{d}$;
5 Set a $P \times 1$ vector $\tilde{\mathbf{p}} = \mathbf{0}$;
6 $m = 1$;
7 **while** $m < M$ **do**
8 Set the matrix $\mathbf{W}_d^m$;
9 Compute the matrix $\mathbf{G}^m$;
10 Compute $\tilde{\mathbf{p}}^m$ (equation 36);
11 $\tilde{\mathbf{p}}[\mathbf{j}^m] \leftarrow \tilde{\mathbf{p}}[\mathbf{j}^m] + \tilde{\mathbf{p}}^m$;
12 $\mathbf{r} \leftarrow \mathbf{r} - \mathbf{G}[:, \mathbf{j}^m]\,\tilde{\mathbf{p}}^m$;
13 $m \leftarrow m + 1$;
14 **end**

Algorithm 3. Generic pseudo-code for the method proposed by Soler and Uieda (2021).

Initialization :
1 Compute a $D \times 1$ vector $\boldsymbol{\Delta}\mathbf{z}$ whose i-th element Δz_i is a vertical distance controlling the depth of the i-th equivalent source, $i \in \{1:D\}$;
2 Set a tolerance ϵ ;
3 Set a maximum number of iterations ITMAX ;
4 Compute $\mathbf{G}$ (equation 3) ;
5 Compute the scale factor $\sigma = \mathbf{d}^\top(\mathbf{G}\mathbf{d})/\mathbf{d}^\top\mathbf{d}$;
6 Set a $D \times 1$ vector $\tilde{\mathbf{p}} = \sigma\,\mathbf{d}$;
7 Set a $D \times 1$ residuals vector $\mathbf{r} = \mathbf{d} - \mathbf{G}\tilde{\mathbf{p}}$;
8 Define the maximum absolute value $r_{\max}$ in $\mathbf{r}$;
9 $m = 1$;
10 **while** $(r_{\max} > \epsilon)$ **and** $(m <$ ITMAX$)$ **do**
11 Define the coordinates $(x_{\max}, y_{\max}, z_{\max})$ and index $i_{\max}$ of the observation point associated with $r_{\max}$;
12 $\tilde{\mathbf{p}}[i_{\max}] \leftarrow \tilde{\mathbf{p}}[i_{\max}] + (\sigma\, r_{\max})$;
13 $\mathbf{r} \leftarrow \mathbf{r} - (\sigma\, r_{\max})\,\mathbf{G}[:, i_{\max}]$;
14 Define the new $r_{\max}$ in $\mathbf{r}$;
15 $m \leftarrow m + 1$;
16 **end**

Algorithm 4. Generic pseudo-code for the method proposed by Cordell (1992).

submatrix $\mathbf{G}^m \equiv \mathbf{G}[\mathbf{i}^m, \mathbf{j}^m]$ (Eq. 32) must be computed for each window. Differently from Leão and Silva (1989), Soler and Uieda (2021) store the computed $\tilde{\mathbf{p}}^m$ for all windows and subsequently use them to obtain a desired potential-field transformation (Eq. 4) as the superposed effect of all windows. The estimated $\tilde{\mathbf{p}}^m$ for all windows are combined to form a single $P \times 1$ vector $\tilde{\mathbf{p}}$, which is an estimate for original parameter vector $\mathbf{p}$ (Eq. 3). For each data window, Soler and Uieda (2021) solve an overdetermined problem (Eq. 22) for $\tilde{\mathbf{p}}^m$ by using $\mathbf{H} = \mathbf{W}_q = \mathbf{I}_{P^m}$ (Eqs. 9, 13), $\mathbf{W}_d^m$ (Eq. 12) equal to a diagonal matrix of weights for the data inside the mth window and $\bar{p} = \mathbf{0}$ (Eq. 14), so that

$$\left[(\mathbf{G}^m)^\top \mathbf{W}_d^m\, \mathbf{G}^m + \mu\, \mathbf{I}_{P^m}\right] \tilde{\mathbf{p}}^m = (\mathbf{G}^m)^\top \mathbf{W}_d^m\, \mathbf{d}^m. \tag{36}$$

Unlike Leão and Silva (1989), Soler and Uieda (2021) do not adopt a sequential order of the data windows; rather, they adopt a randomized order of windows in their iterations. The overall steps of the method proposed by Soler and Uieda (2021) are defined by the Algorithm 3. For convenience, we have omitted the details about the randomized window order, normalization strategy employed and block-averaged sources layout proposed by those authors (see Subsection 2.1). Note that this algorithm starts with a residuals vector $\mathbf{r}$ that is iteratively updated. The iterative algorithm in Soler and Uieda (2021) estimates a solution ($\tilde{\mathbf{p}}^m$ in Eq. 36 using the data and the equivalent sources that fall within a moving-data window; however, it calculates the predicted data and the residual data in the whole survey data. Next, the residual data that fall within a new position of the data window is used as input data to estimate a new solution within the data window which, in turn, is used to calculated a new predicted data and a new residual data in the whole survey data.

The computational cost of Algorithm 3 can be defined in terms of the linear system (Eq. 36) to be solved for each window (line 10) and the subsequent updates in lines 11 and 12. We consider that the linear system cost can be quantified by the matrix-matrix and matrix-vector products $(\mathbf{G}^m)^\top\mathbf{G}^m$ and $(\mathbf{G}^m)^\top\mathbf{d}^m$, respectively, and solution of the linear system (line 10) via Cholesky factorization (Eqs. 25, 26). The following updates represent a saxpy without scalar-vector product (line 11) and a matrix-vector product (line 12). In this case, according to Table 1, the total number of flops associated with Algorithm 3 is given by:

$$f_{\mathrm{SU21}} = M\left[1/3(P')^3 + 2(D')(P')^2 + (4D')P'\right], \tag{37}$$

where P' and D' represent, respectively, the average number of equivalent sources and data at each window.

7.2 Column-action update

Cordell (1992) proposed a *column-action update* strategy similar to those applied to image reconstruction methods (e.g., Elfving et al., 2017). His approach, that was later used by Guspí and Novara (2009), relies on first defining one equivalent source located right below each observed data d_i, $i \in \{1{:}D\}$, at a vertical coordinate $z_i + \Delta z_i$, where Δz_i is proportional to the distance from the ith observation point (x_i, y_i, z_i) to its closest neighbor. The second step consists in updating the physical property p_j of a single equivalent source, $j \in \{1{:}D\}$ and remove its predicted potential field from the observed data vector $\mathbf{d}$, producing a residuals vector $\mathbf{r}$. At each iteration, the single equivalent source is the one located vertically beneath the observation station of the maximum data residual. Next, the predicted data produced by this single source is calculated over all of the observation points and a new data residual $\mathbf{r}$ and the $D \times 1$ parameter vector $\mathbf{p}$ containing the physical property of all equivalent sources are updated iteratively. During each subsequent iteration, Cordell's method either incorporates a single equivalent source or adjusts an existing equivalent source to match the maximum amplitude of the current residual field. The convergence occurs when all of the residuals are bounded by an envelope of prespecified expected error. At the end, the algorithm produces an estimate $\tilde{\mathbf{p}}$ for the parameter vector yielding a predicted potential field $\mathbf{f}$ (Eq. 3) satisfactorily fitting the observed data $\mathbf{d}$ according to a given criterion. Note that the method proposed by Cordell (1992) iteratively solves the linear $\mathbf{G}\tilde{\mathbf{p}} \approx \mathbf{d}$ with a $D \times D$ matrix $\mathbf{G}$. At each iteration, only a single column of $\mathbf{G}$ (Eq. 3) is used. An advantage of this *column-action update approach* is that the full matrix $\mathbf{G}$ is never stored.

Algorithm 4 delineates the Cordell's method. We have introduced a scale factor σ to improve convergence. Note that a single column $\mathbf{G}[:, i_{\max}]$ of the $D \times D$ matrix $\mathbf{G}$ (Eq. 3) is used per iteration, where $i_{\max}$ is the index of the maximum absolute value in $\mathbf{r}$. As pointed out by Cordell (1992), the method does not necessarily decrease monotonically along the iterations. Besides, the method may not converge depending on how the vertical distances Δz_i, $i \in \{1{:}D\}$, controlling the depths of the equivalent sources are set. According to Cordell (1992), the maximum absolute value $r_{\max}$ in $\mathbf{r}$ decreases robustly at the beginning and oscillates within a narrowing envelope for the subsequent iterations.

Guspí and Novara (2009) generalized Cordell's method to perform reduction to the pole and other transformations on

scattered magnetic observations by using two steps. The first step involves computing the vertical component of the observed field using equivalent sources while preserving the magnetization direction. In the second step, the vertical observation direction is maintained, but the magnetization direction is shifted to the vertical. The main idea employed by both Cordell (1992) and Guspí and Novara (2009) is an iterative scheme that uses a single equivalent source positioned below a measurement station to compute both the predicted data and residual data for all stations. This approach entails a computational strategy where a single column of the sensitivity matrix $\mathbf{G}$ (Eq. 3) is calculated per iteration.

The total number of flops in Algorithm 4 consists in computing the scale factor σ (line 5), computing an initial approximation for the parameter vector and the residuals (lines 6 and 7) and finding the maximum absolute value in vector $\mathbf{r}$ (line 8) before the while loop. Per iteration, there is a saxpy (line 13) and another search for the maximum absolute value in vector $\mathbf{r}$ (line 14). By considering that selecting the maximum absolute value in a $D\times 1$ vector is a $D\log_2(D)$ operation (e.g., Press et al., 2007, p. 420), we get from Table 1 that the total number of flops in Algorithm 38 is given by:

$$f_{\mathrm{C92}} = 4D^2 + 6D + D\log_2(D) + \mathtt{ITMAX}\left[2D + D\log_2(D)\right]. \quad (38)$$

7.3 Row-action update

To reduce the total processing time and memory usage of equivalent-layer technique, Mendonça and Silva (1994) proposed a strategy called *equivalent data concept*. The equivalent data concept is grounded on the principle that there is a subset of redundant data that does not contribute to the final solution and thus can be dispensed. Conversely, there is a subset of observations, called equivalent data, that contributes effectively to the final solution and fits the remaining observations (redundant data). Iteratively, Mendonça and Silva (1994) selected the subset of equivalent data that is substantially smaller than the original dataset. This selection is carried out by incorporating one data point at a time.

The method presented by Mendonça and Silva (1994) is a type of algebraic reconstruction technique (ART) (e.g., van der Sluis and van der Vorst, 1987, p. 58) or *row-action update* (e.g., Elfving et al., 2017) to estimate a parameter vector $\tilde{\mathbf{p}}$ for a regular grid of P equivalent sources on a horizontal plane z_0. Such methods iterate on the linear system rows to estimate corrections for the parameter vector, which may substantially save computer time and memory required to compute and store the full linear system matrix along the iterations. The convergence of such methods strongly depends on the linear system condition. The main advantage of such methods is not computing and storing the full linear system matrix, but iteratively using its rows. In contrast to common row-action algorithms, the rows in Mendonça and Silva (1994) are not processed sequentially. Instead, in Mendonça and Silva (1994), the rows are introduced according to their residual magnitudes (maximum absolute value in $\mathbf{r}$), which are computed based on the estimate over the equivalent layer from the previous iteration. The particular row-action method proposed by Mendonça and Silva (1994) considers that

Initialization :
1 Set a regular grid of P equivalent sources at a horizontal plane z_0 ;
2 Set a tolerance ϵ ;
3 Set a $D\times 1$ residuals vector $\mathbf{r}=\mathbf{d}$;
4 Define the maximum absolute value $r_{\max}$ in $\mathbf{r}$;
5 Define the index $i_{\max}$ of $r_{\max}$;
6 Define the list of indices $\mathbf{i}_r$ of the remaining data in $\mathbf{r}$;
7 Define $\mathbf{d}_e=\mathbf{d}[i_{\max}]$;
8 Compute $(\mathbf{F}+\mu\mathbf{I}_{D_e})$ and $\mathbf{G}_e$;
9 Compute $\tilde{\mathbf{p}}$ (equation 40) ;
10 Compute $\mathbf{r}=\mathbf{d}[\mathbf{i}_r]-\mathbf{G}[\mathbf{i}_r,:]\,\tilde{\mathbf{p}}$;
11 Define the maximum absolute value $r_{\max}$ in $\mathbf{r}$;
12 **while** $(r_{\max}>\epsilon)$ **do**
13 Define the index $i_{\max}$ of $r_{\max}$;
14 Define the list of indices $\mathbf{i}_r$ of the remaining elements in $\mathbf{r}$;
15 $\mathbf{d}_e \leftarrow \begin{bmatrix}\mathbf{d}_e \\ \mathbf{d}[i_{\max}]\end{bmatrix}$;
16 Update $(\mathbf{F}+\mu\mathbf{I}_{D_e})$ and $\mathbf{G}_e$;
17 Update $\tilde{\mathbf{p}}$ (equation 40) ;
18 Update $\mathbf{r}=\mathbf{d}[\mathbf{i}_r]-\mathbf{G}[\mathbf{i}_r,:]\,\tilde{\mathbf{p}}$;
19 Define the maximum absolute value $r_{\max}$ in $\mathbf{r}$;
20 **end**

Algorithm 5. Generic pseudo-code for the method proposed by Mendonça and Silva (1994).

$$\mathbf{d}=\begin{bmatrix}\mathbf{d}_e\\ \mathbf{d}_r\end{bmatrix}, \quad \mathbf{G}=\begin{bmatrix}\mathbf{G}_e\\ \mathbf{R}_r\end{bmatrix}, \quad (39)$$

where $\mathbf{d}_e$ and $\mathbf{d}_r$ are $D_e\times 1$ and $D_r\times 1$ vectors and $\mathbf{G}_e$ and $\mathbf{G}_r$ are $D_e\times P$ and $D_r\times P$ matrices, respectively. Mendonça and Silva (1994) designate $\mathbf{d}_e$ and $\mathbf{d}_r$ as, respectively, *equivalent* and *redundant* data. With the exception of a normalization strategy, Mendonça and Silva (1994) calculate a $P\times 1$ estimated parameter vector $\tilde{\mathbf{p}}$ by solving an underdetermined problem (Eq. 23) involving only the equivalent data $\mathbf{d}_e$ (Eq. 39) for the particular case in which $\mathbf{H}=\mathbf{W}_p=\mathbf{I}_P$ (Eqs. 9, 13), $\mathbf{W}_d=\mathbf{I}_{D_e}$ (Eq. 12) and $\tilde{p}=\mathbf{0}$ (Eq. 14), which results in

$$\begin{aligned}\left(\mathbf{F}+\mu\,\mathbf{I}_{D_e}\right)\mathbf{u}&=\mathbf{d}_e\\ \tilde{\mathbf{p}}&=\mathbf{G}_e^{\top}\mathbf{u}\end{aligned}, \quad (40)$$

where $\mathbf{F}$ is a computationally-efficient $D_e\times D_e$ matrix that approximates $\mathbf{G}_e\,\mathbf{G}_e^{\top}$. Mendonça and Silva (1994) presume that the estimated parameter vector $\tilde{\mathbf{p}}$ obtained from Eq. 40 leads to a $D_r\times 1$ residuals vector

$$\mathbf{r}=\mathbf{d}_r-\mathbf{G}_r\tilde{\mathbf{p}} \quad (41)$$

having a maximum absolute value $r_{\max}\le\epsilon$, where ϵ is a predefined tolerance.

The overall method of Mendonça and Silva (1994) is defined by Algorithm 5. It is important noting that the number D_e of equivalent data in $\mathbf{d}_e$ increases by one per iteration, which means that the order of the linear system in Eq. 40 also increases by one at each iteration. Those authors also propose a computational strategy based on Cholesky factorization (e.g., Golub and Van Loan, 2013, p. 163) for efficiently updating $\left(\mathbf{F}+\mu\,\mathbf{I}_{D_e}\right)$ at a given iteration (line 16 in Algorithm 5) by computing only its new elements with respect to those computed in the previous iteration.

7.4 Reparameterization

Another approach for improving the computational performance of equivalent-layer technique consists in setting a $P\times Q$ reparameterization matrix $\mathbf{H}$ (Eq. 9) with $Q\ll P$. This strategy has

been used in applied geophysics for decades (e.g., Skilling and Bryan, 1984; Kennett et al., 1988; Oldenburg et al., 1993; Barbosa et al., 1997) and is known as *subspace method*. The main idea relies in reducing the linear system dimension from the original P-space to a lower-dimensional subspace (the Q-space). An estimate $\tilde{\mathbf{q}}$ for the reparameterized parameter vector $\mathbf{q}$ is obtained in the Q-space and subsequently used to obtain an estimate $\tilde{\mathbf{p}}$ for the parameter vector $\mathbf{p}$ (Eq. 3) in the P-space by using Eq. 9. Hence, the key aspect of this *reparameterization approach* is solving an appreciably smaller linear inverse problem for $\tilde{\mathbf{q}}$ than that for the original parameter vector $\tilde{\mathbf{p}}$ (Eq. 3).

Oliveira Jr. et al. (2013) have used this approach to describe the physical property distribution on the equivalent layer in terms of piecewise bivariate polynomials. Specifically, their method consists in splitting a regular grid of equivalent sources into source windows inside which the physical-property distribution is described by bivariate polynomial functions. The key aspect of their method relies on the fact that the total number of coefficients required to define the bivariate polynomials is considerably smaller than the original number of equivalent sources. Hence, they formulate a linear inverse problem for estimating the polynomial coefficients and use them later to compute the physical property distribution on the equivalent layer.

The method proposed by Oliveira Jr. et al. (2013) consists in solving an overdetermined problem (Eq. 22) for estimating the polynomial coefficients $\tilde{\mathbf{q}}$ with $\mathbf{W}_d = \mathbf{I}_D$ (Eq. 12) and $\bar{q} = \mathbf{0}$ (Eq. 14), so that

$$\left(\mathbf{H}^\top \mathbf{G}^\top \mathbf{G}\, \mathbf{H} + \mu\, \mathbf{W}_q\right) \tilde{\mathbf{q}} = \mathbf{H}^\top \mathbf{G}^\top\, \mathbf{d}, \tag{42}$$

where $\mathbf{W}_q = \mathbf{H}^\top \mathbf{W}_p \mathbf{H}$ is defined by a matrix $\mathbf{W}_p$ representing the zeroth- and first-order Tikhonov regularization (e.g., Aster et al., 2019, p. 103). Note that, in this case, the prior information is defined in the P-space for the original parameter vector $\mathbf{p}$ and then transformed to the Q-space. Another characteristic of their method is that it is valid for processing irregularly-spaced data on an undulating surface.

Mendonça (2020) also proposed a reparameterization approach for the equivalent-layer technique. Their approach, however, consists in setting $\mathbf{H}$ as a truncated singular value decomposition (SVD) (e.g., Aster et al., 2019, p. 55) of the observed potential field. Differently from Oliveira Jr. et al. (2013), however, the method of Mendonça (2020) requires a regular grid of potential-field data on horizontal plane. Another difference is that these authors uses $\mathbf{W}_q = \mathbf{I}_Q$ (Eq. 13), which means that the regularization is defined directly in the Q-space.

We consider an algorithm (not shown) that solves the overdetermined problem (Eq. 22) by combining the reparameterization with CGLS method (Algorithm 1). It starts with a reparameterization step defined by defining a matrix $\mathbf{C} = \mathbf{G}\,\mathbf{H}$ (Eq. 10). Then, the CGLS (Algorithm 1) is applied by replacing $\mathbf{G}$ with $\mathbf{C}$. In this case, the linear system is solved by the reparameterized parameter vector $\tilde{\mathbf{q}}$ instead of $\tilde{\mathbf{p}}$. At the end, the estimated $\tilde{\mathbf{q}}$ is transformed into $\tilde{\mathbf{p}}$ (Eq. 15). Compared to the original CGLS shown in Algorithm 1, the algorithm discussed here has the additional flops associated with the matrix-matrix product to compute $\mathbf{C}$ and the matrix-vector product of Eq. 15 outside the while loop. Then, according to Table 1, the total number of flops given by:

$$f_{\texttt{reparam.}} = 2Q(DP + D) + 2PQ + \texttt{ITMAX}(4QD + 4D). \tag{43}$$

The important aspect of this approach is that, for the case in which $Q \ll P$ (Eq. 9), the number of flops per iteration can be substantially decreased with respect to those associated with Algorithm 1. In this case, the flops decrease per iteration compensates the additional flops required to compute $\mathbf{C}$ and obtain $\tilde{\mathbf{p}}$ from $\tilde{\mathbf{q}}$ (Eq. 15).

7.5 Sparsity induction

Li and Oldenburg (2010) proposed a method that applies the discrete wavelet transform to introduce sparsity into the original dense matrix $\mathbf{G}$ (Eq. 3). Those authors approximate a planar grid of potential-field data by a regularly-spaced grid of equivalent sources, so that the number of data D and sources P is the same, i.e., $D = P$. Specifically, Li and Oldenburg (2010) proposed a method that applies the wavelet transform to the original dense matrix $\mathbf{G}$ and sets to zero the small coefficients that are below a given threshold, which results in an approximating sparse representation of $\mathbf{G}$ in the wavelet domain. They first consider the following approximation

$$\mathbf{d}_w \approx \mathbf{G}_s\, \mathbf{p}_w, \tag{44}$$

where

$$\mathbf{d}_w = \mathcal{W}\, \mathbf{d}\,, \quad \mathbf{p}_w = \mathcal{W}\, \mathbf{p}, \tag{45}$$

are the observed data and parameter vector in the wavelet domain; $\mathcal{W}$ is a $D \times D$ orthogonal matrix defining a discrete wavelet transform; and $\mathbf{G}_s$ is a sparse matrix obtained by setting to zero the elements of

$$\mathbf{G}_w = \mathcal{W}\, \mathbf{G}\, \mathcal{W}^\top \tag{46}$$

with absolute value smaller than a given threshold.

Li and Oldenburg (2010) solve a normalized inverse problem in the wavelet domain. Specifically, they first define a matrix

$$\mathbf{G}_L = \mathbf{G}_s\, \mathbf{L}^{-1} \tag{47}$$

and a normalized parameter vector

$$\mathbf{p}_L = \mathbf{L}\, \mathbf{p}_w, \tag{48}$$

where $\mathbf{L}$ is a diagonal and invertible matrix representing an approximation of the first-order Tikhonov regularization in the wavelet domain. Then they solve an overdetermined problem (Eq. 22) to obtain an estimate $\tilde{\mathbf{p}}_L$ for $\mathbf{p}_L$ (Eq. 48), with $\mathbf{G}_L$ (Eq. 47), $\mathbf{H} = \mathbf{I}_P$ (Eq. 9), $\mu = 0$ (Eq. 11), $\mathbf{W}_d = \mathbf{I}_D$ (Eq. 12) and $\bar{p} = \mathbf{0}$ (Eq. 14) via conjugate-gradient method (e.g., Golub and Van Loan, 2013; Section 11.3). Finally, Li and Oldenburg (2010) compute an estimate $\tilde{\mathbf{p}}$ for the original parameter vector given by

$$\tilde{\mathbf{p}} = \mathcal{W}^\top \left(\mathbf{L}^{-1}\, \tilde{\mathbf{p}}_L\right), \tag{49}$$

where the term within parenthesis is an estimate $\tilde{\mathbf{p}}_w$ of the parameter vector $\mathbf{p}_w$ (Eq. 45) in the wavelet domain and matrix $\mathcal{W}^\top$ represents an inverse wavelet transform.

Barnes and Lumley (2011) also proposed a computationally efficient method for equivalent-layer technique by inducing sparsity into the original sensitivity matrix $\mathbf{G}$ (Eq. 3). Their approach consists in setting a $P \times Q$ reparameterization matrix $\mathbf{H}$ (Eq. 9) with $Q \approx 1.7\,P$. Note that, differently from Oliveira Jr. et al. (2013) and Mendonça (2020), Barnes and Lumley (2011) do not use the reparameterization with the purpose of reducing the number of the parameters. Instead, they use a reparameterization scheme that groups distant equivalent sources into blocks by using a bisection process. This scheme leads to a quadtree representation of the physical-property distribution on the equivalent layer, so that matrix $\mathbf{GH}$ (Eq. 10) is notably sparse. Barnes and Lumley (2011) explore this sparsity in solving the overdetermined problem for $\tilde{\mathbf{q}}$ (Eq. 42) via conjugate-gradient method (e.g., Golub and Van Loan, 2013; sec. 11.3).

It is difficult to predict the exact sparsity obtained from the methods proposed by Li and Oldenburg (2010) and Barnes and Lumley (2011) because it depends on several factors, including the observed potential-field data. According to Li and Oldenburg (2010), their wavelet approach results in a sparse matrix having ≈2% of the elements in $\mathbf{G}_w$ (Eq. 46). The reparameterization proposed by Barnes and Lumley (2011) leads to a sparse matrix $\mathbf{G}\,\mathbf{H}$ (Eq. 10) with only ≈1% of non-zero elements. These sparsity patterns can be efficiently explored, for example, in computing the required matrix-vector products along the iterations of the CGLS method (Algorithm 1).

7.6 Iterative methods using the full matrix G

Xia and Sprowl (1991) introduced an iterative method for estimating the parameter vector $\tilde{\mathbf{p}}$ (Eq. 3), which was subsequently adapted to the Fourier domain by Xia et al. (1993). Their method uses the full and dense sensitivity matrix $\mathbf{G}$ (Eq. 3) (without applying any compression or reparameterization, for example,) to compute the predicted data at all observation points per iteration. More than two decades later, Siqueira et al. (2017) have proposed an iterative method similar to that presented by Xia and Sprowl (1991). The difference is that Siqueira et al.'s algorithm was deduced from the *Gauss' theorem* (e.g., Kellogg, 1967, p. 43) and the *total excess of mass* (e.g., Blakely, 1996, p. 60). Besides, Siqueira et al. (2017) have included a numerical analysis showing that their method produces very stable solutions, even for noise-corrupted potential-field data.

The iterative method proposed by Siqueira et al. (2017) is outlined in Algorithm 6, presumes an equivalent layer formed by monopoles (point masses) and can be applied to irregularly-spaced data on an undulating surface. Instead of using the element of area originally proposed by Siqueira et al. (2017), we introduce the scale factor σ, which can be automatically computed from the observed potential-field data. Note that the residuals $\mathbf{r}$ are used to compute a correction $\boldsymbol{\Delta}\mathbf{p}$ for the parameter vector at each iteration (line 11), which requires a matrix-vector product involving the full matrix $\mathbf{G}$. Interestingly, this approach for estimating the physical property distribution on an equivalent layer is the same originally proposed by Bott (1960) for estimating the basement relief under sedimentary basins. The methods of Xia and Sprowl (1991) and Siqueira et al. (2017) were originally proposed for processing gravity data, but can be potentially applied to any harmonic function

Initialization :
1 Set P equivalent sources on a horizontal plane z_0 ;
2 Set a tolerance ϵ ;
3 Set a maximum number of iterations ITMAX ;
4 Compute $\mathbf{G}$ (equation 3) ;
5 Compute the scale factor $\sigma = \mathbf{d}^\top(\mathbf{G}\mathbf{d})/\mathbf{d}^\top\mathbf{d}$;
6 Set a $D \times 1$ vector $\tilde{\mathbf{p}} = \sigma\,\mathbf{d}$;
7 Compute the $D \times 1$ residuals vector $\mathbf{r} = \mathbf{d} - \mathbf{G}\tilde{\mathbf{p}}$;
8 Compute $\delta = \|\mathbf{r}\|/D$;
9 $m = 1$;
10 **while** $(\delta > \epsilon)$ **and** $(m <$ ITMAX$)$ **do**
11 Compute $\boldsymbol{\Delta}\mathbf{p} = \sigma\,\mathbf{r}$;
12 Update $\tilde{\mathbf{p}} \leftarrow \tilde{\mathbf{p}} + \boldsymbol{\Delta}\mathbf{p}$;
13 Compute $\boldsymbol{\nu} = \mathbf{G}\,\boldsymbol{\Delta}\mathbf{p}$;
14 Update $\mathbf{r} \leftarrow \mathbf{r} - \boldsymbol{\nu}$;
15 Compute $\delta = \|\boldsymbol{\nu}\|/D$;
16 $m \leftarrow m + 1$;
17 **end**

Algorithm 6. Generic pseudo-code for the iterative method proposed by Siqueira et al. (2017).

because they actually represent iterative solutions of the classical *Dirichlet's problem* or the *first boundary value problem of potential theory* (Kellogg, 1967, p. 236) on a plane.

Recently, Jirigalatu and Ebbing (2019) presented another iterative method for estimating a parameter vector $\tilde{\mathbf{p}}$ (Eq. 3). With the purpose of combining different potential-field data, their method basically modifies that shown in Algorithm 6 by changing the initial approximation and the iterative correction for the parameter vector. Specifically, Jirigalatu and Ebbing (2019) replace line 5 by $\tilde{\mathbf{p}} = \mathbf{0}$, where $\mathbf{0}$ is a vector of zeros, and line 11 by $\boldsymbol{\Delta}\mathbf{p} = \omega\mathbf{G}^\top\mathbf{r}$, where ω is a positive scalar defined by trial and error. Note that this modified approach requires two matrix-vector products involving the full matrix $\mathbf{G}$ per iteration. To overcome the high computational cost of these two products, Jirigalatu and Ebbing (2019) set an equivalent layer formed by prisms and compute their predicted potential field in the wavenumber domain by using the Gauss-FFT technique Zhao et al. (2018).

The iterative method proposed by Siqueira et al. (2017) (Algorithm 6) requires computing the scale factor σ (line 5), computing an initial approximation for the parameter vector and the residuals (lines 6 and 7) before the main loop. Inside the main loop, there is a half saxpy (lines 11 and 12) to update the parameter vector, a matrix-vector product (line 13) and the residuals update (line 14). Then, we get from Table 1 that the total number of flops is given by:

$$f_{\texttt{SOB17}} = 4D^2 + 6D + \texttt{ITMAX}\left(2D^2 + 3D\right). \tag{50}$$

Note that the number of flops per iteration in $f_{\texttt{SOB17}}$ (Eq. 50) has the same order of magnitude, but is smaller than that in $f_{\texttt{CGLS}}$ (Eq. 28).

7.7 Iterative deconvolution

Recently, Takahashi et al. (2020, 2022) proposed the *convolutional equivalent-layer method*, which explores the structure of the sensitivity matrix $\mathbf{G}$ (Eq. 3) for the particular case in which 1) there is a single equivalent source right below each potential-field datum and 2) both data and sources rely on planar and regularly spaced grids. Specifically, they consider a regular grid of D potential-field data at points (x_i, y_i, z_0), $i \in \{1{:}D\}$, on a horizontal plane z_0.

The data indices i may be ordered along the $x-$ or $y-$ direction, which results in an $x-$ or $y-$ oriented grid, respectively. They also consider a single equivalent source located right below each datum, at a constant vertical coordinate $z_0 + \Delta z$, $\Delta z > 0$. In this case, the number of data and equivalent sources are equal to each other (i.e., $D = P$) and $\mathbf{G}$ (Eq. 3) assumes a *doubly block Toeplitz* (Jain, 1989, p. 28) or *block-Toeplitz Toeplitz-block* (BTTB) (Chan and Jin, 2007, p. 67) structure formed by $N_B \times N_B$ blocks, where each block has $N_b \times N_b$ elements, with $D = N_B N_b$. This particular structure allows formulating the product of $\mathbf{G}$ and an arbitrary vector as a *fast discrete convolution* via *Fast Fourier Transform* (FFT) (Van Loan, 1992; Section 4.2).

Consider, for example, the particular case in which $N_B = 4$, $N_b = 3$ and $D = 12$. In this case, $\mathbf{G}$ (Eq. 3) is a 12×12 block matrix given by

$$\mathbf{G} = \begin{bmatrix} \mathbf{G}^0 & \mathbf{G}^1 & \mathbf{G}^2 & \mathbf{G}^3 \\ \mathbf{G}^{-1} & \mathbf{G}^0 & \mathbf{G}^1 & \mathbf{G}^2 \\ \mathbf{G}^{-2} & \mathbf{G}^{-1} & \mathbf{G}^0 & \mathbf{G}^1 \\ \mathbf{G}^{-3} & \mathbf{G}^{-2} & \mathbf{G}^{-1} & \mathbf{G}^0 \end{bmatrix}_{D \times D}, \tag{51}$$

where each block $\mathbf{G}^n$, $n \in \{(1 - N_B):(N_B - 1)\}$, is a 3×3 Toeplitz matrix. Takahashi et al. (2020, 2022) have deduced the specific relationship between blocks $\mathbf{G}^n$ and $\mathbf{G}^{-n}$ and also between a given block $\mathbf{G}^n$ and its transposed $(\mathbf{G}^n)^\top$ according to the harmonic function g_{ij} (Eq. 2) defining the element ij of the sensitivity matrix $\mathbf{G}$ (Eq. 3) and the orientation of the data grid.

Consider the matrix-vector products

$$\mathbf{G}\,\mathbf{v} = \mathbf{w} \tag{52}$$

and

$$\mathbf{G}^\top \mathbf{v} = \mathbf{w}, \tag{53}$$

involving a $D \times D$ sensitivity matrix $\mathbf{G}$ (Eq. 3) defined in terms of a given harmonic function g_{ij} (Eq. 2), where

$$\mathbf{v} = \begin{bmatrix} \mathbf{v}^0 \\ \vdots \\ \mathbf{v}^{N_B - 1} \end{bmatrix}_{D \times 1}, \quad \mathbf{w} = \begin{bmatrix} \mathbf{w}^0 \\ \vdots \\ \mathbf{w}^{N_B - 1} \end{bmatrix}_{D \times 1}, \tag{54}$$

are arbitrary partitioned vectors formed by N_B sub-vectors $\mathbf{v}^n$ and $\mathbf{w}^n$, $n \in \{0{:}(N_B - 1)\}$, all of them having N_b elements. Eqs. 52, 53 can be computed in terms of an auxiliary matrix-vector product

$$\mathbf{G}_c\,\mathbf{v}_c = \mathbf{w}_c, \tag{55}$$

where

$$\mathbf{v}_c = \begin{bmatrix} \mathbf{v}_c^0 \\ \vdots \\ \mathbf{v}_c^{N_B - 1} \\ \mathbf{0} \end{bmatrix}_{4D \times 1}, \quad \mathbf{w}_c = \begin{bmatrix} \mathbf{w}_c^0 \\ \vdots \\ \mathbf{w}_c^{N_B - 1} \\ \mathbf{0} \end{bmatrix}_{4D \times 1}, \tag{56}$$

are partitioned vectors formed by $2N_b \times 1$ sub-vectors

$$\mathbf{v}_c^n = \begin{bmatrix} \mathbf{v}^n \\ \mathbf{0} \end{bmatrix}_{2N_b \times 1}, \quad \mathbf{w}_c^n = \begin{bmatrix} \mathbf{w}^n \\ \mathbf{0} \end{bmatrix}_{2N_b \times 1}, \tag{57}$$

and $\mathbf{G}_c$ is a $4D \times 4D$ *doubly block circulant* (Jain, 1989, p. 28) or *block-circulant circulant-block* (BCCB) (Chan and Jin, 2007, p. 76) matrix. What follows aims at explaining how the original matrix-vector products defined by Eqs. 52, 53, involving a $D \times D$ BTTB matrix $\mathbf{G}$ exemplified by Eq. 51, can be efficiently computed in terms of the auxiliary matrix-vector product given by Eq. 55, which has a $4D \times 4D$ BCCB matrix $\mathbf{G}_c$.

Matrix $\mathbf{G}_c$ (Eq. 55) is formed by $2N_B \times 2N_B$ blocks, where each block $\mathbf{G}_c^n$, $n \in \{(1 - N_B):(N_B - 1)\}$ is a $2N_b \times 2N_b$ circulant matrix. For the case in which the original matrix-vector product is that defined by Eq. 52, the first column of blocks forming the BCCB matrix $\mathbf{G}_c$ is given by

$$\mathbf{G}_c[:, :2N_b] = \begin{bmatrix} \mathbf{G}_c^0 \\ \mathbf{G}_c^{-1} \\ \vdots \\ \mathbf{G}_c^{1-N_B} \\ \mathbf{0} \\ \mathbf{G}_c^{N_B - 1} \\ \vdots \\ \mathbf{G}_c^1 \end{bmatrix}_{4D \times 2N_b}, \tag{58}$$

with blocks $\mathbf{G}_c^n$ having the first column given by

$$\mathbf{G}_c^n[:, 1] = \begin{bmatrix} \mathbf{G}^n[:, 1] \\ 0 \\ (\mathbf{G}^n[1, N_b{:}2])^\top \end{bmatrix}_{2N_b \times 2N_b}, \quad n \in \{(1 - N_B):(N_B - 1)\}, \tag{59}$$

where $\mathbf{G}^n$ are the blocks forming the BTTB matrix $\mathbf{G}$ (Eq. 51). For the case in which the original matrix-vector product is that defined by Eq. 53, the first column of blocks forming the BCCB matrix $\mathbf{G}_c$ is given by

$$\mathbf{G}_c[:, :2N_b] = \begin{bmatrix} \mathbf{G}_c^0 \\ \mathbf{G}_c^1 \\ \vdots \\ \mathbf{G}_c^{N_B - 1} \\ \mathbf{0} \\ \mathbf{G}_c^{1-N_B} \\ \vdots \\ \mathbf{G}_c^{-1} \end{bmatrix}_{4D \times 2N_b}, \tag{60}$$

with blocks $\mathbf{G}_c^n$ having the first column given by

$$\mathbf{G}_c^n[:, 1] = \begin{bmatrix} (\mathbf{G}^n[1, :])^\top \\ 0 \\ \mathbf{G}^n[N_b{:}2, 1] \end{bmatrix}_{2N_b \times 2N_b}, \quad n \in \{(1 - N_B):(N_B - 1)\}. \tag{61}$$

The complete matrix $\mathbf{G}_c$ (Eq. 55) is obtained by properly downshifting the block columns $\mathbf{G}_c[:,:2N_b]$ defined by Eq. 58 or 60. Similarly, the nth block $\mathbf{G}_c^n$ of $\mathbf{G}_c$ is obtained by properly downshifting the first columns $\mathbf{G}_c^\ell[:,1]$ defined by Eq. 59 or 61.

Note that $\mathbf{G}_c$ (Eq. 55) is a $4D\times 4D$ matrix and $\mathbf{G}$ (Eq. 51) is a $D\times D$ matrix. It seems weird to say that computing $\mathbf{G}_c\mathbf{v}_c$ is more efficient than directly computing $\mathbf{G}\mathbf{v}$. To understand this, we need first to use the fact that BCCB matrices are diagonalized by the 2D unitary discrete Fourier transform (DFT) (e.g., Davis, 1979, p. 31). Because of that, $\mathbf{G}_c$ can be written as

$$\mathbf{G}_c = \left(\mathcal{F}_{2N_B}\otimes\mathcal{F}_{2N_b}\right)^*\mathbf{\Lambda}\left(\mathcal{F}_{2N_B}\otimes\mathcal{F}_{2N_b}\right), \tag{62}$$

where the symbol "⊗" denotes the Kronecker product (e.g., Horn and Johnson, 1991, p. 243), $\mathcal{F}_{2N_B}$ and $\mathcal{F}_{2N_b}$ are the $2N_B\times 2N_B$ and $2N_b\times 2N_b$ unitary DFT matrices (e.g., Davis, 1979, p. 31), respectively, the superscritpt "*" denotes the complex conjugate and $\mathbf{\Lambda}$ is a $4D\times 4D$ diagonal matrix containing the eigenvalues of $\mathbf{G}_c$. Due to the diagonalization of the matrix $\mathbf{G}_c$, Eq. 55 can be rewritten by using Eq. 62 and premultiplying both sides of the result by $\left(\mathcal{F}_{2N_B}\otimes\mathcal{F}_{2N_b}\right)$, i.e.,

$$\mathbf{\Lambda}\left(\mathcal{F}_{2N_B}\otimes\mathcal{F}_{2N_b}\right)\mathbf{v}_c = \left(\mathcal{F}_{2N_B}\otimes\mathcal{F}_{2N_b}\right)\mathbf{w}_c. \tag{63}$$

By following Takahashi et al. (2020), we rearrange Equation 63 as follows

$$\mathcal{L}\circ\left(\mathcal{F}_{2N_B}\,\mathcal{V}_c\,\mathcal{F}_{2N_b}\right) = \mathcal{F}_{2N_B}\,\mathcal{W}_c\,\mathcal{F}_{2N_b} \tag{64}$$

where "∘" denotes the Hadamard product (e.g., Horn and Johnson, 1991, p. 298) and $\mathcal{L}$, $\mathcal{V}_c$ and $\mathcal{W}_c$ are $2N_B\times 2N_b$ matrices obtained by rearranging, along their rows, the elements forming the diagonal of $\mathbf{\Lambda}$ (Eq. 62), vector $\mathbf{v}_c$ and vector $\mathbf{w}_c$ (Eq. 56), respectively. Then, by premultiplying both sides of Eq. 64 by $\mathcal{F}^*_{2N_B}$ and then postmultiplying both sides by $\mathcal{F}^*_{2N_b}$, we obtain

$$\mathcal{F}^*_{2N_B}\left[\mathcal{L}\circ\left(\mathcal{F}_{2N_B}\,\mathcal{V}_c\,\mathcal{F}_{2N_b}\right)\right]\mathcal{F}^*_{2N_b} = \mathcal{W}_c. \tag{65}$$

Finally, we get from Eq. 62 that matrix $\mathcal{L}$ can be computed by using only the first column $\mathbf{G}_c[:,1]$ of the BCCB matrix $\mathbf{G}_c$ (Eq. 55) according to (Takahashi et al., 2020)

$$\mathcal{L} = \sqrt{4D}\,\mathcal{F}_{2N_B}\,\mathcal{C}\,\mathcal{F}_{2N_b}, \tag{66}$$

where $\mathcal{C}$ is a $2N_B\times 2N_b$ matrix obtained by rearranging, along its rows, the elements of $\mathbf{G}_c[:,1]$ (Eq. 55). It is important noting that the matrices $\mathcal{C}$ and $\mathcal{L}$ (Eq. 66) associated with the BTTB matrix $\mathbf{G}$ (Eq. 51) are different from those associated with $\mathbf{G}^\top$.

The whole procedure to compute the original matrix-vector products $\mathbf{G}\mathbf{v}$ (Eq. 52) and $\mathbf{G}^\top\mathbf{v}$ (Eq. 53) consists in 1) rearranging the elements of the vector $\mathbf{v}$ and the first column $\mathbf{G}[:,1]$ of matrix $\mathbf{G}$ into the matrices $\mathcal{V}_c$ and $\mathcal{C}$ (Eqs. 65, 66), respectively; 2) computing terms $\mathcal{F}_{2N_B}\mathcal{A}\mathcal{F}_{2N_b}$ and $\mathcal{F}^*_{2N_B}\mathcal{A}\mathcal{F}^*_{2N_b}$, where $\mathcal{A}$ is a given matrix, and a Hadamard product to obtain $\mathcal{W}_c$ (Eq. 65); and 3) retrieve the elements of vector $\mathbf{w}$ (Eq. 52) from $\mathcal{W}_c$ (Eq. 65). It is important noting that the steps (i) and (iii) do not have any computational cost because they involve only reorganizing elements of vectors and matrices. Besides, the terms $\mathcal{F}_{2N_B}\mathcal{A}\mathcal{F}_{2N_b}$ and $\mathcal{F}^*_{2N_B}\mathcal{A}\mathcal{F}^*_{2N_b}$ in step (ii) represent, respectively, the 2D Discrete Fourier Transform (2D-DFT) and the 2D Inverse Discrete Fourier Transform (2D-IDFT) of $\mathcal{A}$. These transforms can be efficiently computed by using the 2D Fast Fourier Transform (2D-FFT). Hence, the original matrix-vector products $\mathbf{G}\mathbf{v}$ (Eq. 52) and $\mathbf{G}^\top\mathbf{v}$ (Eq. 53) can be efficiently computed by using the 2D-FFT.

Algorithm 7 and Algorithm 8 show pseudo-codes for the convolutional equivalent-layer method proposed by Takahashi et al. (2020, 2022). Note that those authors formulate the overdetermined problem (Eq. 22) of obtaining an estimate $\tilde{\mathbf{p}}$ for the parameter vector $\mathbf{p}$ (Eq. 3) as an *iterative deconvolution* via *conjugate gradient normal equation residual* (CGNR) Golub and Van Loan (2013, sec. 11.3) or *conjugate gradient least squares* (CGLS) (Aster et al., 2019, p. 165) method. They consider $\mathbf{H}=\mathbf{I}_P$ (Eq. 9), $\mu=0$ (Eq. 11), $\mathbf{W}_d=\mathbf{W}_q=\mathbf{I}_P$ (Eqs. 12, 13) and $\bar{\mathbf{p}}=\mathbf{0}$ (Eq. 14). As shown by Takahashi et al. (2020, 2022), the CGLS produces stable estimates $\tilde{\mathbf{p}}$ for the parameter vector $\mathbf{p}$ (Eq. 3) in the presence of noisy potential-field data $\mathbf{d}$. This is a well-known property of the CGLS method (e.g., Aster et al., 2019, p. 166).

The key aspect of Algorithm 7 is replacing the matrix-vector products of CGLS (Algorithm 1) by fast convolutions (Algorithm 8). A fast convolution requires one 2D-DFT, one 2D-IDFT and an entrywise product of matrices. We consider that the 2D-DFT/IDFT are computed with 2D-FFT and requires $\lambda\,(4D)\log_2(4D)$ flops, where $\lambda=5$ is compatible with a radix-2 FFT (Van Loan, 1992, p. 16), and the entrywise product $24D$ flops because it involves two complex matrices having $4D$ elements (Golub and Van Loan, 2013, p. 36). Hence, Algorithm 8 requires $\lambda\,(16D)\log_2(4D)+26D$ flops, whereas a conventional matrix-vector multiplication involving a $D\times D$ matrix requires $2D^2$ (Table 1). Finally, Algorithm 7 requires two 2D-FFTs (lines 4 and 5), one fast convolution and an inner product (line 8) previously to the while loop. Per iteration, there are three saxpys (lines 12, 15 and 16), two inner products (lines 14 and 17) and two fast convolutions (lines 13 and 17), so that:

$$f_{\texttt{TOB20}} = \lambda\,(16D)\log_2(4D)+26D+\texttt{ITMAX}\left[\lambda\,(16D)\log_2(4D)+58D\right]. \tag{67}$$

7.8 Direct deconvolution

The method proposed by Takahashi et al. (2020, 2022) can be reformulated to avoid the iterations of the conjugate gradient method. This alternative formulation consists in considering that $\mathbf{v}=\mathbf{p}$ and $\mathbf{w}=\mathbf{d}$ in Eq. 52, where $\mathbf{p}$ is the parameter vector (Eq. 3) and $\mathbf{d}$ the observed data vector. In this case, the equality "=" in Eq. 52 becomes an approximation "≈ ". Then, Eq. 64 is manipulated to obtain

$$\mathcal{V}_c \approx \mathcal{F}^*_{2N_B}\left[\left(\mathcal{F}_{2N_B}\,\mathcal{W}_c\,\mathcal{F}_{2N_b}\right)\circ\check{\mathcal{L}}\right]\mathcal{F}^*_{2N_b}, \tag{68}$$

where

$$\check{\mathcal{L}} = \mathcal{L}^*\oslash\left(\mathcal{L}\circ\mathcal{L}^*+\zeta\mathbf{1}\right), \tag{69}$$

$\mathbf{1}$ is a $4D\times 4D$ matrix of ones, "⊘" denotes entrywise division and ζ is a positive scalar. Note that $\zeta=0$ leads to $\mathbf{1}\oslash\mathcal{L}$. In this case, the entrywise division may be problematic due to the elements of

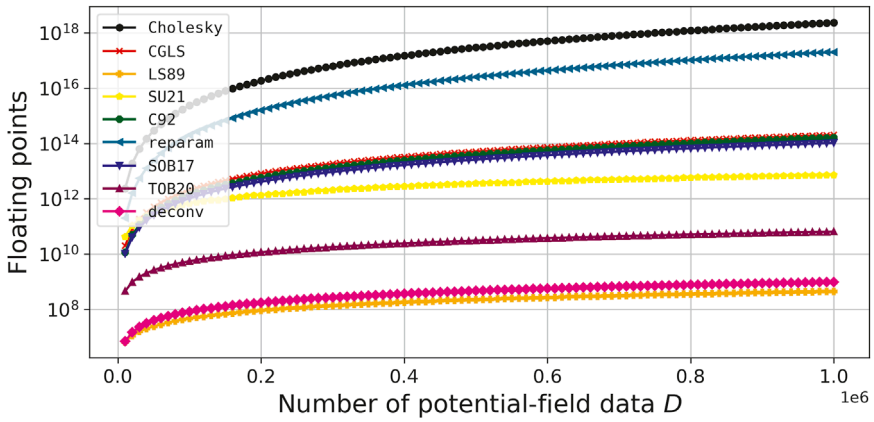

FIGURE 1
Total number of flops for different equivalent-layer methods (Eqs. 27, 28, 35, 37, 38, 43, 50, 67, and 70). The number of potential-field data D varies from 10,000 to 1,000,000.

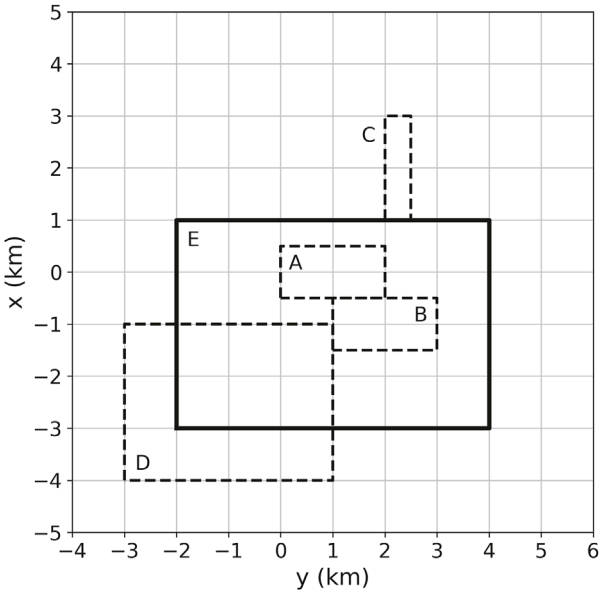

FIGURE 2
Synthetic prisms used in numerical simulations. The prisms A to D with horizontal projections represented by dashed lines have density contrasts of, respectively, 1,500, −1800, −3,000 and 1,200 kg/m^3, tops varying from 10 to 100 m, bottom from 1,010 to 1,500 m and side lengths varying from 1,000 to 4,000 m. The prism E with horizontal projection represented by solid lines has a density contrast −900 kg/m^3, top at 1,000 m, bottom at 1,500 m and side lengths of 4,000 and 6,000 m. Our model also have 300 additional small cubes (not shown), with top at 0 m and side lengths defined according to a pseudo-random variable having uniform distribution from 100 to 200 m. Their density contrasts vary randomly from 1,000 to 2000 kg/m^3.

Initialization :
Set the regular grid of P equivalent sources on a horizontal plane z_0 ;
Set a tolerance ϵ and a maximum number of iterations ITMAX ;
Compute the first column $\mathbf{G}[:,1]$ and row $\mathbf{G}[1,:]$ of the sensitivity matrix $\mathbf{G}$ (equation 3) for the particular case in which it has a BTTB structure (equation 51);
Rearrange the elements of $\mathbf{G}[:,1]$ into matrix $\mathcal{C}$, compute its 2D-DFT via 2D-FFT and multiply by $\sqrt{4D}$ to obtain a matrix $\mathcal{L}'$ (equation 66);
Rearrange the elements of $\mathbf{G}[1,:]$ into matrix $\mathcal{C}$, compute its 2D-DFT via 2D-FFT and multiply by $\sqrt{4D}$ to obtain a matrix $\mathcal{L}''$ (equation 66);
Set $\tilde{\mathbf{p}} = \mathbf{0}$;
Set $\mathbf{r} = \mathbf{d}$ and compute $\delta = \|\mathbf{r}\|/D$;
Compute $\vartheta = \mathbf{G}^\top \mathbf{r}$ (Algorithm 8) and $\rho_0 = \vartheta^\top \vartheta$;
Set $\tau = 0$ and $\boldsymbol{\eta} = \mathbf{0}$;
$m = 1$;
while $(\delta > \epsilon)$ **and** $(m <$ ITMAX$)$ **do**
  Update $\boldsymbol{\eta} \leftarrow \vartheta + \tau\,\boldsymbol{\eta}$;
  Compute $\boldsymbol{\nu} = \mathbf{G}\,\boldsymbol{\eta}$ (Algorithm 8);
  Compute $\upsilon = \rho_0/(\boldsymbol{\nu}^\top \boldsymbol{\nu})$;
  Update $\tilde{\mathbf{p}} \leftarrow \tilde{\mathbf{p}} + \upsilon\,\boldsymbol{\eta}$;
  Update $\mathbf{r} \leftarrow \mathbf{r} - \upsilon\,\boldsymbol{\nu}$ and $\delta \leftarrow \|\upsilon\,\boldsymbol{\nu}\|/D$;
  Compute $\vartheta = \mathbf{G}^\top \mathbf{r}$ (Algorithm 8) and $\rho = \vartheta^\top \vartheta$;
  Compute $\tau = \rho/\rho_0$;
  Update $\rho_0 \leftarrow \rho$;
  $m \leftarrow m + 1$;
end

Algorithm 7. Generic pseudo-code for the convolutional equivalent-layer method proposed by Takahashi et al. (2020, 2022).

Rearrange the elements of $\mathbf{v}$ (equations 52 and 54) into the matrix $\mathcal{V}_c$ (equation 65);
Compute $\mathcal{F}_{2N_B}\,\mathcal{V}_c\,\mathcal{F}_{2N_b}$ via 2D-FFT;
Compute the Hadamard product with matrix $\mathcal{L}$ (equation 66);
Compute 2D-IDFT via 2D-FFT to obtain matrix $\mathcal{W}_c$ (65);
Retrieve $\mathbf{w}$ (equations 52 and 54) from $\mathbf{w}_c$ (equations 55–57);

Algorithm 8. Pseudo-code for computing the generic matrix-vector products given by Eqs. 52, 53 via fast 2D discrete convolution for a given vector $\mathbf{v}$ (Eq. 54) and matrix $\mathcal{L}$ (Eq. 66).

$\mathcal{L}$ having absolute value equal or close to zero. So, a small ζ is set to avoid this problem in Eq. 69. Next, we use $\check{\mathcal{L}}$ to obtain a matrix $\mathcal{V}_c$ from Eq. 68. Finally, the elements of the estimated parameter vector $\tilde{\mathbf{p}}$ are retrieved from the first quadrant of $\mathcal{V}_c$. This procedure represents a *direct deconvolution* (e.g., Aster et al., 2019, p. 220) using a *Wiener filter* (e.g., Gonzalez and Woods, 2002, p. 263).

The required total number of flops associated with the direct deconvolution aggregates one 2D-FFT to compute matrix $\mathcal{L}$ (Eq. 66), one entrywise product $\mathcal{L} \circ \mathcal{L}^*$ involving complex matrices and one entrywise division to compute $\check{\mathcal{L}}$ (Eq. 69) and a fast convolution (Algorithm 8) to evaluate Eq. 68, which results in:

$$f_{\text{deconv.}} = \lambda\ (12D)\log_2(4D) + 72D. \tag{70}$$

Differently from the convolutional equivalent-layer method proposed by Takahashi et al. (2020, 2022), the alternative direct deconvolution presented here produces an estimated parameter vector $\tilde{\mathbf{p}}$ directly from the observed data $\mathbf{d}$, in a single step, avoiding the conjugate gradient iterations. On the other hand, the alternative method presented here requires estimating a set

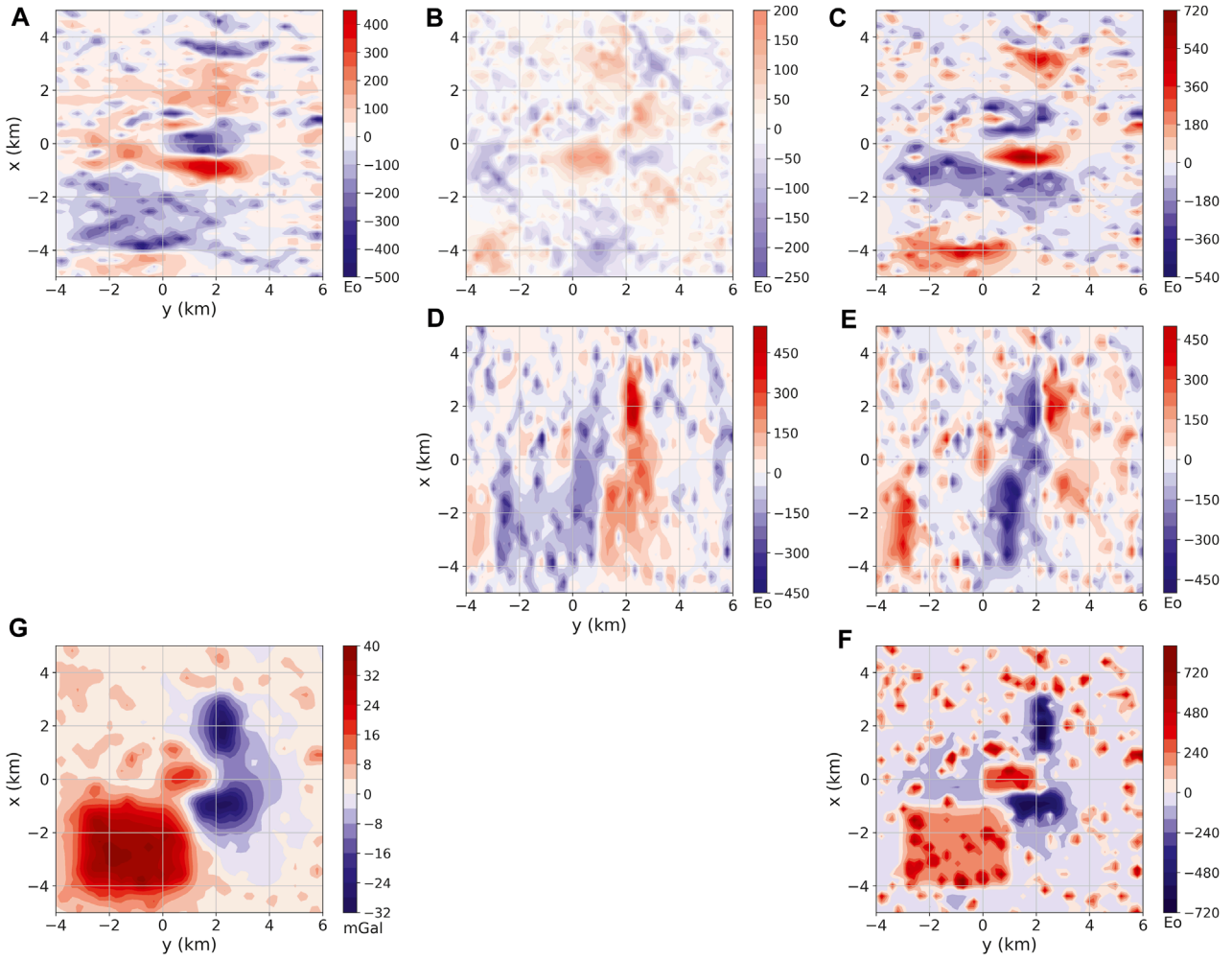

FIGURE 3
Noise-free gravity data produced by an ensemble of rectangular prisms (Figure 2). The data are located on a regular grid of 50 × 50 points. Panels **(A–F)** show, respectively, the *xx*, *xy*, *xz*, *yy*, *yz* and *zz* component of the gravity-gradient tensor in Eötvös (E). Panel **(G)** shows the gravity disturbance in milligals (mGal).

of tentative parameter vectors $\tilde{\mathbf{p}}$ for different predefined ζ. Besides, there must be criterion to chose the best $\tilde{\mathbf{p}}$ from this tentative set. This can be made, for example, by using the well-known *L-curve* (Hansen, 1992). From a computational point of view, the number of CGLS iterations in the method proposed by Takahashi et al. (2020, 2022) is equivalent to the number of tentative estimated parameter vectors required to form the L-curve in the proposed direct deconvolution.

8 Numerical simulations

8.1 Flops count

Figure 1 shows the total number of flops for solving the overdetermined problem (Eq. 22) with different equivalent-layer methods (Eqs. 27, 28, 35, 37, 38, 43, 50, 67 and 70), by considering the particular case in which $\mathbf{H} = \mathbf{I}_P$ (Eq. 9; Subsection 3.2), $\mu = 0$ (Eq. 11), $\mathbf{W}_d = \mathbf{I}_D$ (Eq. 12) and $\bar{\mathbf{p}} = \mathbf{0}$ (Eq. 14), where $\mathbf{I}_P$ and $\mathbf{I}_D$ are the identities of order P and D, respectively. The flops are computed for different number of potential-field data ranging from 10,000 to 1,000,000. Figure 1 shows that the moving data-window strategy by using Leão and Silva's 1989 method and direct deconvolution are the fastest methods.

The control parameters to run the equivalent-layer methods shown in Figure 1 are the following: 1) in CGLS, reparameterization approaches (e.g., Oliveira Jr. et al., 2013; Mendonça, 2020), Siqueira et al. (2017), and Takahashi et al. (2020) (Eqs. 28, 38, 43, 50, 67) we set ITMAX = 50; 2) Cordell (1992) we set ITMAX = 10D; 3) in Leão and Silva (1989) (Eq. (35)) we set $D' = 49(7 \times 7)$ and $P' = 225(15 \times 15)$; and 4) in Soler and Uieda (2021) (Eq. (37)) we set $D' = P' = 900(30 \times 30)$.

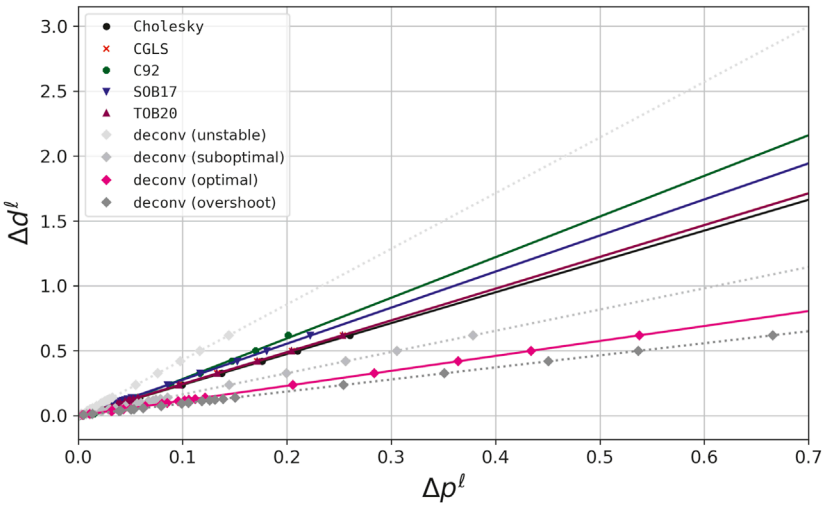

FIGURE 4
Numerical stability curves obtained for the 21 synthetic gravity data sets by using the Cholesky factorization with $\mu \approx 2 \times 10^{-2}$; column-action update (C92) with 25,000 iterations (10× the number D of potential-field data); CGLS, iterative method (S0B17) and iterative deconvolution (T0B20) with 50 iterations each (Algorithm 1, Algorithm 6 and Algorithm 7); and the direct deconvolution (deconv.) computed with four different values for ζ (Eq. 69): 0, 10^{-18} (overshoot), 10^{-22} (optimal) and 10^{-28} (suboptimal). The stability parameter κ (Eq. 29) obtained for the eight curves described above are 2.37 (Cholesky); 2.45 (CGLS); 3.13 (C92); 2.78 (S0B17); 2.44 (T0B20); 4.28, 1.63, 1.15 and 0.93 (deconv. with null, suboptimal, optimal and overshoot ζ).

8.2 Synthetic potential-field data

We create a model composed of several rectangular prisms that can be split into three groups. The first is composed of 300 small cubes (not shown) with top at 0 m and side lengths defined according to a pseudo-random variable having uniform distribution from 100 to 200 m. Their density contrasts are defined by a pseudo-random variable uniformly distributed from 1,000 to 2000 kg/m^3. These prisms produce the short-wavelength component of the simulated gravity data. The 4 prisms forming the second group of our model (indicated by A-D in Figure 2) have tops varying from 10 to 100 m and bottom from 1,010 to 1,500 m. They have density contrasts of 1,500, −1800, −3,000 and 1,200 kg/m^3 and side lengths varying from 1,000 to 4,000 m. These prisms produce the mid-wavelength component of the simulated gravity data. There is also a single prism (indicated by E in Figure 2) with top at 1,000 m, bottom at 1,500 m and side lengths of 4,000 and 6,000 m. This prism has density contrast is −900 kg/m^3 and produces the long-wavelength of our synthetic gravity data.

We have computed noise-free gravity disturbance and gravity-gradient tensor components produced by our model (Figure 2) on a regularly spaced grid of 50×50 points at $z = -100$ m (Figure 3). We have also simulated additional $L = 20$ gravity disturbance data sets $\mathbf{d}^\ell$, $\ell \in \{1{:}L\}$, by adding pseudo-random Gaussian noise with zero mean and crescent standard deviations to the noise-free data (not shown). The standard deviations vary from 0.5% to 10% of the maximum absolute value in the noise-free data, which corresponds to 0.21 and 4.16 mGal, respectively.

8.3 Stability analysis and gravity-gradient components

We set a planar equivalent layer of point masses having one source below each datum at a constant vertical coordinate $z \approx 512.24$ m. This depth was set by following the Dampney's (1969) criterion (see Subsection 2.1), so that the vertical distance Δz between equivalent sources and the simulated data is equal to 3× the grid spacing ($\Delta x = \Delta y \approx 204.08$ m). Note that, in this case, the layer has a number of sources p equal to the number of data D.

We have applied the Cholesky factorization (Eqs. 25, 26), CGLS (Algorithm 1), column-action update method of Cordell (1992) (Algorithm 4), the iterative method of Siqueira et al. (2017) (Algorithm 6), the iterative deconvolution (Algorithm 7 and Algorithm 8) proposed by Takahashi et al. (2020) and the direct deconvolution (Eqs. 68 and 69) with four different values for the parameter ζ to the 21 gravity data sets.

For each method, we have obtained one estimate $\tilde{\mathbf{p}}$ from the noise-free gravity data $\mathbf{d}$ and $L = 20$ estimates $\tilde{\mathbf{p}}^\ell$ from the noise-corrupted gravity data $\mathbf{d}^\ell$, $\ell \in \{1{:}L\}$, for the planar equivalent layer of point masses, totaling 21 estimated parameter vectors and 20 pairs $\left(\Delta p^\ell, \Delta d^\ell\right)$ of model and data perturbations (Eqs. 30, 31). Figure 4 shows the numerical stability curves computed with each method for the synthetic gravity data.

All these 21 estimated parameters vectors were obtained by solving the overdetermined problem (Eq. 22) with the same method for the particular case in which $\mathbf{H} = \mathbf{I}$ (Eq. 9; Subsection 3.2), $\mathbf{W}_d = \mathbf{W}_q = \mathbf{I}$ (Eqs. 12, 13) and $\bar{\mathbf{p}} = \mathbf{0}$ (Eq. 14), where $\mathbf{I}$ is the identity of order D.

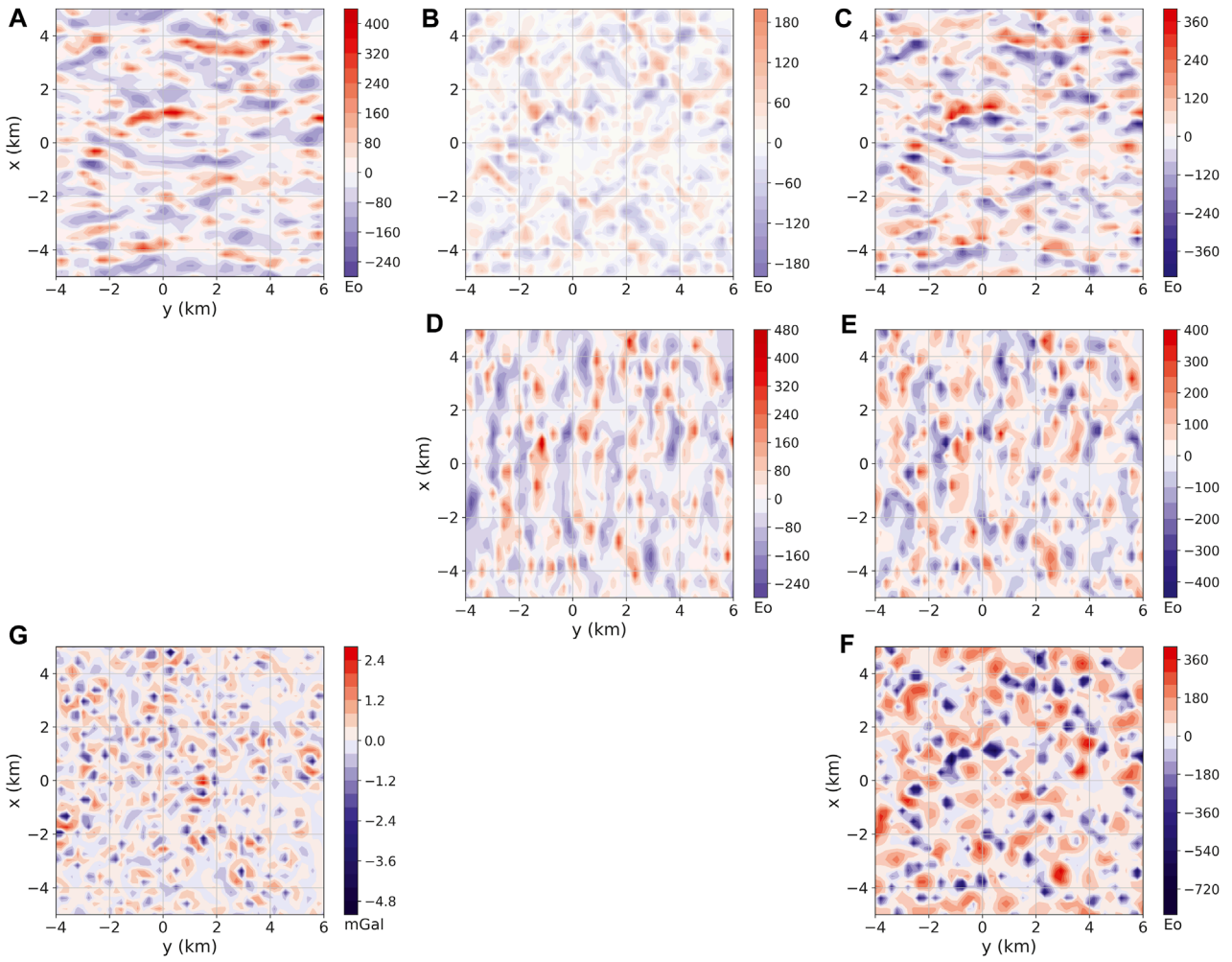

FIGURE 5
Residuals between the gravity data predicted by the equivalent layer estimated with the iterative deconvolution (TOB20) (Algorithm 7). The inverse problems was solved by using the noise-corrupted gravity disturbance having the maximum noise level (not shown). Panels **(A–F)** show the residuals between the predicted and noise-free gravity gradient data (Figure 3) associated with the *xx*, *xy*, *xz*, *yy*, *yz* and *zz* components of the gravity-gradient tensor, respectively. The values are in Eötvös. **(G)** Shows the residuals between the predicted and noise-corrupted gravity disturbances. The values are in milligals (mGal).

Figure 4 shows how the numerical stability curves vary as the level of the noise is increased. We can see that for all methods, a linear tendency is observed as it is expected. The inclination of the straight line indicates the stability of each method. As shown in Figure 4, the direct deconvolution with $\zeta = 0$ exhibits a high slope, which indicates high instability and emphasizes the necessity of using the Wiener filter ($\zeta > 0$ in Eq. 69).

The estimated stability parameters κ (Eq. 29) obtained for the Cholesky factorization, CGLS and iterative deconvolution are close to each other (Figure 4). They are slightly smaller than that obtained for the iterative method of Siqueira et al. (2017). Note that by varying the parameter ζ (Eq. 69) it is possible to obtain different stability parameters κ for the direct deconvolution. There is no apparent rule to set ζ. A practical criterion can be the maximum ζ producing a satisfactory data fit. Overshoot values tend to exaggeratedly smooth the predicted data. As we can see in Figure 4, the most unstable approaches are the direct deconvolution with null ζ (`deconv.unstable`), followed by the column-action update (`C92`).

We inverted the noise-corrupted gravity disturbance with the highest noise level (not shown) to estimate an equivalent layer (not shown) via iterative deconvolution (Algorithm 7). Figure 5G shows the residuals (in mGal) between the predicted and noise-corrupted gravity disturbances. As we can see, the residuals are uniformly distributed on simulated area and suggest that the equivalent layer produces a good data fit. This can be verified by inspecting the histogram of the residuals between the predicted and noise-corrupted gravity disturbances shown in panel **(G)** of Figure 6.

Using the estimated layer, we have computed the gravity-gradient data (not shown) at the observations points. Figure 5A–F show the residuals (in Eötvös) between the predicted (not shown) and noise-free gravity-gradient data (Figure 3). These figures show that the iterative deconvolution (Algorithm 7) could predict the six components of the gravity-gradient tensor with a good precision,

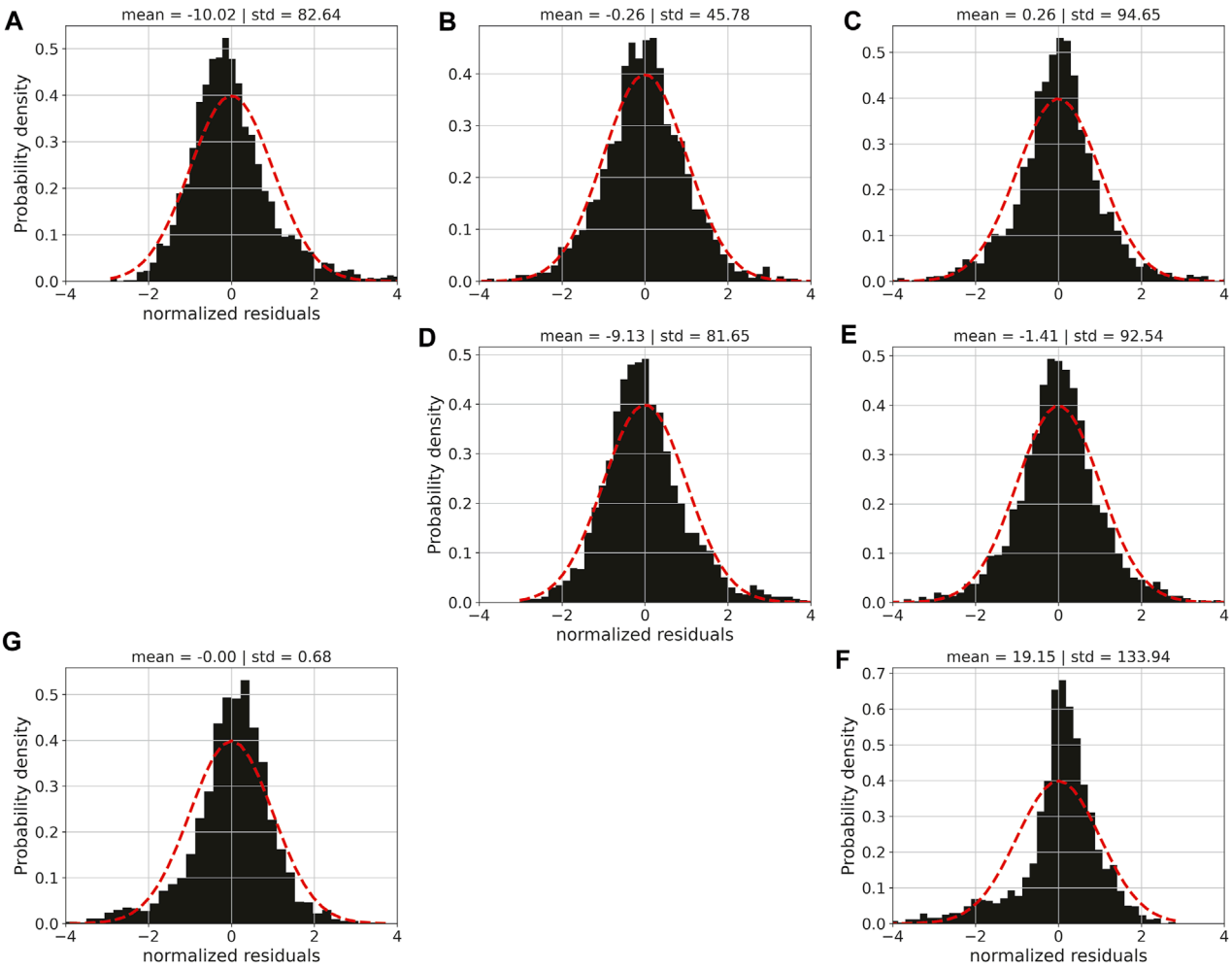

FIGURE 6
Histograms of the residuals shown in Figure 5. The residuals were normalized by removing the mean and dividing the difference by the standard deviation. Panels **(A–F)** show the histograms associated with the *xx*, *xy*, *xz*, *yy*, *yz* and *zz* components of the gravity-gradient tensor, respectively. **(G)** Shows the histogram of the residuals between the predicted and noise-corrupted gravity disturbances.

which can also be verified in the corresponding histograms shown in Figure 6.

In the Supplementary Material, we show the residuals between the gravity data predicted by the equivalent layer estimated by using the following methods: 1) the CGLS method (Algorithm 1); 2) the Cholesky factorization (Eqs. 25, 26); 3) the iterative method proposed by Siqueira et al. (2017) (Algorithm 6); 4) the direct deconvolution with optimal value of $\zeta = 10^{-22}$ (Eq. 69); and 5) the iterative method proposed by Cordell (1992) (Algorithm 4).

9 Applications to field data

In this section, we show the results obtained by applying the iterative deconvolution (Algorithm 7) to a field data set over the Carajás Mineral Province (CMP) in the Amazon craton (Moroni et al., 2001; Villas and Santos, 2001). This area (Figure 7) is known for its intensive mineral exploration such as iron, copper, gold, manganese, and, recently, bauxite.

9.1 Geological setting

The Amazon Craton is one of the largest and least-known Archean-Proterozoic areas in the world, comprehending a region with a thousand square kilometers. It is one of the main tectonic units in South America, which is covered by five Phanerozoic basins: Maranhão (Northeast), Amazon (Central), Xingu-Alto Tapajós (South), Parecis (Southwest), and Solimões (West). The Craton is limited by the Andean Orogenic Belt to the west and the by Araguaia Fold Belt to the east and southeast. The Amazon craton has been subdivided into provinces according to two models, one geochronological and the other geophysical-structural (Amaral, 1974; Teixeira et al., 1989; Tassinari and Macambira, 1999). Thus, seven geological provinces with distinctive ages, evolution, and structural patterns can be observed, namely,: 1) Carajás with two

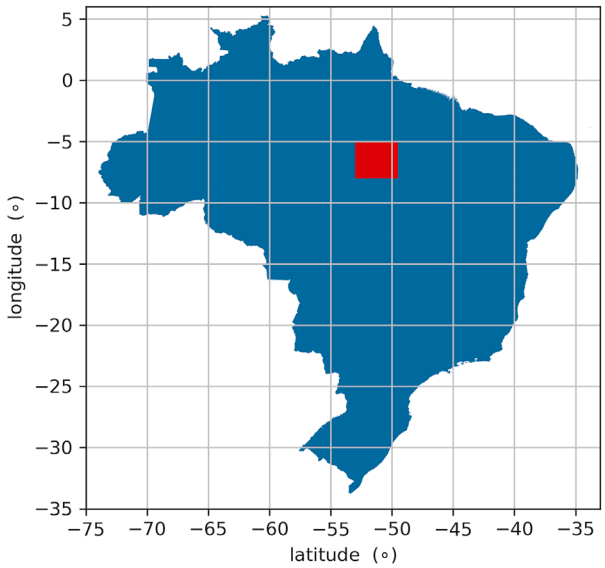

FIGURE 7
Location of the Carajás Mineral Province (CMP), Brazil. The coordinates are referred to the WGS-84 datum. The study area (shown in red) is located at the UTM zone 22S.

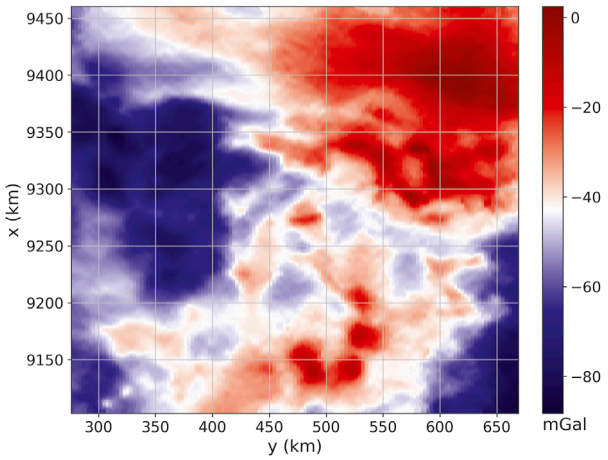

FIGURE 8
Field aerogravimetric data over Carajás, Brazil. There are $D = 500{,}000$ observations located on regular grid of $1{,}000 \times 500$ points.

domains - the Mesoarchean Rio Maria and Neoarchean Carajás; 2) Archean-Paleoproterozoic Central Amazon, with Iriri-Xingu and Curuá-Mapuera domains; 3) Trans-Amazonian (Ryacian), with the Amapá and Bacajá domains; 4) the Orosinian Tapajós-Parima, with Peixoto de Azevedo, Tapajós, Uaimiri, and Parima domains; 5) Rondônia-Juruena (Statherian), with Jamari, Juruena, and Jauru domains; 6) The Statherian Rio Negro, with Rio Negro and Imeri domains; and 7) Sunsás (Meso-Neoproterozoic), with Santa Helena and Nova Brasilândia domains (Santos et al., 2000). Nevertheless, we focus this work only on the Carajás Province.

The Carajás Mineral Province (CMP) is located in the east-southeast region of the craton (Figure 7), within an old tectonically stable nucleus in the South American Plate that became tectonically stable at the beginning of Neoproterozoic (Salomao et al., 2019). This area has been the target of intensive exploration at least since the final of the '60s, after the discovery of large iron ore deposits. There are several greenstone belts in the region, among them are the Andorinhas, Inajá, Cumaru, Carajás, Serra Leste, Serra Pelada, and Sapucaia (Santos et al., 2000). The mineralogic and petrologic studies in granite stocks show a variety of minerals found in the province, such as amphibole, plagioclase, biotite, ilmenite, and magnetite (Cunha et al., 2016).

9.2 Potential-field data

The field data used here were obtained from an airborne survey conducted by Lasa Prospecções S/A. and Microsurvey Aerogeofísica Consultoria Científica Ltda. between April/2013 and October/2014. The survey area covers ≈58000 km^2 between latitudes $-8°/-5°$ and longitudes $-53°/-49.5°$ referred to the WGS-84 datum. We obtained the horizontal coordinates x and y already in the UTM zone 22S. The flight and tie lines are spaced at 3 km and 12 km, with orientation along directions $N-S$ and $E-W$, respectively. The data are placed at an approximately constant distance of 900 m above the ground. Figure 8 shows the $D = 500{,}000$ aerogravimetric data on a grid of $1{,}000 \times 500$ observation points with $\Delta x = 358.12$ m and $\Delta y = 787.62$ m.

9.3 Potential-field transformation

We applied the equivalent-layer technique to the observed data (Figure 8) with the purpose of illustrating how to estimate the gravity-gradient tensor over the study area. We used an equivalent layer layout with one source located below each datum (so that $P = D$) on a horizontal plane having a vertical distance $\Delta z \approx 2362.86$ m from the observation plane. This setup is defined by setting $\Delta z \approx 3dy$, which follows the same strategy of Reis et al. (2020). We solve the linear inverse problem for estimating the physical-property distribution on the layer by using the iterative deconvolution (Algorithm 7) with a maximum number of 50 iterations. Actually, the algorithm have converged with only 18 iterations.

Figure 9G shows the histogram of the residuals between the predicted (not shown) and observed data (Figure 8). As we can see, the iterative deconvolution produced an excellent data fit. By using the estimated layer, we have computed the gravity-gradient tensor components at the observation points. The results are shown in Figure 9A–F.

Considering the processing time, the iterative deconvolution took ≈1.98 s to execute the 18 iterations for estimating the physical-property distribution on the layer by inverting the $D = 500{,}000$ observed data. The code was run in a modest computer with 16,0 GiB of memory and processor 12th Gen Intel® Core™ i9 − 12900H × 20. Given the estimated equivalent layer, the gravity-gradient components shown in

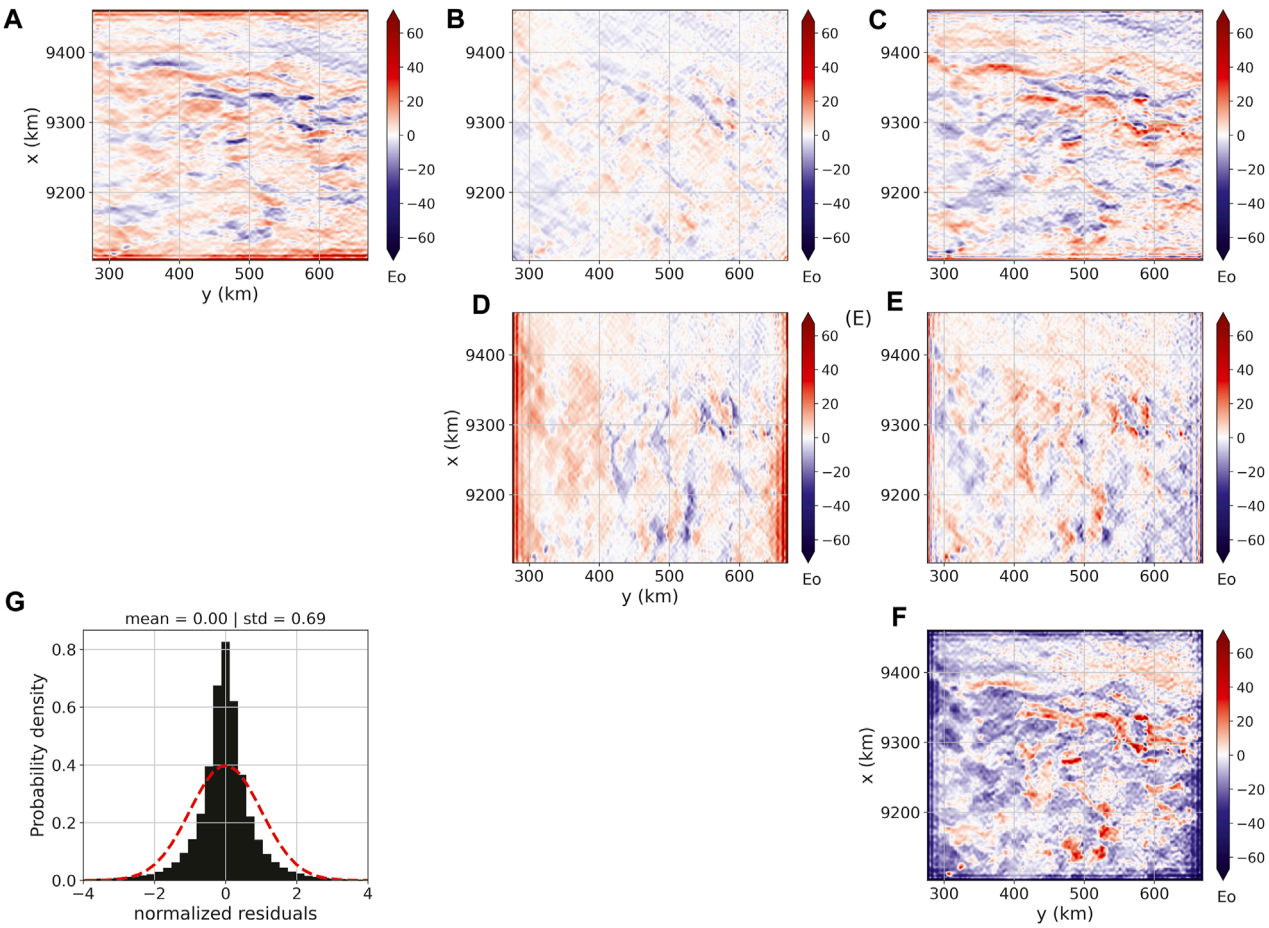

FIGURE 9
Estimated gravity-gradient tensor components over Carajás, Brazil. Panels **(A–F)** show, respectively, the *xx*, *xy*, *xz*, *yy*, *yz* and *zz* components of the gravity-gradient tensor in Eötvös. Panel **(G)** shows the histogram of the residuals between predicted data (not shown) and field data (Figure 8). The residuals were normalized by removing the mean and dividing the difference by the standard deviation. The results were generated by applying the iterative deconvolution (T0B20) (Algorithm 7) with 50 iterations.

Figure 9 were computed in ≈3.41 s. These results demonstrate the efficiency of the iterative deconvolution method in processing large datasets.

10 Discussion

The review discusses strategies utilized to reduce the computational cost of the equivalent-layer technique for processing potential-field data. These strategies are often combined in developed methods to efficiently handle large-scale data sets. Next, the computational strategies are addressed. All results shown here were generated with the Python package gravmag (https://doi.org/10.5281/zenodo.8284769). The datasets generated for this study can be found in the online repository: https://github.com/pinga-lab/eql ayer-review-computational.

The first one is the moving data-window scheme spanning the data set. This strategy solves several much smaller, regularized linear inverse problems instead of a single large one. Each linear inversion is solved using the potential-field observations and equivalent sources within a given moving window and can be applied to both regularly or irregularly spaced data sets. If the data and the sources are distributed on planar and regularly spaced grids, this strategy offers a significant advantage because the sensitivity submatrix of a given moving window remains the same for all windows. Otherwise, the computational efficiency of the equivalent-layer technique using the moving-window strategy decreases because the sensitivity submatrix for each window must be computed.

The second and third strategies, referred to as the column-action and row-action updates, involve iteratively calculating a single column and a single row of the sensitivity matrix, respectively. By following the column-action update strategy, a single column of the sensitivity matrix is calculated during each iteration. This implies that a single equivalent source contributes to the fitting of data in each iteration. Conversely, in the row-action update strategy, a single row of the sensitivity matrix is calculated per iteration, which means that one potential-field observation is incorporated in each iteration, forming a new subset of equivalent data much smaller than the original data. Both strategies (column- and row-action updates) have a great advantage because a single column or a single

TABLE 2 Computational strategies to overcome the intensive computational cost of the equivalent-layer technique for processing potential-field data and the corresponding articles.

Computational strategies	Characteristics	Advantages	Disadvantages	Articles
Moving data-window scheme	A single and small sensitivity submatrix for all moving windows	One of the fastest strategies	Regularly spaced grids of sources and data	Leão and Silva (1989)
Moving data-window scheme	Multiple and small sensitivity submatrices, one for each moving	Irregularly spaced grids of sources and data	Computational speed is reduced	Soler and Uieda (2021)
Column-action updates	A single equivalent source is used, iteratively	A single column of the sensitivity matrix is calculated	Issues related to convergence	Cordell (1992), Guspí and Novara (2009)
Row-action updates	Equivalent data concept	A subset of rows of the sensitivity matrix is calculated	Increasing the order of the linear system of equations, iteratively	Mendonça and Silva (1994)
Reparametrization of the original parameters	Reduction the dimension of the linear system of equations	Lower-dimensional linear system of equations	Undesirable smoothing effect	Oliveira Jr. et al. (2013), Mendonça (2020)
Sparsity induction of the sensitivity matrix	Sparse representation of the original dense sensitivity matrix	Fast iteration of the CG algorithm	Requires computing the full and dense sensitivity matrix	Li and Oldenburg (2010), Barnes and Lumley (2011)
Iterative methods using the full sensitivity matrix	The equivalent layer is updated, iteratively	Fast iterations	Requires computing the full and dense sensitivity matrix	Xia and Sprowl (1991), Xia et al. (1993), Siqueira et al. (2017), Jirigalatu and Ebbing (2019)
Iterative deconvolution	Block-Toeplitz Toeplitz-block (BTTB) matrices concept	One of the fastest strategies	Regularly spaced grids of sources and data	Takahashi et al. (2020), Takahashi et al. (2022)
Direct deconvolution	BTTB matrices concept	One of the fastest strategies	Solution instability	

row of the sensitivity matrix is calculated iteratively. However, to our knowledge, the strategy of the column-action update presents some issues related to convergence, and the strategy of the row-action update can also have issues if the number of equivalent data is not significantly smaller than the original number of data points.

The fourth strategy is the sparsity induction of the sensitivity matrix using wavelet compression, which involves transforming a full sensitivity matrix into a sparse one with only a few nonzero elements. The developed equivalent-layer methods using this strategy achieve sparsity by setting matrix elements to zero if their values are smaller than a predefined threshold. We highlight two methods that employ the sparsity induction strategy. The first method, known as wavelet-compression equivalent layer, compresses the coefficients of the original sensitivity matrix using discrete wavelet transform, achieves sparsity in the sensitivity matrix, and solves the inverse problem in the wavelet domain without an explicit regularization parameter. The regularized solution in the wavelet domain is estimated using a conjugate gradient (CG) least squares algorithm, where the number of iterations serves as a regularization factor. The second equivalent-layer method that uses the sparsity induction strategy applies quadtree discretization of the parameters over the equivalent layer, achieves sparsity in the sensitivity matrix, and solves the inverse problem using CG algorithm. In quadtree discretization, equivalent sources located far from the observation point are grouped together to form larger equivalent sources, reducing the number of parameters to be estimated. Computationally, the significant advantage of the equivalent-layer methods employing wavelet compression and quadtree discretization is the sparsity induction in the sensitivity matrix, which allows for fast iteration of the CG algorithm. However, we acknowledge that this strategy requires computing the full and dense sensitivity matrix, which can be considered a drawback when processing large-scale potential-field data.

The fifth strategy is the reparametrization of the original parameters to be estimated in the equivalent-layer technique. In this strategy, the developed equivalent-layer methods reduce the dimension of the linear system of equations to be solved by estimating a lower-dimensional parameter vector. We highlight two methods that used the reparametrization strategy: 1) the polynomial equivalent layer (PEL) and; 2) the lower-dimensional subspace of the equivalent layer. In the PEL, there is an explicit reparametrization of the equivalent layer by representing the unknown distribution over the equivalent layer as a set of piecewise-polynomial functions defined on a set of equivalent-source windows. The PEL method estimates the polynomial coefficients of all equivalent-source windows. Hence, PEL reduces the dimension of the linear system of equations to be solved because the polynomial coefficients within all equivalent-source windows are much smaller than both the number of equivalent sources and the number of data points. In the lower-dimensional subspace of the equivalent layer, there is an implicity reparametrization of the equivalent layer by reducing the linear system dimension from the original and large-model

space to a lower-dimensional subspace. The lower-dimensional subspace is grounded on eigenvectors of the matrix composed by the gridded data set. The main advantage of the reparametrization of the equivalent layer is to deal with lower-dimensional linear system of equations. However, we acknowledge that this strategy may impose an undesirable smoothing effect on both the estimated parameters over the equivalent layer and the predicted data.

The sixth strategy involves an iterative scheme in which the estimated distribution over the equivalent layer is updated iteratively. Following this strategy, the developed equivalent-layer methods differ either in terms of the expression used for the estimated parameter correction or the domain utilized (wavenumber or space domains). The iterative estimated correction may have a physical meaning, such as the excess mass constraint. All the iterative methods are efficient as they can handle irregularly spaced data on an undulating surface, and the updated corrections for the parameter vector at each iteration are straightforward, involving the addition of a quantity proportional to the data residual. However, they have a disadvantage because the iterative strategy requires computing the full and dense sensitivity matrix to compute the predicted and residual data in all observation stations per iteration.

The seventh strategy is called iterative deconvolutional of the equivalent layer. This strategy deals with regularly spaced grids of data stations and equivalent sources which are located at a constant height and depth, respectively. Specifically, one source is placed directly below each observation station, which results in sensitivity matrices with a BTTB (Block-Toeplitz Toeplitz-Block) structure. It is possible to embed the BTTB matrix into a matrix of Block-Circulant Circulant-Block (BCCB) structure, which requires only one equivalent source. This allows for fast matrix-vector product using a 2D fast Fourier transform (2D FFT). As a result, the potential-field forward modeling can be calculated using a 2D FFT with only one equivalent source required. The main advantages of this strategy are that the entire sensitivity matrices do not need to be formed or stored; only their first columns are required. Additionally, it allows for a highly efficient iteration of the CG algorithm. However, the iterative deconvolutional of the equivalent layer requires observations and equivalent sources aligned on a horizontal and regularly-spaced grid.

The eigth strategy is a direct deconvolution method, which is a mathematical process very common in geophysics. However, to our knowledge, direct deconvolution has never been used to solve the inverse problem associated with the equivalent-layer technique. From the mathematical expressions in the iterative deconvolutional equivalent layer with BTTB matrices, direct deconvolution arises naturally since it is an operation inverse to convolution. The main advantage of applying the direct deconvolution strategy in the equivalent layer is that it avoids, for example, the iterations of the CG algorithm. However, the direct deconvolution is known to be an unstable operation. To mitigate this instability, the Wiener deconvolution method can be adopted.

Table 2 presents a list of computational strategies used in the equivalent-layer technique to reduce the computational demand. The table aims to emphasize the important characteristics, advantages, and disadvantages of each computational strategy. Additionally, it highlights the available methods that use each strategy.

11 Conclusion

We have presented a comprehensive review of the strategies used to tackle the intensive computational cost associated with processing potential-field data using the equivalent-layer technique. Each of these strategies is rarely used individually; rather, some developed equivalent-layer methods combine more than one strategy to achieve computational efficiency when dealing with large-scale data sets. We focuses on the following specific strategies: 1) the moving data-window scheme; 2) the column-action and row-action updates; 3) the sparsity induction of the sensitivity matrix; 4) the reparametrization of the original parameters; 5) the iterative scheme using the full sensitivity matrix; 6) the iterative deconvolution; and 7) the direct deconvolution. Taking into account the mathematical bases used in the above-mentioned strategies, we have identified five groups: 1) the reduction of the dimensionality of the linear system of equations to be solved; 2) the generation of a sparse linear system of equations to be solved; 3) the explicit iterative method; 4) the improvement in forward modeling; and 5) the deconvolution using the concept of block-Toeplitz Toeplitz-block (BTTB) matrices.

We show in this review that the computational cost of the equivalent layer can vary from up to 10^9 flops depending on the method without compromising the linear system stability. The moving data-window scheme and direct deconvolution are the fastest methods; however, they both have drawbacks. To be computationally efficient, the moving data-window scheme and the direct deconvolution require data and equivalent sources that are distributed on planar and regularly spaced grids. Moreover, they both requires choosing an optimun parameter of stabilization. We stress that the direct deconvolution has an aditional disadvantage in terms of a higher data residual and border effects over the equivalent layer after processing. These effects can be seen from the upward continuation of the real data from Carajás.

We draw the readers' attention to the possibility of combining more than one aforementioned strategies for reducing the computational cost of the equivalent-layer technique.

Author contributions

VO and VB: Study conception and mathematical deductions. VO: Algorithms. VO and DT: Python codes and synthetic data applications. VO and AR: Real data applications. VO and VB: Result analysis and draft manuscript preparation.

Funding

VB was supported by fellowships from CNPq (grant 309624/2021-5) and FAPERJ (grant 26/202.582/2019). VO was supported by fellowships from CNPq (grant 315768/2020-7)

and FAPERJ (grant E-26/202.729/2018). DT was supported by a Post-doctoral scholarship from CNPq (grant 300809/2022-0).

Acknowledgments

We thank the brazillian federal agencies CAPES, CNPq, state agency FAPERJ and Observatório Nacional research institute and Universidade do Estado do Rio de Janeiro.

Conflict of interest

The authors declare that the research was conducted in the absence of any commercial or financial relationships that could be construed as a potential conflict of interest.

Publisher's note

Supplementary material

The Supplementary Material for this article can be found online at: https://www.frontiersin.org/articles/10.3389/feart.2023.1253148/full#supplementary-material

References

Amaral, G. (1974). *Geologia Pré-Cambriana da Região Amazônica*. Ph.D. thesis, Universidade de ãão Paulo.

Aster, R. C., Borchers, B., and Thurber, C. H. (2019). *Parameter estimation and inverse problems*. 3 edn. Elsevier.

Barbosa, V. C. F., Silva, J. B., and Medeiros, W. E. (1997). Gravity inversion of basement relief using approximate equality constraints on depths. *Geophysics* 62, 1745–1757. doi:10.1190/1.1444275

Barnes, G., and Lumley, J. (2011). Processing gravity gradient data. *GEOPHYSICS* 76, I33–I47. doi:10.1190/1.3548548

Blakely, R. J. (1996). *Potential theory in gravity and magnetic applications*. Cambridge University press.

Bott, M. H. P. (1960). The use of rapid digital computing methods for direct gravity interpretation of sedimentary basins. *Geophys. J. Int.* 3, 63–67. doi:10.1111/j.1365-246X.1960.tb00065.x

Chan, R. H.-F., and Jin, X.-Q. (2007). *An introduction to iterative Toeplitz solvers*, 5. SIAM.

Cordell, L. (1992). A scattered equivalent-source method for interpolation and gridding of potential-field data in three dimensions. *Geophysics* 57, 629–636. doi:10.1190/1.1443275

Cunha, I. R., Dall'Agnol, R., and Feio, G. R. L. (2016). Mineral chemistry and magnetic petrology of the archean Planalto Suite, Carajás Province – amazonian Craton: implications for the evolution of ferroan archean granites. *J. S. Am. Earth Sci.* 67, 100–121. doi:10.1016/j.jsames.2016.01.007

Dampney, C. N. G. (1969). The equivalent source technique. *GEOPHYSICS* 34, 39–53. doi:10.1190/1.1439996

Davis, P. J. (1979). *Circulant matrices*. John Wiley & Sons, Inc.

Elfving, T., Hansen, P. C., and Nikazad, T. (2017). Convergence analysis for column-action methods in image reconstruction. *Numer. Algorithms* 74, 905–924. doi:10.1007/s11075-016-0176-x

Emilia, D. A. (1973). Equivalent sources used as an analytic base for processing total magnetic field profiles. *GEOPHYSICS* 38, 339–348. doi:10.1190/1.1440344

Golub, G. H., and Van Loan, C. F. (2013). *Johns hopkins studies in the mathematical sciences*. 4 edn. Johns Hopkins University Press.Matrix computations.

Gonzalez, R. C., and Woods, R. E. (2002). *Digital image processing*. 2 edn. Prentice Hall.

Gonzalez, S. P., Barbosa, V. C. F., and Oliveira, V. C., Jr. (2022). Analyzing the ambiguity of the remanent-magnetization direction separated into induced and remanent magnetic sources. *J. Geophys. Res. Solid Earth* 127, 1–24. doi:10.1029/2022JB024151

Guspí, F., Introcaso, A., and Introcaso, B. (2004). Gravity-enhanced representation of measured geoid undulations using equivalent sources. *Geophys. J. Int.* 159, 1–8. doi:10.1111/j.1365-246X.2004.02364.x

Guspí, F., and Novara, I. (2009). Reduction to the pole and transformations of scattered magnetic data using Newtonian equivalent sources. *GEOPHYSICS* 74, L67–L73. doi:10.1190/1.3170690

Hansen, P. C. (1992). Analysis of discrete ill-posed problems by means of the l-curve. *SIAM Rev.* 34, 561–580. doi:10.1137/1034115

Hansen, R. O., and Miyazaki, Y. (1984). Continuation of potential fields between arbitrary surfaces. *GEOPHYSICS* 49, 787–795. doi:10.1190/1.1441707

Horn, R. A., and Johnson, C. R. (1991). *Topics in matrix analysis*. 1 edn. Cambridge University Press.

Jain, A. K. (1989). *Fundamentals of digital image processing*. 1 edn. Pearson.

Jirigalatu, J., and Ebbing (2019). A fast equivalent source method for airborne gravity gradient data. *Geophysics* 84, G75–G82. doi:10.1190/GEO2018-0366.1

Kellogg, O. D. (1967). *Foundations of potential theory*. Springer-Verlag. reprint from the first edition of 1929 edn.

Kennett, B., Sambridge, M., and Williamson, P. (1988). Subspace methods for large inverse problems with multiple parameter classes. *Geophys. J. Int.* 94, 237–247. doi:10.1111/j.1365-246X.1988.tb05898.x

Leão, J. W. D., and Silva, J. B. C. (1989). Discrete linear transformations of potential field data. *Geophysics* 54, 497–507. doi:10.1190/1.1442676

Li, Y., Nabighian, M., and Oldenburg, D. W. (2014). Using an equivalent source with positivity for low-latitude reduction to the pole without striation. *GEOPHYSICS* 79, J81–J90. doi:10.1190/geo2014-0134.1

Li, Y., and Oldenburg, D. W. (2010). Rapid construction of equivalent sources using wavelets. *GEOPHYSICS* 75, L51–L59. doi:10.1190/1.3378764

Mendonça, C. A., and Silva, J. B. C. (1994). The equivalent data concept applied to the interpolation of potential field data. *Geophysics* 59, 722–732. doi:10.1190/1.1443630

Mendonça, C. A. (2020). Subspace method for solving large-scale equivalent layer and density mapping problems. *GEOPHYSICS* 85, G57–G68. doi:10.1190/geo2019-0302.1

Menke, W. (2018). *Geophysical data analysis: Discrete inverse theory*. 4 edn. Elsevier.

Moroni, M., Girardi, V., and Ferrario, A. (2001). The Serra Pelada Au-pge deposit, Serra dos Carajás (pará state, Brazil): geological and geochemical indications for a composite mineralising process. *Miner. Deposita* 36, 768–785. doi:10.1007/s001260100201

Oldenburg, D., McGillivray, P., and Ellis, R. (1993). Generalized subspace methods for large-scale inverse problems. *Geophys. J. Int.* 114, 12–20. doi:10.1111/j.1365-246X.1993.tb01462.x

Oliveira, V. C., Jr., Barbosa, V. C. F., and Uieda, L. (2013). Polynomial equivalent layer. *GEOPHYSICS* 78, G1–G13. doi:10.1190/geo2012-0196.1

Press, W. H., Teukolsky, S. A., Vetterling, W. T., and Flannery, B. P. (2007). *Numerical recipes: The art of scientific computing*. 3 edn. Cambridge University Press.

Reis, A. L. A., Oliveira, V. C., Jr., and Barbosa, V. C. F. (2020). Generalized positivity constraint on magnetic equivalent layers. *Geophysics* 85, 1–45. doi:10.1190/geo2019-0706.1

Roy, A. (1962). Ambiguity in geophysical interpretation. *GEOPHYSICS* 27, 90–99. doi:10.1190/1.1438985

Salomao, G. N., Dall'Agnol, R., Angelica, R. S., Figueiredo, M. A., Sahoo, P. K., Medeiros-Filho, C. A., et al. (2019). Geochemical mapping and estimation of background concentrations in soils of Carajás mineral province, eastern Amazonian Craton, Brazil. *Geochem. Explor. Environ. Anal.* 19, 431–447. doi:10.1144/geochem2018-066

Santos, J. O. S., Hartmann, L. A., Gaudette, H. E., Groves, D. I., Mcnaughton, M. J., and Fletcher, I. R. (2000). A new understanding of the provinces of the Amazon Craton based on integration of field mapping and U-Pb and Sm-Nd geochronology. *Gondwana Res.* 3, 453–488. doi:10.1016/S1342-937X(05)70755-3

Silva, J. B. C. (1986). Reduction to the pole as an inverse problem and its application to low-latitude anomalies. *GEOPHYSICS* 51, 369–382. doi:10.1190/1.1442096

Siqueira, F., Oliveira, V. C., Jr., and Barbosa, V. C. F. (2017). Fast iterative equivalent-layer technique for gravity data processing: A method grounded on excess mass constraint. *GEOPHYSICS* 82, G57–G69. doi:10.1190/GEO2016-0332.1

Skilling, J., and Bryan, R. (1984). Maximum entropy image reconstruction-general algorithm. *Mon. Notices R. Astronomical Soc.* 211(1), 111. doi:10.1093/mnras/211.1.111

Soler, S. R., and Uieda, L. (2021). Gradient-boosted equivalent sources. *Geophys. J. Int.* 227, 1768–1783. doi:10.1093/gji/ggab297

Takahashi, D., Oliveira, V. C., Jr., and Barbosa, V. C. (2022). Convolutional equivalent layer for magnetic data processing. *Geophysics* 87, 1–59. doi:10.1190/geo2021-0599.1

Takahashi, D., Oliveira, V. C., Jr., and Barbosa, V. C. F. (2020). Convolutional equivalent layer for gravity data processing. *GEOPHYSICS* 85, G129–G141. doi:10.1190/geo2019-0826.1

Tassinari, C. C., and Macambira, M. J. (1999). Geochronological provinces of the amazonian craton. *Episodes* 22, 174–182. doi:10.18814/epiiugs/1999/v22i3/004

Teixeira, W., Tassinari, C., Cordani, U. G., and Kawashita, K. (1989). A review of the geochronology of the Amazonian Craton: tectonic implications. *Precambrian Res.* 42, 213–227. doi:10.1016/0301-9268(89)90012-0

van der Sluis, A., and van der Vorst, H. A. (1987). "Numerical solution of large, sparse linear algebraic systems arising from tomographic problems," in *Seismic tomography with applications in global seismology and exploration geophysics*. Editor G. Nolet (D. Reidel Publishing Company). chap. 3. 49–83.

Van Loan, C. F. (1992). Computational frameworks for the fast fourier transform. *Front. Appl. Math. (SIAM)*. doi:10.1137/1.9781611970999

Villas, R. N., and Santos, M. (2001). Gold deposits of the Carajás mineral province: deposit types and metallogenesis. *Miner. Deposita* 36, 300–331. doi:10.1007/s001260100178

Xia, J., Sprowl, D. R., and Adkins-Heljeson, D. (1993). Correction of topographic distortions in potential-field data; a fast and accurate approach. *Geophysics* 58, 515–523. doi:10.1190/1.1443434

Xia, J., and Sprowl, D. R. (1991). Correction of topographic distortion in gravity data. *Geophysics* 56, 537–541. doi:10.1190/1.1443070

Zhao, G., Chen, B., Chen, L., Liu, J., and Ren, Z. (2018). High-accuracy 3D Fourier forward modeling of gravity field based on the Gauss-FFT technique. *J. Appl. Geophys.* 150, 294–303. doi:10.1016/j.jappgeo.2018.01.002

Zidarov, D. (1965). Solution of some inverse problems of applied geophysics. *Geophys. Prospect.* 13, 240–246. doi:10.1111/j.1365-2478.1965.tb01932.x

Frontiers in Earth Science

Investigates the processes operating within the major spheres of our planet

Advances our understanding across the earth sciences, providing a theoretical background for better use of our planet's resources and equipping us to face major environmental challenges.

Discover the latest Research Topics

See more →

Frontiers

Avenue du Tribunal-Fédéral 34
1005 Lausanne, Switzerland
frontiersin.org

Contact us

+41 (0)21 510 17 00
frontiersin.org/about/contact